Lecture Notes in Civil Engineering

Subashisa Dutta
Vinay Chembolu *Editors*

Recent Development in River Corridor Management

Select Proceedings of RCRM 2022

Springer

Lecture Notes in Civil Engineering

Volume 376

Lecture Notes in Civil Engineering (LNCE) publishes the latest developments in Civil Engineering—quickly, informally and in top quality. Though original research reported in proceedings and post-proceedings represents the core of LNCE, edited volumes of exceptionally high quality and interest may also be considered for publication. Volumes published in LNCE embrace all aspects and subfields of, as well as new challenges in, Civil Engineering. Topics in the series include:

- Construction and Structural Mechanics
- Building Materials
- Concrete, Steel and Timber Structures
- Geotechnical Engineering
- Earthquake Engineering
- Coastal Engineering
- Ocean and Offshore Engineering; Ships and Floating Structures
- Hydraulics, Hydrology and Water Resources Engineering
- Environmental Engineering and Sustainability
- Structural Health and Monitoring
- Surveying and Geographical Information Systems
- Indoor Environments
- Transportation and Traffic
- Risk Analysis
- Safety and Security

To submit a proposal or request further information, please contact the appropriate Springer Editor:

– Pierpaolo Riva at pierpaolo.riva@springer.com (Europe and Americas);
– Swati Meherishi at swati.meherishi@springer.com (Asia—except China, Australia, and New Zealand);
– Wayne Hu at wayne.hu@springer.com (China).

All books in the series now indexed by Scopus and EI Compendex database!

Subashisa Dutta · Vinay Chembolu
Editors

Recent Development in River Corridor Management

Select Proceedings of RCRM 2022

Springer

Editors
Subashisa Dutta
Department of Civil Engineering
Indian Institute of Technology Guwahati
Guwahati, Assam, India

Vinay Chembolu
Department of Civil Engineering
Indian Institute of Technology Jammu
Jammu, India

ISSN 2366-2557 ISSN 2366-2565 (electronic)
Lecture Notes in Civil Engineering
ISBN 978-981-99-4422-4 ISBN 978-981-99-4423-1 (eBook)
https://doi.org/10.1007/978-981-99-4423-1

This Springer imprint is published by the registered company Springer Nature Singapore Pte Ltd.
The registered company address is: 152 Beach Road, #21-01/04 Gateway East, Singapore 189721, Singapore

Preface

The escalating human activities, control efforts over river flow, and disturbances to river systems in recent years have necessitated sustainable protection and careful management of river corridors. These actions can disrupt the natural water-ecological balance within these systems. Furthermore, activities within the river corridor, such as inland transport, damming, generating hydroelectric power, intervening in river dynamics, and tourism, need to be conducted while minimizing environmental effects. It's crucial to gain a comprehensive understanding of these issues to effectively develop guidelines for river corridor development. To address these concerns, an international conference focused on River Corridor Research and Management was held from May 30 to June 1, 2022. The conference aimed to identify the specific problems, discuss the challenges, and outline future directions for managing river corridors.

Recent Development in River Corridor Management is a compiled volume of selected research papers from the 2nd International Conference on River Corridor Research and Management (RCRM 2022), focusing on fluvial-hydro-ecological processes of riverine systems. The book, structured into five distinct sections, encompasses 26 chapters. Part I, "River Corridor Issues and Challenges," addresses concerns like flooding in dynamic braided river systems, dam and barrage impacts, and responses to tectonic and glacial activities. Part II explores numerical and physical modeling techniques to understand flow-vegetation interactions, the turbulence in sinuous channels, and the effect of simulated macro-microporosity on soil infiltration. River ecology, including topics such as river recovery, ecological biodiversity in river corridors, and the impact of human activities on water quality, is the focus of Part III. Part IV delves into the effects of climate change on floods, streamflow extremes, and land use and landcover changes. The final section, Part V, investigates upland catchment management, including aspects like watershed-scale soil moisture dynamics, applications of satellite remote sensing, soil erosion, and crop irrigation water requirements.

We extend our gratitude towards IIT Guwahati and IIT Jammu for their administrative support and cooperation. We also wish to acknowledge the contributions of our keynote speakers, who shared insights in their areas of expertise through

plenary lectures and technical interactions. Our appreciation further extends to Dr. Chandan Pradhan and Mr. Mridupawan Deka in reviewing processes and minor editing of all the chapters. Contribution of research scholars working in Geoinformatics laboratory IIT Guwahati in meticulous organization of the conference is sincerely acknowledged. Lastly, we are grateful for the financial support received from the National Mission on Himalayan Studies (NMHS) project, which was instrumental in facilitating this conference.

We anticipate that this book will serve as a significant resource for academicians, practitioners, and emerging researchers, providing a valuable addition to the current literature on river processes and river sciences.

Guwahati, India — Subashisa Dutta
Jagti, India — Vinay Chembolu

Contents

About the Editors

Prof. Subashisa Dutta is working at Department of Civil Engineering, Indian Institute of Technology Guwahati. He is currently working as a professor of Civil Engineering and a professor-in-charge of Space Technology Cell, IIT Guwahati. He was a visiting fellow in Technical University of Munich, Germany, and Kyoto University in Japan and visited several other countries for research and academic collaborations. His research interests include fluvial hydraulics, hydro-informatics and advanced remote sensing for water resources applications, hill slope hydrology, urban hydrology and climatic change. He was a member in water resources thematic group in Ganga River Basin Environment Management Plan, the Brahmaputra Board and several other academic and research organizations. He has published more than 100 research articles in reputed water resources journals and conferences. He has been the associate editor of Journal of Hydrology and Hydrological Sciences Journal and an active reviewer for many reputed journals. He was awarded prestigious S. N. Gupta memorial, R. J. Garde Research Award, DAAD fellowship and many others for his wide contribution in the Water Resources Engineering in India. He has supervised 12 Ph.D. research thesis (and other in progress) in different areas of hydrological sciences and in advanced satellite remote sensing.

Dr. Vinay Chembolu is currently working as an assistant professor in Civil Engineering Department at Indian Institute of Technology Jammu. He obtained his B.Tech. (Civil) from UCEK-JNTU Kakinada and M.Tech. and Ph.D. in Water Resources Engineering from Indian Institute of Technology Guwahati. His major research interests include River Engineering, River Dynamics, Experimental and Field Hydraulics, Environmental Fluid Mechanics and Satellite Remote Sensing for River Management Studies. He has published his research work in reputed international journals. He also got varied experience of working with research and consultancy projects for river training, development of waterways, dam break analysis, flood inundation modeling and environmental flows, all those pertaining to Indian Rivers. He has been actively involved in conducting hydrographic surveys in

challenging rivers like the Brahmaputra, Kosi, Brahmani and Himalayan Rivers using advanced river surveying equipment. He is a member of British Society of Geomorphology, International Association of Sedimentologists and Association of Sciences of Liminology and Oceanography.

River Corridor: Issues and Challenges

Influence of Lateral Connectivity on Channel Characteristics in (Post)Glacial Landscapes

Marwan A. Hassan, Mike Turley, David A. Reid, Stephen Bird, and Porter Abbey

Abstract Postglacial mountainous regions are characterized by wide valleys with steep walls, over-deepened valley segments linked with abrupt topographic steps, and thick sediment deposits on valley floors which grow and decay as the paraglacial period progresses. In many formerly glaciated regions, despite over ten thousand years of modification by non-glacial processes, the landscape characteristics and process behaviors are still dominantly controlled by the glacial legacy. In this paper we examine the pace and style of landscape evolution in paraglacial mountainous settings in comparison to fluvially-dominated systems. In particular, the paper will explore how variable valley geometries control lateral connectivity and influence sediment sources, sediment delivery to the channel network, and the geometry and morphology of contemporary channels in previously glaciated mountainous basins.

Keywords Channel morphology · Flooding · Glaciation · Landscape history · Sediment supply · Coupling · Connectivity · Sediment connectivity

1 Introduction

Mountain drainage basins are dynamic, complex systems shaped by a variety of active geomorphic and hydrologic processes, their interactions, and climatic and tectonic history. The spatial variability of channel reach morphology and geometry influences aquatic ecosystems and is, in turn, affected by the geomorphic processes that are directly connected to the channel network. Understanding the processes

The original version of this chapter was revised: The spelling of the last author's name has been corrected. The correction to this chapter is available at https://doi.org/10.1007/978-981-99-4423-1_27

M. A. Hassan (✉) · M. Turley · D. A. Reid · P. Abbey
Department of Geography, The University of British Columbia, Vancouver, BC V6T 1Z2, Canada
e-mail: marwan.hassan@geog.ubc.ca

S. Bird
Fluvial Systems Research Inc., 130-1959 152 Street, No. 501, Surrey, BC, Canada

S. Dutta and V. Chembolu (eds.), *Recent Development in River Corridor Management*, Lecture Notes in Civil Engineering 376, https://doi.org/10.1007/978-981-99-4423-1_1

driving both landscape evolution and in-channel morphology conditions requires a knowledge of the spatial pattern and linkages between channel morphology and processes that shape the drainage basins. The shape and dimensions of stream channels are formed not only by water flowing from upstream and from hillslopes, but also by the sediment flux from upstream, adjacent hillslopes, and streambanks. This is especially the case for small, headwater streams in mountainous terrain that are directly coupled to adjacent hillslopes through active mass movement processes which transfer substantial amounts of sediment to low-relief areas, valleys, and the channel network [40, 54]. The location and volume of sediment inputs to the channel and landscape heterogeneity affect the spatial variability of channel morphology, channel geometry, and the texture of the bed [11, 12, 36, 46, 48, 49, 52]. Additionally, lag material within the channel from nonfluvial sources (e.g., mass movement, glacial processes) can control channel stability and the geomorphic effectiveness of floods [18, 34]. In contrast to small, coupled stream systems, most watersheds tend to be fragmented [29] with only a small portion of the watershed supplying sediment to the channel (e.g., [30, 39]).

In mountainous regions with a history of intense glaciation, such as British Columbia (e.g., [11, 12], landscapes have generally been sculpted by glacial erosion and deposition, which has resulted in the formation of glacial cirques and U-shaped valleys, as well as widespread accumulation of glacial deposits [8, 33, 45]. Glacial erosion conditions subsequent fluvial geomorphic change, and alters the spatial organization and relative importance of geomorphic processes. In these settings, slope-area relationships reveal a generalized process-form disequilibrium, with a mismatch between topographic signatures and currently active geomorphic process domains (e.g., [11]). Glacial processes have redistributed sediment over large areas, often leading to thick deposits of erodible material through which rivers flow. This sediment can make its way into high-order lowland streams as a result of both colluvial and fluvial processes [19, 21]. Based on suspended sediment data collected from basins in British Columbia, [21] reported a positive relation between specific sediment yield and drainage area for basins up to 30,000 km^2 as a result of reworking glacial sediments. Building on this finding, [59] developed a postglacial sediment budget for the Chilliwack River Valley (British Columbia) and showed that specific sediment yields are lowest in small basins (<10 km^2) implying sediment deposition, while sediment yields in basins > 10 km^2 increase through the remobilization of glacial and glaciofluvial valley fills [13, 21]. In modeling the postglacial adjustment of an idealized glacial trough, [25] show a rapid adjustment of hillslope processes, but a comparatively slow adjustment of the fluvial system in the range of 5,000–10,000 years. While glacial sediment deposits may stabilize through time, terraces composed of glacial material have recently been identified as a major sediment source to lowland streams [55]. These terraces, however, also act as buffers that prevent hillslope sediment from reaching the channel network [29], adding complexity to the spatial patterns of landscape connectivity [5]. In summary, contemporary non-glacial processes operating on relict glacial topography results in unique and poorly understood sediment transfer dynamics, network configurations, and patterns of landscape connectivity, each changing over time.

The legacy of past glacial episodes has resulted in disconnectivity between sediment sources on hillslopes and river networks, leading to unique watershed configurations at a range of spatial scales [19, 21, 56]. This disconnectivity limits our capacity to predict river response to disturbance [28] and has implications for geohazard mitigation [42, 50] and aquatic habitat function [10]. Sediment connectivity/disconnectivity depends on the spatial organization of hillslope-channel coupling which dictates sediment inputs to the channel and hence channel morphology (e.g., [36, 51]). Coupling is the transmission of matter and energy between two components of the landscape and in this paper refers to the transfer of sediment between hillslopes and channels unless otherwise specified. Similarly, connectivity is defined as the efficient transfer of matter and energy within and between component parts of the landscape and applies at all scales.

In the last three decades, researchers have predominantly focused on landscape adjustment to accelerated hillslope processes and reworking of glacial sediment deposited along valleys [6, 7, 21, 60]. An overlooked aspect of glacial erosion is the effect of valley characteristics (e.g., width, depth, topography) on the postglacial sediment flux [14]. Glacial valleys tend to have discontinuous geometries, such as alternating flat and stepped long profiles, and wide valley floors, which reduces the sediment transport capacity of contemporary streams and increases the storage of hillslope sediments in the valley bottom. The increased disconnectivity in previously glaciated landscapes reduces the volume of sediment exported from the landscape on a watershed scale by current erosional processes [61, 62].

Knowledge of the spatial extent of landscape-shaping geomorphic processes is critical for the prediction of the spatial organization of hillslope and channel characteristics, degree of coupling between hillslopes and channels, and ultimately the efficiency of sediment transfer within the landscape (i.e., connectivity) which, in turn, has direct implications for channel morphology and ecology. Also, such research is important to understand the response of a landscape to changes in climate and land use. While research in paraglacial landscapes has advanced significantly (e.g., [6, 7, 44]), there is a need to explore watershed-scale sediment dynamics in mountain regions with a complex landscape history [61].

This paper aims to integrate recent research to illustrate the diverse consequences of past and contemporary glaciation on disconnectivity and associated channel characteristics. We aim to describe how landscape organization by glacial erosion, transport, and deposition determines the location and the amount of sediment inputs to channels and their associated channel morphology. The specific objectives are to: (1) develop a conceptual model to describe sediment (dis)connectivity in a variety of glaciated watersheds, (2) identify controls on sediment supply, in the form of buffers of sediment input from hillslopes to channels, and barriers that reduce downstream transport, and (3) provide case studies to demonstrate how disconnectivity influences channel characteristics. Three case studies were selected to demonstrate different aspects of our conceptual model. These case studies from the Pacific Northwest of North America represent widely varying, although not exhaustive, examples of mountainous glacial landscapes encompassing both erosional and depositional

glacial features, semi-arid to temperate rainforest biomes, and low-gradient plateau to high-gradient glaciated stratovolcano topography.

2 Conceptual Model

Here we describe a conceptual model for comparing spatial trends in sediment connectivity, and their impacts on channel characteristics, in mountainous unglaciated basins with those in mountainous deglaciated basins (Fig. 1). Specifically, this model integrates components from a model proposed by [36] that looks at landsliding within a connectivity framework and a model by [51] that does the same for channel widening to provide a more holistic description of (dis)connectivity in glacial landscapes. Like these existing models, we consider glacial and paraglacial landforms to be primary controls on sediment connectivity through the intermediaries of valley width and channel confinement. Our model similarly emphasizes the high spatial heterogeneity of connectivity trends in (de)glaciated mountain landscapes. Our conceptualization departs from the previously mentioned models by (1) including three types of postglacial landscapes and (2) by incorporating barriers and buffers to sediment transfer (in the sense of Fryirs et al. [29]) to provide a more nuanced understanding of controls on sediment connectivity. Our intention in proposing this conceptual model is to synthesize general observations from the diverse case studies we present.

In unglaciated headwater basins (Fig. 1a) we expect to see relatively continuous downstream trends including steadily decreasing slope (creating a smooth, concave-up long profile), increasing valley width, and bed material coarsening up until an inflection point after which a gentle fining trend occurs [15]. Lateral connectivity decreases downstream as valley width increases.

In small, high-relief (post)glacial basins carved primarily by a single ice flow (Fig. 1b), the downstream trends in slope, valley width, bed material, and coupling may be similar to unglaciated headwater basins (Fig. 1a). Glacial landforms increase landscape heterogeneity and may lead to unique spatial patterns of disconnectivity. Additionally, sediment availability and yield are likely still elevated above rates in comparable unglaciated basins [19, 21].

In formerly glaciated basins with high-relief topography (Fig. 1c), the mainstem channel's long profile may be complex and stepped, a characteristic imposed by glacial macroforms such as cirques and hanging valleys. Moving down the long profile, lateral connectivity oscillates between coupled and uncoupled states according to valley width. Where the gradient is steep and the valley bottom is narrow, hillslopes are coupled with the channel. As the slope decreases (e.g., in a hanging valley) the valley widens, and lateral connectivity decreases.

In formerly glaciated basins with subdued topography due to overtopping glaciers (Fig. 1d), long profiles may also be stepped, with lateral connectivity oscillating in a similar manner to the previous scenario. However, the low-relief topography in these

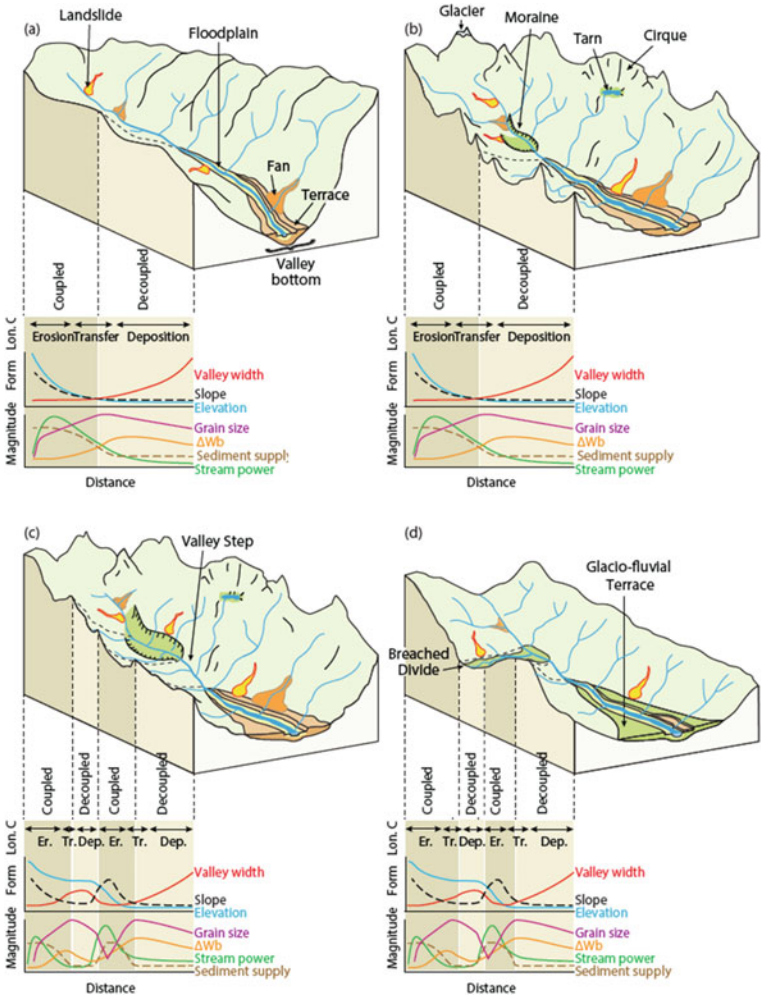

basins—particularly the wide valleys and rounded drainage divides—has less gravitational potential energy for sediment transport processes than high-relief, formerly glaciated basins. This manifests as a distinct scarcity of paraglacial depositional landforms, which could act as barriers or buffers. In this scenario, spatial patterns of lateral connectivity are primarily determined by valley geometry, with a prevailing state of hillslope-channel decoupling. Any lateral connectivity may take the form of fluvial erosion of glaciofluvial terraces.

◀**Fig. 1** Conceptual model of lateral connectivity and channel characteristics in mountainous post-glacial basins. (a) Unglaciated basin for comparison. This scenario features lateral connectivity which decreases in the downstream direction, relatively continuous downstream trends, and may include non-glacial barriers and buffers including fans, alluvial terraces, and floodplains. (b) Small, high-relief (post)glacial basin carved primarily by a single ice flow. Like panel (a), lateral connectivity tends to decrease downstream but with added complexity due to paraglacial disconnectivity features (see Table 1) including wide, U-shaped valleys, cirques and associated tarns, and lateral moraines. (c) Large, high-relief glacial basin with valley step. Lateral connectivity oscillates downstream according to glacially imposed valley width. Each valley step effectively "resets" the downstream trend of decreasing lateral connectivity [11] with corresponding grain size trends resetting in tandem. As described in [51], stream power and sediment availability change downstream as dictated by valley width and channel gradient. (Para)glacial features may act as buffers, inhibiting lateral sediment input to channels, or barriers, inhibiting downstream transmission of sediment. (d) Formerly glaciated basin with subdued topography due to breached divides. Hillslope-channel decoupling prevails due to glacially imposed low-gradient valley geometry but there may be fluvially-initiated lateral connectivity in the form of glaciofluvial terrace erosion. Lateral drainage divide breaching may locally reduce connectivity by forming low-gradient valley walls and may cause discontinuous channel bed grain size trends (e.g., [52]). Figure modified from [36, 51]

3 Small, High-Relief (Post)Glacial Basins—Tahoma Creek

The Tahoma Creek watershed inspires panel (b) of Fig. 1, which is a conceptual model of connectivity in small, high-relief (post)glacial watersheds. However, this site also has breached divides as shown in panel (d) and discussed in more detail in this section. In the following paragraphs we discuss the glacial history of Tahoma Creek, the resulting glacial landforms and valley geometry characteristics that cause disconnectivity, and the spatial patterns of connectivity and hillslope-channel coupling. Turley et al. [61] leveraged a suite of semi-quantitative connectivity indices to provide a more holistic estimation of connectivity within the basin. The reader is referred to the original paper for more details on the methodologies, while a summary of the results is presented here.

The Tahoma Creek watershed is approximately 40 km^2 and is located on the southwest flank of təqʷuʔmaʔ (Mt. Rainier) in the Cascade Range of Washington, USA, in the territory of the dxʷsqʷaliʔ abš (Nisqually) and spuyaləpabš (Puyallup) tribes (Fig. 2). The watershed is the product of volcanic activity [26], edifice collapse [56], and repeated glaciations [24]. The resulting landscape is topographically complex and characterized by a mix of low-gradient ridges, high-relief valley walls with local relief exceeding 1000 m, cirque basins, large valley margin paraglacial sediment storage reservoirs, and a wide and flat valley floor.

Although much of the Tahoma Creek watershed is ice-free today, the landscape preserves a record of past glaciations of much greater extent. At many times throughout the Pleistocene, much of the watershed was covered in a thick ice cap, and the main ice flow extended beyond the modern watershed boundary [24]. In fact, as late as ~80–40 ka and corresponding to the Salmon Springs Glaciation, the ice cap over Rainier extended as far west as Mount Wow overtopping Mount Ararat and leaving Tumtum Peak as a nunatak [24], (Fig. 2). Remnant glacial features on the

Table 1 Description and characteristics of selected glacial sources of disconnectivity

Feature	Type	Scale	Description/comments
Wide/flat, U-shaped valleys	Buffers/barriers	Macro	Glacially carved valleys tend to be wide and U-shaped with relatively flat valley bottoms. Wide/flat valley floors promote deposition over transport, increasing disconnectivity
Cirques/glacial overdeepenings	Buffers/barriers	Macro	Cirques form when glacial ice carves a concave amphitheater-shaped headwall, leading to convergent ice flow and rapid subglacial erosion producing an overdeepening at the base of the headwall. Overdeepenings also occur downvalley as a result of ice flow dynamics. As the ice retreats, water often fills these depressions (see tarns/lakes below). Reverse slope at base of cirque promotes disconnectivity
Hanging valleys/ valley steps	Buffers/barriers	Macro	Hanging valleys are U-shaped tributary valleys perched above the main valley due to reduced subglacial erosion in the tributary. Valley steps along the main valley may also occur at ice stream confluences as a result of increased basal erosion or due to lithological changes. Valley steps "reset" and disrupt trends in downvalley (de)coupling and channel characteristics
Valley constrictions	Barriers	Macro	Valley constrictions, or abrupt reductions in valley width, may occur as a result of ice flow dynamics, lateral moraines, etc. Constrictions prevent the river from migrating laterally and can cause backwater areas and aggradation upstream as a result of the bottleneck effect
Breached divides	Buffers	Macro	Glaciers breaching valley divides results in more subdued and lower relief topography, and subsequently reduced gravitational potential energy available for sediment transport processes. Low-gradient upland surfaces are likely to be disconnected from the channel network
Lateral moraines	Buffers	Meso	Sharp-crested linear accumulation of glacially transported rocks and debris dropped by the ice along its' lateral margins as it melts. Lateral moraines disrupt the sediment cascade by causing localized deposition of hillslope sediment on the distal slope of the moraines while the proximal slope often acts as a sediment supply

(continued)

Table 1 (continued)

Feature	Type	Scale	Description/comments
Tarns/lakes	Buffers/barriers	Meso	Proglacial mountain lakes formed in a cirque excavated by a glacier and lakes formed in glacial over-deepening's. Glacial lakes effectively disconnect all upstream areas with respect to coarse sediment, and likely trap a high proportion of the suspended sediment
Grain size/ competence	Barriers/blankets	Micro	Sediment transported and deposited by glaciers is commonly unsorted, with clasts ranging in size from clay to boulders (diamictic). Fluvial reworking of this material may lead to lag deposits consisting of material too coarse for fluvial transport due to differences in process competence, increasing longitudinal disconnectivity through persistent aggradation and/or non-transport

hillslopes include cirque basins containing tarns, breached divides at Emerald Ridge and Round Pass (Fig. 1d), and parklands at the base of Pyramid Peak and Copper Mountain (Fig. 2). These features increase landscape heterogeneity and complexity and, in turn, sediment disconnectivity by fragmenting the sediment cascade (Table 1), [5]. Many of these glacial features, such as cirque basins and tarns, are long-term sediment reservoirs that hillslope sediment must pass through before eventually reaching the channel network. Other glacial features which are low gradient, such as breached divides and parklands, result in reduced gravitational potential energy which promotes deposition and longer residence times over transport (Table 1).

Later during the Last Glacial Maximum (LGM; locally termed the Fraser Glaciation, 17–18 ka) the South Tahoma Glacier was likely confined to the valley floor but still extended beyond the watershed boundary [24]. During this time, erosion was concentrated along the main valley, producing a wide, U-shaped valley with steep sidewalls. Locally, the Pleistocene-Holocene transition corresponded to a cold and dry climate without glacier advances, in contrast to many other areas globally [37]. More recently, neoglacial advances during the sixteenth and nineteenth centuries (e.g., 1550 AD, 1840 AD) formed impressive lateral and terminal moraines 3.5 km below the modern-day glacier termini [57]. Today, rapidly retreating glaciers are exposing a thick blanket of unconsolidated glacial till within the proglacial zone.

The resulting glacial landscape morphology is a unique canvas over which contemporary processes operate. Today, Tahoma Creek flows through three distinct zones after issuing from the South Tahoma Glacier. From river kilometer (RKM) 0–3.5 the river flows through the proglacial zone where it is deeply incised in a narrow canyon of unconsolidated neoglacial drift (Figs. 2 and 3a). In applying the hillslope-channel coupling method proposed by Whiting and Bradley [64], Turley et al. [61] found that this reach of channel is coupled (AD—pink in Fig. 4) to the adjacent hillslopes. This is supported by fieldwork observations of bank erosion along the entire length of this

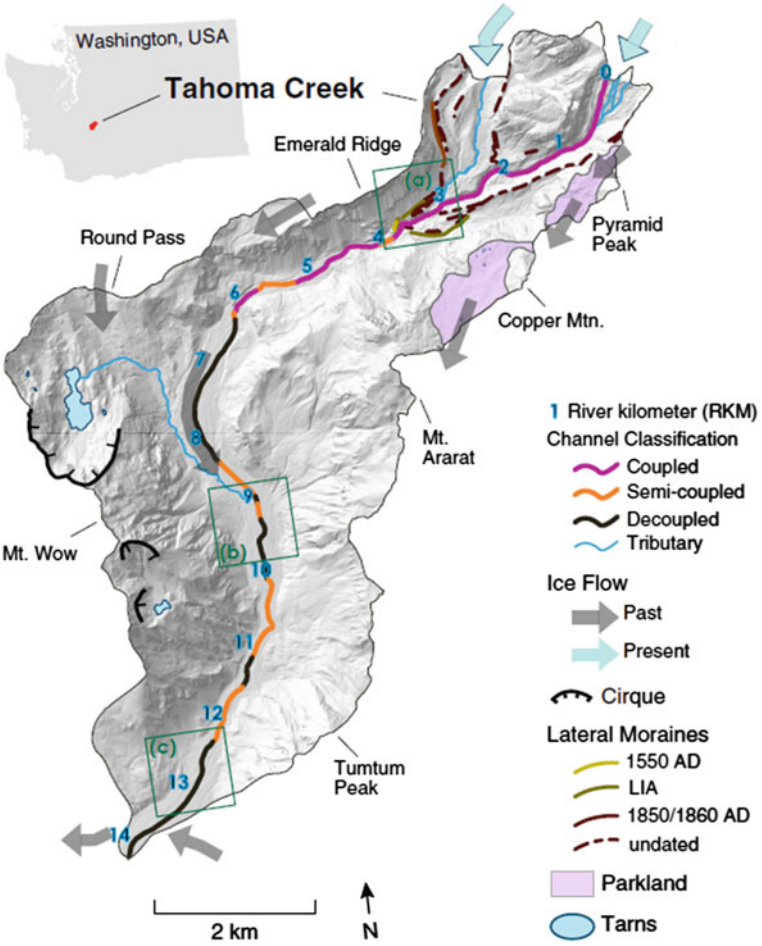

Fig. 2 Overview map of the Tahoma Creek watershed including watershed location, glacial landforms, (paleo) ice flow patterns, hillslope-channel coupling estimates (visualized as valley bottom centerline), and Fig. 3 extent indicators (green boxes)

reach. However, lateral moraines delineate the proglacial area and prevent hillslope sediment from outside of the proglacial zone from reaching the channel network, while also creating a valley constriction where they come together as end moraines (Fig. 3a). Additionally, at least 33 debris flow/flood events have been recorded since 1967 (Fig. 4a; [9, 61]). These events begin as glacial outburst floods or failure of proglacial gully walls [41, 63] and are responsible for mobilizing large volumes of diamictic sediment and carving the deep canyon. Between 2002 and 2008, a period encompassing a large debris flow/flood event [4], up to 40 m of incision occurred within this reach, smoothing out the minor irregularities visible in the otherwise concave-up long profile (Fig. 4c). Through this same zone (RKM 0-3.5), the effective

catchment area method [30] and Index of Connectivity [16] suggest that connectivity is high [61].

From RKM 3.5–6 the glacial trough is moderately narrow, and the active channel occupies much of the valley floor (Fig. 4ab). Because of this configuration, hillslope sediment that reaches the valley margin is readily entrained and transported downstream. This observation is supported by hillslope-channel coupling estimates which suggest the channel is coupled (AD) or semi-coupled (MD, OD—yellow in Fig. 4) with the adjacent hillslopes [61, 64], and morphometric analysis results suggesting relatively little net change occurs within the active channel (Fig. 4c), [3, 60]. Connectivity indices estimate moderate connectivity that is decreasing in the downvalley direction [61].

Much of the debris flow/flood material mobilized from the proglacial zone is deposited where the valley abruptly widens beginning at RKM 6. The coarsest fraction of these deposits includes boulders greater than 2 m in diameter and can likely only be reworked during extreme events. This results in channel widening and coarsening. The Residual Flow method [27] also predicts a zone of persistent aggradation in this location based on proximity to sediment sources and sediment routing patterns [61].

From RKM 6-14 the glacial trough becomes wide (Fig. 4b), and paraglacial valley margin reservoirs are common (Fig. 3b). Despite the wide valley floor, channel confinement fluctuates along this reach as a result of debris cones, and extensive terraces (Fig. 3bc). Historical records suggest that four debris flows have occurred since 2003 at RKM 8.5. Five large paraglacial landslides (i.e., rockfall and rock avalanches) were also identified along this lower reach through geomorphic mapping, while bank erosion was found to be negligible (Fig. 4a). Quantitative indices indicate that the hillslopes are predominantly decoupled (SD—grey in Fig. 4) or semi-coupled, and connectivity decreases to a minimum value [61].

Taking Tahoma Creek as an example, we can conclude that small, high-relief (post)glacial basins (Fig. 1b) maintain a record of past glaciations that increases landscape complexity and results in unique patterns of connectivity. In these basins, hillslope-channel coupling and sediment connectivity tend to decrease in the downvalley direction. Making a space-for-time substitution, sediment yields are also likely to decrease in the downvalley direction as landforms stabilize [19], (Fig. 4c), unless secondary reworking of glacial sediment becomes important [21].

4 Moderate Relief Postglacial Basins with Breached Divides—Riley Creek

The Riley Creek watershed inspires panel (d) of Fig. 1, which is a conceptual model of lateral connectivity for low-relief postglacial basins with breached divides (Table 1). However, the watershed also contains a mix of high-gradient slopes similar to panel (c). In the following paragraphs we discuss the recent glacial history of Riley

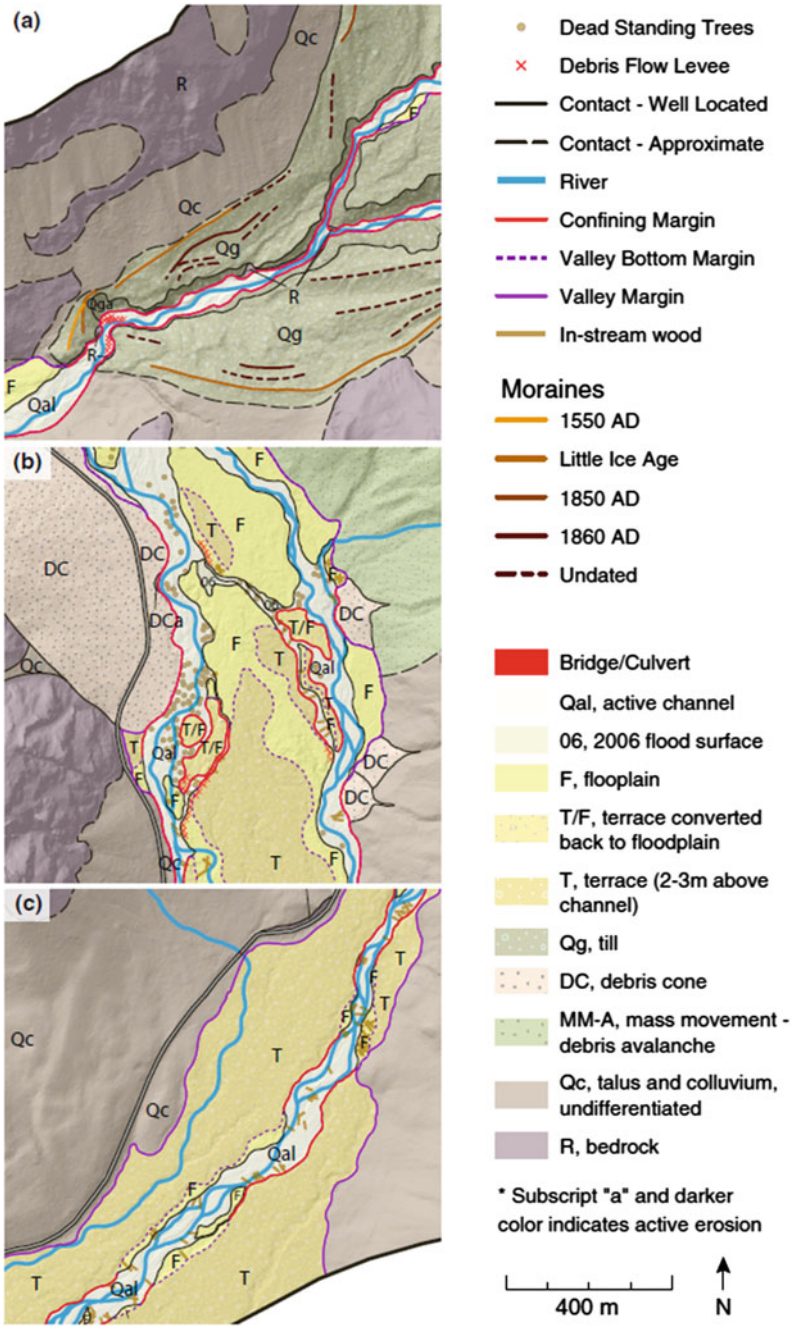

Fig. 3 Geomorphic map of select locations within the Tahoma Creek watershed. Mapping extents are shown in Fig. 2. Lateral moraine dates are based on [57]. Mapping was completed in the field by M. Turley during the summer of 2019

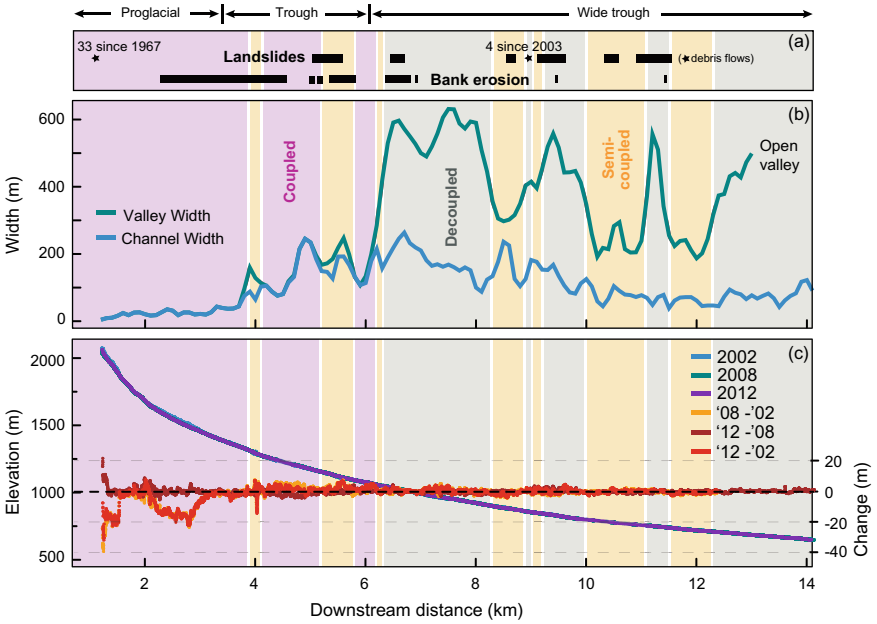

Fig. 4 Summary characteristics for the Tahoma Cr. Watershed. **a** Hillslope inputs based on fieldwork. Frequency of debris flows (stars) noted for period of record. **b** Valley and channel width, and hillslope-channel coupling based on the method proposed by [64]. **c** Longitudinal profiles based on Lidar from 2002, 2008, and 2012 and net channel change between these years [3]

Creek, valley geometry characteristics, and the resulting downstream changes in the lateral input of sediment and wood (lateral connectivity) and its' control on channel characteristics.

Riley Creek drains 28 km^2 of terrain along the western edge of the Skidegate Plateau in the archipelago of Haida Gwaii, British Columbia, territory of the Haida Nation (Fig. 5). The islands were last overridden by ice during the Fraser Glaciation when valley glaciers emerged from the Queen Charlotte Ranges along a northwest-southeast oriented ice divide, and at times coalescing with the Cordilleran ice sheet to the east [23, 58]. West of the divide and in the region of Riley Creek, ice flowed westward toward the ocean [1, 58]. In Riley Creek and in neighboring basins, the landscape is represented by glacial troughs generally aligned east to west with divide breaches aligned northeast to southwest, the latter due to past glacial transfluence [36]. Cirques in hanging valleys are evident in the basin and oriented primarily to the north [1, 36].

The Riley Creek basin is characterized by a mix of high-gradient hillslopes, with a relative relief of 870 m and about 8 km^2 of slopes with a gradient > 30°, and low-relief breached divides. The hillslopes are generally covered by a veneer of colluvium with thicknesses in the range of 0.1–1.0 m [1]. The postglacial landscape has been heavily modified by hillslope processes. The basin receives more than 3600 mm of

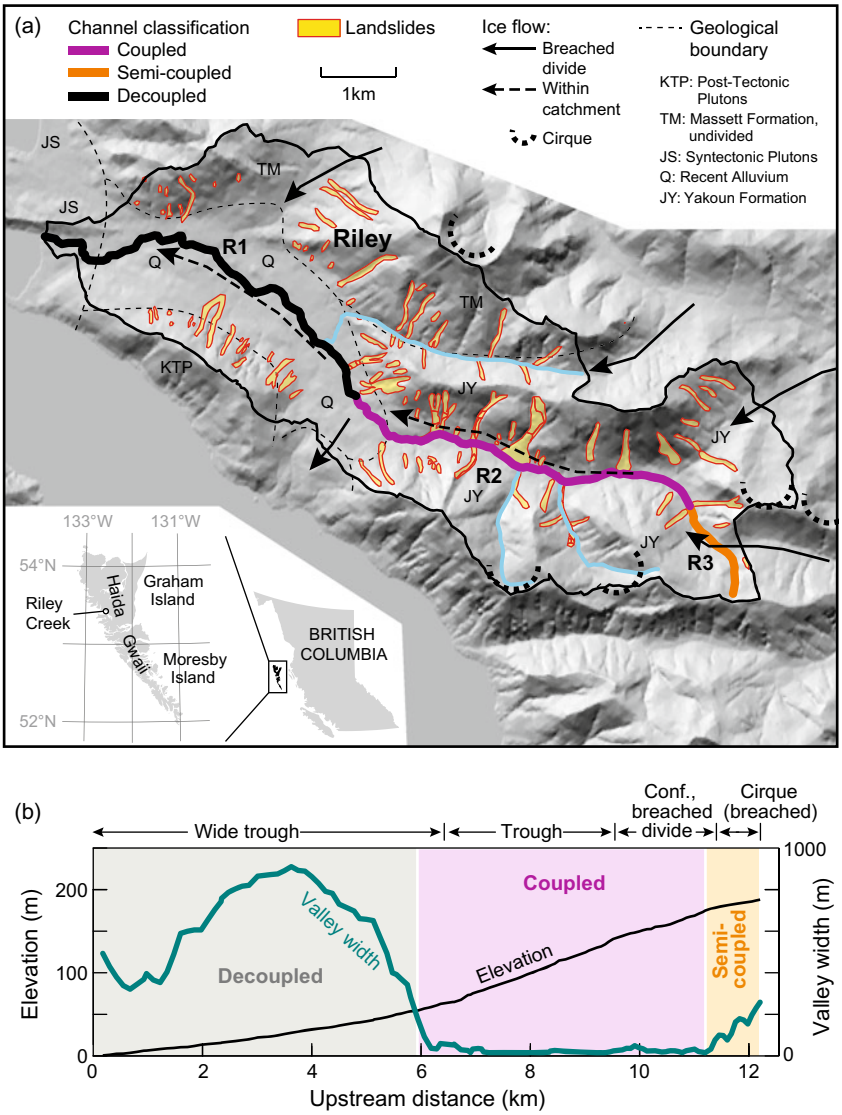

Fig. 5 **a** Location map, watersheds, geology, landslides, glacial history, and study reaches of Riley Creek, British Columbia. Ice flow direction is indicated by solid (flow is within a catchment) and dashed (ice flow crosses catchment divide) lines with arrows. **b** Longitudinal profiles, valley width, and hillslope-channel coupling. Modified from [36]

precipitation per year, most of which falls as rain in the fall and winter months [65]. This, in combination with a weak, heavily fractured volcanic lithology, and regional seismic activity produces widespread landsliding from glacially oversteepened hillslopes [32, 43]. Most landslides in Riley Creek occur as debris avalanches, debris torrents, and debris slides that transfer sediment and trees from hillslopes to either the valley bottom or directly to the channel network depending on valley geometry (e.g., [38]) (Fig. 5).

Riley Cr. Flows through three distinct reaches (Fig. 5, R1-R3) which we will discuss from upstream to downstream. The longitudinal profile of the mainstem channel is variable, alternating between concave-up and concave-down reaches (Fig. 5b). In the headwaters (R3; Fig. 5), the channel is generally flanked by a relatively narrow ribbon of vegetated fluvial deposits set into the basal till (non-sorted sand, silt, and clay) that forms the valley bottom (where present). Steep, headwater channels generally flow through gullies that serve as conduits for debris flows (upper coupled slopes in Fig. 1d). The location of debris flow-prone tributaries is given in Fig. 5. The largest tributaries are 9–10 m in width and 0.07–0.08 in gradient and transfer coarse sediment and large wood (LW) to the mainstem channel in a mix of fluvial and hillslope processes [38]. However, the mainstem of Riley Creek begins in a cirque where an area of plateau-like topography developed from a divide breaching by valley glaciers, leaving behind gently sloping valley sidewalls that do not generally reach the threshold of slope failure (upper decoupled reach in Fig. 1d). In areas where the threshold is exceeded and slope failures occur, colluvial sediments and debris are deposited on a relatively wide valley bottom of up to 200 m formed mainly due to a breached dived from the northeast (Fig. 5), but may approach the channel margin [36]. Hillslope coupling in this reach is limited to that of small, steep tributaries that transfer lag materials derived from the veneer of upslope colluvium to the mainstem channel, especially in drainage areas < 0.3 km^2 and thus the reach is considered only semi-connected to the hillslopes. Additional sediments are transferred to the channel through lateral erosion of alluvium and relict glacial till stored along the banks and in the valley bottom [35]. Areas of higher sediment storage generally reflect the location of tributary confluences (Fig. 6).

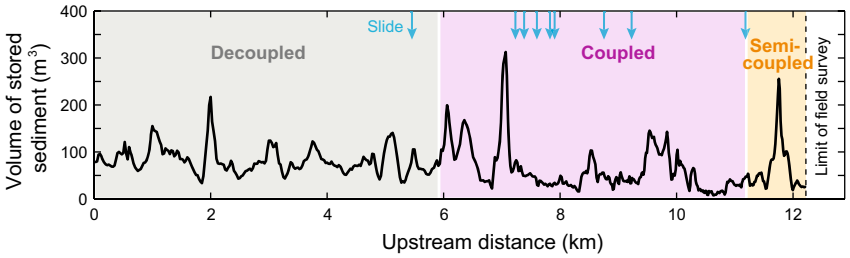

Fig. 6 Sediment storage along the mainstem of Riley Creek

Bed slope averages 0.013 and increases in the downstream direction (Fig. 7). The channel is relatively stable flowing through a series of pools and riffles among mature coniferous trees that populate the streambanks in an old growth forest (Fig. 8). Riffles are short (<0.5 bankfull widths in length) (Fig. 8a) and pools are frequent, typically occurring every 2 bankfull widths (Fig. 8b). LW inputs to the channel are mostly derived from riparian sources [35] and logjams are generally absent from the reach although remnants of a logjam at least 300 years in age was observed in the lower portion of the reach where the valley begins to narrow (see [38]). Channel width is about 10 m in the upper portion of the reach but approaches 30 m in the vicinity of the old logjam in the lower portion of the reach after side channels formed as the channel adjusted laterally across the unconfined valley bottom (Fig. 7). Depth generally decreases and width increases with basin area. Grain size in this portion of the reach is 0.1 m in diameter and declines in the downstream direction (although data here is sparse).

Moving downstream to reach 2 (R2 in Fig. 5), the channel enters a glacial trough and the valley becomes narrow and confined by steep valley walls where sediment and debris are transferred to the channel. The channel is directly connected to the hillslope (e.g., the lower coupled reach in Fig. 1d). Induvial landslides can transfer > 10,000 m^3 of sediment (Fig. 7) and over 3000 m^3 of LW to the channel [35]. During the past century, at least seven landslides have reached the channel and debris flows occurred in 10 steep tributaries [36]. Logjams related to landslide deposits are frequent in this reach and generally store anywhere from 10 to 500 m^3 of LW (Fig. 7). Bed slope appears almost cyclical ranging from 0.01 to 0.03 and typically in relation to locations of recently formed logjams with the steepest gradients found downstream of the jam [38]. The downstream fining of the bed surface material noted in R3 reverses, increasing to a grain size of 0.5 m for drainage areas ranging from 1–2 km^2 to about 10 km^2 and attributed to the presence of logjams and inputs of colluvium from landslides. Channel width averages 19 m and is relatively independent of basin area for most of R2 as the channel is confined by the valley walls (Fig. 7). Channel adjustment is generally restricted to the vertical dimension as the channel aggrades and degrades in response to logjam and landslide inputs of LW and sediment and channel depths range from 1 to 3 m (Fig. 7). Sediment storage loci are generally found downstream of recent landslide inputs (Fig. 6). Riffles in R2 are relatively long and typically up to a bankfull width in length but reach five widths upstream of a large and recently formed logjam (Fig. 8a). Compared to R3, pools are less frequent and are spaced up to 12.5 widths in a section of channel severely impacted by a landslide (Fig. 8b). Bedrock outcrops are rare throughout Haida Gwaii [58] and are localized to valleys differentially scoured by glacial ice [1]. This is likely the case in the lower portion of R2 as the channel flows through a narrow bedrock canyon. Here the channel gradient reaches up to 0.08 and a single step over a debris pile anchored by a bedrock knob creates a 2 m hydraulic jump.

Moving further downstream to reach 1 (R1), the channel enters a wide glacial trough where the valley broadens to over 200 m in width and the valley walls are relatively gentle in slope given glacial breaching of the divide from the north to the south (Fig. 5; Table 1). Although one landslide enters the channel near the upstream

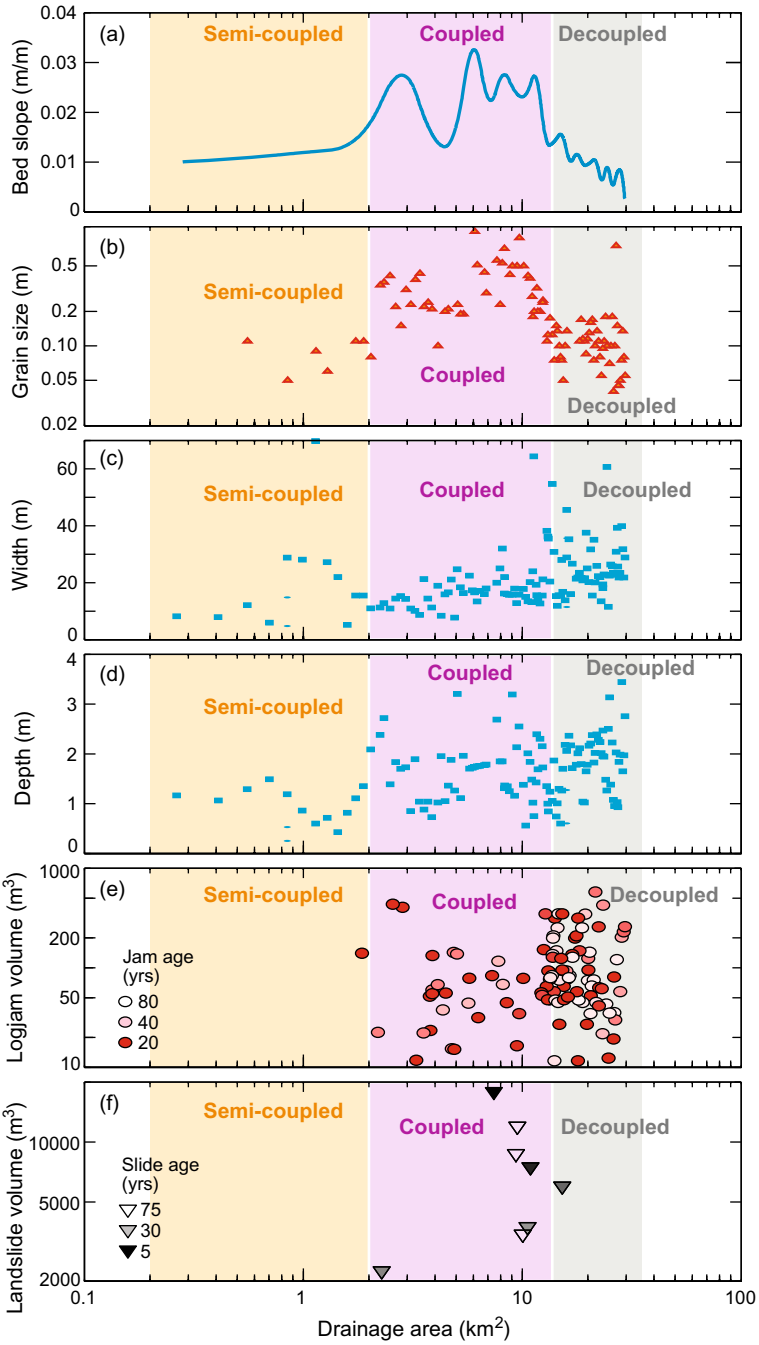

Fig. 7 Plots of relations between **a** slope, **b** grain size (D_{90}), **c** bankfull width, **d** bankfull depth, **e** wood volume and age of logjams, and **f** landslide age and volume of sediment delivered to the channel versus drainage basin area of Riley Creeks. Modified from [36]

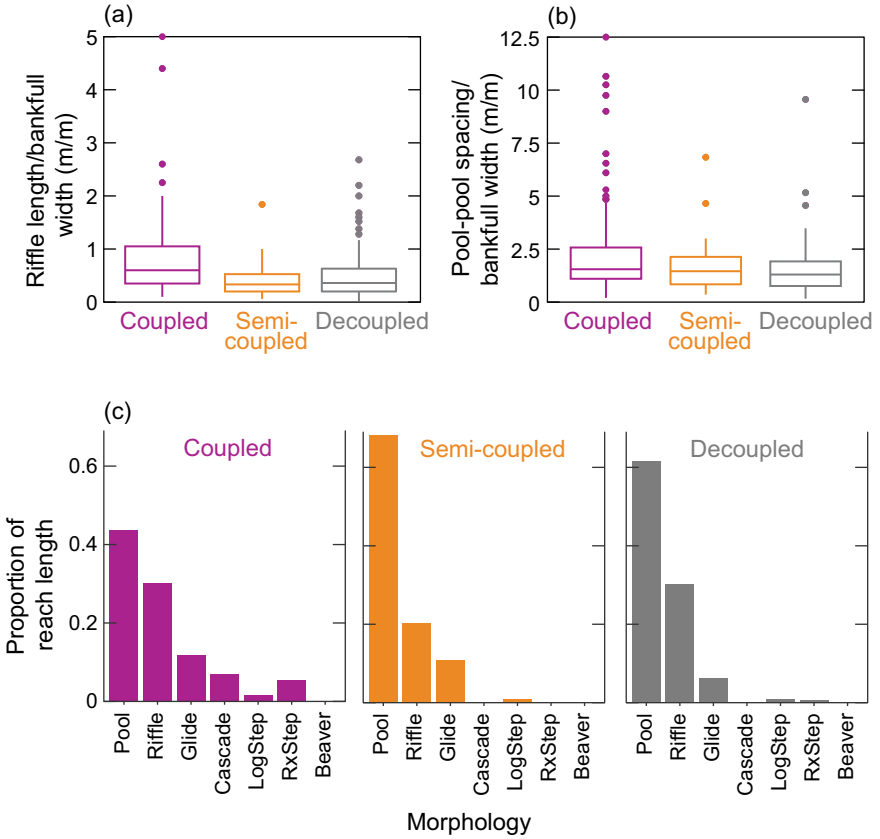

Fig. 8 Channel morphology of the mainstem of Riley Creek. **a** Riffle length (scaled by channel bankfull width), pool-pool spacing (scaled by bankfull channel width) (**b**), and length (proportion of the total length) of the geomorphological units (**c**)

boundary with R2, the channel is generally decoupled from surrounding hillslopes (e.g., the lower decoupled reach in Fig. 1d). Bed slope declines with basin area from about 0.01 to 0.001 while grain size declines from 0.2 to 0.05 m (Fig. 7). The channel also becomes wider and shallow along the reach in the downstream direction but there is relatively large scatter around these relations imposed by the frequency, size, and age of logjams (Fig. 7). As in R3, inputs of LW to the channel are derived from riparian sources [35]. The bed aggrades upstream of a logjam and then adjusts laterally across the valley bottom often creating multiple side channels around and through the structure of the logjam [38]. Sediment transfer to the reach comes in the form of transport from both R2 and several small tributaries flowing across the valley floor, and from erosion of alluvium and glacial till stored on the valley bottom. Local sediment storage increases (Fig. 6) as sediments are transferred to the valley bottom

and eventually stabilized by riparian vegetation. Compared to R2, riffle length, and pool spacing decreases and generally matches conditions in R3.

5 Lateral Erosion of Glaciofluvial Deposits—Guichon Creek, B.C.

Guichon Creek presents a watershed where sediment dynamics continue to be dominated by relic glacial features, despite a lack of direct hillslope-channel connectivity along much of the main stem. While the connection between the legacy erosional features (i.e., oversteepened valley walls, hanging valleys) can provide a long-term signature to geomorphic processes in formerly glaciated regions (e.g., [36]), the Guichon Creek case study provides an illustration of how the depositional environment created by past glaciation continues to dominate fluvial processes. Guichon Creek presents an example of a watershed corresponding most closely to panel (d) in Fig. 1—though the headwaters hillslope connectivity is also comparatively muted.

The Guichon Creek watershed is located in the southern interior of British Columbia in the territory of the Nlaka'pamux people. Guichon Creek flows off the Thompson Plateau in a southerly direction, joining the Nicola River 10 km west of the town of Merritt and draining an area of approximately 1200 km^2 (Fig. 9).

As with most of B.C., the regional topography and surficial geology have been strongly shaped by past glaciation. While the region has been repeatedly overrun by ice during glacial episodes (as many as 20 over the last one million years), the most recent glacial episode (Fraser Glaciation) began approximately 30,000 years ago and terminated 10,000 years ago [20]. The dominant direction of ice flow was from the north toward the south over the interior plateau of British Columbia [20]. This glacial event resulted in extensive morainal deposits in upland areas, and major valleys in the region are filled with lacustrine, glaciofluvial, and contemporary alluvial deposits [22]. Along Guichon Creek, the channel mainstem and major tributaries flow through such deposits including unconsolidated gravel terraces, lacustrine sediment, relic fans, and contemporary alluvium ([31], Fig. 9). Upland areas consist of till-covered bedrock, with till depth varying substantially over short distances. Since the last glacial retreat, the channel has eroded laterally into sediment deposits adjacent to the active channel along the lower 15 km of the creek (Fig. 10b). A wide (200–500 m) contemporary floodplain is apparent (Fig. 10a) along the lower 6 km of channel, slightly incised within a large lateral fan deposited during ice melt from the most recent glacial retreat [22].

Watershed elevation spans from 575 m to approximately 2000 m and is fairly low-relief with a watershed-average slope of 12%. Floodplain-adjacent terrace fronts compose the few steep areas exceeding 30°. Watershed climate is semi-arid, with precipitation averaging 321 mm/year. Precipitation is even throughout the year, but occasional thunderstorms deliver intense localized rainfall. Peak flows are snowmelt driven and usually occur in mid May. In spite of the large catchment area, the highest

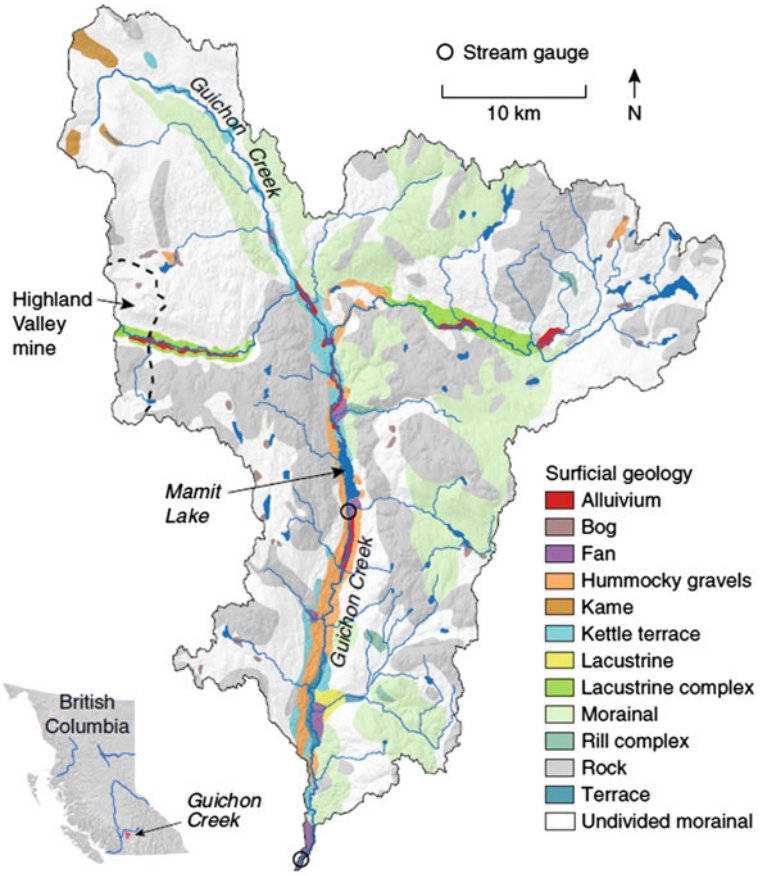

Fig. 9 Hillshade map of Guichon Creek. Photo locations shown in Fig. 10 are marked as green dots. Note the location of Mamit Lake. Surficial geology of the Guichon Creek watershed, is also shown with features digitized from maps generated by Fulton [31]

mean daily flows near the creek outlet average below4 m^3/s. The largest lake in the watershed, Mamit Lake, is located 32 km upstream from the Nicola River confluence (Fig. 9).

As opposed to the typical concave longitudinal profile [53], Guichon Creek contains a generally linear and then convex longitudinal profile. Mamit Lake lies approximately at the transition in the profile with channel gradients ranging from 0.2 to 1% upstream and at the outlet of the lake, and increasing gradient downstream of the outlet reaching a maximum of 3.5% (Fig. 11b). Above Mamit Lake, floodplain width varies but generally increases in a downstream direction from ~150 m to a maximum of nearly 800 m near the lake, with small confined sections located adjacent to relic glaciofluvial terraces (Fig. 11a). Below the lake, floodplain width is

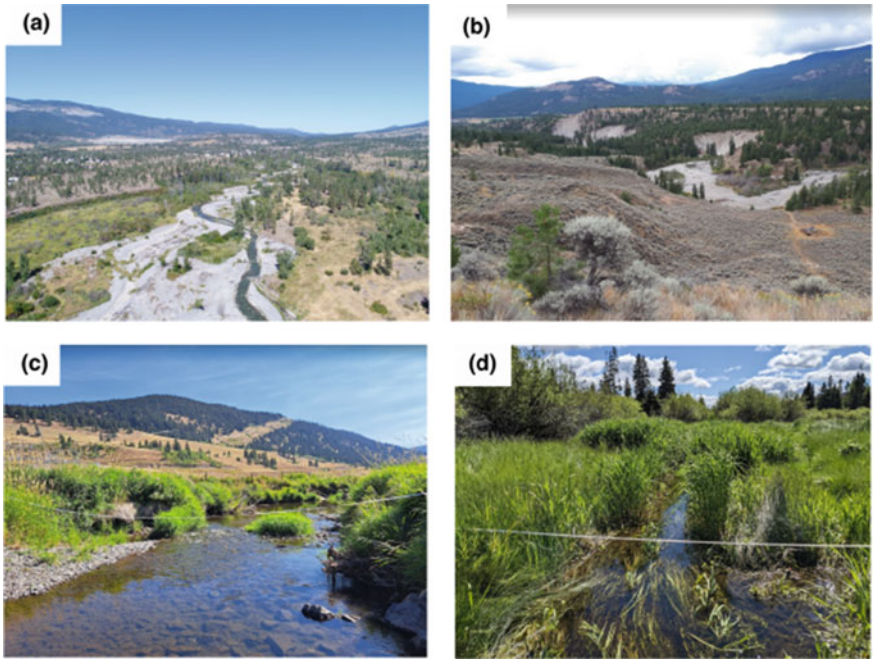

Fig. 10 **a** Image looking upstream from the lower portion of Guichon Creek. Note the wide active channel area following flooding in 2018. **b** Examples of eroding terrace material along lower Guichon Creek, approximately 8 km upstream of the confluence with the Nicola River. **c** Guichon Creek approximately 3 km above Mamit Lake with gentle hillslopes shown in the background. **d** Headwaters of a tributary to Guichon Creek. Many headwater areas are relatively flat and contain wetlands

reduced to less than 75 m before increasing again and reaching a maximum of 800 m near the confluence with the Nicola River.

Landscape organization and topography, which is a result of past glacial episodes, have led to a distinct spatial pattern of sediment disconnectivity. The connectivity characteristics can be broadly divided into regions up and downstream of Mamit Lake, the only major disruptor of longitudinal connectivity (Table 1). However, several lower gradient areas near 52 km upstream likely represent a depositional region and a minor barrier. The more interesting characteristics lie in the nature of hillslope-floodplain coupling, which varies notably along the length of the channel (Fig. 11a). It is important to note that in this section we report coupling based on the floodplain width rather than channel width to represent the long-term potential for coupling. The floodplain is considered coupled when the adjacent terrace or slope exceeds 30° grade [51]. Above Mamit Lake (Fig. 11a), coupling is present near 41 and 51 km (Fig. 11a). The floodplain is closely coupled along at least one side from 32.5 to within 6 km of the Nicola River confluence. Approximately 50% of this length contains coupling along both floodplain margins. Much of this portion of coupled floodplain is lined with large (height > 20 m) terraces composed of glaciofluvial

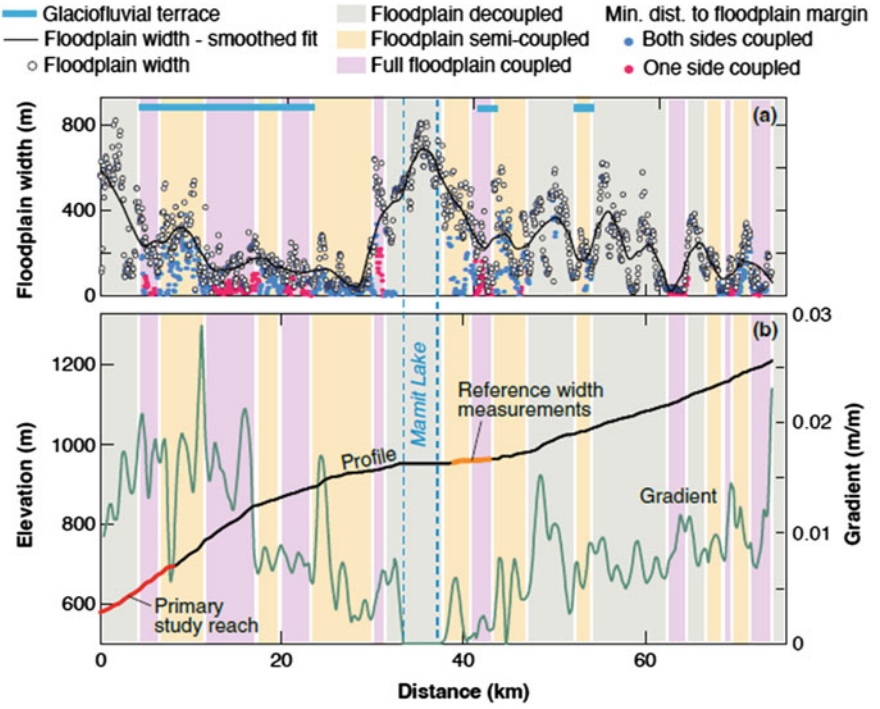

Fig. 11 **a** Plot of floodplain width along Guichon Creek. Each point corresponds to a width measurement made from a digital elevation model combined with aerial imagery. Sufficiently steep slopes adjacent to the floodplain would result in an indicator of "coupled." However, hillslopes were rarely coupled directly to the channel. **b** Longitudinal profile and channel gradient along Guichon Creek. Floodplain coupling shaded from (**a**) is also indicated in (**b**)

deposits (see Fig. 11a for site location and Fig. 10b for an image example). Overall, the spatial patterns of connectivity are largely a function of past glacial deposition of sediment which buffers much of the channel from direct hillslope input. Instead, lateral sediment input is driven by fluvial processes, namely, erosion into glacial terrace material.

The glacially imposed pattern of sediment availability and disconnectivity is reflected in the sediment dynamics and changes in channel width along Guichon Creek following two recent flooding events. Flooding occurred during May of 2017 and again in 2018. These floods were of relatively high magnitude and long duration with flows exceeding twice the mean annual freshet value on 42 days in 2017 and 22 days in 2018. Analysis of flow data return periods of the flood events are likely in the range of 1:20 years for 2017 and 1:40 years for 2018.

Changes in channel width along the downstream portion of Guichon Creek and a portion just 2 km upstream of Mamit Lake were evaluated using aerial imagery and Lidar. This analysis spans the lower 15 km for the first flood event and the lower 6.5 km for the second flood event. Sediment delivery to the channel was also

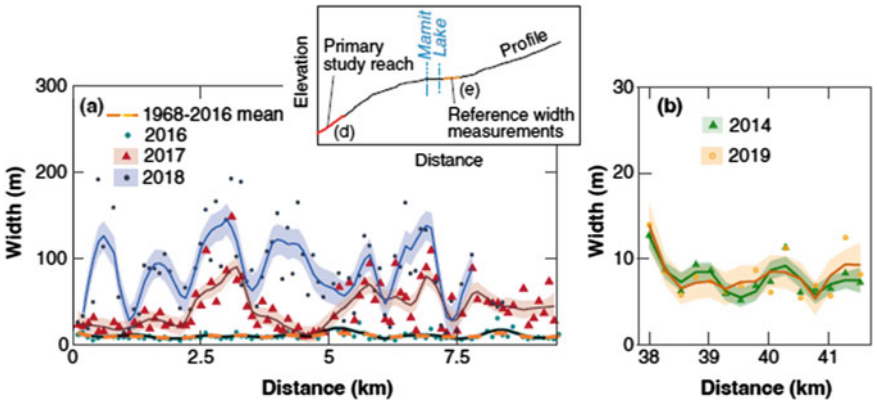

Fig. 12 **a** Channel width during three time periods along the lower 10 km of Guichon Creek. Dark lines correspond to a smoothed fit of the raw data; **b** channel width upstream of Mamit Lake during two time periods spanning the major flood events

estimated using two sets of Lidar data collected after each flood event. Additional details of the analysis can be found in [51].

Figure 12a displays longitudinal variation and temporal change in width along the lower 10 km of Guichon Creek. In 2016, downstream width variation is minor, with values ranging from approximately 8 m to just over 20 m. However, the channel had widened to well over 20 m in most locations and approached 100 m in multiple locations following the 2017 flooding. During the 2018 flooding, the channel widened again, approaching 200 m in several locations. The average channel width for 2016 is 10.1 m, 41.4 m after the 2017 flood season, and 84.6 m after the 2018 flood season. In contrast to the change in channel width downstream of Mamit lake in the region of terrace erosion, locations upstream of Mamit lake showed very little change in width (Fig. 12b).

In addition to causing substantial channel widening, the proximity of erodible terrace material to the active channel led to widespread erosion of glacial deposits. Following analysis of channel change from Lidar and imagery, erosion associated with the flooding event in 2017 was estimated as 163,000 ± 83,000 m^3. 73,890 ± 11,752 m^3 of additional material was eroded along the lowermost 7.5 km of channel during the 2018 flood season. These two years of input sum to 237,190 ± 95,052 m^3 of eroded sediment, which is likely an underestimate given the partial extent of available imagery and Lidar coverage. This input exceeds the mean annual transport capacity by a factor of 200.

Sediment source reactivation and resultant channel response in Guichon Creek provides an example of "late-stage paraglacial conditions", where stabilized post-glacial landscape features have been reactivated via contemporary fluvial processes [7]. Past glacial episodes have largely influenced the spatial organization and characteristics of erodible material within Guichon Creek (see Fig. 9), and also the patterns of connectivity within the system (Fig. 10a). The unusual shape of the longitudinal

channel profile demonstrates numerous signatures of a glaciated landscape, with the stepped profile form being an important indicator [2, 36]. This form disrupts downstream connectivity, as sediment is deposited in Mamit Lake. Unlike many mountain areas where glaciation has occurred, the dry climate and absence of large and steep hillslopes within the watershed reduces the occurrence of sediment input to channels driven by hillslope processes. As a result, lateral fluvial erosion of glacial deposits is likely the key input source. Past incision into lacustrine and glaciofluvial deposits has provided the channel a disconnection from direct colluvial input, but the river is also in a position to migrate laterally into these sediment deposits during periods of enhanced channel instability. The interaction between lateral erosion and glaciofluvial terraces has not been broadly quantified or documented, but recent studies indicate that terrace erosion may compose a large fraction of the total sediment budget in some watersheds, such as those in Puget Sound [55]. A positive feedback mechanism may be present in incised channels adjacent to erodible terraces: at locations where the channel is able to expand or migrate across a floodplain with erodible terraces on the margins, added sediment may lead to further channel widening and consequently more contact between the active channel margin and terrace fronts. This form of feedback has been documented in gravel channels with alluvial banks [17, 49].

6 Summary

In this paper, we present a conceptual model of lateral connectivity and subsequent channel characteristics in mountainous (post)glacial basins. This conceptual model illustrates that glacial landscapes have a unique valley geometry and landform assemblage which controls lateral connectivity and subsequently characteristics of contemporary channels in addition to catchment sediment yield. Glacial landforms increase landscape complexity and fragment the sediment cascade, ultimately increasing sediment disconnectivity. Glacial processes condition hillslope-channel connectivity on two spatial scales: valley scale and landform scale. Postglacial valley geometry often leads to an oscillating downstream trend in hillslope-channel coupling on which (para)glacial landforms impose finer-scale complexity (Fig. 1b, c). Past glacial activity can influence two subsets of contemporary lateral connectivity: (1) hillslope-channel coupling patterns in high-gradient watersheds, and (2) glaciofluvial terrace-floodplain coupling in low-gradient watersheds with depositional glacial landforms, each of which alters channel characteristics. Lateral connectivity influences channel characteristics through past and present sediment transport dynamics. Glacially conditioned lateral connectivity is a control on contemporary channel response to floods. Over steepened valley walls, thick blankets of unconsolidated till, and accessible glaciofluvial terraces may still result in high sediment yields, paraglacial sedimentation, and rapid adjustment of the channel profile during extreme events and periods of channel instability.

Acknowledgements This paper benefited from the help and support of a large number of students and colleagues. Tahoma Creek–Scott Beason, Taylor Kenyon, and Robby Jost. Riley Creek–Sid Tsang, Alan Paige, Tony Cheong, Dave Ramsey, Jim Schwab, Dan Hogan, and Steve Rice. Guichon Creek–Leona Antoine, Hyrum Petersen, Mike Simpson, Tracy Thomas, Tom Willms, and Leonora King. Eric Leinberger prepared many of the figures. The research was funded by NSERC Discovery (to MAH) and Canada Foundation for Innovation (to MAH).

References

1. Alley NF, Thomson B (1978) Aspects of environmental geology, parts of Graham Island, Queen Charlotte Islands. Brit Columb Ministry Environ Resource Anal Branch Bull 2, 65 p
2. Anderson R, Molnar P, Kessler M (2006) Features of glacial valley profiles simply explained. J Geophys Res 111:F01004. https://doi.org/10.1029/2005JF000344
3. Anderson S, Pitlick J (2014) Using repeat lidar to estimate sediment transport in a steep stream. J Geophys Res Earth Surf 621–643. https://doi.org/10.1002/2013JF002933
4. Anderson S, Shean D (2021) Spatial and temporal controls on proglacial erosion rates: a comparison of four basins on Mount Rainier, 1960 to 2017. Earth Surf Process Landforms 1–50. https://doi.org/10.1002/esp.5274
5. Baartman JEM, Masselink R, Keesstra SD, Temme AJAM (2013) Linking landscape morphological complexity and sediment connectivity. Earth Surf Proc Land 38(12):1457–1471. https://doi.org/10.1002/esp.3434
6. Ballantyne CK (2002) Paraglacial geomorphology. Quatern Sci Rev 21(18–19):1935–2017
7. Ballantyne C (2002) A general model of paraglacial landscape response. The Holocene 3(3):371–376. https://doi.org/10.1191/0959683602hl553fa
8. Barsch D, Caine N (1984) The nature of mountain geomorphology. Mt Res Dev 4:287–298
9. Beason SR, Legg NT, Kenyon TR, Jost RP, Kennard PM (2019) Forecasting and seismic detection of debris flows in pro-glacial rivers at Mount Rainier National Park, Washington, USA, 7Th International Conference on Debris-Flow Hazards Mitigation
10. Benda L, Leroy N, Miller D, Dunne T, Reeves G, Pess G, Pollock M (2004) The network dynamics hypothesis: how channel networks structure riverine habitats. Bioscience 54:413–427
11. Brardinoni F, Hassan MA (2006) Glacial erosion, evolution of river profiles, and the organization of process domains in mountain drainage basins of coastal British Columbia. J Geophys Res 111:F01013. https://doi.org/10.1029/2005JF000358
12. Brardinoni F, Hassan MA (2007) Glacially induced organization of channel-reach morphology in mountain streams. J Geophys Res 112(F03013):2007. https://doi.org/10.1029/2006JF000741
13. Brardinoni F, Hassan MA, Rollerson T, Maynard D (2009) Colluvial sediment dynamics in mountain drainage basins. Earth Planet Sci Lett 284:310–319
14. Brocklehurst SH, Whipple KX (2006) Assessing the relative efficiency of fluvial and glacial erosion through simulation of fluvial landscapes. Geomorphology 75:283–299
15. Brummer CJ, Montgomery DR (2003) Downstream coarsening in headwater channels. Water Resourc Res 39(10). https://doi.org/10.1029/2003WR001981
16. Cavalli M, Trevisani S, Comiti F, Marchi L (2013) Geomorphometric assessment of spatial sediment connectivity in small Alpine catchments. Geomorphology 188:31–41. https://doi.org/10.1016/j.geomorph.2012.05.007
17. Church M (2002) Geomorphic thresholds in riverine landscapes: geomorphic thresholds. Freshw Biol 47(4):541–557. https://doi.org/10.1046/j.1365-2427.2002.00919.x
18. Church M, Ham D, Hassan M, Slaymaker O (1999) Fluvial clastic sediment yield in Canada: scaled analysis. Can J Earth Sci 36(8):1267–1280

19. Church M, Ryder JM (1972) Paraglacial sedimentation: a consideration of fluvial processes conditioned by glaciation. Geol Soc Am Bull 83:3059–3071
20. Church M, Ryder J (2010) Physiography of British Columbia. In: Pike R, Redding T, Moore R, Winkler R, Bladon K (eds) Compendium of forest hydrology and geomorphology in British Columbia. Victoria, BC, pp 17–44
21. Church M, Slaymaker O (1989) Disequilibrium of Holocene sediment yield in glaciated British Columbia. Nature 337(2):452–454
22. Clague J (1989). Quat Geol Canad Cordillera. https://doi.org/10.1130/dnag-gna-k1.15
23. Clague J, Harper JR, Hebda RJ, Howes DE (1982) Late Quaternary sea levels and crustal movements, coastal British Columbia. Can J Earth Sci 19:597–618
24. Crandell DR, Miller RD (1974) Quaternary stratigraphy and extent of glaciation in the Mount Rainier region, Washington. US Geol Surv Prof Paper 59
25. Dadson SJ, Church M (2005) Postglacial topographic evolution of glaciated valleys: a stochastic landscape evolution model. Earth Surf Proc Land 30:1387–1403
26. Fiske RS, Hopson CA, Waters AC (1963) Geology of mount rainier national park. Geological Survey Professional Paper, Washington, p 444
27. Fressard M, Cossart É (2019) A graph theory tool for assessing structural sediment connectivity: development and application in the Mercurey vineyards (France). Sci Total Environ 651:2566–2584. https://doi.org/10.1016/j.scitotenv.2018.10.158
28. Fryirs K (2013) (Dis)Connectivity in catchment sediment cascades: a fresh look at the sediment delivery problem. Earth Surf Proc Land 38:30–46. https://doi.org/10.1002/esp.3242
29. Fryirs KA, Brierley GJ, Preston NJ, Kasai M (2007) Buffers, barriers and blankets: the (dis)connectivity of catchment-scale sediment cascades. CATENA 70(1):49–67. https://doi.org/10.1016/j.catena.2006.07.007
30. Fryirs KA, Brierley GJ, Preston NJ, Spencer J (2007) Catchment-scale (dis)connectivity in sediment flux in the upper Hunter catchment. New South Wales, Aust Geomorphol 84(3–4):297–316. https://doi.org/10.1016/j.geomorph.2006.01.044
31. Fulton R (1960) Surficial geology: Merritt West of 6th Meridian. Geological Survey of Canada
32. Gimbarzevsky P (1988) Regional inventory of mass wasting on the Queen Charlotte Islands. BC Ministry of Forests, Victoria, BC. Land Management Report No 29, 96 p
33. Hallet B, Hunter L, Bogen J (1996) Rates of erosion and sediment evacuation by glaciers: a review of field data and their implications. Glob Planet Change 12:213–235
34. Hassan MA, Brayshaw D, Alila Y, Andrews E (2014) Effective discharge in small formerly glaciated mountain streams of British Columbia: limitations and implications. Water Resour Res 50:4440–4458. https://doi.org/10.1002/2013WR014529
35. Hassan MA, Bird S, Reid D, Hogan D (2016) Simulated wood budgets in two mountain streams. Geomorphology 259:119–133
36. Hassan MA, Bird S, Reid D, Ferrer-Boix C, Hogan D, Brardinoni F, Chartrand S (2019) Variable hillslope-channel coupling and channel characteristics of forested mountain streams in glaciated landscapes. Earth Surf Proc Land 44(3):736–751. https://doi.org/10.1002/esp.4527
37. Heine JT (1998) Extent, timing, and climatic implications of glacier advances Mount Rainier, Washington, USA, at the pleistocene/holocene transition. Quat Sci Rev 17(12):1139–1148. https://doi.org/10.1016/S0277-3791(97)00077-2
38. Hogan DL, Bird SA, Hassan MA (1998) Spatial and temporal evolution of small coastal gravel-bed streams: the influence of forest management on channel morphology and fish habitats. Gravel-Bed rivers in the environment. Water Resources Publications, Colorado, pp 365–392
39. Khan S, Fryirs K, Bizzi S (2021) Modelling sediment (dis)connectivity across a river network to understand locational-transmission-filter sensitivity for identifying hotspots of potential geomorphic adjustment. Earth Surf Proc Land 46:2856–2869. https://doi.org/10.1002/esp.5213
40. Lancaster N, Casebeer NE (2007) Sediment storage and evacuation in headwater valleys at the transition between debris-flow and fluvial processes. Geology 35:1027–1030
41. Legg NT, Meigs AJ, Grant GE, Kennard P (2014) Debris flow initiation in proglacial gullies on Mount Rainier, Washington. Geomorphology 226:249–260. https://doi.org/10.1016/j.geomorph.2014.08.003

42. Marchi L, Comiti F, Crema S, Cavalli M (2019) Channel control works and sediment connectivity in the European Alps. Sci Total Environ 668:389–399. https://doi.org/10.1016/j.scitotenv.2019.02.416
43. Martin Y, Rood K, Schwab JW, Church M (2002) Sediment transfer by shallow landsliding in the Queen Charlotte Islands, British Columbia. Can J Earth Sci 39(2):189–205
44. McColl ST (2012) Paraglacial rock-slope stability. Geomorphology 153–154:1–16. https://doi.org/10.1016/j.geomorph.2012.02.015
45. Montgomery DR (2002) Valley formation by fluvial and glacial erosion. Geology 30(11):1047–1050. https://doi.org/10.1130/0091-7613(2002)030%3c1047:VFBFAG%3e2.0.CO;2
46. Montgomery DR, Buffington JM (1997) Channel reach morphology in mountain drainage basins. Geol Soc Am Bull 109:596–611
47. Montgomery DR, Brandon MT (2002) Topographic controls on erosion rates in tectonically active mountain ranges. Earth Planet Sci Lett 201(3–4):481–489
48. Montgomery DR, Foufoula-Georgiou E (1993) Channel network source representation using digital elevation models. Water Resour Res 29(12):3925–3934
49. Mueller E, Pitlick J (2014) Sediment supply and channel morphology in mountain river systems: 2. Singlethread to braided transitions. J Geophys Res 300–316. https://doi.org/10.1002/2013JF002871
50. Persichillo MG, Bordoni M, Cavalli M, Crema S, Meisina C (2018) The role of human activities on sediment connectivity of shallow landslides. Catena 160:261–274. https://doi.org/10.1016/j.catena.2017.09.025
51. Reid DA, Hassan MA, McCleary R (2021) Glacial landscape configuration influences channel response to flooding. Earth Surf Proc Land. https://doi.org/10.1002/esp.5240
52. Rice SP (1998) Which tributaries disrupt downstream fining along gravel-bed rivers? Geomorphology 22(1):39–56. https://doi.org/10.1016/S0169-555X(97)00052-4
53. Schumm S (1977) The fluvial system. Wiley, New York
54. Stock JD, Dietrich WE (2003) Valley incision by debris flows: evidence of a topographic signature. Water Resour Res 39(4):2003. https://doi.org/10.1029/2001WR001057
55. Scott DN, Collins BD (2021) Frequent mass movements from glacial and lahar terraces, controlled by both hillslope characteristics and fluvial erosion, are an important sediment source to Puget sound rivers. Water Resourc Res 57:e2020WR028389. https://doi.org/10.1029/2020WR028389
56. Scott KM, Vallance JW, Pringle PT (1995) Sedimentology, behavior, and hazards of debris flows at mount rainier. Geological Survey Professional Paper, Washington, p 1547
57. Sigafoos RS, Hendricks EL (1972) Recent activity of glaciers of mount rainier, Washington, Geological Survey Professional Paper, 387-B
58. Sutherland Brown A (1968) Geology of the queen Charlotte Islands, British Columbia. Brit Columb Dept Mines Petrol Resource Bull 54, 226 p
59. Tunnicliffe JF, Church M (2011) Scale variation of post-glacial sediment yield in Chilliwack Valley, British Columbia. Earth Surf Proc Land 36:229–243
60. Turley M (2020) Exploring the importance of sediment disconnectivity and connectivity in Glacierized Catchments, Tahoma Creek, WA, Master Thesis, Department of Geography, University of British Columbia
61. Turley M, Hassan MA, Slaymaker O (2021) Quantifying sediment connectivity: moving toward a holistic assessment through a mixed methods approach. Earth Surf Proc Land 46(12):2501–2519. https://doi.org/10.1002/esp.5191
62. Tsuruta K, Hassan MA (2022) Large-scale sediment transport modelling: development, application, and insights. In Mandal S, Maiti R, Nones M, Beckedahl HR (eds) Applied geomorphology and contemporary issues. Geography of the physical environment. Springer, Cham. https://doi.org/10.1007/978-3-031-04532-5_1
63. Walder JS, Driedger CL (1995) Frequent outburst floods from South Tahoma Glacier, Mount Rainier, USA: relation to debris flows, meteorological origin, and implications for subglacial hydrology. J Glaciol 41(137):1–10. https://doi.org/10.1017/S0022143000017718

64. Whiting PJ, Bradley JB (1993) A process-based classification system for headwater streams. Earth Surf Proc Land 18:603–612
65. Williams GDV (1968) Climate of the Queen Charlotte Islands. In: Calder JA, Taylor RL (eds) Flora of the Queen Charlotte Islands. Canadian Department of Agriculture, Plant Research Institute, Ottawa, Ontario, pp 16–49

Challenges of River Corridor Management in Dynamic Braided River Systems

Arup Kumar Sarma

Abstract Delineating River Corridor of a large braided river from the mainland is a challenging task, as diverse human activities are often observed within the sand bars and in the point bars of such river. Large spatiotemporal variation in their width adds further complexities to River Corridor management of braided reaches. Dynamic nature and hence the complexities in river corridor delineation are demonstrated by analysing pattern of progressive changes in the river cross-section of the Brahmaputra River within the period 1971 to 2011. Various prevailing human activities within the flow path of some of the large braided rivers of the world are presented to show its genuine utility. Scope and challenges of channelizing braided river are finally demonstrated through application of hydrodynamic model BRAHMA in a 130 km long braided reach of Brahmaputra River. Need of field-based research along with application of modelling techniques to utilize the river corridor of a braided river advantageously without disturbing the river ecology is advocated.

Keywords BRAHMA · Braided-river · River corridor

1 Introduction

Width of river corridor of a braided river system can vary significantly and, therefore, its management involves different challenges and opportunity. In some situations, defining a river corridor itself becomes challenging for a large braided river. Because of exponential population growth, pressure on the land is increasing globally leading to unaffordable cost of land. Apart from the factor of high cost, people started living within the river corridor in different ways due to certain other advantages. Floating village in the Mekong River, habitation and farming in sand bars of the Brahmaputra River are some of such examples. Because of the existence of different economic classes and different means of livelihood, high-rise building also may not serve as the ultimate solution to population pressure, at least in near future. Development of River

A. K. Sarma (✉)
Department of Civil Engineering, IIT Guwahati, Guwahati, India
e-mail: aks@iitg.ac.in

S. Dutta and V. Chembolu (eds.), *Recent Development in River Corridor Management*,
Lecture Notes in Civil Engineering 376, https://doi.org/10.1007/978-981-99-4423-1_2

Front by encroaching into the existing natural river bank alignment in a systematic way is another example of augmenting natural river corridor. Construction of storage structure to augment river flow, collection of bed material through river mining for constructional activities also influences the natural flow characteristic of a river and influence river corridor. Maintenance of navigation channel is another challenge in braided river. With increasing concerns about ecology and water quality, utilizing river corridor for habitation or agricultural activities should also be regulated in a more scientific manner with due emphasis on river ecology. With advancement in the capability of mathematical model and geoinformatics, consequences of various activities mentioned above or impact of any river training work for maintaining river corridor can now be investigated more conveniently. Need and scope of managing river corridor using advanced technology are presented in this chapter.

2 Variation in River Corridor of Braided River

Because of high variation in the seasonal precipitation and in longitudinal gradient, Himalayan Rivers of the sub-tropical region experience high seasonal variations in flow and sediment load. This leads to frequent changes in the river course. Management of River Corridor in a braided river is therefore quite challenging because of huge spatiotemporal variation in their width. In some situations, defining a river corridor itself becomes challenging for a large braided river. While such variations generally create problem to people residing near the river, people with their long experiences have also utilized the river taking advantage of such spatial variation. A morphological study carried out for the Brahmaputra River has shown some interesting facts about spatiotemporal variations of River Corridor in braided river system.

Pattern of progressive changes in the river cross-section, particularly in terms of the total section width, was analysed in the Brahmaputra River starting from Sadia in the east to Dhubri on the west by dividing the river reach into 65 cross sections. Data referred for the purpose are tabulated below (Table 1). It was observed that the river width in some sections has increased significantly during 1970–2011. However, at the nodal points, which exist primarily due to having either hill or rocky formation on both sides, the river width does not change. Some stable bank reach with clay formation was also observed in this reach of the Brahmaputra River. Figure 1 shows the decadal temporal variation of width in different sections of the river Brahmaputra from 1973 to 2011.

From Fig. 1, it is clear that for some of the reaches (sections 2-4, 20-22, 35-37, 51-53, 58-60, 62-64), the change in width exceeds 5 km, and, in some cases, change is reaching nearly 10 km. As such, defining or fixing a river corridor for large braided river, even with a range of few kilometres, needs extensive observation and will have to be made reach specific.

Table 1 Data used for temporal change detection of Brahmaputra River

Year	Data used (Toposheets/satellite data)
1973–1974	GSI Toposheet; 1:50,000 scale
1976–1980	Landsat MSS; 80 m resolution
1993–1995	IRS 1B LISS 1; 72.5 m resolution
2003–2004	IRS P6 LISS 3; 23.5 m resolution
2008–2011	IRS P6 LISS 3; 23.5 m resolution

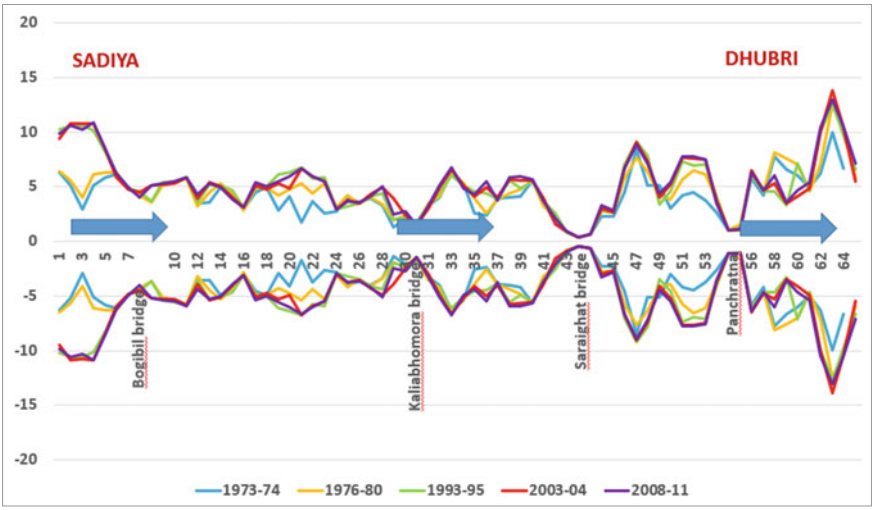

Fig. 1 Plot of river width (km) of Brahmaputra in 65 sections from Dhubri to Sadia

3 Utility of River Corridor

Because of exponential population growth, pressure on the mainland is increasing globally leading to unaffordable cost of favourable land. Because of this, many communities, more particularly those falling in the category of low-income group, encroach into the bank line of river to utilize the land in the lean period for their diverse benefits. Apart from the factor of high cost, people also started utilizing the river corridor in different ways due to certain other advantages. The possible impacts of such utilizations and their relevance to the concept of river corridor in case of large braided river are presented below.

Floating village in the Mekong River and Tonle-sap Lake is an example of utilizing river corridor for living purpose and business activities. However, this kind of utilization basically uses the water bodies of the river and, being floating structures, they allow flow even in the location where they exist, particularly when such floating structures are located in a flowing river and not in the lake portion with relatively stagnant water. There can be direct dumping of solid waste and wastewater from

these establishments into the river and thus can affect the water quality as well as the flow cross-section of the river.

Habitation and farming in the mid sand bar or in the point sand bar attached to the river bank are common practices in the Brahmaputra River, which is highly braided in nature. Because of the availability of fertile land within the river, people carry on cultivation in such sand bars almost on a regular basis during the period of lean flow. Some of the sand bars have now become almost permanent with well-established vegetation and people have started living in these sand bars. In some cases, people also claim such sand bars as their own land, as they have lost their original land due to river erosion. These forms of river utilization have direct relevance to the concept of demarcating river corridor, as people utilize the land masses located within the bank line of the river. The presence of these forms of river utilization has raised a question as to whether we can really demarcate a river corridor in large braided river and can keep it completely free dedicating the space solely for movement of flow alone. Considering the prevailing practices, we can also think of allowing such activities within the river corridor in a more planed manner by analysing the process scientifically and arranging it in a way that ecological disturbance to the system is minimum. A study carried out on utilization of sand bar [3] of river Brahmaputra is perhaps the first attempt in this direction. While optimal combination of crops for deriving maximum benefit from sand bar cultivation can be decided considering various constraints, impact of such agriculture on the water quality also should be considered with due emphasis. For example, the use of chemical fertilizer should not be allowed in sand bar cultivation and they can affect the aquatic habitat.

River mining is another common exercise of braided river, which changes the river bathymetry. Need of soil for various constructional activities cannot be denied. In developing countries, such activities will continue for many years to come. Collection of river sand is therefore essential for such activities, as the alternative to this at similar cost is the hill cutting, which is far more detrimental to environment and ecology. While the concept of sustainable mining can easily be applied in a small river, quantification of sustainable mining is quite a difficult task in case of braided river. Barman et al. [1] carried out some study to identify best sediment transport equation applicable in mining pit constructed in laboratory using sand of river Brahmaputra. Continuous monitoring of aggradation, degradation, sand bar formation and their washing out is essential for taking a scientifically acceptable decision about sustainable river mining in braided river. With denudation of hills in the upper catchment, sediment influx and subsequent deposition of the same in the river bed is increasing at a faster rate reducing flow carrying capacity of the river with time. Considering this, river mining in a sustainable manner should be permitted in braided river and more research in this direction is necessary to understand sediment dynamics in a better way.

Construction of storage structure or diversion structure to augment river flow is very common in almost all countries. Generally, such structures are not made in the mainstream of large braided river, rather they are made in the tributary of such large braided river. Such tributaries can also take a braided form in its alluvial reach. Operation of such reservoirs can influence the flow and significant flow variation, both

seasonal and diurnal, can be experienced at downstream. Flow variation becomes more significant when the flow from one tributary is diverted and transferred for power production to power house located on the bank of another tributary to have higher head difference. Such river flows through a narrow channel during the period of normal flow, as power release goes to another tributary, and therefore, people start different activities in the free space of the river corridor. In countries having low population density, such river reaches are generally barricaded and no activities are allowed in such segments. However, in a developing country, having high population density, it becomes extremely difficult to regulate and prohibit activities in such river reach. Sensor-based real-time monitoring and coupled reservoir operation and hydrodynamic modelling [2] can help in providing a dynamic warning system to facilitate safe utilization of such otherwise risky corridor of river reach.

4 Scope of Channelizing Braided River

Large braided river generally moves in multiple channels even in the flood period except for the nodal points, where the river covers its full width. Even though the river does not cover the entire width, its banks suffer severe erosion because of existence of active near bank channel. Therefore, to get rid of erosion problem and also to acquire land from such wide braided river, scope of channelizing such river through a designed waterway of smaller width is now in active consideration for troublesome river reach of braided channel. Navigation in braided river is another important aspect, so far management of river corridor is concerned. For maintaining waterway, it becomes necessary to dredge the identified channel to maintain require depth. Channelization can, therefore, help in navigation as well. So far narrowing down of channel width is concerned, it is possible to reduce the width to a much narrow width without increasing the velocity alarmingly. For example, the present width of the Brahmaputra River varies approximately from 2.00 km to 20.00 km. A mathematical model study of Brahmaputra River carried out by us for a length of about 130 km starting from Bhumuraguri near Tezpur to Pandu near Guwahati has shown that the width of the river reach can be reduced to a much smaller width without increasing the velocity significantly. The maximum velocity computed by the hydrodynamic model BRAHMA-2D (Braided River Aid: Hydro-Morphological Analyzer) considering the entire width is 3.65 m/s, which changes to 3.53 m/s, 3.73 m/s and 3.74 m/s for maximum channel width of 5.00 km, 4.00 km and 3.00 km, respectively. Although from the consideration of velocity, channelization appears to be a feasible task, many other socio-economic considerations need to be examined for establishing feasibility from socioeconomic and ecological viewpoint. For example, many small streams flow into the braided river from the nearby areas. People use small boats to move from the interior area to the main river through these small channels. Such connectivity has lots of implications and can affect the livelihood of people. Therefore, any measures taken for augmenting or maintaining river corridor should be done with a detailed investigation.

5 Conclusion

Encroachment into the waterway of river by human beings for various needs has raised a concern among scientific community regarding need of maintaining river corridor. The problem becomes more complex in developing country because of economic need of encroaching into river corridor. Because of the existence of different economic classes and different means of livelihood, high-rise building also may not serve as the ultimate solution to population pressure, at least in near future and therefore, such encroachment into unfavourable habitats like river corridors and hills will continue in a haphazard manner if not planned scientifically. Unplanned urbanization and deforestation in hilly area will also indirectly contribute to the reduction in river corridor space by releasing excessive sediment from the catchment to make the river shallow. With increasing concerns about ecology and water quality, utilizing river corridor for habitation or agricultural activities should also be regulated in a more scientific manner with due emphasis on river ecology. With advancement in the capability of mathematical model and geoinformatics, consequences of various activities mentioned above or impact of any river training work taken up for maintaining river corridor can now be investigated more conveniently. Therefore, we should always take recourse to such technology to utilize the river corridor advantageously without disturbing the river ecology.

References

1. Barman B, Sharma A, Kumar B, Sarma AK (2017) Multiscale characterization of migrating sand wave in mining induced alluvial channel. Ecol Eng 102:199–206. Elsevier
2. Devi D, Baruah A, Sarma AK (2022) Characterization of dam-impacted floods hydrograph and its degree of severity as potential hazard. Nat Hazard. https://doi.org/10.1007/s11069-022-05253-7
3. Talukdar G, Sarma AK, Bhattacharjya RK (2020) Mapping agricultural activities and their temporal variations in the riverine ecosystem of the Brahmaputra River using geospatial techniques. Rem Sens Appl Soc Environ. https://doi.org/10.1016/j.rsase.2020.100423

Some Adverse Effect of Kosi and Farakka Barrages in India

S. K. Mazumder

Abstract Kosi and Farakka barrages were constructed on rivers Kosi and Ganga in the years 1963 and 1971, respectively. During the period 1731–1954, river Kosi had been shifting its course from east to west by a distance of 112 km causing devastating floods in Bihar. Kosi breached its flood embankments both upstream and downstream of the barrage on many occasions resulting in devastation in several districts in Bihar causing loss of life and damage to crops and properties. Similarly, river Ganga has breached its left marginal flood embankment upstream and erosion of right bank downstream of Farakka barrage occasionally causing loss of life and properties, damage of crops in Malda and Murshidabad districts in West Bengal. Author has described some salient features and discussed the adverse impacts of both the barrages on the respective rivers. In this paper, author has made an in-depth analysis of the different causes of the breaches of flood embankments and erosion of river banks resulting in failure of the flood embankments upstream and downstream of Kosi barrage and breaches in left marginal flood embankment upstream and erosion of right bank downstream of Farakka barrage.

Keywords Kosi barrage · Farakka barrage · Flood embankments · Erosion · Energy dissipation

1 Introduction

After a great deal of investigations [2] for selection of site, Kosi and Farakka barrages were constructed on rivers Kosi and Ganga in the years 1963 and 1971, respectively. While Kosi barrage was built to divert flow into eastern and western Kosi canals, purpose of Farakka barrage was to forcefully divert flow from Ganga to Bhagirathi/Hoogly as its offtake at Jangipur was silting up resulting in huge dredging cost for survival of Kolkata port, loss of navigation and water supply. During the period 1731–1954, river Kosi had been shifting its course from east to west by a distance of 112 km

S. K. Mazumder (✉)
Former Delhi College of Engineering (DCE/DTU), Delhi, India
e-mail: somendrak64@gmail.com

S. Dutta and V. Chembolu (eds.), *Recent Development in River Corridor Management*,
Lecture Notes in Civil Engineering 376, https://doi.org/10.1007/978-981-99-4423-1_3

causing devastating floods in Bihar. It was decided to Jacket the river by building flood embankments 144 km on east side and 123 km on west side. Kosi breached its flood embankments on several occasions and 284 number of spurs (Appendix 1) had to be built on either side to save the embankments and to ensure that the barrage is safe and the river does not outflank the barrage. Yet, the river breached the flood embankments both upstream and downstream of the barrage (Appendix 2) on several occasions. Its left embankment got breached in the year 2008 at Kusaha about 15 km upstream of the barrage resulting in devastation in nine districts in Bihar.

River Ganga has also breached its left marginal flood embankment upstream of Farakka barrage occasionally causing loss of life and properties, crop damage in Malda district in West Bengal. Estimated cost of damages due to 1998 flood alone is Rs.1000 crore [15] On the downstream side of Farakka barrage, river Ganga has severely eroded right bank of the river washing out important townships in the district Murshidabad in West Bengal. 76 spurs were built to protect the right bank downstream of the barrage to arrest erosion [6]. These were washed out in the floods and the river is severely threatening the feeder canal, National Highway (NH-34) and Railway connecting Kolkata with North-East of India. 27 spurs that were constructed on the left embankment on east side to protect the flood embankment and train the river up to the barrage were washed out. Yet the river breached the flood embankment 7 times and retired embankments were built 7 times to avoid outflanking of the barrage [11]. Unless the breach is controlled, the river is likely to wash out NH-34, railway line, loss of life and properties and damage to crops. Malda town will be severely affected and utility of the barrage for flow diversion will be lost. Needless to mention that the river training measures that had to be adopted to protect life and properties in a periodic manner involved huge cost. But even then, the measures are found ineffective. In this paper, author discusses the case histories of the Kosi barrage at Bhimnagar on Kosi River and Farakka barrage on Ganga River at Farakka and tries to analyse the different reasons for such devastations brought out post-barrage construction.

2 Some Salient Features of Kosi and Farakka Barrages

Figure 1a, b shows the plan and sectional views of Kosi barrage indicating eastern and western canals and flood embankments. Figure 2a shows a plan view of Farakka barrage illustrating feeder canal, NH-34 and rail lines linking North East with rest of India. While Kosi barrage was constructed to divert flow to eastern and western canals for irrigation and.

hydro-power (Fig. 1a), the purpose of Farakka barrage was to forcefully divert 1135 cumec (40,000 cusec) flow to Bhagirathi/Hoogly River to save Kolkata port, navigability of Hoogly River (National waterways 1 and 2), water supply for Farakka super thermal power plant and municipal water supply to numerous cities/towns on the banks of Hoogly River, which is the lifeline of Kolkata metropolitan city. River link-1 [8] proposed by [18] connecting Brahmaputra with Ganga for transfer of surplus water of Ganga–Brahmaputra basins to the water deficit basins in the south.

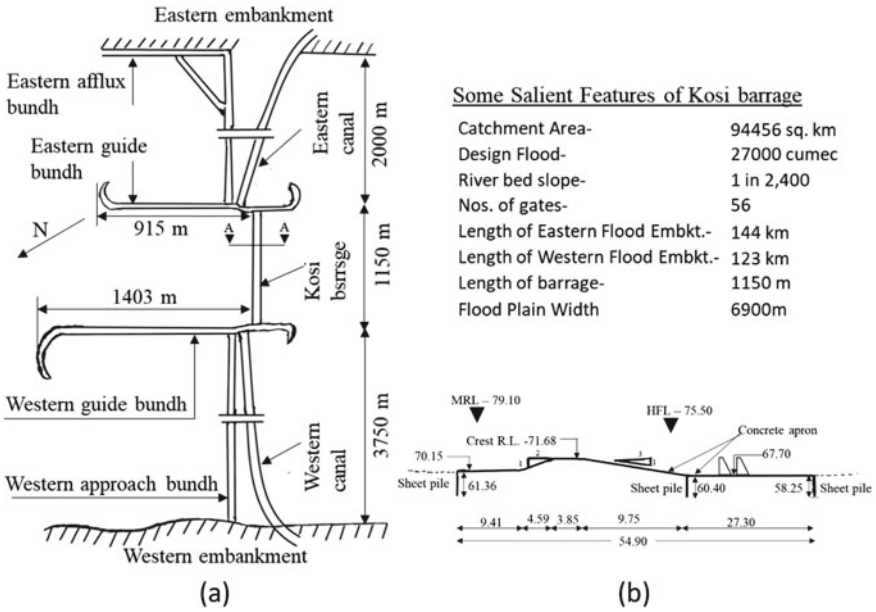

Fig. 1 **a** Plan view of Koshi barrage, **b** sectional (A-A) view of Kosi barrage

3 Case Histories and Purpose of Kosi and Farakka Barrages

River Kosi originates in Tibet and travels 468 km before joining Ganga River at Kursela. Kosi is known to have changed its course across a width of 112 km from east to west during 1731–1954 (Fig. 3) with its appex at Chatra (in Nepal) where it comes down from hills to the plains. In 1946, there was a proposal to construct a 239 m high dam at Barakshtra in Nepal with a storage capacity of 8500 million cubic meter at a cost of Rs.175 crore. But the proposal was dropped by the then British Govt. and a barrage was built at Bhimnagar/Hanuman Nagar in the year 1963 by the Indian Govt. Primary objective of Kosi barrage was to control flooding of Bihar by jacketing it with flood embankments on either side—152 km on eastern side and 123 km on the west—on the flood plain of 6,900 m width having a spillway width of 1190 m as shown in Fig. 1a. Cross-section of the barrage is shown in Fig. 1b. Kosi barrage is used to divert flow through eastern and western canals for irrigation in Bihar and Nepal, respectively. It also helps in generating hydro-power.

Farakka barrage is constructed in the alluvial flood plain of lower Ganga basin where the river has been in a meandering state [7, 9]. In pre-historic days, river Bhagirathi/Hoogly was the main Ganga flowing by the side of Kolkata. Gradually, the main course of parent Ganga (known as Padma in Bangladesh) was shifting towards the east side resulting in silting of its Hoogly off-take on right bank near Jangipur (Fig. 2a) thereby cutting off Hoogly River from upland discharge of Ganga

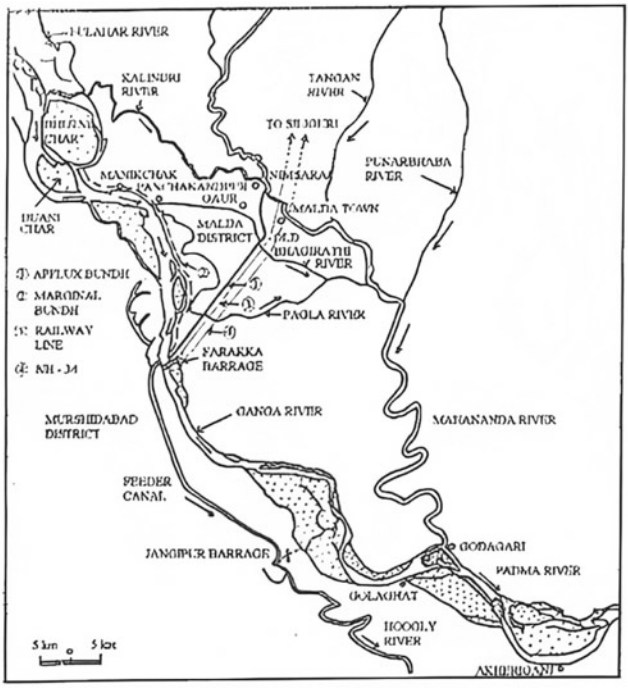

Fig. 2 **a** Plan view of Farakka barrage, Feeder Canal, NH-34 etc. **b** Sectional view of Farakka barrage

during lean flow season. Farakka site in Malda district in West Bengal was selected for the barrage after a prolonged investigation and model study by eminent river engineers like Sir Arthur Cotton from UK, Dr. Hansen from West Germany, Dr. K.L. Rao and Joglekar from India. Farakka barrage was constructed to forcibly divert 1135 cusec flow from Ganga to Hooghly through a 26 km long feeder canal (Fig. 2a) for improving navigability of the river Bhagirathi/Hooghly serving Kolkata port, desalination of water of Hooghly River (a tidal river) for drinking and industrial water supply to Kolkata and other townships on both the banks of Bhagirathi/Hoogly.

Fig. 3 Swinging Kosi River d/s of Chatra (1731–1954)

NTPC super-thermal power project receives cooling water from feeder canal. The broad gauge railway and the National Highway (NH-34), which are important links to north-east India, cross Ganga passing over the barrage. Both National Waterways NW-1(from Prayag to Haldia) and NW-2 (from Sadia to Haldia) meet upstream of Farakka barrage and pass through feeder canal linking Ganga and Brahmaputra rivers with Bhagirathi/Hooghly. Farakka barrage is a nodal point for transfer of surplus flow of Brahmaputra and Ganga basins through the proposed Brahmaputra-Tista-Ganga Link (No.1) under the National perspective plan by [18]. Figure 2a shows the Farakka barrage on Ganga River and Jangipur barrage on river Bhagirathi, Feeder canal, NH-34, railway line and other details. Section of the barrage is shown in Fig. 2b.

4 Some Adverse Impacts of Kosi and Farakka Barrages

Planners of Kosi project did not perhaps anticipate the various problems being faced by the project authorities subsequently. Kosi brings large amount of sediments, which deposits upstream (u/s) of the barrage. It flows in multiple channels u/s of the barrage due to typical delta type formations where the river is unstable and often swings its course. Construction of long impermeable type spurs to channelize the river has resulted in further instability of the river [17] periodically attacking both left and right embankments and causing breach of flood embankments both upstream and downstream of the barrage. A total of 378 number of impermeable spurs—264 on eastern embankment and 114 on western embankment—were constructed (Appendix 1) to save the flood embankments but still the river had been breaching its embankments (Appendix 1). The river caused a 2200 m wide breach of eastern flood embankment

on August 8, 2008 at Kushaha, about 15 km upstream of the barrage, resulting in devastating floods in 13 districts in Bihar (Photo 1). Western Kosi canal passing through Nepal is almost defunct due to heavy sediment deposition. The situation of eastern canal passing through Bihar is also not good due to sediment deposition and its carrying capacity has considerably reduced [4].

Similar to Kosi, there is an occasional breach in the eastern marginal flood embankment u/s of Farakka barrage near Manikchak about 15 km u/s of the barrage. Devastating flood occurred in Malda district in West Bengal (Photo 2). Estimated cost of damages due to 1998 flood alone is Rs.1000 crore. 27 spurs that were constructed on the left embankment on east side to protect the flood embankment and train the river up to the barrage were washed out. Yet the river breached the flood embankment 7 times and retired embankments were built 7 times to avoid outflanking of the barrage [14, 22]. Unless the breach is controlled, the river is likely to wash out NH-34, railway line, loss of life and properties and damage to crops. Severe erosion occurred d/s of Farakka barrage washing out several townships on the right bank of Ganga River in Murshidabad district in West Bengal [21]. 76 spurs and revetments were built to arrest erosion of the right bank downstream of the barrage. These were washed out in the floods and the river is severely threatening the feeder canal, National Highway NH-34 and Railway line connecting Kolkata with North-East of India.

5 In-Depth Analysis of Problems

In India, it is customary to take remedial measures like plugging the breaches that occur in flood embankments and damage due to erosion on war footing unmindful of costs in order to arrest further damages that may be caused by the rivers. There is little effort to understand and analyse the basic causes triggering such events. Author wishes to discuss the basic cause of adverse impact of the Kosi and Farakka barrages in the following paragraphs.

5.1 Analysis of Causes of Breaches in Kosi Barrage

As mentioned before, river Kosi had been swinging like a pendulum [3] with its apex at Barakhsetra/Chapra (Fig. 3). Even after jacketing the river by flood embankments, the river has a tendency to move east and west due to inherent instability of the river attacking both the embankments and causing breaches (Appendix 1, Appendix 2). It would have been perhaps wiser to build a dam at Barakshetra as proposed in 1946. The enormous cost of embankments, spurs and their maintenance could be perhaps avoided [23].

Downstream of Barakshetra, Kosi River has to shed its sediment load since carrying capacity of a mountainous river drastically reduces as per Einstein's [5] bed load theory

Photo 1 Devastating flood in Bihar due to breach in Eastern Embankment in 2018

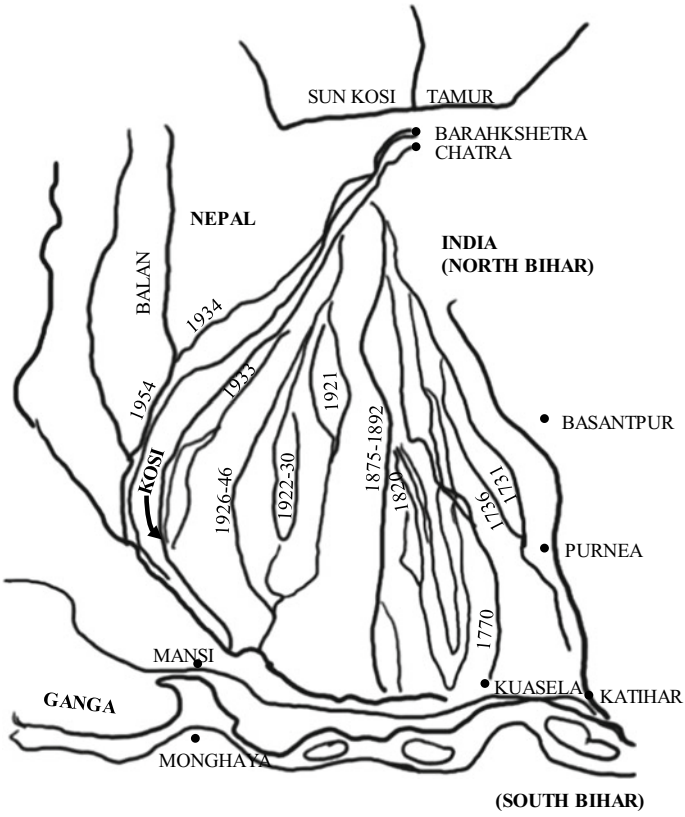

Photo 2 Flood in Malda Town due to breach in Flood Embankment at Manikchak in 1998

$$q_s s_s \propto q^2 s^2 / d^{1.5} \tag{1}$$

where q and q_s are flow of water and sediments per unit width of river; s_s is the specific gravity of sediments, s is the bed slope and d is the sediment diameter. Keeping d, s and s_s constant

$$q_s \propto q^2 \tag{2}$$

q_s being proportional to q^2, sediments must be dropped whenever a narrow mountainous river expands to its flood plain of larger width. Since the flood plain width of Kosi near Bhimnagar/Hanumangar is about 6.9 km, and there is ponding due elevated crest, most of the sediments being carried by Kosi up to Barakshetra get deposited upstream of the barrage. This has resulted in multiple channel formation of Kosi upstream of Kosi barrage.

In the Kusaha breach (2.2 km wide) in August 2008, Kosi had flood discharge substantially less than the design flood. It is reported that nearly 85% incoming flow (4081cusec) was flowing through the left channel hugging the eastern embankment, just before the breach. [11] analysed the cause of the Kusaha breach and found that the embankment failed due to choking of flow in the left channel (hugging the left embankment), as a result of high degree of constriction owing to the presence of a 269 m long spur (at 12.9 km) in the left channel of about 800 m mean width. Choked flow resulted in high degree of instability of flow [10], which attacked the embankment in between spurs at 12.1 km and 12.9 km measured upstream from barrage axis.

5.2 Analysis of Causes of Breaches in Farakka Barrage

River Ganga periodically breaches the left marginal afflux embankment near Manikchak (Figs. 2a and 4). It is due to shifting of river course after the barrage construction as shown in Fig. 4. As mentioned earlier, main course of Ganga had been shifting towards left resulting in siltation near off-take of Bhagirathi/Hooghly River near Jangipur (Fig. 2a). Breaches occurred 7 times near Manikchak and 7 retired embankments were constructed to block the breach as shown in Fig. 5. Prior to construction of Farakka barrage, Bhagirathi and Pagla rivers (near Manikchak) used to divert some flow of Ganga to Mahananda river as shown in Fig. 2a. After the barrage construction, the off-take of these tributaries has been blocked by the afflux embankment near Manikchak. The main Ganga has a tendency to open up these blockages by repeated breaching of the embankment near Manikchak, which lies on the outer bank of the main Ganga after its main course shifted about 7 km towards Malda (Figs. 2a and 4). If the breach continues, Ganga may join Mahananda through the old tributaries bringing devastation to Malda district. Railway line and NH-34 will be washed out and the very purpose of the barrage will be lost.

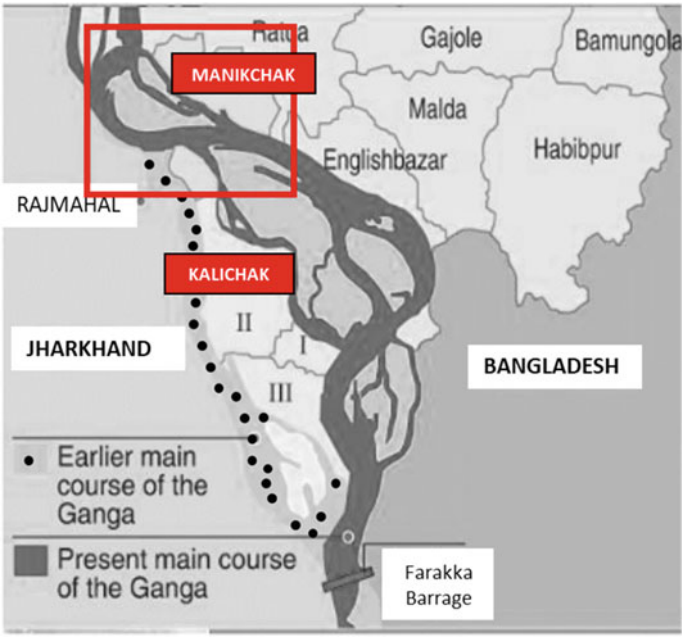

Fig. 4 Shifting Ganga (Blue) u/s of Farakka (1973–2000)

Fig. 5 Retired embankments to close the breach of embankment near Manikchak

5.3 Meandering of Kosi and Ganga Rivers

When a river enters flood plains after its journey in mountains, it flows in a meandering path. Both Kosi and Farakka barrages are built on flood plains and are in meandering state. A natural meander always moves outward (Fig. 6). It also moves along the length at a very small rate compared to its lateral movement in the flood plain [19]. When a barrage is constructed on a meandering river, meander pattern alters with barrage as a fixed point. In case of Farakka Barrage, Malda lies on the outer side of upstream meander and Murshidabad lies on the outer side of downstream meander with Farakka barrage as a fixed point. This has resulted in deep scour as shown in Fig. 7 [20]. With such deep scour near the embankments/spurs, poor shear strength of bed soil (0.15 mm), it is almost impossible to prevent breaching with protective pitching/spurs/porcupines etc. [12].

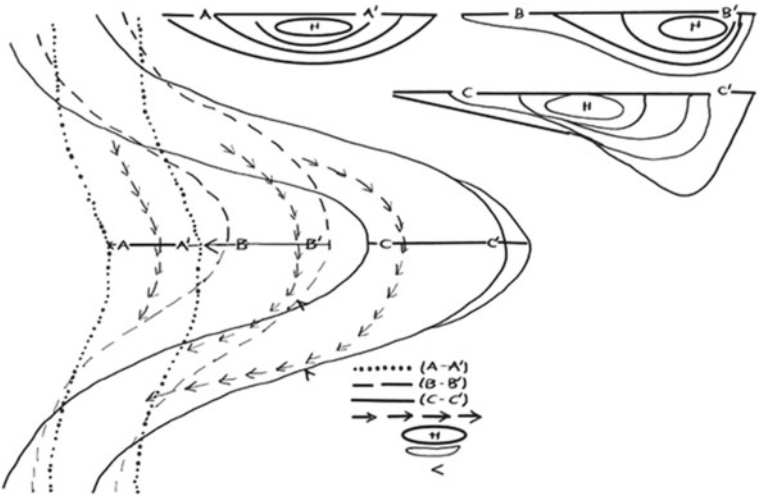

Fig. 6 Flow concentration and scour of outer bank in a meandering river

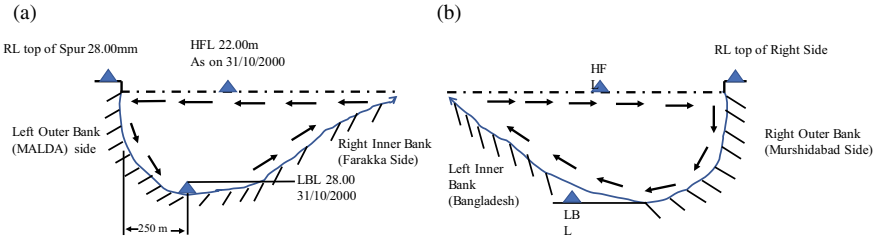

Fig. 7 Typical cross-section of Ganga **a** upstream and **b** downstream of Farakka barrage

5.4 *Inadequate Energy Dissipation and Flow Distortion*

It is reported that deep erosion of banks occurred d/s of both the Kosi and Farakka barrages. Although stilling basins have been provided, the basins are not effective at low inflow pre-jump Froude's no. F_1, which are 2.4 and 1.8 in Kosi and Farakka barrages, respectively. Residual K.E. of flow (Fig. 8) leaving the basin is responsible for flow distortion and wall jet type flow (as illustrated in Fig. 9a, b) since the only way a given flow with a given depth and mean flow velocity can contain the residual energy is by flow distortion either in vertical plain (Fig. 9a) or in horizontal plain (Fig. 9b).

6 Flow Expansion Due to Gate Operation in Barrage

Mode of gate operation for flow release d/s is found to have great importance in scour d/s of a barrage [16]. In a model study on barrage on River Nyle in Egypt, Ahmed et al. [1] studied the effect of expansion ratio (Eq. 3), defined as the ratio between width of gate opening and channel width defined as

$$e = W_g/W_b \tag{3}$$

where, W_g = Waterway under number of gates actually opened and

W_b = Total Waterway in the barrage when all gates are opened.

Average scour depth downstream (d_s) was found to be governed by expansion ratio e. Scour depth $d_s/a_g = 0.24$ when $e = 1.21$ (All gates open) and $d_s/a_g = 2.76$ when $e = 6.12$ (when only one gate open) i.e. 11.5 times more. Here, a_g is height of gate opening above crest of barrage.

Defining average scour depth downstream of barrage as d_s and vertical height of gate opening above barrage crest as a_g, it was observed that $d_s/a_g = 0.24$ for $e = 1.21$. When all gates were opened and $d_s/a_g = 2.76$ for $e = 6.12$. (There were five piers with six gates in the model). Thus, the scour depth was 11.5 times more or percentage increase was 1046%.

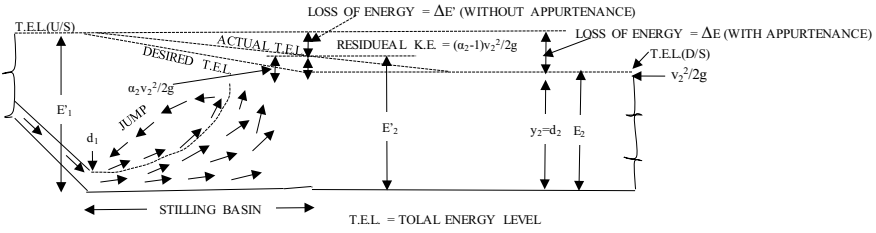

Fig. 8 Showing hydraulic jump, total energy line (TEL) and residual kinetic energy (ΔE-$\Delta E^{/}$) leaving a stilling basin

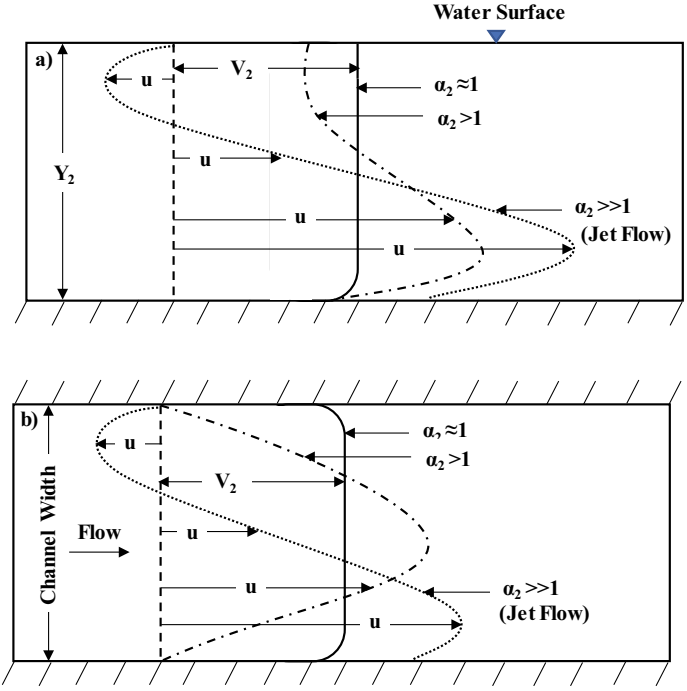

Fig. 9 Showing distortion of flow velocity in a channel D/S of basin due to residual kinetic energy **a** along depth and **b** along width

7 Summary and Conclusions

Long impermeable type spurs should not be constructed as it causes flow concentration. It is not understood why the Govt. is allowing only the conventional measures for controlling erosion again and again inspite of the fact they are not effective. There is no sincere effort to analyse the causes of erosion and adopt other alternative measures of control-both short and long term. As impermeable spurs can not be kept in position, permeable spurs of Ballis or bamboos should be constructed for dampening of flow velocity (i.e. flow intensity) and energy dissipation in microturbulence produced by such permeable spurs. Filter is essential below stone apron to prevent loss of fines both during back flow, seepage and winnowing effect when high flow passes over an area. During launching of mattress, the filter must also launch uniformly. This does not happen. The use of geo filter of proper mesh size (depending on type of material to be protected) is going to more effective both in launching as well as uniformity of pitching. Tarza mat that was used in place of filter requires thorough testing regarding its effectiveness as filter.

Since flow above 26,000 cusec is causing bank erosion. An attempt should be made to divert excess flow through Pagla or other natural or artificial diversion channel bypassing the flow through the barrage. It may also be feasible to construct another

barrage u/s of Rajmahal for diverting excess flow through the Jharkhand state. Shear strength of embankment soil and bank soil may be artificially improved by the use of geo-synthetics, cement–soil grouting, etc. Afforestation of the bank will help in improvement of soil strength. The flow should be diverted through Fulahar side of Ganga by using groins on Rajmahal side or by dredging. Instead of launching apron, an attempt should be made to construct vertical cut-off like sheet piling etc. at the end of apron up to estimated scour depth. Filter being the most important part of pitching, geo-filter should be used in place of tarza mat (for which nothing is known) for continuous launching and uniformity after launching. GI wire crates are not as flexible as Nylon rope nets filled with stones. Such nylon mattresses will be also useful in maintaining uniformity after launching. Since submerged bed spurs cause high flow concentration at head of spurs, it will be desirable to omit it and design the weight of cribs so that these can not be removed by drag. Due to larger size of nylon cribs their combined weight will be sufficient. Otherwise, dagger-type bed spurs may be used to avoid excessive flow concentration at the head. As a long-term measure, dredging has to be commenced near head of pointed bed bars to control growth of bars, consequent meandering and rise in stream curvature. Attempt should be made to measure annual deposition of sediments u/s of barrage [13] since the root cause of the problem is sediment deposition u/s and char formation. Instead of retired embankment, it will be wise to construct arrays of curved submerged vanes as recommended by Odgaard [19].

Appendix 1

Details of Spurs on Kosi Embankments

Embankment	Location	Number of Spurs
Eastern afflux bund	Nepal (upstream of barrage)	60 numbers
Western afflux bund	Nepal (upstream of barrage)	21 numbers
Eastern Embankment	India (downstream of barrage)	204 numbers
Western embankment	Nepal (downstream of barrage)	29 numbers
Western embankment	India (downstream of barrage)	64 numbers

Appendix 2

Summary of Past Breaches in Kosi Flood Embankments

Year	Location of breach	Embankment
1963	Dalwa, Nepal	West Embankment
1968	Jamalpur, Bihar (India)	West Embankment
1971	Matniyaband ha, Bihar	East Embankment
1980	Barharawa, Bihar	East Embankment
1984	Hempur, Bihar	East Embankment
1987	Gandaul and Samani in Bihar	West Embankment
1991	Joginiyan, Nepal	West Embankment
2008	Kusaha, Nepal	East Embankment

References

1. Ahmed L, Basiouni F, Abdel Haleem FS, Nasrallah TH (2020) Scour downstream of submerged parallel radial gates. J Water Energy Int 50–56
2. CBIP (1989) River behaviour, management and training. Central Board of Irrigation and Power, Malcha Marg, Chanakyapuri, New Delhi
3. Chakraborty T et al (2010) Kosi mega fan: historical records, geomorphology and the recent avulsion of the Kosi River). Quatern Int 227(2):143–160
4. Chitale SV (2009) Kosi disaster-caution and pre caution. ISH J Hydraul Eng 15(1):101–107

5. Eoinstein HA (1942) Formulas for transportation of bed load. Trans ASCE 107:561–573
6. Keskar Committee Report (1996) Bank erosion problem of river Ganga-Padma in the districts of Malda and Murshidabad in West Bengal, vol I and II, Planning Commission, Govt. of India
7. Mandal S (2017) Assessing the instability and shifting character of the river bank ganga in Manikchak Diara of Malda district, West Bengal using bank erosion hazard index (Behi), Rs & Gis. Eur J Geogr 8(4):6–25. Association of European Geographers, pp 6–27
8. Mazumder SK (2021) National perspective plan for Ganga-Brahmaputra link-1 for benefit of both India and Bangladesh. J Inst Publ Health Eng (IPHE) Kolkata
9. Mazumder SK (2021) Discussion on the paper assessment of planform changes of the Ganga River from Bhagalpur to Farakka During 1973–2019 using satellite imageries by Chandan Raj and Vivekanand Singh. ISH J Hydraul Eng
10. Mazumder SK (2013) Discussion on the paper "Experimental study on performance of spurs. In: Burele SA, Gupta ID, Singh M, Sharma N, Ahmad Z (eds). ISH J Hydraul Eng 18(3)
11. Mazumder SK (2011) Breaching of flood embankments with particular reference to Kosi & Farakka barrages in India. J Water Energy
12. Mazumder SK (2010) Critical tractive stress in straight and curved channels with non-cohesive soil. ISH J Hydraul Eng 16(2)
13. Mazumder SK (2004) Aggradation/degradation of Ganga near Farakka barrage. In: Proceedings of Seminar on "Silting of Rivers-Problems and Solutions" org. by Min of Water Resources, Govt of India, New Delhi Feb 12–13
14. Mazumder SK (2001) Training of river Ganga near Farakka barrage. In: Proceedings of national conference on hydraulics and water resources HYDRO—2001. Indian Society for Hydraulics (ISH) & CWPRS, Pune, Dec 6–7
15. Mazumder SK (2000) Role of Farakka barrage on the disastrous flood at Malda (West Bengal) in 1998. In Proceedings of 8th ICID international drainage workshop 'role of drainage and challenges of 21st century, vol III, sponsored by ICID—CIID and Min of Water Resources and org by ICD & WAPCOS, New Delhi Jan 31–Feb 4, New Delhi 25
16. Mazumder SK, Sen P (1991) Design, operation and maintenance of diversion structures in alluvial rivers. J Inst Eng 72, Part CV 3
17. Mazumder SK (1985) Effectiveness of impermeable type Groyens in river training with particular reference to river Kosi in India. In: 2nd International conference on "The hydraulics of floods and flood control" org by British Hydromechanics Research Association, Fluid Engineering Centre, Cambridge, England 24–26 Sept
18. NWDA (2005) Water for life. In: 11th National water convention, org. by National Water Development Agency, Govt. of India Delhi, May 11th. 2
19. Odgaard AJ (1986) Meander flow model 1: development. J Hydraul Eng ASCE HY-12, pp 1117–1136
20. Rozovski JL (1957) Flow of water in bends of open channels. Acadamy of Sciences of the Ukranian SSR, Translated in English by Prushansky, Y. Israel Programme of Scentific Translation
21. Rudra K (1996) Problems of river bank erosion along the Ganga in Murshidabad district of West Bengal. Indian J Geogr Environ 1:25–32
22. Rudra K (2000) Will Ganga outflanks the Farakka Barriage? (in Bengali) Desh 58–68
23. Sanyal N (1980) Effect of embankment of River Kosi. In: Proceedings of international workshop on 'alluvial rivers' org by University of Roorkee, March 18–20

A Non-stationary Hydrologic Drought Index Using Large-Scale Climate Indices as Covariates

Arya Sajeev and Subrahmanya Kundapura

Abstract The dry and wet periods can be analyzed based on different drought indices. Most existing drought studies are based on stationary assumptions, and environmental changes are not considered. This study proposes a non-stationary streamflow-based drought index, incorporating large-scale climate indices to study hydrological drought for 45 years. Climate indices are used as covariates for building the non-stationary model fitted to streamflow. Correlation analysis is carried out to determine the best covariates for the streamflow in the Netravati River basin in India. The Southern Oscillation Index (SOI) exhibited a significant influence on streamflow at all time scales. The non-stationary model is compared with the stationary model, and the best model is chosen based on the Akaike information criterion (AIC). Under statistical measures, non-stationary models performed better than stationary ones at all time scales. The generalized additive model for location, scale, and shape (GAMLSS) is used for non-stationary modeling. The models are developed for short-term (3 and 6 months) and long-term (12 and 24 months) droughts. The influence of climate variables on drought classes is analyzed, and more severe drought is observed under the non-stationary scenario. The deficiency in streamflow was more than 60% in the basin in 1987 and 2002. The non-stationary drought index detected more severe drought events than the stationary index under short-term scales. Hydrological drought properties such as drought severity, duration, and peak are calculated under stationary and non-stationary scenarios, and a noticeable difference is observed. Compared to stationary models, the non-stationary model yields more logical and satisfactory findings because it effectively takes into account non-stationarities in the streamflow caused by climate change.

Keywords Stream flow · Drought · Non-stationary · Generalized additive model for location · scale · and shape (GAMLSS) · Stream flow drought index

A. Sajeev (✉) · S. Kundapura
Department of Water Resources and Ocean Engineering, National Institute of Technology, Karnataka, India
e-mail: aryasaji93@gmail.com

S. Kundapura
e-mail: subrahmanyakundapura@nitk.edu.in

S. Dutta and V. Chembolu (eds.), *Recent Development in River Corridor Management*, Lecture Notes in Civil Engineering 376, https://doi.org/10.1007/978-981-99-4423-1_4

1 Introduction

Drought is a complicated natural phenomenon that occurs due to the deficiency in the availability of rainfall, and it is also associated with a deficiency in the runoff, groundwater level, agricultural production, and socio-economic situations [9, 18, 26]. Hydrological drought is related to a deficiency of streamflow [4]. It is represented by using various drought indices such as Streamflow Drought Index (SDI) [15], the Standardized Streamflow index (SSI) [19], Standardized Terrestrial Water Storage Index (SWSI) [28]. The calculation of those indices is based on the stationary assumption, but in the changing climate, non-stationarities in the streamflow cannot be ignored, and stationary indices lead to inaccurate results [12]. Previous research has established the impact of large-scale climate variables on the rainfall pattern in India [1].

Recent research has mostly focused on drought studies using non-stationary indices, like the Non-stationary Standardized Precipitation Index (NSPI) [14], time-dependent Standardized Precipitation Index (SPIt) [24], and non-stationary Reconnaissance Drought Index (RDI_N) [6]. These indices were developed for the analysis of meteorological drought. The hydrological drought is associated with streamflow deficiency, so it is also essential to consider climate change in the hydrological drought index. Because of its simplicity, Standardized Streamflow Index (SSI) has been used by various researchers globally for drought studies [3, 10, 19]. Various researchers examined the influence of the Southern Oscillation Index (SOI) and ENSO index on the Indian climate [1, 2, 27]. In non-stationary modeling, the generalized additive model for location, scale, and shape (GAMLSS) is a widely used algorithm [5, 20, 25].

In terms of the geographical area experiencing drought, Rajasthan is first, with Karnataka coming in second [21]. Most of the droughts were reported in arid regions. Although Dakshina Kannada experiences heavy rain during the monsoon, recent years have reported drought situations throughout the summer [8]. Water scarcity exists due to the extensive expansion of industries during the past two decades. Revadekar et al. [16] examined a declining trend in heavy rainfall along the coastal region of Karnataka in the future. Dakshina Kannada's economic development is significantly influenced by the Netravati River. There is no research on the Netravati River basin's drought conditions. So, it is necessary to study the drought situations in the river basin and to implement necessary water management programs to reduce the water scarcity problems. The primary goal of this research is to create a non-stationary standardized streamflow drought index using climate indices for the Netravati River basin. It is compared with the traditional hydrological drought index. Drought severity, peak, and duration are also calculated and compared under both scenarios.

2 Study Area

2.1 Overview of the Basin

The Netravati River basin covers 3401 km^2 and is chosen as the study area. It originates in the Indian state of Karnataka's Western Ghats and flows west. The basin is situated between 12°30′ N and 13°10′ N latitude and 74°50′ E–75°50′ E longitude. The gauging station of the river is located in Bantwal. The annual average rainfall is 3076 mm, and the temperature is 20–26 °C. The monsoon season begins in June and lasts until September. The water from the river is mainly used for agricultural purposes, and the main crop in the region is paddy. Sandy clay loam and clay loam are the main types of soil found in the region [13]. This river is the primary water source for nearby cities such as Mangalore, Bantwal, Dharmasthala, and Puttur (Fig. 1).

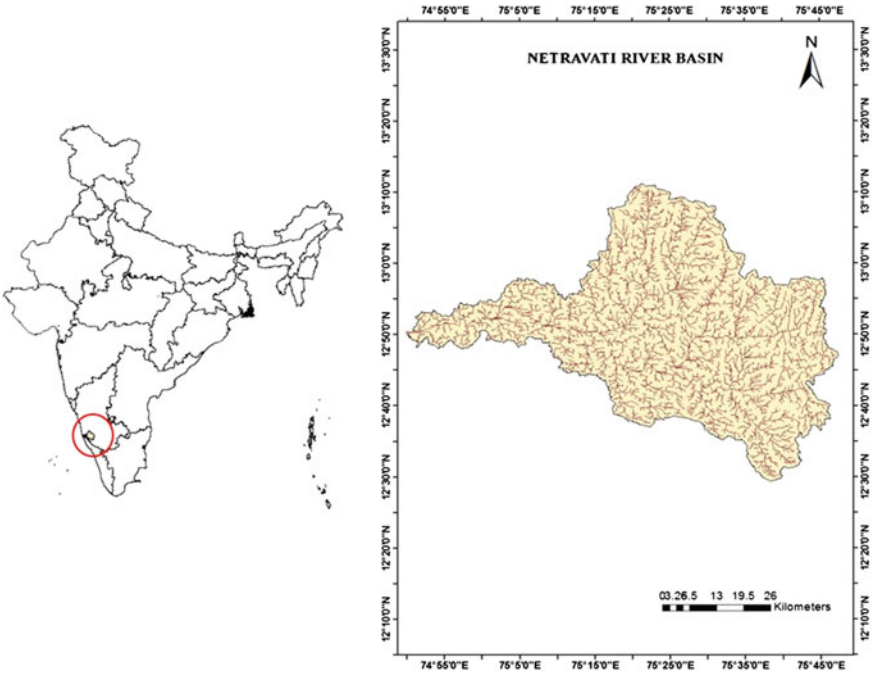

Fig. 1 Location of the Netravati river basin

2.2 Data Used

The monthly streamflow data of the Netravati River are obtained from the Water Resources Information System, India, database (http://www.india.wris.nrsc.gov.in). It is the observed data at the Bantwal River gauging station from 1971 to 2016. The climate indices such as Sea Surface Temperature (SST), Southern Oscillation Index (SOI), and Indian Ocean Dipole (IOD) are obtained for the same period from www.esrl.noaa.gov.

3 Methodology

3.1 Percentage Departure of Streamflow

The streamflow's departure from its long-term mean is measured as a percentage departure in streamflow, and it can be obtained using Eq. (1). Annual and seasonal departure with respect to long-term (45 years) mean values are calculated.

$$Departure(\%) = \frac{y_i - \overline{y}_i}{\overline{y}_i} \times 100 \tag{1}$$

where y_i = streamflow for the season i; and $\overline{y}_i$ = long-term average for the considered period.

3.2 Climate Indices

In this study, three climate variables, such as IOD, SOI, and SST, are taken as covariates for constructing non-stationary models. The streamflow data are arranged to 3-, 6-, 12-, and 24 months time scales. The monthly data of climate indices are arranged to 0–12-month lag. The Kendall correlation test is performed at a 5% significance level to find the best lag of climate data correlated with the streamflow data arranged on different time scales. Different combinations of selected climate indices are also checked to find the best combination for non-stationary modeling.

3.3 Hydrologic Drought Index

This study defines the hydrological drought using the streamflow-based Standardized Streamflow Index, and a new drought index based on climate variables is developed. The SSI is calculated based on the SPI concept. The first step is to identify the

Table 1 Classification of drought

Index values	Class	
$-1 \leq \text{SSI} < 0$	Mild drought	C1
$-1.5 \leq \text{SSI} < -1$	Moderate drought	C2
$-2 \leq \text{SSI} < -1.5$	Severe drought	C3
$\text{SSI} < -2$	Extreme drought	C4

marginal distribution that fits the data the best. For instance, the gamma distribution is selected as the best-fitted probability distribution [3]. The probability density function of a Gamma distribution shape parameter α and scale parameter β is given as:

$$g(x) = \frac{1}{\beta^{\alpha}\Gamma(\alpha)} x^{\alpha-1} \mathrm{e}^{\frac{-x}{\beta}} \tag{2}$$

Its cumulative probability density is given below:

$$F(x) = q + (1-q)G(x) \tag{3}$$

where $G(x)$ is the cumulative distribution function for the non-zero streamflow q is the probability of zero values. The cumulative distribution is then changed to a normal distribution with zero mean value and unit standard deviation to get SSI values. The drought is classified into different categories and is given in Table 1 [23].

3.4 Calculation of the Non-Stationary Index

The generalized additive model for location, scale, and shape (GAMLSS) is used for non-stationary modeling [17]. The non-stationary gamma distribution with linearly varying location parameters is used to calculate the non-stationary Standardized Streamflow Index (NSSI), and it is given as follows:

$$X_t \ \ gamma\,(\mu_t,\ \sigma) \tag{4}$$

$$\mu_t = c_0 + c_1 I_1(t) + c_2 I_2(t) \ldots\ldots\ldots\ldots + c_n I_n(t) \tag{5}$$

where, constants are $c_0, c_1, .., c_n$, and the covariates are $I_1, I_2, .., I_n$ at time t. The parameters are computed using the maximum likelihood approach. NSSI is classified similarly to SSI (Table 1) and can monitor drought events on various time scales.

The stationary and non-stationary indices based on drought properties are calculated. The duration is defined by the number of consecutive months with an index value below the threshold, where the threshold value is typically -1. The severity is

Table 2 Significant lag of climate indices

Climate oscillations	SST	SOI	IOD
Time scale			
3 months	–	9	11
6 months	–	0	–
12 months	2	1	0
24 months	0	1	2

the total of those index values for that duration. Peak is the index's lowest value for that specific period.

4 Results and Discussion

4.1 Significant Lag of Climate Indices

For the time scales of 3, 6, 12, and 24 months, the cumulative streamflow data are calculated. The lag of the climate oscillations ranges from 0 to 12 months. The correlation between streamflow on various time scales and climate oscillation on 0–12 lags was tested using the Kendall correlation method at a significance level of 5%. The significant lag obtained is listed in Table 2. At all time scales, only SOI exhibited a significant influence on streamflow. SST had no significant correlation on streamflow at 3-month and 6-month time scales. Except for the 6-month time scale, IOD showed a significant correlation at all other time scales, and at the 12-month time scale, there was a concurrent association between IOD and streamflow. There was a concurrent association of SST and SOI with the flow at 24- and 6-month time scales, respectively. So, the climate oscillations with significant lag are taken as a covariate for developing a non-stationary index.

4.2 Non-Stationary Drought Index

The gamma distribution is identified to be the best fit for streamflow data in this study. The stationary model is made using gamma distribution with both parameters as constant. For the non-stationary model, the distribution's location parameter is considered to be varied linearly with the selected covariates. Various combinations of climate oscillations at significant lags are tested to find the best model based on AIC values, and the results are tabulated in Table 3. The table also includes the AIC values of stationary and non-stationary models. Combination of SST and IOD was the best for non-stationary models at 12- and 24-month time scales. At all time scales, the AIC values of non-stationary models were less than the stationary models. The

Table 3 Selected covariates and AIC values of models

Time scale	Selected covariates and lag	AIC value of non-stationary	AIC value of stationary
3 months	IOD_{11}	8053.60	8230.86
6 months	SOI_0	9486.72	9592.23
12 months	SST_2, IOD_0	9445.99	9482.70
24 months	SST_0, IOD_2	9774.04	9813.20

Table 4 Equations of Mu and Sigma values

Time scale	Equations
3 months	$\mu(t) = 6.92615–0.29054\ IOD_{11}(t)$ $\sigma = 1.701114$
6 months	$\mu(t) = 7.692151 + 0.007906\ SOI_0(t)$ $\sigma = 1.121142$
12 months	$\mu(t) = 8.36594–0.07928\ SST_2(t) + 0.18086\ IOD_0(t)$ $\sigma = 0.3568845$
24 months	$\mu(t) = 9.06111–0.09120\ SST_0(t) + 0.18638\ IOD_2(t)$ $\sigma = 0.2914951$

non-stationary model is selected as better than the stationary model at all scales based on the statistical measure.

The non-stationary gamma with constant sigma and linearly varying Mu is taken for calculating the non-stationary hydrologic drought index NSSI. The equation of Mu and Sigma is given in Table 4. The distribution parameters are computed using the Maximum Likelihood Estimation (MLE) approach.

4.3 Comparison of Drought Classes

The drought classes, based on the index values based on Table 1, are mild (C1), moderate (C2), severe (C3), and extreme (C4) droughts. Fig. 2 compares and illustrates the frequency of occurrence of various drought classes under stationary and non-stationary conditions. Based on both approaches, C1 has a higher percentage of occurrence at all time scales. C2 has a higher frequency based on non-stationary than stationary index at all scales except 24-months. At all time scales, the occurrence frequency of all types of drought classes for stationary and non-stationary indices varies; hence it can be postulated that climate oscillations influence the drought class in the basin.

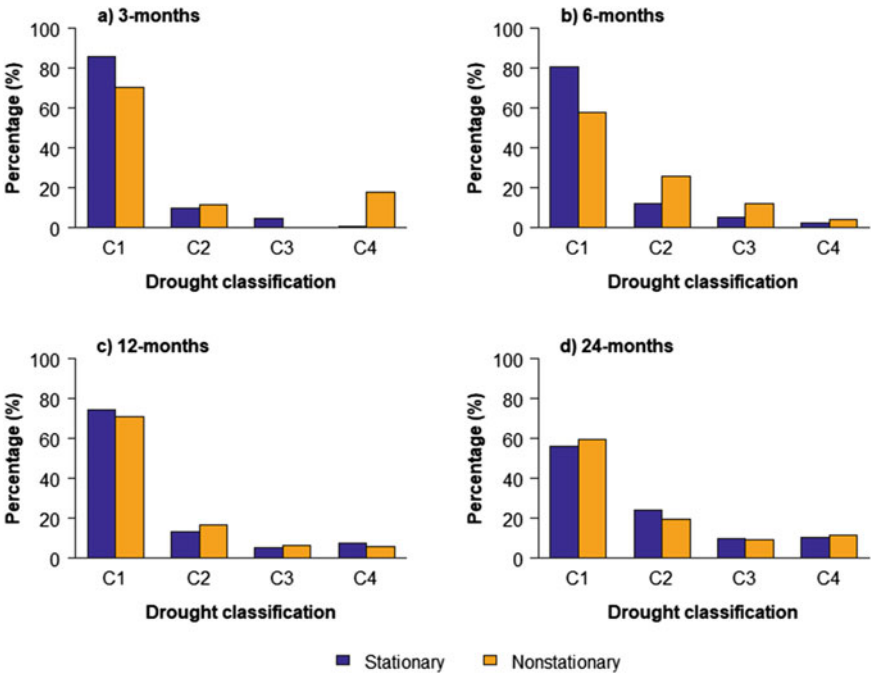

Fig. 2 Percentage occurrence of drought classes

4.4 Comparison of Drought Properties

The peak, severity, and duration of drought events are calculated from SSI and NSSI values, and its statistical characteristics are given in Table 5. The mean duration, severity, and peak values obtained from NSSI are higher than those obtained from SSI at all the time scales except at 12 months. In every case, drought properties under stationary conditions differ from non-stationary conditions. For the comparative study, the density plot of drought duration is also plotted in Fig. 3. At all the time scales, a noticeable difference is observed in the density plots of duration. The density plot for non-stationary is shifted towards the right of the stationary plot at the time scales of 6-month and 12-month. This variation shows the association of climate indices to vary drought properties.

Table 5 Statistical characteristics of drought properties

	SSI			NSSI		
	Duration (in months)	Severity	Peak	Duration (in months)	Severity	Peak
3 months						
Mean	1.71	2.35	1.33	2.38	4.17	1.57
Maximum	4.00	6.85	2.13	4.00	8.80	2.24
Minimum	1.00	1.01	1.01	1.00	1.00	1.00
6 months						
Mean	2.16	3.09	1.35	2.22	3.46	1.88
Maximum	7.00	13.47	2.29	4.00	7.55	3.89
Minimum	1.00	1.00	1.00	1.00	1.00	1.00
12 months						
Mean	9.25	14.17	1.49	5.92	9.12	1.46
Maximum	26.00	41.61	2.30	24.00	40.70	2.50
Minimum	1.00	1.00	1.00	1.00	1.01	1.01
24 months						
Mean	13.62	21.42	1.44	16.00	26.27	1.72
Maximum	48.00	80.31	2.52	49.00	79.13	2.68
Minimum	1.00	1.02	1.02	1.00	1.22	1.17

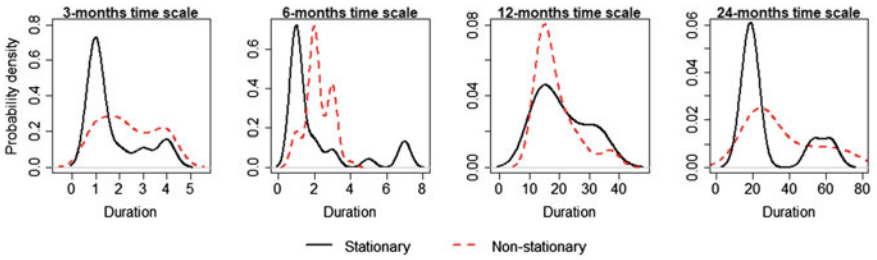

Fig. 3 Probability density of duration

4.5 Departure Analysis of Streamflow and Comparison with Historical Droughts

The annual and seasonal departure of streamflow of the Netravati basin is computed using Eq. (1), plotted in Fig. 4. Cyclic up and down behavior can be observed in the graph. The maximum deficiency observed in seasonal and annual rainfall was 69.68% and 64.37%, respectively, in 2002. In 1987 also, the deficiency was more than 60%. A continuous deficiency was observed in the annual and seasonal flow from 1984 to 1989, 1999 to 2004, and 2011 to 2016. According to the Indian meteorological department, 110% of long-period average seasonal rainfall was obtained in India in

Fig. 4 Annual and seasonal departure of streamflow

1994; hence, excess flow can be observed in the river in the same year. Both stationary and non-stationary indices were plotted and depicted in Fig. 5. The deficiency in the streamflow is the primary reason for hydrological drought in a basin. From Fig. 5, the drought events can be observed during the streamflow deficiency years.

India experienced the worst drought situations in 1917, 1918, 1965, 1966, 1986, 1987, 2002, 2009, and 2012 during the last century [7]. According to previous studies, Karnataka faced severe drought from 2001 to 2004, 2009, and 2012 [11, 22]. In the same years, the deficiency in the streamflow of Netravati can be observed. NSSI also clearly showed the drought conditions during the same period (Fig. 5). The drought events number is higher under short-term compared to longer-duration drought in the basin. Even though Dakshina Kannada receives much rain during the monsoon, recent years have been noted as drought conditions throughout the summer [8]. After 2000, the severity of drought is observed to be increased in the basin, and this is well captured by NSSI than SSI.

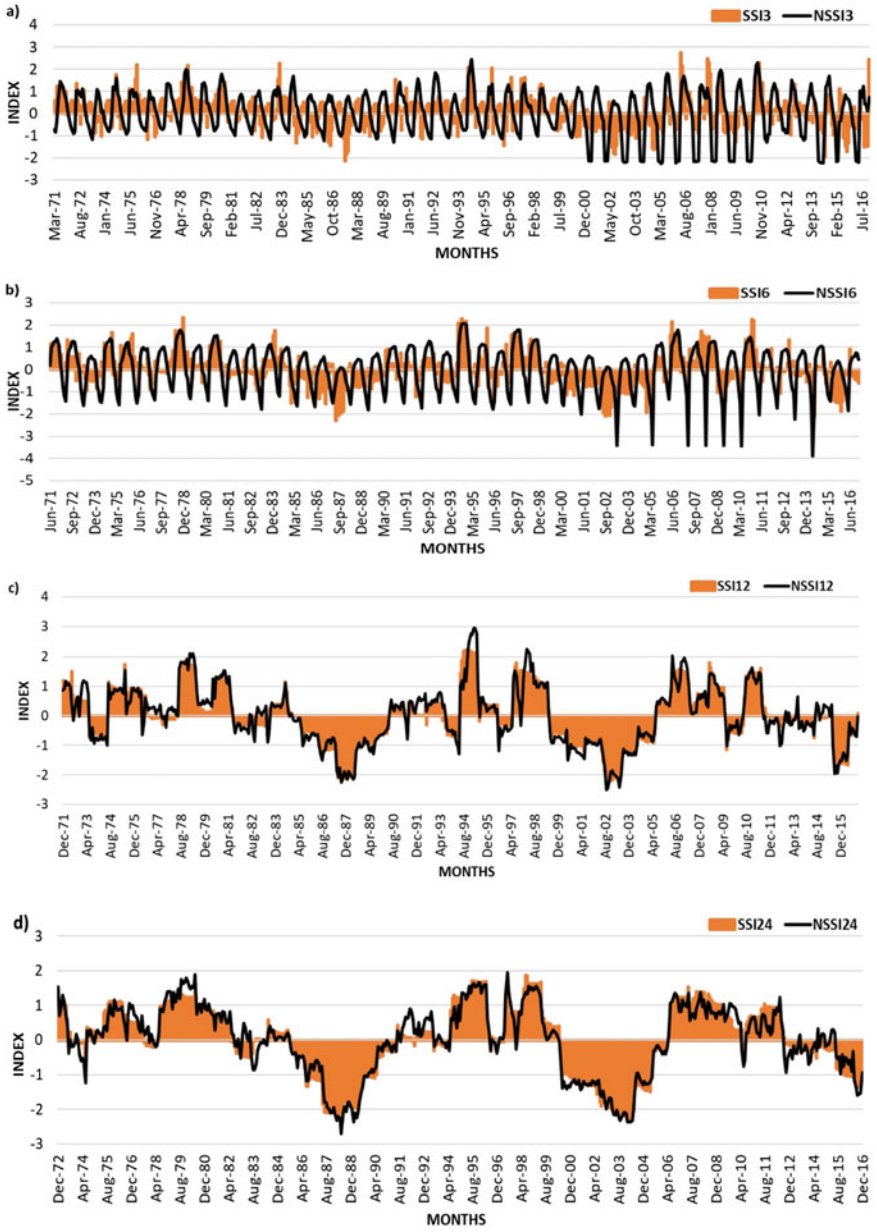

Fig. 5 Stationary and non-stationary indices

5 Conclusion

The streamflow at various time scales significantly correlated with various climate indices with different lags. Hence, the non-stationary models were constructed with the GAMLSS algorithm and compared with the traditional stationary models. From statistical measures, non-stationary models were the best at all the time scales. The influence of climate variables on drought classes, drought properties, and probability density plots was observed. From the comparison of NSSI with streamflow departure and historical drought events, it was found that the NSSI is better than SSI at detecting more severe drought events at short-term scales.

Further analysis based on the non-stationary index will be more helpful in reducing drought risk in the future. The hydrological drought in the basin was the main focus of this study. Many factors other than streamflow lead to drought in a region. Hence, future studies on drought should focus on other types of droughts. In addition, for water resource policymakers to effectively manage water resources, it is crucial to investigate the joint behavior of drought properties and determine the drought return periods in the basin.

Acknowledgements The first author would like to thank the Ministry of Education (MoE), Government of India, for providing Institutional Fellowships to carry out the research.

References

1. Agilan V, Umamahesh NV (2018) El Niño Southern Oscillation cycle indicator for modeling extreme rainfall intensity over India. Ecol Indic 84(Jan): 450–458
2. Ajayamohan RS, Rao SA (2008) Indian ocean dipole modulates the number of extreme rainfall events over India in a warming environment. J Meteorol Soc Jpn 86(1):245–252
3. Botai CM, Botai JO, De Wit JP, Ncongwane KP, Murambadoro M, Barasa PM, Adeola AM (2021) Hydrological drought assessment based on the standardized streamflow index : A case study of the three Cape Provinces of South Africa. Water 13(24):3498
4. Chemeda D, Mukand E, Babel S (2010) Drought analysis in the Awash River Basin, Ethiopia. Water Resour Manage 24:1441–1460
5. Das J, Jha S, Goyal MK (2020) Non-stationary and copula-based approach to assess the drought characteristics encompassing climate indices over the Himalayan states in India. J Hydrol 580(Jan): 124356
6. Das S, Das J, Umamahesh NV (2021) Nonstationary modeling of meteorological droughts: Application to a region in India. J Hydrol Eng 26(2):05020048
7. GOI (2016) Drought Management Manual 1: 154
8. Gowda HCC, Girisha K, Gowda CC (2015) Nethravathi river—water supply scheme in Dakshina Kannada district—a case study. Aquat Procedia 4(Icwrcoe): 625–632
9. Hangshing L, Dabral PP (2018) Multivariate frequency analysis of meteorological drought using copula. Water Resour Manage 32(5):1741–1758
10. Harisuseno D (2020) Comparative study of meteorological and hydrological drought characteristics in the Pekalen River basin, East Java, Indonesia. J Water Land Dev 45:19–41
11. Jayasree V, Venkatesh B (2015) Analysis of rainfall in assessing the drought in semi-arid region of Karnataka State, India. Water Resour Manag 29(15):5613–5630

12. Jehanzaib M, Shah SA, Yoo J, Kim TW (2020) Investigating the impacts of climate change and human activities on hydrological drought using non-stationary approaches. J Hydrol 588(March):125052
13. Kumar R, Eldho STI (2018) Effects of historical and projected land use/cover change on runoff and sediment yield in the Netravati river basin, Western Ghats, India. Environ Earth Sci 77(3):1–19
14. Li JZ, Wang YX, Li SF, Hu R (2015) A nonstationary standardized precipitation index incorporating climate indices as covariates. J Geophys Res 120(23):12082–12095
15. Myronidis D, Ioannou K, Fotakis D, Dörflinger G (2018) Streamflow and hydrological drought trend analysis and forecasting in cyprus. Water Resour Manage 32(5):1759–1776
16. Revadekar JV, Patwardhan SK, Rupa Kumar K (2011) Characteristic features of precipitation extremes over India in the warming scenarios. Adv Meteorol 2011:1–11
17. Rigby RA, Stasinopoulos DM (2005) Generalized additive models for location, scale and shape (with discussion). Appl Stat 54(3):507–554
18. Sajeev A, Deb Barma S, Mahesha A, Shiau J-T (2021) Bivariate drought characterization of two contrasting climatic regions in India using copula. J Irrig Drain Eng 147(3):05020005
19. Shamshirband S, Hashemi S, Salimi H, Asadi E, Shadkani S, Kargar K, Nabipour N, Chau K (2020) Mechanics predicting standardized streamflow index for hydrological drought using machine learning models predicting standardized streamflow index for hydrological drought using. Eng Appl Comput Fluid Mech 14:339–350
20. Shiau J (2020) Effects of gamma-distribution variations on SPI-based stationary and nonstationary drought analyses. Water Resour Manage 34(6):2081–2095
21. Srinivasa Reddy GS, Prabhu CN (2017) Natural disaster monitoring system—Karnataka model 5: 178–187
22. Srinivasareddy GS, Shivakumarnaiklal HS, Keerthy NG, Garag P, Jothi EP, Challa O (2019) Drought vulnerability assessment in Karnataka: Through composite climatic index. Mausam 70(1):159–170
23. Tsakiris ING (2009) Assessment of hydrological drought revisited. Water Resour Manage 23(April 2007): 881–897
24. Wang Y, Li J, Feng P, Hu R (2015) A time-dependent drought index for non-stationary precipitation series. Water Resour Manage 29(15):5631–5647
25. Yu J, Kim T (2019) Future hydrological drought risk assessment based on nonstationary joint drought management index. Water 11(3):532
26. Zhang J, Lin X, Zhao Y, Hong Y (2017) Encounter risk analysis of rainfall and reference crop evapotranspiration in the irrigation district. J Hydrol 552:62–69
27. Zhang Q, Li J, Singh VP, Xu CY, Deng J (2013) Influence of ENSO on precipitation in the East River basin, south China. J Geophys Res Atmos 118(5):2207–2219
28. Zhu N, Xu J, Zeng G, Cao X (2021) Spatiotemporal response of hydrological drought to meteorological drought on multi-time scales concerning endorheic basin. Int J Environ Res Public Health 18(17):9074

Tectonism and Drainage Responses: Insights from the Siang River Basin

M. Uma Narayan, Rishikesh Bharti, and Archana M. Nair

Abstract Siang River, the upstream subbasin of the mighty Brahmaputra in north-east India, enters the Indian territory from the Tibetan plateau through the Namche Barwa massif carrying the footprints of tectonic perturbations. This study uses morphometric, morphotectonic and profile analyses of the Siang basin to quantify the landscape responses to tectonics and spatiotemporal variability in the responses. The tectonic imprints on the river basin's morphological characteristics were studied using SRTM DEM-based morphometric analysis and geomorphic indices. The hypsometric integral ('H.I'), asymmetry ratio ('A_f') and stream length gradient index ('S.L') are to mention a few morphotectonic parameters analysed in this study. The higher asymmetry value with the sigmoidal to slightly convex up hypsometric curve of the Siang River indicates an unstable tectonic setting of the river basin. An increasing trend for the 'S.L' index is visible along the upstream Siang River. The gradient changes with sharp elevation differences were evident from the river's long profile. The 'chi' plot displays disequilibrium from the steady state, as diversions from linearity, indicating an imbalance between the rate of erosion and upliftment at the upstream reach of the river. These drainage responses of the Siang basin can be attributed as typical landscape responses to the ongoing upliftment and the active tectonics of the area.

Keywords Active tectonics · Morphotectonic analysis · Geomorphic indices · Fluvial responses

1 Introduction

Quantitative morphological studies bestow a better perception of the active deformation of an area. The diversity in landforms within a given area is often related to landscape responses to tectonic forcing [10, 12, 15]. Such techniques can quantify

M. Uma Narayan · R. Bharti · A. M. Nair (✉)
Earth System Science and Engineering, Department of Civil Engineering, Indian Institute of Technology Guwahati, Assam, India
e-mail: nair.archana@iitg.ac.in

S. Dutta and V. Chembolu (eds.), *Recent Development in River Corridor Management*, Lecture Notes in Civil Engineering 376, https://doi.org/10.1007/978-981-99-4423-1_5

the spatiotemporal variability in a region's tectonic upliftment rate [22]. Systematic methodologies using GIS and high-resolution remote sensing data enable the quantitative analysis of landscape deformations and erosions with high precision [12, 19]. The earlier notions prove that the topography contains information about the spatial and temporal changes due to differential uplift and associated tectonic deformations [9, 14, 25]. The rivers respond to tectonic deformation through erosion, sedimentation and deposition [16]. Any tectonic activity can increase a river's gradient and hydraulic energy, resulting in increased sediment deposition in the mountain front [33]. Extreme mass flow events and climatic factors create the present longitudinal and transient river profiles [8, 42]. The current planar features of a river system guide the past drainage characteristics and the tectonic events that have shaped the fluvial morphology. Thus, drainage network analysis can provide insight into the landscape evolutionary pattern of the area [16]. Analysing the river characteristics using geomorphic parameters explains the equilibrium between tectonic upliftment and surface erosion [6].

The Siang River belongs to the seismically active Brahmaputra valley of northeast India. Originated in Tibet as Yarlung Tsangpo, the river makes a horseshoe-shaped bend around the Namche Barwa Grand Canyon and Giala Peri ranges before entering the Arunachal Pradesh as Siang [7, 13, 29, 33]. Thereafter, the river flows southward to join the Dibang and Lohit Rivers and follows a southwestern course as the Brahmaputra River [29]. High exhumation rates of Himalayan ranges have resulted in a massive influx of sediments into the drainage area [11, 34]. Other distinct features like braiding pattern, anabranching, bank line shift, paleochannels, and records of past megafloods indicate the coupling between exogenous and endogenous processes [4, 5, 28, 29].

In this study, the morphotectonic analysis of the Siang River is carried out using GIS and remote sensing techniques. Siang River belongs to a tectonically unstable area of northeast India. These studies establish the relation between uplift and erosion by quantifying the drainage characteristics. The geomorphic indices analysed include the bifurcation ratio (R_b), asymmetry factor (A_f), Hypsometric Integral (H.I) and Stream length Gradient index (S.L). Further, the interpretation of the river profile helps to establish the influence of various tectonic elements on the drainage characteristics.

2 Study Area

The Brahmaputra Valley, of which the Siang River shares a major part, belongs to a seismically active converging zone. The movement and subduction of the Indian Plate with the Burmese Plate and the Eurasian Plate account for the formation of the Himalayas, leaving the region highly unstable [2, 41]. The V-shaped Siang valley, located south of the Eastern Himalayan Syntaxis, undergoes a sudden change in slope descending from the Tsangpo gorges (Fig. 1). The prominent rock types include metamorphosed Eocene phyllite–schist–limestone–quartzite [4].

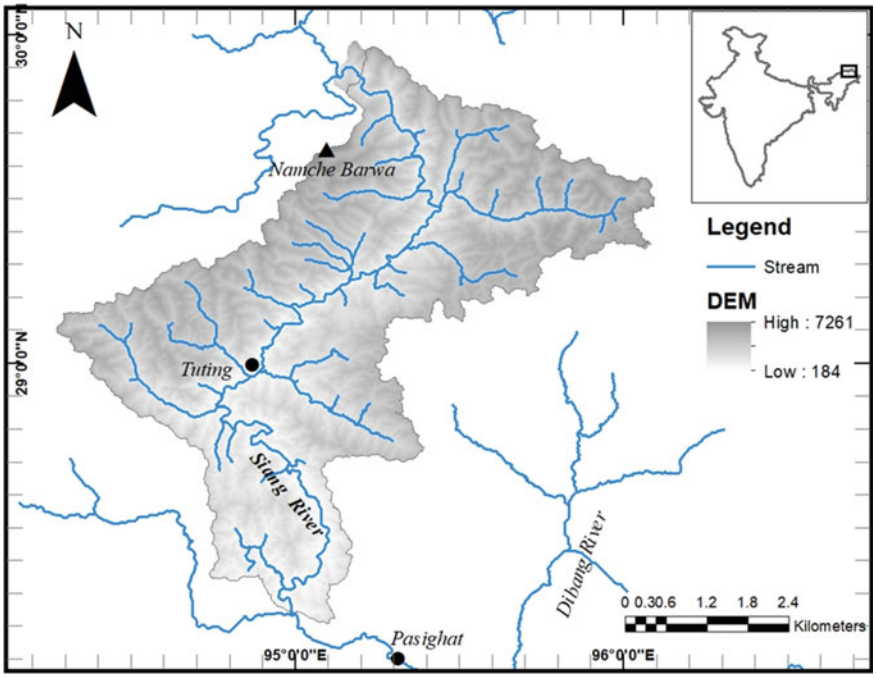

Fig. 1 The DEM of the Siang River basin *(Source*: SRTM) with major tributaries and important locations. The study area location is presented on the top right-hand side

The area has witnessed some of the continent's great earthquakes, like the 1897-Shilong earthquake and the 1950-Assam earthquake. [3, 27]. The influence of Himalayan orogeny, the rapidly uplifting mountains and the movement of alluvial deposits make the Brahmaputra River a young, active, and exceptionally massive river with colossal discharge [37]. The Main Central Thrust (MCT) and Main Boundary Thrust (MBT) form the two major tectonic domains in Eastern Himalayas. The MCT marks a separation between two topographically different zones—the southern Lesser Himalayas and the northern Higher Himalayas. The sub-Himalayan and lesser Himalayan zones are primarily separated by the MBT, showing some high-intensity seismic activities [38]. The Tidding Suture, N.W.–S.E. trending tectonic lineament, spots the borderline between the Indian and Central Burmese plates. The Lohit Thrust is a tectonic plane between the Tidding Formation and Mishmi granodiorite. The Po Chu Fault is a major fault lying to the northeast of the Lohit Thrust. The Assam syntaxis zone, where the Himalayan arc and the Burmese arc intersect the Mishmi block, is considered the source of the 1950 great earthquake. Two major thrust faults, Lohit and Mishmi thrusts, are active at the two ends of this syntaxis and this area [26, 38].

3 Methodology

The present study advocates the techniques of remote sensing, and GIS aims to quantify the prevailing neotectonic features of the region. Using ArcGIS, the Shuttle Radar Topography Mission (SRTM) digital elevation model (DEM) with 90 m resolution can be made seamless by filling the voids and further employed to extract the flow accumulation grid. Later, the DEM was subjected to the calculation of various morphometric and morphotectonic parameters like Bifurcation ratio ('R_b'), Hypsometric Integral ('H.I'), Asymmetry Factor ('A_f') and Stream-length gradient index ('S.L'). These indices are excellent geomorphic tools for assessing the tectonic activity of the area. The TopoTool box in MATLAB advocated the profile analysis to investigate the variations in tectonic forcing along the river.

3.1 Morphometric Parameters

3.1.1 Bifurcation Ratio

The ratio between the stream number in a particular order ('N_u') with the stream number in the consecutive higher order ('N_{u+1}') gives the bifurcation ratio ('R_b'). It gives an insight into the relief of the area and dissection of the drainage system [17]:

$$R_b = \frac{N_u}{N_{u+1}} \tag{1}$$

The bifurcation ratio varies with different orders and environments depending upon the lithological and tectonic setting of the area [36]. Using the method of stream order by Strahler [36], the arithmetic mean of the bifurcation ratio for each subbasin can be calculated. The higher bifurcation ratio indicates the presence of any tectonic activity or structural distortion.

3.1.2 Basin Asymmetry Factor ('A_f')

The tectonic tilting of an area is often evaluated using the Basin Asymmetry factor ('A_f'), given by

$$A_f = \left(A_r / A_t\right) 100 \tag{2}$$

As it is a ratio between the basin area to the right of the main channel ('A_r') and the total area ('A_t'), it accounts for stability in an area's tectonic setting. When there is an equilibrium between the forces acting, the value should be equal to 50. A

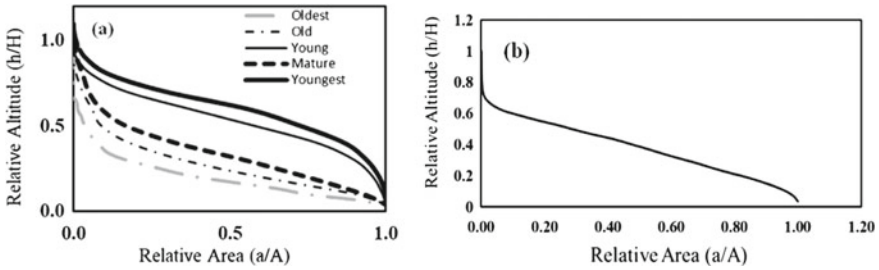

Fig. 2 **a** The schematic representation of the hypsometric curve of different evolutionary stages. **b** The hypsometric curve of the Siang River, A is the total surface area of the basin, and H is the highest elevation, a is the basin area for a given elevation h

variation in 'A_f' from the neutral value 50 denotes the asymmetric basin. It is clear from Eq. (2) that the basin tilting towards the left tends to have a higher value [21].

3.1.3 The Hypsometric Curve and the Hypsometric Integral

Hypsometry determines the basin developmental stage. It gives the elevation-wise distribution of the basin area [31, 36]. The area under the hypsometric curve denotes the uneroded segment of the river basin [21].

$$HI = \frac{(Average\ Elevation - Minimum\ Elevation)}{(Maximum\ Elevation - Minimum\ Elevation)} \tag{3}$$

Convex curves and high 'H.I' values denote the young stage. S-shaped and concave curves with low 'H.I' values denote mature and old stages [36]. Figure 2(a) shows the schematic representation of the Hypsometric curve.

3.1.4 Stream Length Gradient Index ('S.L')

The 'SL' index gives an insight into the hydraulic capacity of a river to transport its sediments and erode the basin [6]. The stream length gradient index is given by

$$S.L = \left(\Delta h / \Delta l\right) l \tag{4}$$

where l is the channel length, and $\Delta h/\Delta l$ is the slope of the channel. It gives an idea of the rock resistance of the area [14]. The 'S.L' index can have a high value while flowing through an area of uplift and low values in the valleys [20].

3.2 Profile Analysis

In a tectonically active area, the river profiles adjust to balance uplift and erosion [18]. Hence river longitudinal profiles can be analysed to deduce the spatio-temporal variability due to the tectonic forcing of a region [39, 40]. Investigating the longitudinal river profile gives an insight into the factors affecting the fluvial landscapes [22, 39]. An equilibrium between the erosion and the uplift shows a smooth concave upward river profile. Deviations from the concave upward profile can be associated with tectonic perturbations or lithological control. The changes in the rock uplift rate can create a disequilibrium in response to which there can be deviations in the river profile. The location of abrupt changes in the elevation along the profile is called knickpoints. The reasons for the formation of the knickpoints can be tectonic uplift, active faults and lithological control.

The longitudinal variations of the drainage area are analysed in an alternate way using integral transformation of the horizontal component of the stream power incision model into a variable called 'χ' (Chi). The initial step is to identify the steady-state channels. For this, a series of 'χ' values were calculated for each '*m/n*' value varying from zero to one. Then, regression analysis of elevation with variation Chi ('χ') is performed to determine the 'R^2'. Finally, a plot of '*m/n*' and 'R^2' is made to find the best-fit '*m/n*' value [26].

4 Results and Discussion

Various morphometric parameters used to analyse an area's topography and drainage responses from the erosional and depositional landscape feature aid in quantifying the disequilibrium reminiscence [15].

4.1 Morphotectonic Analysis

The morphotectonic analysis of the Siang basin was performed quantitatively by calculating the different geomorphic parameters. The segmentation of the drainage network into different hierarchical orders of the Siang River resulted in the highest stream order of 5 [36]. The bifurcation ratio for a typical drainage basin ranges from 3 to 4. However, for the Siang basin, this is calculated as 4.6 (Table 1), indicating the presence of some drainage distortions. The influence of external tectonic force is evident from these observations.

Table 1 The morphotectonic parameters of the Siang River estimated in this study

Morphometric indices	Highest stream order	Mean R_b	A_f	Average H.I
Siang	5	4.6	54	0.5

4.1.1 Basin Asymmetry Factor ('A_f')

The ('A_f') value gives an idea about the tectonic tilting of a drainage basin in response to tectonics or lithology. The value tends to be 50 under stable conditions. A higher value indicates tilting. An asymmetry factor of 54 for the Siang basin indicates the absence of tilting. However, the presence of an asymmetry in the basin topography cannot be dismissed.

4.1.2 Hypsometric Curve and Hypsometric Integral

Hypsometric Curve gives the distribution of the basin area at different elevations. It helps in picturing the basins' developmental stages (Fig. 2(a)) [31, 36]. A plot between altitude and basin area represents it. The hypsometric curve of the Siang River shows a sigmoidal-convex-up plot indicating comparatively less erosion than uplift (Fig. 2(b)). An average hypsometric integral of H.I = 0.5 depicts a young stage with active tectonics. The shape of the hypsometric curve cogitates the predominant geomorphic process. A convex curve of the Siang River indicates that most of the drainage area is held at higher elevations (Fig. 3). Hill slope processes such as landslide and soil creep are prominent in such cases [9].

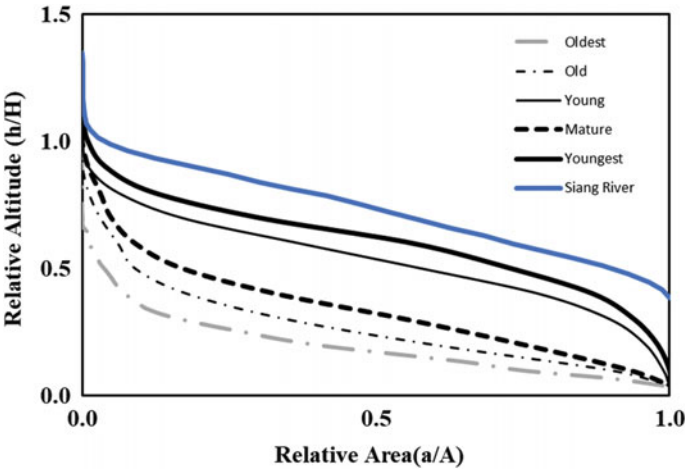

Fig. 3 Normalised hypsometric curve showing the position of the developmental stage of the Siang basin. The original plot has been offset by a scale of 0.35 units for better visualisation

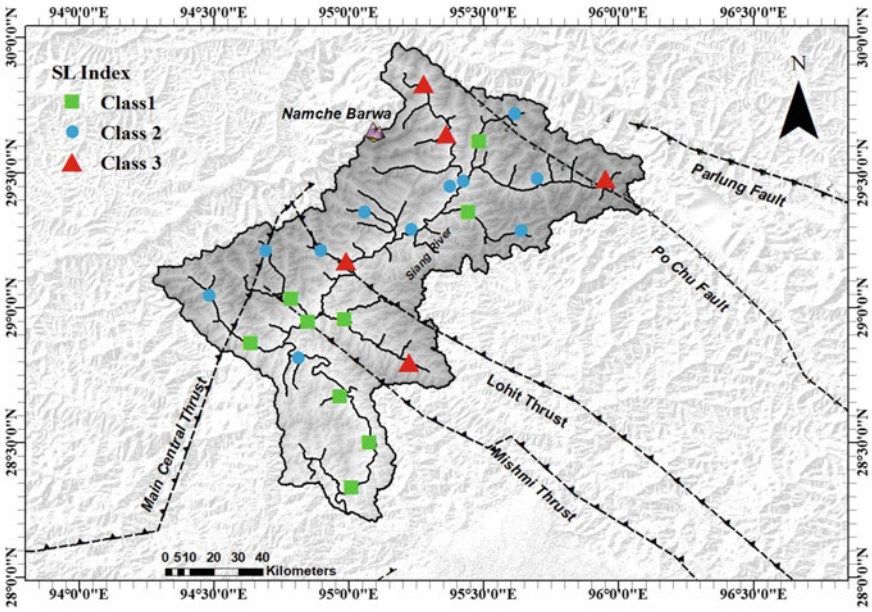

Fig. 4 The stream length gradient index of the Siang basin plotted along the locations with the most prominent tectonic elements

4.1.3 Stream Length Gradient Index ('S.L')

The 'S.L' index gives an insight into rock resistance [14]. It can have a high value while flowing through an area of uplift and low values in the valleys [21]. It also gives an insight into the hydraulic capacity of a river to transport its sediments and erodes the basin [6]. Uplift zones show relatively high 'S.L' values. It is an important tool in identifying the neotectonic activities of the basin. In this analysis, the streams were segregated into different contours of equal interval. The drainage response of the Siang.

The high 'S.L' values reveal the ongoing tectonics as the river pass by the Namche Barwa massif (Fig. 4). Towards the northwest end of the Lohit thrust, the Siang River shows an abruptly high 'S.L' value (Fig. 4), signifying the gradient variations imposed by the active Lohit thrust on the Siang River.

4.2 Profile Analysis

The 'long profile' is representative of the spatial and temporal uplift patterns. The entire morphology of the river channel represents tectonic activity with abrupt gradient changes known as 'knickpoints' [1, 22]. The gradient changes along the river

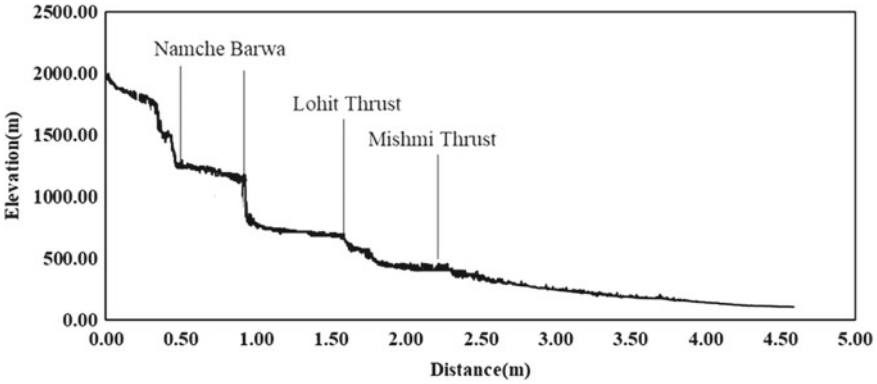

Fig. 5 Longitudinal profile of the Siang River. The knick points are mapped at the disequilibrium locations caused by the major tectonic elements

profile can be assumed to indicate uplift along with the various tectonic elements of the region. The ongoing tectonic activities of the Himalayan ranges are evident from the long profile of the Siang River (Fig. 5). The abrupt variation in the river profile can be seen where the river carves around the Namche Barwa Massif (Fig. 5). Lohit thrust has also induced variations along with the Siang River profile. The locations' knickpoints coincide with the S.L. index anomalies through the basin, especially along the major tectonic elements (Fig. 5).

The Chi ('χ') plot was created using MATLAB software from the DEM data. At first, the DEM was processed, and the flow direction, stream network and drainage area were extracted. To determine the 'χ', a series of concavity values, '*m/n*', were selected. The good-fit value of the '*m/n*' ratio is taken to be 0.48. The drainage shift seen above the steady-state trend on a 'χ' plot can be ascribed to the dominance of erosion over the tectonic uplift, whereas the migration below the trend is due to the dominance of tectonic uplift than erosion [25]. The 'χ' plots of the Siang River rivers were seen diverting from linearity, showing disequilibrium. This divergence can be due to tectonics or lithology. The 'χ' plot reveals that the Siang River shows an erosion-dominated landscape in the lower reaches and a tectonic-dominated landscape in the upstream area (Fig. 6).

5 Conclusions

Landscape responses to active tectonics can be characterised by analysing the morphology of an area. Morphotectonic indices are established as a convenient and valuable method to elucidate the tectonic characteristics of an area. The current study

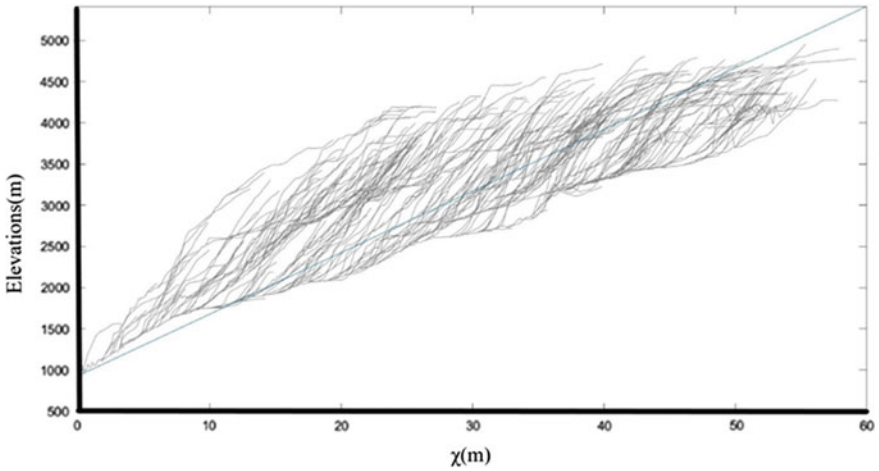

Fig. 6 The variations Chi(χ) with elevations with respect to the steady state line at an *m/n* ratio of 0.48. The transient stream migration seen above the steady-state line indicates an increased erosion compared to tectonic uplift, whereas a channel below the steady-state trend is due to enhanced tectonic uplift with less erosion [25]. The Siang River shows an uplift-dominated characteristic at higher elevations and erosional dominance at the lower reaches

quantifies the transient drainage responses of the Siang River basin with the aid of geomorphic parameters. The conclusions are as follows.

- The Siang Valley belongs to a seismically active converging zone. The transient drainage responses of the Siang basin foreshow the quaternary tectonism. The topography seems to be still adjusting to the disequilibrium caused by the tectonic forcing and associated movements.
- The Siang River basin displays a highly asymmetric nature. A convex-up hypsometric curve stipulates the young stage of the Siang River basin, which is typical of a tectonically active landscape. The stream length gradient index displays an increasing trend upstream of the Siang River. The high 'S.L' values at the upstream river can indicate the influence of ongoing tectonics of the Namche Barwa massif.
- The analysis of the river profile shows an abrupt variation as the river carves around the Namche Barwa Massif. As the river displays rapid gradient changes at Lohit and Mishmi faults, both can be considered active faults.
- Diversion from linearity in the 'χ' plot suggests an imbalance in the erosional and upliftment rates. The higher reaches of the river exhibit an uplift dominant landscape.

These studies help understand the morphological features and drainage responses induced by tectonic forcing. The results can be valuable input in the challenging river engineering and management field.

References

1. Ambili V, Narayana AC (2014) Tectonic effects on the longitudinal profiles of the Chaliyar River and its tributaries, southwest India. Geomorphology 217:37–47
2. Angelier J, Baruah S (2009) Seismotectonics in Northeast India: A stress analysis of focal mechanism solutions of earthquakes and its kinematic implications. Geophys J Int 178:303–326
3. Bilham R, England P (2001) Plateau Pop-up during the 1897 Assam earthquake. Nature 410:806–809
4. Borgohain B, Mathew G, Chauhan N, Jain V, Singhvi AK (2020) Evidence of episodically accelerated denudation on the Namche Barwa massif by megafloods. Quat Sci Rev
5. Bracciali L, Najman Y, Parrish RR, Akhter SH, Millar I (2015) The Brahmaputra tale of tectonics and erosion: Early Miocene river capture in the Eastern Himalaya. Earth Planet Sci Lett 415:25–37
6. Burbank DW, Anderson RS (2012) Tectonic geomorphology. Wiley-Blackwell
7. Burg JP, Nievergelt P, Oberli F, Seward D, Davy P, Maurin JC, Diao Z, Meier M (1998) The Namche Barwa syntaxis: evidence for exhumation related to compressional crustal folding. J Asian Earth Sci 16(2–3):239–252
8. Clark MK, Schoenbohm LM, Royden LH, Whipple KX, Burchfiel BC, Zhang X, Tang W, Wang E, Chen L (2004) Surface uplift, tectonics, and erosion of eastern Tibet from large-scale drainage patterns. Tectonics 3
9. Davis WM (1899) The geographical cycle. Geogr J 14:481–504
10. Donnaloia M, Giachetta E, Capolongo D, Pennetta L (2019) Evolution of fluviokarst canyons in response to the Quaternary tectonic uplift of the Apulia Carbonate Platform (southern Italy): Insights from morphometric analysis of drainage basins. Geomorphology 336:18–30
11. Enkelmann E, Ehlers TA, Zeitler PK, Hallet B (2011) Denudation of the Namche Barwa antiform, Eastern Himalaya. Earth Planet Sci Lett 307:323–333
12. Gioia D, Schiattarella M, Mattei M, Nico G (2011) Quantitative morphotectonics of the Pliocene to Quaternary Auletta basin, Southern Italy. Geomorphology 134:326–343
13. Goswami DC (1985) Brahmaputra river, Assam, India: physiography, basin denudation, and channel aggradation. Water Resour Res 21:959–978. https://doi.org/10.1029/WR021i007p00959
14. Hack JT (1973) Stream-profile analysis and stream-gradient index. J Res US Geol Surv
15. El Hamdouni R, Irigaray C, Fernández T, Chacón J, Keller EA (2008) Assessment of relative active tectonics, southwest border of the Sierra Nevada (southern Spain). Geomorphology 96:150–173
16. Holbrook J, Schumm SA (1999) Geomorphic and Sedimentary response of rivers to tectonic deformation: a brief review and critique of a tool for recognising subtle epeirogenic deformation in modern and ancient settings. Tectonophysics 287–306
17. Horton R, E. (1945) Erosional development of streams and their drainage basins, hydrophysical approach to quantitative morphology. Bull Geo Soc Am 56:275–370
18. Howard A D (1994) A detachment limited model of drainage-basin evolution. Water Resour Res 30(7):2261–2285
19. Jordan G, Meijninger BML, van Hinsbergen DJJ, Meulenkamp JE, van Dijk PM (2005) Extraction of morphotectonic features from Dems: Development and applications for study areas in Hungary and N.W. Greece. Int J Appl Earth Obs Geoinf 7:163–182
20. Keller EA (1986) Investigation of active tectonics: Use of surficial Earth processes. In: Keller EA, Pinter N (eds) 2002 Active tectonics, earthquakes, uplift and landscape, 2nd edn. Prentice Hall, Upper Saddle River
21. Keller EA, Pinter N (2002) Active tectonics, earthquakes, uplift and landscape, 2nd edn. Prentice Hall, Upper Saddle River
22. Kirby LC, KX Whipple (2001) Quantifying differential rock uplift rates via stream profile analysis. Geology 29:415–418
23. Kirby E, Whipple KX (2012) Expression of active tectonics in Erosional landscapes. J Struct Geol 54–75

24. Penck W (1953) Morphological analysis of land forms. Macmillan and Co., Limited
25. Perron JT, Royden L (2013) An integral approach to bedrock river profile analysis. Earth Surf Process Landforms 38:570–576
26. Poddar MC (1950) The Assam earthquake of 15th August 1950. Ind Mineral 4:167–176
27. Reddy DV, Nagabhushanam P, Kumar D, Sukhija BS, Thomas PJ, Pandey AK, Sahoo RN, Ravi Prasad GV, Datta K (2009) The great 1950 Assam Earthquake revisited: Field evidences of liquefaction and search for paleoseismic events. Tectonophysics 474(3–4):463–472
28. Sarma JN (2005) Fluvial process and morphology of the Brahmaputra River. Geomorphology 70:226–256
29. Sarma JN, Phukan MK (2004) Origin and some geomorphological changes of Majuli island of the Brahmaputra River in Assam, India. Geomorphology 60:1–19
30. Schumm SA, Dumont JE, Holbrook JM (2000) Active tectonics and Alluvial rivers. Cambridge University Press, pp 21–42
31. Schumm SA (1956) Evolution of drainage systems and slopes in badlands at perth amboy, new jersey. Geolical Soc Am Bull 67:464–597. https://doi.org/10.1130/0016-7606(1956)67[597:EODSAS]2.0.CO;2
32. Seward D, Burg JP (2008) Growth of the Namche Barwa Syntaxis and associated evolution of the Tsangpo Gorge: Constraints from structural and thermochronological data. Tectonophysics 451:282–289
33. Srivastava P, Bhakuni SS, Luirei K, Misra DK (2009) Morpho-sedimentary records at the Brahmaputra River exit, N.E. Himalaya: Climate–tectonic interplay during the Late Pleistocene–Holocene. J. Quaternary Sci 24:175–188
34. Stewart RJ, Hallet B, Zeitler PK, Malloy MA, Allen CM, Trippett D (2008) Brahmaputra sediment flux dominated by highly localised rapid erosion from the easternmost Himalaya. Geology 36:711–714
35. Strahler AN (1952) Hypsometric (area-altitude) analysis of erosional topography. Geol Soc Am Bull 63:1117–1142
36. Strahler AN (1957) Quantitative analysis of watershed geomorphology. Eos Trans AGU 38(6):913–920. https://doi.org/10.1029/TR038i006p00913
37. Thorne CR, Russell APG, Alam MK (1993) Planform pattern and channel evolution of the Brahmaputra river, Bangladesh. Geol Soc Lond Spec Publ 75:257–276
38. Valdiya KS (1976) Himalayan transverse faults and folds and their parallelism with subsurface structures of North Indian plains. Tectonophysics 353–386
39. Whipple KX (2004) Bedrock rivers and the geomorphology of active orogens. Annu Rev Earth Planet Sci 32:151–185
40. Whipple KX, Tucker GE (1999) Dynamics of the stream-power river incision model: Implications for height limits of mountain ranges, landscape. J Geophys Res 104:17661–17674
41. Yin A, Harrison TM (2000) Geologic evolution of the Himalayan-Tibetan orogen. Ann Rev Earth Planet Sci 28:211–280. https://doi.org/10.1146/annurev.earth.28.1.211
42. Yu G-A, Lu J, Lyu L, Han L, Wang Z (2020) Mass flows and river response in rapid uplifting regions—A case of lower Yarlung Tsangpo basin, southeast Tibet, China. Int J Sedim Res 35(6):609–620

Numerical and Physical Modelling

Numerical Modelling of Flow-Vegetation Interactions in Rivers and Coastal Environments: Recent Trends and Future Research Directions

Timothy I. Marjoribanks

Abstract Vegetation is a common occurrence within natural rivers and coastal systems. It can have a profound effect on flow and sediment dynamics which means it may be utilised as a nature-based solution or may require management to prevent adverse effects. Understanding the complex interaction between flow and vegetation is essential to effective management. This two-way interaction is a function of both the flow and vegetation properties. There are a broad range of methods that have been used to represent flow-vegetation interactions within numerical models, ranging from the rigid cylinder approximation to flexible and complex morphologies. Here, I review recent methods employed to represent flow-vegetation interactions and identify key future research directions. In particular, this chapter focuses on the role of vegetation characteristics including morphology and biomechanics on determining flow and sediment dynamics. I conclude that there is a need to both improve our understanding of the impact of such vegetation characteristics, and improve the representation of these impacts, within reach-scale models used for river and coastal management.

Keywords Eco-hydrodynamics · Flow-vegetation interactions · Numerical modelling · Computational fluid dynamics · Aquatic ecology

1 Introduction

Vegetation is a common feature of riverine and coastal systems globally. Within rivers, it can occur as riparian, or in-channel macrophytic vegetation, while examples of coastal vegetation include seagrasses, intertidal marsh halophytes, dune grasses and mangroves. In each case, vegetation can directly affect the evolution of these

T. I. Marjoribanks (✉)
School of Architecture, Building and Civil Engineering, Loughborough University, Loughborough LE11 3TU, UK
e-mail: t.i.marjoribanks@lboro.ac.uk

S. Dutta and V. Chembolu (eds.), *Recent Development in River Corridor Management*, Lecture Notes in Civil Engineering 376, https://doi.org/10.1007/978-981-99-4423-1_6

systems, through the impact, it has on flow and sediment dynamics. Vegetation represents a blockage to the flow, extracting energy from the mean flow via drag and producing turbulence at a number of different scales, from stem, through patch to canopy scales [23, 55]. The alteration to the mean flow and turbulence creates heterogeneity in channel processes, which can alter flow structure and secondary circulation [24, 26] and has a direct impact on sediment transport, causing both local erosion and deposition depending on location, scale and flow parameters (e.g. [35, 70, 81]).

The scale of the impact that vegetation can have on system dynamics has long been recognised, and traditionally vegetation has been seen as a nuisance and consequently removed from river channels to increase conveyance [33, 54]. However, recently aquatic vegetation has been viewed in a more positive light due to its potential use as a nature-based solution to climate change, biodiversity losses, and disaster risk prevention and mitigation [29, 52, 57].

Therefore, understanding the complex interactions between flow, vegetation and sediment is crucial to effective management of river and coastal systems. As a result, much work has been undertaken over the last ~30 years regarding the representation of vegetation with numerical models used for predictive purposes (see Fig. 1). These models range from one-dimensional shallow water equation models, through to three-dimensional computational fluid dynamics approaches and encompass a broad range of vegetation types.

This paper reviews the existing methods for modelling flow-vegetation interactions, with a particular focus on the representation of vegetation biomechanics (Sect. 2) and morphology (Sect. 3). It is worth noting that, due to the broad interest in vegetated flows, the literature is extensive. Therefore, the review is not exhaustive but aims to provide examples that cover the full variety of methods adopted, with a focus on aquatic rather than terrestrial flows. Having reviewed the current state-of-the-art, the chapter then presents the case for further developing models to account for heterogeneity in vegetation characteristics (Sect. 4). Finally, some important future research challenges are highlighted that emerge from the review (Sect. 5).

2 Vegetation Biomechanics

Many aquatic plants reconfigure to both the mean flow (static reconfiguration) and temporally-dynamic turbulent flow (dynamic reconfiguration) [67] as a survival strategy. Reconfiguration is determined by plant biomechanics and aquatic plants can be broadly categorised into two types depending on their reconfiguration biomechanics: semi-rigid plants, whose reconfiguration is dominated by bending forces, and highly flexible plants, controlled predominantly by tensile forces [55]. This section reviews the three common model representations of vegetation biomechanics: rigid, semi-rigid and highly flexible.

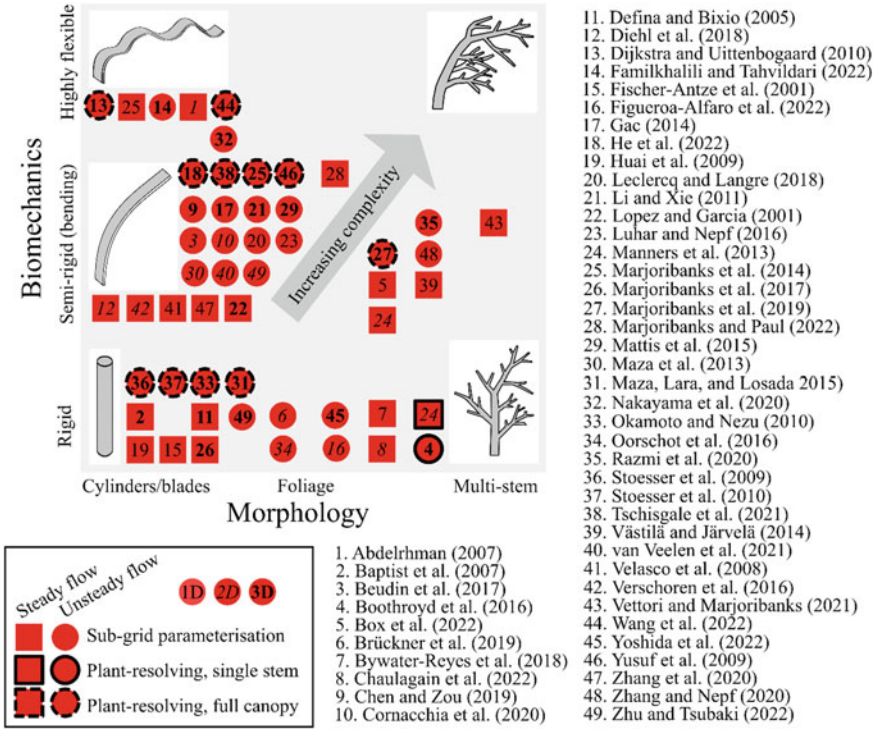

Fig. 1 Summary of existing numerical models for flow-vegetation in terms of their representation of morphology and rigidity. Positions on the scale are approximate. Some studies appear twice as they use multiple models. Model dimensionality is denoted by font type (normal = 1D, italic = 2D, bold = 3D). Scale of parameterisation is given by the line style. Steady/unsteadiness of the flow model is given by shape. *Note* This corresponds to the flow model rather than the vegetation model

2.1 Rigid Vegetation

Traditionally, vegetation has been represented within hydrodynamic models as rigid objects, typically cylinders or rectangular blades. The advantage of this approach is that drag coefficients for these objects, $C_D = 1$ and $C_D = 1.95$, respectively, are relatively well-constrained over the relevant range of Reynolds numbers [59, 79]. For dense canopies where stems interact, methods for calculating canopy-sale drag coefficients have also been developed (e.g. [10]). For sub-grid parameterisation models, where the numerical model grid resolution is larger than the vegetation stem width, vegetation is represented by a bulk drag force term and included as a momentum sink within the hydrodynamic model momentum equations. The drag force is calculated using the drag coefficient, the vegetation density and the vegetation geometry (height, width). Such an approach has been used across many models of different dimensionality from one-dimensional velocity profile momentum models

(e.g. [2]), through two-dimensional depth-averaged models [7] to fully spatially explicit three-dimensional models (e.g. [12, 18, 39, 45]).

For one-dimensional analytical velocity profile models, the velocity profile is typically split into two or three layers, each governed by different velocity/momentum equations [2, 30]. These approaches can lead to roughness formulations (e.g. Darcy, Chezy, Manning's) that incorporate vegetative drag effects [2, 5] and perform reasonably in representing the impact of vegetation on bulk flow. However, such models fail to reproduce the three-dimensional flow structure and turbulence caused by vegetation that can be crucial in driving channel processes.

For models that go beyond an analytical momentum balance to solve a form of the Navier–Stokes equations, e.g. the Reynolds-averaged Navier–Stokes Equations (RANS) or Large Eddy Simulation (LES), the drag force is applied throughout the canopy region such that the flow structure is then solved by the model. As well as the additional drag term, an adjustment is sometimes made to the turbulent kinetic energy equations to reflect the impact of vegetation on turbulence production and dissipation [2, 39].

When using plant-resolving models (i.e. where the grid resolution is substantially less than the vegetation width), a drag coefficient is not required as the flow separation around the vegetation and subsequent form drag are explicitly represented within the model [50, 56, 68, 69]. Similarly, the friction drag, though small (<10%) for cylinders perpendicular to the flow [68], can be directly included too. Such simulations can capture the fine-scale wake turbulence through canopy-scale vortices and allow a full characterisation of the vegetative drag. Importantly, from a practical modelling perspective, Kim and Stoesser [34] demonstrated that reasonable accuracy was still possible with a relatively coarse mesh, using an immersed boundary method. However, despite the ability of these methods to capture the flow processes in detail, they do not account for the two-way interaction between flow and vegetation.

2.2 Semi-Rigid Bending Vegetation

The majority of vegetation reconfiguration models have focussed on bending-dominated plants. Beam and rod bending models have been widely used to simulate reconfiguration in canopy-scale models. These models include one-dimensional models (e.g. [75]), through to two-dimensional shallow water models (e.g. [11, 76]) and fully three-dimensional models including plant-resolving approaches (e.g. [72]) and sub-grid parameterisations (e.g. [37, 62]). Plant-resolving three-dimensional LES models that calculate vegetation forcing directly [28, 43, 72, 83] are ideal as they do not rely on parameterisation of drag coefficients and permit investigation of the time-varying interaction between vegetation and turbulence at multiple scales [44]. While increased computing power has enabled simulations with both impressive spatial resolution (<1 mm) and scale (800 stems) [72], such models are still impractical for river/coastal management applications where models still rely on sub-grid vegetation parameterisation.

As with the rigid vegetation case, sub-grid parameterisation models represent vegetation as a drag force in the momentum equations and, where appropriate, through adjustments to the turbulence model [9, 49]. There are two methods for accounting for vegetation reconfiguration. First, it can be represented by fully solving the deflection of the sub-grid stems in response to the flow and calculating vegetation heights and spatial distribution of the drag forces within the fluid model [21, 36, 40, 48, 74]. Second, instead of calculating the vegetation deflection directly, it can be accounted for through experimentally or numerically pre-defined relationships between flow and vegetation properties. Examples include modifications of drag coefficients (e.g. [84]) and relationships between the local velocity and stem height [37] or bending angle [11, 76].

A key development in the use of pre-defined relationships in canopy-scale simulation of vegetation bending came through the seminal paper by Luhar and Nepf [41] which defined the effective stem length that can be used in the standard drag equation to account for the impacts of reconfiguration. The effective stem length is a function of the Cauchy number, which represents the balance between the drag and bending forces. This relationship permits the inclusion of vegetation bending within larger scale models, without a biomechanical model, as long as the flexural rigidity, vegetation geometry and local velocity are known. This approach has been used for simulating coastal vegetation [3] and within river morphodynamic and eco-geomorphic models [13, 87].

2.3 Highly Flexible Tensile Vegetation

For highly flexible, tensile plants, biomechanical models have been developed that are able to simulate large deflections and flapping behaviour of plant stems. Such models are typically characterised by a local expression of rigidity and include n-pendula-type approaches [1, 14, 15, 43, 53] and pellet-rope models [80]. These models allow the analysis of the reconfiguration of plants that typically occupy a more horizontal position within the flow and are not well represented by a beam-bending model.

Model applications with highly flexible vegetation are not as common as semi-rigid vegetation (see Fig. 1), partly due to the dominance of research on saltmarshes, mangroves and riparian vegetation, which tend to be well-represented by the semi-rigid bending models. Nevertheless, development of highly flexible models, or indeed models that can adequately capture the full range of motion dynamics, is important for river macrophytes, seagrasses and vegetation with varied morphology (e.g. leaves and foliage).

3 Vegetation Morphology

In addition to vegetation flexibility, another important consideration is the representation of vegetation morphology. Aquatic vegetation may exhibit multiple stems as well as leaves/foliage which can significantly impact on the flow-vegetation interaction. The approach described in Sect. 2 is therefore inaccurate for modelling vegetation beyond simple single-stemmed plants.

A number of studies have sought to represent the complex nature of vegetation morphology within hydrodynamic models. The simplest approach is to represent multiple stems/foliage as an extra sub-grid component, which contributes an additional drag force. This approach has been used for static vegetation models [42, 82] as well as for dynamic vegetation models, where the foliage can either be treated as a static component attached to the bending stem [31, 46] or as a dynamic term that adjusts with the velocity to account for variation in flow-leaf interaction [62, 73, 86]. In the above examples, methods such as terrestrial laser scanning (TLS) and image analysis as well as stem sampling are used to help define the morphological characteristics. Larger-scale remote sensing approaches such as LiDAR and satellite imagery have also been applied to capture broad-scale vegetation morphology for parameterisation of numerical models [8, 17].

Fewer studies have resolved complex morphology and foliage explicitly within models. Boothroyd et al. [4] used TLS to capture high resolution cm-scale plant morphology with and without foliage. They demonstrated that foliage can increase the drag by an order of magnitude and that the inclusion of both complex morphology and foliage produced flow structure not simulated by rigid cylinders. Manners et al. [42] applied a multi-scale approach, whereby stem-resolving simulations using fine-scale TLS data were used to calculate roughness values for reach-scale simulations. While these approaches represent significant advances in the representation of complex morphology, there remains a significant gap in the representation of reconfiguration of morphologies beyond single stems (Fig. 1).

4 Heterogeneity of Natural Aquatic Vegetation

Regardless of the extent to which flexibility and morphology are considered, vegetation is typically represented as homogenous in terms of biomechanics (along a single plant and between different plants) and morphology (between individual plants). However, all but the simplest vegetation forms contain spatial and temporal heterogeneity/variation (Fig. 2), which is often not represented in laboratory or numerical studies (see [71]).

At the single plant scale, observed changes in geometry and biomechanics along stems for saltmarsh vegetation [16, 63], river macrophytes [51], seaweed [78] and seagrasses [77] will impact on flow-vegetation interactions. Recent studies have applied models with variable rigidity (e.g. [15]) and shown that the assumption of a

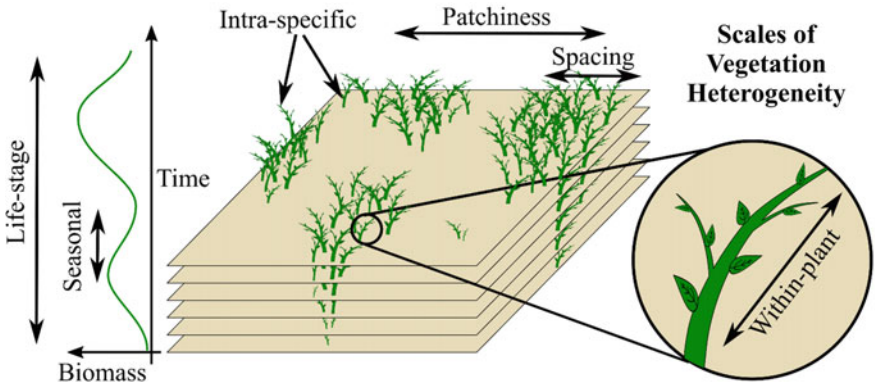

Fig. 2 Spatial and temporal scales of vegetation heterogeneity with respect to geometry and biomechanics

long-stem homogeneity can lead to over-prediction of stem drag forces and under-prediction of deflected stem heights [47]. Furthermore, similar components within a plant (e.g. stems, blades, leaves) may exhibit variability in geometry and biomechanics dependent on their location/rank within the plant, which may be related to age [64, 77]. For seagrass, it has been shown that accounting for the heterogeneity between rank can reduce the simulated drag force by 10% compared to a homogeneous approximation [77].

At the patch/canopy scale, intraspecific variability in biomechanics has been evidenced across a range of aquatic plant types [46, 51, 60] due to environmental conditions (e.g. thigmomorphogenesis and nutrient loading) and also variation with age (e.g. [66]). The same is true for morphology, where each plant will have unique morphology. Considering this in the simplest terms as a variation in stem height, [27] demonstrated the impact of heterogeneity of morphology on effective canopy height and turbulent momentum exchange.

Another common simplification made in canopy models is the assumption of regular spacing of plants. Different arrangements of stems within the canopy (e.g. aligned, staggered or random) have different impacts on dispersion [25] and flow/wave attenuation [71]. At a larger scale, fragmentation, or patchiness is a common natural feature within aquatic vegetation canopies [19, 65] and recent simulations have demonstrated the distinct turbulent signature within canopy gaps [61] and interactions between patches [22, 38, 44].

Finally, vegetation is temporally heterogeneous too, with variation in geometry and biomechanics throughout the life cycle of the plant, as well as in different seasons. For seagrasses, simplified modelling of flow-vegetation demonstrated drag forces ~45% larger on average in summer than in spring [77]. At the reach scale and beyond, models have been developed to include the growth and decay of vegetation patches through time [6, 11, 58]. In some cases, changes to vegetation characteristics with season and life stage have been explicitly included [6]. These models, though

simplified, represent a significant opportunity to study longer-term dynamic flow-vegetation interactions, which will be further improved through the availability of additional field data to more accurately inform the parameterisation.

5 Conclusion and Future Research Directions

This review has shown the development of parametrisations of vegetation within hydrodynamic models, from the simple rigid cylinder approach to flexible plants with complex morphology. Choice of parameterisation depends on the complexity and scale of processes being simulated and therefore there is no single 'best' approach. However, a few clear needs and opportunities emerge.

First, there is the need to develop plant-resolving numerical models that account for both complex morphology and biomechanics (Fig. 1). Existing models typically only represent single stems or two-dimensional reconfiguration (in the streamwise and vertical plane). While some basic 'multi-stem' models have been applied [77], research should focus on developing biomechanical models that can fully represent three-dimensional reconfiguration of complex plants including plant-plant interactions to better understand the complex physics of the problem.

Second, the accuracy of existing sub-grid parameterisations needs to be examined in the case of heterogeneity. Currently, there are no parameterisations that account for spatially heterogeneous geometry and biomechanics. Inclusion of these factors is essential for improving predictive models used for management of vegetated flows [20, 85]. Luhar and Nepf's [41] approach has been successfully used to upscale plant motion dynamics to the reach scale. However, it is not clear how the Cauchy number approach applies to heterogeneous stems [47] and there is also the need to include heterogeneity between stems. One possible method for doing so is through using sub-grid parameterisation based on an experimentally-informed distribution of plant characteristics rather than a single value.

Finally, and related to the previous point, the advancement of numerical models is also dependent on the availability of appropriate and accurate field data to inform parameter choice [20]. New developments in measurement methods such as laser scanning provide promising methods for capturing complex plant morphology for inclusion within numerical models [4, 32, 46]. Relatively few studies have characterised geometric and biomechanical variability within and between plants and given the observed order of magnitude intraspecific range in these values [46, 51, 60], this is an important avenue for further work.

References

1. Abdelrhman MA (2007) Modeling coupling between Eelgrass Zostera marina and water flow. Mar Ecol Prog Ser 338:81–96. https://doi.org/10.3354/meps338081
2. Baptist MJ, Babovic V, Rodríguez Uthurburu J, Keijzer M, Uittenbogaard RE, Mynett A, Verwey A (2007) On inducing equations for vegetation resistance. J Hydraul Res 45(4):435–450. https://doi.org/10.1080/00221686.2007.9521778
3. Beudin A, Kalra TS, Ganju NK, Warner JC (2017) Development of a coupled wave-flow-vegetation interaction model. Comput Geosci 100:76–86. https://doi.org/10.1016/j.cageo.2016.12.010
4. Boothroyd RJ, Hardy RJ, Warburton J, Marjoribanks TI (2016) The importance of accurately representing submerged vegetation morphology in the numerical prediction of complex river flow. Earth Surf Proc Land 41(4):567–576. https://doi.org/10.1002/esp.3871
5. Box W, Järvelä J, Västilä K (2022) New formulas addressing flow resistance of floodplain vegetation from emergent to submerged conditions. Int J River Basin Manag 1–17. https://doi.org/10.1080/15715124.2022.2143512
6. Brückner MZM, Schwarz C, van Dijk WM, van Oorschot M, Douma H, Kleinhans MG (2019) Salt Marsh establishment and eco-engineering effects in dynamic Estuaries determined by species growth and mortality. J Geophys Res Earth Surf 124(12):2962–2986. https://doi.org/10.1029/2019JF005092
7. Bywater-Reyes S, Diehl RM, Wilcox AC (2018) The influence of a vegetated bar on channel-bend flow dynamics. Earth Surf Dyn 6(2):487–503. https://doi.org/10.5194/esurf-6-487-2018
8. Chaulagain S, Stone MC, Dombroski D, Gillihan T, Chen L, Zhang S (2022) An investigation into remote sensing techniques and field observations to model hydraulic roughness from Riparian vegetation. River Res Appl 38(10):1730–1745.https://doi.org/10.1002/rra.4053
9. Chen H, Zou Q-P (2019) Eulerian–Lagrangian flow-vegetation interaction model using immersed boundary method and OpenFOAM. Adv Water Resour 126:176–192. https://doi.org/10.1016/j.advwatres.2019.02.006
10. Cheng N-S, Hui CL, Chen X (2019) Estimate of drag coefficient for a finite patch of rigid cylinders. J Hydraul Eng 145(2):06018019. https://doi.org/10.1061/(ASCE)HY.1943-7900.0001561
11. Cornacchia L, Wharton G, Davies G, Grabowski RC, Temmerman S, van der Wal D, Bouma TJ, van de Koppel J (2020) Self-organization of river vegetation leads to emergent buffering of river flows and water levels. Proc Royal Soc B: Biol Sci 287(1931):20201147. https://doi.org/10.1098/rspb.2020.1147
12. Defina A, Bixio AC (2005) Mean flow and turbulence in vegetated open channel flow. Water Resour Res 41(7):1–12. https://doi.org/10.1029/2004WR003475
13. Diehl RM, Wilcox AC, Merritt DM, Perkins DW, Scott JA (2018) Development of an eco-geomorphic modeling framework to evaluate riparian ecosystem response to flow-regime changes. Ecol Eng 123(November):112–126. https://doi.org/10.1016/j.ecoleng.2018.08.024
14. Dijkstra JT, Uittenbogaard RE (2010) Modeling the interaction between flow and highly flexible aquatic vegetation. Water Resour Res 46(12):W12547–W12547. https://doi.org/10.1029/2010WR009246
15. Familkhalili R, Tahvildari N (2022) Computational modeling of coupled waves and vegetation stem dynamics in highly flexible submerged meadows. Adv Water Resour 165(July):104222. https://doi.org/10.1016/j.advwatres.2022.104222
16. Feagin RA, Irish JL, Möller I, Williams AM, Colón-Rivera RJ, Mousavi ME (2011) Short communication: engineering properties of wetland plants with application to wave attenuation. Coast Eng 58(3):251–255. https://doi.org/10.1016/j.coastaleng.2010.10.003
17. Figueroa-Alfaro RW, van Rooijen A, Garzon JL, Evans M, Harris A (2022) Modelling wave attenuation by saltmarsh using satellite-derived vegetation properties. Ecol Eng 176(March):106528. https://doi.org/10.1016/j.ecoleng.2021.106528

18. Fischer-Antze T, Stoesser T, Bates P, Olsen NRB (2001) 3D Numerical modelling of open-channel flow with submerged vegetation. J Hydraul Res 39(3):303–310. https://doi.org/10.1080/00221680109499833
19. Folkard AM (2019) Biophysical interactions in fragmented marine canopies: fundamental processes, consequences, and upscaling. Front Marine Sci 6. https://www.frontiersin.org/articles/10.3389/fmars.2019.00279
20. Fringer OB, Dawson CN, He R, Ralston DK, Joseph Y, Zhang (2019) The future of coastal and estuarine modeling: findings from a workshop. Ocean Model 143:101458–101458. https://doi.org/10.1016/j.ocemod.2019.101458
21. Gac JM (2014) A large Eddy based Lattice-Boltzmann simulation of velocity distribution in an open channel flow with rigid and flexible vegetation. Acta Geophys 62(1):180–198. https://doi.org/10.2478/s11600-013-0178-1
22. Ghani U, Anjum N, Pasha GA, Ahmad M (2019) Investigating the turbulent flow characteristics in an open channel with staggered vegetation patches. River Res Appl 35(7):966–978. https://doi.org/10.1002/rra.3460
23. Ghisalberti M (2002) Mixing layers and coherent structures in vegetated aquatic flows. J Geophys Res 107(C2):3011–3011. https://doi.org/10.1029/2001JC000871
24. Ghisalberti M (2010) The three-dimensionality of obstructed shear flows. Environ Fluid Mech 10(3):329–343. https://doi.org/10.1007/s10652-009-9161-4
25. Golzar M, Sonnenwald F, Guymer I, Stovin V (2018) A CFD based comparison of mixing due to regular and random cylinder arrays. In: Kalinowska MB, Mrokowska MM, Rowiński PM (eds) Free surface flows and transport processes. GeoPlanet: Earth and Planetary Sciences. Springer International Publishing, Cham, pp 195–205. https://doi.org/10.1007/978-3-319-70914-7_11.
26. Gurnell AM, Van Oosterhout MP, De Vlieger B, Goodson JM (2006) Reach-scale interactions between aquatic plants and physical habitat: river Frome, Dorset. River Res Appl 22(6):667–680. https://doi.org/10.1002/rra.929
27. Hamed AM, Sadowski MJ, Nepf HM, Chamorro LP (2017) Impact of height heterogeneity on canopy turbulence. J Fluid Mech 813:1176–1196. https://doi.org/10.1017/jfm.2017.22
28. He S, Liu H, Shen L (2022) Simulation-based study of turbulent aquatic canopy flows with flexible stems. J Fluid Mech 947(September):A33. https://doi.org/10.1017/jfm.2022.655
29. van Hespen R, Hu Z, Borsje B, De Dominicis M, Friess DA, Jevrejeva S, Kleinhans MG et al (2022) Mangrove forests as a nature-based solution for coastal flood protection: biophysical and ecological considerations. Water Sci Eng. https://doi.org/10.1016/j.wse.2022.10.004
30. Huai WX, Zeng YH, Xu ZG, Yang ZH (2009) Three-layer model for vertical velocity distribution in open channel flow with submerged rigid vegetation. Adv Water Resour 32(4):487–492. https://doi.org/10.1016/j.advwatres.2008.11.014
31. Ikeda S (2001) Numerical study on turbulent flow and Honami in and above flexible plant canopy. Int J Heat Fluid Flow 22(3):252–258. https://doi.org/10.1016/S0142-727X(01)00087-X
32. Jalonen J, Järvelä J, Virtanen J-P, Vaaja M, Kurkela M, Hyyppä H (2015) Determining characteristic vegetation areas by terrestrial laser scanning for floodplain flow modeling. Water 7(2):420–437. https://doi.org/10.3390/w7020420
33. Kadlec RH (1990) Overland flow in wetlands: vegetation resistance. J Hydraul Eng 116(5):691–706. https://doi.org/10.1061/(ASCE)0733-9429(1990)116:5(691)
34. Jin KS, Stoesser T (2011) Closure modeling and direct simulation of vegetation drag in flow through emergent vegetation. Water Resour Res 47(10):W10511–W10511. https://doi.org/10.1029/2011WR010561
35. Larsen LG (2019) Multiscale flow-vegetation-sediment feedbacks in low-gradient landscapes. Geomorphology 334(June):165–193. https://doi.org/10.1016/j.geomorph.2019.03.009
36. Leclercq T, de Langre E (2018) Reconfiguration of elastic blades in oscillatory flow. J Fluid Mech 838(March):606–630. https://doi.org/10.1017/jfm.2017.910
37. Li CW, Xie JF (2011) Numerical modeling of free surface flow over submerged and highly flexible vegetation. Adv Water Resour 34(4):468–477. https://doi.org/10.1016/j.advwatres.2011.01.002

38. Lima PHS de, Janzen JG, Nepf HM (2015) Flow patterns around two neighboring patches of emergent vegetation and possible implications for deposition and vegetation growth. Environ Fluid Mech 15(4): 881–898.https://doi.org/10.1007/s10652-015-9395-2
39. Lopez F, Garcia MH (2001) Mean flow and turbulence structure of open-channel flow through non-emergent vegetation. J Hydraul Eng 127(5):392–402. https://doi.org/10.1061/(ASCE)0733-9429(2001)127:5(392)
40. Luhar M, Nepf HM (2016) Wave-induced dynamics of flexible blades. J Fluids Struct 61:20–41. https://doi.org/10.1016/j.jfluidstructs.2015.11.007
41. Luhar M, Nepf HM (2011) Flow-induced reconfiguration of buoyant and flexible aquatic vegetation. Limnol Oceanogr 56(6):2003–2017. https://doi.org/10.4319/lo.2011.56.6.2003
42. Manners R, Schmidt J, Wheaton JM (2013) Multiscalar model for the determination of spatially explicit riparian vegetation roughness. J Geophys Res Earth Surf 118(1):65–83. https://doi.org/10.1029/2011JF002188
43. Marjoribanks TI, Hardy RJ, Lane SN, Parsons DR (2014) High-resolution numerical modelling of flow—vegetation interactions. J Hydraul Res 52(6):775–793. https://doi.org/10.1080/00221686.2014.948502
44. Marjoribanks TI, Hardy RJ, Lane SN, Parsons DR (2017) Does the canopy mixing layer model apply to highly flexible aquatic vegetation? Insights from numerical modelling. Environ Fluid Mech 17(2):277–301. https://doi.org/10.1007/s10652-016-9482-z
45. Marjoribanks TI, Hardy RJ, Lane SN, Tancock MJ (2017) Patch-scale representation of vegetation within hydraulic models. Earth Surf Proc Land 42(5):699–710. https://doi.org/10.1002/esp.4015
46. Marjoribanks TI, Lague D, Hardy RJ, Boothroyd RJ, Leroux J, Mony C, Puijalon S (2019) Flexural rigidity and shoot reconfiguration determine wake length behind Saltmarsh vegetation patches. J Geophys Res Earth Surf 124(8):2176–2196. https://doi.org/10.1029/2019JF005012
47. Marjoribanks TI, Paul M (2022) Modelling flow-induced reconfiguration of variable rigidity aquatic vegetation. J Hydraul Res 60(1):46–61. https://doi.org/10.1080/00221686.2020.1866693
48. Mattis SA, Dawson CN, Kees CE, Farthing MW (2015) An immersed structure approach for fluid-vegetation interaction. Adv Water Resour 80:1–16. https://doi.org/10.1016/j.advwatres.2015.02.014
49. Maza M, Lara JL, Losada IJ (2013) A coupled model of submerged vegetation under oscillatory flow using Navier-Stokes equations. Coast Eng 80(October):16–34. https://doi.org/10.1016/j.coastaleng.2013.04.009
50. Maza M, Lara JL, Losada IJ (2015) Tsunami wave interaction with mangrove forests: a 3-D numerical approach. Coast Eng 98(April):33–54. https://doi.org/10.1016/j.coastaleng.2015.01.002
51. Miler O, Albayrak I, Nikora V, O'Hare M (2012) Biomechanical properties of aquatic plants and their effects on plant-flow interactions in streams and rivers. Aquat Sci 74(1):31–44. https://doi.org/10.1007/s00027-011-0188-5
52. Möller I, Kudella M, Rupprecht F, Spencer T, Paul M, Van Wesenbeeck BK, Wolters G et al (2014) Wave attenuation over coastal salt marshes under storm surge conditions. Nat Geosci 7(10):727–731. https://doi.org/10.1038/NGEO2251
53. Nakayama K, Shintani T, Komai K, Nakagawa Y, Tsai JW, Sasaki D, Tada K et al (2020) Integration of submerged aquatic vegetation motion within hydrodynamic models. Water Resour Res 56 (8):e2020WR027369. https://doi.org/10.1029/2020WR027369.
54. Nepf H, Ghisalberti M, White B, Murphy E (2007) Retention time and dispersion associated with submerged aquatic canopies. Water Resour Res 43(4):10–10. https://doi.org/10.1029/2006WR005362
55. Nikora V (2010) Hydrodynamics of aquatic ecosystems: an interface between ecology, biomechanics and environmental fluid mechanics. River Res Appl 26(4):367–384. https://doi.org/10.1002/rra.1291
56. Okamoto T-A, Nezu I (2010) Large Eddy simulation of 3-D flow structure and mass transport in open-channel flows with submerged vegetations. J Hydro-Environ Res 4(3):185–197. https://doi.org/10.1016/j.jher.2010.04.015

57. Ondiviela B, Losada IJ, Lara JL, Maza M, Galván C, Bouma TJ, van Belzen J (2014) The role of seagrasses in coastal protection in a changing climate. Coast Eng 87:158–168. https://doi.org/10.1016/j.coastaleng.2013.11.005
58. van Oorschot M, Kleinhans M, Geerling G, Middelkoop H (2016) Distinct patterns of interaction between vegetation and morphodynamics. Earth Surf Proc Land 41(6):791–808. https://doi.org/10.1002/esp.3864
59. Panton RL (1996) Incompressible flow, 2nd edn. John Wiley and Sons, New York
60. Paul M, Henry PYT, Thomas RE (2014) Geometrical and mechanical properties of four species of northern European brown macroalgae. Coast Eng 84:73–80. https://doi.org/10.1016/j.coastaleng.2013.11.007
61. Ranjan P, Mittal K, Chamorro LP, Tinoco RO (2022) Impact of gaps on the flow statistics in an emergent rigid canopy. Phys Fluids 34(6):066601. https://doi.org/10.1063/5.0088527
62. Razmi AM, Chamecki M, Nepf HM (2020) Efficient numerical representation of the impacts of flexible plant reconfiguration on Canopy posture and hydrodynamic drag. J Hydraul Res 58(5):755–766. https://doi.org/10.1080/00221686.2019.1671511
63. Rupprecht F, Möller I, Evans B, Spencer T, Jensen K (2015) Biophysical properties of salt marsh canopies—Quantifying plant stem flexibility and above ground biomass. Coast Eng 100:48–57. https://doi.org/10.1016/j.coastaleng.2015.03.009
64. Santos CB de los, Vicencio-Rammsy B, Lepoint G, Remy F, Bouma TJ, Gobert S (2016) Ontogenic variation and effect of collection procedure on leaf biomechanical properties of Mediterranean Seagrass Posidonia Oceanica (L.) Delile. Marine Ecol 37(4):750–759.https://doi.org/10.1111/maec.12340
65. Schoelynck J, de Groote T, Bal K, Vandenbruwaene W, Meire P, Temmerman S (2012) Self-organised patchiness and scale-dependent bio-geomorphic feedbacks in aquatic river vegetation. Ecography 35(8):760–768. https://doi.org/10.1111/j.1600-0587.2011.07177.x
66. Silinski A, Schoutens K, Puijalon S, Schoelynck J, Luyckx D, Troch P, Meire P, Temmerman S (2018) Coping with waves: plasticity in Tidal Marsh plants as self-adapting coastal ecosystem engineers. Limnol Oceanogr 63(2):799–815. https://doi.org/10.1002/lno.10671
67. Siniscalchi F, Nikora V (2013) Dynamic reconfiguration of aquatic plants and its interrelations with upstream turbulence and drag forces. J Hydraul Res 51(1):46–55. https://doi.org/10.1080/00221686.2012.743486
68. Stoesser T, Kim SJ, Diplas P (2010) Turbulent flow through idealized emergent vegetation. J Hydraul Eng 136(12):1003–1017. https://doi.org/10.1061/(ASCE)HY.1943-7900.0000153
69. Stoesser T, Palau Salvador G, Rodi W, Diplas P (2009) Large Eddy simulation of turbulent flow through submerged vegetation. Transp Porous Media 78 (3 SPEC. ISS.):347–65. https://doi.org/10.1007/s11242-009-9371-8
70. Tinoco RO, Coco G (2018) Turbulence as the main driver of resuspension in oscillatory flow through vegetation. J Geophys Res Earth Surf 123(5):891–904. https://doi.org/10.1002/2017JF004504
71. Tinoco RO, San Juan JE, Mullarney JC (2020) Simplification bias: lessons from laboratory and field experiments on flow through aquatic vegetation. Earth Surf Process Landf 45(1):121–43. https://doi.org/10.1002/esp.4743
72. Tschisgale S, Löhrer B, Meller R, Fröhlich J (2021) Large Eddy simulation of the fluid-structure interaction in an abstracted aquatic canopy consisting of flexible blades. J Fluid Mech 916(June):A43. https://doi.org/10.1017/jfm.2020.858
73. Västilä K, Järvelä J (2014) Modeling the flow resistance of woody vegetation using physically based properties of the foliage and stem. Water Resour Res 50(1):229–245. https://doi.org/10.1002/2013WR013819
74. van Veelen TJ, Karunarathna H, Reeve DE (2021) Modelling wave attenuation by quasi-flexible coastal vegetation. Coastal Eng 164(March):103820.https://doi.org/10.1016/j.coastaleng.2020.103820
75. Velasco D, Bateman A, Medina V (2008) A new integrated, hydro-mechanical model applied to flexible vegetation in riverbeds. J Hydraul Res 46(5):579–597. https://doi.org/10.3826/jhr.2008.2986

76. Verschoren V, Meire D, Schoelynck J, Buis K, Bal KD, Troch P, Meire P, Temmerman S (2016) Resistance and reconfiguration of natural flexible submerged vegetation in hydrodynamic river modelling. Environ Fluid Mech 16(1):245–265. https://doi.org/10.1007/s10652-015-9432-1
77. Vettori D, Marjoribanks TI (2021) Temporal variability and within-plant heterogeneity in blade biomechanics regulate flow-seagrass interactions of Zostera Marina. Water Resour Res 57(3):e2020WR027747. https://doi.org/10.1029/2020WR027747
78. Vettori D, Nikora V (2017) Morphological and mechanical properties of blades of Saccharina Latissima'. Estuar, Coast Shelf Sci 196. https://doi.org/10.1016/j.ecss.2017.06.033
79. Vogel S (1994) Life in moving fluids: the physical biology of flow, 2nd edn
80. Wang J, He G, Dey S, Fang H (2022) Influence of submerged flexible vegetation on turbulence in an open-channel flow. J Fluid Mech 947(September):A31. https://doi.org/10.1017/jfm.2022.598
81. Yang JQ, Nepf HM (2018) A turbulence-based bed-load transport model for bare and vegetated channels. Geophys Res Lett 45(19):10428–10436. https://doi.org/10.1029/2018GL079319
82. Yoshida K, Kajikawa Y, Nishiyama S, Islam MT, Adachi S, Sakai K (2022) Three-dimensional numerical modelling of floods in river corridor with complex vegetation quantified using airborne LiDAR imagery. J Hydraul Res 1–21.https://doi.org/10.1080/00221686.2022.2106596
83. Yusuf B, Karim OA, Osman SA (2009) Numerical solution for open channel flow with. Int J Eng Technol 6(1):12
84. Zhang X, Lin P, Gong Z, Li B, Chen X (2020) Wave attenuation by Spartina Alterniflora under macro-tidal and storm surge conditions. Wetlands 40(6):2151–2162. https://doi.org/10.1007/s13157-020-01346-w
85. Zhang X, Lin P, Nepf H (2022) A wave damping model for flexible marsh plants with leaves considering linear to weakly nonlinear wave conditions. Coast Eng 175(August):104124. https://doi.org/10.1016/j.coastaleng.2022.104124
86. Zhang X, Nepf H (2020) Flow-induced reconfiguration of aquatic plants, including the impact of leaf sheltering. Limnol Oceanogr 65(11):2697–2712. https://doi.org/10.1002/lno.11542
87. Zhu R, Tsubaki R (2022) The role of Riparian vegetation flexibility in a bio-hydro-morphodynamic simulation. Earth Surf Process Landf. https://doi.org/10.1002/esp.5469

Numerical Investigation of Various Turbulence Models for a Sinuous Channel with Sand Mining Pit

Om Prakash Maurya, Ketan Kumar Nandi, Suresh Modalavalasa, and Subashisa Dutta

Abstract This study aims to assess the performance of three turbulence models, namely, k-ω, k-ε, and RNG k-ε, for a regular low sinuous channel setup with a sand mining pit on the floodplain of the IIT Guwahati laboratory, using the FLOW-3D software. The results indicate that the k-ω turbulence model is better suited to the experimental results than the other two models. The maximum stream-wise velocity in the mainstream is 10% less in the case of the k-ω model than in the k-ε model, and the secondary current is more concentrated at the outer bank in the case of the k-ω model than in the RNG k-ε model. Additionally, the turbulence kinetic energy (TKE) is more concentrated at the inner bank with the k-ε model than in the other two models. These findings have significant implications for similar types of research in the field of sediment transport and channel stability in models for a sand bed sinuous channel. By using the most suitable turbulence model for the problem at hand, researchers can improve the accuracy of their prediction, leading to better decision-making in the design and management of natural channels.

Keywords Turbulence-model · Sinuosity · Sand mining pit · Numerical simulation

1 Introduction

Flow characteristics in the sinuous or meander channel are much different from those in the rectangular compound channel [1, 2]. The meandering shape of the river may be caused by river bank instability during flooding and also due to anthropogenic stresses [3, 4]. Momentum transfer happens at the junction of shallow and deep flow during flood season or over bank flow conditions, and a shear layer zone separates the high and low-velocity zones [5–8].

Sediment erosion and deposition in river systems are influenced by several factors, but the most important factor is the energy of flow [9]. Many factors contribute to

O. P. Maurya (✉) · K. K. Nandi · S. Modalavalasa · S. Dutta
Indian Institute of Technology, Guwahati, India
e-mail: om1996@iitg.ac.in

S. Dutta and V. Chembolu (eds.), *Recent Development in River Corridor Management*, Lecture Notes in Civil Engineering 376, https://doi.org/10.1007/978-981-99-4423-1_7

energy loss in the river corridor system, including floodplain obstructions (mining pits, bridge piers, etc.), and natural channel formations like sinuosity or bends, sediment movement, vegetation, channel stepping, etc. [10–13]. Sand mining has benefits, such as in-stream mining improves navigation and economy, and further, floodplain mining improves the economy and channel stability. However, these activities must be done in accordance with proper guidelines [14, 15]. It is well documented that sand mining without discrimination can cause river geometry instability and bridge failure in fluvial systems [16, 17]. River geometry is unstable when erosion and deposition occur, altering geometric parameters such as bed slope, bank slope, depth, width, and channel armoring [18, 19]. There are several negative impacts that can occur downstream if there is a sudden change in the width of a river. These impacts may include negative effects on vegetation, the local economy, agriculture, and the groundwater table [20, 21]. If a mining pit is close to a bridge pier or abutment, it can speed up scour by enhancing secondary currents and mining pit migration [22, 23]. Anthropogenic activities, such as sand mining, have been found to have detrimental effects on the environment. Various investigations, including experimental, and theoretical studies, as well as field observations, have examined the consequences of these pressures [24–35]. There are various studies also carried out numerically using Open FOAM, FLOW-3D, and more, that have been utilized in various studies related to open channel flow, such as analyzing bridge pier scour and investigating the interaction between vegetation and flow [36–46]. However, most experimental and numerical studies on sand mining have focused only on straight channels. This narrow focus may limit our understanding of the impacts of sand mining, as it fails to account for the complexities of natural waterways. Therefore, further research is needed to explore the effects of sand mining on meandering and braided channels and their associated ecosystems. Such research will enable the development of more comprehensive strategies to mitigate the negative impacts of sand mining and promote sustainable resource management.

A lot of studies were carried out to solve the open channel flow problem experimentally and numerically, so many turbulence models are proposed by the researcher with some applications and limitations, therefore it is necessary to choose the best one for a particular problem. In light of this, this study seeks to identify the most appropriate turbulence model for a sinuous channel with a floodplain sand mining pit.

2 Material and Method

2.1 FLOW-3D

FLOW-3D is a computational fluid dynamics software application that is capable of modeling and analyzing various types of fluid flow problems such as air entrainment, multiphase flow, granular flow, sediment transport, turbulence flow, and more. This

is achieved through the use of a finite volume method to discretize and solve the governing equations of fluid dynamics, and specialized modules and features that are designed to handle specific types of fluid flow problems. This study is only based on turbulence modeling because here we are interested to investigate the flow characteristics only such as secondary current, streamwise velocity, and turbulence kinetic energy. For turbulence modeling, there are mainly four turbulence models given in FLOW-3D. The present study compares the flow characteristics among the three turbulence models (k-ω, k-ε, and RNG k-ε).

2.2 Governing Equations

There are two governing equations: continuity, which describes mass conservation, and momentum conservation, which describes the motion of fluid. For Cartesian coordinates and incompressible flow, the continuity equation is as follows:

3 Continuity Equation

$$A_x \frac{\partial u}{\partial x} + A_y \frac{\partial v}{\partial y} + A_z \frac{\partial w}{\partial z} = \frac{R_{SOR}}{\rho} \tag{1}$$

where ρ is the fluid density, u, v, and w are the velocity components in the x, y, and z-direction respectively. A_x, A_y, and A_z are the fractional area that is open to flow in the x, y, and z-direction respectively, R_{SOR} is the source mass (Eq. 1).

4 Momentum Equations

The Navier–Stokes equation with additional terms for the fluid velocity components (u, v, and w) is used to calculate fluid motion in the three coordinate directions (Eq. 2).

$$\frac{\partial u_i}{\partial t} + \frac{1}{V_F}\left[u_j A_j \frac{\partial u_i}{\partial x_j}\right] = -\frac{\partial P}{\partial x_i} + g_i + f_i \tag{2}$$

where f_i is acceleration due to viscous, g_i is acceleration due to body, and V_F is the fractional volume.

4.1 Configuration of Numerical Simulations

In this study, a sinuous channel with sand mining is built using Solidworks, with the dimension followed in the laboratory experiments, were conducted in Fluvial laboratory at IIT Guwahati. The channel setup details are provided in the table below [31]. Figure 1 depicts the configuration of the channel, while Fig. 2 presents a cross-sectional view of the channel (Table 1).

4.2 Numerical Simulation

The study focuses on a non-mobile bed low sinuous channel with a roughness height of 0.0016 m and smooth metal side walls. The channel has a bed slope of 1 in 1000, and clean water flowing into it. The laboratory setup has specific physical conditions that require two physical models (Turbulence model, and Gravity model) to be used to solve the same problem.

Fig. 1 CAD modeling of the low sinuous channel

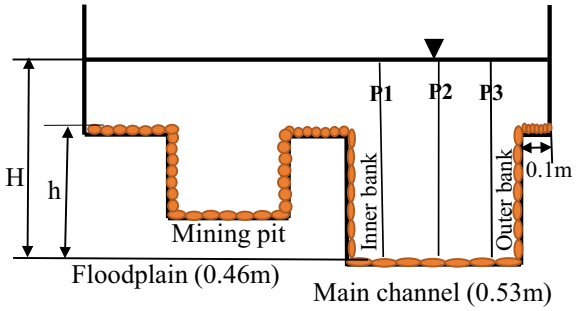

Fig. 2 Cross-sectional (CS1) view of the channel

Table 1 Configuration of numerical simulation

Dimension of the channel	18 m × 1 m × 0.3 m
Sinuosity index	1.1
Width of the main channel	0.53 m
Height of the flood plain	0.08 m
Size of the sand pit	0.4 m × 0.2 m × 0.06 m
Bed roughness height	0.0016 m
Meandering channel length	9.6 m

4.2.1 Turbulence and Viscosity Model

Turbulence models are a set of mathematical equations, which solve non-linear terms of the Navier Stokes equation. The concept behind it is solving fluid flow non-linear partial differential equations. There are three turbulence models that are used in this study (k-ω, k-ε, and RNG k-ε).

4.3 Boundary and Initial Condition

The simulation's accuracy is influenced by the mesh size, boundary conditions, and initial conditions. The accuracy of the model will be almost constant at a certain limit of mesh size [16], but it is very sensitive to the boundary and initial conditions. In this study, the mesh size was set to 0.01 m throughout the channel, and the total number of cells was 2,520,000. The boundary conditions were selected as follows: the inlet was specified with a volume flow rate, while the outlet was set with an outflow boundary condition and a fluid height of 0.14 m in the channel. The lateral directions were treated with wall boundary conditions, assuming a zero-roughness height for the side walls. At the bed, a wall boundary condition was considered. Finally, at the free stream, the boundary condition was specified as atmospheric pressure (Table 2).

5 Results and Discussion

The results of several flow characteristics are discussed in this section such as secondary current, streamwise velocity, and turbulence kinetic energy (TKE) due to floodplain sand mining pit in a low sinuous (SI = 1.1) channel.

Table 2 Hydraulic parameters of numerical setups

Serial number	Simulation run conditions	Discharge (m^3/s)	Flow depth (m)	Initial velocity (m^3/s)	Pressure distribution
1 2 3	k-ω k-ε RNG k-ε	0.01536	0.14	0.11	Hydrostatic

5.1 *Comparison of Turbulence Models Using Experimental and Numerical Results*

For validating the numerical simulation and turbulence model, IIT Guwahati fluvial lab experimental results are used. For this purpose, there are three points (P1, P2, and P3) considered in the main channel at cross-Sect. 1 (Fig. 2). Figure 3 depicts the streamwise velocity distribution in the main channel at three different points, namely P1, P2, and P3. The maximum streamwise velocity at the inner bank (P1) of the main channel is observed just below the free surface, as shown in Fig. 4a. At the mid (P2) of the main channel, the maximum streamwise velocity is slightly shifted below as compared to point P1, as depicted in Fig. 4b. Furthermore, at the outer bank (P3), the maximum streamwise velocity is observed at almost half of the depth of flow, as illustrated in Fig. 4c.

According to Priego et al. [47], a shift in the maximum streamwise velocity occurs from the inner bank of the main channel to the outer bank, from just below the free surface to almost mid-depth. This phenomenon is commonly attributed to the presence of unbalanced forces between centrifugal forces and hydrostatic pressure gradients. Experimental results were collected at three distinct points labeled P1, P2, and

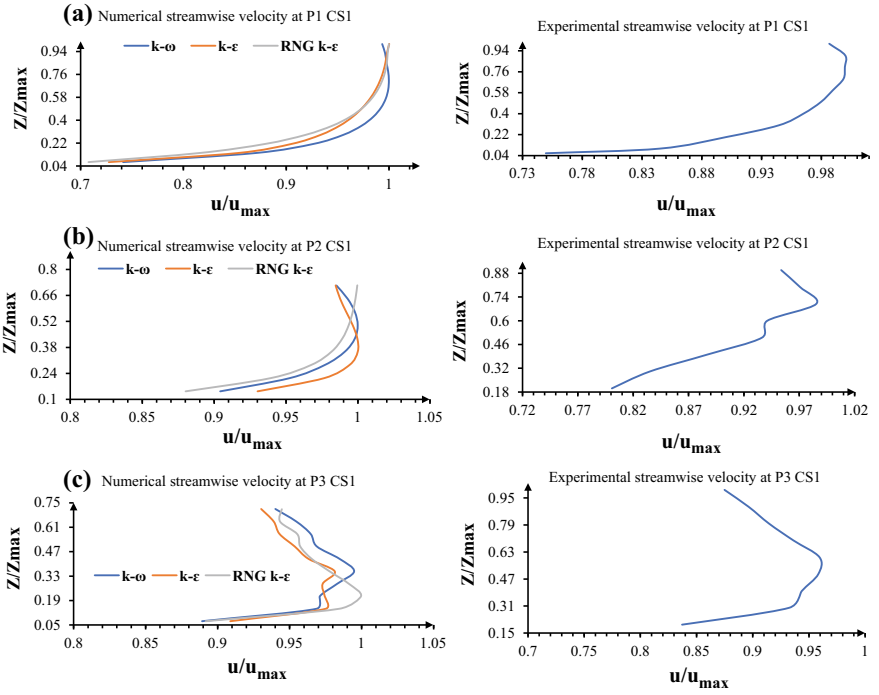

Fig. 3 Vertical stream-wise velocity, **a** at the inner bank, **b** at the mid of the main channel, **c** at the outer bank

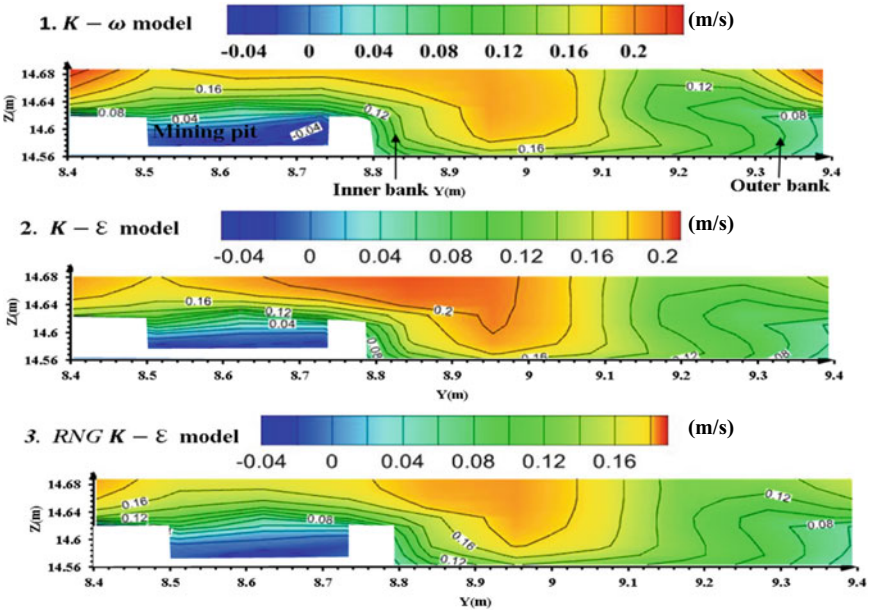

Fig. 4 Streamwise velocity contour plots near the mining pit at (CS1)

P3 to be best suited to the k-ω turbulence model. In summary, the shift in maximum streamwise velocity from the inner bank to the outer bank and from just below the free surface to almost mid-depth can be explained by the unbalanced forces between centrifugal forces and hydrostatic pressure gradients. The experimental streamwise velocity profiles collected at points P1, P2, and P3 were found to be best suited to the k-ω turbulence model than the other two turbulence models for a sand bed sinuous channel with lateral metal walls.

5.2 *Comparison of Turbulence Models Using Numerical Simulation*

5.2.1 Streamwise Velocity at CS1

Figure 4 depicts the simulated contour plots of streamwise velocity at cross-section 1 (CS1) using the three turbulence models: k-ω, k-ε, and RNG k-ε. The dashed line on the plot represents the negative magnitude of streamwise velocity within the flood-plain sand mining pit. The results indicate that the maximum streamwise velocity is concentrated near the inner bank of the main channel, which is consistent with previous studies [48, 49]. However, the magnitude of the maximum streamwise velocity varies by 10% among the three turbulence models. The k-ω model exhibits

the highest maximum streamwise velocity, while the k-ε model shows the lowest. Overall, these results suggest that the k-ω turbulence model is better suited for simulating streamwise velocity in low sinuosity channels with floodplain sand mining pits.

5.2.2 Secondary Current at CS1

In Fig. 5, simulated contour plots of the secondary current at cross-section (CS1) are displayed with the three turbulence models, namely, k-ω, k-ε, and RNG k-ε. The concentration of the secondary current is observed inside the mining pit and at the outer bank. The presence of secondary currents at the outer bank leads to scouring, which is a common phenomenon in sinuous rivers or channels and accelerates the thalweg shifting phenomena. The concentration of the secondary current is more pronounced in the case of k-ω and k-ε models as compared to the RNG k-ε model. These observations are consistent with previous studies [47]. Therefore, the results suggest that k-ω and k-ε models are more suitable for predicting the concentration of secondary currents and the associated scour phenomenon in low sinuosity channels.

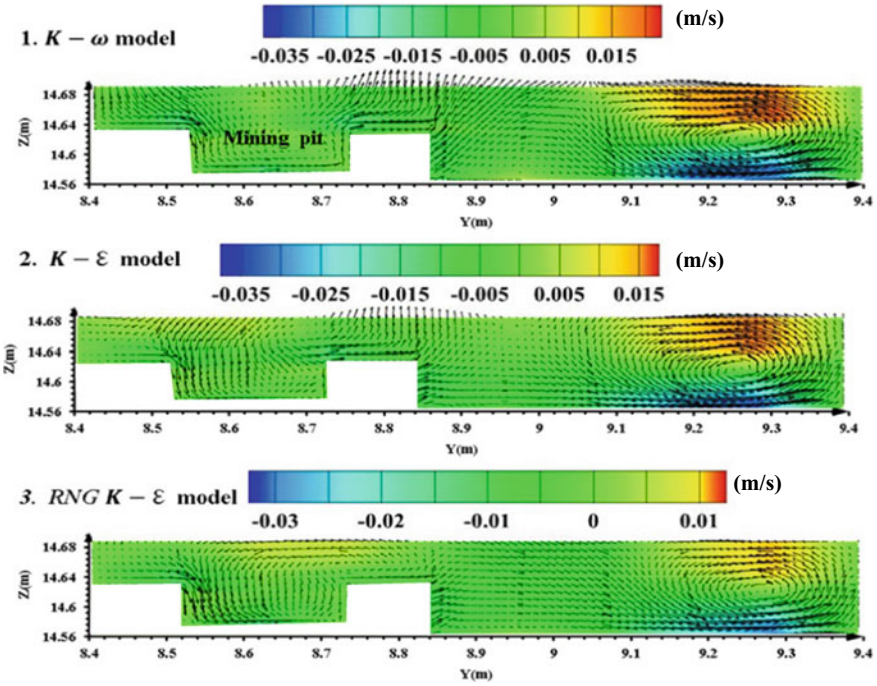

Fig. 5 Secondary current contour plots near the mining pit (at CS1)

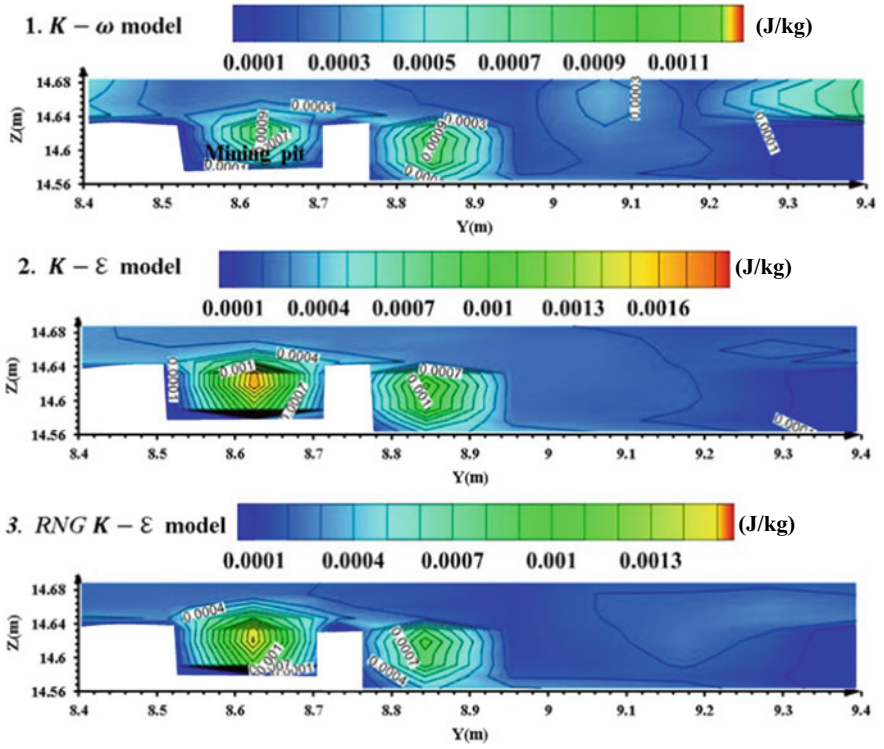

Fig. 6 Turbulent kinetic energy contour plots near the mining pit (at CS1)

5.2.3 Turbulent Kinetic Energy at CS1

Figure 6 in the study shows the simulated contour plots of turbulence kinetic energy (TKE) at cross-section (CS1) using three different turbulence models: k-ω, k-ε, and RNG k-ε. The results indicate that TKE is mainly concentrated within the floodplain sand mining pit and near the inner bank of the main channel. Previous research has also identified similar patterns [50]. However, the concentration of TKE in the k-ε model is observed to be higher at the inner bank in comparison to the other two models.

6 Conclusion

The present study investigated the applicability of turbulence models for predicting the flow characteristics in a channel with a low sinuosity and a rectangular sand mining pit located on the floodplain adjacent to the channel. The study found that the k-ω turbulence model was the best suited for analyzing the sinuous channel with

sand bed and metal side walls, as it yielded the closest results to the experimental data. The study also found that the maximum streamwise velocity in the channel shifted from the free surface (inner bank) to almost the mid-flow depth (outer bank). Additionally, the secondary current was more concentrated at the outer bank when using the k-ω model, compared to the RNG k-ε model. This suggests that the K-ω model was better at capturing the flow behavior in a sand bed sinuous channels with lateral metal walls. Furthermore, the turbulence kinetic energy was found to be more concentrated at the inner bank when using the k-ε model, compared to the k-ω and RNG k-ε models.

Overall, this study provides valuable insights into the selection of turbulence models for simulating flow in sinuous channels with floodplains and highlights the importance of accurately predicting flow characteristics for a better understanding of sediment transport and channel stability.

References

1. Pacheco-Ceballos R (1983) Energy losses and shear stresses in channel bends. J Hydraul Eng 109(6):881–896
2. Prinos P, Townsend R, Tavoularis S (1985) Structure of turbulence in compound channel flows. J Hydraul Eng 111(9):1246–1261
3. Callander RA (1978) River meandering. Annu Rev Fluid Mech 10(1):129–158
4. Pradhan C et al (2022a) Assessment of fluvial controls and cross-sectional recovery indicators in a large regulated river. In: Recent trends in river corridor management: select proceedings of RCRM 2021. Springer Nature Singapore, Singapore, pp 39–48
5. Myers WRC (1978) Momentum transfer in a compound channel. J Hydraul Res 16(2):139–150
6. Modalavalasa S et al (2023) Laboratory investigation on flow structure and turbulent characteristics in low sinuous compound channels with vegetated floodplains. J Hydrol 129178
7. Rajaratnam N, Ahmadi RM (1979) Interaction between main channel and flood-plain flows. J Hydraul Div 105(5):573–588
8. Sellin RHJ (1964) A laboratory investigation into the interaction between the flow in the channel of a river and that over its flood plain. La Houille Blanche 7:793–802
9. Yang CT (1971) On river meanders. J Hydrol 13:231–325
10. Bagnold RA (1960) Some aspects of the shape of river meanders. US Government Printing Office
11. Kondolf GM (2002) Freshwater gravel mining and dredging issues: white paper. Washington Department of Fish and Wildlife
12. Molnár P, Ramírez JA (1998) Energy dissipation theories and optimal channel characteristics of river networks. Water Resour Res 34(7):1809–1818
13. Padmalal D, Maya K (2014) Sand mining: environmental impacts and selected case studies. Springer
14. Hübler M, Pothen F (2021) Can smart policies solve the sand mining problem? PLoS ONE 16(4):e0248882
15. Khan S, Ai Sugie (2015) Sand mining and its social impacts on local society in rural Bangladesh: a case study of a village in Tangail district. J Urban Regional Stud Contemp India 2(1):1–11
16. Daneshfaraz R et al (2021) Investigation of local scouring around hydrodynamic and circular pile groups under the influence of river material harvesting pits. Water 13(16):2192
17. Hackney CR et al (2020) River bank instability from unsustainable sand mining in the lower Mekong River. Nat Sustain 3(3):217–225

18. Nandi KK et al (2022a) How dynamic is the Brahmaputra? Understanding the process–form–vegetation interactions for hierarchies of energy dissipation. Ecohydrology 15(3):e2416
19. Nandi KK et al (2022b) Understanding the entropy-based morphological variability and energy expenditure mechanism of a large braided river system. J Hydrol 615:128662
20. Gavriletea MD (2017) Environmental impacts of sand exploitation. Analysis of sand market. Sustainability 9(7):1118
21. Koehnken L et al (2020) Impacts of riverine sand mining on freshwater ecosystems: a review of the scientific evidence and guidance for future research. River Res Appl 36(3):362–370
22. Lee H-Y, Fu D-T, Song M-H (1993) Migration of rectangular mining pit composed of uniform sediments. J Hydraul Eng 119(1):64–80
23. Neyshabouri SAAS, Farhadzadeh A, Amini A (2002) Experimental and field study on mining-pit migration. Int J Sediment Res 17(4):323–331
24. Haghnazar H, Saneie M (2020) Impacts of pit distance and location on river sand mining management. Model Earth Syst Environ 5(4):1463–1472
25. Zolghadr M et al (2021) Migration of sand mining pit in rivers: an experimental, numerical and case study. Measurement 172:108944
26. Thi Kim T et al (2020) Assessment of the impact of sand mining on bottom morphology in the Mekong River in an Giang Province, Vietnam, using a hydro-morphological model with GPU computing. Water 12(10):2912
27. Lade AD, Deshpande V, Kumar B (2020) Study of flow turbulence around a circular bridge pier in sand-mined stream channel. In: Proceedings of the Institution of Civil Engineers-Water Management, vol. 173. no. 5. Thomas Telford Ltd.
28. Barman B, Kumar B, Sarma AK (2019) Impact of sand mining on alluvial channel flow characteristics. Ecol Eng 135:36–44
29. Chen S et al (2018) Effect of sand mining on bridge capacity and safety under the bridge. J Highw Transport Res Dev (English Edition) 12(2):51–58
30. Chembolu V, Kakati R, Dutta S (2019) A laboratory study of flow characteristics in natural heterogeneous vegetation patches under submerged conditions. Adv Water Resour 133:103418
31. Modalavalasa S et al (2022b) Combined effect of bridge piers and floodplain vegetation on main channel hydraulics. Exp Thermal Fluid Sci 136:110669
32. Pradhan C et al (2021a) Role of effective discharge on morphological changes for a regulated macrochannel river system. Geomorphology 385:107718
33. Pradhan C et al (2021b) Regulated rivers in India: research progress and future directions. ISH J Hydraul Eng 1–13
34. Pradhan C et al (2022b) A process-based recovery indicator for anthropogenically disturbed river system. Sci Rep 12(1):1–14
35. Zhang B et al (2021) Experimental study on the flow behaviour of water-sand mixtures in fractured rock specimens. Int J Min Sci Technol 31(3):377–385
36. Alasta MS et al (2022) Modeling of local scour depth around bridge pier using FLOW 3D. CRPASE: Trans Civ Environ Eng 8(2):1–9
37. Fard ART (2020) Influence of vegetation on shear stress and flow rate in open channel using flow 3D. Civil Eng Res J 9(5):555774
38. Kocaman S, Seckin G, Erduran KS (2010) 3D model for prediction of flow profiles around bridges. J Hydraul Res 48(4):521–525
39. Karami H et al (2014) Verification of numerical study of scour around spur dikes using experimental data. Water Environ J 28(1):124–134
40. Kakati R, Chembolu V, Dutta S (2022) Experimental and numerical investigation of hybrid river training works using OpenFOAM. Water Resour Manag 36(8):2847–2863
41. Man C et al (2019) Assessment of turbulence models on bridge-pier scour using flow-3D. World J Eng Technol 7(2):241–255
42. Maurya OP et al (2022) Effect of sinuosity variation on flow characteristics of sand mined sinuous channel using numerical modeling
43. Maurya OP et al (2023) Flow hydrodynamics influences due to flood plain sand mining in a meandering channel. In: Sustainable environment: proceedings of NERC 2022. Springer Nature Singapore, Singapore, pp 245–251

44. Modalavalasa S et al (2022a) Numerical and experimental investigation of effect of green river corridor on main channel hydraulics. In: Recent trends in river corridor management: select proceedings of RCRM 2021. Springer Nature Singapore, Singapore, pp 165–176
45. Nazari-Sharabian M et al (2020) Sacrificial piles as scour countermeasures in river bridges a numerical study using flow-3D. Civ Eng J 6(6):1091
46. Shamohamadi B, Mehboudi A (2016) Numerical modeling of local scour at the junction of open channels in Flow3d numerical model. Civ Eng J 2(9):474–483
47. Priego-Hernández GA, Rivera-Trejo F (2016) Secondary currents: measurement and analysis. Atmósfera 29(1):23–34
48. Bathurst JC et al (2002) Overbank sediment deposition patterns for straight and meandering flume channels. Earth Surf Proc Land 27(6):659–665
49. Xu D, Bai Y (2013) Experimental study on the bed topography evolution in alluvial meandering rivers with various sinuousnesses. J Hydro-Environ Res 7(2):92–102
50. Biron PM et al (2004) Comparing different methods of bed shear stress estimates in simple and complex flow fields. Earth Surf Process Landf: J Br Geomorphol Res Group 29(11):1403–1415

Structure of Turbulent Flow in a Meander Gravel Bed Channel

Abhimanyu Kumar, Pritam Kumar, and Anurag Sharma

Abstract Various types of bed materials are present in rivers or canals, and they have important effects on hydrodynamic characteristics such as velocity distribution and turbulence characteristics. Study of the flow behavior in gravel bed channels is limited until the flow structures are described and their origin explained. In the meandering river consisting of gravel as bed material, eddies can be seen at the surface due to which flow turbulence is not random. The experimentations were performed in a prismatic rectangular concrete meander channel having a slope of 0.001 and sinuosity of 1.06 and this channel bed is arranged with non-uniform gravel with D_{50} as 12 mm to study the turbulent flow characteristics such as time-averaged velocity and turbulent intensity along longitudinal and vertical directions at two different discharges. The experimental data were collected by a 3D Acoustic Doppler Velocimeter. In this investigation, longitudinal velocity decreases in the downstream direction near the bed surface but increases along the free surface and vertical velocity reduces in the direction of the stream. Analysis and comparison of turbulent flow properties in a gravel bed meander channel at two different discharges and different sections are studied in this chapter. It will give a better impact on the field of hydraulics and provide a comprehensive idea for studying some important flow characteristics in a more advanced manner for different conditions.

Keywords Meander · Gravel · Flow velocity · Turbulent

1 Introduction

To determine the intensity and character of river processes, one of the main factors is turbulence. These consist of sediment transport, erosion, deposition, flow resistance, transfer of heat, diffusion of matter, and origin of bed and channel systems. Turbulence in free surface flows is currently the subject of extensive research. Turbulent fluctuations are thought to be chaotic and unpredictable, so it is expected that

A. Kumar · P. Kumar · A. Sharma (✉)
Department of Civil Engineering, National Institute of Technology, Rourkela, India
e-mail: sharmaan@nitrkl.ac.in

S. Dutta and V. Chembolu (eds.), *Recent Development in River Corridor Management*,
Lecture Notes in Civil Engineering 376, https://doi.org/10.1007/978-981-99-4423-1_8

all turbulent structures would be elucidated experimentally and conceptually using standard statistical techniques. At the origin of analysis of extensive turbulent variations, a series of "rolling" vortices of depth-wise were included in the mathematical model of free surface flow [13]. The kinematic structure of the flow in lab channels through rough and smooth beds was carefully considered by Fidman [2]. He discovered that the small-frequency turbulent variations brought on by the biggest turbulent instabilities contain the most turbulence energy. In the flume studies with moveable gravel beds, Klaven and Kopaliani [7] used the visualization method.

A significant and recognized element of flow through the curvature of a meandering bend induced secondary motion that develops in the bend's center as a result of a discrepancy between the transverse pressure gradient and the centrifugal force close to the bed [4]. A streamwise coherent vortical structure is created as a result of this imbalance, and its sense of rotation causes it to steer near-bed flow along the inner bank and surface flow along the outer bank. Johannesson and Parker [5] created a mathematical model for the analysis of secondary flow in slightly sinuous channels, and Kalkwijk and De Vriend [6] devised a mathematical model characterizing primary and secondary flow velocities in large and slightly curved bends in open channel. Frothingham and Rhoads [3] used field experiment in irregular compound meander bend to look at the 3D flow structure and streambed modifications. They observed inside a lobe that no mean streamlines complete a full cycle of helical rotation and that helical mean flow motion connected to the center area cell gradually degrades as the flow approaches inflections in curvature. In the investigation of flow in a meandering gravel bed watercourse, Thompson [11] noted a region of upwelling along the stream's concave bend and inward flow along water's surface into a region of convergence over pool's deepest portion. Van Balen et al. [12], in order to replicate the flow in a sinuous flume with a rectangular cross-section, used Large-Eddy Simulation (LES) which they used to confirm that centrifugal force and cross-stream turbulent loads are key factors in the creation of outer bank cell. Sukhodolov et al. (2012) effort was motivated by mounting evidence that the riffle-pool geometry in bends can have major effects on flow structure. This study uses field data to examine the flow in a lowland river bend with a shallow riffle and a deep pool. According to the investigation, the reach flow in the riffle is nearly uniform. Two layers make up the vertical structure of the stream in the pool, which has a nearly uniform flow along the riverbed. Ferguson et al. [1] performed 3D Reynolds Averaged Navier–Stokes (RANS) simulations. He noted the recirculation region along the convex bend of the meander and solved flow in natural bends. They claimed that by forming clumps of fine sediment, the slow flow in the convex bend recirculation region can alter the dynamics of sediment. The creation of bars at the convex bend of the bank is associated with flow separation, which has a significant impact on meander morpho-mechanics, according to all previous field and laboratory research.

The aforementioned literature study demonstrates the difficulty of meander bend flows and displays that even through substantial advancements, there are numerous features of such flows that are not fully understood. Therefore, there is a need for more study on turbulent flow properties in a gravel bed meander channel. In this paper, we

experimentally investigate turbulent flow properties in a gravel bed meander channel at different sections and compare them with two different discharges.

2 Experimental Setup

The experiment was performed in a 10 m long, 1.7 m wide, and 0.9 m depth compound meandering channel with a bed slope of 0.001. The cross-section of the main meandering channel was rectangular with a breadth of 0.28 m and depth of 0.10 m. Sinuosity of the main channel was 1.06 with a bend angle of 30 degrees. An overhead reinforced cement concrete tank was erected upstream of the channel to carry water to the testing flume. Steady head conditions are beneficial for testing purposes. To maintain a constant water supply, the overflow water is routed through line links directly to the sump tank, and the volumetric tank collects all the channel water before directing it to the sump tank as well. The distribution of water along the channel is provided by three 10HP diffusive syphons together with suction and conveyance pipes. In order to straighten and minimize the flow turbulence, a stilling chamber with a baffle arrangement is placed at the beginning of the channel. An almost uniform flow was achieved by adjusting the tailgate. The 2.2-m test section was selected at a distance of $3.85 < \times < 6.05$ (x is the distance of examination section from the inlet in the direction of flow) because it was in a location where the flow was fully developed and unimpeded by backwater. The bed of the main channel was covered by river gravel whose particle size (D_{50}) is 12 mm. Over the breadth of the canal where the experimentation setup was located, the moveable bridge arrangement is positioned. Two different discharges of 0.011971 m^3/s and 0.0106 m^3/s were taken for this investigation. Three-dimensional velocity was measured using a SonTek 16 MHz Micro-Acoustic Doppler Velocimetry system (ADV). The bend apex and cross-over parts of the examination section were measured for their respective velocities. Section S1 and S3 are bend apex, and S2 and S4 are cross-over of the channel cross-section shown in Fig. 1, and experimental setup in laboratory is shown in Fig. 2. All the data are taken at the middle of channel cross-section. To provide correct datasets, each point velocity was filtered via WIN ADV software with a signal to noise ratio (SNR) of 15 and a correlation value of 70 [8].

3 Results and Discussion

In this segment, different turbulent flow characteristics have been discussed for flow in the gravel bed meandering channel in the direction of the stream and compared between two different discharges Q1 and Q2 of 0.01197 m^3/s and 0.0106 m^3/s, respectively. Due to ADV's limitations, it was not able to measure the flow field in the area that was 5 cm below the free surface. Therefore, the flow region close to the free surface is outside the possibility of this investigation.

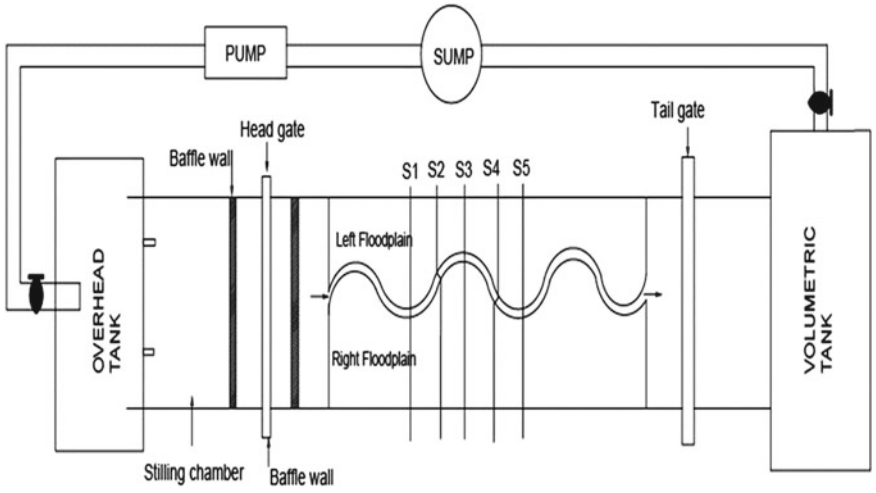

Fig. 1 Plan view of experimental setup and test section

Fig. 2 Experimental setup in laboratory

3.1 Longitudinal Velocity

Vertical distribution of longitudinal velocity at different sections with respect to normalized depth of flow (y/H, where y = height from bed surface and H = total depth of flow) are shown in Fig. 3. A comparison of the differences in discharge illustrates the variation in longitudinal velocity at the 4 sections. Bend apex sections are shown by Section S1 and S3, whereas S2 and S4 are the cross-over sections. On observing the profiles across streamwise and comparing with two different discharges Q1 and Q2, where Q1 > Q2; it is seen that the velocity remains higher towards upper surface. Near the bed, velocity is minimum for both discharges under the case of

gravel bed. Near the bed surface, velocity is smaller for cross-over sections than bend apex sections. In the comparison of discharge, velocity is higher for Q2 than Q1 for all sections. The roughness of bed increases in a channel would suggest a greater value of Manning's 'n' and hence velocity will decrease. A meandering waterway should have also allowed for such an observation. However, as seen in bend apex sections (S1 and S3), the longitudinal velocity for lesser discharge (Q2) is lower than the longitudinal velocity for larger discharge (Q1) towards the free surface but in inner layer higher longitudinal velocity for smaller discharge in the gravel bed meandering channel. However, longitudinal velocity is higher for smaller discharge than higher discharge throughout the flow depth at cross-over sections. The gravel bed meandering channel's velocity distribution is seen to be higher for increased discharge for the bend apex section as depth increases. The curvature is the sole additional impact, and it is same for both discharges. As a conclusion, the resistance brought on by the meandering effect is more pronounced at the curve apex than at the cross-over. Thus, it may be concluded that channel curvature, rather than only bed roughness, affects velocity variation significantly.

3.2 Vertical Velocity

Distribution of vertical velocity at bend apex and cross-over are shown in Fig. 4 of S1, S3 and S2, S4; respectively. On observing the profile of vertical velocity, found that close to the bed surface water particles move in upward direction after that it tends towards downward direction at a normalized depth of 0.05 to 0.1. In case of vertical velocity in outer layer, water particles moved towards upward direction. Intensity of vertical velocity is higher for bend apex than cross-over near the bed surface and smaller for bend apex towards the outer layer. In this experimentation, we also observed that smaller discharge has smaller vertical velocity intensity than higher discharge at bend apex section. At cross-over section, smaller discharge has higher intensity than higher discharge. In general, when water particles moved along streamwise direction from bend apex with higher discharge then transverse velocity is also higher than the smaller discharge of water flowing through meandering gravel bed channel but at the cross-over, it is opposite from bend apex, that is, when water particles moved along streamwise direction from cross-over then smaller discharge have higher vertical velocity intensity than higher discharge.

3.3 Longitudinal Turbulence Intensity

The turbulent intensity is analyzed by the value of the root-mean-square (rms) of longitudinal velocity variations. Distribution of longitudinal turbulent intensity at different sections with respect to normalized depth of flow (y/H, where y = height from bed surface and H = total depth of flow) is shown in Fig. 5. The results

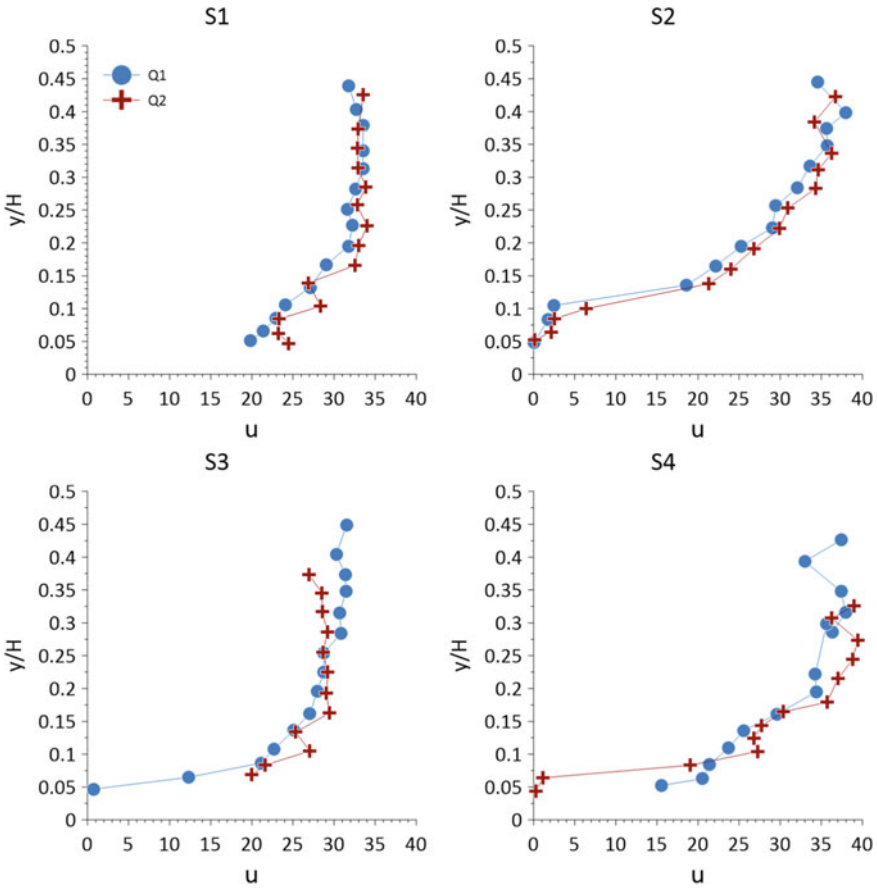

Fig. 3 Longitudinal velocity profile at different section

display a respectable agreement with the experimental results [9]. We observed that longitudinal turbulence intensity is slightly higher for smaller discharge than higher discharge at bend apex sections, but at cross-over section, it is slightly higher for higher discharge than smaller discharge. Hence, turbulent intensity in gravel bed meander channel decreases when flow discharge increases at bend apex section and increases when flow discharge increases at cross-over of the channel cross-section. Magnitude of longitudinal turbulence intensity is higher for cross-over sections as compared to bend apex sections. It means when water particles move in the direction of stream through bend apex section then longitudinal turbulence intensity decreases, while at cross-over section increases.

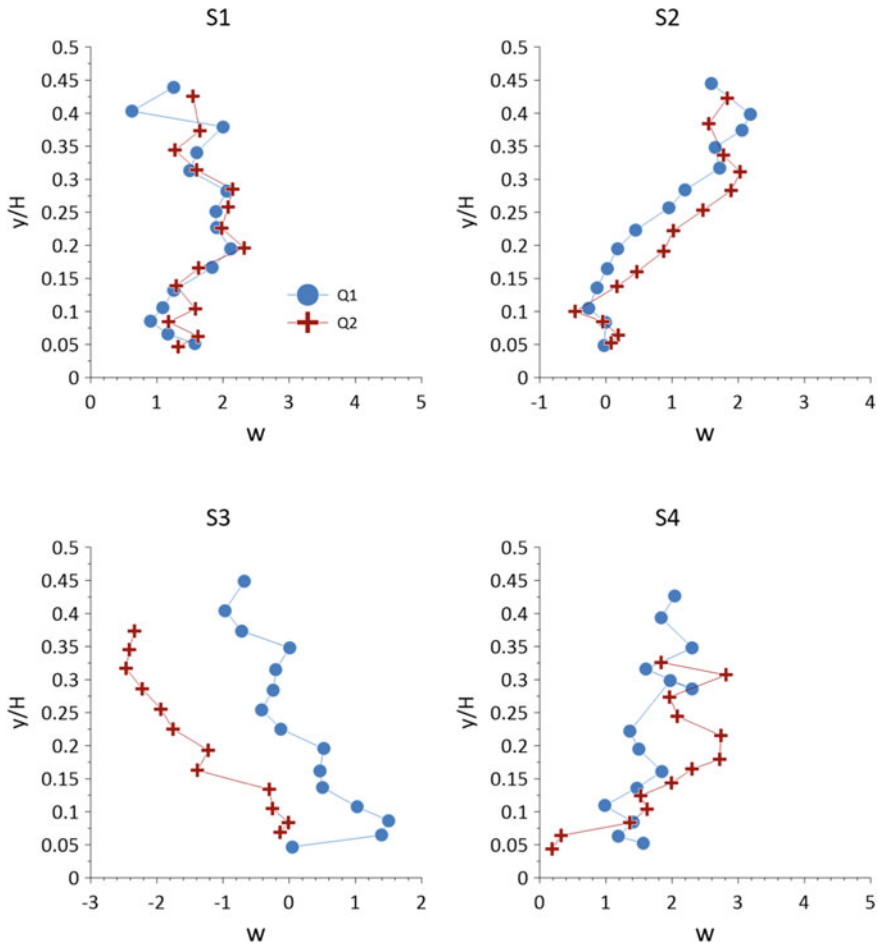

Fig. 4 Vertical velocity profile at different section

3.4 Vertical Turbulent Intensity

Distribution of vertical turbulent intensity at different sections with normalized depth of flow is shown in Fig. 6, where S1 and S3 are bend apex sections and S2 and S4 are cross-over sections for two different discharges (Q1 > Q2) in a gravel bed meander channel. The result shows that vertical turbulent intensity is smaller near the bed surface. Near the bed surface, it is higher for bend apex than cross-over. Vertical turbulent intensity is higher for smaller discharge (Q2) than higher discharge (Q1) at bend apex section, but smaller for smaller discharge at cross-over section in gravel bed meander channel. In the comparison of bend apex and cross-over section, vertical turbulent intensity is higher for bend apex section than cross-over section near the bed surface.

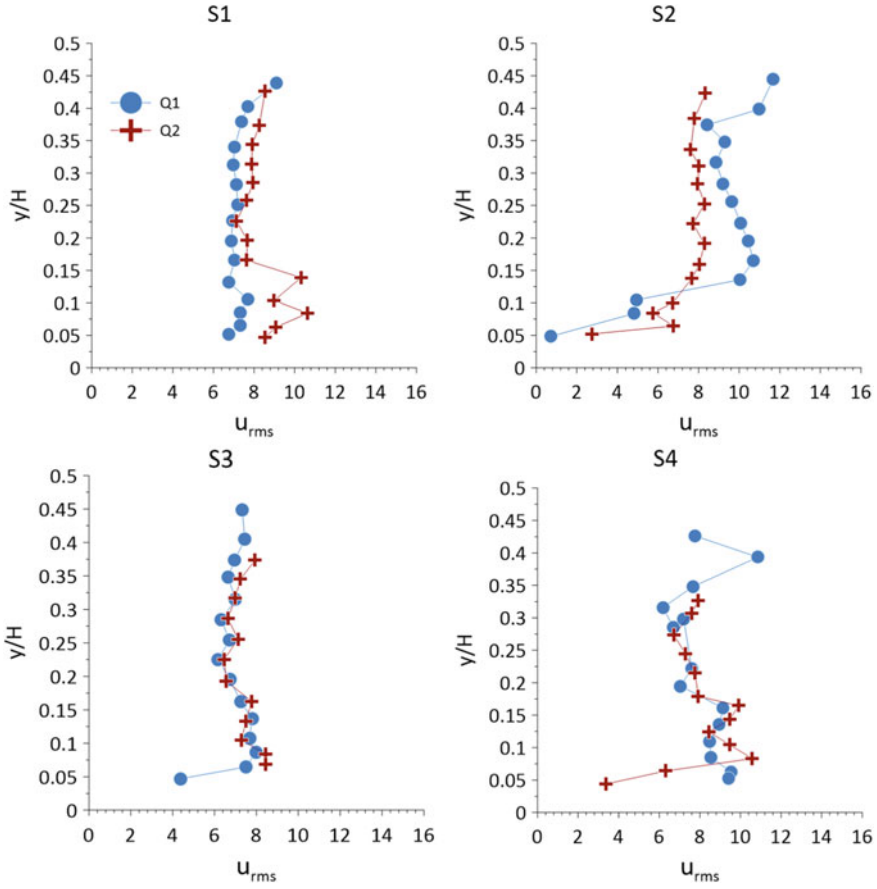

Fig. 5 Longitudinal turbulent intensity profile for different section

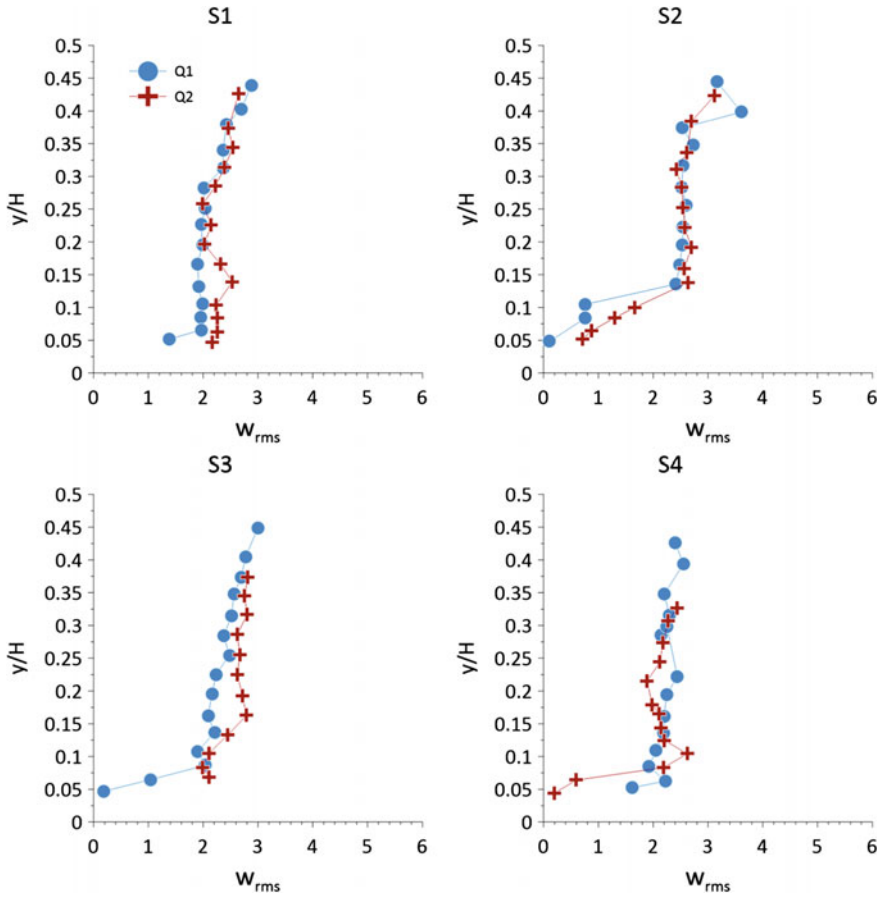

Fig. 6 Vertical turbulent intensity at different sections

4 Conclusion

This chapter presents an experimental investigation of two-dimensional flow property in a meandering compound channel whose bed is covered by gravel. This investigation is done under two different flow discharges 0.011971 m^3/s and 0.0106 m^3/s. The flow properties such as the two-dimensional time-averaged velocity and turbulent intensity are examined in this chapter. Further, the results of the vegetation zone at two different bend apex and two different cross-over are analyzed and compared between two different discharges.

The results conclude that the longitudinal velocity decreases near-bed surface for both discharge and higher for bend apex than cross-over. For smaller discharge, longitudinal velocity is smaller for higher discharge at cross-over section but at bend apex section, it is smaller in outer layer for bend apex sections. Thus, the

velocity variation may be affected by discharge variation significantly in the gravel bed meander channel. When discharge increases in gravel bed meander channel, then vertical velocity increases in upward direction at bend apex section. However, it decreases when flow passes from cross-over section for higher discharge. Longitudinal turbulent intensity decreases at bend apex section when discharge of flow increases, while it increases at cross-over section. Vertical turbulent intensity is higher for smaller discharge in gravel bed meander channel. The investigations show the two-dimensional flow property in a gravel bed meandering channel, which has implications on the understanding of the behavior of a gravel bed meandering channel.

References

1. Ferguson RI, Parsons DR, Lane SN, Hardy RJ (2003) Flow in meander bends with recirculation at the inner bank. Water Resour Res 39(11)
2. Fidman BA (1953) Principal results of experimental study of the structure of turbulent flows. Prob Channel Process 138–150
3. Frothingham KM, Rhoads BL (2003) Three-dimensional flow structure and channel change in an asymmetrical compound meander loop, Embarras River, Illinois Earth Surface Processes and Landforms. J Br Geomorphol Res Group 28(6):625–644
4. Humphrey JAC, Whitelaw JH, Yee G (1981) Turbulent flow in a square duct with strong curvature. J Fluid Mech 103:443–463
5. Johannesson H, Parker G (1989) Secondary flow in mildly sinuous channel. J Hydraul Eng 115(3):289–308
6. Kalkwijk JT, De Vriend HJ (1980) Computation of the flow in shallow river bends. J Hydraul Res 18(4):327–342
7. Klaven AB, Kopaliani ZD (1973) Laboratory investigations of the kinematic structure of turbulent flow over a rough bed. Trans State Hydrol Inst 209:67–90
8. Kumar P, Sharma A (2022) Experimental investigation of 3D flow properties around emergent rigid vegetation. Ecohydrology 15(8):e2474
9. Muto Y (1997) Turbulent flow in two-stage meandering channels. PhD thesis, University of Bradford, UK
10. Sukhodolov AN, Nikora VI, Katolikov VM (2011) Flow dynamics in alluvial channels: the legacy of Kirill V Grishanin. J Hydr Res 49(3):285–292
11. Thompson A (1986) Secondary flows and the pool-riffle unit: A case study of the processes of meander development. Earth Surf Proc Land 11(6):631–641
12. Van Balen W, Uijttewaal WS, Blanckaert K (2009) Large-eddy simulation of a mildly curved open-channel flow. J Fluid Mech 630:413–442
13. Velikanov MA (1949) Dynamics of Alluvial Flows. *Gidrom-eteoizdat, Leningrad, Russia*

Experimental Investigation of Infiltration Influenced by Simulated Macro-microporosity

Lohit Jain and Sumedha Chakma

Abstract The modelling of the infiltration process for the field conditions requires the study of macro-microporosity and their primary controlling factors such as slope, land use land cover (LULC), surface condition and soil characteristics. Macropores are found relatively in a smaller percentage than the micropores, yet govern the higher portion of the infiltrated volume in the soil system. In the present study, double-ring infiltrometer experiments were performed on grassland, bare surface, harvested agricultural land and earth cover of a solid waste landfill to understand the participation of active macropores and micropores for different surface slopes with diurnal temperature variation. An average and maximum water flow from macropores were estimated as 64.4% and 84% of the total infiltrated volume for all LULC. Macropore flow was found to be proportional to the temperature by showing higher macro-flow (70.7%) of total infiltration in afternoon sessions than (58.4%) in the forenoon sessions. Macroflow has also demonstrated a positive correlation with the surface slope for all focused LULC. The present study of cumulative infiltration through macropores and micropores individually for different LULC will help understand the water flow mechanism with time beneath the surface. These experimentally derived quantitative infiltration data for different LULCs can have a broad range of applications in this region for drainage system design, agricultural management, and groundwater pollution study.

Keywords Infiltration · Macroporosity · LULC · Slope · Temperature

L. Jain (✉) · S. Chakma
Department of Civil Engineering, Indian Institute of Technology, Delhi 110016, India
e-mail: Lohit.Jain@civil.iitd.ac.in

S. Chakma
e-mail: Sumedha.Chakma@civil.iitd.ac.in

S. Dutta and V. Chembolu (eds.), *Recent Development in River Corridor Management*,
Lecture Notes in Civil Engineering 376, https://doi.org/10.1007/978-981-99-4423-1_9

1 Introduction

A soil system is considered a very complex system due to micropores, macropores, earthworm burrows and cracks, which effectively take part in the infiltration process by connecting to subsurface fractures and generating rapid water drainage flow [1]. Macropore is defined as connecting pores of different shapes and sizes, in which the flux rate occurring in the smallest size of the pore is greater than or equal to the saturated hydraulic conductivity of the soil [8]. Physics-based popular models like Green Ampt and Richard equations have not been justified to represent the whole soil matrix because both models follow the assumption of laminar flow having Reynolds number (Re) < 1, which is valid for the presence of micropores only [3, 8]. It was suggested that preferential flow under ponded conditions could not be described by laminar flow theory adequately due to the presence of macropores either on the surface or in the subsurface [24]. Further, Reynolds numbers for ponded infiltration are observed between 50 and 80 (non-laminar) due to macropores of the natural field, and flow from partially saturated 6 mm macropore is considered turbulent flow with Re > 1000 [21]. Generally, macropores have been observed from 0.32% to 5% of total porosity [3, 44]. It is noted that Richard's model underestimates the infiltration for the field conditions by avoiding the higher flow through macropores, and quoted as "justified misuse of physics" [45], and is considered inefficient for in-situ field conditions. Still, Richard model is considered as one of the popular models because of its comfortable applicability [3]. Few studies support the Darcy-Richard model for the non-ponded infiltration by neglecting acceleration in moment-balance and preferential flow, however, it cannot be neglected for ponded infiltration in the natural field [21]. In the preferential flow generation, macropore distributions plays an important role, which can be categorised based on average equivalent pore diameter. Development of macropores are caused mainly by biopores due to earthworms (2–12 mm), cracks due to wetting and drying loop of soil, and decayed roots have been observed as major reasons for macropore generation [21]. It is not easy to describe preferential flow through macropores quantitatively [5], therefore macropores, macrostructures and cracks have been expressed conceptually as single lumped expressions as total macropore area to simplify the approach [8]. A similar approach has been used based on MDA (Macropore drainage area) by estimating the numbers of macropore per m^2 area of soil, which concluded that macropores capture 50–80% of runoff [46]. Based on several studies, the equivalent diameter of the minimum–maximum size of macropores has been decided as 30 μm and 5000 μm, respectively [6–8, 22, 32, 36]. However, more field studies are required to understand the complexity of the macropores arrangements in natural soil so that infiltration models can be updated by adopting the variations of active macropores.

Therefore, it is necessary to conduct an experimental study of infiltrated volume for the application of more general scenarios on various LULC and understand the different mechanisms for flow through micropores and macropores. In the present

chapter, the participation of macropores and micropores is studied using the field-experimental data for targeted LULC with their soil characteristics, precedent moisture content and field density, incorporating the effects of slope and temperature variation. The purpose of the experimental analysis is to investigate the differences in infiltrated volume from macropores for ponded water conditions between various permeable LULC in urban areas incorporating the combined impacts of temperature variation and slope.

2 Study Area

The experiments were conducted on the field sites located in Delhi, the capital of India, situated in the northern part of India and covering an area of 1483 km^2 (Fig. 1). In the last 14 years, the highest annual rainfall was recorded as 1531.4 mm in 2013, and the annual minimum was 559.4 mm in 2012, with an average rainfall of 879.2 mm [16]. Delhi has a sub-tropical climate, where summers are very hot, with temperatures attained till 45 °C and winters are very cold, with temperatures falling to 2 °C. The annual average difference in maximum and minimum diurnal temperature in Delhi has been observed at approximately 11 °C [27]. The soils in the study area are chiefly found in categories of sand, loamy, sandy loam and silty loam [2].

The chosen metropolitan city, which majorly includes grass area, forest area and bare area surrounded by the agricultural area apart from impermeable built-up area, has been dealing with the rapid growth of industrialisation and increasing population

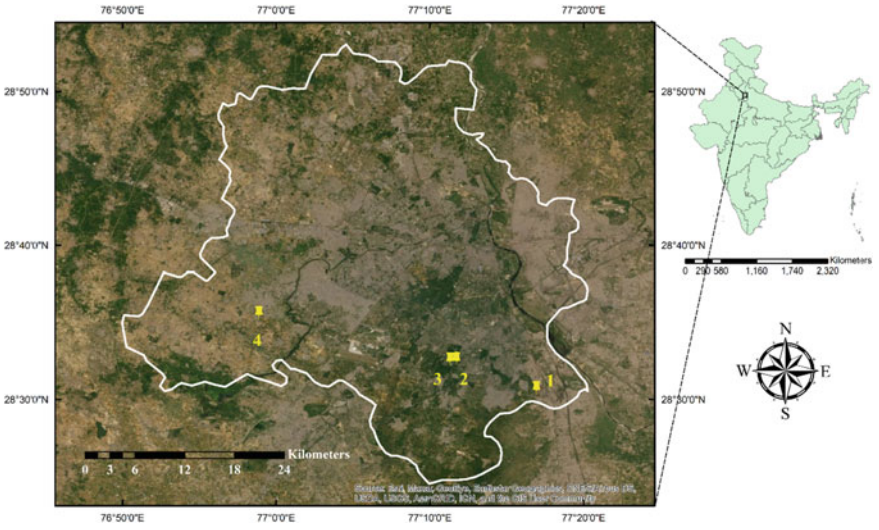

Fig. 1 Experimental locations in Delhi (India): 1. Landfill (Okhla), 2. Grassland, 3. Bare surface (South Delhi) and 4. Agricultural land (Nazafgarh)

rate due to the migration of people from villages and towns to metro cities which promotes a large amount of solid waste generation [39] along with water scarcity in the area [4]. Delhi is also suffering from frequent urban flooding, which has been the result of rapid population growth [26]. Landfills were also found to be one of the most impactful permeable zones in the chosen urban region covering 0.67 km^2 of the area, including all three major landfills (Okhla, Gazipur and Bhalswa) in Delhi [34]. These factors led to the selection of four different LULCs as bare surface, agricultural surface, landfill surface and grass surface in Delhi for studying the effects of slope and temperature on infiltration mechanism as shown in Fig. 1.

3 Methodology

3.1 Experimental Methods and Data Collection

The double-ring infiltrometer method was selected for studying the infiltration characteristics of opted LULC, as it is a well-known and commonly used technique for directly measuring the infiltration rate on the field [10, 35]. The experimental design includes infiltration affecting three major factors: diurnal temperature variation, surface slope and different LULC, which were focused on investigating their impacts on infiltration mechanism quantitatively, as shown in Fig. 2.

Experiments were divided into morning and afternoon sessions for approximately 3.5–4 h duration each to incorporate the temperature variation. The temperature was measured by calibrated digital temperature meter at the surface level for measuring the local temperature variation along with each reading of the infiltrometer. Three sets of experiments were conducted on each inclined surface to study the effect of slope on the infiltration process, and based on the available scenario on fields. The slope was categorised into three parts—flat surface (0°–5°), gentle slope range (6°–15°) and moderate slope range (16°–25°). The agricultural surface was examined for flat surfaces only due to the unavailability of a further range of slopes, and Okhla (landfill) surfaces were available for flat and moderate slope categories as well; however, inclination in grassland and bare surfaces were found in all three slope ranges and examined accordingly. Soil characteristics like field density, moisture content, specific gravity, maximum dry density, particle size distribution and hydraulic conductivity were measured by standard laboratory experiments [17, 19] for soil samples from all experimental sites to characterise the top surface soil, as mentioned in Table 1. Standard proctor experiments were carried out for all the soil samples to understand the dry density variation with change in moisture content, and a comparative chart of maximum dry density and optimum moisture content is shown in Fig. 3. Dry densities of landfill samples and bare field samples were experimentally observed as highest and lowest, respectively, among all targeted sites.

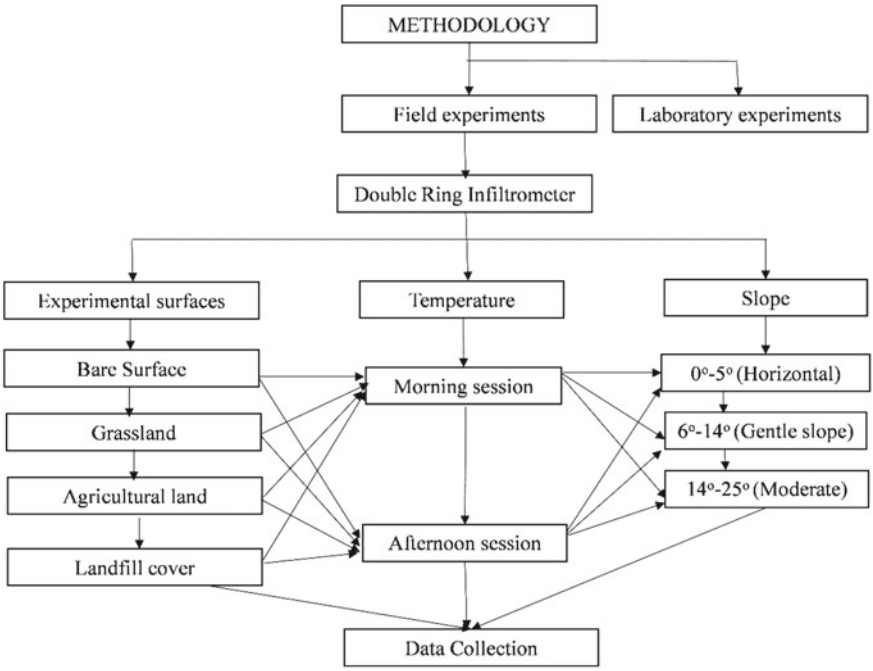

Fig. 2 Experimental flow diagram of the data collection

3.2 Macroporosity Estimation and Participation

Evidently, field infiltration does not include darcian flow or laminar flow only but also non-laminar flow due to the presence of cracks, wormholes, roots and soil aggradation [21]. The General infiltration model was used to examine the participation of micropores considering darcian flow and macropores for non-laminar flow using different mechanisms [20]. Estimation of the percentage of microporosity and macroporosity in the topsoil layer is needed before deciding the weightage of each type of flux. Stolf et al. [40] generated the empirical models using bulk density, particle density and % of sand present in the soil to estimate the microporosity, microporosity and total porosity. After the validation of the estimated porosity from Eq. (3) with the calculated porosity from experimental observation, an average error of 4.49% was observed, as presented in Fig. 4, and thus, Eqs. (1) and (2) were selected for the macro-microporosity estimation.

$$\text{Macroporosity} = 0.693 - 0.465\,FD + 0.212\,Sa \tag{1}$$

$$\text{Microporosity} = 0.337 + 0.120\,FD - 0.294\,Sa \tag{2}$$

Table 1 Soil characteristics of selected LULC based on laboratory experiments

Experiment	Agricultural surface	Grass surface	Landfill soil cover	Bare surface
Initial moisture content (%)	11.84	15.65	6.42	10.12
Hydraulic conductivity (cm/min)	1.77×10^{-2}	1.60×10^{-2}	6.25×10^{-3}	2.76×10^{-2}
Field (Bulk) density (gm/cm^3)	1.50	1.58	1.81	1.21
Gravel (%)	7.6	5.3	20.3	18.6
Sand (%)	74.6	61.5	59.3	41.4
Silt (%)	13.2	28.2	14.1	39.8
Clay (%)	4.5	4.9	2.7	3.8
Specific gravity	2.56	2.58	2.69	2.54
Porosity (calculated/estimated)	0.48/0.45	0.47/0.43	0.37/0.36	0.55/0.56
Micropores (Estimated)	0.349	0.345	0.353	0.409
Macropores (Estimated)	0.100	0.080	0.005	0.155

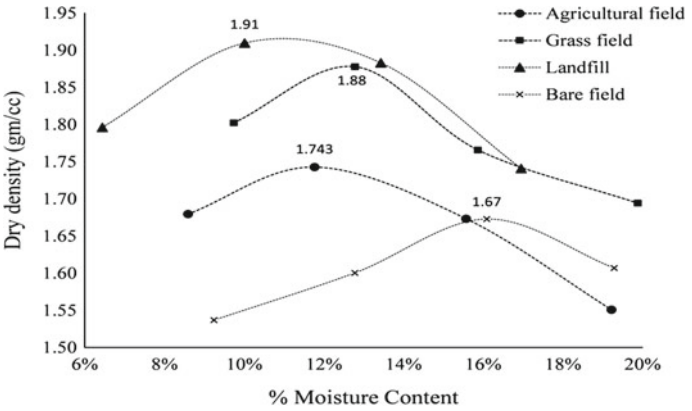

Fig. 3 Variation of dry density with increment in moisture content of all focused LULC and landfill

$$\text{Total porosity} = 1.03 - 0.345\,FD - 0.082\,Sa \tag{3}$$

where, *FD* is the field density of the experimental location, and *Sa* is the percentage of sand in the field soil.

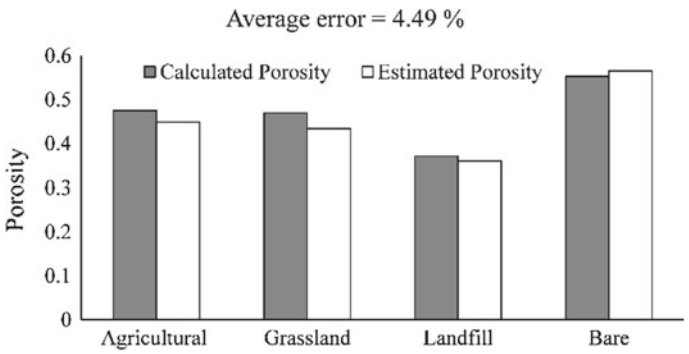

Fig. 4 Comparison in porosity estimated by the empirical model and calculated based on laboratory experiments

Preferential flow is a major part of infiltration volume but is very difficult to describe quantitatively [5]. The macropore area theoretically includes macropores and macrostructures that can be articulated in terms of lumped expression representing all pores and cracks [8]. The minimum and maximum radius of macropores were identified by many researchers as 15–30 μm to 2500–5000 μm [6, 8, 14]. Although, Radulovich found the critical macro-diameter as 100 μm after which the flow converts laminar to non-laminar with Re > 3 [32]. In the present study, minimum and maximum equivalent diameter sizes are considered as 30 μm and 5000 μm for covering all the possible ranges. Weights are calculated for minimum–maximum-sized macropores and microporosity based on the experimental data and used to validate the weights with infiltration data observed in another scenario with different combinations of slope and temperature variation.

4 Results and Discussion

4.1 Infiltration Characteristics with Slope and Temperature Variation

The key features of DRI experimental observations with temperature and slope variations are presented in Table 2 for the focused LULC. The average temperature near the experimental surface showed variation with the LULC and presented 17.23 °C and 52 °C as the minimum and maximum values measured at grassland and landfill, respectively. The trend of average initial and final infiltration rates was observed from the LULC-wise data, which presented f_o in increasing order as 0.25 cm/min, 0.96 cm/min, 1.35 cm/min and 1.48 cm/min for landfill, grass field, agricultural, bare field respectively. Similarly, average steady-state infiltration rates were found in the same increasing order as landfill > Grass > Agricultural > Bare field, varied between

0.015 cm/min and 0.260 cm/min, which can be deduced from Table 2. The reason for the higher infiltration rate in bare surface than grassland is probably due to the pronounced structural changes in the bare ground than in the vegetated area, especially because of the absence of the soil-binding root system. The attributes of land use and land covers, such as soil characteristics, % sand, % silt, % clay, average field density, initial moisture content and surface cover, can affect the infiltrated volume significantly [38]. Although analysis of the study shows that the infiltration process is mostly governed by the density and distribution of porosity in the soil system [41], higher porosity ensures more connectivity in the soil matrix which reflects increased infiltration as compared to soil with lower porosity [33]. Initial and final infiltration rates were also found to be affected by soil characteristics by showing negative correlation coefficients as −0.57 and −0.63 with field densities and positive correlation coefficients as 0.58 and 0.67 with porosity, respectively.

Table 2 Observed infiltration characteristics with various field experimental scenarios for selected LULC

LULC	Slope (°)	Temperature range (°C)	Average temperature (°C)	f_o (cm/min)	f_c (cm/min)	F (200 min) (cm)
Landfill	4	26.0–35.0	30.1	0.1	0.01	2.3
		34.0–42.0	36.9	0.2	0.02	4.5
	23	31.0–38.0	32.8	0.3	0.02	3.7
		38.0–42.0	39.4	0.4	0.01	10.5
Agricultural	2	30.0–50.7	42.5	1.4	0.27	26.4
		52.1–38.9	48.1	1.3	0.15	37.1
		26.8–40.1	27.6	0.6	0.09	22.7
		40.4–36.5	38.2	0.6	0.09	21.6
Bare	1	35.2–37.2	36.3	0.8	0.17	39.8
		44.8–50.7	46.2	1.3	0.26	65.3
	13	30.9–36.4	31.9	1.7	0.21	53.7
		38.5–33.1	37.2	1.7	0.26	77.8
	21	35.9–45.2	38.4	1.9	0.27	77.8
		48.5–52.7	52.1	1.5	0.38	104.1
Grass	2	17.2–33.4	23.1	0.8	0.04	10.9
		33.0–24.2	32.1	0.8	0.05	14.4
	8	16.5–21.2	17.2	0.7	0.08	12.5
		26.7–22.2	26.8	1.7	0.09	22.8
	18	17.5–23.5	19.8	0.8	0.08	19.1
		23.5–26.8	24.1	1.0	0.06	31.5

4.2 Participation of Macropores

Based on past experimental findings, macroporosity was estimated using % of sand and bulk density, which estimated higher macroporosity for bare surface soil systems having lower field density and higher total porosity [40]. The lowest infiltration was observed in landfill surfaces due to minimum active macropores, which mostly depend on land use rather than soil characteristics for the top 20 cm [37]. The average participation of active macropores is found to be 58.4% for morning experimental sessions and 70.7% for afternoon experimental sessions of the total infiltrated volume, respectively. An increasing trend can be noticed for total infiltrated volume and macro-infiltrated volume from landfill to bare surface in a sequence of landfill > grass > agricultural > bare, as depicted by Fig. 5, which depicts the significance of macroporosity in the ponded water infiltration process.

Figure 5b presents the infiltration in the afternoon session (higher temperature), which shows approximately 62.6%, 63.3%, 33.8% and 36.4% higher macro-flow compared to macro-flow estimated in the morning session (morning session) in landfill, grassland, agricultural land, and bare surface, respectively. Thus, Fig. 5a presents an average of 49% lower macroflow in the morning session than Fig. 5b because the higher temperature ranges lead to more thermal movement of the water molecules, reducing the relative mutual friction, which helps in the qualitative clarification of the reduction in viscosity and increment in hydraulic conductivity for the higher temperature [47]. The rise in temperature affects the water movement by increasing hydraulic conductivity due to a decrease in water density and viscosity, which increases fluidity [18]. The present results coincide with the past experiments at the scale of seasonal variation, which documented an increment of 15 cm/day in the summer season as compared to the winter season [23, 31]. The scale of increment was found as a function of soil–water interactions and soil characteristics [23], which justifies the variation in increment of infiltrated volume in the afternoon session for different land uses and land covers.

The Model was calibrated with the soil characteristics, ponding depth, observed temperature data and surface slope. After model setup, it was run using other sets of temperature data and surface slope for all four locations to generate infiltration values which were compared with the corresponding observation data. Table 3 shows the performance of the General Infiltration Model using statistical tools such as the coefficient of determination (R^2), Nash Sutcliffe Efficiency (*NSE*), percentage biased (*PBIAS*) and Root mean Square Error- observations standard deviation ratio (*RSR*).

The variation of simulated cumulative macroflow curves with time, slope and diurnal temperature differences for bare surface (Fig. 6), grassland (Fig. 9), landfill (Fig. 7) and agricultural land (Fig. 8) are investigated. The cumulative infiltration through macropores is found to be 1.2 and 1.6 times higher when the bare surface slope is increased from flat to gentle and moderate, respectively, as shown in Fig. 6a for the morning session. Simulation data showed the similar trend of infiltrated volume via macropores in the afternoon session as well, as shown in Fig. 6b, which

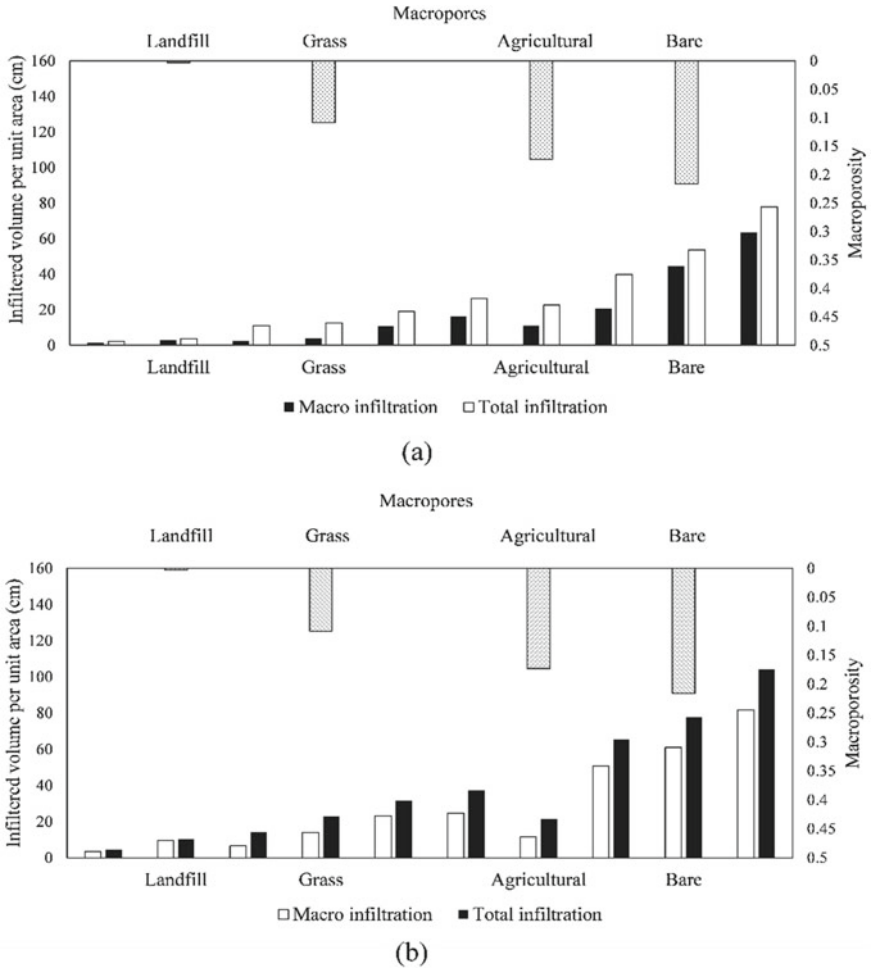

Fig. 5 Variation of infiltrated volume by macropores and total infiltration in **a** lower temperature range (morning session), **b** higher temperature range (afternoon session)

Table 3 Statistical comparison of model outcomes (simulated cumulative infiltration) for parameters as a function of temperature and slope with the observed data

	R^2	NSE	PBIAS	RSR
Landfill	0.995	0.834	21.010	0.406
Agricultural	0.995	0.968	−10.920	0.177
Bare surface	0.999	0.963	−15.120	0.192
Grassland	0.989	0.933	11.500	0.259

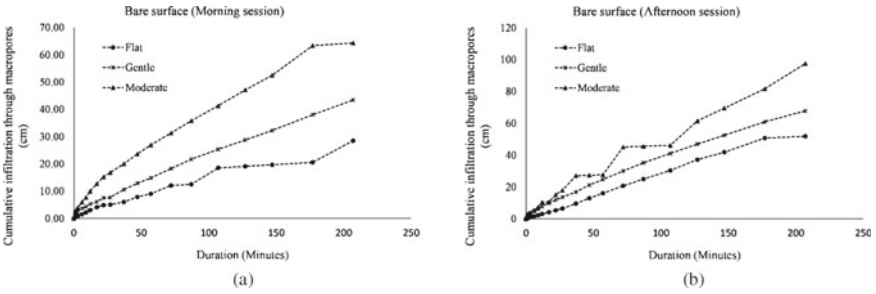

Fig. 6 Simulated variation in cumulative infiltration through macropores with the surface slope for bare surface in **a** morning sessions and **b** afternoon sessions

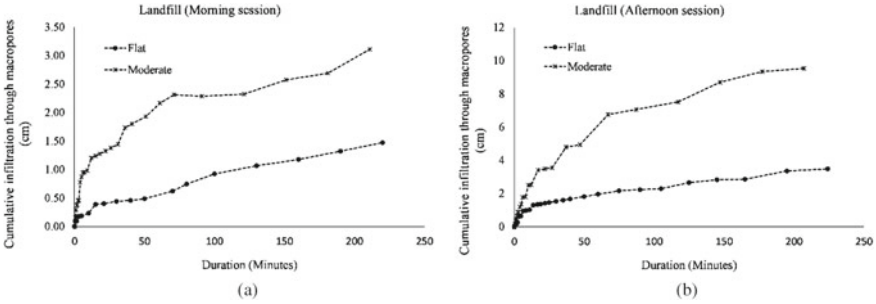

Fig. 7 Simulated variation in cumulative infiltration through macropores with the surface slope for landfill cover in **a** morning session and **b** afternoon session

showed 2.1 and 3.0 times higher macroflow participation for gentle and moderate slopes compared to the flat surface.

Okhla landfill was filled with solid waste in a layer-on-layer structure, which creates the possibility of subsurface flow with higher macrostructures, depending on the compaction of the earth cover. The lowest moisture content was measured for the landfill at the time of the experiment, yet it showed the minimum infiltration among other experimental sites, as presented in Table 2, which can be justified by the increased soil temperature due to exothermic reaction, which reduces the active porosity by filling voids with gases [43]. Cumulative infiltration from macropores for landfill earth surface is analysed, which showed approximately 2.4 and 3.1 times higher macroflow in the afternoon session (Fig. 7b) than in the morning session (Fig. 7a) for flat and moderate slope surfaces, respectively. Landfill earth cover showed the increased macroflow for higher slope and presented 2.1–2.7 times higher macroflow when the slope is increased from the flat surface to a moderate slope surface in the morning and afternoon sessions, respectively.

Cumulative macroflow is observed approximately twice higher for grassland when the slope is increased from flat surface to gentle slope and 3.5 times higher when the slope is increased to moderate, as shown in Fig. 8. Double-ring infiltrometer

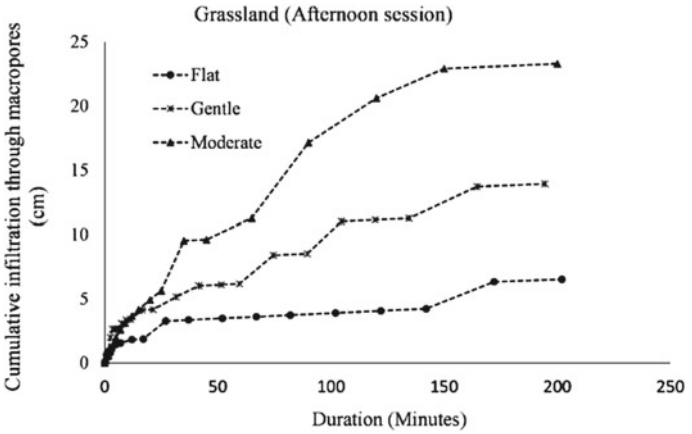

Fig. 8 Simulated variation in cumulative infiltration through macropores with surface slope for grassland

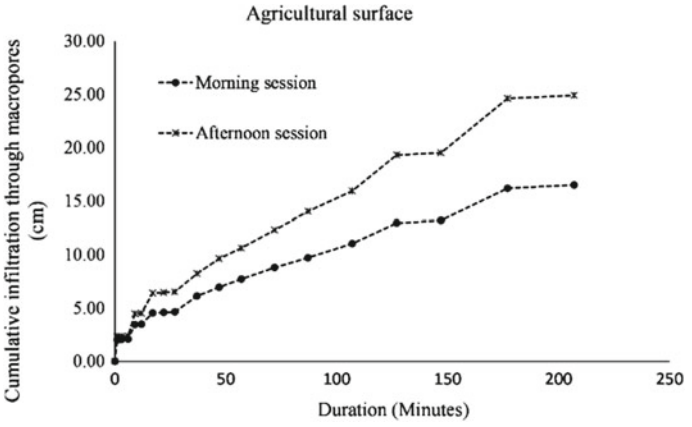

Fig. 9 Simulated variation of cumulative infiltration through macropores for morning and afternoon sessions on agricultural land

obstructs the runoff, and the impact of the slope cannot be measured on direct runoff; however, the effect of the slope can be understood on subsurface flow as parallel flow through macropores due to gravitational acceleration. As the slope increases, the lateral component of flow beneath the surface increases as well [42], which is why the higher infiltrated volume can be seen in Fig. 8. Similar results were seen in a laboratory experiment by Lv [25], where the effect of the slope was noted more on the subsurface and is slow rather than any normal component and the observed moisture content were 13%, 29%, and 44% at 15 cm depth for slopes at 9°, 19° and 28°, respectively. Richard equation and Green-Ampt model were modified for the infiltration measurement on 0° and 30° slopes and found lower infiltrated volume

Fig. 10 Cross section of agricultural soil showing macropores due to decayed roots and bio-pore at 20 cm depth

for the flat surface compared to the 30° inclined surface [9], which is similar to the presented results.

A similar trend of macro flow with temperature is noticed for agricultural land, which showed approximately 1.5 times higher flow through macropores for higher temperature sessions than lower temperature sessions, as shown in Fig. 9. Among green covers (grass and agricultural), infiltration was observed to be relatively higher in harvested agricultural surfaces, possibly due to the presence of higher macropores generated by decayed root under ponded infiltration, as shown in Fig. 10, which agrees with the past experimental studies [12, 15, 30].

Most scientific studies on the effect of slope on infiltration affirm the opposite and are sighted as a decrement in vertical infiltration from the surface as the slope increases [28]. The contrary remarks can be justified by the adopted method of experiments. In the present study, a Double ring infiltrometer was used for stagnated and ponded water to study the impact of macropores and micropores on subsurface lateral flow parallel to the surface slope. However, in the previous studies, a rainfall simulator or runoff generation mechanism was used to see the impact of slope on runoff and then derived the quantitative effects on the infiltration process [11, 13, 28, 29]. This analysis opens the scope of further research based on a physical-based model and experimental approach to understand the slope effects precisely.

The model has limitations in considering the soil characteristics like field density, hydraulic conductivity, and particle size distribution, homogeneous and isotropic for each set of experiments. These values were estimated from the soil samples extracted from the top 20 cm of the surface. The average soil properties were measured based on the samples extracted from the 2- to 3-m radius of the experimental setup; hence the homogeneity of the soil can be justified. The validity of the generated model parameters needs to be verified using the field data from the heterogeneous system at a larger scale due to the spatial variability of the current land uses. The model does not include the effect of temperature on the soil–water interaction but only on the water properties, which is needful to incorporate and is part of the future scope.

The model targets the flow process of the individual domains (macropores and soil matrix) and does not incorporate the water exchange mechanism between micro–macro pores beneath the surface. The model performance was evaluated based on the limited range of temperature and slope as per the availability and required to be assessed for the more extensive data set. The research findings could still be helpful for comparative study and deliver valuable information for the better understanding of the impact of the slope, temperature and LULC on the dual-domain approach regarding soil infiltration.

5 Conclusion

Flow through the macropores in the natural soil system analysed here accounts for a dominant part of the saturated condition and its variability. These outcomes from the present study reveal that the percentage contribution of the macro-flow to the total cumulative infiltration is found to increase with the surface slope and higher temperature. Macropores are found relatively in a smaller percentage in the soil system than the micropores yet govern the higher portion of the infiltrated volume. An average and maximum water flow from macropores were estimated as 64.4% and 84% of the total infiltrated volume for all LULC. Macropore flow was found to be proportional to the temperature by showing higher macro-flow (70.7%) of total infiltration in afternoon sessions than (58.4%) in the forenoon sessions. Macroflow has also demonstrated a positive correlation with the surface slope under ponding water conditions for all focused LULC. The study may be helpful for assessing the effects of different LULC and green cover management on soil structures and should provide a better idea of macropore flow occurring beneath the natural surfaces. The spatial variability of macropores and soil matrix flow characteristics needs to be evaluated for various other LULCs with different ranges of slope and temperature variations.

Author Contribution *Lohit Jain*: Conceptualisation, methodology, writing-original draft preparation, investigation, data curations. *Sumedha Chakma*: Reviewing and editing, supervision.

Conflict of Interest Lohit Jain and Sumedha Chakma declare no conflict of interest.

References

1. Akay O, Fox GA (2007) Experimental investigation of direct connectivity between macropores and subsurface drains during infiltration. Soil Sci Soc Am J 71(5):1600–1606. https://doi.org/10.2136/sssaj2006.0359
2. Ali QSW, Pandey S, Chaudhuri RR, Behera S, Jeyakumar L (2021) Development of rainfall-infiltration measurement system and recharge strategies for urban flooding areas: a case study of Delhi. Model Earth Syst Environ, India. https://doi.org/10.1007/s40808-020-01050-y

3. Beven K, Germann P (2013) Macropores and water flow in soils revisited. Water Resour Res 49(6):3071–3092. https://doi.org/10.1002/wrcr.20156
4. Bhattacharyya R, Prasad S (2020) Water scarcity in Delhi: mapping for solutions and the way forward. In: Singh RB, Srinagesh B, Anand S (eds) Urban health risk and resilience in Asian cities. Springer. https://books.google.co.in/books?id=iajbDwAAQBAJ&dq=water+scarcity+in+delhi&lr=&source=gbs_navlinks_s
5. Bouma J (1981) Soil morphology and preferential flow along macropores. Agric Water Manag 3(4):235–250. https://doi.org/10.1016/0378-3774(81)90009-3
6. Bouma J, Wösten JHM (1979) Flow patterns during extended saturated flow in two, undisturbed swelling clay soils with different macrostructures. Soil Sci Soc Am J 43(1):16–22. https://doi.org/10.2136/SSSAJ1979.03615995004300010003X
7. Cameira MR, Fernando RM, Pereira LS (2003) Soil macropore dynamics affected by tillage and irrigation for a silty loam alluvial soil in southern Portugal. Soil Tillage Res 70(2):131–140. https://doi.org/10.1016/S0167-1987(02)00154-X
8. Chen C, Wagenet RJ (1992) Simulation of water and chemicals in macropore soils Part 1. Representation of the equivalent macropore influence and its effect on soilwater flow. J Hydrol 130(1–4):105–126. https://doi.org/10.1016/0022-1694(92)90106-6
9. Chen L, Young MH (2006) Green-Ampt infiltration model for sloping surfaces. Water Resour Res 42(7):1–9. https://doi.org/10.1029/2005WR004468
10. Clancy K, Alba VM (2011) Temperature and time of day influence on double-ring infiltrometer steady-state infiltration rates. Soil Sci Soc Am J 75(1):241–245. https://doi.org/10.2136/sssaj2009.0355n
11. Essig E, Corradini C, Morbidelli R, Govindaraju RS (2009) Infiltration and deep flow over sloping surfaces: comparison of numerical and experimental results. J Hydrol 374(1–2):30–42. https://www.sciencedirect.com/science/article/pii/S0022169409003163?casa_token=xuKYXJlePCQAAAAA:b1_BIykoPp2ckOfTz0osZrGA8uvtivpldvu_5E9SptOKEtCgOJQBNVEYLQz2DkzE1O0cp5EM
12. Fischer C, Tischer J, Roscher C, Eisenhauer N, Ravenek J, Gleixner G, Attinger S, Jensen B, de Kroon H, Mommer L, Scheu S, Hildebrandt A (2015) Plant species diversity affects infiltration capacity in an experimental grassland through changes in soil properties. Plant Soil 397(1–2):1–16. https://doi.org/10.1007/s11104-014-2373-5
13. Fox DM, Bryan RB, Price AG (1997) The influence of slope angle on final infiltration rate for interrill conditions. Geoderma 80(1–2):181–194. https://doi.org/10.1016/S0016-7061(97)00075-X
14. Fu Z, Hu W, Beare M, Thomas S, Carrick S, Dando J, Langer S, Müller K, Baird D, Lilburne L (2021) Land use effects on soil hydraulic properties and the contribution of soil organic carbon. J Hydrol 602(July):126741. https://doi.org/10.1016/j.jhydrol.2021.126741
15. Ganesan G, Rainwater K, Gitz D, Hall N, Zartman R, Hudnall W, Smith L (2016) Comparison of infiltration flux in playa lakes in grassland and cropland basins, southern high plains of Texas. Texas Water J 7(1):25–39. https://doi.org/10.21423/TWJ.V7I1.7007
16. Indian Council of Agricultural Research (2020) Daily weather data. https://www.iari.res.in/index.php?option=com_content&view=article&id=402&Itemid=103
17. Indian Standard (1994) IS-2720 (PART 4)-1985-Indian standard methods of test for soils grain size analysis(second revision). https://civilengineer.co.in/indian-standard-codes/is-2720-part-4-1985-indian-standard-methods-of-test-for-soils-grain-size-analysissecond-revision/
18. Ioannou I, Charalambous C, Hall C (2017) The temperature variation of the water sorptivity of construction materials. Mater Struct/Materiaux et Constructions 50(5):1–12. https://doi.org/10.1617/s11527-017-1079-6
19. IS 2720-17 (1986): Methods of test for soils, Part 17: laboratory determination of permeability, Pub. L. No. IS code 2720 (Part 17) (2002). https://law.resource.org/pub/in/bis/S03/is.2720.17.1986.pdf
20. Jain L (2022) Assessment of infiltration process considering slope and diurnal temperature variation in humid subtropical region [Indian Institute of Technology]. http://103.27.10.17/bitstream/handle/2074/9528/TH-6866.pdf?sequence=1&isAllowed=y

21. Jarvis NJ (2007) A review of non-equilibrium water flow and solute transport in soil macropores: principles, controlling factors and consequences for water quality. Eur J Soil Sci 58(3):523–546. https://doi.org/10.1111/j.1365-2389.2007.00915.x
22. Li L, Li XA, Lei H, Hong B, Wang L, Zheng H (2020) On the characterization of the shrinkage behavior and soil-water retention curves of four soils using centrifugation and their relation to the soil structure. Arab J Geosci 13(23). https://doi.org/10.1007/s12517-020-06273-y
23. Lin C, Greenwald D, Banin A (2003) Temperature dependence of infiltration rate during large scale water recharge into soils. Soil Sci Soc Am J 67(2):487–493. https://doi.org/10.2136/sssaj2003.4870
24. Logsdon SD (1995) Flow mechanisms through continuous and buried macropores. Soil Science 160(4):237–242. https://journals.lww.com/soilsci/Abstract/1995/10000/FLOW_MECHANISMS_THROUGH_CONTINUOUS_AND_BURIED.1.aspx
25. Lv M, Hao Z, Liu Z, Yu Z (2013) Conditions for lateral downslope unsaturated flow and effects of slope angle on soil moisture movement. J Hydrol 486:321–333. https://doi.org/10.1016/j.jhydrol.2013.02.013
26. Manawi SMA, Nasir KAM, Shiru MS, Hotaki SF, Sediqi MN (2020) Urban flooding in the northern part of Kabul City: causes and mitigation. Earth Syst Environ 4(3):599–610. https://doi.org/10.1007/S41748-020-00165-7/TABLES/5
27. Mohan M, Kandya A (2015) Impact of urbanization and land-use/land-cover change on diurnal temperature range: a case study of tropical urban airshed of India using remote sensing data. Sci Total Environ 506–507:453–465. https://doi.org/10.1016/J.SCITOTENV.2014.11.006
28. Morbidelli R, Saltalippi C, Flammini A, Govindaraju RS (2018) Role of slope on infiltration: a review. J Hydrol 557:878–886. https://doi.org/10.1016/j.jhydrol.2018.01.019
29. Mu W, Yu F, Li C, Xie Y, Tian J, Liu J, Zhao N (2015) Effects of rainfall intensity and slope gradient on runoff and soil moisture content on different growing stages of spring maize. Water 7(6):2990–3008. https://doi.org/10.3390/W7062990
30. Neris J, Jiménez C, Fuentes J, Morillas G, Tejedor M (2012) Vegetation and land-use effects on soil properties and water infiltration of Andisols in Tenerife (Canary Islands, Spain). CATENA 98:55–62. https://doi.org/10.1016/j.catena.2012.06.006
31. Qiao X, Ma S, Pan G, Liu G (2019) Effects of temperature change on the soil water characteristic curve and a prediction model for the Mu us Bottomland, Northern China. Water (Switzerland) 11(6). https://doi.org/10.3390/w11061235
32. Radulovich R, Solorzano E, Sollins P (1989) Soil macropore size distribution from water breakthrough curves. Soil Sci Soc Am J 53(2):556–559. https://doi.org/10.2136/sssaj1989.03615995005300020042x
33. Rasool T, Dar AQ, Wani MA (2021) Comparative evaluation of infiltration models under different land covers. Water Resour 48(4):624–634. https://doi.org/10.1134/S0097807821040175
34. Rawat M, Ramanathan A (2011) Assessment of methane flux from Municipal Solid Waste (MSW) landfill areas of Delhi India. J Environ Protect 2(4):399–407. https://doi.org/10.4236/jep.2011.24045
35. Ronayne MJ, Houghton TB, Stednick JD (2012) Field characterization of hydraulic conductivity in a heterogeneous alpine glacial till. J Hydrol 458–459:103–109. https://doi.org/10.1016/j.jhydrol.2012.06.036
36. Shakya NM, Chander S (1998) Modelling of hillslope runoff processes. Environ Geol 35(2–3):115–123. https://doi.org/10.1007/s002540050298
37. Shougrakpam S, Sarkar R, Dutta S (2010) An experimental investigation to characterise soil macroporosity under different land use and land covers of northeast India. J Earth Syst Sci 119(5):655–674. https://doi.org/10.1007/s12040-010-0042-5
38. Shukla MK, Lal R, Owens LB, Unkefer P (2003) Land use and management impacts on structure and infiltration characteristics of soils in the north appalachian region of Ohio. Soil Sci 168(3):167–177. https://doi.org/10.1097/01.SS.0000058889.60072.AA
39. Singh RP, Tyagi VV, Allen T, Ibrahim MH, Kothari R (2011) An overview for exploring the possibilities of energy generation from municipal solid waste (MSW) in Indian scenario. Renew Sustain Energy Rev 15(9):4797–4808. https://doi.org/10.1016/J.RSER.2011.07.071

40. Stolf R, de Thurler ÁM, Bacchi OOS, Reichardt K (2011) Method to estimate soil macroporosity and microporosity based on sand content and bulk density. Revista Brasileira de Ciência Do Solo 35(2): 447–459https://doi.org/10.1590/s0100-06832011000200014
41. Sun D, Yang H, Guan D, Yang M, Wu J, Yuan F, Jin C, Wang A, Zhang Y (2018) The effects of land use change on soil infiltration capacity in China: a meta-analysis. Sci Total Environ 626:1394–1401. https://doi.org/10.1016/j.scitotenv.2018.01.104
42. Ticehurst JL, Cresswell HP, Jakeman AJ (2003) Using a physically based model to conduct a sensitivity analysis of subsurface lateral flow in south-east Australia. Environ Model Softw 18(8–9):729–740. https://doi.org/10.1016/S1364-8152(03)00075-6
43. Tupsakhare S, Moutushi T, Castaldi MJ, Barlaz MA, Luettich S, Benson CH (2020) The impact of pressure, moisture and temperature on pyrolysis of municipal solid waste under simulated landfill conditions and relevance to the field data from elevated temperature landfill. Sci Total Environ 723:138031. https://doi.org/10.1016/J.SCITOTENV.2020.138031
44. Watson KW, Luxmoore RJ (1986) Estimating macroporosity in a forest watershed by use of a tension infiltrometer. Soil Sci Soc Am J 50(3):578–582. https://doi.org/10.2136/SSSAJ1986.03615995005000030007X
45. Weiler M (2017) Macropores and preferential flow—A love-hate relationship. Hydrol Process 31(1):15–19. https://doi.org/10.1002/hyp.11074
46. Weiler M, Naef F (2003) Simulating surface and subsurface initiation of macropore flow. J Hydrol 273(1–4):139–154. https://doi.org/10.1016/S0022-1694(02)00361-X
47. Wright PG (1977) The variation of viscosity with temperature. Phys Educ 12(5):323–325. https://doi.org/10.1088/0031-9120/12/5/012

River Ecology

Exploring Large Braided River Systems: Understanding the Dynamics and Pathways of River Recovery

C. Pradhan, S. Dutta, and Rishikesh Bharti

Abstract In the twenty-first century, it is crucial to recognize the heterogeneity in fluvial controls along the Indian river systems. In addition, tracking the river recovery, and associated geomorphic and vegetative attributes' evolutions are crucial for Indian Himalayan river systems, where archival fluvial benchmark information was inadequately maintained. The present chapter focuses on the issue of river recovery trajectory assessment along complex fluvial systems and has highlighted the importance of integrating Google Earth Engine and cloud computing, fine resolution images and advanced river surveying equipment in assessing the fluvial health.

1 Introduction

The present persisting fluvial issues emphasize the need of nature-based water resources management for environmental sustainability. In the last couple of decades, many such global goals like UN Millennium Development Goals (2000–2015), the UN Sustainable Development Goals (2016–2030) and the UN Decade on Ecosystem Restoration (2021–2030) have been synthesized [25]. Within the Indian context, the Namami Gange Program under National Mission for Clean Ganga was commissioned in 2014 with objectives of river surface cleaning, bio-diversity conservation, river-front development and enhanced afforestation.

C. Pradhan (✉)
Post-Doctoral Fellow, TIH-TIDF, IIT Guwahati, Guwahati 781039, India
e-mail: c.pradhan@iitg.ac.in

S. Dutta · R. Bharti
Department of Civil Engineering, IIT Guwahati, Guwahati 781039, India

S. Dutta and V. Chembolu (eds.), *Recent Development in River Corridor Management*,
Lecture Notes in Civil Engineering 376, https://doi.org/10.1007/978-981-99-4423-1_10

Building on these global and national efforts, it is crucial to recognize the diverse nature of river systems in India, which exhibit considerable heterogeneity in fluvial controls [22]. In particular, Himalayan braided rivers are defined by a complex arrangement of geomorphic units due to high stream power and sediment transport [5]. The distinctive morphology of the multi-channel flow network and associated ecological landforms develop challenges in braided river management and planning [10, 15, 20, 28] (Surian, 2006; Bertoldi et al. 2020). Further, anthropogenic stresses in terms of river regulation, channelization, vegetation clearance and deforestation have altered the boundary conditions of channel functions [26, 12, 29] (Giller 2005). River recovery is defined as the capacity of the river system to adjust to the prevailing boundary conditions [8]. River recovery also facilitates an understanding of the past system trajectories and future scenarios, where each reach needs to be analyzed within its catchment context [9]. Tracking the river recovery, and associated geomorphic and vegetative attributes' evolutions are crucial for Indian Himalayan river systems, where archival fluvial benchmark information was inadequately maintained. The present concept paper focuses on the issue of river recovery assessment along Himalayan rivers, which are characterized by flash floods, high sediment (debris load), complex morphology and growing anthropogenic stresses. Further, this chapter encourages the use of advanced remote sensing, river surveying instruments, and cloud computing techniques to understand the intricate process-form relationship along Indian braided river systems.

2 Study Area

Trans-Himalayan rivers like the Manas, the Kameng and the Subansiri significantly contribute to the flow and sediment transport processes of the mighty Brahmaputra River. The Manas River catchment in Bhutan (Himalaya) is dominated by deforestation, and the friable soils contribute to a high sediment load [11]. The channel gradient is as steep as 19 m/km, and the river shows signatures of transitional meandering-braided planform in the flatland of Assam, India. The Kameng and the Subansiri are among the flashiest rivers in the world [11] and were governed by increased deforestation, river regulation and land use practices in the late twentieth and early twenty-first centuries. The Kameng River has a mean annual discharge of 0.0858 $m^3/s/km^2$, with frequent bank erosion, thalweg shifting, and bar sculpting migration [22]. The changes in land use land cover are also dominant in the Subansiri catchment, where river regulation by a large dam has increased in recent years [6] (Fig. 1).

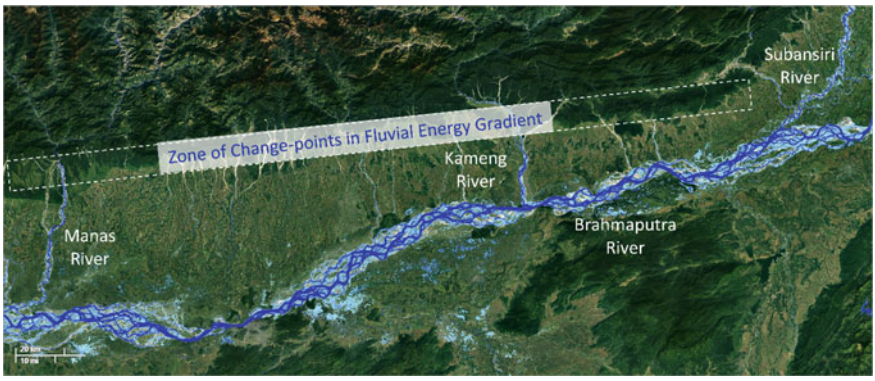

Fig. 1 Large braided river systems in the Eastern Himalaya and zone of change-points in fluvial energy gradient

3 Understanding Pathways of River Recovery for Large Braided River

3.1 Implication of Google Earth Engine and Cloud Computing

Google Earth Engine is a cloud-based platform for geospatial analysis that allows users to view and examine satellite imagery of Earth. The advancement of cloud-based computing techniques will help to process the reach-to-catchment-scale behavioral regime of the river. Certain geomorphic indicators like increased complexity of geomorphic unit assemblages, increase in definition of low flow channel, decrease in low flow number in high flow duration percentiles, and well-defined pool-riffle structures can be identified through the analysis of satellite images captured over an extended time period, followed by the application of band ratio and remote sensing classification techniques. For example, the JRC Global Surface Water Mapping Layers include maps that display the spatial distribution and temporal variations of surface water from 1984 to 2021, offering data on the scope and alterations of these water surfaces (GEE Catalog). Additionally, parameters such as occurrence (how often water is present), absolute change in occurrence (comparison between 1984–1999 and 2000–2021), normalized change in occurrence, seasonality (the number of months water is present), recurrence (the frequency of water reappearing annually), transition (a categorical classification of change between the first and last year), and maximum extent (a binary image marking areas where water has ever been detected) can be utilized to analyze the spatio-temporal variability of geomorphic indicators and their stability properties.

Figure 2 shows spatial variability of JRC water seasonality across the Himalayan foothills. These reaches are subjected to breakpoints of channel bed slope and the change in energy gradient forces the river systems to dissipate the excess fluvial

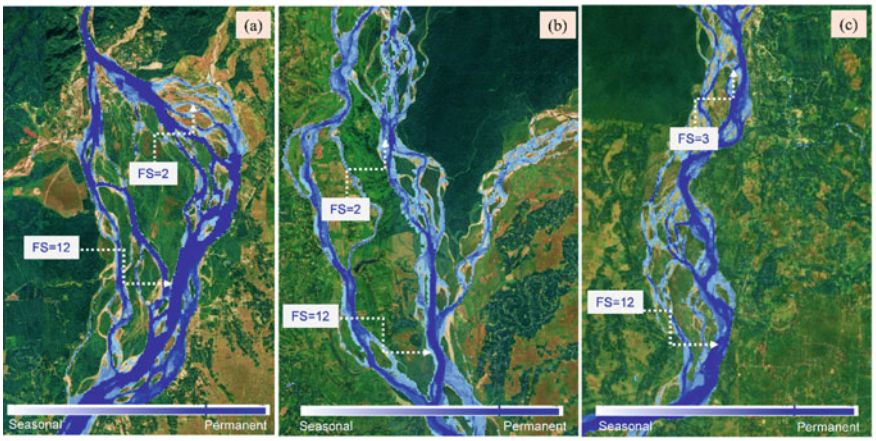

Fig. 2 JRC Global Surface Water Mapping Layer-seasonality variation at the fluvial energy change point zones of Himalaya for **a** Subansiri River, **b** Kameng River and **c** Manas River

energy and increase the probability of braiding [23]. In these dynamic reaches, redefinition of low flow channel is an important indicator of river recovery as increased braiding has disturbed the channel bed configuration [9]. The flow seasonality (FS) image shows stability of low flow channels (FS = 12) along the hilly terrain and gradual increase of flow-division in the plain region (FS < 5). The stability characteristics of low flow channels, bars and islands require intrinsic understanding of fluvial hydrodynamic processes and associated ecological linkages. Figure 2 further establishes that reaches with vegetated bars, flood plain vegetated zones and islands are forcing the low-flow channel to develop a low width-depth ratio. The observed transformation is indicative of a potential recovery stage of the river, but a more comprehensive analysis of longer-term data using texture-based classification is necessary to confirm this interpretation.

Instream vegetation directly affects the formation of vegetated landforms and engineer river recovery (Gurnell 2014) [9]. As per Pradhan et al. [24], the presence of instream vegetation is considered as an additional degree of freedom, which further controls the hierarchy of energy dissipation and morphological continuum in the weakly braided macrochannel settings. However, the concept of recovery for complex braided (and meandering) reaches of Himalayan rivers needs a careful understanding of past fluvial information and future system trajectories of geomorphic units. This owes to the fact that similar landforms may represent degradation or recovery depending upon the river under investigation [9]. Therefore, for Indian river systems, where archival fluvial benchmark information was inadequately maintained, textural analysis of CORONA declassified imagery will provide valuable information regarding self-organization and adjustment capacity of instream vegetated landforms (Fig. 3).

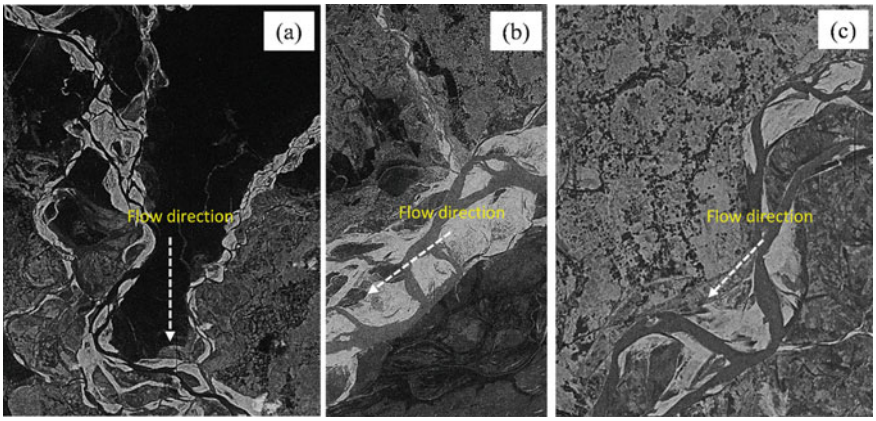

Fig. 3 Declassified CORONA satellite imagery of 1976 for **a** Kameng River, **b** Brahmaputra River, **c** Subansiri River (Obtained from USGS, Earth explorer)

3.2 Role of Advanced River Surveying Equipment

In this scientific era, advanced river surveying equipment is designed to assess detailed fluvial datasets of the river and the surrounding environments. Recent innovations like Multi-Beam Echo Sounders (MBES) [1, 7], Acoustic Doppler Current Profiler (aDcp) (Muste et al. 2014; [18], Side-Scan Sonar [21, 33], Global Navigation Satellite Systems (GNSS) [16, 31], Light Detection and Ranging (LIDAR) [30] (Paul et al. 2020) are helpful in understanding the complex fluvial process-form relationships.

The braided rivers are characterized by shallow, multi-channel flow networks with complex mobile bed topography. In such river systems, the pathways of river recovery are associated with large-scale sediment mobilization and heterogenous erosional-depositional processes. In addition, it is essential to identify the reach and its relation with catchment-scale sediment transport processes [4]. For example, the recovery indicators and their trajectories may vary for source zone ($E > E_{min}$), transfer zone ($E \sim E_{min}$) and deposition zone ($E < E_{min}$) (Where, E: available energy and E_{min}: energy that is required to transport available sediment). Further, it is imperative to assess the degree of sediment connectivity present within the channel to gain a comprehensive understanding of the channel evolution and function [14, 17]. The upslope and downslope components of sediment connectivity will depend upon the contributing area characteristics, gradient, and length of the flow path. In the large Himalayan river, longitudinal profile of the river along with the formation of pool-riffle sequences affects the connectivity process [17]. In these river systems, integration of advanced river surveying instruments collected datasets with past fluvial information may provide an idea of river health status and future trajectories. For example, An aDcp transect conducted on a braided section of the Kameng River revealed a division in the low flow channel network, highlighting the prevalence

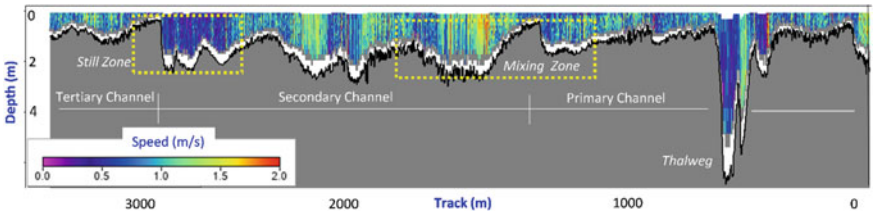

Fig. 4. **a** Dcp transect showing spatial variation of depth and velocity at a highly braided section of the Kameng River

of spatial heterogeneity in both depth and flow velocity magnitude (Fig. 4). In the mixing zone of the primary channel, the flow velocity is close to 2 m/s, highlighting intense momentum transfer between the anabranches. The slow-moving pools are observed close to the left bank and thalweg. For such braided rivers, the formation of benches, well-defined low flow channels through the reorganization of bed materials, and the re-establishment of pool scour can be key indicators of geomorphic river recovery [9].

Ashmore [2] identified four dominant braid bar formation mechanisms: middle bar accretion, transverse bar conversion, chute cutoff and multiple bar dissection. Units bars are defined as unmodified bars whose morphologies are governed mostly by depositional processes [27] (Herbert et al. 2019). Compound bars have a complex history of erosion–deposition and are formed by the amalgamation of multiple unit bars [32]. In multi-channel flow, the appearance of compound bars with vegetated landforms and bed heterogeneity can be adopted as a sign of recovery. High-resolution images reveal evidence of recovery in the plain regions of large Himalayan rivers (Fig. 5). However, these fluvial systems are subjected to intense fluvial energy (floods exceeding 6000 cumecs) during monsoon and may disturb the existing biomorphology linkages and ecosystem hotspot zones. As per the findings of [24], the dominance between self-organization of vegetated landforms and fluvial disturbances control the recovery trajectory of the weakly braided system. Therefore, in highly braided river, tracking the formation of unit (or compound) bars along with the status of vegetated landforms after the monsoon season seems as an option to understand the recovery trajectory.

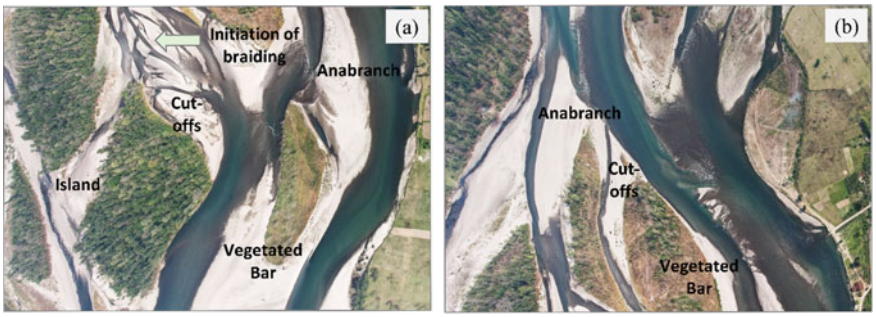

Fig. 5 High-resolution imagery of large Himalayan rivers showing complex bio-morphodynamic processes

4 Conclusions

The chapter has highlighted the importance of integrating Google Earth Engine and cloud computing, fine resolution images and advanced river surveying equipment in assessing fluvial health and recovery trajectory. The major conclusions are:

1. The advancement of cloud-based computing techniques will help to process the reach-to-catchment-scale behavioral regime of the river. The spatial variability of JRC water seasonality across the Himalayan foothills shows breakpoints of channel bed slope and the change in energy gradient forces the river systems to dissipate the excess fluvial energy and increase the probability of braiding.
2. In Indian river systems, textural analysis of CORONA declassified imagery will provide valuable information regarding self-organization and adjustment capacity of instream vegetated landforms
3. For highly braided river, the formation of unit (or compound) bars along with the status of vegetated landforms can be tracked with advanced river surveying equipment, which will be helpful to understand the recovery trajectory.

References

1. Amiri-Simkooei A, Snellen M, Simons DG (2009) Riverbed sediment classification using multi-beam echo-sounder backscatter data. J Acoust Soc Am 126(4):1724–1738
2. Ashmore P (1991) Channel morphology and bed load pulses in braided, gravel-bed streams. Geogr Ann Ser B 73(1):37–52
3. Bertoldi W, Zanoni L, Tubino M (2010) Assessment of morphological changes induced by flow and flood pulses in a gravel bed braided river: the Tagliamento River (Italy). Geomorphology 114(3):348–360
4. Brierley G, Fryirs K, Cullum C, Tadaki M, Huang HQ, Blue B (2013) Reading the landscape: Integrating the theory and practice of geomorphology to develop place-based understandings of river systems. Prog Phys Geogr 37(5):601–621

5. Chembolu V, Dutta S (2018) An entropy based morphological variability assessment of a large braided river. Earth Surf Proc Land 43(14):2889–2896
6. Dutta R, Sarma SK (2012) Lower Subansiri hydroelectric power project and future of the Subansiri river ecosystem. Ann Biol Res 3(6):2953–2957
7. Eleftherakis D, Snellen M, Amiri-Simkooei A, Simons DG, Siemes K (2014) Observations regarding coarse sediment classification based on multi-beam echo-sounder's backscatter strength and depth residuals in Dutch rivers. J Acoust Soc Am 135(6):3305–3315
8. Fryirs K, Brierley G (2000) A geomorphic approach to the identification of river recovery potential. Phys Geogr 21(3):244–277
9. Fryirs KA, Brierley GJ, Hancock F, Cohen TJ, Brooks AP, Reinfelds I, Raine A (2018) Tracking geomorphic recovery in process-based river management. Land Degrad Dev 29(9):3221–3244
10. Gilvear DJ (1993) River management and conservation issues on formerly braided river systems; the case of the River Tay, Scotland. Geol Soc, Lond, Spec Publ 75(1):231–240
11. Goswami DC (1985) Brahmaputra River, Assam, India: Physiography, basin denudation, and channel aggradation. Water Resour Res 21(7):959–978
12. Gurnell A, Surian N, Zanoni L (2009) Multi-thread river channels: a perspective on changing European alpine river systems. Aquat Sci 71:253–265
13. Herbert CM, Alexander J, Amos KJ, Fielding CR (2020) Unit bar architecture in a highly-variable fluvial discharge regime: Examples from the Burdekin River Australia. Sedimentology 67(1):576–605
14. Hooke J (2003) Coarse sediment connectivity in river channel systems: a conceptual framework and methodology. Geomorphology 56(1–2):79–94
15. Le Lay YF, Piégay H, Rivière-Honegger A (2013) Perception of braided river landscapes: Implications for public participation and sustainable management. J Environ Manage 119:1–12
16. Li X, Zhong B, Li J, Liu R (2023) Joint inversion of GNSS and GRACE/GFO data for terrestrial water storage changes in the Yangtze River Basin. Geophys J Int
17. Mishra K, Sinha R, Jain V, Nepal S, Uddin K (2019) Towards the assessment of sediment connectivity in a large Himalayan river basin. Sci Total Environ 661:251–265
18. Moradi G, Vermeulen B, Rennie CD, Cardot R, Lane SN (2019) Evaluation of aDcp processing options for secondary flow identification at river junctions. Earth Surf Proc Land 44(14):2903–2921
19. Muste M, Yu K, Spasojevic M (2004) Practical aspects of ADCP data use for quantification of mean river flow characteristics; part I: moving-vessel measurements. Flow Meas Instrum 15(1):1–16
20. Piégay H, Grant G, Nakamura F, Trustrum N (2006) Braided river management: from assessment of river behaviour to improved sustainable development. Braided Rivers: Process, Depos, Ecol Manag 36:257–275
21. Połap D, Wawrzyniak N, Włodarczyk-Sielicka M (2022) Side-scan sonar analysis using roi analysis and deep neural networks. IEEE Trans Geosci Remote Sens 60:1–8
22. Pradhan C, Chembolu V, Bharti R, Dutta S (2023) Regulated rivers in India: Research progress and future directions. ISH J Hydraul Eng 29(1):58–70
23. Pradhan C, Chembolu V, Dutta S, Bharti R (2021) Role of effective discharge on morphological changes for a regulated macrochannel river system. Geomorphology 385:107718
24. Pradhan C, Padhee SK, Bharti R, Dutta S (2022) A process-based recovery indicator for anthropogenically disturbed river system. Sci Rep 12(1):1–14
25. Russell K, Fryirs K, Reid D et al (2023) Evolution of a river management industry in Australia reveals meandering pathway to 2030 UN goals. Commun Earth Environ 4:93. https://doi.org/10.1038/s43247-023-00748-y
26. Sedell JR, Reeves GH, Hauer FR, Stanford JA, Hawkins CP (1990) Role of refugia in recovery from disturbances: modern fragmented and disconnected river systems. Environ Manage 14:711–724
27. Smith ND (1974) Sedimentology and bar formation in the upper Kicking Horse River, a braided outwash stream. J Geol 82(2):205–223

28. Smith, G. H. S., Best, J. L., Bristow, C. S., & Petts, G. E. (2009). Braided Rivers Process, Deposits, Ecology and Management. John Wiley & Sons, Ltd
29. Tockner K, Pusch M, Borchardt D, Lorang MS (2010) Multiple stressors in coupled river–floodplain ecosystems. Freshw Biol 55:135–151
30. Tonina D, McKean JA, Benjankar RM, Wright CW, Goode JR, Chen Q, Edmondson MR (2019) Mapping river bathymetries: Evaluating topobathymetric LiDAR survey. Earth Surf Proc Land 44(2):507–520
31. Wang Y, Morton YJ (2021) River slope observation from spaceborne GNSS-R carrier phase measurements: a case study. IEEE Geosci Remote Sens Lett 19:1–5
32. Wheaton JM, Fryirs KA, Brierley G, Bangen SG, Bouwes N, O'Brien G (2015) Geomorphic mapping and taxonomy of fluvial landforms. Geomorphology 248:273–295
33. Wolfenkoehler W, Long JM, Gary R, Snow RA, Schooley JD, Bruckerhoff LA, Lonsinger RC (2023) Viability of side-scan sonar to enumerate Paddlefish, a large pelagic freshwater fish, in rivers and reservoirs. Fish Res 261:106639

Assessment of Ichthyofaunal Diversity and Habitat Variables in Himalayan Brahmaputra River of Assam, North-Eastern India

Niti Sharma, Birendra Kumar Bhattacharjya, Dipesh Debnath, Shyamal Chandra Sukla Das, Amulya Kakati, and Basanta Kumar Das

Abstract In the present communication, we report ichthyofaunal diversity and habitat variables from eight major landing centers spread across three stretches (upper, middle and central) of River Brahmaputra in Assam from 2019 to 2021. The environmental variables such as temperature (21.2–28.6 °C), dissolved oxygen (6.52–8.27 mg/l), pH (7.1–8.2), alkalinity (62–87 mg/l), nitrate (0.018–0.038 mg/l) and phosphate (0.003–0.016 mg/l) were observed to be in a suitable range for aquatic fauna and flora. From the studied region, 110 fish species belonging to 33 families and 69 genera were reported. Among the families, Cyprinidae was the most prevalent family representing 42.73% then Bagridae (6.38%), Channidae (6.36%), Ambassidae and Osphronemidae (3.63%), Badidae, Mastacembelidae, Schilbeidae Siluridae, and Sisoridae (2.73%), and other families contributing about 1%. According to the International Union for Conservation of Nature and Natural Resources (IUCN) status, two species were included under Endangered category, two species under Vulnerable category, 6 species under Near threatened, 4 species have Data deficient and 96 species under Least concern category. Most of the fish species observed were indigenous, with a few endemic and rare species in the region. Small indigenous fishes (such as *Cabdio morar* and *Ailia coila*) are the most abundant fish species. Fish species richness and diversity indices showed seasonal fluctuation. Highest species richness (105) was observed during pre-monsoon, then post-monsoon (88), and monsoon (82) seasons. The Shannon (H′) indices varied from 3.45 (monsoon) to 3.86 (pre-monsoon), with an evenness index between 0.38 (monsoon) to 0.45 (pre-monsoon) indicating a slightly impacted pattern of the studied river stretch i.e., (H′) > 3.0. Various natural and man-made threats are presumed to affect biodiversity in River Brahmaputra. Therefore, strategies such as fish harvest regulation, desiltation, controlling of water pollution and anthropogenic activities are suggested for conservation of the aquatic biodiversity in the River.

N. Sharma (✉) · B. K. Bhattacharjya · D. Debnath · S. C. S. Das · A. Kakati
ICAR-Central Inland Fisheries Research Institute, Regional Centre, Guwahati, Assam, India

B. K. Das
ICAR-Central Inland Fisheries Research Institute, Barrackpore, West Bengal, India

S. Dutta and V. Chembolu (eds.), *Recent Development in River Corridor Management*,
Lecture Notes in Civil Engineering 376, https://doi.org/10.1007/978-981-99-4423-1_11

Keywords Brahmaputra river · Fish diversity · Environmental variables · Threats · Conservation

1 Introduction

One of the largest river systems in South Asia, the River Brahmaputra flows approximately 3000 km transboundary through China, India, and Bangladesh, covering 1625 km, 918 km, and 337 km, respectively, before it merges with the Ganges and flows into the Bay of Bengal. More than half of its basin area is spread across China (50.5%), followed by India (33.6%), Bangladesh (8.1%) and Bhutan (7.8%) [22, 34, 36]. The River descends to India through a network of tributaries beginning in the northern Himalayas as Tsangpo. Through the Siang hills of Arunachal Pradesh, Brahmaputra reaches India; however, when it arrives at the plains, it is called Dihang. Dibang and Lohit, two tributaries in Assam, join the Brahmaputra to form a very wide river. It descends in Assam from east to west over approximately 650 km having 42 important tributaries in Northeast India, including 15 on the south bank and 27 on the north bank. As the River passes through the valley of Assam many Himalayan streams comprising Kameng, Subansiri, Bharali, Dhansiri, Manas, Saralbhanga, Champamati and Sankosh rivers join the Brahmaputra. Numerous floodplain wetlands, or beels, are created by these rivers as they travel through the valley. The Brahmaputra and its tributaries are the lifeline of millions of people in the region, who are dependent on agricultural activities. It contributes to almost 17% of the gross domestic product of India [30, 31]. River provides numerous benefits in the form of and not limited to, irrigation, ecosystem services, domestic use, navigation, tourism, wildlife areas and hydropower, thereby supporting livelihoods and food security.

Brahmaputra basin comes under one of the mega biodiversity hotspots of the Indo-Burma biodiversity hotspot region as recognized by the IUCN. The region is blessed with enormous floral and faunal diversity. The unique physiographic and climatic characteristics make the region rich in biodiversity. The Brahmaputra basin has the highest forest cover of 59% in the country. Different types of endemic vegetation including about 600 plant species, more than 800 orchid species and nearly 67 species of animals are endemic and endangered to the region supported by nearly 75 protected areas in the basin. Brahmaputra River system is home to many indigenous and endemic freshwater fishes as well [21, 27, 40]. Reportedly, there are 422 fish species found in different water-bodies of northeast India, and 141 finfishes in River Brahmaputra of Assam [7, 20]. However, the available scientific information on aquatic biology and fisheries is fragmented and not up-to-date. Impact of rivers on fisheries and habitat variables are poorly studied. Therefore, the present chapter focused on assessing habitat variables and ichthyofaunal diversity in selected stretches of River Brahmaputra including seasonal variations in fish species richness and diversity indices.

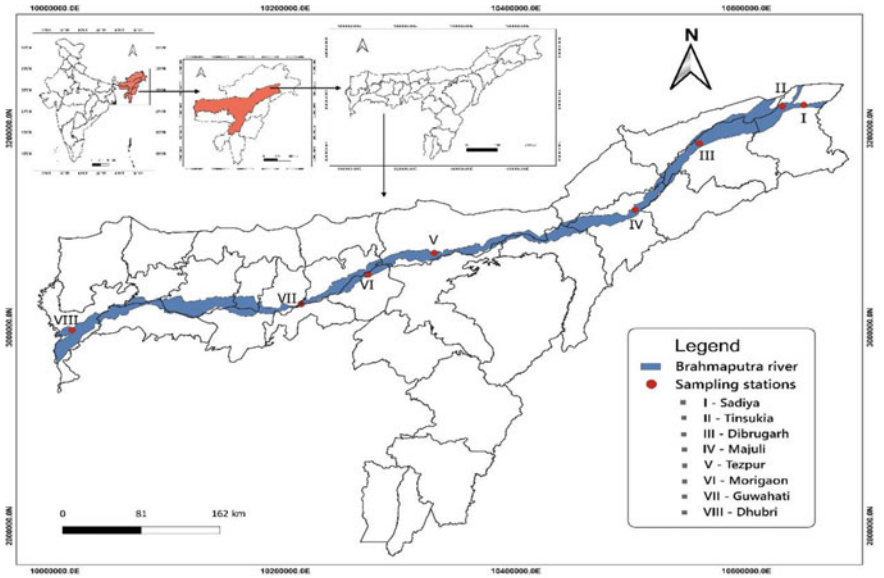

Fig. 1 Brahmaputra River, Assam along with sampling sites

2 Study Area

The present investigation was carried out in River Brahmaputra, Assam from November 2019 to December 2021 from Sadiya to Dhubri, Assam. Sampling was carried out on seasonal basis from eight major landing centers (Fig. 1), marked as site I (Sadiya; 95°40′52″ E & 27°49′14″ N), II (Tinsukia; 95°32′49″ E & 27°57′79″ N), III (Dibrugarh; 94°54′13″ E & 27°29′9″ N), IV (Majuli; 94°29′85″ E & 26°91′67″ N), V (Tezpur; 92°47′27″ E & 26°36′58″ N), VI (Morigaon; 92°06′40.8″E & 26°17′20.7″N), VII (Guwahati; 91°45′20″E & 26°11′43″N) and VIII (Dhubri; 89°59′41″ E & 26°1′20″ N).

3 Methodology

3.1 Water and Sediment Quality

Water samples were collected from each sampling station using clean 1000 ml polypropylene bottles for the determination of various physico-chemical parameters. At each point of water sample collection, pH, water temperature, specific conductivity and total dissolved solids were measured using a portable water testing kit. Winkler's method was used to measure dissolved oxygen. Total water alkalinity and free carbon

dioxide were assessed using standard methods [1, 2]. Phosphate–phosphorus content of water was estimated with the help of a spectrophotometer. Phenol disulphonic acid reduction method was used to assess Nitrate–nitrogen [25]. An Ekman dredger was used to collect sediment samples in the study area. Three samples were collected from each sampling site. In order to produce uniform composite samples, debris, as well as other parts from plants and animals, were removed and thoroughly mixed. Samples were brought to the laboratory in plastic pouch bags for further analysis. The sediment samples that were collected were air-dried and ground into a fine powder, strained through a 2 mm mesh sized sieve and air-dried again. Determination of sediment quality was done by standard procedures given by [25]. Mechanical analysis with a Bouyocos hydrometer (graduated in g/l) was used to determine the texture of the sediment, which was expressed as percentages of sand, clay, and silt particles. A pH meter was used to estimate the pH of the sediment. Total organic carbon and organic matter were analyzed using Walkley–Black's method (1934) and loss-on-ignition method, respectively and the results were expressed in percentages. Available phosphorous and nitrogen in the sediments were estimated by Trougss (Bray's) method (1945) and the alkali permanganate method, respectively.

3.2 Fish Diversity

Fish species were collected through fishing by local fishermen with different fishing gears such as cast net, gill net, hook and lines, and various types of traps and also recorded from study area, landing centers and local markets of the sampling area. Most of the fish species were identified on the spot and unidentified specimens were brought to the laboratory in well-preserved 5–10% formalin and further identification was done using standard manuals of [24, 38] and Viswanath (2002). Conservation status evaluation was done according to the IUCN Red List of threatened species (IUCN 3.1). Data on threats to fish fauna were collected from both primary (direct observations and interactions with local fishermen and stakeholders) and secondary sources. Abundance, diversity and species richness were determined by following [29, 37] and diversity indices (Evenness Index and Shannon-Weinner Index,).

3.3 Data Analysis

Relative abundance (RA) of fish species was calculated as

$$\text{RA}\ (\%) = \text{Isi}/\sum \text{Nsi} \times 100 \tag{1}$$

where, Isi is the no. of samples of particular species, $\sum$ and Nsi is the total no. of samples.

The Shannon and Weiner diversity index (H′) was estimated for fishes employing the following formula.

$$H\prime = \sum\{pi \times \ln(pi)\} \quad (2)$$

where, s is the no. of fish species, p is the proportion (n/N) of individuals of one particular fish species observed (n) divided by the total no. of individuals observed (N), ln is the natural log and Σ is the sum of the calculations.

The Evenness index (E) was assessed using the following formula

$$E = H/\text{In}S \quad (3)$$

where, H = diversity index; S = total no. of fish species

4 Results and Discussion

4.1 Water and Sediment Quality

The water and sediment quality variables were found to be in a suitable range for aquatic fauna and flora (Table 1). It was characterized by alkaline pH (7.1–8.2), rich dissolve oxygen (6.52–8.27 mg/l) and poor nutrients (nitrate: 0.018–0.038 mg/l and phosphate: 0.003–0.016 mg/l). Water temperature, pH, DO and alkalinity were satisfactory for the survival and growth of aquatic organisms. The sediments were dominated by sandy soil and loamy-sandy soil from upper to lower stretches, having mostly alkaline pH (6.82–8.64), low organic carbon (0.347–0.495%), organic matter (0.596–0.851%) and low available nutrients. Similar observations were reported by [7] in River Brahmaputra except for some tributaries. Kotoky and Sarma [26] studied the water quality of the river in Kamrup district of Assam. They suggested that the water was not fit for drinking, and might be used for agricultural purposes. Many researchers studied the physico-chemical parameters of Brahmaputra river and its tributaries and the water was found to be suitable for aquatic organisms [3, 12–14].

4.2 Ichthyofaunal Diversity of Brahmaputra River

In the present investigation, a total of 110 fish species belonging to 33 families and 69 genera were reported from the studied region. Among the families, Cyprinidae was the most dominant one representing 42.73% of the species followed by Bagridae (6.38%), Channidae (6.36%), Ambassidae and Osphronemidae (3.63%), Badidae, Mastacembelidae, Schilbeidae Siluridae, and Sisoridae (2.73%), and other families

Table 1 Water and sediment quality of River Brahmaputra, Assam

Water parameters	Range	Soil parameters	Range
Temperature	21.2–28.6 °C	Soil texture	Sandy (dominant) to Loamy Sandy (lower stretches) Sand: (80.64–93.64) % Silt: (4.64–14.64) % Clay: (1.72–4.72) %
pH	7.1–8.2		
Dissolve Oxygen	6.52–8.27 mg/l		
Free CO_2	0–2.21 mg/l		
Total alkalinity	62–87 mg/l	pH	6.82–8.64
Total Dissolve Solids	46–78 mg/l	Organic Carbon	0.347–0.495%
Salinity	0.01–0.12 ppt	Available P	0.28–1.9 mg/100 g sediment
Phosphate (PO_4)	0.003–0.016 mg/l	Available N	9.84–22.84 mg/100 g sediment
Nitrate (NO_3)	0.018–0.038 mg/l	Organic matter content	0.596–0.851%

contributing about 1% (Fig. 2). Fishes having both ornamental and/ or food values were found abundantly in the river and its tributaries.

Most of the fish species observed were indigenous by habitat, with a few endemic to the region and a few rare species. During our field visits, majority of the fishes were available in the form of live, fresh, frozen, smoked and dried forms in local markets. *Cabdio morar* and *Ailia coila* were the most abundant fish species from the River. The Indian major carps (*Labeo catla*, *Labeo rohita, Cirrhinus mrigala)*, minor carps (*Bangana dero, C. reba, L. gonius*, *L. bata*, *L. calbasu)*, air breathing fishes

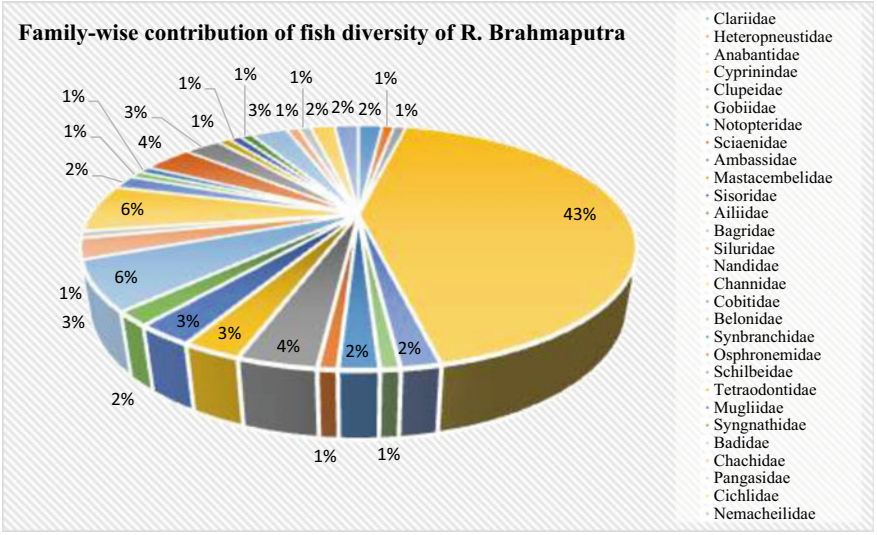

Fig. 2 Family-wise contribution of fish diversity of selected stretches of River Brahmaputra, Assam

(*Channa* spp., *Clarias magur, Heteropneustes fossilis, Anabas testudineus)*, catfishes (*Wallago attu, Sperata aor, S. Seenghala, Mystus tengara, M. cavasius, M. bleekeri, Ompok pabda, Eutrophiichthys vacha, Clupisoma garua, Rita rita)* and several prawn species were reported from all the stretches. Migratory fishes such as anadromous Hilsa (*Tenualosa ilisha*) were observed in the lower stretches, amphidromous fishes (*Otolithoides pama*) and catadromous migrant (*Anguilla bengalensis bengalensis*) were also observed in lower stretches of the River. *Tor tor, T. putitora*, *Neolissocheilus hexagonolepis*, *Bangana dero, L. dyocheilus*, *Raimas bola*, *Cyprinion semiplotus*, *Barilius* spp. and *Silonia silondia* were some of the fishes that migrate between the main river and tributaries.

Among exotic fishes recorded from the main river were common carp (*Cyprinus carpio*), grass carp (*Ctenopharyngodon idella*), silver carp (*Hypophthalmichthys molitrix*), bighead carp (*Hypophthalmichthys nobilis*), African catfish (*Clarias gariepinus)*, pangas (*Pangasius* spp.,) tilapia (*Oreochromis* spp.) and pacu (*Piaractus brachypomus*) were recorded in associated wetlands and Brahmaputra valley. According to IUCN (2021), the conservation status of the recorded fishes was classified into five categories such as Endangered, Near Threatened, Least Concern, Vulnerable and Data Deficient. Accordingly, two species were included under Endangered category, two species under Vulnerable category, 6 species under Near threatened, 4 species have Data deficient and 96 species under Least concern category. Due to large-scale diversity in environments in river Brahmaputra, fishes thriving in it comprises of plainwater forms, estuarine forms, torrential forms, coldwater forms and it is also home to river dolphin *Platanista gangetica* [7, 8, 11, 33, 39]. [20] recorded 422 fish species from Northeast states of India belonging to 133 genera and 38 families having commercial importance as food and/ or ornamental values. Bhattacharjya et al. [6] recorded 216 fish species from Brahmaputra and Barak river systems in Assam and 141 finfish species including 29 families and 84 genera were reported from the Brahmaputra alone [7]. Ninety seven fish species were recorded from lower reaches of river Brahmaputra [32], 57 fish species from Kulsi river [23] and 50 fish species from Dihing river, a tributary of river Brahmaputra [17]. Although there are differences in ichthyofaunal diversity recorded in the present and earlier studies, the message which comes out profoundly is that there is rich diversity in fish species thriving in river Brahmaputra and its tributaries. Our experience also suggests that fishes undertake migration within the river(s) to adjust to changes in climatic variables. Studies related to generating updated information on ichthyofaunal diversity and distribution range of species in river Brahmaputra are encouraged.

4.3 Diversity Indices and Relative Abundance

Indicators of fish species richness and diversity showed seasonal fluctuation (Table 2). Highest species richness (105) was observed during pre-monsoon, followed by post-monsoon (88) and monsoon (82) seasons. Shannon-Weiner indices (H′) varied from 3.45 (monsoon) to 3.86 (pre-monsoon) indicating slightly impacted pattern of

Table 2 Diversity indices of fishes of River Brahmaputra, Assam

	Pre-monsoon	Monsoon	Post-monsoon
No. of Species	105	82	88
Individual	849	516	544
Shannon (H)	3.861	3.451	3.66
Evenness (e^H/S)	0.4523	0.3847	0.4416

the selected river stretch [10, 28]. Evenness index varied from 0.38 (monsoon) to 0.45 (pre-monsoon) indicating the frequency of dominating species present during pre-monsoon season. Margalef index was maximum for pre-monsoon season (15.42) indicating highest species richness during the season.

Relative Abundance of species measures how rare or common a species is in comparison to other species in a given area or population [28]. In the present study, SIFs dominated among the fishes in the River Brahmaputra of Assam (Fig. 3). *Cabdio morar* dominated in all the seasons; *Ailia coila* and *Clarias magur* dominated during pre-monsoon season. *Channa punctata*, *Parambassis baculis* and *P. ranga* dominated during monsoon season. High fish diversity in terms of species richness and evenness was observed in River and its associated tributaries by many researchers [4, 5, 15, 16, 18, 28, 35].

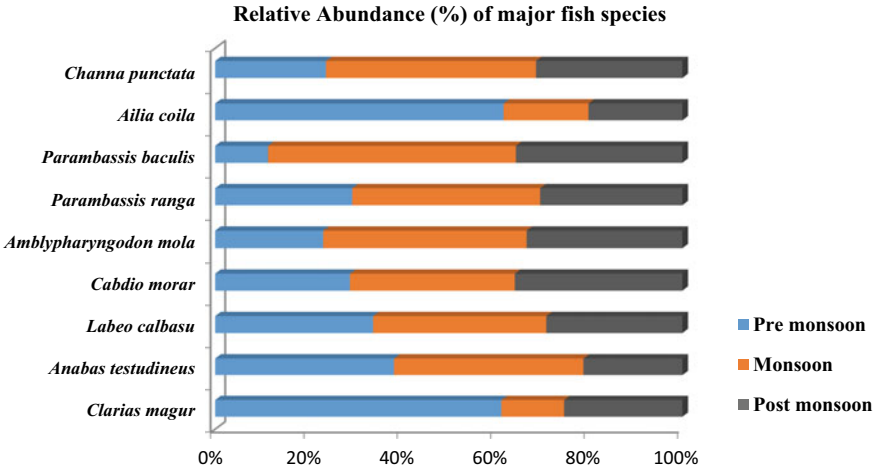

Fig. 3 Relative abundance of major fish species in R. Brahmaputra, Assam

5 Conclusion

The present study on Brahmaputra river provided updated important information on hydrobiological conditions and ichthyofaunal diversity of selected stretches. Although the river is rich in fish diversity indicating good ecosystem health, however, it is facing many challenges. The major threats in the river is recognized as siltation of river bed and connected channels, habitat destruction/alteration, construction of flood-control embankments, construction of dams, over-exploitation of fish, illegal fishing, pollution and climate change. Majority of these threats are caused due to anthropogenic factors that are in the hands of mankind to control. Rational fishing practices and desiltation of selected stretches of the river might help in conserving aquatic biodiversity. It is strongly felt that mass awareness on sustainable utilization and management of the river among riparian fishers and other stakeholders would contribute significantly in this direction.

Acknowledgements The authors are thankful to the Director, ICAR-Central Inland Fisheries Research Institute, Barrackpore for his support and encouragement. We are grateful to the fishers of river Brahmaputra for providing information and assisting in field sampling.

References

1. APHA (1998) Standard Methods for the Examination of Water and Wastewater, 20th edn. American Public Wealth Association, Washington, DC, USA
2. APHA (2005) Standard methods for examination of water and wastewater. 17th edn. APHA, AWWA, WPCF, Washington DC, USA
3. Bailung B, Biswas SP (2021) Determination of water quality and ecology of river Dihing river: A tributary of almighty Brahmaputra, Assam, NE India. AGBIR 37(5):172–176
4. Baishya RA, Basumatary S, Kalita HK, Talukdar B, Dutta A, Sarma D (2016) Present status and diversity of small indigenous fish species (SIS) in the upper reaches of river Brahmaputra in Assam, north-eastern India. Indian J Fish 63(1):1–7
5. Baro DC, Sharma S, Sharma D (2015) Coldwater fish diversity and abundance of upper reaches of Sonkosh river, Kokrajhar Assam. Sci Vision 15(1):8–18
6. Bhattacharjya BK, Choudhury M, Sugunan VV (2004) Icthyofaunistic resources of Assam with a note on their sustainable utilization. In: Mahanta PC, Tyagi LK (Eds.), Participatory approach for fish biodiversity conservation in North East India, workshop proceedings, NBFGR, Lucknow. pp. 87–105
7. Bhattacharjya BK, Bhaumik U, Sharma AP (2017) Fish habitat and fisheries of Brahmaputra River in Assam, India. Aquat Ecosyst Health Manag 20:102–115
8. Biswas SP, Baruah S (2000) Ecology of the river dolphin (*Platanista gangetica*) in the upper Brahmaputra. Hydrobiologia 430:97–111
9. Biswas SP (2014) An Overview on the threats of aquatic ecosystem in Upper Brahmaputra Basin. In Rivers for Life-Proceedings of the International Symposium on River Biodiversity: Ganges-Brahmaputra-Meghna River System; IUCN: Patna, India, pp. 45–53
10. Bode RW, Novak MA, Abele LE (1993) 20 Year trends in water quality of rivers and streams in New York State Dodge D.P. (ed.): Proceedings of the International Large River Symposium (LARS). Can Spec Publ Fish Aquat, pp 106

11. Bordoloi B, Saharia S (2021) Current status of the endangered Ganges River Dolphin (*Platanista gangetica*), the aquatic megafauna in the Brahmaputra River system. Curr World Environ 16(2):600–606
12. Borthakur, T. A., Kumar, D. and Singhal, A. (2016). Assessment of water quality of river Brahmaputra in Guwahati city of Assam. Conference paper, national conference on sustainable water resources development and management (SWARDAM-2016) volume: ISBN: 978-93-85777-75-2
13. Das BK, Boruah P, Kar D (2014) Study of seasonal variation of water quality of River Siang in Arunachal Pradesh, India. IOSR J Environ Sci, Toxicol Food Technol 8(2IV): 11–20
14. Das N, Das BK, Das S, Singh NR, Kar D (2015) Preliminary studies on Icthyofauna diversity and PhysicoChemical Parameters of River Bhogdoi during Winter and PreMonsoon Season in Assam. IOSR J Agric VetY Sci 8 (6): 35–41
15. Das SCS, Khan A, Alam A, Dubey VK, Joshi KD (2020) Piscine diversity, Community structure and distributional patterns of the west Ramganag river: a Mid Himalayan tributary of river Ganga. Indian J Anim Sci 90(1):109–115
16. Das SCS, Jha DN, Kumar V, Alam A, Srivastava K, Sahoo AK, Das BK (2022) Fish diversity, community structure, and environmental variables of River Tamas, a tributary of River Ganga. India Aquat Ecosyst Health Manag 25(2):62–69
17. Deori DJ, Abujam SK, Biswas SP (2015) Fish diversity and habitat ecology of Dihing river-A tributary of Brahmaputra River. Int J Fish Aquat Stud 2(4):190–197
18. Dey A, Sarma D (2018) Diversity, distribution and conservational approach of hillstream ornamental fishes in Manas River, India: An eastern hotspot region. Journal of Coldwater Fisheries 1(1):103–112
19. Goswami C, Zade VS (2015) Ornamental fish diversity across Brahmaputra Valley of Assam. Int J Innov Sci, Eng & Technol 2(1):547–549
20. Goswami UC, Basistha SK, Bora D, Shyamkumar K, Saikia B, Changsan K (2012) Fish diversity of North East India, inclusive of the Himalayan and Indo Burma biodiversity hotspots zones: A checklist on their taxonomic status, economic importance, geographical distribution, present status and prevailing threats. Int J Biodivers Conserv 4(15):592–613
21. Gupta N, Mishra A, Agrawal NK, Shrestha AB (2019) Potential impacts of climate change on water resources and adaptation policies in the Brahmaputra River Basin; Working Paper 2019/8; ICIMOD: Kathmandu, Nepal
22. India-WRIS, 2014. Brahmaputra Basin. Version 2.0. India-Water Resources Information System: www.india-wris.nrsc.gov.in
23. Islam MR, Das B, Baruah D, Biswas SP, Gupta A (2013) Fish Diversity and Fishing Gears used in the Kulsi River of Assam, India. Ann Biol Res 4(1):289–293
24. Jayaram KC (1999) The freshwater fishes of Indian region. Narendra Publishing House, Delhi, 551 pp Jhingran, V.G. 1991. Fish and Fisheries of India. 3rd Edn. Hindustan Publishing Corporation, Delhi, India
25. Jhingran VG, Natarajan AV, Banerjea SM, David A (1988) Methodology on reservoir fisheries investigations in India. Bull. No. 12
26. Kotoky P, Sarma B (2017) Assessment of water quality index of the Brahmaputra River of Guwahati City of Kamrup District of Assam, India. Int J Eng Res Technols 6(3):536–540
27. Kottelat M, Whitten T (1996) Freshwater biodiversity in Asia with special reference to fish. World Bank Tech. Pap., 343
28. Kumar D, Maurya AK, Prasad L, Singh CP, Radhakrishnan KV, Somasekara SR (2020) Fish biodiversity and its diversity indices in the Himalayan River Ghaghara at Northern India. J Entomol Zool Stud 8(6):1559–1564
29. May RM (1975) Patterns of species abundance and diversity. In: Cody ML, Diamond JM (eds) Ecology and evolution of communities. Belknap Press, Cambridge, Mass, pp 81–120
30. Pradhan NS, Das PJ, Gupta N, Shrestha AB (2021) Sustainable management options for healthy rivers in South Asia: the case of Brahmaputra. Sustainability 2021(13):1087. https://doi.org/10.3390/su13031087

31. Rasul G (2015) Water for growth and development in the Ganges, Brahmaputra, and Meghna basins: an economic perspective. Int J River Basin Manag 13:387–400
32. Sarma D, Das J, Bhattacharyya RC, Dutta A (2012) Ichthyofaunal diversity of lower reaches of the Brahmaputra River, Assam. Int J Appl Biol Pharm Technol 3(2):126–130
33. Sen N (2000) Occurrence, distribution and status of diversified fish fauna of north east India, In: Ponniah AG, Sarkar UK (Eds.), Fish Biodiversity of North East India pp. 31–48. NATP Publ. No. 2, NBFGR, Lucknow
34. Sharma JN (2004) An overview of the Brahmaputra River system. In: Singh VP, Sharma N, Ojha CSP (eds.), The Brahmaputra basin water resources. Water science and technology library, Vol. 47. Springer, Dordrecht
35. Sharma S, Das B (2009) Study of fish diversity of river Kopili in Assam. Proceedings of the Zoological Society of India 8(2):87–92
36. Singh V, Sharma N, Ojha CSP (Eds.), (2004) The Brahmaputra basin water resources (Vol. 47). Springer Science & Business Media
37. Solow AR (1993) A simple test for change in community structure. J Anim Ecol 62:191–193
38. Talwar PK, Jhingran AG (1991) Inland Fishes of India and Adjacent countries. Oxford & IBH Publishing Co. Pvt. Ltd, New Delhi
39. Vishwanath W (2002) Fishes of North East India. Maipur University, Imphal, India
40. Vishwanath W (2014) Freshwater fish diversity of the Ganges-Brahmaputra-Meghna River Basin. In: Rives for Life: Proceedings of the International Symposium on River Biodiversity: Ganges-Brahmaputra-Meghna River System, Ecosystems of Life, A Bangladesh-India Initiative; Sinha, R.K., Ahmed, B., Eds.; IUCN, International Union for Conservation of Nature: Dhaka, Bangladesh, 340p.

Initial Assessment of Air and Water Temperature in Western Nayar River Basin in Garhwal Himalaya

Dhruv Pandey and Soukhin Tarafdar

Abstract The thermal regime of streams and rivers is critical for freshwater ecosystems. The temperature regimes could be regulated by many factors and the most important could be the land surface air temperature as well as the groundwater contribution to the river-groundwater hydrological continuum. Further, the likely impacts of climate change on surface and groundwater warming could result in loss of habitat. In the present study, one of the largest spring-fed river systems of the western Nayar River basin, which acts as an ecologically sensitive habitat is being investigated. Satellite-based temperature data (MODIS LST product) was used to analyzed the monthly, seasonal as well as daytime and nighttime average temperature lapse rate for the selected stations in Western Nayar River. The lapse rate for the 2001 year was found to be 0.4 ~ 0.45 °C per 100 m while in the year 2021 the average TLR for Western Nayar River valley, annual and seasonal fell to 0.4 °C per 100 m. The previous studies reported from stations-based observation during monsoon period a lapse rate of 0.6 ~ 0.65 °C per 100 m (Kattel and Yao in J Earth Syst Sci 122:215–227, 2013), but due to cloud cover influence on MODIS data, the reported value is an underestimation of the actual lapse rate during monsoon season. Monthly to biweekly year-round measurements for the years 2011 and 2022 of Western Nayar, Nayar, and River Ganga water temperature were combined into average seasonal temperature data and spatially interpolated using Inverse Distance Weighted (IDW) interpolation technique for the generation of the spatiotemporal temperature profile of the river system. The Ganga River is colder by 4 to 5 °C during monsoon and post-monsoon whereas the water temperature difference during pre-monsoon and winter is around 1 °C. The initial results indicate a good correlation between monthly nighttime average air temperature and the monthly river water temperature. The preliminary results highlight that the warmest stretch of the river body starting from the confluence of West and East Nayar to its confluence till it meets River Ganga could be the most ecologically sensitive area and thus might require utmost protection.

D. Pandey · S. Tarafdar (✉)
GBPNIHE, Garhwal Regional Centre, Uttrarakhand 246174, India
e-mail: tarafdar101s@gmail.com

S. Dutta and V. Chembolu (eds.), *Recent Development in River Corridor Management*,
Lecture Notes in Civil Engineering 376, https://doi.org/10.1007/978-981-99-4423-1_12

Keywords Mid-Himalayan basin · Temperature Lapse Rate (TLR) · River thermal regime · Lotic ecosystem

1 Introduction

Globally, accelerated rise in minimum temperature, diminishing temperature range, and reduced asymmetric daily range in temperature patterns have been identified as indicators of climate change [13]. Conversely, the observation from western Himalaya covering Jammu and Kashmir and Himachal Pradesh during the twentieth century indicate temperature range has been expanding [3, 8]. Baidya et al. [1] analyzed the temperature data from eight stations in Nepal for 46 years span (1971–2006) and highlighted that the southern facing hillslopes observation through meteorological stations in the central Himalayas are observing an increase in the diurnal temperature range. Kattel and Yao [14] also reported that the average and maximum temperatures in the southern slope of the central Himalayas during 1980–2009 period have dramatically increased, especially in the last decade in the early twenty-first century. The findings indicated a sharp temperature regime shift occurred in 1997. The increase in mean temperature over the previous decade of observation is in line with the findings of recent research conducted in the Indian Himalayan region and Upper Indus Basin, where greenhouse gas emissions by humans could be linked to warming. The study by [3] in the northwest Himalayan (NWH) region observed that the air temperature has increased significantly over the past century by almost 1.6 °C, with winters warming more quickly. The report of IPCC (2018) states that the Asian mountains have warmed in recent decades at a pace of about 0.3 °C per decade, and it is extremely likely that this warming will continue, with a likely range of about 0.2 °C, with even higher values locally for some regions. Under a projected scenario with significant greenhouse gas emissions, atmospheric warming in mountains will be more pronounced after the mid-twenty-first century, and the rate at which this occurs will depend on regional and complex elevational factors [10].

In a mountainous topography, the air temperature decreases with the increase in elevation, and the rate of change of temperature with varying altitude is termed as temperature lapse rate (TLR). Prior work on free-air TLR [7, 9, 11, 16] has been conclusive that the average temperature lapse rate, or the rate at which air cools with elevation change, varies from around $10°Ckm^{-1}$ for dry air (i.e., the dry adiabatic lapse rate) to about $6.5°Ckm^{-1}$ for wet air (i.e., the saturated adiabatic lapse rate). [15] found through analysis of 56 stations in the central Himalayas(Nepal) that the pre-monsoon has the strongest dry convection causing the largest temperature lapse rate. The second highest lapse rate occurs during the post-monsoon, which has a similar cause attributed to the summer season but a much smaller thermal forcing impact following the wet summer. Winter time has the minimum lapse rate, which is accompanied by intense radiative cooling and cold air flows over low-lying locations. Several studies [9, 18, 20, 22] have also found the same variance in lapse rates with

changing seasons due to temperature inversions, where dry convection is most intense in the summer and least intense in the winter. It is also important to distinguish between near-surface and free-air lapse rates. Near-surface and free-air lapse rates may differ significantly at a certain time and location because they are affected by distinct processes. Compared to free-air lapse rates at the 14 stations of south-central Ihado from 1989 to 2004, the near-surface lapse rates are more unpredictable [5]. The present study is solely concerned on the near-surface temperature lapse rates.

To accurately estimate the altitudinal variability, it is imperative to quantify the distribution of temperature in complex terrain, particularly the link between temperature and altitude. But this quantification is difficult due to the scarcity of long-term surface temperature measurements in mountains, as well as it requires an understanding of the effects of regional variables like cold air pooling and inversions. Dense networks of sensors with great temporal precision are necessary to accurately characterize surface temperature trends that occur over rugged terrain in the region of Cascade mountains [18]. The land surface temperature data from the Moderate Resolution Imaging Spectroradiometer (MODIS) have been extensively utilized in establishing the temperature lapse rate (TLR) in various regions of the Himalayas. Several studies have demonstrated that the MODIS LST corresponds well with observed air temperatures during the night due to a lack of solar radiation [26, 30]. The TLR is a crucial metric for interpolating surface temperature data in mountainous locations. In regions with varying topography and unavailabilty of in-situ data, high-resolution satellite imageries can be valuable sources. The MODIS LST is a high-resolution (1 km) data and was found suitable for the study in the western Nayar basin for assessment of seasonal and monthly variations.

In lotic ecosystems, river water temperature is a very crucial factor for aquatic ecosystems. For instance, high summertime temperatures those made worse by land-use activities can have a negative impact on cold-water fish. Caissie et al. [6] in Catamaran Brook stream in New Brunswick and [21] in river Drava in Croatia observed that aquatic life becomes more sensitive to temperature resulting from an upsurge in water temperature due to a lack of dissolved oxygen. Lee and Rinne [17] and Bjornn and Reiser [4] stated that salmonid mortality has been impacted by high stream temperatures between 23 and 25°. These changes in the river water temperature are very much affected by the air temperature fluctuations in the region due to climate change.

The statistical correlations between water and air temperatures have frequently been studied when examining the thermal regimes of streams and rivers, which are important for aquatic ecology, water quality, and the use of water resources [6, 27]. A study on Devon river system [28] states that water temperature is significantly related to macro-air temperature, and even hourly fluctuations in water temperature are well related to changes in air temperature. Although linear regression models are frequently used for studying the correlation of air and water temperatures, several studies have also claimed that with the increase in frequency from hourly to daily or weekly, the air–water temperature regression relationship gets steeper and less scattered [23].

The aim of this study is to analyze the monthly and seasonal surface air temperature lapse rate of the western Nayar River valley using MODIS LST day and night time product for an elevation difference of 420 m for the years 2001 and 2021. The spatiotemporal variability of the river temperature profile at a seasonal scale is also being investigated to understand the thermal regime of the Nayar system as well as the Garga River. The air-river water temperature relationship is also investigated at a monthly scale to decipher the upgradient change in river water temperature with changing elevation for assessment of its ecological significance.

2 Study Area

The Western Nayar River sub-basin lies in the Pauri district between 29.938° to 30.213° latitude and 78.706° to 79.111° longitude (Fig. 1). The sub-basin covers an area of 752 km^2 with nearly 45% of area being dominated by pine and oak forest. The elevation of the basin varies from 530 to 2970 m. The sub-basin of Nayar River covers an area of 192 km^2 dominated by broad inner valley and steep slope. The average channel slope of the Western Nayar River between Jwalpa and Vyasghat is $\leq$2% with bedform morphology of riffle and pool configuration. The average summer temperature is 24.2 °C while the average winter temperature is 12.8 °C with more than 75% rainfall occurring during the monsoon period. The basin is underlain by metasedimentary rocks mainly quartzite and phyllite of Precambrian age.

3 Data Used and Methodology

3.1 MODIS Land Surface Temperature

The Moderate Resolution Imaging Spectroradiometer (MODIS) land surface temperature (LST) day and night data has been used for deriving the temperature values of the region. The MODIS-LST is derived from two thermal infrared (TIR) band channels, 31 (10.78–11.28 μm) and 32 (11.77–12.27 μm) with a 1 km spatial resolution. Split-window algorithm for the retrieval of the land surface temperature (LST) is used for the product results. The split-window algorithm is the estimation of emissivity in bands 31 and 32 by the division of the lower boundary air surface temperature, atmospheric column water vapor, and land cover types into compliant sub-ranges for ideal retrieval [2]. Temperature and emissivity values for each pixel are provided by the MODIS LST and emissivity (LST/E) products. Due to its extensive global coverage, radiometric resolution, dynamic ranges, and precise calibration in multiple TIR bands (better than 1% absolute) intended for retrieving sea-surface temperature (SST), long-term sea-surface temperature (LST), and atmospheric properties, MODIS is particularly helpful [12].

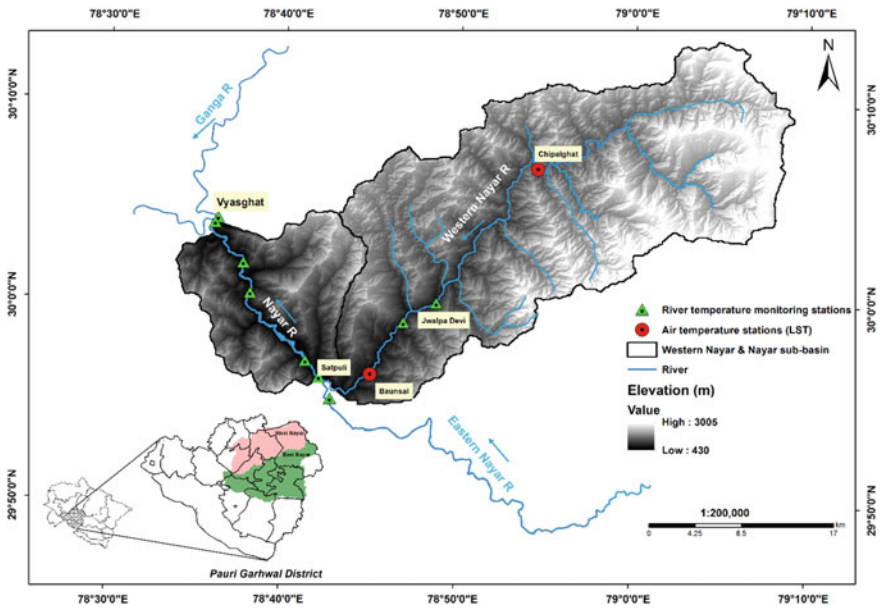

Fig. 1 West Nayar and Nayarsub-basinin middle Himalaya with locations of spot river water monitoring station as well as air temperature locations used for TLR estimation. Index map shows the coverage of west and east Nayar in Pauri district

MODIS version MOD11A1 LST products with a spatial resolution of 1 km^2 have been acquired from the LAADS DAAC of the Earthdata NASA portal. Daily LST data for daytime as well as nighttime data was acquired for the years 2001 and 2021 and lapse rate for the western Nayar River sub-basin between Baunsal (604 m) and Chipalghat (1024 m) stations was derived from the data retrieved after converting the pixel value into degree Celsius. MODIS data had its own limitations as cloud cover over a region severely affects the values of that particular spatial grid, with 0 being depicted as a temperature value, due to the inefficiency of the sensor to penetrate through clouds.

3.2 Estimation of the Temperature Lapse Rate (TLR)

The LST (land surface temperature) values derived from the MODIS LST day and nighttime products were used for the estimation of the TLR across the western Nayar valley for the two elevations transects, namely, Baunsal located at an elevation of 604 m and Chipalghat at an elevation of 1024 m.

The average lapse rate can be calculated as the rate of change in the temperature values with changes in the altitude, i.e.,

$$TLR = -\frac{dt}{dz}$$

where t and z are the temperature and elevation, respectively, of a particular location. One of the most crucial aspects of local and regional climate is TLR which varies with macro-topography [5, 9, 19, 22, 24, 25]. Additionally, its magnitude varies depending on the energy balance regimes which include surface characteristics, elevation, air moisture content, wind speed, cloudiness, radiative conditions, and proximity to the ocean [14].

3.3 In-Situ Water Temperature Data of the Nayar River

A calibrated handheld pH-temperature multi-parameter device (PCS Tester 35-Eutech Instrument) has been used for spot measurements of the water temperature of the Western Nayar, Nayar River, and the Ganga River at Vyasghat. Nine locations expanding from Jwalpa station to Vyasghat station in Ganga River, approximately covering a river length of 40 km, were covered during the daytime between 8 am and 2 pm at a biweekly to monthly interval. The in-situ data collected were classified into seasonal data for further generation of spatiotemporal variability of river water temperature along the course selected river using interpolating techniques.

4 Results and Discussion

4.1 Seasonal Air Temperature Variability and Temperature Lapse Rate

Interseasonal variation using MODIS LST dataset at average daily, daytime, and nighttime air temperature was analyzed for the years 2001 and 2021. The daytime summer temperature varies from 25 °C to 36 °C, whereas during the nighttime temperature ranges between 14 °C and 19 °C. The monsoons temperature of 26.5–33.5 °C was observed during the daytime but the nighttime temperature dropped between 14 °C and 22 °C. Winter records the seasonal minimum temperature during daytime (15.4–16 °C) and nighttime (7–10 °C). In all the seasonal observations the temperature recorded was minimum in the Chipalghat station and maximum in the Baunsal station in the western Nayar sub-basin as governed by the lapse rate.

Since the macro environment of the inner mountain valley could be significantly different from the complex sloping mountainous landscape, the altitudinal temperature lapse rate was computed over a time difference of two decades in the western Nayar sub-basin between Baunsal to Chipalghat having an elevation difference of 420 m. The monthly lapse rate for the sub-basin varied from 0.03 °C to 0.78 °C per

100 m for the year 2001, with the lowest record for the month of January and the highest for the month of September. However, the year 2021 recorded the lowest and highest TLR during January and August, respectively, beginning with 0.05–1.1 °C per 100 m. Table 1 and Fig. 2a highlight the annual and the seasonal values of lapse rates of the western Nayar catchment. The annual average lapse rate for the year 2001 was around 0.4 ~ 0.45 °C per 100 m, while in the year 2021 recorded a similar the mean lapse rate of 0.4 °C per 100 m. The study also showed that the maximum lapse rate is in summers (0.7 °C to 1 °C per 100 m) and the lowest lapse rates in winters (0.02 °C to 0.04 °C per 100 m). The bi-modal pattern with two maxima can also be observed from the western Nayar sub-basin as reported by Kettal et al. (2013) from Nepal Himalaya caused by seasonal differences in stronger dry convection during summer and intense radiative cooling and cold air flows during the winter period.

The lapse rates for the day and nighttime were also analyzed as it has significant ecological importance for river systems [29]. Figure 2b, c shows that the daytime average maximum temperature lapse rate was during the month of May (1.3 °C per 100 m) and the minimum was observed during December (0.01 °C per 100 m). The nighttime lapse rate ranges between 0.07 and 0.8 °C per 100 m. The underlying reason for daytime maxima and nighttime minimum value could due to the cool air advection from the Nayar River during nighttime as reported by [19] from the regions of Northern England.

Table 1 Monthly and seasonal lapse rate (in °C) between the selected two stations of the Western Nayarsub-basin

	Monthly TLR (°C/100 m)		Seasonal TLR (°C/100 m)		
	Year 2001	Year 2021		Year 2001	Year 2021
January	−0.028	−0.048	*Summer*	−0.524	−0.510
February	−0.061	−0.078	*Monsoon*	−0.665	−0.793
March	−0.303	−0.295	*Post-monsoon*	−0.545	−0.163
April	−0.508	−0.587	*Winter*	−0.096	−0.057
May	−0.738	−0.749			
June	−0.547	−0.411			
July	−0.630	−0.833			
August	−0.582	−1.099			
September	−0.783	−0.447			
October	−0.686	−0.210			
November	−0.405	−0.117			
December	−0.199	−0.044			
Average TLR	−0.456	−0.410			

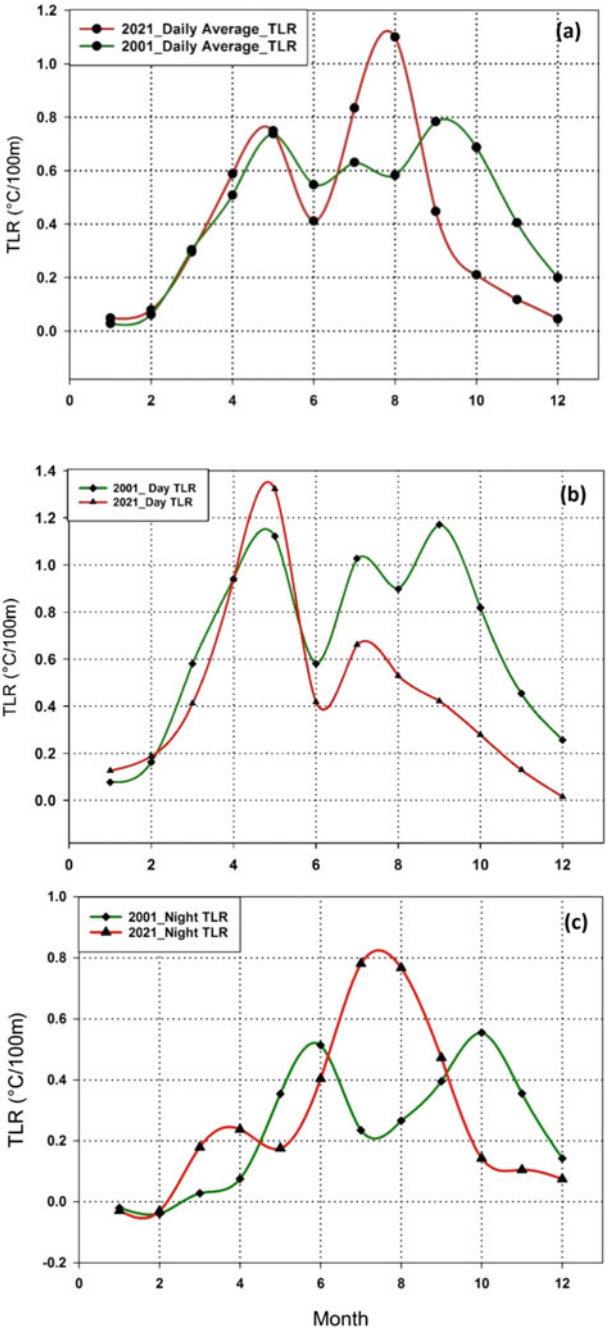

Fig. 2 Monthly variability in TLR in the western Nayar basin for the year 2001 and 2021; Daily average temperature (**a**), Daytime temperature (**b**), and Nighttime temperature (**c**)

4.2 Spatiotemporal Variability of River Water Temperature

Figure 3 depicts the spatiotemporal seasonal temperature difference in the western Nayar and Nayar Rivers sub-basin till its confluence in the Ganga River. The spot *in-situ* measurements of river water temperature at biweekly to monthly interval were interpolated using ARCGIS to generate spatiotemporal maps of the river. In general, the seasonal temperature maps (Fig. 3) highlight river temperature decrease up gradient in the western Nayar River whereas river water temperature decreases down gradient in the Nayar River till its confluence at River Ganga. The Ganga River being coldest as it receives significant snow and glacier melt contribution as compared to groundwater dominated spring-fed system of Nayar Basin.

The monsoon, post-monsoon, and the winter periods of the year marked similar patterns of temperature variability across the Western Nayar and Nayar Rivers formed after the confluence of East and West Nayar near Satpuli. However, the pre-monsoon period showed a complete reversal within the inner valley between Satpuli and Vyasghat and was found to be considerably cooler than the western Nayar river course. Figure 3 and Table 2 show that the spot temperature values for each station in the inner valley (like Chopda, Badayun, etc.) being almost colder by 3 °C as compared with the temperature of the western Nayar River observed at Baunsal, Jwalpa, and Patisain, thus making that portion of the transect warmer than the inner valley. Table 2 also highlights the highest variance in temperature values observed during the pre-monsoon season, with temperature fluctuating by more than 3 °C. It can also be observed in Table 2 that the temperature of the Ganga River compared with that of Nayar is almost colder by 1–5 °C.

The average water temperature fall along the course of Western Nayar and Nayar is around 0.57 °C and 0.59 °C per 100 m, respectively, which agrees well with the average surface air temperature lapse rate for the terrain. The highest average water temperature fall was observed during the post-monsoon period (1.4° and 0.86 °C per 100 m in west Nayar and Nayar, respectively) followed by the pre-monsoon period with an average water temperature fall of 0.8 °C, while the minimum was recorded during the winter period with the values 0.01° and 0.2 °C per 100 m.

4.3 Air–Water Temperature Relationship

River water temperature fluctuations could be very well correlated to the fluctuations in the surrounding air temperature. Regression analysis was performed between the average daytime spot river water temperatures with the monthly average daily value, average daytime, and average nighttime values obtained from MODIS LST temperature data. Figure 4 shows the correlation between the nighttime average monthly air and average monthly water temperature in the western Nayar Valley. The R^2 value of 0.66 indicates a good correlation with 75% of the values falling under the 95% confidence interval line. However, poor correlation was observed between

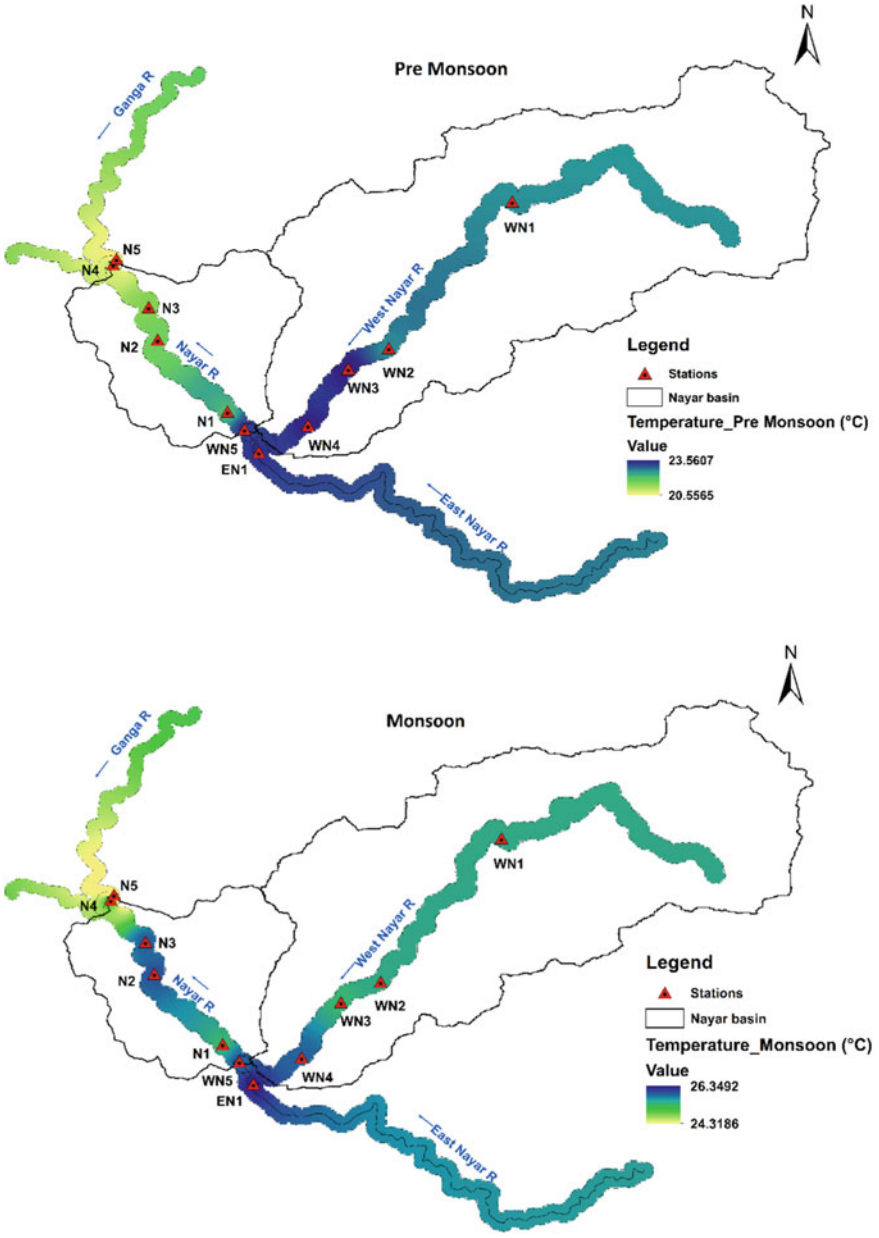

Fig. 3 Temperature variability across the western Nayar valley and Nayar River during the pre-monsoon and monsoon season. The spot river water temperature monitoring locations are represented as WN1 to WN5: Chipalghat, Jwalpa, Patisain and Baunsal; EN1: Satpuli (East Nayar); N1 to N5: CWC(Satpuli), Banghaat, Badayun, Chopda, Vyasghat and Vyasghat (Ganga)

Table 2 Seasonal average water temperature of Western Nayar, Nayar, and Ganga Rivers for 2021–2022

Stations	Mean water temperature (°C)			
	Winter	Pre-monsoon	Monsoon	Post-monsoon
Jwalpa Devi	16.40	21.98	25.05	20.65
Patisain	17.14	23.56	24.88	21.12
Baunsal	17.41	23.44	25.69	21.32
Satpuli(E.Nayar)	16.79	23.23	26.35	21.75
CWC (Satpuli)	17.09	23.15	25.71	21.82
Banghaat bridge	17.11	21.10	24.81	21.65
Badayun	16.84	20.51	25.85	21.37
Chopda	16.76	20.08	25.76	21.22
Vyas Ghat(Nayar)	16.45	19.78	25.4	20.82
Vyas Ghat(Ganga R.)	16.17	18.35	20.28	18.12

*__Pre-monsoon__: March to June, __Monsoon__: July to September, __Post-monsoon__: October and November, __Winter__: December to February

monthly and daytime average monthly air temperature data with water temperature data. More clarity will emerge when continuous data on air and water temperature will be collected from the network of paired air–water sensors installed in the river valley of Nayar. The studies in the Devon River system in the United Kingdom reported R^2 above 90% at mean weekly values of water and air observations [28].

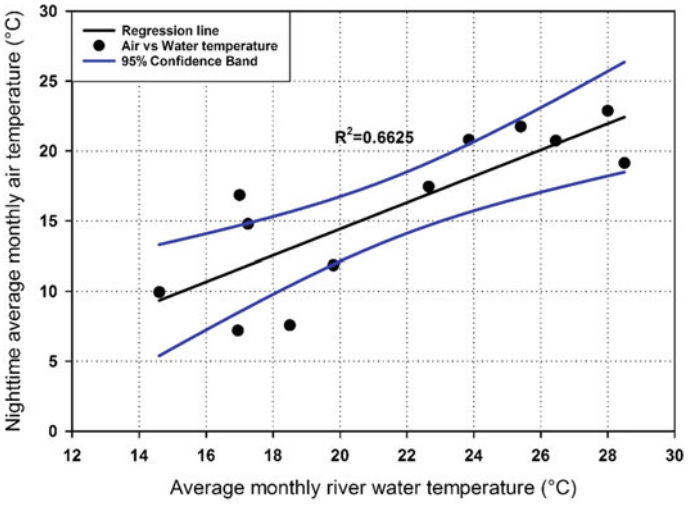

Fig. 4 Linear regression chart depicting the correlation between the air and river water temperature

5 Conclusion

Near-surface temperature lapse rate was analyzed using the MODIS LST temperature data for the two stations in the western Nayar Valley. A nominal variation in the TLR was observed for the years 2001 and 2021, as the mean yearly TLR ranges between 4.5 °C/Km and 4 °C/Km which is low compared to the reported yearly TLR of 5.5 °C/Km in Himalaya. The maximum TLR was observed during the summer season and the minimum was recorded in winter months with a bi-modal distribution of average monthly TLR as observed from Nepal Himalaya. The daytime average maximum temperature lapse rate was recorded during May (1.3 °C per 100 m) and the minimum was observed during December (0.01 °C per 100 m). A lower night time lapse rate between 0.07 and 0.8 °C per 100 m was recorded from the study area. Initial linear regression results showed a good correlation of monthly river water temperature with monthly nighttime air temperature as compared to the daytime monthly or monthly daily averaged of MODIS LST data. Spatiotemporal analysis of seasonal river water temperature indicates an average water temperature decline of around 0.57 °C and 0.59 °C per 100 m along the course of Western Nayar and Nayar Rivers, respectively. The decline in water temperature matches well with the average surface air temperature lapse rate for the terrain. The snow and glacier melt-fed Ganga River is colder than the groundwater dominated Nayar basin. Sensor-based paired air and river water monitoring network will throw more light to the specific relationship of air–water in the Nayar Basin.

Acknowledgements The authors express gratitude to the National Mission on Himalayan Studies (NMHS), implemented by the Ministry of Environment, Forest and Climate Change (MoEF&CC), New Delhi Nodal and Serving hub with G.B. Pant National Institute of Himalayan Environment and Sustainable Development (GBPNIHESD), Almora, Uttarakhand for providing the funding and research facilities during this research work. The all-round support of Prof. S. Dutta is gratefully acknowledged.

References

1. Baidya SK, Shrestha ML, Sheikh MM (2008) Trends in daily climatic extremes of temperature and precipitation in Nepal. J Hydrol Meteorol 5(1):38–51
2. Benali A, Carvalho AC, Nunes JP, Carvalhais N, Santos A (2012) Estimating air surface temperature in Portugal using MODIS LST data. Remote Sens Environ 124:108–121
3. Bhutiyani MR, Kale VS, Pawar NJ (2007) Long-term trends in maximum, minimum and mean annual air temperatures across the Northwestern Himalaya during the twentieth century. Clim Change 85(1):159–177
4. Bjornn TC, Reiser DW (1991) Habitat requirements of salmonids in streams. Am Fish Soc Spec Publ 19(837):138
5. Blandford TR, Humes KS, Harshburger BJ, Moore BC, Walden VP, Ye H (2008) Seasonal and synoptic variations in near-surface air temperature lapse rates in a mountainous basin. J Appl Meteorol Climatol 47(1):249–261
6. Caissie D, El-Jabi N, St-Hilaire A (1998) Stochastic modelling of water temperatures in a small stream using air to water relations. Can J Civ Eng 25(2):250–260

7. Dodson R, Marks D (1997) Daily air temperature interpolated at high spatial resolution over a large mountainous region. Climate Res 8(1):1–20
8. Fowler HJ, Archer DR (2006) Conflicting signals of climatic change in the Upper Indus Basin. J Clim 19(17):4276–4293
9. Gardner AS, Sharp MJ, Koerner RM, Labine C, Boon S, Marshall SJ, Burgess DO, Lewis D (2009) Near-surface temperature lapse rates over Arctic glaciers and their implications for temperature downscaling. J Clim 22(16):4281–4298
10. Hock R, Rasul G, Adler C, Cáceres B, Gruber S, Hirabayashi Y, Jackson M, Kääb A, Kang S, Kutuzov S, Milner A (2019) High mountain areas
11. Immerzeel WW, Van Beek LPH, Konz M, Shrestha AB, Bierkens MFP (2012) Hydrological response to climate change in a glacierized catchment in the Himalayas. Clim Change 110(3):721–736
12. Jain SK, Goswami A, Saraf AK (2008) Determination of land surface temperature and its lapse rate in the Satluj River basin using NOAA data. Int J Remote Sens 29(11):3091–3103
13. Karl TR, Jones PD, Knight RW, Kukla G, Plummer N, Razuvayev V, Gallo KP, Lindseay J, Charlson RJ, Peterson TC (1993) Asymmetric trends of daily maximum and minimum temperature. Pap Nat Resour 185
14. Kattel DB, Yao T (2013) Recent temperature trends at mountain stations on the southern slope of the central Himalayas. J Earth Syst Sci 122(1):215–227
15. Kattel DB, Yao T, Yang K, Tian L, Yang G, Joswiak D (2013) Temperature lapse rate in complex mountain terrain on the southern slope of the central Himalayas. Theoret Appl Climatol 113(3):671–682
16. Kattel DB, Yao T, Yang W, Gao Y, Tian L (2015) Comparison of temperature lapse rates from the northern to the southern slopes of the Himalayas. Int J Climatol 35(15):4431–4443
17. Lee RM, Rinne JN (1980) Critical thermal maxima of five trout species in the southwestern United States. Trans Am Fish Soc 109(6):632–635
18. Minder JR, Mote PW, Lundquist JD (2010) Surface temperature lapse rates over complex terrain: lessons from the Cascade mountains. J Geophys Res: Atmos 115(D14)
19. Pepin N (2001) Lapse rate changes in northern England. Theoret Appl Climatol 68(1):1–16
20. Pepin N, Losleben M (2002) Climate change in the Colorado Rocky Mountains: free air versus surface temperature trends. Int J Climatol: J R Meteorol Soc 22(3):311–329
21. Rabi A, Hadzima-Nyarko M, Šperac M (2015) Modelling river temperature from air temperature: case of the River Drava (Croatia). Hydrol Sci J 60(9):1490–1507
22. Rolland C (2003) Spatial and seasonal variations of air temperature lapse rates in Alpine regions. J Clim 16(7):1032–1046
23. Stefan HG, Preud'homme EB (1993) Stream temperature estimation from air temperature 1. JAWRA J Am Water Resour Assoc 29(1):27–45
24. Tarafdar S (2016) The study of spatial distribution of precipitation and stable isotope content in a mountainous watershed of the Mid-Himalaya, Northern India from short-term records of monsoon period. J Hydrogeol Hydrol Eng 5. https://doi.org/10.4172/2325-9647.1000138
25. Thayyen RJ, Gergan JT, Dobhal DP (2005) Slope lapse rates of temperature in Din Gad (Dokriani glacier) catchment, Garhwal Himalaya, India. Bull Glaciol Res 22:31–37
26. Wang Y, Wang L, Li X, Chen D (2018) Temporal and spatial changes in estimated near-surface air temperature lapse rates on Tibetan Plateau. Int J Climatol 38(7):2907–2921
27. Webb BW (1987) The relationship between air and water temperatures for a Devon river. Rep Trans Devon Ass Advmt Sci 119:197–222
28. Webb BW, Clack PD, Walling DE (2003) Water–air temperature relationships in a Devon river system and the role of flow. Hydrol Process 17(15):3069–3084
29. Wilby RL, Johnson MF, Toone JA (2014) Nocturnal river water temperatures: spatial and temporal variations. Sci Total Environ 482:157–173
30. Zhang H, Immerzeel WW, Zhang F, De Kok RJ, Gorrie SJ, Ye M (2021) Creating 1-km long-term (1980–2014) daily average air temperatures over the Tibetan Plateau by integrating eight types of reanalysis and land data assimilation products downscaled with MODIS-estimated temperature lapse rates based on machine learning. Int J Appl Earth Obs Geoinf 97:102295

Effect of Anthropogenic Activities on the Water Quality in Tarafeni River of Jhargram District, Bankura

Amlan Mahata and Chiranjit Singha

Abstract The water quality of the Tarafeni River was analyzed during the COVID-19 period, from March 2020 to March 2021. The seasonal variation of water quality standards is compared with the Water Quality Index (WQI). The survey areas are contaminated with a different type of untreated sewage that impacts the anthropogenic activities when the results of the analyzed water quality parameters (WQP) of the river dam are significantly ($p < 0.05$) inter-association with the different water quality parameters. The study involves analyzing the various biological and physiological parameters of the river at 18 locations. The water quality parameters were analyzed, namely, pH, BOD, COD, DO, TDS, PO_4, NO_3, Cl^-, and Total Alkalinity. Water quality conditions in wet session for Total coliform P value was 1.671 ($p < 0.05$) and *E.coli* P value was 4.063 ($p < 0.05$). The correlation of COD and BOD is very strong with pH (above 0.85) in pre-monsoon. The results indicated that the water quality of the river location was low, In addition, the pH and bacterial load levels crossed the acceptable limits. The quality of water is hygienic for local people as well as for domestic purposes but not for the industrial and agricultural fields so that may need rectification for improved water quality management and their diversity.

Keywords Water Quality Index (WQI) · Anthropogenic parameter · Pre-monsoon · Tarafeni river

1 Introduction

Without fresh water, life on Earth would not be able to survive. Rivers are the primary source of nourishment for various life forms on this planet. Unfortunately, they are being exploited and polluted by various activities, which are endangering the river's

A. Mahata
Department of Microbiology, Burdwan University, Burdwan, West Bengal, India

C. Singha (✉)
Department of Agricultural Engineering, Visva-Bharati, Santiniketan, West Bengal, India
e-mail: singha.chiranjit@gmail.com

S. Dutta and V. Chembolu (eds.), *Recent Development in River Corridor Management*,
Lecture Notes in Civil Engineering 376, https://doi.org/10.1007/978-981-99-4423-1_13

health and environment. It is therefore important that the various activities that affect the river's quality are studied [1, 8] (Singha and Swain 2021). A comprehensive survey is also needed to rectify the water of the Tarafeni River that flows in the river. This process involves conducting a microbiological survey to define the microorganisms living in the water [7, 9]. Besides being used for drinking water, the river also serves as a vital part of the aquatic ecosystem [10]. It is therefore important that the various activities that affect the river's quality are studied. A microbiological survey is also needed to determine water quality. With diversity and the ability to respond quickly to environmental changes, bacteria are the ideal indicators of the pollution of surface waters (Kavka and Poetsch 2006). The soil conditions at the surface layer of the river negatively affect the productivity of the agricultural yield. This area also has sporadic agricultural lands that can be used for the production of vegetables such as mustard and cabbage. The lower part of the river, which is located in the Belpahari block, is suitable for various crops and is also used for the production of mustard seeds. The increasing urbanization and the increasing number of people living in the region have caused the demand for subsurface water to rise. This is also linked to the region's socioeconomic development. It is therefore important that the government and the private sector take measures to address the issue of surface water shortages. The objective of the study was to identify a process that could be carried out in the evaluation of the surface water resources of the River to improve their hygiene and quality. The water quality parameters were analyzed, namely, pH, BOD, COD, DO, TDS, PO_4, NO_3, Cl^-, and total alkalinity condition from March 2020 to March 2021.

2 Materials and Methods

2.1 Study Location

The undulating tracts in Belpahari block, which are located in the block of Binpur I and II at Jhargram District, have lateritic soil and various streamlets and rivulets that are situated along the river's route (Fig. 1). The monsoonal channels that run through the river bring water into the next-ordered streams. The river, which is a 5th-order stream, flows over a rugged surface for a length of approximately 48.7 km. The river passes through the Binpur I and Binpur II blocks of Jhargram District and joins the Bhairabbaki River. It is located within the boundaries of the Binpur I and Binpur II blocks. It is tracking within 22.6321°N and 86.7643°E and falls under the jurisdiction of the Belpahari and Binpur police stations. Its geographical position indicates that it is situated in the eastern part of the Chhoto Nagpur plateau. The area around the river slopes down into the undulating terrain, and it experiences hot and humid weather with temperatures of up to 46° Celsius.

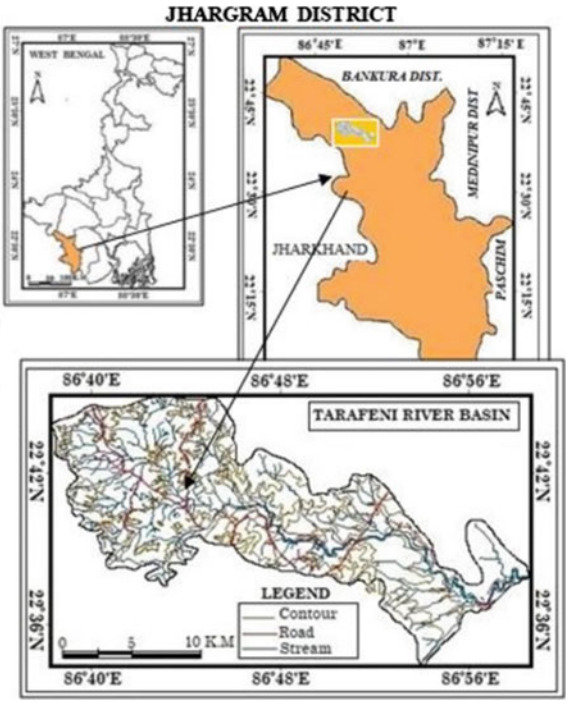

Fig. 1 The study area

2.2 Collection of Sample

The water samples were taken from various areas of the Tarafeni River, which is located in the Belpahari block. They were collected from March 2020 to March 2021. The water samples are usually collected from pre-monsoon, monsoon, and post-monsoon seasons. Table 1 shows the locations site of sampling sites and eighteen water samples are used for testing in anthropometric parameters.

2.2.1 Collection and Preservation of Samples

The samples were collected from the Tarafeni River to determine the water quality that was used by the neighboring areas for their needs. One bottle of water was in gaseous condition and kept at a pH of 2–4° Celsius until COD measurement and the analysis of the data was carried out. After the sample was poured into a bottle, it was carefully transported to the microbiology laboratory and subjected to analysis. The bottle was labeled with the name of the sample and stored in a dark place so it was estimated to be laboratory [3].

Table 1 The GPS based water sample location for the anthropogenic stress identification of the study station

Sl. no	Sample no	Name of places	Latitude and longitude	Session
1	S1	Bansgar	22.656055, 86.806256	Pre-monsoon low flow
2	S2	Nalkhalia	22.653482, 86.812365	Pre-monsoon low flow
3	S3	Jamboni	22.655591, 86.817227	Pre-monsoon low flow
4	S4	Bansgar	22.656055, 86.806256	Pre-monsoon High flow
5	S5	Nalkhalia	22.653482, 86.812365	Pre-monsoon High flow
6	S6	Jamboni	22.655592, 86.817227	Pre-monsoon High flow
7	S7	Bansgar	22.656869, 86.824508	Monsoon High flow
8	S8	Nalkhalia	22.652354, 86.829401	Monsoon High flow
9	S9	Jamboni	22.346752, 86.832416	Monsoon High flow
10	S10	Bansgar	22.656869, 86.824508	Monsoon low flow
11	S11	Nalkhalia	22.652354, 86.829401	Monsoon low flow
12	S12	Jamboni	22.346752, 86.832416	Monsoon low flow
13	S13	Bansgar	22.656869, 86.824508	Post monsoon low flow
14	S14	Nalkhalia	22.652354, 86.829401	Post monsoon low flow
15	S15	Jamboni	22.346752, 86.832416	Post monsoon low flow
16	S16	Bansgar	22.656869, 86.824508	Post monsoon High flow
17	S17	Nalkhalia	22.652354, 86.829401	Post monsoon High flow
18	S18	Jamboni	22.346752, 86.832416	Post monsoon High flow

2.3 Water Quality Index (WQI)

The water quality index of the River is affected by anthropogenic factors. This parameter is used to evaluate the overall health of the river. Eleven different water parameters were analyzed in the study to check the validity of the WQI. The calculation of the WQI was executed through the weighted arithmetic index method [1, 4]. The WQI is a measure of the adverse state of the river's water flow. It takes into account the various environmental factors that negatively affect its quality. The weight that the various water parameters are given is taken into account to evaluate the significance of the parameter. The final aggregate of the index is then calculated using the arithmetic mean.

The Water Quality Index was calculated by following steps:

First: Parameter formulated using factors of Unit weight (Wn)

Unit weight (Wn) for nth parameter = Proportionality constant (K)/Standard permissible value for nth parameter (Sn).

Where n is the number of water quality parameters.

Second: Formulated the value:

Sub-index (Qn) $= \frac{Vn-Vi}{Vs-Vi} \times 100$, where, Observed value indicates—Vn

The ideal value indicates—Vi, Standard value—Vs, Vi–Ideal value (Generally Vo = 0 for most parameters except pH and DO is 6.9 and 14.7)

Third; WQI is calculated with a combination of the First and Second formula

$$\text{WQI} = \sum_{n=1}^{n} q_n \, w_n / \sum_{n=1}^{n} w_n$$

where Unit weight (Wn) is using factors, n is the number of water quality parameters, and Qn is the sub-index.

3 Results and Discussion

The objective of this survey determines the various water parameters that affect the Tarafeni River's water quality. It also included the parameters of chemical and biological. The results of various factors in water are characterized in (Table 2). Tarafeni River of surface water parameters is analyzed according to CPCB standards, followed in (Table 3). The water pH level was also analyzed. It is a negative representation of the hydrogen ion concentration in the water. Various factors create gases. Acidity and alkalinity can affect the pH level of water. In this survey, the lowest value was found in S9 which is 6.19 while the highest value was found in S1 which is 7.65. The data collected from the water sample were analyzed using the ANOVA method. All of the parameters were under the permeable limit of the Central Pollution Control Board (CPCB India). The total coliform values depended on the nature of the water in the river basin. The BOD value also revealed that river water is not suitable for aquatic life. Water has been used for irrigation areas after it has been treated properly. However, the maximum amount of dissolved organic matter (DO) that can be reported from the river is still below the permissible limit. Their DO value is 6.1–7.6 mg/L. This means water is still usable. Although the phosphate values are still high, the nitrate and chloride levels are within the permissible limit. The increase in the phosphate limits has been linked to the development of algae blooms and their effect on the river's water quality. This is because the nutrients are contributing to the river's eutrophication load [2, 6]. The hardness of the water is a vital property that prevents it from being used as a soap solution. The permissible limit is increased according to standard value so it can cause the fatal unhealthy condition. The highest value that the river water quality was reported at 87 mg/L, while the lowest one was at 6.5 mg/L. This means that the river water is still safe to drink even though it has been treated properly. However, the high levels of dissolved particles and suspended wastes in the water are not ideal for aquatic life. The high levels of this contaminant can be caused by the sewage and sediments coming from local places [5]. The data collected from the Tarafeni River shows that it is not suitable for drinking water. It requires treatment and disinfection to maintain its quality.

The microbiological parameters of Tarafeni River's water were analyzed for the last two years (Table 5). Determination of Total coliform bacterial activities unstable in a different session (Fig. 2). The data collected from different sessions were analyzed according to their respective locations. The study Sites of Water quality index were assigned through the CPCB standards in the study sites domain (Fig. 3). The average total chemical counts (TC counts) of the river were 8916/100 ml, which indicates that it is in the moderately polluted category of the CPCB. The index of water is a statistical tool for aims to analyze the quality of river water. Index of Water Quality formulated according to CPCB standards A+++++ , A++++ , A+++ , A++ , and A+, to check water quality (Table 4). It takes into account the various factors that affect its water quality, such as its use of it, its nutrients, and its biological composition. The variability of the water quality index was dynamically changeable in different seasons with their climatic condition [4]. The river water from different places is unusable water for domestic purposes. On the other hand, the water from location A3 is in the poor water quality category. The high levels of phosphate values in the river have been identified as factors that affect water which gradually decreases the water quality of the region's water supply. Results of the survey revealed that the water of the river basin is unsuitable for industrial and local purposes. The correlation matrix between the various parameters of the water showed that the high levels of organic factors and the phosphate values were related to the WQI rating. During the monsoon season, the strong correlation between the various parameters, such as the BOD and pH, became apparent. The correlation matrix between the anthropogenic parameters, such as the pH and the BOD, became interesting during the monsoon season. The strong correlation between these two became apparent during the post-monsoon season. On the other hand, the negative correlation between the DO and Chlorine was also observed during the pre-monsoon seasons (Tables 6, 7 and 8).

4 Statistical Analysis

Statistical analysis of the water sample was carried out by ANOVA method through the statistical SPSS software. The variability of the different physicochemical parameters is inter-association in pre and post-monsoon periods. This relationship quantified the importance of the physicochemical properties conforming to the water quality status in the study area. This study evaluated to correlation coefficient between Total coli form (TC), *E.coli* in water sources at the dry periods for TC, P value of 3.091 ($P < 0.05$) and *E.coli* P value of 3.517 ($P < 0.05$). The correlation of COD and BOD is very strong with pH (above 0.85) in pre-monsoon. In addition, the correlation of TH and PO4 is very strong with pH and BOD (above 0.92) in post-monsoon. Water quality conditions in the wet session for Total coliform P value 1.671 ($P < 0.05$) and *E.coli* P value 4.063 ($P < 0.05$). The statistical significance revealed that the water source of session for total coliform P value 5.369 ($P < 0.05$) and *E.coli* P value 6.933 ($P < 0.01$). Water sources of Kechanda region showed the higher total coliform and

Table 2 Physicochemical parameters variation of Tarafeni River water (2020–2021)

Sample no	pH	COD (mg/L)	BOD (mg/L)	DO (mg/L)	Phosphate (mg/L)	Chloride (mg/L)	Nitrate (mg/L)	Turbidity NTU	TA (mg/L)	TH (mg/L)	TDS (mg/L)
S1	7.65	27.1	6.5	7.4	8.6	23.21	7.3	273	77	76	197.1
S2	7.34	22.4	3.1	6.1	7.1	31.10	6.6	198	74	71.1	199.3
S3	7.20	25	6.2	6.9	7.5	26	6.8	219	83	69	245.5
S4	6.36	18	6.7	7.3	9.2	27	7.7	224	79	66	232
S5	7.34	21.6	7.3	7.0	8.6	24.3	7.3	279	81	74	247
S6	7.50	23.8	2.8	6.5	8.0	21.31	6.8	189	86	78	285
S7	7.23	27	6.4	6.9	8.2	30	6.3	224	72	71	255
S8	7.31	29.1	6.0	6.9	7.3	24	7.4	254	77	68	203.1
S9	6.19	31	3.7	6.4	6.9	26	7.9	201	87	79	244
S10	7.62	26	3.0	6.5	8.1	33.21	7.3	177	78	75	234
S11	7.90	28.8	2.9	7.6	7.7	26.90	6.9	261	76	71	248
S12	7.52	26	3.56	6.5	8.0	28	7.2	199	84	82	188
S13	6.85	31	6.9	6.3	7.8	26	6.8	217	89	72	212.4
S14	7.69	16.5	6.1	6.6	7.4	22	7.9	261	71	77	236
S15	7.42	28	5.9	7.5	8.5	23.45	7.6	272	86	87	178.3
S16	6.92	22.2	6.5	6.1	8.9	31.10	7.6	241	87	76	199
S17	7.45	30	7.1	7.1	7.3	24.51	5.9	211	74	80	241
S18	7.59	24.5	6.9	6.2	7.5	30	7.0	231	87	71	248

Table 3 Central Pollution Control Board (CPCB India) standard for water quality

Sl. No	Parameters	CPCB of river surface water	CPCB Limit mg/L	CPCB standards 2006
1	PH	6.7–8.5	6.0–8.5	6.0–8.5
2	TDS mg/l	250	20	20
3	Chloride (Cl^-) mg/l	250	250	600
4	Phosphate (PO_4) mg/l	6	–	–
5	Nitrate (NO_{3-}) mg/l	45	20	20
6	BOD mg/l	30	15	15
7	DO mg/l	3	5	6
8	COD mg/l	250	–	125
9	Turbidity	5	10	–
10	Total hardness mg/l	300	200	200
11	Total alkinity mg/l	200	200	300

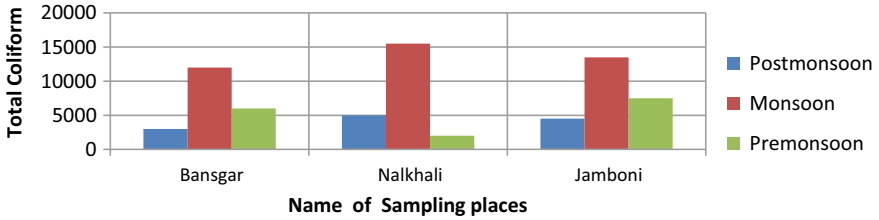

Fig. 2 Determination of Total Coliform in different session

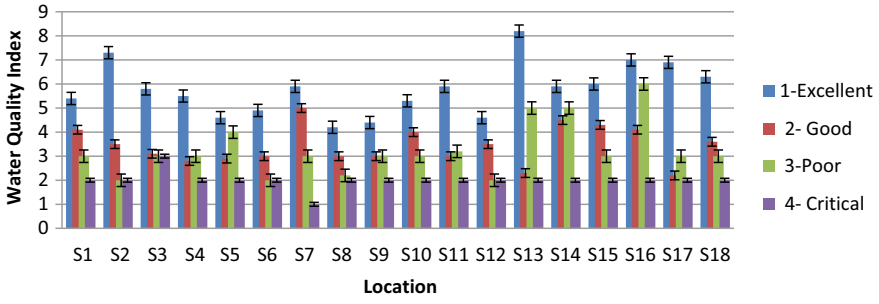

Fig. 3 Water quality index of Tarafeni river based on CPCB standards

E.coli concentration. Diarrheal and other water-related diseases spread from these sources.

Table 4 Water quality index of collected water sample

Water quality index	Quality	% of Samples	Grade
0–25	Excellent	0	A+++++
26–50	Good	3	A++++
51–75	Poor	50	A+++
76–100	Very poor	35	A++
100>	Unsuitable	12	A+

5 Conclusions

River pollution is a major public health issue that affects the lives of many people in developing nations. The lack of proper government policies and planning is the main reason why this issue occurs. This study aims to identify the current state of the Tarafeni River water quality and its impact on public health. The study involves analyzing the various biological and physiological parameters of the river at 18 locations. The water quality parameters of the Tarafeni River were analyzed. These included the biological and physiological parameters. The survey results revealed that the quality of river water is not fitting for consumption due to the excessive amount of pollution and sewage that it has received. Aside from being a major issue for public health, the presence of industrial waste and inorganic pollutants in the river water has also been known to cause various health problems. During the monsoon season, the river is prone to natural disasters such as flooding. Various measures with purification have to be taken to prevent further contamination of the Tarafeni River.

To maintain further contamination of Tarafeni River water, certain measures have to be taken. These include the implementation of stricter regulations regarding the discharge and drainage systems of public toilets into the river. Besides these, other measures have to be taken to prevent the floodwater from flowing into the river due to the accumulation of debris and silt in the area surrounding it. This can be done through the establishment of a plantation along the riverbank. This will help in controlling the floodwater's load and prevent it from flowing into the river. A floodwater reservoir can also be created in the river's lower valley to allow agricultural activities to use it. The natural bodies have limited capacities to self-degrade and recover from the effects of their pollution. When the amount of pollutants that they receive exceeds their capacity to degrade the wastes, the river's water quality can be negatively affected. Due to the presence of excessive amounts of sewage and pollution in the Tarafeni River, it has been identified that the local population and government should work together to prevent it from deteriorating. This is why regular measures should be implemented to combat the effects of pollution. In addition to regular measures, the people of the Belpahari I and II blocks should also be involved in the management of the river.

Table 5 Microbiological parameters of the water in Tarafeni River (February 2020 and 2021)

Month/ Year	Total coliform (MPN/ 100 ml)		Vibrio cholera		Staphylococcus aureus		Pseudomonas aeruginosa		Salmonella typhi	
	2020	2021	2020	2021	2020	2021	2020	2021	2020	2021
January	12,000	19,000	A	P	A	A	A	A	A	A
February	6000	9000	P	A	A	A	A	A	A	A
March	2000	2700	P	A	A	A	A	A	A	A
April	11,000	13,000	A	A	A	A	A	A	A	A
May	3000	7000	A	A	A	A	A	A	A	A
June	6000	13,000	P	A	A	A	A	A	A	A
July	27,000	16,000	A	P	A	P	A	A	A	A
August	5000	8000	A	P	A	A	A	P	A	A
September	9000	11,000	P	P	A	A	A	A	A	A
October	10,000	18,000	A	A	A	A	P	A	A	A
November	7000	20,000	P	A	A	A	A	A	A	A
December	9000	17,000	A	P	A	A	A	A	A	A

Note P → Present, A → Absent

Table 6 Physicochemical parameters Correlation coefficient matrix in pre-monsoon samples water

	PH	COD	BOD	DO	PO_4	Cl	NO_3	TH	TA	TDS	Turbidity
PH	1										
COD	−53*	1									
DO	0.71**	−0.92**	1								
BOD	−57*	0.95**	0.93*	1							
PO_4	−0.59**	0.94**	0.93**	−0.92**	1						
NO_3	−0.41	0.57*	0.68**	−0.47*	0.65**	1					
Cl	−0.89**	0.78**	0.77**	−0.93**	0.82**	0.28	1				
TH	0.96**	−0.71**	−0.78**	0.87**	−0.77**	−0.75**	−0.77**	1			
TA	0.65**	−0.77**	−0.97**	0.96**	−0.81**	−0.69**	−049**	0.70**	1		
TDS	−0.07	0.23	0.29*	−0.014	0.28	−0.36	0.86**	−0.52*	−0.31	1	
Turbidity	0.22	0.10	0.01*	0.05	0.39*	-0.01	0.24	0.22	0.20	−0.05	1

Dissolved Organic matter (DO), Total Hardness (TH), Total Dissolved Solids (TDS), Bio-chemical Oxygen Demand (BOD), Chemical Oxygen demand (COD), * Correlation significant level P = 0.05 level (2-tailed), ** Correlation significant level P = 0.01

Table 7 Physicochemical parameters correlation coefficient matrix in monsoon

	PH	COD	BOD	DO	PO_4	Cl	NO_3	TH	TA	TDS	Turbidity
PH	1										
COD	0.88**	1									
DO	−0.65**	−0.55**	1								
BOD	0.86**	0.84**	−0.75*	1							
PO_4	−0.03	−0.04	−0.13	−0.15	1						
NO_3	−0.55	0.57*	0.68**	−0.47*	0.65**	1					
Cl	0.88**	0.82**	0.87**	−0.93**	0.23	0.28	1				
TH	0.96**	−0.71**	−0.78**	0.87**	−0.77**	−0.75**	−0.77**	1			
TA	0.65**	−0.77**	−0.97**	0.96**	−0.81**	−0.69**	−0.49**	0.70**	1		
TDS	−0.07	0.23	0.29*	−0.014	0.28	−0.36	0.86**	−0.52*	−0.31	1	
Turbidity	0.22	0.10	0.01*	0.05	0.39*	−0.01	0.24	0.22	0.20	−0.05	1

Dissolved Organic matter (DO), Total Hardness (TH), Total Dissolved Solids (TDS), Bio-chemical Oxygen Demand (BOD), Chemical Oxygen demand (COD), * Correlation significant level P = 0.05 level (2-tailed), ** Correlation significant level P = 0.01

Table 8 Physicochemical parameters of post-monsoon samples water correlation coefficient matrix

	PH	COD	BOD	DO	PO_4	Cl	NO_3	TH	TA	TDS	Turbidity
PH	1										
COD	0.39*	1									
DO	−0.36	−0.91**	1								
BOD	0.45	0.99**	−0.88*	1							
PO_4	0.44**	0.88**	0.93**	−0.71**	1						
NO_3	0.78**	0.27	0.32	−0.17	0.65**	1					
Cl	0.66**	0.32	0.38*	−0.19	0.44*	0.85**	1				
TH	0.92**	0.76**	0.72**	−0.67**	0.77**	0.75**	0.79**	1			
TA	0.27	−0.33	−0.44	0.22	−0.29	0.46	0.12	−0.23	1		
TDS	0.72**	0.35**	0.41*	−0.44	0.53**	0.83**	0.86**	0.81**	0.27	1	
Turbidity	0.66	0.83**	0.88*	−0.61	0.39**	0.65	0.47	0.78*	−0.55*	0.57**	1

Dissolved Organic matter (DO), Total Hardness (TH), Total Dissolved Solids (TDS), Bio-chemical Oxygen Demand (BOD), Chemical Oxygen demand (COD), * Correlation significant level P = 0.05 level (2-tailed), ** Correlation significant level P = 0.01

Acknowledgements We acknowledge the Dept. of Microbiology, Burdwan University, and Dept. of Agricultural Engineering, Visva Bharati University in West Bengal for the necessary support by the laboratory staffs in many ways during this study. We are also thankful to the tribal peoples of Belpahari block for supporting this work.

References

1. Abbasi SA (2002) Water quality indices, state of the art report, National Institute of Hydrology, scientific contribution no. INCOH/SAR-25/2002, Roorkee: INCOH. pp 73
2. Adeola Fashae O, Abiola Ayorinde H, Oludapo OA et al (2019) Landuse and surface water quality in an emerging urban city. Appl Wat Sci 9(2):25
3. APHA (American Public Health Association). 2017. Standard methods for the examination of water and wastewater (23rd edn). American Public Health Association, Washington, DC
4. Brown RM, McCleiland NJ, Deininger RA, O'Connor MF (1972) A water quality index-crossing the psychological barrier. In: Jenkis SH (ed) Proceedings of international conferences on water pollution Research, Jerusalem, vol 6, pp 787–797
5. Gupta N, Pandey P, Hussain J (2017) Effect of physicochemical and biological parameters on the quality of river water of Narmada, Madhya Pradesh, India. Wat Sci 31(1):11–23
6. Isiuku GO, Enyoh CE (2020) Pollution and health risks assessment of nitrate and phosphate concentrations in water bodies in South Eastern, Nigeria. Environ Adv 2:100018
7. Kavka G, Poetsch E (2002) Microbiology. In: Literáthy P, Koller Kreimel V, Liska I (eds) Technical report of the international commission for the protection of the Danube river. Eigenverlag ICPDR, Vienna, Austria, pp 138–150
8. Kumara A, Sharma MP, Rai SP (2017) A novel approach for river health assessment of Chambalusing fuzzy modelling, India. Desalin Wat Treat 58:72–79. https://doi.org/10.5004/dwt.2017.0144
9. Mahata A, Singha C (2020) The status of microbiological quality of water samples at Bankura District, West Bengal, at publish the entitled – "Water resources: current and future challenges and research directions" Kolkata, India, pp 24–33
10. Singha C, Swain KC (2022) Using earth observations and GLDAS model to monitor water budgets for river basin management. In: Rao CM, Patra KC, Jhajharia D, Kumari S (eds) Advanced modelling and innovations in water resources engineering. Lecture notes in civil engineering, vol 176. Springer, Singapore. https://doi.org/10.1007/978-981-16-4629-4_34

Effects of Anthropogenic Stress and Water Security in Himalayan Urban River Watershed

Avinash Kumar, Ketan Kumar Nandi, and Subashisa Dutta

Abstract This study investigates the impact of changing land use and land cover patterns on the surface water deficit in the Rispana River Watershed in Dehradun, India, from 1991 to 2020. Using Landsat TM, ETM+, and OLI images in the GEE platform, the authors assess changes in vegetation, land cover, and land use, as well as climatic variables such as precipitation, evapotranspiration, and temperature. Find that the rapid expansion of urban/built-up areas, from 20% in 2005 to 64% in 2020, is one of the primary reasons for the decline in surface water area. Over the past 30 years, the maximum and average variations of surface water areas have shown a declining trend. In addition, the study find that LST has risen by 2.74 °C during the study period, and meteorological parameters have changed with the declining surface water area. Field surveys conducted in the pre- and post-monsoon periods confirm these findings. The study suggest that a proper management policy for watershed restoration and rejuvenation initiatives should be designed and implemented to mitigate the negative impacts of urbanization and overexploitation of natural resources. The findings of this study are relevant not only for the Rispana River Watershed but also for other regions facing similar challenges. The study highlights the need for sustainable land use practices and ecosystem management strategies that balance economic development with environmental conservation. The integration of geospatial data with hydrological, meteorological, and environmental variables at a regional scale can help policymakers and stakeholders make informed decisions for the sustainable management of river watersheds in the face of rapid urbanization and climate change.

Keywords Cloud computing · LST · LULC · Anthropogenic stress

A. Kumar (✉) · K. K. Nandi · S. Dutta
Indian Institute of Technology, Guwahati-781039, India
e-mail: avi32@rnd.iitg.ac.in

S. Dutta and V. Chembolu (eds.), *Recent Development in River Corridor Management*,
Lecture Notes in Civil Engineering 376, https://doi.org/10.1007/978-981-99-4423-1_14

1 Introduction

Water resources are critical in promoting sustainable development because they support human communities, ecosystem functions, and economic growth. Surface water is an important indicator of water resource availability. It is an important land cover type in many ways, including climate regulation, biogeochemical cycling, and surface energy balance. Many countries, particularly developing countries, have experienced rapid urbanization in recent decades. Human-caused surface water changes significantly impact surface temperature, soil moisture, biological diversity, ecosystem functioning, and even human well-being.

Surface water remote sensing studies began in the years following 1970s. The methods used in this study mainly include the single-band threshold method [1], the water index method [22], the application of machine learning algorithms [29], etc. The near-infrared and mid-infrared bands are typically used in the single-band threshold approach, whose water properties are visible while other ground objects are not noticeable [28]. The Modified Normalized Difference Water Index (mNDWI) and the Normalized Difference Water Index (NDWI) are two types of water indexes that are commonly used in water and non-water body feature detection [27]. The fundamental idea is to emphasize water body features while decreasing non-water body features using the band ratio calculation approach [12], to determine surface water coverage. Several passive and active remote sensors with visible and microwave bands, such as the Moderate Resolution Imaging Spectrometer (MODIS), Landsat Thematic Mapper (TM), and Synthetic Aperture Radar (SAR) have been used to estimate inundation areas and delineate water boundaries. The acquisition and storage of data have historically posed significant barriers to the effective use of these images, especially for large-scale and long-term applications [10, 9]. Utilizing later on, large amounts of remote sensing imageries have been stored and processed using the open cloud computing platform Google Earth Engine (GEE). The GEE provides the power of specialized cloud storage and processing hardware, as well as a copy of remote sensing imagery and a graphical user interface [26]. It has been applied in the extensive mapping of vegetation cover [14], population and settlement monitoring [26], and identification of urban areas [8]. Landsat satellite data allow for high-spatial-resolution LST estimates, which are especially useful for local and small-scale research. There have been several LST methods described for the Landsat series [18, 24, 25]. Even though most algorithms are simple to use, some do require users to provide calibration coefficients and input data, which can sometimes be challenging to locate. Some datasets are accessible to online users, for example [13], meanwhile, in Google Earth Engine, they frequently need to be able to manage enormous amounts of data most algorithms are straightforward to apply.

The main goals of this research are to suggest a faster way of estimating annual surface water levels by using a well-established surface water index, and then to use this method to analyze how surface water has changed between 1991 and 2020. Additionally, the study will examine the reasons for any changes in surface water that are

caused by human activities, such as land use/land cover changes, temperature fluctuations, rainfall patterns, and evaporation rates. By using remote sensing and cloud computing, this methodology will provide a fresh perspective on studying surface water, and the outcomes will aid in understanding the distribution and dynamics of water resources. The results of this research will also help in developing effective strategies for water resource management and conservation.

2 Study Area

The once-perennial Rispana River in Dehradun has now become a small stream that is polluted with commercial and residential waste. Despite this, the buildings erected around the river and watershed highlight their functional significance. The area was once known for producing type-3 basmati, litchi cultivation, and was home to over 315 bird species, deer, panthers, and other creatures. The river originates as a small spring on the Lal Tibba peaks of the Mussorie Hills and flows through Dehradun City, located at roughly 2228 m above MSL. Additionally, the Bindal River also runs through Dehradun and converges with the Rispana River at Mothrowala to form the Suswa River. The Suswa River flows between Rishikesh and Haridwar and joins the Ganga near Satyanarayana as a tributary of the Song River. The Rispana watershed covers a total area of 58.78 km^2 and is located between 30° 29′ 15″ N and 78° 06′ 98″ E. Formerly a bustling transportation hub with active flour mills, the degradation of the Rispana River and its surrounding area is an unfortunate reminder of the importance of preserving natural resources and ecosystems (Fig. 1).

3 Data and Methods

3.1 Data Preparation

Surface water in the Rispana watershed is extracted using Landsat 4, 5, 7, and 8 from 1991 to 2020. We utilize atmospherically corrected SR images with a 20% cloud cover to minimize the impacts of the atmosphere and solar irradiation [4], Clouds, cloud shadows, and snow pixels are all removed by the data quality band. The Landsat imagery from 1991 to 2020 was chosen for analysis due to the lack of Landsat imagery since before 1990. Landsat 7-based verification has a spatial resolution of 30 m and similar producer accuracy, it has lower user accuracy [30]. Furthermore, imageries from Landsat 7 ETM + after 2003 contain scan line errors. As a result, Landsat 7 imagery is only used as a supplement when the annual data volume is insufficient. Finally, 1063 Landsat SR images with a cloud cover of 20% from 1991 to 2020 are screened using the GEE platform (https://earthengine.google.com/).

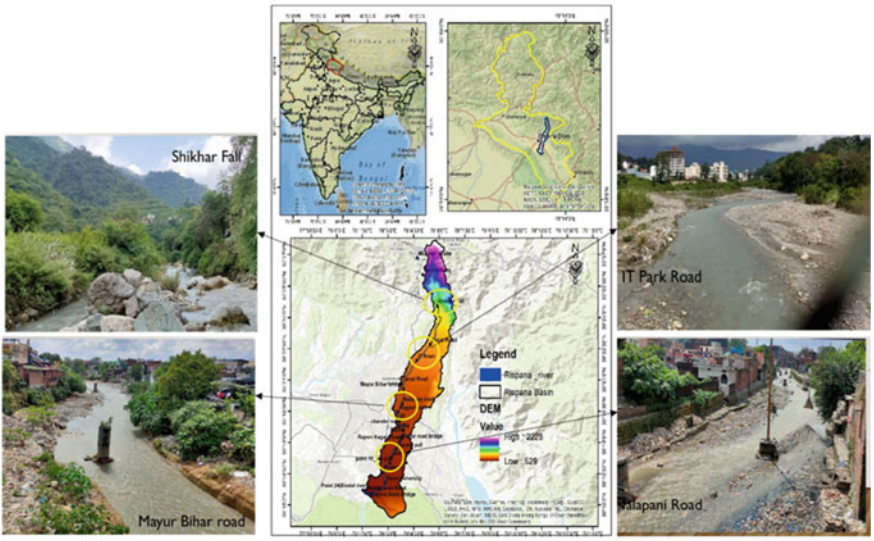

Fig. 1 The study area of Rispana Watershed (Dehradun)

3.2 Methodology

The least and maximal surface water for a certain period were retrieved in order to gather extensive information regarding surface water coverings. In this study, the minimal surface water is all seasonal surface water, while the maximum water is all permanent. As explained in the section below, the wettest and greenest pixel composite images for each time were used to compute the yearly minimal and maximal surface water (Fig. 2).

3.3 Water Body Extraction

Two widely used water body extraction indices such as Normalized Difference Water Index (NDWI), and Modification of Normalized Difference Water Index (MNDWI) were calculated for each image and added to the image collections, using Eqs. (1) and (2). NDWI developed by [17] and MNDWI developed by [27] were utilized to enhance the water-related features of the landscapes.

$$NDWI = \frac{\rho_{NIR} - \rho_{SWIR}}{\rho_{NIR} + \rho_{SWIR}} \tag{1}$$

$$MNDWI = \frac{\rho_{Green} - \rho_{SWIR}}{\rho_{Green} + \rho_{SWIR}} \tag{2}$$

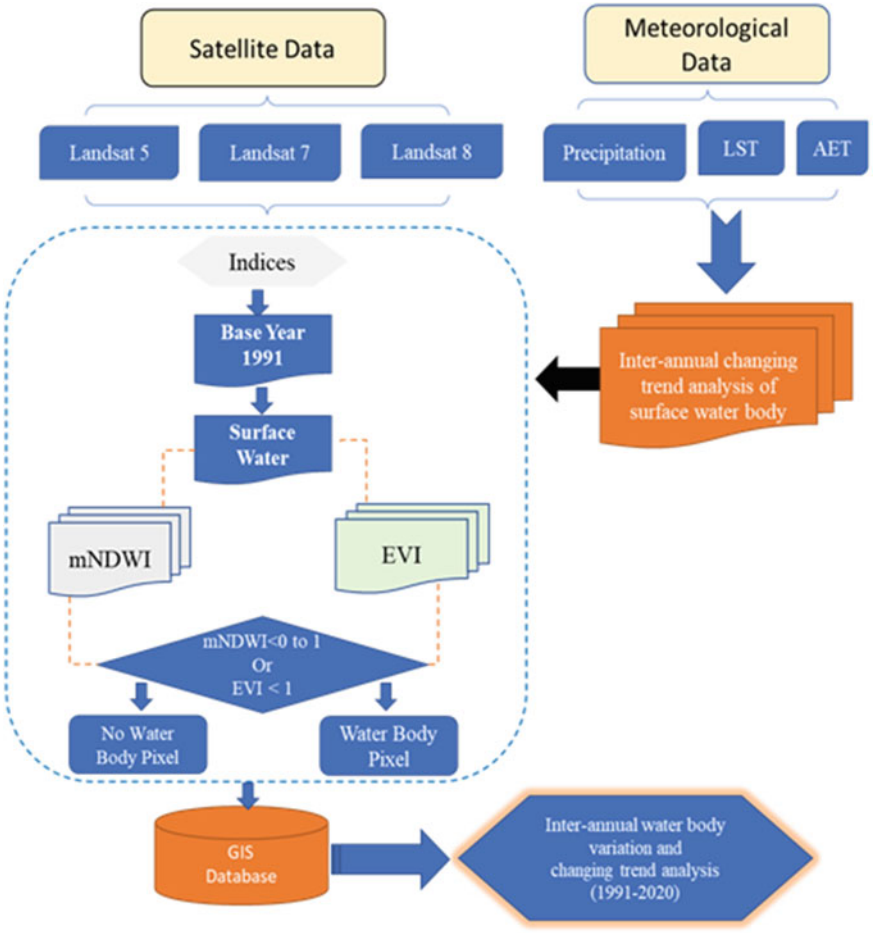

Fig. 2 Schematic flowchart performed to the study on Anthropogenic study and water security

where, ρ_{NIR}, respects the values of the near-infrared band, ρ_{GREEN} respects the values of the green band, and ρ_{SWIR} respects the values of the shortwave infrared band in the Landsat Images.

3.4 LU/LC Information Extraction

Regarding the characteristics of the remote sensing image, we categorized the LU/LC into five types Forest cover, Water body, Agricultural land, Built-up land, and Plantation. According to the high-resolution Google Earth images and field survey, we identified training samples to classify the LULC using the Random Forest classification techniques in the google earth engine.

3.5 Meteorological and Statistics Data

Surface water frequency dynamics can investigate how the Rispana Watershed is affected by meteorological circumstances, including climate and human activity (Dehradun). During three decadal series from 1991 to 2020, the land surface temperature [5] was studied and forecast using the Landsat dataset records on the Google Earth Engine (GEE) cloud computing platform.

4 Results

The share of the natural land cover such as agricultural land, plantations, forests, and water bodies decreased significantly from 85.6% to 25.4% between 1991 and 2020 (Fig. 3a). This is further evident in the deviation of the categorical share of various LULC classes in the Rispana watershed (Fig. 3b). Overall, the three-decade rapid urbanization period witnessed an increase in urban/built-up land to cover 64% of the total area, while agricultural land area cover decreased to a mere 3% followed by the 1% coverage by water bodies.

4.1 Robustness and Accuracy of the Assessment

The Kappa statistic was employed to assess the accuracy of the LULC classification. This was achieved by evaluating the agreement between classification results and reference data after removing the proportion of agreement that could be expected to occur by chance. Overall accuracy (OA) and Kappa (KA) statistics for LULC maps generated between 1991 and 2020 ranged from 83.7% and 0.85 in 1991 to 86.3% and 0.86 in 2005 and 84.3% and 0.84 in 2020 (Table 1). Therefore, the assessment is robust and accurate as per prevalent methods.

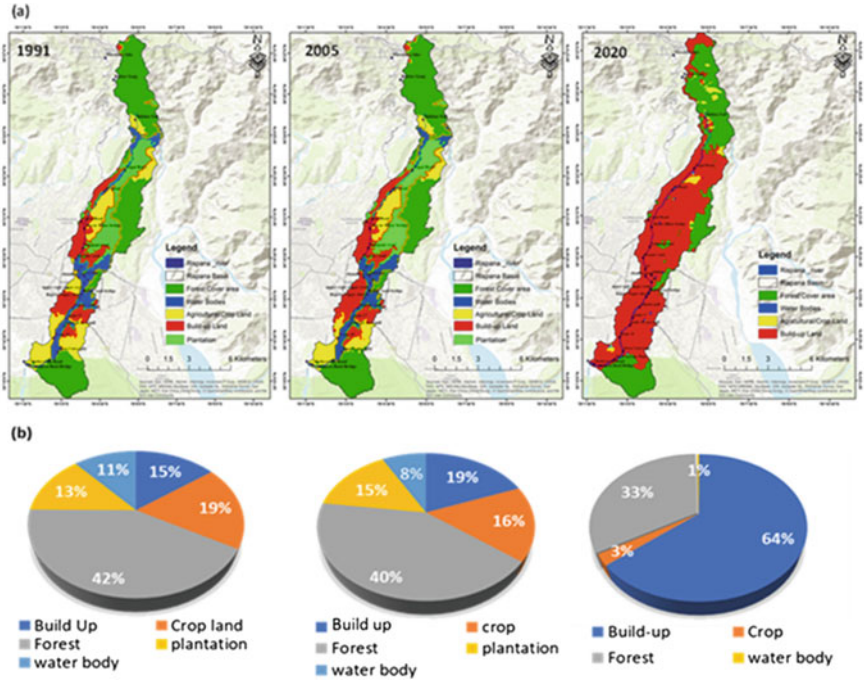

Fig. 3 **a** Land use Land cover Map and; **b** Area (%) distribution over the Rispana Watershed (Dehradun)

Table 1 The accuracy of classified LULC of Rispana Watershed (Dehradun)

Year	Region	Overall accuracy %	Kappa coefficient
1991	Rispana Watershed	83.7	0.84
2005	Rispana Watershed	86.3	0.85
2020	Rispana Watershed	84.3	0.83

4.2 Spatial and Temporal Distribution of Surface Water During the Study Period

Waterbodies are crucial for ecosystems to function sustainably and often regulate the migration, range, and mobility of species. However, a constant and significant decrease in the annual surface water availability (1991–2020) was observed owing to the transformation of permanent bodies of water to non-water bodies and changes in land use patterns (Fig. 4). Surface water frequency varied significantly between

individual pixels in the Rispana Watershed (Dehradun), and indicates that annual fluctuations in water frequency between 1991 and 2000 were appreciably different.

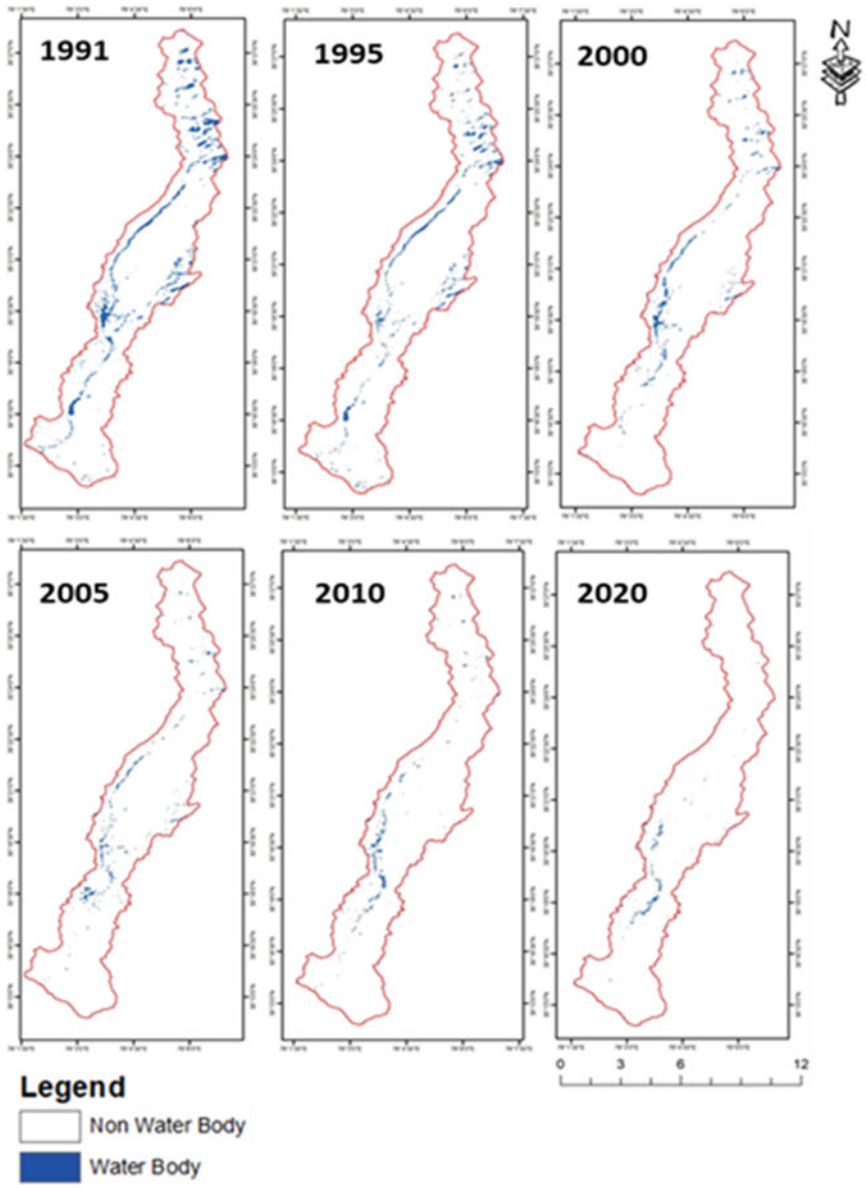

Fig. 4 Spatial distribution of the Surface water body in the Rispana Watershed (Dehradun)

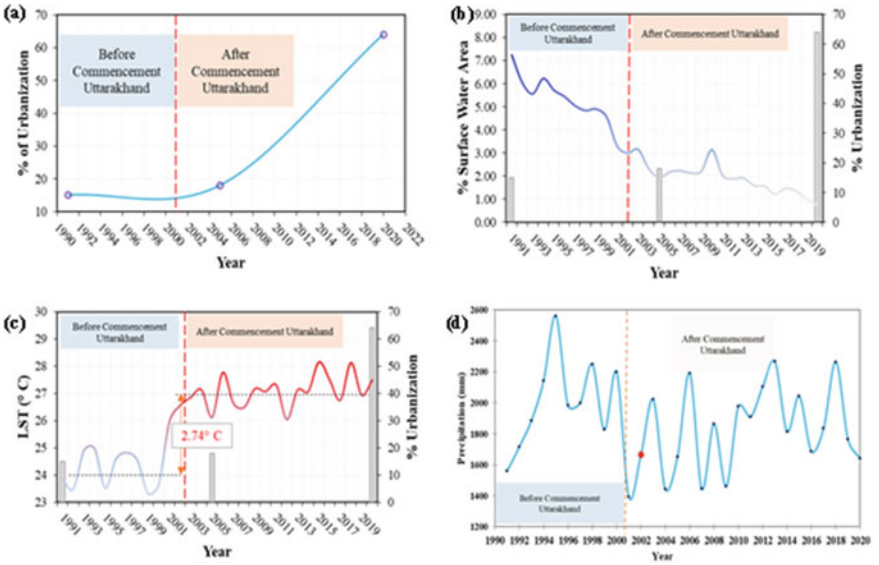

Fig. 5. **a** Changing trend of the urbanization in Rispana Watershed (Dehradun) from 1991 to 2020, **b** Annual surface water body area changes in the Rispana Watershed (Dehradun) from 1991 to 2020, **c** LST annual trend of Rispana Watershed (Dehradun), **d** Annually Precipitation trend of the Rispana Watershed (Dehradun).

4.3 Temporal and Change Analysis of Meteorological Data, Urbanization, and Surface Water Body

The rate of urbanization in the Rispana watershed (Dehradun) fluctuated between 10 to 20% until 2000 but sharply increased post-2005, reaching around 65% by 2020 (Fig. 5a). This rapid urbanization coincided with a significant decrease in surface water availability, which had previously remained relatively stable but began to exponentially decrease after 2005 (Fig. 5b). As a result of this urbanization, approximately 65% of the urban area competes for only 1% of surface water, creating water deficit. Moreover, the temperature has increased by 2.7 °C since urbanization began in 2005, with the current average being around 27 °C (Fig. 5c). The increase in built-up area in the Rispana watershed (Dehradun) has also led to a gradual change in precipitation trends (Fig. 5d), exacerbating the underdevelopment of the city's urban areas.

5 Discussion

The rapid expansion of urban/built-up land has been a major trend in many regions across the world, and its consequences for the environment and human well-being have been a subject of concern among researchers and policymakers alike. The

conversion of natural land cover to urban/built-up land has been identified as a significant driver of habitat loss and biodiversity decline [7, 23]. Further, studies have shown that urbanization can lead to the fragmentation and isolation of natural habitats, which can disrupt ecological processes and reduce the viability of species populations [6]. The loss of natural land cover can also lead to a decrease in ecosystem services such as water purification, carbon sequestration, and climate regulation [3, 19].

Moreover, the expansion of urban areas can exacerbate the risk of natural disasters such as floods, landslides, and droughts, by altering water flows and reducing the capacity of ecosystems to absorb and mitigate the impacts of extreme weather events [11]. The decline in the coverage of water bodies due to urbanization can also have significant implications for water availability and quality, which can affect the ecological and social well-being of the region [16].

In addition to the ecological consequences, the expansion of urban areas can also have social and economic impacts, such as increased energy consumption, air pollution, and social inequality. The urban heat island effect, which occurs when urban areas absorb and re-emit more heat than surrounding rural areas, can have implications for human health and comfort, and increase the demand for energy-intensive cooling systems [21].

The Rispana watershed in Dehradun, India, is an example of a region where urbanization has had significant impacts on the environment and the well-being of local communities. The decline in surface water availability in the region, as discussed in the previous section, is a concerning issue that requires urgent attention from policymakers and stakeholders. Studies have shown that unsustainable land use practices and inadequate water management strategies have contributed to the degradation of the watershed's ecosystems [15].

To address these challenges, it is crucial to develop effective conservation and management strategies that balance the needs of urbanization and environmental protection. The integration of ecosystem-based approaches in urban planning and development can help to mitigate the impacts of urbanization on the environment and improve the well-being of local communities [20]. Additionally, the adoption of sustainable land use practices, such as green infrastructure, can help to enhance the resilience of ecosystems to environmental stressors and provide multiple benefits, such as improved air and water quality, climate regulation, and biodiversity conservation [2].

Furthermore, the rapid expansion of urban/built-up land has significant implications for the environment, human well-being, and social and economic development. The Rispana watershed is an example of a region where urbanization has led to a severe water deficit and other environmental challenges. Addressing these challenges requires the adoption of sustainable land use practices and effective water management strategies that balance the needs of urbanization and environmental protection. The integration of ecosystem-based approaches in urban planning and development can provide multiple benefits for the environment and local communities and contribute to the achievement of sustainable development goals (Fig. 6).

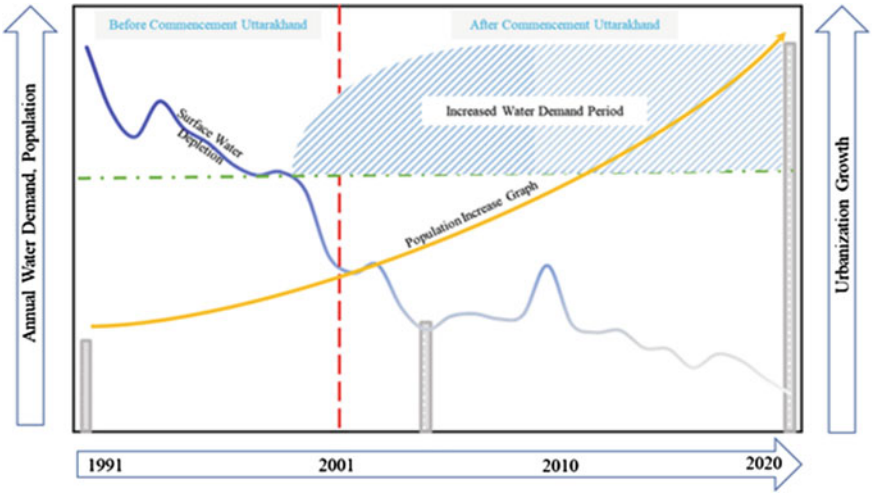

Fig. 6 Conceptual summarization of the current scenario happening in the Rispana watershed (Dehradun)

6 Conclusions

In conclusion, the loss of natural land cover and its associated impacts highlights the urgency for sustainable land use practices. Policymakers should prioritize the conservation of natural land cover and encourage the adoption of sustainable land use practices. Innovative solutions are also needed to increase food production and improve water management in regions with limited water resources. The implementation of these measures requires the active involvement of all stakeholders, including governments, local communities, and the private sector, to ensure the long-term sustainability of land use practices. The success of such efforts will depend on the commitment and collaboration of all stakeholders toward achieving a balance between economic development and environmental protection. Overall, sustainable land use practices are crucial for the preservation of biodiversity, essential ecosystem services, and the well-being of communities and the planet.

References

1. Alesheikh AA, Ghorbanali A, & Nouri N (2007) Coastline change detection using remote sensing. Int J Environ Sci & Technol 4:61–66. https://link.springer.com/article/10.1007/BF03325962 (2007). https://doi.org/10.1007/BF03325962
2. Benedict MA, McMahon ET (2012) Green infrastructure: linking landscapes and communities. Island Press
3. Costanza R, De Groot R, Sutton P, Van der Ploeg S, Kubiszewski I, Turner RK (2014) Changes in the global value of ecosystem services. Glob Environ Chang 26:152–158

4. Deng Y, Jiang W, Tang Z, Ling Z, Wu Z (2019) Long-term changes of open-surface water bodies in the Yangtze River Basin based on the google earth engine cloud platform. Remote Sens 11:2213. https://doi.org/10.3390/rs11192213
5. Ermida SL, Soares P, Mantas V, Göttsche FM, Trigo IF (2020) Google earth engine open-source code for land surface temperature estimation from the landsat series. Remote Sensing 12(9):1471. https://doi.org/10.3390/rs12091471
6. Fahrig L (2003) Effects of habitat fragmentation on biodiversity. Annu Rev Ecol Evol Syst 34(1):487–515
7. Foley JA, DeFries R, Asner GP, Barford C, Bonan G, Carpenter SR, Snyder PK (2005) Global consequences of land use. Science 309(5734):570–574. DOI: https://doi.org/10.1126/science.1111772
8. Goldblatt R, You W, Hanson G, Khandelwal AK (2016) Detecting the boundaries of urban areas in india: a dataset for pixel-based image classification in google earth engine. Remote Sens 8(8):634
9. Gong P, Liu H, Zhang M, Li C, Wang J, Huang H, Clinton N, Ji L, Li W, Bai Y, Chen B (2019) Stable classification with limited sample: transferring a 30-m resolution sample set collected in 2015 to mapping 10-m resolution global land cover in 2017. Sci Bull 64:370–373. https://doi.org/10.1016/j.scib.2019.03.002
10. Gorelick N, Hancher M, Dixon M, Ilyushchenko S, Thau D, Moore R (2017) Google Earth Engine: planetary-scale geospatial analysis for everyone. Remote Sens Environ 202:18–27. https://doi.org/10.1016/j.rse.2017.06.031
11. Grimm NB, Faeth SH, Golubiewski NE, Redman CL, Wu J, Bai X, Briggs JM (2008) Global change and the ecology of cities. Science 319(5864):756–760
12. Guo Q, Pu R, Li J, Cheng J (2017) A weighted normalized difference water index for water extraction using Landsat imagery. Int J Remote Sens 38:5430–5445. https://doi.org/10.1080/01431161.2017.1341667
13. Hulley G, Shivers S, Wetherley E, Cudd R (2019) New ECOSTRESS and MODIS land surface temperature data reveal fine-scale heat vulnerability in cities: A case study for Los Angeles County, California. Remote Sensing 11(18):2136. https://doi.org/10.3390/rs11182136
14. Johansen K, Phinn S, Taylor M (2015) Mapping woody vegetation clearing in Queensland, Australia from Landsat imagery using the Google Earth Engine. Remote Sens App Soc Environ 1:36–49
15. Joshi M, Levy O, Weld DS, Zettlemoyer L (2019) BERT for coreference resolution: baselines and analysis. ArXiv preprint arXiv:1908.09091
16. Kumar S, Singh A (2015) Biopesticides: present status and the future prospects. J Fertil Pestic 6(2):100–129
17. McFeeters SK (1996) The use of the Normalized Difference Water Index (NDWI) in the delineation of open water features. Int J Remote Sens 17(7):1425–1432. https://doi.org/10.1080/01431169608948714
18. Meng X, Cheng J, Zhao S, Liu S, Yao Y (2019) Estimating land surface temperature from Landsat-8 data using the NOAA JPSS enterprise algorithm. Remote Sens 11(2):155
19. Millennium ecosystem assessment, M. E. A. (2005) Ecosystems and human well-being (Vol. 5, p. 563). Washington, DC: Island press
20. Nagendra H, Bai X, Brondizio ES, Lwasa S (2018) The urban south and the predicament of global sustainability. Nat Sustain 1(7):341–349
21. Oke TR (1982) The energetic basis of the urban heat island. Q J R Meteorol Soc 108(455):1–24
22. Rokni K, Ahmad A, Selamat A, Hazini S (2014) Water feature extraction and change detection using multitemporal Landsat imagery. Remote Sens 6:4173–4189. https://doi.org/10.3390/rs6054173
23. Seto KC, Güneralp B, Hutyra LR (2012) Global forecasts of urban expansion to 2030 and direct impacts on biodiversity and carbon pools. Proc Natl Acad Sci 109(40):16083–16088
24. Sobrino JA, Raissouni, N, Li ZL (2001) A comparative study of land surface emissivity retrieval from NOAA data. Remote Sens Environ 75(2):256–266. https://www.sciencedirect.com/science/article/pii/S0034425700001711#:~:text=https%3A//doi.org/10.1016/S0034%2D4257(00)00171%2D1

25. Stroppiana D, Antoninetti M, Brivio PA (2014) Seasonality of MODIS LST over Southern Italy and correlation with land cover, topography, and solar radiation. Eur J Remote Sens 47:133–152. https://doi.org/10.5721/EuJRS20144709
26. Trianni G, Angiuli E, Lisini G, Gamba P (2014) Human settlements from LandsatLandsat data using google earth engine. In Proceedings of the 2014 IEEE International Geoscience and Remote Sensing Symposium (IGARSS), Quebec City, QC, Canada, 13–18 July 2014; pp. 1473–1476. https://doi.org/10.1109/IGARSS.2014.6946715
27. Xu H (2005) A study on information extraction of water bodies with the modified normalized difference water index (MNDWI). J Remote Sens-Beijing 9(5):595
28. Yang H, Wang Z, Zhao H, Guo Y (2011) Water body extraction methods study based on RS and GIS. Procedia Environ Sci 10:2619–2624. https://doi.org/10.1016/j.proenv.2011.09.407
29. Zamil KS, Mim & M. A. (2018) Gis-based analysis of changing surface water in Rajshahi city corporation area using support vector machine (svm), decision tree & random forest technique. Mach Learn Res 3(2):11
30. Zhou Y, Dong J, Xiao X, Xiao T, Yang Z, Zhao G, ... , Qin Y (2017) Open surface water mapping algorithms: a comparison of water-related spectral indices and sensors. Water 9(4):256

Climate Change and Flood Modelling

Future Climate Change Impacts on the Stream Flow—A River Basin Scale Assessment

T. I. Eldho and Rakesh Kumar Sinha

Abstract The effect of climate change (CC) variation results in considerable changes in hydrology leading to large-scale socio-economic impacts. Further studies demonstrate that long-term climate change in the river basins is giving rise to frequent hydro-meteorological extremes such as floods and droughts. In this study, the future CC impacts on a river basin scale are assessed and effects on stream flow are estimated using a hydrological model SWAT (Soil and Water Assessment Tool). The methodology adopted is demonstrated using a case study of the Muvattupuzha river basin (MRB) in Kerala, South India. The CC impacts for the future up to 2100 are obtained from the ensembled values of 5 GCMs including CCCMA CanESM2; CNRM CM5; MPI ESM MR; MPI ESM LR and BNU ESM. The hydrologic model was calibrated and validated at two river gauge stations using monthly river streamflow data. The results indicated that mean annual surface runoff in the near, mid, and far future would be decreasing under both RCP 4.5 and 8.5 while RCP 8.5 showing worse conditions than RCP 4.5, in the future. Furthermore, the projected results indicate that the surface runoff would be higher in both RCP scenarios during winter and summer, while the monsoon period largely demonstrates a reverse trend, that can lead the water scarcity in the river basin. The results of this study can be helpful to policymakers for appropriate water resource management, considering climate change scenarios for moderate and worse conditions in the future period.

Keywords Climate change · River basin · SWAT model · Surface runoff · Hydrology

T. I. Eldho (✉) · R. K. Sinha
Department of Civil Engineering, Indian Institute of Technology Bombay, Powai, Mumbai 400076, India
e-mail: eldho@civil.iitb.ac.in

S. Dutta and V. Chembolu (eds.), *Recent Development in River Corridor Management*, Lecture Notes in Civil Engineering 376, https://doi.org/10.1007/978-981-99-4423-1_15

1 Introduction

In the last few decades, throughout the world, the adverse impacts of climate change (CC) on the water resources are widely reported. As per the IPCC report [4], in the future this impact is expected to be more severe. However, the CC impacts can considerably vary from one region to another. Due to CC and its impacts, many places may face scarcity of freshwater, flooding or may subject to water quality issues. Thus, especially in tropical regions, sustainable use of water resources becomes the core of the local and national strategies and politics. Due to increase in population and various activities, the demand for water has increased many times, causing an imbalance in the supply and demand of water [16]. In maintaining the global water balance, the tropical regions play a key role. The humid tropics cover almost 25% of Earth's land surface, with tropical forests covering approximately 50% of this area [11]. The land use changes in this region drastically changes the annual mean streamflow [12, 14, 15].

In India, there is a huge variation of climatic conditions, ranging from tropical in the south to temperate and alpine in the Himalayan north. In most of India, the monsoon is the major source of precipitation (i.e., 80% of precipitation is from monsoon). In most parts of India, the climate variation is reflected by the rising temperature leading to high evapotranspiration, and the intensities and nature of precipitation are considered to have a significant impact on various hydrological processes. Many of the available studies show that the effect of climate variation on hydrological regimes is significant, and such effects will likely continue to increase in the future. In the literature, number of studies are available that tried to investigate river basin scale CC impacts [5, 14]. As reported by Kim et al. [6], the CC impacts under different RCP (Representative Concentration Pathways) emission scenarios on surface runoff in the Hoyea River basin, Korea, and is more than the effects of LULC change. Givati et al. [3] reported the impacts of CC on runoff for the Upper Jordan basin. According to them, due to CC, there can be a significant decrease of runoff approximately by 11% and 16% for the near and far future, respectively, under RCP 4.5 and 16% and 44%, respectively, under RCP 8.5. Thus, there is a need to investigate the hydrological response related to CC on a river basin scale. In this study, a methodological framework is presented for the river basin scale CC impact assessment. The changes in streamflow were analyzed using the SWAT watershed simulation model. The Muvattupuzha river basin (MRB) located in central Kerala, South India is taken as a case study. The main objectives of this paper are the assessment of climate change impacts at the sub-basins scale for near (2016–2040), mid (2041–2070), and far (2071–2100) future for RCP 4.5 and RCP 8.5 emission scenarios.

2 Study Area

The Muvattupuzha River is one of the major perennial rivers in Central Kerala (Fig. 1). It has a length of about 121 km and has a catchment area of 1554 km^2 (Table 1). The river basin lies between north latitudes 9° 40′–10° 10′ and east longitudes 76° 30′–77°. Due to data availability issues, the present study is confined up to Vettikkattumukku in the downstream, covering the river course of almost 116 km length. The remaining length of river is part of other river confluences and backwaters. The region receives an annual mean rainfall of about 3500 mm. The area enjoys a tropical humid climate. Figure 1 shows the location of MRB. Figure 1b shows the DEM (Digital Elevation Model) of the river with basin, 1c shows the sub-basins and 1d shows the soil map [2].

In MRB, in most months of the year, rainfall is significant and has short dry seasons. In this humid tropical basin, the annual temperature typically varies from 22 °C to 35 °C and is rarely below 20 °C or above 37 °C. The average wind speed over the basin is more than 9.2 km/hr. It also experiences a seasonal variation in perceived relative humidity. In the river basin, the surface soil pattern is more than 70% of lateritic soil and the remaining riverine alluvium and brown hydromorphic soil (Fig. 1d).

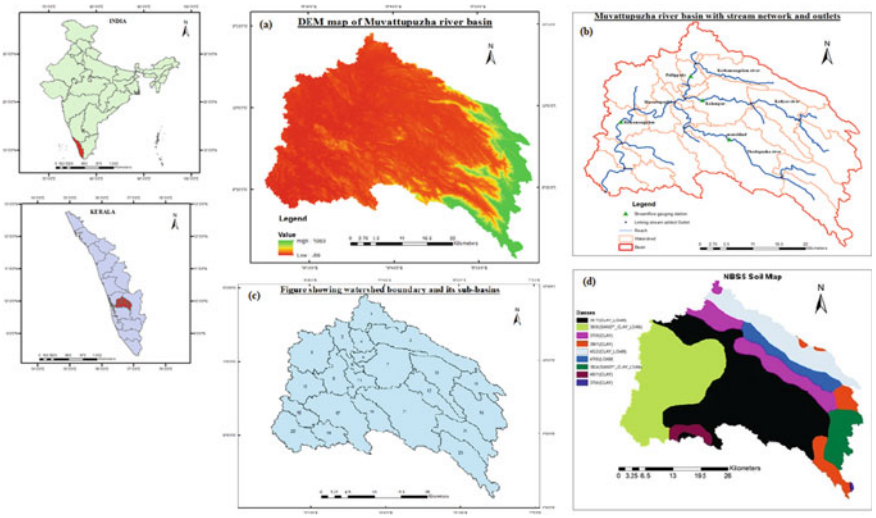

Fig. 1 Details of Muvattupuzha river basin—Location map, **a** digital elevation model, **b** stream network, **c** sub-basins, and **d** soil of the study area

Table 1 Input data used for Muvattupuzha River Basin

Input data	Resolution	Source
Digital Elevation Model (DEM) Cartosat	30 m	NRSC: National Remote Sensing Centre (http://www.nrsc.gov.in/)
LULC map	30 m	Landsat imageries (http://earthexplorer.usgs.gov/)
Basin Soil data	Toposheet	National Bureau of Soil Survey (NBSS)
Meteorological data (precipitation and temperature (min. and max.))	0.25° (daily)	Indian Meteorological Department (IMD)
Meteorological data (solar radiation, relative humidity, and wind velocity)	0.25° (daily)	Climate Forecast System Reanalysis (CFSR)
Hydrological data (streamflow)	Daily	Central Water Commission (http://www.india-wris.nrsc.gov.in/)

3 Materials and Methodology

3.1 Data Description

The DEM (digital elevation model) was generated using Cartosat, with 30 m resolution. The required soil data was collected from Government agencies (NBSS, Nagpur). The land use land cover (LULC) was obtained using Landsat data (30 m resolution). The meteorological data (IMD, 0.25°) such as rainfall and temperature were used as input data for the simulation of the hydrologic model. The Climate Forecast System Reanalysis data of relative humidity, solar radiation, and wind velocity were collected and interpolated at 0.25° as the same grid points to precipitation data. Gauge-discharge data at the Ramamangalam and Kalambur measuring stations were taken from IWRIS (Indian-Water Resources Information System) open data source for the time 1986–2015 (http://www.india-wris.nrsc.gov.in). The soil data used in the present study were acquired from the National Bureau of Soil Survey and Land Use Planning (NBSS & LUP), Nagpur. The DEM used for delineating watershed was Cartosat DEM of 30 m (1 arc-second) resolution. Table 1 gives input data details, resolutions, and sources.

3.2 Future GCM Database

For the future data, the statistical downscaled climate variables, namely precipitation, minimum and maximum temperature, relative humidity, and wind were collected from other INCCC projects for five Coupled Model Intercomparison Project 5 (CMIP5) using GCM (general circulation model) simulations in daily time steps (Table 2) [2]. As a part of the project funded by the Indian National Committee on

Table 2 Input data used for the future period in the present study

Model	Institution	Spatial resolution	Scenarios
CanESM2	Canadian Centre for Climate Modeling and Analysis	2.8° × 2.8°	RCP 4.5 and 8.5
BNU ESM	Beijing Climate Center, China Meteorological Administration	2.8° × 2.8°	RCP 4.5 and 8.5
CNRM CM5	Centre National de Recherches Meteorologiques/ Centre Europeen de Recherche et Formation Avancees en Calcul Scientifique	1.4° × 1.4°	RCP 4.5 and 8.5
MPI ESM LR	Max Planck Institute for Meteorology (MPI-M)	1.8° × 1.8°	RCP 4.5 and 8.5
MPI ESM MR	Max-Planck-Inst. for Meteorology	1.87 × 1.87	RCP 4.5 and 8.5

Climate Change (INCCC), Ministry of water resources, Government of India, statistically downscaled climate variables were made available for India (http://www.regclimindia.in/). For the CC impact assessment using RCP 4.5 and RCP 8.5 emissions scenarios, all GCMs contained essential variables corresponding to historic and projected climate data. The output from the five GCMs including CCCMA CanESM2; MPI ESM LR; CNRM CM5; MPI ESM MR; and BNU ESM, respectively, are the source of predictor data used for precipitation downscaling for future RCP scenarios. A brief description of the GCM datasets, resolution, and scenarios is given in Table 2.

3.3 GCM Climate Data Analysis

After the bias correction, the statistics of the observed and GCM-simulated climate variables of rainfall, maximum (T_{max}), and minimum temperature (T_{min}) for the MRB are illustrated for ensemble data in a Taylor diagram as shown in Fig. 2. This indicates all variables correlation are in an acceptable range. Hence, they are used for further hydrological parameter analysis, for the river basin.

3.4 Hydrologic Modeling Using SWAT Model

The hydrologic model SWAT was developed by the United States Department of Agriculture–Agricultural Research Service (USDA–ARS) [1]. The SWAT model can be used to predict various hydrological variables and assess the impact of land use land cover changes, sediment, and agricultural chemical yields. It is a semi-distributed continuous-time varying model that can be used for the prediction of

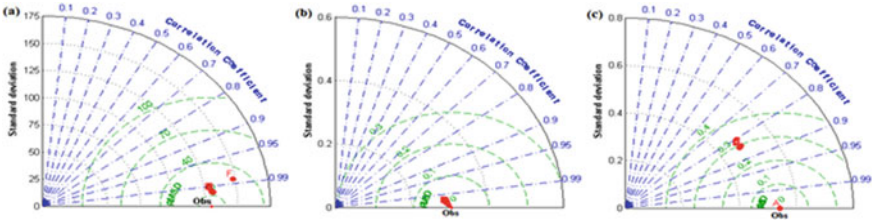

Fig. 2 Taylor diagram for study area: **a** rainfall (mm/month), **b** T_{max} (°C), and **c** T_{min} (°C) for the MRB

various hydrological variables and water quality parameters at a watershed scale. We can use various time steps of daily, weekly, or monthly. In the SWAT model, the major components include weather conditions, hydrology, soil properties, plant growth, land management, nutrients, pesticides, bacteria, etc. In SWAT model, we divide the basin into sub-basins and then into units of unique soil/land use characteristics called hydrological response units (HRUs). In the modeling process, the HRUs are defined as homogeneous spatial units characterized by similar geomorphologic and hydrological properties. While modeling, a specific HRU land unit considered may contain a sandy loam, walnut orchards, and a slope of up to 5%. For the problem considered, user can specify land cover, soil area, and slope thresholds. A complete description of SWAT model can be found in [9]. SWAT model provides several water management options to improve its ability to predict streamflow such as irrigation, water transfer, etc. The model provides five sources of water for irrigation including reservoirs, shallow and deep aquifers, and sources from outside the watershed. Further details of SWAT hydrological model can be also found in Neitsch et al. [10].

3.5 Methodological Framework

For the hydrological impact assessment of CC, a general methodological framework was developed in this study for river basin scale analysis. The flow chart of the methodological framework developed is given in Fig. 3.

Following are the step-by-step procedures adopted in this study.

- Extraction and database development of input data such as DEM, LULC, Soil, and climatic parameters.
- Data preprocessing such as making inputs data for SWAT model and Landsat image classification for historical LULC.
- Obtain the future climate data after bias correction for the selected 5 GCMS [2] (the GCMS used are BNU, CNRM, CAN-ESM, MPI-LR, and MPI-MR) http://www.regclimindia.in/.
- Develop the SWAT model for the considered study area.

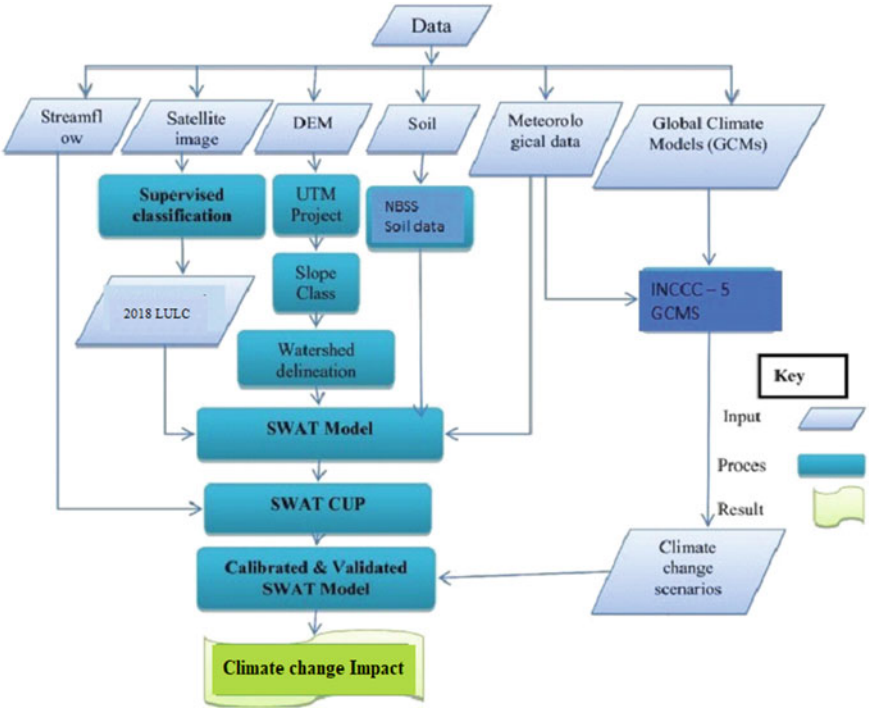

Fig. 3 SWAT Modeling procedure for climate change impact assessment on River Basin Scale

- SWAT model calibration and validation.
- Assessing the impact of historical and future CC and its effects on hydrological components and streamflow.

Based on the analysis, derive the conclusions and recommendations.

4 Results and Discussion

4.1 LULC Analysis

For the Muvattupuzha river basin, the classified LULC (land use land cover) of 2018 was utilized to analyze condition of the basin. Landsat image was procured for 2018 to determine the land cover variation. Before classification and topographic correction, the selected Landsat image was corrected for atmospheric interference by using the dark-object subtraction method. To avoid the cloud related issues, the image used in this study was obtained in the post-monsoon season (October). For image classification, the supervised maximum likelihood technique was used [7].

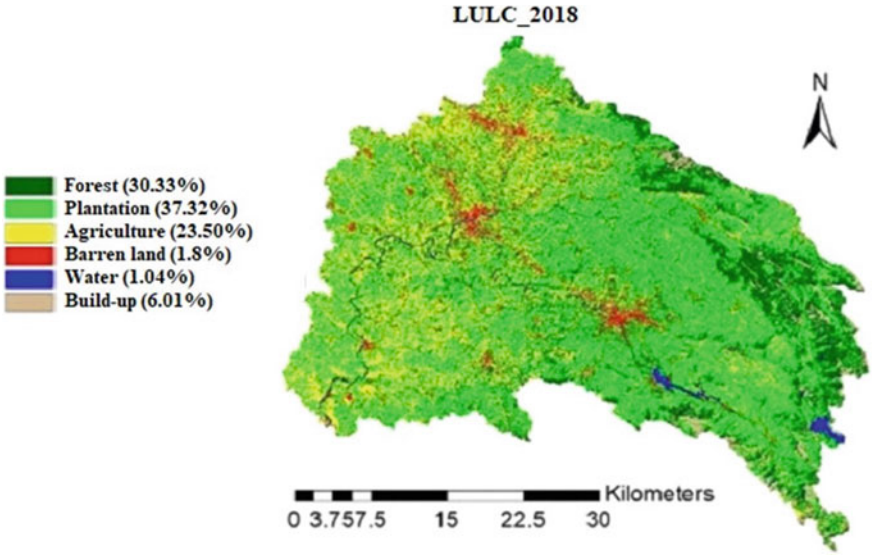

Fig. 4 Land use land cover map of Muvattupuzha basin–2018

Figure 4 shows the result of maximum likelihood classification of Landsat image for the year 2018. The area of each class was calculated considering the pixel count and total area (study area). The types of land use present in the study area are identified as 6 classes of: water bodies (WATR), agricultural land (AGRL), forest land (FRST), barren land (BARR), urban land (URBN), and plantations (RUBR). As per the LULC classification, plantation is the most prominent land use with 37.32%, followed by forest with 30.33%, agriculture with 23.5%, built-up with 6.01%, water with 1.04%, and barren land with 1.8%.

4.2 Calibration and Validation of the SWAT Model

The hydrological model SWAT is calibrated for streamflow at two gauge stations Kalambur (Sub-basin 7) and Ramamangalam (Sub-basin 15) for a period of 10 years starting from 1991 to 2000. The model was run monthly, and 5 years were given as warm-up period to the model before the simulation output starts. We have taken 1000 simulations for the identification of sensitive parameters for discharge in SWAT-CUP for calibration using SUFI2 by LH procedure, in which observed and computed outputs were compared at the considered river gauging station. The model was calibrated by adjusting ten sensitive parameters for streamflow which includes five related to surface runoff (CN2, SOL_AWC, EPCO, ESCO, SUR_LAG) and other five related to base flow (ALPHA_BF, GW_DELAY, GW_REVAP, RCHRG_DP, GWQMN) as given in Table 3.

Table 3 SWAT model parameters and their fitted values used in calibration and sensitivity analysis

No	Parameters	Description	Process range		Fitted value
1	CN2	SCS CN II Value–initial	Runoff	±0.1	0.06 (r)
2	SOL_AWC	Available water capacity of the soil layer	Soil	0–1	0.42 (v)
3	SURLAG	Surface runoff lag time	Runoff	0.1–10	0.18 (v)
4	ESCO	Compensation factors for soil evaporation	Evaporation	0–0.8	0.23 (v)
5	EPCO	Compensation factors–Plant uptake	Soil	0.1–0.7	0.37 (v)
6	ALPHA_BF	Base flow alpha factor (day)	Groundwater	0–1	0.52 (v)
7	GW_DELAY	Groundwater delay (days)	Groundwater	10–300	35.88 (v)
8	GW_REVAP	Groundwater "revap" coefficient	Groundwater	0.02–0.2	0.07 (v)
9	GWQMN	Threshold depth of water in the shallow aquifer required for return flow to occur (mm)	Groundwater	0–300	2.9 (v)
10	RCHRG_DP	Deep aquifer percolation factor	Groundwater	0–1	0.82 (v)

Note Here (r) is the value existing that is multiplied; (v) is the value existing that is replaced by the given value

Figure 5 shows the output from SWAT-CUP after calibration, which clearly shows that simulated streamflow closely matches with the observed value for both stations with an R^2 and NSE value of 0.87 and 0.86 respectively for Kalambur station and an R^2 and NSE value of 0.89 and 0.85 respectively for Ramamangalam station (Table 4). According to Moriasi et al. [8], calibration results are in an acceptable range.

4.3 Impact of Climate Change on Streamflow at the Basin Scale

In this study, to investigate the impacts of CC on streamflow, simulations were carried out by keeping LULC fixed for 2018 and altering the climate continuously for the baseline period (1986–2015) and future (2016–2100). For future periods, the outputs are aggregated into three-time slices: T1 (2016–2040), T2 (2041–2070), and T3 (2071–2100) for both emission scenarios (RCP 4.5 and 8.5). To quantify the changes in streamflow, the SWAT model was simulated using 5 downscaled, bias-corrected

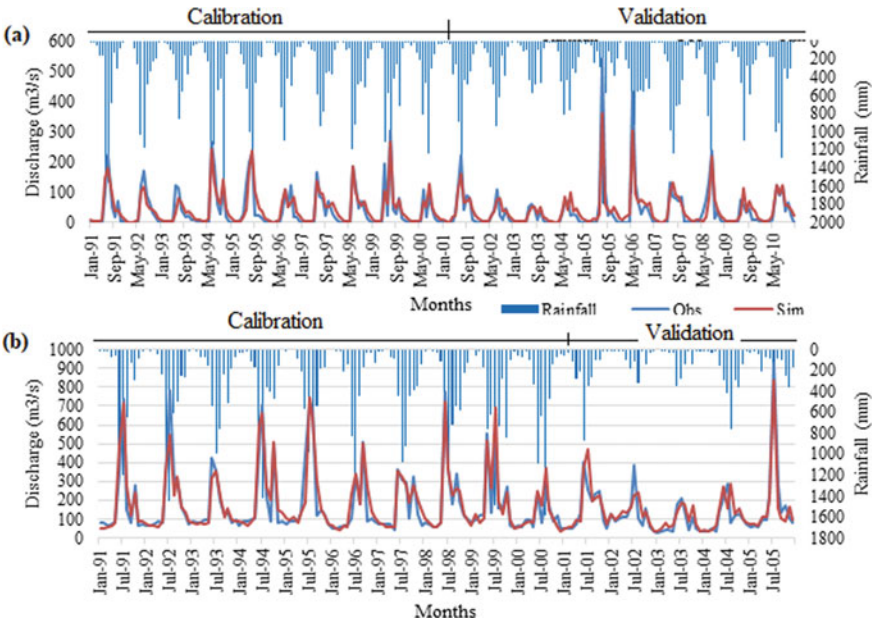

Fig. 5 Comparison of monthly streamflow value between the observed and calculated for the calibration and validation **a** Kalambur, **b** Ramamangalam

Table 4 Calibration and validation—Hydrologic model performance criteria

Gauging Site	Calibration (1991–2000)			Validation (2001–2005)		
	R^2	NSE	PBIAS	R^2	NSE	PBIAS
Kalambur	0.87	0.86	−9.0	0.90	0.89	−8.7
Ramamangalam	0.89	0.85	−2.4	0.81	0.75	−10.5

GCMs ensemble outputs (RCP 4.5 and 8.5), and the simulation results obtained are compared with baseline period (1986 to 2015) simulation results. In this study, the model simulation results obtained are referred to as Q_{clim}. In the next section, the results are presented using ensembled data of all 5 GCMs.

4.4 Ensemble of All Five GCMs Analysis

Figure 6 shows the mean precipitation of all five GCMs and ensembled for RCP 4.5 and 8.5 for near, mid, and far future. These indicated rainfall will be more in north part areas and less in the south part areas and sub-basins. The rainfall varies between mostly 1400–4500 mm among the sub-basins level in the MRB but showed a slightly decrease in comparison to historical rainfall. Using the projected rainfall and climate

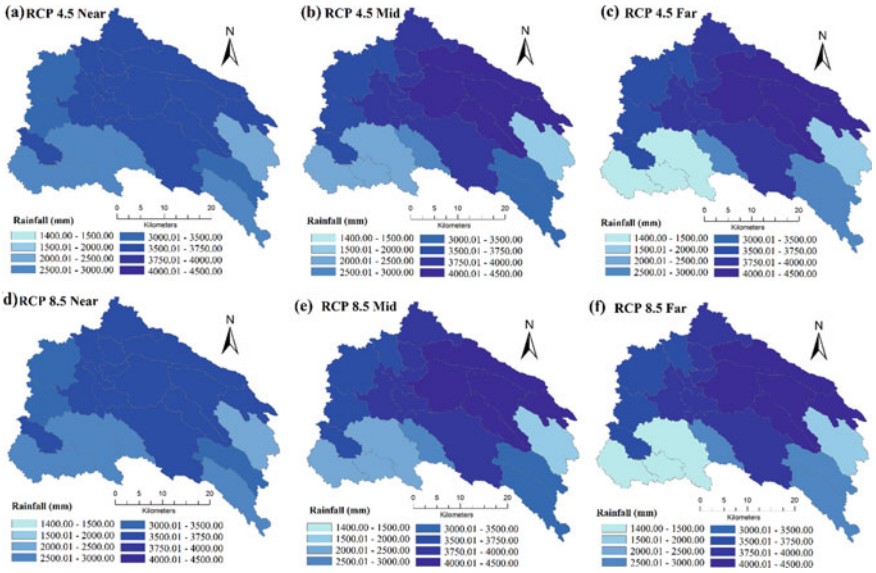

Fig. 6 Spatial distributions of precipitation for near, mid, and far future time slices of RCP 4.5 and 8.5 emission scenarios

parameters such as temperature, wind, solar radiation, etc., SWAT model has run for various scenarios, and results are presented here.

Figure 7 shows the variation of evapotranspiration (ET) for each sub-basin for the considered near, mid, and far future for both RCP 4.5 and 8.5 at sub-basin scale. The ET is mostly depending upon the precipitation, temperature, and land use variations of the study area. In MRB, ET is more in north side areas and less in south side because of high precipitation and more plantation and agriculture in respective regions. Figure 7 shows slight variations in ET among different time slices as well as RCPs scenarios because of variations in rainfall and temperature.

Figure 8 shows the simulated mean surface runoff of each sub-basins for all different time slices and scenarios. Figure 9 shows the simulated time series of runoff at the watershed outlet for various scenarios. Figure 10 gives the time series intercomparison of runoff at the watershed outlet for RCP 8.5 and 4.5 scenarios for near, mid, and far future continuously.

The simulated Q_{clim} (change in surface runoff) for the future period under both scenarios (RCP 4.5 and 8.5) were compared to the corresponding values of all sub-basins from the baseline period (1986 to 2015), as given in Fig. 11. It can be observed that change in annual Q_{clim} for all the time slices is moderate to highly significant for the future periods to RCP 4.5 and 8.5 CC scenarios. In general, Q_{clim} was predicted to decrease in sub-basins more toward the main stream. In particular, the Q_{clim} decreased from the baseline period by 8.33%, 6.5%, and 11.24% in RCP 4.5 and 11.7%, 8.72%, and 17.33% for RCP 8.5 from T1, T2, and T3 period, respectively.

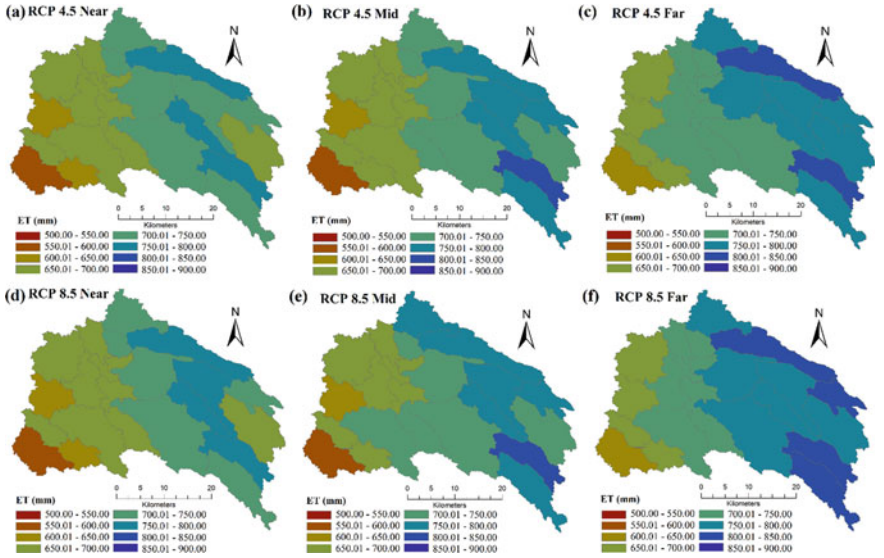

Fig. 7 Spatial distributions of actual ET for near, mid, and far future of RCP 4.5 and RCP 8.5 emission scenarios

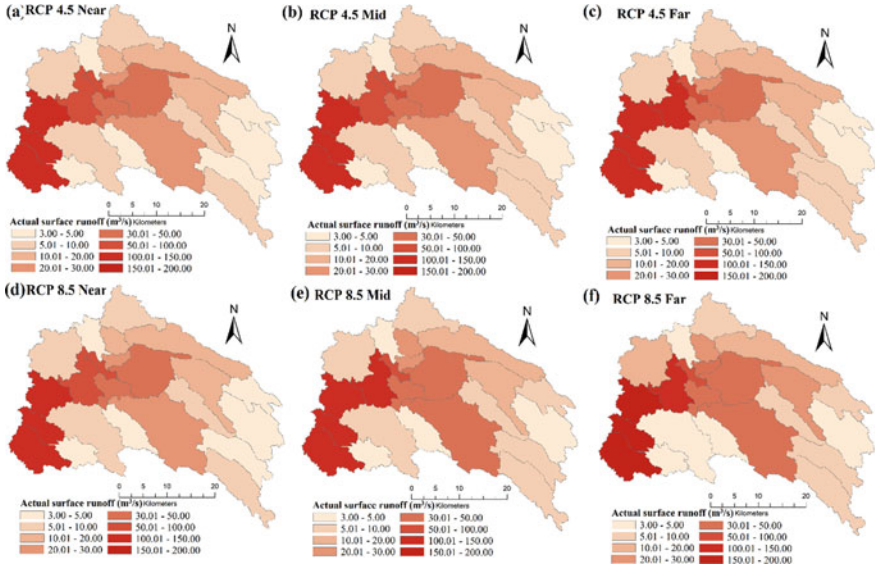

Fig. 8 Spatial distribution of surface runoff (m^3/s) for near, mid, and far future of RCP 4.5 and RCP 8.5 emission scenarios

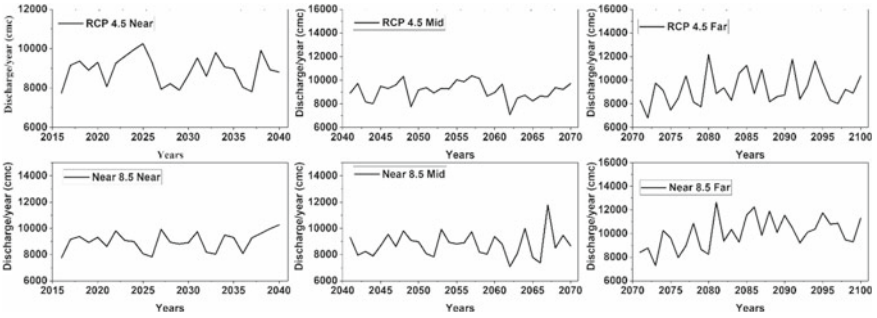

Fig. 9 Simulated time series of runoff at the watershed outlet for various scenarios-(i) RCP4.5-near; (ii) RCP4.5-mid; (iii) RCP4.5-far; (iv) RCP8.5-near; (v) RCP8.5-mid; (vi) RCP8.5-far

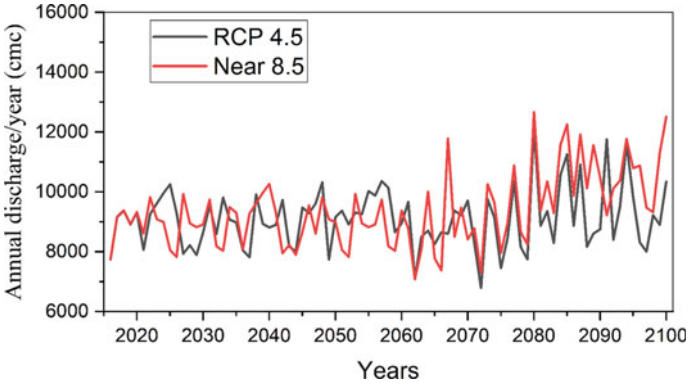

Fig. 10 Comparison of simulated time series of runoff at the watershed outlet for various scenarios of RCP 4.5 and RCP 8.5 for 2010–2100

The result shows more urbanization in downstream showing less rainfall in the future and affecting surface runoff. In most of the cases considered, change in Q_{clim} for all the time slices of near, mid, and far future are found to be moderate to highly significant indicating possible impacts of CC on the hydrologic response of the catchment. The monthly, seasonal, and annual changes in streamflow for the future periods are shown in Fig. 12 according to RCP 4.5 and 8.5 CC scenarios. It is observed that streamflow was predicted to decrease in the wet season (June to September) and increase in the dry season (October to May), though there were some variations between various scenarios and among the future periods.

In particular, the maximum streamflow increased by 2.45–65.30% under RCP 4.5, and 288.29% under RCP 8.5 in April. Meanwhile, the streamflow decreases in monsoon months mostly June and July approximately 40–48% under both RCP 4.5 and 8.5. Because of the higher unexpected precipitation during the summer rain and early monsoon period (March–May), it is important to forecast seasonal changes in water resources within the catchment associated with future CC. The impacts

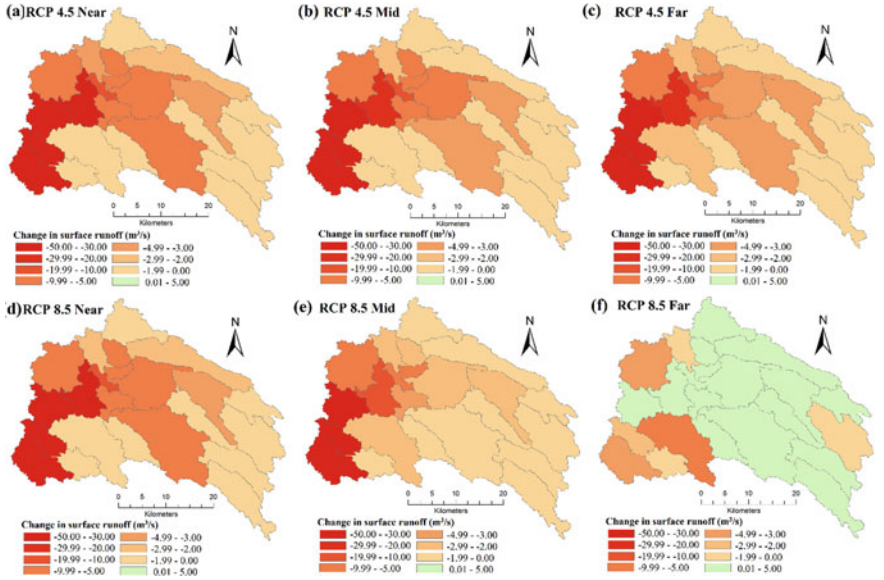

Fig. 11 For MRB, the spatial distribution of changes in the future surface runoff for the three different scenarios of CC between 2011 and 2099 for RCP 4.5 and RCP 8.5. **a** RCP4.5 (2011–2040); **b** RCP4.5 (2041–2070); **c** RCP4.5 (2071–2099); **d** RCP8.5 (2011–2040); **e** RCP8.5 (2041–2070); **f** RCP8.5 (2071–2099) in the MRB

of distinct climate change are more visible in the seasonal streamflow than does the monthly streamflow. The general pattern indicated an increase in winter and summer flow and a decrease in monsoon flow (but not all months) though there were some variations among the RCP 4.5 and 8.5 scenarios. The streamflow in winter and summer increased by 4.46–7.76% and 34.13–47.96%, respectively, under RCP 4.5 and by 4.0–30.16%, and −13.21–195.66%, under RCP 8.5.

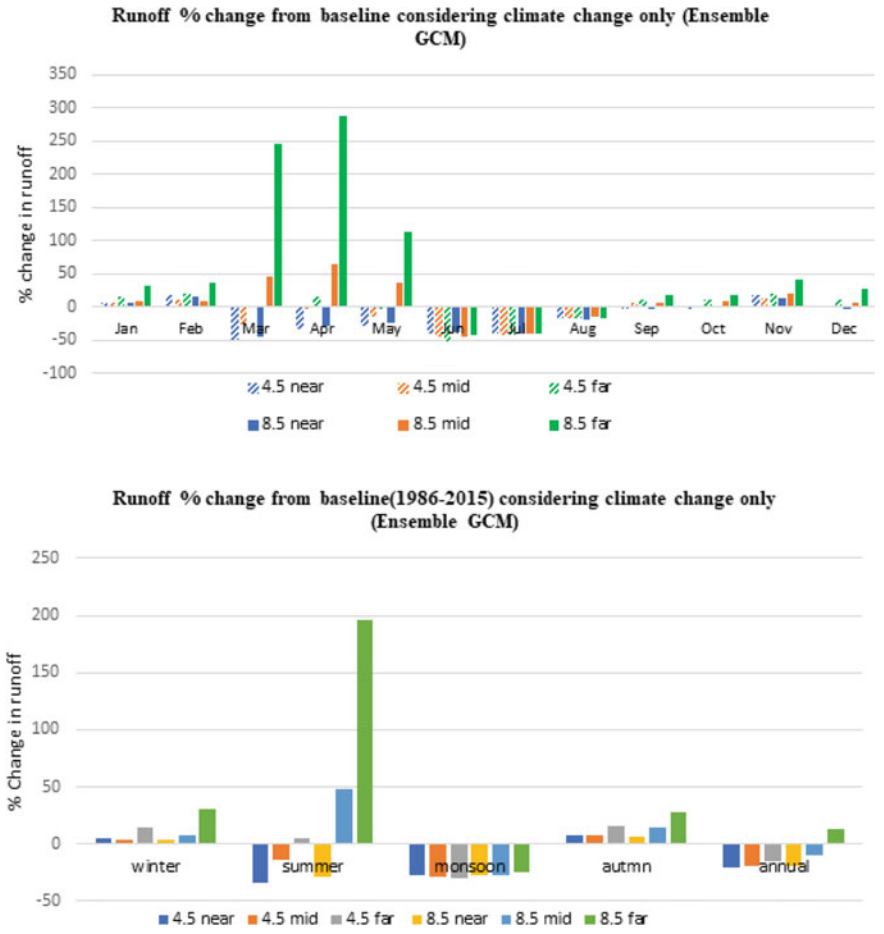

Fig. 12 Quantification in changes in streamflow for the three-time periods (near, mid, and future) relative to the baseline period. **a** Mean monthly streamflow changes. **b** Mean seasonal and annual streamflow changes in the MRB

5 Conclusions

In this study, a methodological framework for climate change (CC) impact assessment on a river basin scale is presented and used for assessment of the impacts of CC on streamflow in the Muvattupuzha river basin, in Kerala, India. The different climate scenarios for RCP 4.5 and RCP 8.5 till 2100 were used in the study. The SWAT model has been used in the hydrological modeling. Ensembled rainfall for near, mid, and far future showed a decrease due to CC by 6.05%, 5.90%, and 4.52% for RCP 4.5 and 7.32%, 6.52%, and 5.72% for RCP 8.5 emission scenarios, in comparison to the baseline. Ensemble of surface runoff show decreasing trend from the baseline

period by 8.33%, 6.5%, and 11.24% in RCP 4.5 and 11.7%, 8.72%, and 17.33% for RCP 8.5 from T1, T2, and T3 period, respectively. For monthly and seasonally, the results indicated that the monthly streamflow decreased mainly in monsoon months like June, July, and August, and other remaining months showing increasing in streamflow under both RCP 4.5 and 8.5 emission scenarios.

For the considered river basin, the water resources planning for the long term must be adjustable and resilient to the changing pattern of CC impacts. Furthermore, both planners and policymakers should develop a land use strategy for reducing the adverse impacts of LULC changes in the river basin considered. The present study will be useful for long-term climate change impacts assessment and long-term water resources planning of the concerned basin and the same methodology can be extended to other river basins.

Acknowledgements We wish to express our deep gratitude to Central Water Commission and Indian Meteorological Department India for providing hydrological and meteorological data. The authors also acknowledge the sponsorship of the project entitled "Impacts of Climate Change on Water Resource in River Basin from Tadri to Kanyakumari" by INCCC, Ministry of Water Resource, Gov. of India.

References

1. Arnold JG et al (1998) Large area hydrologic modeling and assessment part I: model development. JAWRA J Am Water Resour Assoc 34(1):73–89
2. Eldho TI (2022) Impact of climate change on water resourcres in river basins from Tadri to Kanyakumari. *Technical report* (unpublished) submitted to Ministry of Jal Shakti, Govt. of India, Project No. 17MWR0009-001
3. Givati A, Thirel G, Rosenfeld D, Paz D (2019) Climate change impacts on streamflow at the upper Jordan river based on an ensemble of regional climate models. J Hydrol: Region Stud 21:92–109
4. IPCC (2021) Climate Change 2021: The Physical Science Basis. Contribution of Working Group I to the Sixth Assessment Report of the Intergovernmental Panel on Climate Change [Masson-Delmotte, V., P. Zhai, A. Pirani, S.L. Connors, C. Péan, S. Berger, N. Caud, Y. Chen, L. Goldfarb, M.I. Gomis, M. Huang, K. Leitzell, E. Lonnoy, J.B.R. Matthews, T.K. Maycock, T. Waterfield, O. Yelekçi, R. Yu, and B. Zhou (eds.)]. *Technical Report*, Cambridge University Press
5. Islam SA, Bari MA, Anwar AHMF (2014) Hydrologic impact of climate change on Murray-Hotham catchment of Western Australia: a projection of rainfall–runoff for future water resources planning. Hydrol Earth Syst Sci 18(9):3591–3614
6. Kim J, Choi J, Choi C, Park S (2013) Impacts of changes in climate and land use/land cover under IPCC RCP scenarios on streamflow in the Hoeya River Basin, Korea. Sci Total Environ 452:181–195
7. Lu D, Weng Q (2007) A survey of image classification methods and techniques for improving classification performance. Int J Remote Sens 28(5):823–870
8. Moriasi DN et al (2007) Model evaluation guidelines for systematic quantification of accuracy in watershed simulations. Trans ASABE 50(3):885–900. https://doi.org/10.13031/2013.23153
9. Neitsch SL, Arnold JG, Kiniry JR, Williams JR, King KW (2005) Soil and water assessment tool theoretical documentation. Version 2005. Texas Water Resource Institute, College Station, Texas, USA

10. Neitsch SL, et al. (2011) Soil and water assessment tool theoretical documentation version 2009**.** Texas: Texas Water Resources Institute, Texas A&M University, College Station
11. Ogden FL, Crouch TD, Stallard RF, Hall JS (2013) Effect of land cover and use on dry season river runoff, runoff efficiency, and peak storm runoff in the seasonal tropics of Central Panama. Water Resour Res 49(12):8443–8462. https://doi.org/10.1002/2013WR013956
12. Sinha RK, Eldho TI (2018) Effects of historical and projected land use/cover change on runoff and sediment yield in the Netravati river basin, Western Ghats, India. Environ Earth Sci 77(3):111
13. Sinha RK, Eldho TI, Ghosh S (2020a) Assessing the impacts of historical and future land use and climate change on the streamflow and sediment yield of tropical mountainous river basin South India. Environ Monit Assess J 192 679:1–21
14. Sinha RK, Eldho TI, Subimal G (2020) Assessing the impacts of land cover and climate on runoff and sediment yield of a river basin. Hydrol Sci J 65(12):2097–2115
15. Yan B, Fang NF, Zhang PC, Shi ZH (2013) Impact of land use change on watershed stream flow and sediment yield: an assessment using hydrologic modeling and Partial least regression. J Hydrol 484:26–37
16. Zuo D et al (2016) Assessing the effects of changes in land use and climate on runoff and sediment yields from a watershed in the Loess Plateau of China. Sci Total Environ 544:238–250

Modelling of Streamflow Considering the Effects of Land Use Land Cover Change Over the Sabari River Basin, India

Subbarao Pichuka and Nandikanti Siva Sai Syam

Abstract Land Use Land Cover (LULC) significantly affects hydrological variables like streamflow. This chapter studies the effects of change in LULC over streamflow in the Sabari Basin, India. The LULC change detection analysis has been carried out for three decades (1985–1995, 1995–2005, 2005–2020). The LULC classes (Barren land, Built-up Area, Cropland, Fallow land, Forest, Grassland, Plantations, Shrubland, Wasteland, and Waterbodies) are analyzed. The change for individual classes and converted area analysis from one class to another is also conducted. By the end of 2005, the built-up area, cropland, and shrubland were increasing by 12.1%, 0.43%, and 3.25%, respectively, when compared to 1985, and the remaining classes were decreasing by each decade. Monthly streamflow is modeled for 30 years (1982–2012) using the Soil and Water Assessment Tool (SWAT). Two Sub-basins (Saradaput and Konta) are considered for the analysis. The R^2 between the modeled and the observed data in the Saradaput and Konta Sub-basins is 0.78 and 0.74, respectively. The results indicate that urbanization and agricultural intensification have contributed to increased streamflow. These LULC change detection can be further used in modeling this basin using different hydrological models to compare the performance of the different models in this basin.

Keywords SWAT · Sabari basin · LULC change · Streamflow

1 Introduction

India is one of the most water-stress countries in the world. The impending water supply in India is becoming most uncertain. Anthropogenic activities such as deforestation, overconsuming water resources and releasing aerosols into the atmosphere in their daily life, and many more aspects lead the climate to change rapidly. Climate

S. Pichuka (✉) · N. S. S. Syam
Department of Civil Engineering, National Institute of Technology Andhra Pradesh, Tadepalligudem 534101, India
e-mail: subbarao@nitandhra.ac.in

S. Dutta and V. Chembolu (eds.), *Recent Development in River Corridor Management*, Lecture Notes in Civil Engineering 376, https://doi.org/10.1007/978-981-99-4423-1_16

and Land use changes are some of the significant factors in altering the hydrological cycle. In recent years, the implication of these changes has been investigated. They increased the extreme events in magnitude and intensity, creating and intensifying many other water resources-related problems [12]. Rainfall is a crucial resource for worldwide socio-economic activity and is vital in the hydrological cycle. In India, most of the agriculture is rainfed. Rainfall and baseflow influence the high and low streamflow extremes, which are crucial for flood management, hydropower, navigation, and ecological concerns [17]. Hence, understanding the consequences of LULC change on the hydrological cycle is necessary [4]. The hydrology of river basins is significantly affected by LULC changes, mainly through variations in baseflow during floods [6] and average annual discharge [7]. Several investigations demonstrated a connection between land use changes and other mechanisms in the local hydrological cycle [3, 20, 21]. Akbar et al. [1] followed the Markov approach to forecast the future LULC after generating the historical LULC maps to study its effects on urbanization. It resulted in a decrease in the water bodies and vegetation and increased the urban area by 2040.

The effects of climate change and LULC on basin hydrology can be analyzed using hydrologic models. SWAT is a semi-distributed hydrological model that can simulate more precisely by considering several hydrological parameters and their interconnections. Along with them, it considers the topographical features of the watershed and decentralizes the watershed at a continuous time step [23]. Using SWAT, a study on Kenya's Sondu Basin shows the model's ability in African watersheds [13]. Zhang et al. [24] compared SWAT with their developed SWAT-T model regarding the response of a hydrological catchment to LULC change. The Change in LULC affected all hydrological variables, among which streamflow is prominent. Sahana and Timbadiya [19] considered the Upper Godavari Basin to study the climate change and LULC effects for different GCMs in different scenarios using SWAT. A thorough knowledge of the river basin's water balance and parameters is crucial when constructing a reliable hydrologic model [16]. The conventional fixed parameterization is compared with the varied parameterization approach resulting in a better performance of the varied approach. Du et al. [8] used this approach in studying the watershed hydrology in urban regions of China. This chapter has two objectives—(i) to find the LULC changes over Sabari River Basin (SRB) from 1985 to 2015, (ii) using the classified LULC map, model the streamflow in the Sabari basin and to observe the anomalies.

2 Study Area and Data Source

2.1 Sabari River Basin (SRB)

The GRB is the second-longest and third-largest river in India. The Sabari Basin is located between 17°31′33″ N to 19°6′42″ N latitudes and 81°3′36″ E to 83°3′5″ E longitudes. The annual average rainfall is approximately 1250 mm. Saradaput and Konta sub-basins are considered to study streamflow anomalies. The Konta is the largest sub-basin of SRB. The Saradaput and Konta stations are located at 18°36′45”N, 82°08′34”E and 17°47′56″ N, 81°23′34″ E, respectively. The basin map and its position in India are presented in Fig. 1.

2.2 Data Used

The Landsat images for the years 1985, 1995, 2005, and 2015 are collected from the USGS web portal. ASTER Digital Elevation Model (DEM) of 30 m resolution is downloaded from the NASA web portal (https://www.earthdata.nasa.gov/news/new-aster-gdem). The daily rainfall data at 0.25° × 0.25° resolution [18] and temperature

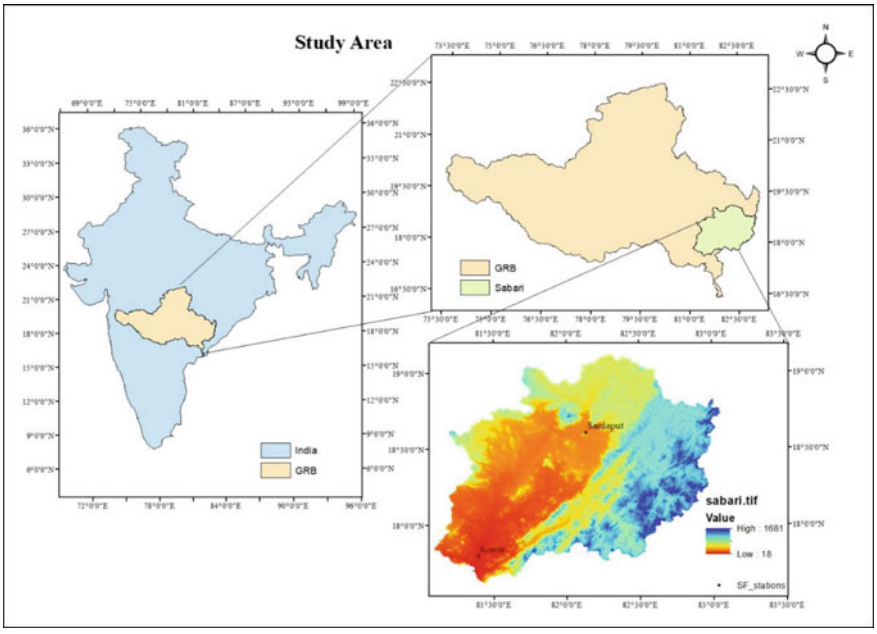

Fig. 1 Study area map

data at 1° × 1° resolution [22] for the GRB are obtained from IMD, Pune. The weather data is collected from the NCEP- NCAR website. FAO (Food and Agriculture Organization) soil map is utilized for this sub-basin.

3 Methodology

See Fig. 2.

3.1 LULC Change Detection

The raw Landsat images for the years 1985, 1995, 2005, and 2015 are classified using the Normalized Difference Vegetation Index (NDVI). Among different normalized difference indices developed for remotely sensed imagery, NDVI is the most widely used index [5]. The image is classified into six classes: cropland, built-up area, dense vegetation, sparse vegetation, range land, and waterbodies, depending on the NDVI

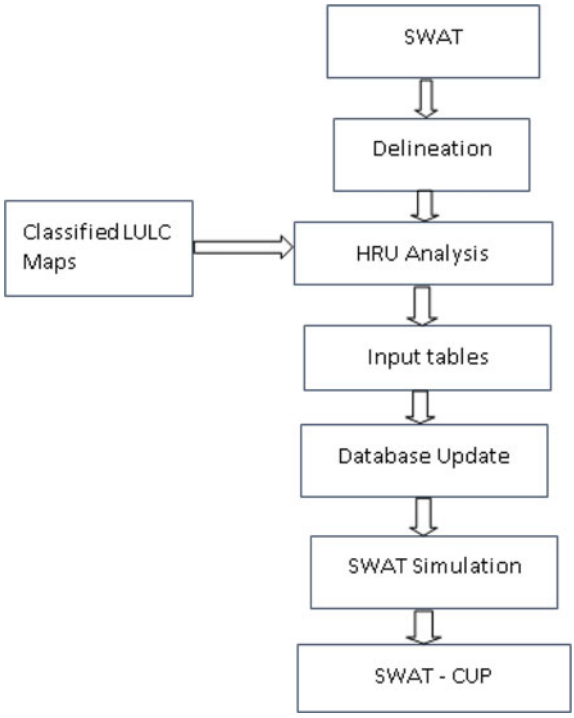

Fig. 2 Methodological flowchart

ranges. The NDVI classification is used due to the vegetative occupancy in the Sabari basin. The two LULC maps are overlaid to detect the change in each class.

3.2 SWAT Model

SWAT is developed by (USDA-ARS) [2] and is used to find the anomalies in the streamflow concerning the change in the LULC for different decades. The model works based on the water balance equation represented by Eq. 1 and SWAT distributes the basin into sub-basins that will eventually connect with the system. Hydrologic Response Units are also generated with the sole allocation of gradient, soil type, and land cover [14]. The weather data is defined using the observed data. To estimate the surface runoff for the selected catchments, the model utilizes the SCS-CN method represented by Eqs. 2 and 3. The model is simulated monthly from 1979 to 2014, skipping three years by considering the lag effect.

$$SW_f = SW_0 + \sum_{j=1}^{n}(P_d - Q_s - ET_j - W_{\text{seep}} - Q_g) \tag{1}$$

$$\begin{aligned} Q &= \tfrac{(P-0.2\,s)^2}{P+0.8s} \quad \text{if } R > 0.2\,s \\ Q &= 0 \qquad\qquad\quad \text{if } R \leq 0.2\,s \end{aligned} \tag{2}$$

$$s = 254\left(\frac{100}{CN} - 1\right) \tag{3}$$

where SW_f = Final Soil water content; SW_0 = Initial Soil Water content; P_d = daily Precipitation; Q_s = Surface flow; Q_g = Return flow; ET_j = Evapotranspiration on jth day; W_{seep} = Soil interflow; n = time. All units are in mm. CN is the curve number; s is the retention parameter depending on the topographical features and soil water content. The equation for the retention parameter is represented by Eq. 3.

3.3 Model Calibration and Validation

SWAT is calibrated using SWAT-CUP by optimizing the parameters and determining the parameters' sensitivity toward hydrological processes such as streamflow [11]. Therefore, in many significant applications, the calibration process might become challenging. Because of SWAT, CUP's intelligence, model parameters can be set, optimized, and manually modified after every iteration of calibration. Multi-objective optimization has been carried out by considering NSE, R^2, and PBias as the objective functions. For this study, 11 parameters were priorly selected, corresponding to their sensitivity and impact on the water balance [9].

$$R^2 = 1 - \frac{\text{Sum of Squares of Residuals}}{\text{Total sum of the squares}} \tag{4}$$

$$SE = 1 - \frac{\sum_{t=1}^{T} X_m^t - X_0^t}{\sum_{t=1}^{T} X_0^t - \underline{X_0}} \tag{5}$$

$$\text{PBIAS} = \frac{\sum_{t=1}^{T} (X_0^t - X_m^t)}{\sum_{t=1}^{T} X_0^t} \times 100 \tag{6}$$

where X_m^t = Modeled data at time t; X_0^t = Observed data at time t; $\underline{X_0}$ = Observed mean.

4 Results and Discussions

4.1 LULC Analysis

The classified decadal LULC maps are shown in Fig. 3. The magnitude of each class in each decade, along with the proportionate change in the LULC from 1985 to 2015, is represented in Table 1. The analysis shows that the SRB is a dominant vegetative basin with overall vegetation (cropland, dense vegetation, and sparse vegetation) area of 19,974 km^2 in a total basin area of 20,840 km^2. The remaining area is covered by a built-up area of 125 km^2 and water bodies of 740 km^2. It is observed that from 1985 to 2015, the built-up area almost doubled (94.95%), whereas the dense and sparse vegetation was reduced by 5% and 4%, respectively. The cropland in the Sabari basin increased by 8.8%, and waterbodies decreased by 32% during 1985–2015. The reduced area of the water bodies, dense and sparse vegetation, is converted into cropland and built-up area. Most of the reduced dense and sparse vegetated area is converted into cropland.

4.2 Performance of the SWAT Model

The model is developed using the topographical and meteorological data for 1979–2014, considering three years (1979–1982) as a lag time. The performance, sensitivity analysis, calibration, and validation of the model using SWAT-CUP are performed. The slope of the SRB varies between 0 and 70%. There are four different soil classes as per the FAO soil map in the study area. The SWAT generates a total of 180 HRUs in the SRB.

The hydrographs of the Sardaput and Konta basins are presented in Figs. 4 and 5. The hydrographs are plotted for three decades 1985–1995, 1995–2005, and 2005–2015. The observed average decadal streamflow during pre-monsoon, monsoon, and

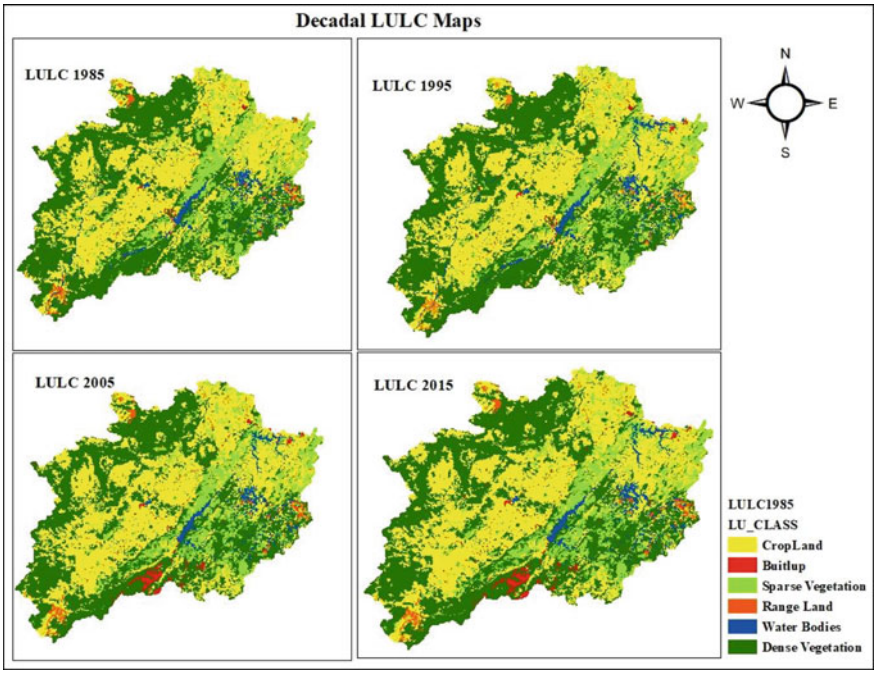

Fig. 3 Decadal LULC maps of Sabari basin

Table 1 Magnitude and % change in the LULC

Class	Decade				% Change between 1985 and 2015
	1985	1995	2005	2015	
Built-up area	125.8	138.1	126.8	245.3	94.96
Cropland	8274	8288	8293	9007	8.86
Dense vegetation	8944	8926	8908	8490	−5.08
Sparse vegetation	2755	2623	2815	2635	−4.35
Water bodies	740.3	864	697.9	502.5	−32.12

post-monsoon seasons in the Saradaput is increased by 4 m^3/s (3.7%), decreased by 25 m^3/s (8.15%) and increased by 3.75 m^3/s (5.09%), respectively, by 2015. In comparison with the first decade 1985–95. For the Konta basin, it has increased by 8 m^3/s (3.1%), decreased by 195 m^3/s (34%), and decreased by 35 m^3/s (5%) in pre-monsoon, monsoon, and post-monsoon seasons, respectively. However, the simulated values are quite converse to the observed data. The simulated decadal streamflow data for pre-monsoon, monsoon, and post-monsoon seasons in Saradaput are decreasing by 9 m^3/s (4%), 9 m^3/s (5.8%), and 1.8 m^3/s (15.27%), respectively. In the Konta basin, it has decreased by 35 m^3/s (5%), increased by 355 m^3/s (5%) and 22 m^3/s (10%) in pre-monsoon, monsoon and post-monsoon seasons, respectively. The

plots of Saradaput and Konta for the decadal analysis of the observed and modeled streamflow are presented in Figs. 4 and 5, respectively.

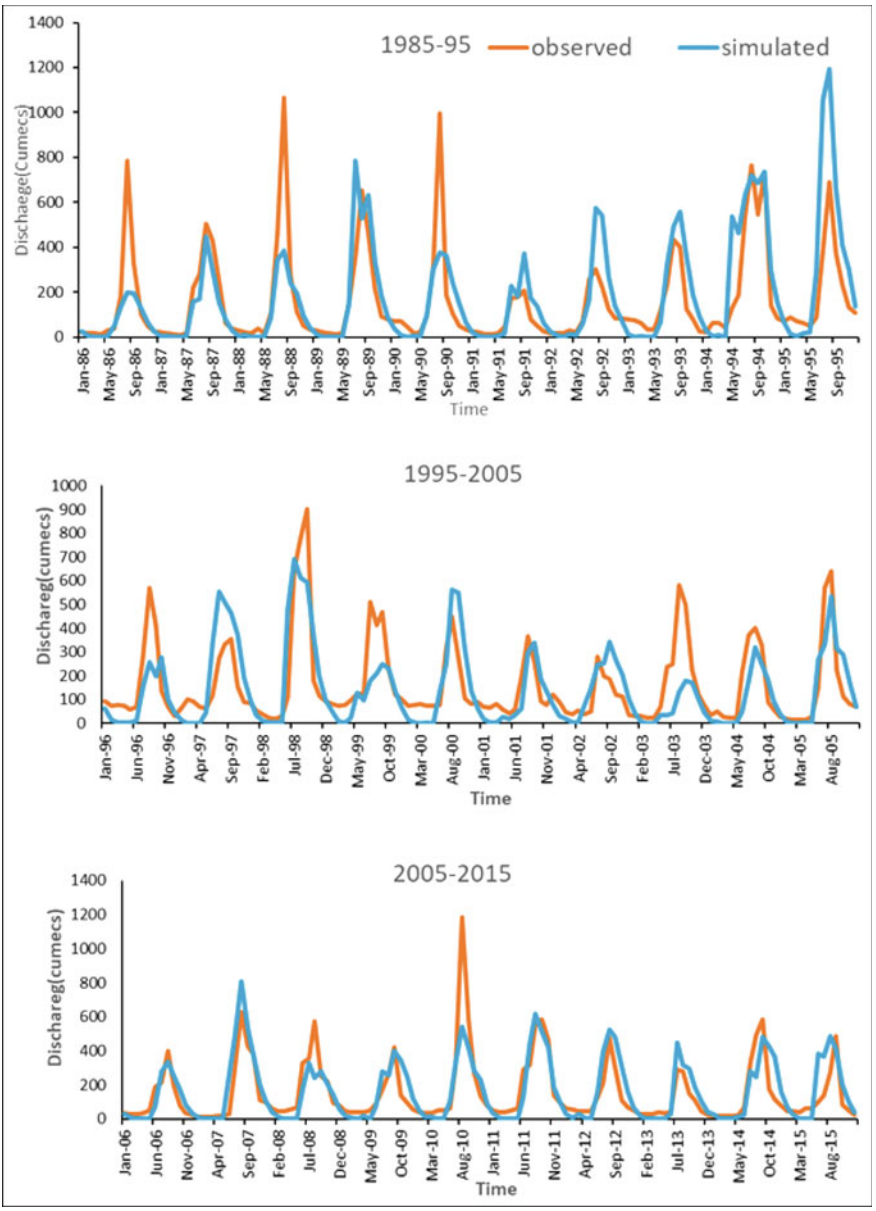

Fig. 4 Observed versus simulated discharge for saradaput sub-basin

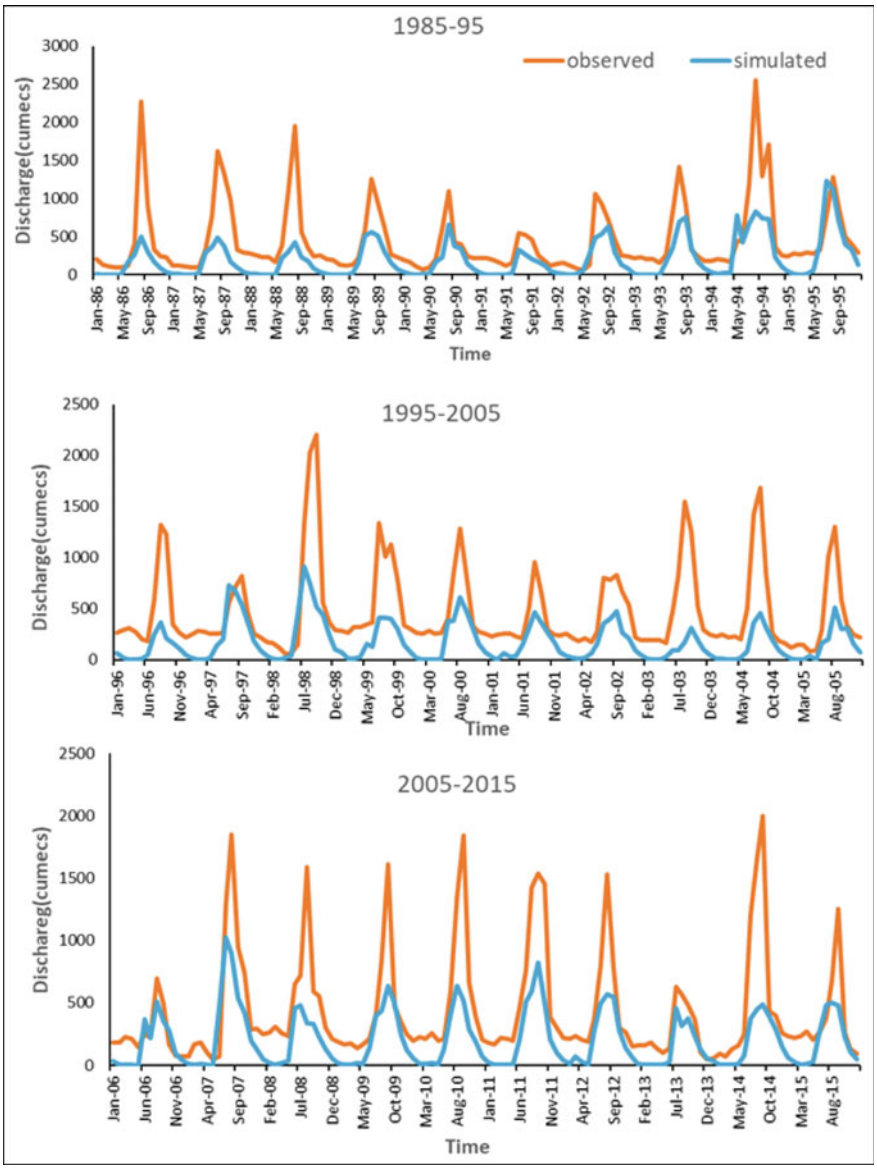

Fig. 5 Observed versus simulated discharge for Konta sub-basin

NSE, PBias, and R^2 are used to check the SWAT performance regarding the sensitivity of parameters. The model is calibrated (1979–2003) and validated (2004–2013) monthly using SWAT-CUP. 11 parameters are selected for sensitivity analysis and after nine iterations of each 400 simulations, a specific value is fitted within the described range. The parameters, description, and fitted value for the best simulation

Table 2 Selected parameters and their fitted values

Sl. No.	Parameter_ Name	Description	Fitted_Value
1	CN2	Curve number for moisture condition II	67.270103
2	ALPHA_BF	Baseflow alpha factor	0.536313
3	GW_DELAY	Groundwater delay	226.575745
4	GWQMN	Threshold depth of water for return flow	753.507507
5	GW_REVAP	Groundwater re-evaporation coefficient	0.020185
6	REVAPMN	Threshold depth of water in the shallow aquifer for "revap" to occur	656.408997
7	CH_N2	Manning's 'n' value in the main channel	0.083838
8	CH_K2	Effective hydraulic conductivity	28.366709
9	SOL_AWC	Soil available water capacity	1.002764
10	ESCO	Soil evaporation compensation facto	0.583095
11	EPCO	Plant uptake compensation Factor	0.612328

Table 3 Performance stats for Saradaput and Konta sub-basins

Period	Performance metric	Saradaput	Konta
Calibration	R^2	0.78	0.58
	NSE	0.51	0.35
	PBIAS (%)	−5.8	−4.2
Validation	R^2	0.74	0.62
	NSE	0.53	0.42
	PBIAS (%)	−3.8	−4.6

are shown in Table 3. Further, the values of the selected objective functions for the best simulation in both the Saradaput and Konta locations are shown in Table 2. Irrespective of the catchment area, the correlation between the extreme events is 0.42. In the case of ordinary events, if the catchment area is small such as Saradaput, the correlation is 0.81, and for a larger sub-basin area, the correlation is 0.75. In Sadaraput, the model performs well with R^2 coefficients of 0.78 and 0.74 with an efficiency of 0.52 and 0.53 in calibration and validation, respectively. For Konta, the R^2 is reduced to 0.58 and 0.62 with an efficiency of 0.35 and 0.42 in calibration and validation, respectively. Therefore in both cases, the model is overestimated.

4.3 Water Balance Components

In SRB, evapotranspiration is the prominent water balance component that consumes about 74% of the rainfall, as it is a vegetation-dominant sub-basin. The surface flow

is 8% due to more infiltration in the basin. The remaining rainfall is percolated into the soil depending on the soil condition. From the percolated soil, 4% returns to the surface flow (return flow). The aquifer recharge is 1% for the deep and the remaining precipitation is stored in the shallow aquifer which is readily available. A similar study on a high vegetation basin is conducted by Koneti et al. [15] and Guug et al. [10] also showed that evapotranspiration is the highest component of these types of basins.

5 Conclusion

The increased built-up area might decrease the infiltration capacity, leading to increased surface runoff in the Saradaput sub-basin. The LULC maps represent that most of the decreased cropland is converted into a built-up area. The modeled streamflow contains bias, due to a considerable difference between the observed and the modeled data for the Konta sub-basin in terms of the catchment area. In this study, the SWAT model showed relatively low accuracy in capturing the hydrograph peaks in Konta sub-basin than in the Saradaput sub-basin. It is due to the larger area of the Konta sub-basin consisting of vegetation which leads to the more evapotranspiration when compared to Saradaput sub-basin. While in both the sub-basins, the recession limbs are almost all properly captured due to the range of the groundwater delay and base flow parameters. Overall, the streamflow variations are associated with the change in LULC and it is evident from this study that the built-up area doubled in 2015 when compared with the land cover data of 1985. It is due to the drastic increase in population over the SRB. The growing population demands more land resources for their basic needs, i.e., food and shelter. Therefore, the vegetated land is turned into agriculture and built-up land. The present study is very helpful in understanding the effects of LULC changes on streamflow in other similar basins.

Acknowledgements The authors acknowledge the financial support received from the Department of Science and Technology (DST), Startup Research Grant (SRG) Scheme, Ministry of Science and Technology, Government of India (**Ref No. DST/SRG/2020/000823**) to carry out present work. The authors are also thankful to Central Water Commission (CWC) and IMD Pune for providing the necessary data to carry out this work.

References

1. Akbar TA, Hassan QK, Ishaq S, Batool M, Butt HJ, Jabbar H (2019) Investigative spatial distribution and modelling of existing and future urban land changes and its impact on urbanization and economy. Remote Sens 11(2). https://doi.org/10.3390/rs11020105
2. Arnold JG, Srinivasan R, Muttiah RS, Williams JR (1998) large area dyrologic modeling and assessment part 1. J Am Water Resour Assoc 34(1):73–89

3. Astuti IS, Sahoo K, Milewski A, Mishra DR (2019) Impact of land use land cover (LULC) change on surface runoff in an increasingly urbanized tropical watershed. Water Resour Manag 33(12):4087–4103. https://doi.org/10.1007/s11269-019-02320-w
4. Babar S, Ramesh H (2015) Streamflow response to land use-land cover change over the Nethravathi River Basin, India. J Hydrol Eng 20(10):05015002. https://doi.org/10.1061/(asce)he.1943-5584.0001177
5. Beck HE, McVicar TR, van Dijk AIJM, Schellekens J, de Jeu RAM, Bruijnzeel LA (2011) Global evaluation of four AVHRR-NDVI data sets: intercomparison and assessment against Landsat imagery. Remote Sens Environ 115(10):2547–2563. https://doi.org/10.1016/j.rse.2011.05.012
6. Brath A, Montanari A, Moretti G (2006) Assessing the effect on flood frequency of land use change via hydrological simulation (with uncertainty). J Hydrol 324(1–4):141–153. https://doi.org/10.1016/j.jhydrol.2005.10.001
7. Costa MH, Botta A, Cardille JA (2003) Effects of large-scale changes in land cover on the discharge of the Tocantins River, Southeastern Amazonia. J Hydrol 283(1–4):206–217. https://doi.org/10.1016/S0022-1694(03)00267-1
8. Du J, Rui H, Zuo T, Li Q, Zheng D, Chen A, Xu Y, Xu CY (2013) Hydrological simulation by SWAT model with fixed and varied parameterization approaches under land use change. Water Resour Manag 27(8):2823–2838. https://doi.org/10.1007/s11269-013-0317-0
9. Gitau MW, Chaubey I (2010) Regionalization of SWAT model parameters for use in ungauged watersheds. Water (Switzerland) 2(4):849–871. https://doi.org/10.3390/w2040849
10. Guug SS, Abdul-Ganiyu S, Kasei RA (2020) Application of SWAT hydrological model for assessing water availability at the Sherigu catchment of Ghana and Southern Burkina Faso. HydroResearch 3:124–133. https://doi.org/10.1016/j.hydres.2020.10.002
11. Ha LT,Bastiaanssen WGM, van Griensven A, van Dijk AIJM, Senay GB, Ha LT (2017) SWAT-CUP for calibration of spatially distributed hydrological processes and ecosystem services in a Vietnamese River Basin using remote sensing. J Hydrol Earth Syst Sci, 1–35 https://doi.org/10.5194/hess-2017-251
12. Hengade N, Eldho TI (2019) Relative impact of recent climate and land cover changes in the Godavari River Basin, India. J Earth Syst Sci 128(4). https://doi.org/10.1007/s12040-019-1135-4
13. Jayakrishnan R, Srinivasan R, Santhi C, Arnold JG (2005) Advances in the application of the SWAT model for water resources management. Hydrol Process 19(3):749–762. https://doi.org/10.1002/hyp.5624
14. Khatun S, Sahana M, Jain SK, Jain N (2018) Simulation of surface runoff using semi distributed hydrological model for a part of Satluj Basin: parameterization and global sensitivity analysis using SWAT CUP. Model Earth Syst Environ 4(3):1111–1124. https://doi.org/10.1007/s40808-018-0474-5
15. Koneti S, Sunkara SL, Roy PS (2018) Hydrological modeling with respect to impact of land-use and land-cover change on the runoff dynamics in Godavari River Basin using the HEC-HMS model. ISPRS Int J Geo-Inf 7(6). https://doi.org/10.3390/ijgi7060206
16. Malik MA, Dar AQ, Jain MK (2022) Modelling streamflow using the SWAT model and multi-site calibration utilizing SUFI-2 of SWAT-CUP model for high altitude catchments, NW Himalaya's. Model Earth Syst Environ 8(1):1203–1213. https://doi.org/10.1007/s40808-021-01145-0
17. Osei MA, Amekudzi LK, Wemegah DD, Preko K, Gyawu ES, Obiri-Danso K (2019) The impact of climate and land-use changes on the hydrological processes of Owabi catchment from SWAT analysis. J Hydrol Reg Stud, 25https://doi.org/10.1016/j.ejrh.2019.100620
18. Pai DS, Sridhar L, Rajeevan M, Sreejith OP, Satbhai NS, Mukhopadyay B (2014) Development of a new high spatial resolution (0.25° × 0.25°) long period (1901–2010) daily gridded rainfall data set over India and its comparison with existing data sets over the region. MAUSAM 65(1):1–18
19. Sahana V, Timbadiya PV (2020) Spatiotemporal variation of water availability under changing climate: case study of the upper Girna Basin, India. J Hydrol Eng 25(5). https://doi.org/10.1061/(asce)he.1943-5584.0001890

20. Schilling KE, Jha MK, Zhang YK, Gassman PW, Wolter CF (2008) Impact of land use and land cover change on the water balance of a large agricultural watershed: historical effects and future directions. Water Resour Res 45(7). https://doi.org/10.1029/2007WR006644
21. Son NT, le Huong H, Loc ND, Phuong TT (2022) Application of SWAT model to assess land use change and climate variability impacts on hydrology of Nam Rom Catchment in Northwestern Vietnam. Environ Dev Sustain 24(3):3091–3109. https://doi.org/10.1007/s10668-021-01295-2
22. Srivastava AK, Rajeevan M, Kshirsagar SR (2009) Development of a high resolution daily gridded temperature data set (1969–2005) for the Indian region. Atmos Sci Lett 10(4):249–254. https://doi.org/10.1002/asl.232
23. Wang Y, Jiang R, Xie J, Zhao Y, Yan D, Yang S (2019) Soil and water assessment tool (SWAT) model: a systemic review. J Coast Res 93(sp1):22–30. https://doi.org/10.2112/SI93-004.1. Coastal Education Research Foundation Inc.
24. Zhang H, Wang B, Liu DL, Zhang M, Leslie LM, Yu Q (2020) Using an improved SWAT model to simulate hydrological responses to land use change: a case study of a catchment in tropical Australia. J Hydrol 585. https://doi.org/10.1016/j.jhydrol.2020.124822

Simulating Flood Exposure Due to Meteorological Extremes in GWMC

S. Vinay, D. Sai Manideep, P. Yeshwanth, and C. H. Saishivaram

Abstract Hazard assessment and forecasting are vital for enhancing the resilience of a region. The current research communication integrates Synthetic Aperture Radar and Multispectral Remote Sensing Satellites to determine the extent and exposure of floods in Greater Warangal Municipal Corporation (GWMC). GWMC is located in the tropical semi-arid zone and is characterized by a hot and dry climate and witnesses an average annual rainfall of 863 mm. Warangal was considered under the smart city mission of India in 2015, in this process of transformation urban areas are expanding at the cost of agrarian landscapes. Assessment of land use between 2016 and 2022 in GWMC indicates the built-up spaces that have increased from 11.50% to over 20.25% promoting local climatic modifications. Changing global climate has led to meteorological extremes, in the last decade maximum intensity ~200 mm/day in August 2020 was observed in GWMC. Flood inundation ranging from 58.39 to 107.82 km^2 was observed with discrete precipitation events such as ranging from 100 to 200 mm/day. Exposure maps show that 6.5 km^2 to 11.4 km^2 area under built-up spaces and about 50–95 km^2 of cultivable landscapes are inundated due to floods. With the exiting trends in landscape and climate changes, hazard exposure tends to increase causing a negative impact on human livelihood. The analysis also aids in developing action plans, enabling appropriate policies to ensure the sustenance of society and the regional ecosystem.

Keywords Meteorological extreme · GWMC · Land use · Smart city · Flood exposure

S. Vinay (✉) · D. S. Manideep · P. Yeshwanth · C. H. Saishivaram
Department of Civil Engineering, SR University, Warangal, India
e-mail: vinay86169@gmail.com; s.vinay@sru.edu.in

S. Vinay
Civil Engineering, Alvas Institute of Engineering and Technology, Moodbidri, India

S. Dutta and V. Chembolu (eds.), *Recent Development in River Corridor Management*,
Lecture Notes in Civil Engineering 376, https://doi.org/10.1007/978-981-99-4423-1_17

1 Introduction

Extreme meteorological events pose tremendous pressure on the community at regional to global scales [2]. With global warming and changing climatic patterns, the frequency of severe precipitation events is increasing leading to loss of habitat, disrupting livelihood, increasing societal imbalance, and affecting the sustainability of the region. In other words, the hydrological cycle is disrupted by global warming and climatic changes [39] which has led to meteorological and hydrological extremes.

Intense precipitation events are intensifying globally due to cyclones or convective currents. According to the global disaster database [9] , in the last 120 years about 16,462 natural disasters have been recorded of which about 31%, i.e., 5186 are meteorological disasters and 40%, i.e., 6518 are hydrological disaster (Fig. 1). A total of 10,308 storms and floods have occurred globally of which 521 are observed in India with 317 floods and 204 storms. Floods in India are increasing at a rate of 12 per decade (Fig. 2) due to increased intensity of precipitation, climate change, and landscape dynamics [15, 31].

Flow regimes (flow rates, flow duration, peak flows) are key drivers for lotic, lentic, and dependent ecosystems that are governed by climate (meteorology), vegetation (landscape), geology, soil, topography, catchment physical characteristics, and human interventions [29, 36]. The changes in climate alter precipitation intensities and durations influence the regime [13], higher rainfall intensities will increase the peak discharge and runoff volumes in the catchment, thereby increasing floods [22, 30]. In addition to climatic patterns, land use modification influences the flow characteristics in the riverscape. Alterations in the land use at the global or local level either through natural or cultural (anthropogenic forces can alter the functioning capability of landscape that has a direct influence on the hydrological cycle, viz., changes in precipitation pattern, surface and subsurface flow regime, evaporation, transpiration,

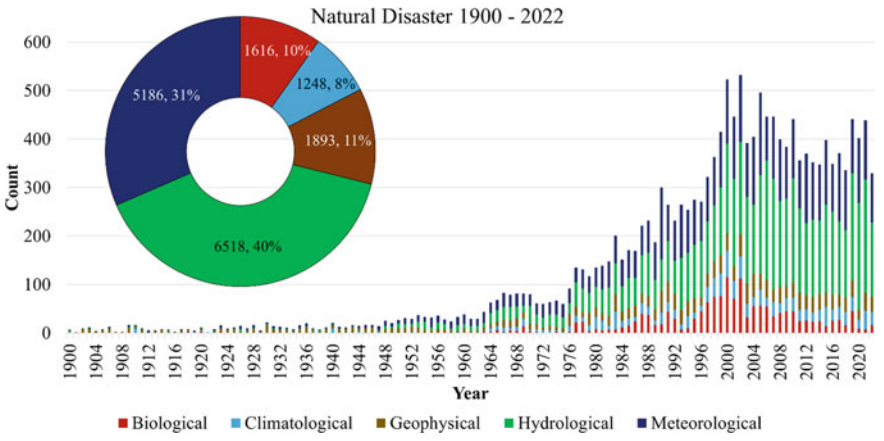

Fig. 1 Global natural disasters

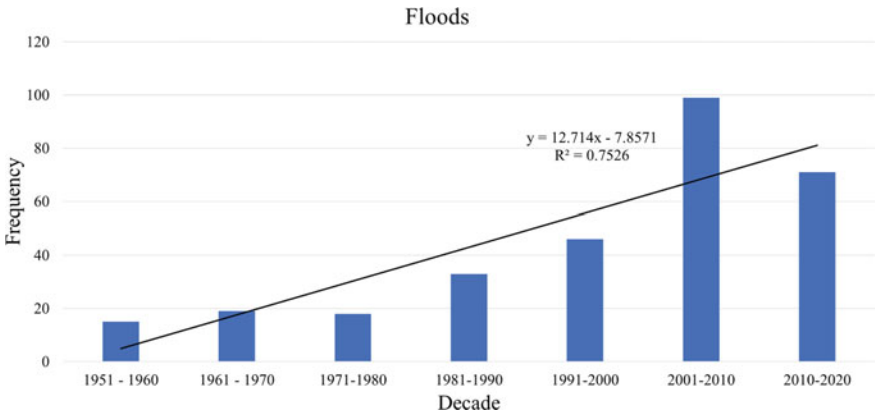

Fig. 2 Floods in India

infiltration, etc. [33, 44]. Figure 3 depicts the influence of land use modifications on flow characteristics [5, 7].

The ever-growing concerns and demand for natural resources have led to unabated alterations in the landscape over time leading to an imbalance in the ecosystem. The modifications in the landscape triggering and escalating natural hazards/disasters over space and time can be visualized using Remote Sensing data and Geospatial tools.

Remote Sensing and GIS technologies have evolved with innumerable applications at a global scale. The process of Remote Sensing involves acquiring, processing, and interpreting data to derive information about an object/area/phenomenon [20]. The term "geographic information system" (GIS) refers to a collection of programs used in tandem with a spatial database to accomplish the tasks such as collecting, storing, retrieving, transforming, relating, and displaying for a particular set of purposes. GIS is multidisciplinary, it involves database management systems, mathematical operations, modeling abilities, involving bio-geo-physical chemical-climatic, and other aspects [32].

Integrating the advances in the geospatial technologies with very high-resolution remote sensing data, viz., Synthetic Aperture Radar and Multispectral Satellite data enables one to (i) quantify and visualize land use change patterns, (ii) identify inundation exposures, (iii) derive terrain, (iv) analyze the likely risk as a result of floods. Numerous using physical, mathematical, predictive models, agent-based models, regression models, rule-based models [8, 11, 28, 35],) have been used globally to identify, model, simulate and predict the land use changes, shoreline dynamics.

In addition the regional climate changes, flood exposures are fueled by the socioeconomic drivers viz., population density, assets, and value of economic activities over time [45]. In the absence of risk mitigation strategies/measures and control over regional development, unabated socioeconomic developments can lead to tragic scenarios. Studies indicate that the absence of any such measures would increase the flood risk by 20 folds by 2100 [34]. Recognizing exposures and impacts of disasters

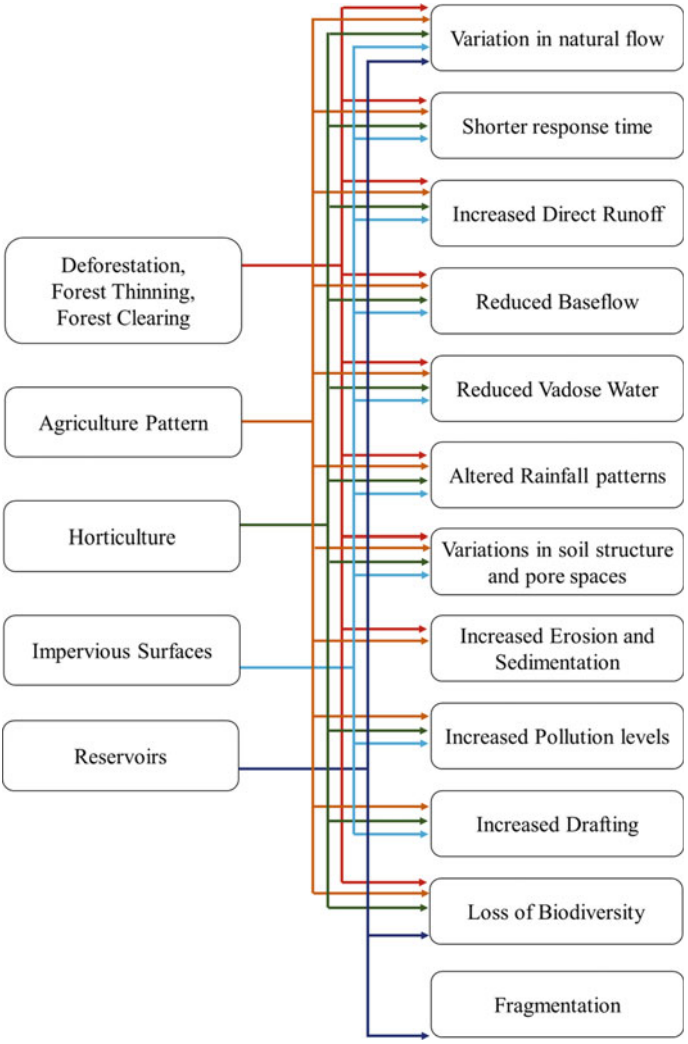

Fig. 3 Influence of land use modifications on riverscape characteristics

are essential for the societal well-being and need to be carried out at regional scales in the developing countries.

Both the disaster management report 2011 and Vulnerability Atlas [3] (BMTPC, 2019) of India, both emphasize on the regions and their habitats, resources exposure toward flooding. According to the global and national frameworks [12, 17, 26, 42], mapping and anticipating hazard intensities, exposures, vulnerabilities, and forecasting risks are essential for understanding the nature of risks. This helps to reduce risks, by improving the response patterns, and coping capacity through

sustainable adaptive planning and mitigative measures, viz., ecosystem, societal, or infrastructure-based approaches.

The current communication uses Geospatial abilities to simulate the expanses of exposure due to floods caused by varied rainfall intensities at a daily scale in Warangal, one of the three smart cities in the state of Telangana [21] so as to provide insights to reduce the flood exposures through appropriate management strategies.

2 Study Area

Greater Warangal Municipal Corporation (GWMC) is located in the state of Telangana, India (Fig. 4). Extending between 17.869° N to 18.105° N and 79.432° E to 79.678° E, GWMC has an area of 408.33 km^2 with 58 Wards [19]. Agro-climatically, GWMC is situated in the Central Telangana Zone i.e., in the Deccan Interiors. Climate is hot and dry with temperatures swaying between just below 10 degrees Celsius to over 46 degree Celsius between 1982 and 2022 in winter and summer [24]. On an average GWMC receives rainfall of 863 mm, increasing at a rate of 2.7 mm per year. In the last decade highest rainfall intensity of 200 mm per day was observed in the month of August 2020 [18]. Region is dominated by Red Soil, followed by calcareous and black soils supporting Paddy, Cotton. Topographically the region is relatively flat, located about 250 m above mean sea level, due to which a large number of interconnected lake systems were created to cater to the regional water needs. With water drafted from Godavari, Warangal caters about 168 MLD of water catering to a population of over 10 lakh people (estimated). The population in GWMC has increased by 32% in the last two censused decades (2001 and 2011) [27]. Being second largest city in Telangana state, Warangal was considered as Smart city in the year 2015–16 [21], post which large-scale developments are taking place in the city. This development has enabled population influx leading to rampant changes in landscapes, i.e., from agrarian to paved. Warangal witnessing the unprecedented high intensity of rainfall, with the current growth in population and the city would increase the risks toward meteorological disasters, necessitating to visualize the landscape modifications and influence of extreme meteorological events, with a focus on Sustainable Development Goals [41].

3 Methodology

The method involved in evaluating flood exposures is depicted in Fig. 5. The method involves five phases, (i) Data collection, (ii) Land use analysis, (iii) Precipitation analysis and scenario development, (iv) Inundation mapping, and (v) Flood exposure analysis [38].

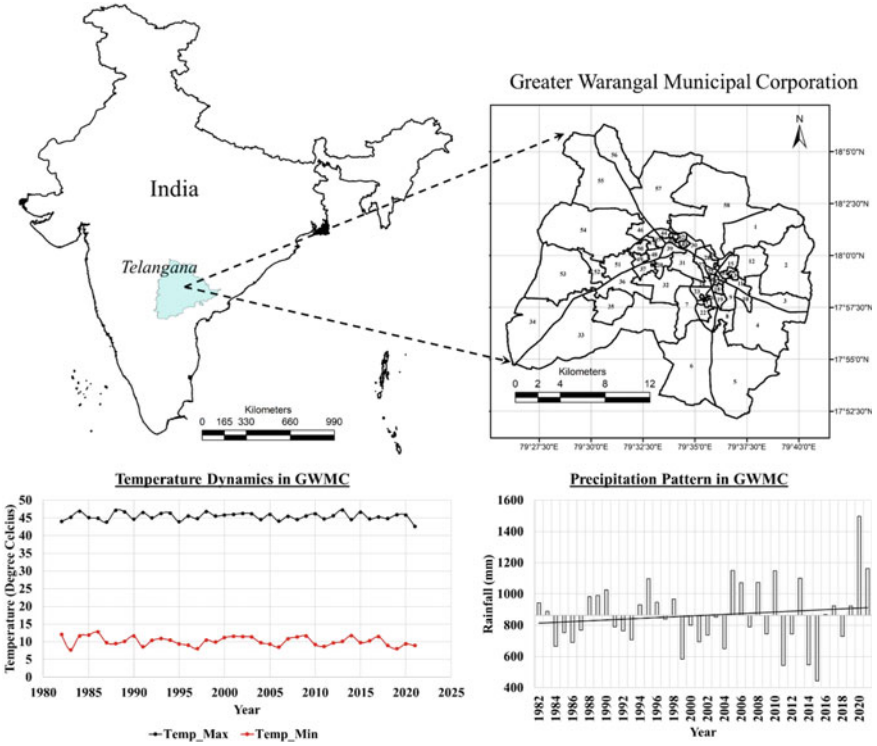

Fig. 4 Study area Greater Warangal Municipal Corporation with plots of climate variables

3.1 Data Collection

Data to understand and visualize flooding and its effects on society were obtained from various sources. The administrative data, i.e., Ward boundaries were obtained from the state web portal [19], Daily rainfall data were downloaded from Indian Meteorological Department [16] and from the Telangana Open Data Portal [18]. The daily rainfall data were used to determine the anomalies according to which the SAR data were downloaded [1, 10]. Sentinel 2 data from ESA across two time periods were collated, i.e., for the year 2016 and 2022 to visualize the changes in landscape after Warangal as Declared as Smart City in 2015–16. Virtual satellite data such as Google earth [14] and Bhuvan [25] were used to identify various land use features to train the machine learning algorithm to classify the satellite data into various land use classes. SAR data due to its cloud penetration potential was used to determine the extent of flooding. SAR data were downloaded on the day or next day of extreme events to capture the original extent of inundation.

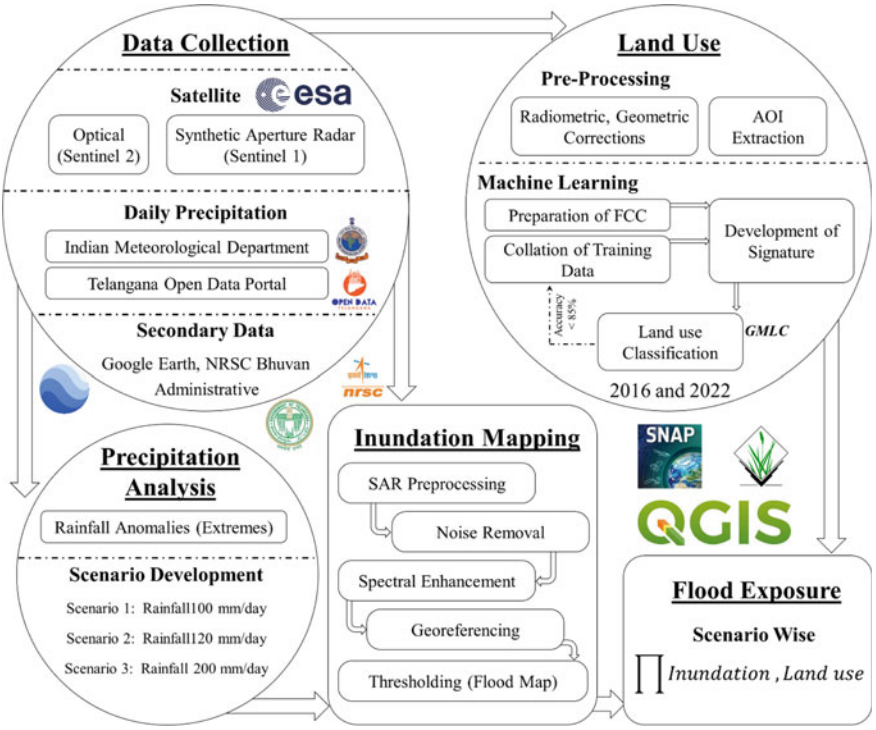

Fig. 5 Method involved to model flood exposure

3.2 Land Use Analysis

Temporal land use analysis is carried out using machine learning tools based on the knowledge gained from field investigations and virtual earth data. The land use was classified into four level one classes, viz., Built-up, Water, Vegetation, and Others. Built-up class typically considers all paved surfaces such as buildings and roads, while vegetation contains all areas containing current sown agriculture lands, grasslands, scrub jungles, avenue trees, plantations, and others class consists of barren lands, rocky outcrops, sand, current fallow agriculture lands. Water class includes all waterscapes, viz., canal, stream, river, lakes, and ponds.

The training sites were delaminated in Google earth covering about 15% of the study area, of which 60% were used for training the algorithm to classify land use and 40% for accuracy assessment. Machine learning algorithm, viz., Gaussian Maximum Likelihood Classifier (GMLC) algorithm has been extensively used [4] to categorize the satellite data into various landscapes based on the spectral reflectance characteristics. GMLC was used to classify temporal satellite data, accuracy assessment was carried out using Kappa statistics [20]. If the accuracy of the classified data was less than 85% additional training sites were used and the program was rerun.

Due to extreme cases where the classifier failed to categorize (particularly at mining sites), visual image interpretation techniques were used and overlaid on the classified outcomes in order to ensure the actual ground information is reflected on the classification outcomes.

3.3 Precipitation Analysis

Daily rainfall databases were acquired for three stations, namely, Hanamkonda, Kazipet, and Warangal from IMD and the state open data portal for the past 10 years. This was only to ensure that the SAR data would be available (note: SAR data from Sentinel 1A/B is available post-2012). The data were checked for inconsistencies, viz., missing data or erroneous data, and rectified using mass curves [22]. Daily data were analyzed for rainfall extremes and the data pertaining to rainfall over 100 mm/day were considered. These dates of extreme precipitation events were used to download the SAR datasets.

Three scenarios were developed based on the extreme rainfall intensities

1. Scenario 1 (Sc1): Rainfall intensity is about 100 mm/day. These rainfall events are common and have a return period of 2 years.
2. Scenario 2 (Sc2): Rainfall intensity is about 120 mm/day. These rainfall events are rare and have a return period of three to four years from June 2021 to July 2018.
3. Scenario 3 (Sc3): Rainfall intensity is about 200 mm/day. These are extreme rainfall events, the last reported was in August 2020.

3.4 Inundation Mapping

Sentinel 1 data was processed using SNAP tool box [10], to map flood [6] using a standard protocol. The step involves preprocessing that includes radiometric calibration of data, followed by noise removal. The preprocesses data was georeferenced and thresholding was carried out to identify water and moisture. The process was carried out for all the select data during rainfall events (Scenarios 1, 2, and 3), The difference in water bodies arrived based on land use analysis carried out using Sentinel 2 data and the extent of water spread based on the three different scenarios provides the exact extent of flooding.

3.5 Flood Exposure Analysis

Flood exposure [23] defines the extent of land that gets inundated and is having influence on the assets, society, and livelihood. Analyzing flood exposure entitles

delineating flood hazard extent and aggregating the intersecting society and assets across the space [40, 43].

4 Results and Discussions

4.1 Land Use Analysis

The Spatio-Temporal Land use changes between the years 2016 and 2022 are shown in Fig. 6. The result shows an increase in built-up area from 12.71% in 2016 to 21.39% in 2022. The waterbodies are increased from 1.63% in 2016 to 3.53% in 2022 due to a higher amount of rainfall in the past 2–3 years, leading to an increase in groundwater level and higher crop yield. Vegetation has increased from 48.82% in 2016 to 58.21% in 2022 because of higher antecedent annual rainfall in the previous years. Others (including the cultivation lands, barren lands, open lands, mines, hilly areas, etc.) have changed from 36.81% in 2016 to 16.85% in 2022 due to high vegetation and urbanization. Overall accuracy was found to be over 90% for both the land use classification and the kappa was just over 0.85

Ribbon development was seen in along Hasanparthy, Kazipet, Mamnoor, and Gorrekunta areas. In the areas such as Gopalpur, Madikonda, Rampur, Bhattupally, Deshaipet, Ayyappa Colony, and Chintagattu, showed the tendency of urban sprawl where the agricultural landscape was being converted to new layouts. Due to the National Highway 163 that was recently laid from Rampur to Mulugu Road, (via Devannapet, Unikicherla, Palvelpula, Reddypuram) proximal areas are getting urbanized and can be explained by the ribbing and leapfrog development. The core urban areas in Hanmakonda, Warangal, and Kazipet are getting more compacted (infilling) and expanding radially (edge growth).

4.2 Flood Inundation and Exposure

Figure 7 depicts flood inundation maps across three scenarios, viz., Scenario-1 rainfall intensity 100 mm/day, Scenario-2 rainfall intensity 120 mm/day, Scenario-3 rainfall intensity 200 mm/day. In Scenario-1, the area inundated is 5389 Hectares followed by 6842 Hectares in Scenario-2. Less deviations were observed between the two scenarios as the variation in rainfall intensity is about 20 mm. In Scenario-3 about 10,782 Hectares of landscapes get inundated. The inundations in GWMC are due to the local topography, land use, and less porous soils (Clayey).

Exposure is defined mathematically as the intersection of land use and flood inundation evaluated across the three observed flood maps (Fig. 7). In the first scenario, i.e., rainfall intensity of 100 mm/day 6.58 km^2 of built-up spaces are exposed to flooding, followed by vegetation and other landscape encompassing 51.8 km^2

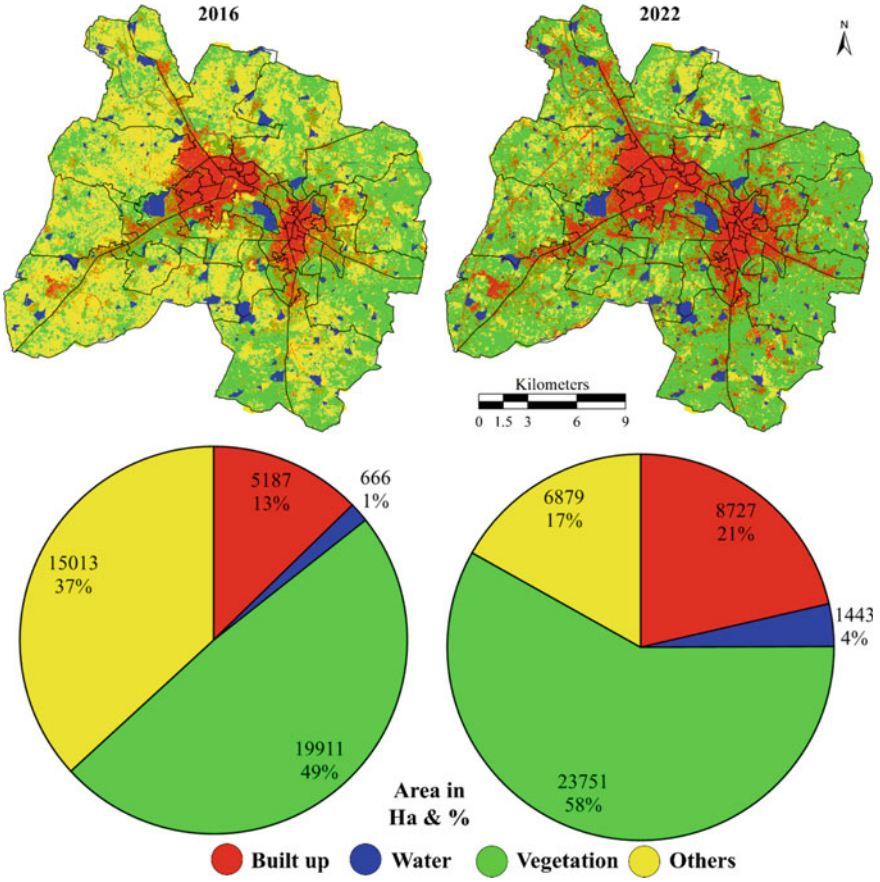

Fig. 6 Land use dynamics in GWMC

exposed to flooding. Similarly in scenario 2 an area of 7.56 km^2 of built-up spaces has been exposed in addition to this 60.5 km^2 of agrarian and other landscapes are exposed to flood. For an extremely severe and rare events such as 200 mm/day flash floods have been reported, due to which an area of 11.42 km^2 of built-up spaces are exposed to flood, additional 96.4 km^2 of agrarian on other landscapes would inundate and are exposed to flood conditions. The above three scenarios are applied to the land use of 2022, further, there is a large scope for simulating the relative land use changes and climate changes and deriving hazard risk maps at the regional scale ensuring the NDMA, and Sendai objectives are met.

SENDAI framework 2015–2030 emphasizes on reducing the risks caused by natural disasters through effective management based on global targets defined by the SDG (Sustainable Management Goals), i.e., (i) reducing mortalities and morbidity, (ii) reducing loss of infrastructure, services, and economy, (iii) increasing the resilience through local disaster risk reduction strategies, (iv) improving early

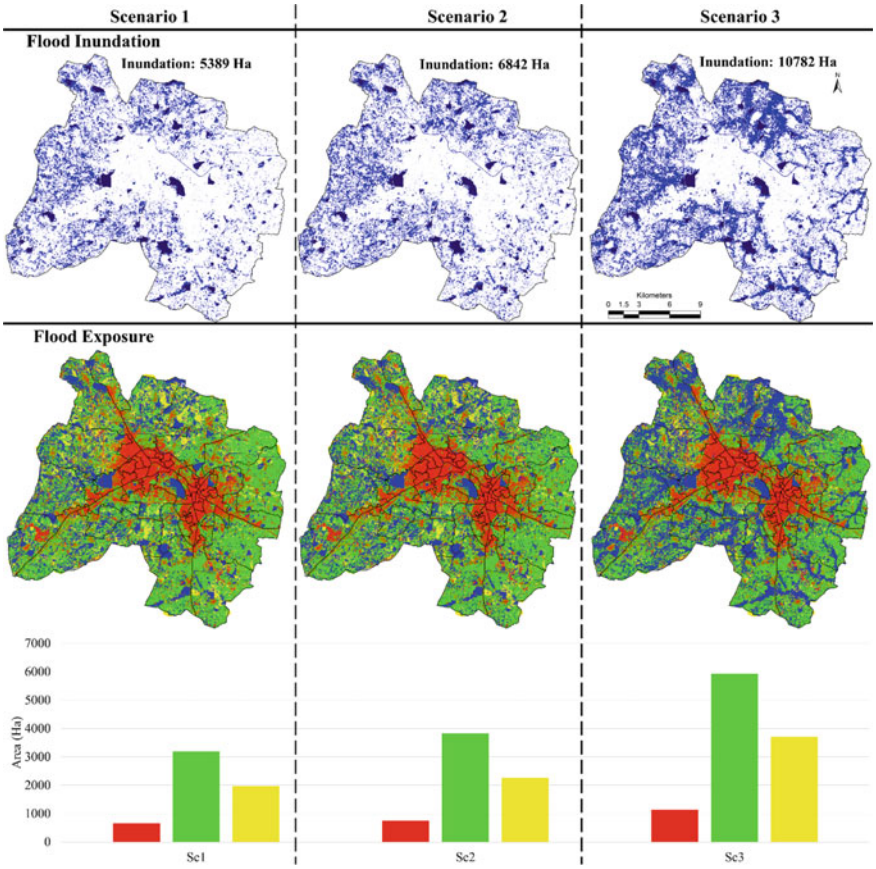

Fig. 7 Flood expanses and exposure in GWMC

warning systems and assess ability toward disaster risk information. Some of the disaster risk reduction and adaption measures [26, 42] are (i) Anticipating Risks, Reducing exposure and vulnerability; Multi-dimensional Iterative learning; Protect, Retreat and Accommodate people, habitat, environment; Capacity Building; Mapping Hazard exposure and risk; Identifying alternate livelihood and source of food; Conserving, restoring river, lake beds, interconnectivity and drainage systems; Recognizing importance and protecting lentic and lotic ecosystems; providing amenities (motorable roads, health facilities. Addition to this accounting the ecosystem services in the region would persuade the regional authorities to maintain and rejuvenate the ecosystem [37].

The population in GWMC is increasing at a rate of 32% per decade. The population in the year 2022 is estimated to be just over 10 lakhs with a density of 2450 persons per km^2. With the same rate of growth, population density by 2041 would be 4247 persons per km^2. With increasing climatic extremes, population, and paved surfaces,

aided by the clayey nature of soils, and flatter terrain, the risk toward flood hazards is likely to increase. This necessitates the Master Plan 2041 to consider the future likely flood risks and taking the advantage of the floods to rejuvenate the surface (lakes) and subsurface (groundwater) waters through appropriate policy measures, also the regional government needs to have prior preparedness strategies to abate risks caused by flooding, viz., (i) suitable laws and regulations, (ii) training, (iii) infrastructure, (iv) communication, (v) dedicated disaster management cell with financial support, (vi) zonation, etc.

The current communication aids simulate the likely flood risk, this enables the local community, governance and decision-makers to understand the spatial expanses of flood and predict the exposures. This enables to develop region-specific strategies for effective management.

5 Conclusion

The deterioration of global climatic conditions has resulted in the increase in the frequency and rate of disasters occurring in India. Meteorological extremes causing hydrological disasters, particularly floods are increasing at an alarming rate of 12 per decade in India.

Located in the hot-semi-arid zone, Warangal is the second largest city in the state of Telangana and is one of the smart cities. The increase in population flux, followed by societal demands has led to large-scale alterations of the regional lotic, lentic, and agricultural ecosystem. This can be explained by the increasing built-up spaces from 12% in 2016 to 21% in 2021 within GWMC at the cost of 40 km^2 of agrarian landscapes. The changes in regional climate and landscapes have paved the way for flooding, catalyzing the process of erosion and sedimentation in the surface water bodies. In the last 1.5 years, field investigations show that few spells of precipitation would rampantly fill up the lakes indicating large volumes of silt being deposited. Further land use assessment also indicated an increase in greenspaces and water bodies. This can be attributed to the antecedent rainfall events in 2021 and 2020, followed by a selection of small-scale irrigation projects and major irrigation projects such as the Kaleshwaram Lift Irrigation project, due to which the current sown agriculture lands and water bodies have increased.

Analysis of rainfall events with respect to daily precipitation intensity indicates 100 mm/day as an annual event while 120 mm/day repeats in 2 to 4 years and 200 mm/day was the highest recorded in the last decade (2012–2022). Accordingly, three different scenarios were developed. SAR data was used to visualize flooded areas in GWMC. With varying inundation extents, the assets and people exposed to hazard varies. In the first scenario, i.e., about 5839.69 hectares get submerged of which 658 hectares of Built-up spaces and 3203 hectares of Vegetated spaces get inundated. Likewise in the scenario there are about 10,782 hectares, i.e., 25% of GWMC is inundated of which 1142 hectares of built-up and 5937 hectares of agriculture spaces get exposed to floods.

In the current article, we integrate mapping flood inundation exposures by considering land use change, demographics, and climate. This would aid in anticipating the effects of hazards and helps the local administration and planning authorities to plan and reduce the damages, mortalities due to hazard at the regional scale through appropriate planning and management interventions that are well-matched to the ecosystem ensuring that the Sendai framework, COP 21/26 goals are met, and the city become both smart and sustainable.

Acknowledgements We are grateful Alaska Satellite Facility, European Space Agency, United States Geological Survey, Google Earth for providing data for analysis, SR University and SRU Workstation Laboratory for infrastructure facility and support.

References

1. Alaska Satellite Facility (2018) Vertex: ASF's data portal. https://www.asf.alaska.edu/doi/palsar-documents-tools/
2. Ali H, Modi P, Mishra V (2019) Increased flood risk in Indian sub-continent under the warming climate. Weather Clim Extrem 25:100212. https://doi.org/10.1016/j.wace.2019.100212
3. Anandha Kumar KJ, Walia A, Chaturvedi S (2012) India disaster report 2011. https://nidm.gov.in/PDF/pubs/IndiaDisasterReport2011.pdf
4. Bharath HA, Ramachandra TV (2016) Visualization of urban growth pattern in Chennai using geoinformatics and spatial metrics. J Indian Soc Remote Sens 44(4):617–633. https://doi.org/10.1007/s12524-015-0482-0
5. Brown C, King J (2003). Environmental flows: concepts and methods. In: Water resources and environment: technical note C.1., 1st ed. The World Bank. http://documents.worldbank.org/curated/en/828931468315285821/pdf/263200NWP0REPL1Concepts0and0Methods.pdf
6. Carreño Conde F, de Mata Muñoz M (2019) Flood monitoring based on the study of sentinel-1 SAR images: the ebro river case study. Water 11(12):2454. https://doi.org/10.3390/w11122454
7. Debortoli NS, Dubreuil V, Hirota M, Filho SR, Lindoso DP, Nabucet J (2017) Detecting deforestation impacts in Southern Amazonia rainfall using rain gauges. Int J Climatol 37(6):2889–2900. https://doi.org/10.1002/joc.4886
8. Dhiman R, VishnuRadhan R, Eldho TI, Inamdar A (2019) Flood risk and adaptation in Indian coastal cities: recent scenarios. Appl Water Sci 9(1):5. https://doi.org/10.1007/s13201-018-0881-9
9. EM-DAT (2022) The international disaster database. CRED. https://public.emdat.be/
10. ESA (2022) Copernicus open access hub. European space agency. https://scihub.copernicus.eu/dhus/#/home
11. Feloni E, Mousadis I, Baltas E (2020) Flood vulnerability assessment using a GIS-based multicriteria approach—the case of Attica region. J Flood Risk Manag 13(S1). https://doi.org/10.1111/jfr3.12563
12. FEMA (2018) Floods and floodplain management. https://www.fema.gov/pdf/floodplain/nfip_sg_unit_1.pdf
13. Georgakakos A, Fleming P, Dettinger M, Peters-Lidard C, Richmond T, Reckhow K, White K, Yates D (2014) Climate change impacts in the United States. Third Natl Clim Assess 69–112. https://doi.org/10.7930/J0G44N6T.On
14. Google (2020) Google earth. https://www.google.com/intl/en_in/earth/
15. Halder S, Parekh A, Chowdary JS, Gnanaseelan C (2022) Dynamical and moist thermodynamical processes associated with Western Ghats rainfall decadal variability. Npj Clim Atmos Sci 5(1):8. https://doi.org/10.1038/s41612-022-00232-y

16. Indian Meteorological Department (2020) Hydrometeorological services. Ministry of earth sciences government of India. http://www.imd.gov.in/pages/services_hydromet.php
17. IPCC (2012) Managing the risks of extreme events and disasters to advance climate change adaptation. In: Intergovernmental panel on climate change.https://doi.org/10.1017/cbo9781139177245
18. IT E&C (2022) Telangana open data platform. Information technology, electronics & communication department (IT E&C), Government of Telangana. https://data.telangana.gov.in/
19. Kakatiya Urban Development Authority (2022, Nov 11) Master plan 2041. Government of Telangana. https://gwmc.gov.in/masterplan2041.aspx
20. Lillesand TM, Kiefer RW, Chipman JW (2004) Remote sensing and image interpretation. In: Lloydia Cincinnati, 7th ed. Wiley. http://www.osti.gov/energycitations/product.biblio.jsp?osti_id=6028047
21. Ministry of Housing and Urban Affairs, & Government of India (2015) Smart cities mission. smartcities.gov.in
22. Mutreja KN (1995) Applied hydrology, 4th ed. Tata McGraw-Hill
23. Narendr A, Das S, Vinay S, Bharath HA (2020) Adaptive capacity assessment for a flood vulnerable region through land use modelling and socio economic and physical indicators. J Environ Inform Lett. https://doi.org/10.3808/jeil.202000031
24. NASA (2022) NASA prediction of world energy resources. The power project. https://power.larc.nasa.gov/data-access-viewer/
25. National Remote Sensing Centre (2016) Bhuvan. Indian space research organisation, Government of India. http://bhuvan.nrsc.gov.in/
26. NDMA (2020) National disaster management authority. Ministry of home affairs, Government of India. https://ndma.gov.in/
27. Office of the Registrar General & Census Commissioner (2011) Census of India. Ministry of home affairs, Government of India. http://www.censusindia.gov.in
28. Percival S, Teeuw R (2019) A methodology for urban micro-scale coastal flood vulnerability and risk assessment and mapping. Nat Hazards 97(1):355–377. https://doi.org/10.1007/s11069-019-03648-7
29. Poff NL, Allan JD, Bain MB, Karr JR, Prestegaard KL, Richter BD, Sparks RE, Stromberg JC (1997) The natural flow regime: a paradigm for river conservation and restoration. Bioscience 47(11):769–784. https://doi.org/10.2307/1313099
30. Raghunath HM (1985) Hydology-principles, analysis and design. Wiley Eastern Limited
31. Ramachandra TV, Bharath S (2019) Global warming mitigation through carbon sequestrations in the central western ghats. Remote Sens Earth Syst Sci 2(1):39–63. https://doi.org/10.1007/s41976-019-0010-z
32. Ramachandra TV, Bharath HA (2016) Bengaluru's reality: towards unliveable status with unplanned urban trajectory. Curr Sci 110(12):2207–2208
33. Ramachandra TV, Vinay S, Bharath S, Chandran MDS, Bharath HA (2020) Insights into riverscape dynamics with the hydrological, ecological and social dimensions for water sustenance. Curr Sci 118(9):1379–1393. https://doi.org/10.18520/cs/v118/i9/1379-1393
34. Rentschler J, Salhab M, Jafino BA (2022) Flood exposure and poverty in 188 countries. Nat Commun 13(1):3527. https://doi.org/10.1038/s41467-022-30727-4
35. Rincón D, Khan U, Armenakis C (2018) Flood risk mapping using GIS and multi-criteria analysis: a greater Toronto area case study. Geosciences 8(8):275. https://doi.org/10.3390/geosciences8080275
36. Schneider SC, Petrin Z (2017) Effects of flow regime on benthic algae and macroinvertebrates-a comparison between regulated and unregulated rivers. Sci Total Environ 579:1059–1072. https://doi.org/10.1016/j.scitotenv.2016.11.060
37. SEEA Central Framework (2012) System of environmental-economic accounting: a central framework. In: White cover publication. ST/ESA/STAT/Ser.F/109
38. Siddayao GP, Valdez SE, Fernandez PL (2014) Analytic hierarchy process (AHP) in spatial modeling for floodplain risk assessment. Int J Mach Learn Comput 4(5):450–457. https://doi.org/10.7763/IJMLC.2014.V4.453

39. Tabari H (2020) Climate change impact on flood and extreme precipitation increases with water availability. Sci Rep 10(1):13768. https://doi.org/10.1038/s41598-020-70816-2
40. Tate E, Rahman MA, Emrich CT, Sampson CC (2021). Flood exposure and social vulnerability in the United States. Nat Hazards 106(1). https://doi.org/10.1007/s11069-020-04470-2
41. UNDESA (2022) Sustainable development goals. Division for sustainable development goals
42. UNDRR (2015) Sendai framework for disaster risk reduction 2015–2030. In: UNDRR. https://www.undrr.org/publication/sendai-framework-disaster-risk-reduction-2015-2030
43. Vinay S, Narendr A, Bharath HA (2022) Forecasting and evaluation of impacts and risk due to tidal anomalies on a coastal Island. J Indian Soc Remote Sens 50(1). https://doi.org/10.1007/s12524-021-01458-8
44. Wagner PD, Bhallamudi SM, Narasimhan B, Kantakumar LN, Sudheer KP, Kumar S, Schneider K, Fiener P (2016) Dynamic integration of land use changes in a hydrologic assessment of a rapidly developing Indian catchment. Sci Total Environ 539:153–164. https://doi.org/10.1016/j.scitotenv.2015.08.148
45. Winsemius HC, Aerts JCJH, van Beek LPH, Bierkens MFP, Bouwman A, Jongman B, Kwadijk JCJ, Ligtvoet W, Lucas PL, van Vuuren DP, Ward PJ (2016) Global drivers of future river flood risk. Nat Clim Chang 6(4):381–385. https://doi.org/10.1038/nclimate2893

Identifying the Potential Impacts of Climate Change on Streamflow in a Humid Tropical Basin

Alka Abraham and Subrahmanya Kundapura

Abstract The preservation of ecosystems in a river is based upon the replication of its original pristine conditions in the river regime. One of the main variables influencing a region's hydrology is climate change. The research investigated the impact of climate change on the streamflow within the Meenachil River basin located in Kerala, India. The present study employed the Soil and Water Assessment Tool (SWAT) model to simulate the hydrological processes of the basin. The calibration and validation of the model are done, and the model performance is determined considering the Nash Sutcliffe Efficiency (NSE), coefficient of determination (R^2), and percentage bias (PBIAS), and it is observed to be good. The data for the future climate are taken from National Aeronautics and Space Administration (NASA) Earth Exchange Global Daily Downscaled Projections (NEX-GDDP) data for Representative Concentration Pathway (RCP) 4.5. The response of streamflow to the climate in the future time period (2025–2099) is evaluated by considering three scenarios, S1, S2, and S3, with reference to a baseline scenario. In order to analyze the impact of climate change in the basin, the high and low flow indices (Q5 and Q95) of the scenarios under consideration are established using the flow duration curve of annual streamflow. Q5 showed a reduction of 20, 8.3, and 1.6% for the considered scenarios compared to the baseline period. The low flow index, Q95, showed an increase of 9.8, 15.3, and 15.1% in the scenarios concerning the baseline period. The findings of the present study will aid in developing adaption techniques for improved basin-wide management of water resources.

A. Abraham (✉)
Department of Water Resources and Ocean Engineering, National Institute of Technology Karnataka, Mangaluru 575 025, India
e-mail: alka.ezrin@gmail.com

Department of Civil Engineering, Mar Athanasius College of Engineering, Kothamangalam, Kerala, India

S. Kundapura
Faculty of Water Resources Engineering, Department of Water Resources and Ocean Engineering, National Institute of Technology Karnataka, Mangaluru 575 025, India
e-mail: subrahmanyakundapura@nitk.edu.in

S. Dutta and V. Chembolu (eds.), *Recent Development in River Corridor Management*, Lecture Notes in Civil Engineering 376, https://doi.org/10.1007/978-981-99-4423-1_18

Keywords Climate change impact · SWAT model · Flow duration curve · Flow indices

1 Introduction

Water is a valuable natural resource and the basis of all other natural resources [10]. The environmental protection and sustainable growth of an area are highly dependent on its water resources [5]. At global, regional, and local levels, climate change is seen as a key factor impacting the availability and quality of water [8]. Increasing temperatures since the middle of the twentieth century may be directly attributed to the warming effects of increased quantities of greenhouse gases, which have been documented across the climate system. The intricate interdependence of the worldwide climate system is underscored by the fact that forthcoming climatic conditions and their impacts on ecological systems are contingent upon not only greenhouses gas emissions but also economic status and developmental strategies [14]. The extent of these alterations will be contingent upon forthcoming human activities alongside technological and economic advancements [15]. It is expected that climate change and the subsequent increase in atmospheric CO_2 concentration will have an impact on hydrological systems across the globe [14].

The phenomenon of climate change can disrupt the typical hydrological processes, potentially resulting in significant consequences for the water resources of a region [6]. Any changes in the distribution of climate variables affect surface water and water vapor circulation [17]. This indicates that the implications of climate change give rise to various adverse impacts on society [11]. Climate change directly affects the hydrology cycle, triggering a cascade of effects that affect, among other things, agriculture, energy, and ecology. Assessing how climate change may affect local and regional water supplies comes first before designing mitigating efforts. The topic of climate change has been the subject of extensive research in numerous large-scale watersheds worldwide. Further investigation is necessary to evaluate the influence of climate change on watersheds at a more localized level. Implementing improved water management strategies can be facilitated through this approach [11].

Studies on the effect of climate change on water resources, especially at the catchment scale, are important as the developmental activities of the region depend on these resources [6, 12]. The most advanced tools for predicting climate variability and changes are General Circulation Models (GCM) [7]. To examine the consequences of climate change, GCM models are most often used to analyze the manner in which various scenarios will affect hydrological systems. To perform an effect assessment at the basin size, we downscale the GCM's global-scale simulation to the basin scale [17]. The Coupled Model Intercomparison Project (CMIP) of the World Climate Research Programme (WCRP) has produced GCMs that serve as valuable instruments for comprehending the mechanisms of historical climate and predicting potential future climate alterations based on hypothetical emission scenarios [14]. The coarser scale GCM simulations are scaled down to a finer scale, and simulations

under different emission scenarios are incorporated in impact assessments [17]. The need for hydrologic models to understand the effects of the changing climate on the water balance is growing. Climate, Soil, and Land use land cover (LULC) are just a few examples of the critical inputs required to run hydrologic models. The incorporation of climate data is a crucial factor in determining the output of computer models' simulations. The climate projections necessary for conducting climate research are obtainable at a less detailed resolution from various GCMs. However, to utilize these data in hydrologic simulations, it must be refined at the Regional Climate Model (RCM) level. The conversion of data from GCMs to RCMs necessitates the implementation of bias correction and downscaling techniques. Future climate data resolution and simulation accuracy are critical for the success of climate change research evaluation [11]. The most common method for impact assessment is to drive a hydrological model with GCM outputs [12, 14].

This research investigates the effects of climate change on the hydrology of the Meenachil basin in Kerala, India. To simulate the climate change effects in the research, the SWAT hydrological model is used. Possible applications of these findings include improved water resource management and implementing measures to mitigate the regional impact of climate change.

2 Methodology

2.1 Study Area

The Meenachil Basin (Fig. 1) in Kerala, India's southernmost state, is selected for study. This is a west-flowing river, which discharges into Vembanad Lake before flowing onto the Arabian Sea. The Western Ghats mountain range defines the basin's eastern border. The Meenachil River originates at Araikunnumudi, which is located at an elevation of 1097 MSL; the basin's drainage area is 1272 km^2. The study area has a hot and humid climate. The southwest monsoon, which lasts from the month of June to September, contributes to the majority of the region's rainfall and is followed by the northeast monsoon, which continues from October to November. The region receives around 3000 mm of rain on average each year, and the temperature falls between 17 and 37 °C. The region gets sufficient rainfall during the monsoon yet experiences water shortages throughout the summer.

2.2 Dataset

The inputs to hydrological modeling include Digital Elevation Model (DEM), climate data, soil map, hydrological data, and LULC maps. The ASTER DEM of 30 m resolution and the Food and Agriculture Organization (FAO) soil map is used in the study.

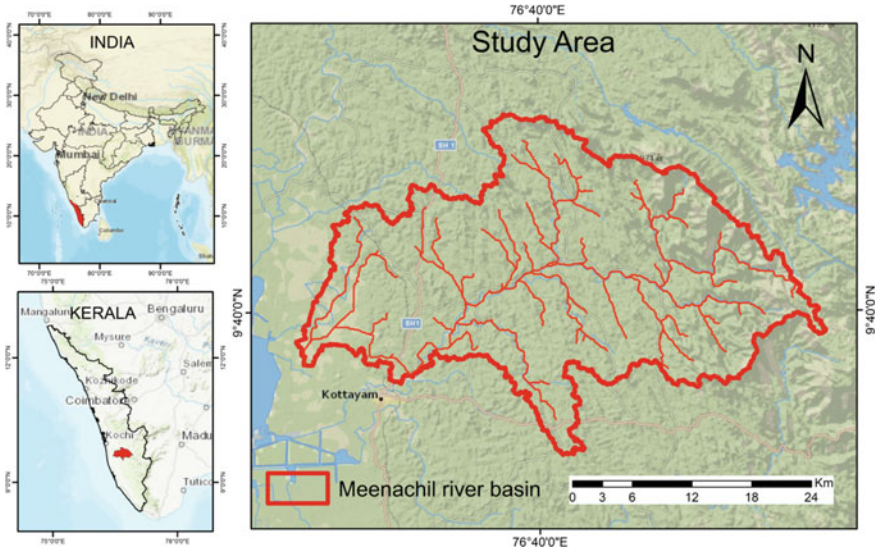

Fig. 1 Location of the study area

The Landsat satellite imagery is extracted from the Google Earth Engine platform and classified with a Random Forest algorithm to prepare the study's LULC map [3]. India Meteorological Department (IMD) gridded rainfall, maximum and minimal temperatures, as well as NASA power grid data for solar radiation, relative humidity, and wind speed, serve as the climatic data for the historic period. The NEX-GDDP dataset of resolution $0.25° \times 0.25°$ under the emission scenario RCP 4.5 is considered for the future. The models (Table 1) are considered based on ranking for selecting a suitable subset of GCM [2]. For future precipitation, the ensemble mean of MIROC-ESM-CHEM (Model for Interdisciplinary Research on Climate Earth system models CHASER-coupled version), MIROC-ESM (Model for Interdisciplinary Research on Climate Earth system models), BCC-CSM1-1 (Beijing Climate Center Climate System Model. Version 1) and NorESM1-M (Norwegian Earth System Model, Intermediate Resolution) is taken. The ensemble mean of MIROC-ESM-CHEM, MIROC-ESM, MPI-ESM-MR (Max Planck Institute Earth System Model at the mixed resolution version), and MPI-ESM-LR (Max Planck Institute Earth System Model at the low-resolution version) are employed for maximum temperature, whereas for minimum temperature, the models MIROC-ESM-CHEM, MRI-CGCM3 (Meteorological Research Institute coupled atmosphere–ocean general circulation model 3), BNU-ESM (Beijing Normal University Earth System Model), and MIROC-ESM are applied. The streamflow data collected from the Central Water Commission (CWC), India website are used in model calibration and validation.

Table 1 GCMs considered in the study [2]

Model	Modeling institution
BNU-ESM	Institute of Global Change and Earth System Sciences, Beijing Normal University, China
MIROC-ESM MIROC-ESM-CHEM	Atmosphere and Ocean Research Institute, Japan
MPI-ESM-LR MPI-ESM-MR MRI-CGCM3	Max Planck Institute for Meteorology, Germany
NorESM1-M	Norway Consumer Council, Norway
BCC-CSM1-1	Beijing Climate Centre, China

2.3 Hydrological Modeling with SWAT

Streamflow is a crucial component of the hydrologic cycle, and alterations in precipitation and evapotranspiration brought about by climate change can significantly impact streamflow [18]. The interconnections and associations between flow regimes and ecosystems hold significant value in forecasting the reactions of riverine ecosystems to global transformations. Additionally, they aid watershed managers in identifying efficacious strategies to sustain the equilibrium of riverine and wetland ecosystems. Environmental alterations exert a direct influence on the hydrological mechanisms of a watershed, thereby affecting its flow dynamics. Distributed hydro-ecological models have proven to be efficacious instruments for examining the impacts of alterations in water flow on riverine ecosystems. These models have limits in forecasting riverine ecosystem responses to environmental changes such as climate change, LULC, and water and soil management for conservation methods such as the implementation of vegetation filter strips, agricultural management practices such as alterations in fertilizer application methods, and rules governing water retention structures. Enhancing the predictive capabilities of said models regarding low flow has emerged as a prevalent issue among hydrological and hydro-ecological communities [20].

The hydrological processes in the research basin are simulated using the SWAT model [4]. The division of the watershed into sub-basins is followed by a further subdivision into Hydrologic Response Units (HRUs), which take into consideration the regional variation based on LULC and soil. The land phase and the routing phase make up the majority of the SWAT modeling of the hydrologic cycle. Water, nutrients, sediments, and pesticide loadings for each HRU are first calculated during the land phase. Sub-basin loadings are then calculated by adding the loads from all HRUs located within that sub-basin. The sub-basin major channel is loaded with the resultant sediment [20]. The hydrological processes in the model are determined by the water balance calculation, which serves as the governing equation. The soil conservation service (SCS) curve number (CN) approach is used in the model to determine the surface runoff from a watershed [19] and is determined as

$$Q_{\text{surf}} = \frac{(R_{\text{day}} - 0.2S)^2}{(R_{\text{day}} + 0.8S)} \tag{1}$$

where 'Q_{surf}' is the surface runoff in mm, 'R_{day}' is the precipitation in mm, and 'S' is the potential maximum retention. The methodological framework of the study is shown in Fig. 2.

The model is calibrated and validated by the use of the SUFI-2 in SWAT CUP [1]. The model's efficacy in modeling streamflow is evaluated with a coefficient of determination (R^2), Nash–Sutcliffe efficiency (NSE), and Percent Bias (PBIAS). The mathematical expression for determining the performance indicators is as follows:

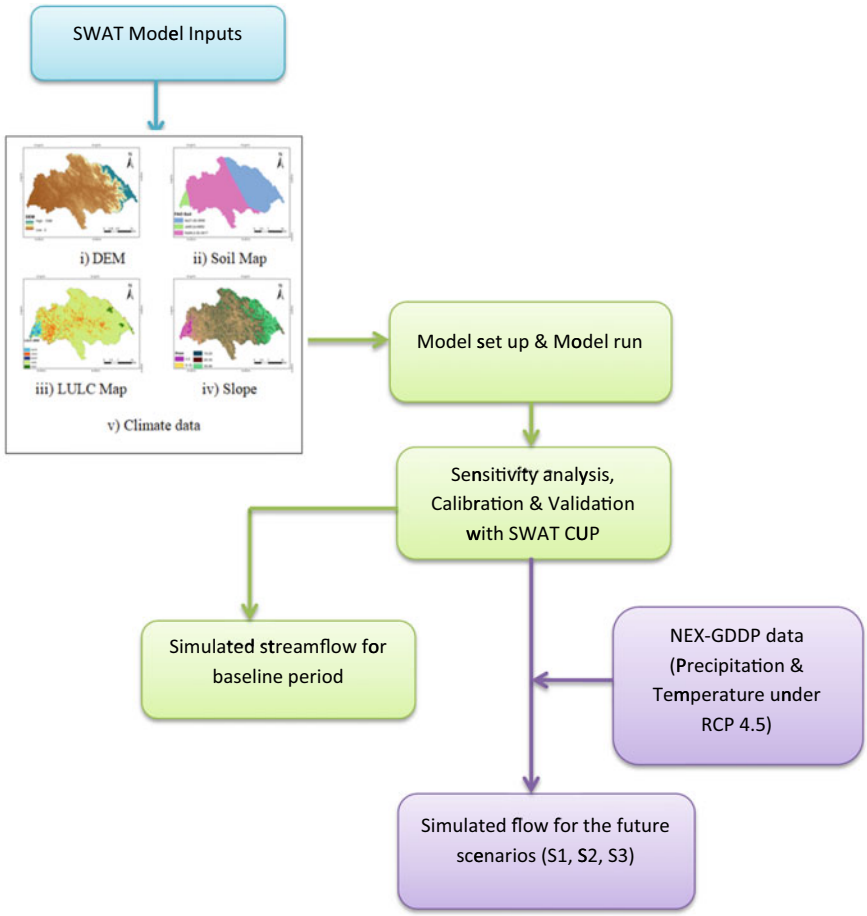

Fig. 2 The methodological framework of the study

$$R^2 = \frac{\sum_{i=1}^{n}\left(Q_{\text{obs}} - \overline{Q_{\text{obs}}}\right) * \left(Q_{\text{sim}} - \overline{Q_{\text{sim}}}\right)}{\sqrt{\sum_{i=1}^{n}\left(Q_{\text{obs}} - \overline{Q_{\text{obs}}}\right)^2} * \sqrt{\sum_{i=1}^{n}\left(Q_{\text{sim}} - \overline{Q_{\text{sim}}}\right)^2}} \tag{2}$$

$$\text{NSE} = 1 - \frac{\sum_{i=1}^{n}\left(Q_{\text{sim}} - Q_{\text{obs}}\right)^2}{\sum_{i=1}^{n}\left(Q_{\text{obs}} - \overline{Q_{\text{obs}}}\right)^2} \tag{3}$$

$$\text{PBIAS} = \frac{\sum_{i=1}^{n}\left(Q_{\text{sim}} - Q_{\text{obs}}\right)}{\sum_{i=1}^{n} Q_{\text{obs}}} \tag{4}$$

where Q_{obs} and $\overline{Q_{\text{obs}}}$ are the observed and the average streamflow; Q_{sim} and $\overline{Q_{\text{sim}}}$ are the simulated flow and the mean simulated flow, respectively. The variable 'n' represents the quantity of data points related to the flow. Several researchers have utilized the model to examine the hydrological events at the river basin scale [5–8, 14, 16].

3 Results and Discussion

3.1 Future Climate in the Study Area

The expected changes to the climate variables, maximum and minimum temperature, and precipitation are determined (Fig. 3) by considering the baseline period from 1991 to 2015. Three-time slices are selected from the future, P1 (2025–2049), P2 (2050–2074), and P3 (2075–2099). The three-time slices exhibited a rise in the mean annual, monthly, and seasonal temperatures compared to the baseline period. The mean annual maximum temperature rises by 1.4%, 3%, and 4.4%, respectively. The minimum temperature showed a higher increase with a 6, 9, and 11% rise compared to the baseline. The mean temperature showed the highest value during the Pre-monsoon season (April). At the end of the century, it is anticipated that the percentage change in the maximum and minimum temperature will be significant in the time slice P3. The warming climate expected in the future increases the susceptibility to drought in the region [16]. Also, temperature rise accelerates the hydrological cycle, which leads to changes in the timing and quantity of rainfall and runoff in the area [10]. The average annual precipitation for the future scenarios is found to be less compared to the baseline scenario by 9%, 27%, and 10%, respectively, suggesting a decrease in rainfall in the basin. Monthly analysis reveals that there is a reduction in precipitation during the monsoon months, June and July, whereas there is an increase during August and September. The pattern of seasonal precipitation is likewise similar, with the exception of winter, where the precipitation is found to be increasing compared to baseline scenario.

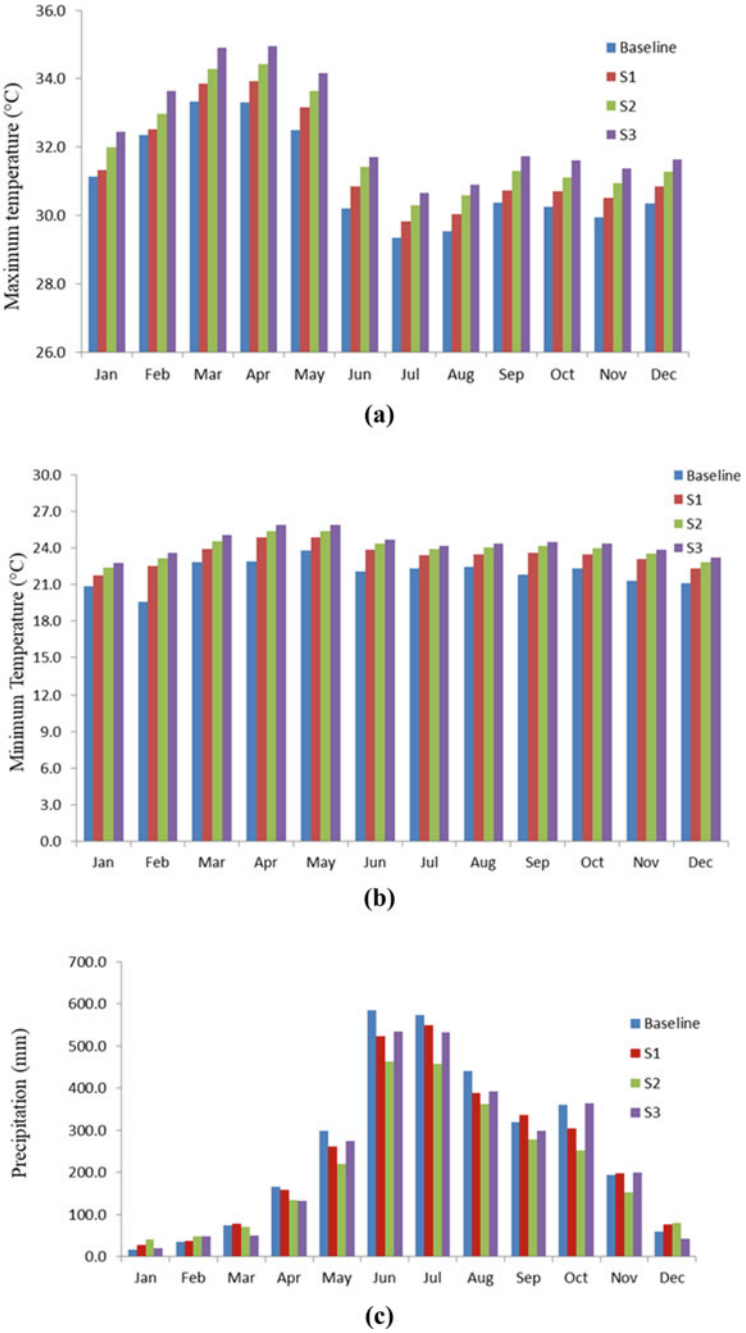

Fig. 3 Monthly variation of climate variables in the study basin: **a** Maximum temperature (°C), **b** Minimum temperature (°C), **c** Precipitation (mm)

3.2 Model Calibration and Validation

Before beginning the calibration process, the sensitivity analysis is taken into consideration. The SUFI 2 technique included in SWAT CUP is used for calibration and validation of the SWAT model. The parameters for sensitivity analysis are selected based on previous literature. The rank obtained for the selected parameters after sensitivity analysis is shown in Table 2. The most critical parameter is found to be SCS-CN (SCS curve number for moisture condition II), followed by SOL_BD (Moist bulk density), ESCO (Evaporation compensation factor), and other parameters. The SWAT model is calibrated for streamflow using historical climate data and LULC for the year 2000. The observed monthly flow at the gauging station, Kidangoor, during (1988–2001) is used for calibration, and (2009–2015) is used for validation. The R^2 and NSE values obtained are greater than 0.8, and PBIAS within $\pm 10\%$ for calibration as well as validation (Table 3). From the validation, it is found that satisfactory results are obtained in the simulation of the streamflow in the Meenachil basin (Fig. 4).

The climate change impact is further studied with the calibrated validated model. The simulated streamflow from 1991 to 2015 is considered a baseline scenario. The future time period from 2025 to 2099 is considered in three-time slices to generate three scenarios, S1, S2, and S3. Scenario S1 indicates simulated streamflow from

Table 2 Parameters considered and ranks obtained in hydrological modeling

Parameters	Lower limit	Upper limit	Fitted value	t-stat	Rank
r__CN2.mgt	−0.2	0.2	−0.18	6.75	1
r__SOL_BD().sol	0	1	0.65	4.989	2
v__ESCO.hru	30	450	166.69	2.217	3
v__CANMX.hru	0	2	1.78	1.055	4
v__GWQMN.gw	0	500	147	0.828	5
v__REVAPMN.gw	−0.25	0.25	0.036	0.719	6
v__GW_REVAP.gw	−0.25	0.25	0.306	0.151	7
r__SOL_Z().sol	−0.25	0.25	−0.0167	0.1172	8
v__EPCO.hru	−0.25	0.25	−0.13	0.1088	9
r__SOL_K().sol	0	1	0.235	0.1013	10
v__GW_DELAY.gw	0	1	0.61	0.0746	11
r__SOL_AWC().sol	0	50	4.1	0.0646	12
v__ALPHA_BF.gw	0	0.2	0.18	0.0374	13

Table 3 Performance of the hydrological model during calibration and validation

Evaluation criteria	R^2	NSE	PBIAS
Calibration	0.84	0.84	5.5
Validation	0.82	0.82	3.0

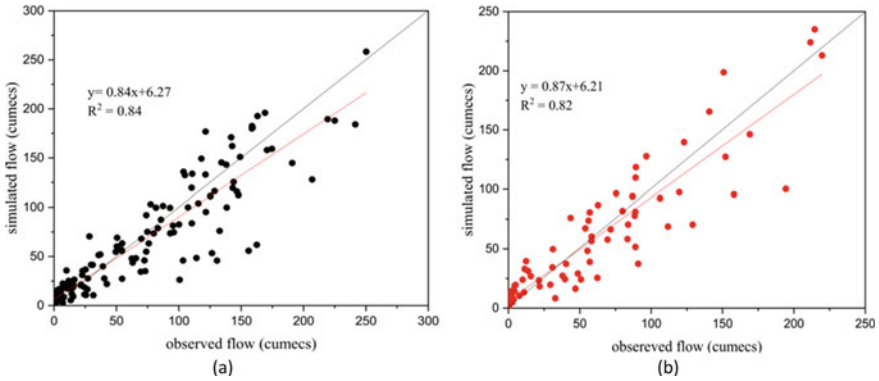

Fig. 4 Scatter plot of simulated versus observed monthly streamflow during **a** calibration and **b** validation

2025 to 2049, S2 for 2050 to 2074, and the simulated streamflow in the period 2075 to 2099 is considered as scenario S3. For all the scenarios, the LULC for the year 2000 is taken.

3.3 Impacts of Climate Change Impact Streamflow

The climate change impact is predicted and analyzed by comparing the streamflow during the three future scenarios with the baseline. The meteorological variables considered for the model are precipitation and temperature. The future scenarios are explored using the calibrated model, and the annual flow duration curve is plotted for the baseline, S1, S2, and S3 cases (Fig. 5). This helps to understand the flow variability between the baseline and the future scenarios.

For scenarios S1, S2, and S3, the annual average streamflow is predicted to decline by 6.8%, 5.5%, and 1%, respectively, relative to the baseline. Also, the percentage changes in the low flow (Q95) and high flow (Q5) indices are evaluated in the study. Q95 is among the most common low-flow indices [9]. Watershed modeling studies need to pay greater attention to low flows since they are crucial for the biotic diversity of aquatic and riparian environments. All of the scenarios for the future predict an increase in the basin's low flows over the baseline. The percentage increase in Q95 for the considered scenarios is expected as 9.8%, 15.3%, and 15.1%, respectively, with respect to baseline. This indicates more water availability during the dry season in the area. The increase in low flow results in lowering the total discharge deficits due to the changes in climate [13]. The high flow indicators (Q5), on the other hand, indicated a significant reduction in the future. The Q95 is found with a decrease of 20, 8.3, and 1.6% compared to the baseline scenario. The patterns of stream flow in the three scenarios are similar but with differences in magnitude.

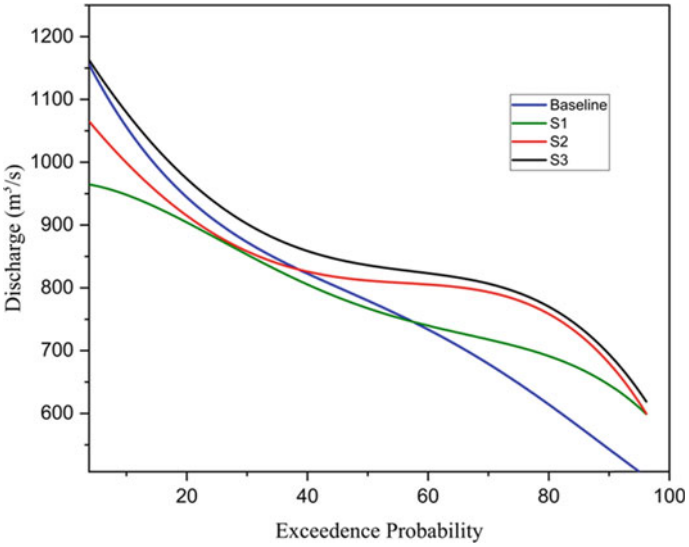

Fig. 5 Annual flow duration curve

4 Conclusion

The research findings suggest that Meenachil may experience a reduction in precipitation and an upsurge in temperature under the RCP 4.5 scenario in comparison to the baseline period that was analyzed. The study employs the SWAT model to examine the possible impacts and alterations on streamflow due to the changing climates. The annual average discharge in Meenachil is predicted to decline in all the considered future scenarios. The reduction in flow is expected to be less for the S3 scenario. The low flow indices (Q95) are found to have a rise, and high flow indices (Q5) showed a decline in the predicted scenarios compared to the baseline. The percentage reduction in the two indices is anticipated to be more in the upcoming future. The study may be useful for comprehending the effects of a changing climate in the Meenachil basin and could be taken into account when developing adaptation measures. In this research, an effort was made to determine how streamflow might respond to climate change by taking into consideration basically the moderate emission scenario. In addition, research is needed to estimate the LULC changes and the impacts of LULC changes and other emission scenarios on the hydrology of the study basin, which is the future scope of the study.

References

1. Abbaspour KC (2007) User manual for SWAT-CUP, SWAT calibration and uncertainty analysis programs. In Eawag, Duebendorf, Switzerland: swiss federal institute of aquatic science and technology. https://doi.org/10.1007/s00402-009-1032-4
2. Abraham A, Kundapura S (2022) Selection of suitable general circulation model outputs of precipitation for a humid tropical basin. In: Lecture notes in civil engineering, Vol 234, pp 417–431. https://doi.org/10.1007/978-981-19-0304-5_30
3. Abraham A, Kundapura S (2022) Spatio-temporal dynamics of land use land cover changes and future prediction using geospatial techniques. J Indian Soc Remote Sens 7. https://doi.org/10.1007/s12524-022-01588-7
4. Arnold JG, Srinivasan R, Muttiah RS, Williams JR (1998) Large area hydrologic modeling and assessment part i: model development. J Am Water Resour Assoc 34(1):73–89. https://doi.org/10.1016/S0899-9007(00)00483-4
5. Dhami B, Kumar S, Ashish H, Amar P, Gautam K (2018) Evaluation of the SWAT model for water balance study of a mountainous snowfed river basin of Nepal. Environ Earth Sci 77(1):1–20. https://doi.org/10.1007/s12665-017-7210-8
6. Fita T, Abate B (2022) Impact of climate change on streamflow of Melka Wakena catchment, Upper Wabi Shebelle sub-basin, south-eastern Ethiopia. J Water Clim Chang 13(5):1995–2010. https://doi.org/10.2166/wcc.2022.191
7. Getachew B, Manjunatha BR, Bhat HG (2021) Modeling projected impacts of climate and land use/land cover changes on hydrological responses in the Lake Tana Basin, upper Blue Nile River Basin, Ethiopia. J Hydrol 595(January). https://doi.org/10.1016/j.jhydrol.2021.125974
8. Glavan M, Ceglar A, Pintar M (2015) Assessing the impacts of climate change on water quantity and quality modelling in small Slovenian Mediterranean catchment–lesson for policy and decision makers 3144(February), 3124–3144. https://doi.org/10.1002/hyp.10429
9. Jha R, Sharma KD, Singh VP (2008) Critical appraisal of methods for the assessment of environmental flows and their application in two river systems of India. KSCE J Civ Eng 12(3):213–219. https://doi.org/10.1007/s12205-008-0213-y
10. Ketema A, Dwarakish GS (2021) Hydro-meteorological impact assessment of climate change on Tikur Wuha watershed in Ethiopia. Sustain Water Resour Manag 3.https://doi.org/10.1007/s40899-021-00547-3
11. Mehan S, Kannan N, Neupane RP, McDaniel R, Kumar S (2016) Climate change impacts on the hydrological processes of a small agricultural watershed. Climate 4(4):1–22. https://doi.org/10.3390/cli4040056
12. Pandey BK, Khare D, Kawasaki A, Mishra PK (2018) Climate change impact assessment on blue and green water by coupling of representative CMIP5 climate models with physical based hydrological model. Water Resour Manag 33(1):141–158
13. Phi Hoang L, Lauri H, Kummu M, Koponen J, Vliet MTHV, Supit I, Leemans R, Kabat P, Ludwig F (2016) Mekong River flow and hydrological extremes under climate change. Hydrol Earth Syst Sci 20(7):3027–3041. https://doi.org/10.5194/hess-20-3027-2016
14. Rashid H, Yang K, Zeng A, Ju S, Rashid A, Guo F (2022) Predicting the hydrological impacts of future climate change in a humid-subtropical watershed. Atmosphere 13(12)
15. Safeeq M, Fares A (2012) Hydrologic response of a Hawaiian watershed to future climate change scenarios. Hydrol Process 26(18):2745–2764. https://doi.org/10.1002/hyp.8328
16. Sinha RK, Eldho TI, Subimal G (2020) Assessing the impacts of land cover and climate on runoff and sediment yield of a river basin. Hydrol Sci J. https://doi.org/10.1080/02626667.2020.1791336

17. Sun JQ, Li HY, Wang XJ, Shahid S (2021) Water resources response and prediction under climate change in Tao'er River Basin, Northeast China. J Mt Sci 18(10):2635–2645. https://doi.org/10.1007/s11629-020-6635-9
18. Tan X, Liu S, Tian Y, Zhou Z, Wang Y, Jiang J, Shi H (2022) Impacts of climate change and land use/cover change on regional hydrological processes: case of the Guangdong-Hong Kong-Macao greater bay area. Front Environ Sci 9(January):1–16. https://doi.org/10.3389/fenvs.2021.783324
19. USDA-SCS (1972) (United States Department of Agriculture–Soil Conservation Service). National engineering handbook, section 4 hydrology. Chapter 4–10. USDA-SCS, Washington, USA. https://directives.sc.egov.usda.gov/OpenNonWebContent.aspx?content=18393.wba
20. Zhang D, Chen X, Yao H, Lin B (2015) Improved calibration scheme of SWAT by separating wet and dry seasons. Ecol Model 301:54–61. https://doi.org/10.1016/j.ecolmodel.2015.01.018

Changing Hydro-climatological Response of Bhadar Basin in Western India

Bhanu Parmar, Suvarna Shah, and Hiteshri Shastri

Abstract Climate change is a global issue of today's modern world. The global temperature is increasing and attaining new records with each passing year [Intergovernmental Panel on Climate Change (2018) Global warming of 1.5 °C: an IPCC special report on the impacts of global warming of 1.5 °C above pre-industrial levels and related global greenhouse gas emission pathways, in the context of strengthening the global response to the threat of climate change, sustainable development, and efforts to eradicate poverty. Intergovernmental Panel on Climate Change]. The changes in temperature affect the hydrological cycle and through changing rainfall patterns. As a result, some areas receiving more and more rainfall and experiencing flood while others have less rainfall and have to deal with drought. The increased frequency of extreme rainfall events is another noted feature of climate change. Rainfall is the key element for well-being of the people in the country like India for larger dependency on the agricultural activities. Different studies highlight significant changes in rainfall pattern over western part of India, Gujarat. The peninsular region of Gujarat, known as Saurashtra is recognized for its flashy rivers and dry hydro-geo-morphology. Bhadar is one of the major rivers of Gujarat and largest river in the Saurashtra region. The Bhadar River basin is observed to experience frequent flooding in the recent years with 2021 flood causing heavy loss in the region. This study is taken up to access system behavior and understand different hydrological processes for Bhadar River basin. Hydrological model is useful to present the real-world system in the simplified form. Here, in this study, a physically based, semi-distributed model, namely, Soil and Water Assessment Tool (SWAT) was used. The study reveals changing hydro-climatological response of Bhadar basin. Findings of this study provide useful inputs to policymakers, farmers, disaster management authorities for management and planning of water resources in the region.

B. Parmar · S. Shah
Faculty of Technology and Engineering, Department of Civil Engineering, The Maharaja Sayajirao University of Baroda, Vadodara, Gujarat, India

H. Shastri (✉)
Department of Civil Engineering, CSPIT, CHARUSAT, Charotar University of Science and Technology (CHARUSAT), CHARUSAT Campus, Changa, India
e-mail: hitesehrishastri.cv@charusat.ac.in; shastrihiteshri@hotmail.com

S. Dutta and V. Chembolu (eds.), *Recent Development in River Corridor Management*, Lecture Notes in Civil Engineering 376, https://doi.org/10.1007/978-981-99-4423-1_19

Keywords Hydro-climatological response · SWAT · Bhadar basin · Saurashtra · India

1 Introduction

Rainfall is an important element of the global circulation of the Earth's system [12]. Temporal as well as spatial pattern of precipitation is more likely to change during twenty-first century due to increase in average global temperature [9]. Hydrologic responses of most of the river basins are expected to change due to the change in climatic conditions. With this in the current century, water scarcity and flooding are projected to affect a larger percentage of the global population [5].

The increased surface temperature caused by rise in greenhouse gas concentration resulted into the increased atmospheric moisture variability. Therefore, regional precipitation variability increases and the hydrological cycle is accelerated [10]. Temperature strongly affects precipitation and evaporation, which directly influence runoff [3]. The higher surface temperature results in an increase of evaporation and enhances regional variability in characteristics of precipitation (e.g., variability, total amount, and extremes frequency), this in turn is likely to influence intensity and frequency of hydrological extremes like droughts and floods. Different components of hydrological cycle such as mean runoff, groundwater recharge, soil moisture, and availability of water for irrigation and hydroelectric generation are also affected through this.

A major consequence of future climate change will be the increase in water stress and alteration of river flows [8, 11, 13]. During monsoon season, the velocity of flow is higher in rivers having steep slope. As a result, extreme high precipitation events caused by projected climate change may result in severe flash flood condition. This condition has also been reported in India [2, 8, 14]. It is also anticipated that sea levels will rise as a result of thermal expansion of seawater and melting of ice from high latitudes and altitudes. This will have a greater impact on coastal agricultural ecosystems due to the frequent seawater intrusion and secondary salination, particularly in low-lying countries such as Bangladesh and India with a long coast line.

The influence of climate change on the surface water is evidently visible by alterations in the water level and water quality. At the same time, the potential impact on the groundwater is also of serious concern because it is widely distributed source of water supply. The change in precipitation pattern has a direct effect on the groundwater recharge while indirectly affecting the groundwater withdrawals or discharge. As a result of negative impact of climate change, modification in hydrological cycle will lead to diverse socio-economic impacts and risks [16]. For long-term management strategies and adaptation measures, a reliable assessment of potential changes in hydrological conditions is important [15].

The major purpose of hydrological modeling is to determine how a watershed responds to changes in climatic parameters, soil types, land uses, and management conditions. This in turn has important implications for water resources planning,

flood forecasting, pollution control, and many other areas [6]. After taking variety of hydrological processes (e.g. precipitation, evaporation, transpiration, groundwater, interflow etc.) into accounts, rainfall-runoff model depicts the process of creating streamflow hydrographs as a result of the surplus rainfall onto the catchment.

Soil and Water Assessment Tool (SWAT) provides computationally efficient, physically based, and capable of continuous simulation of hydrological processes over long time periods [4]. SWAT model is suitable to assess the hydrologic response of the river basin under the effect of changes in soil, land use and climate. The SWAT model functioning divides a watershed into several sub-watersheds. These sub-watersheds are then further segmented into Hydrologic Response Units (HRUs). The HRUs consist of soil characteristics, land use, and management practices.

2 Study Area

Bhadar is one of the major and longest rivers of Saurashtra region. The river originates about 26 km north-west of Jasdan in Rajkot district near Vaddi (Aniali Village) at an elevation of 261 m above mean sea level and confluence with Arabian Sea at Navibandar (Porbandar). The Bhadar River travels in the south west direction mainly in the Rajkot, Junagadh and Porbandar district with total length of 198 km. The basin lies between geographical latitudes 21° 25′ and 22° 10′ N and 69° 45′ and longitudes 71° 20′ E with drainage area of 7094 km^2 accounting for one seventh of the total area of Saurashtra. Bhadar River receives nine major tributaries; six feeding from the right (Chapparwadi, Gandali, Phopal, Utawali, Venu andMoj) and three feeding from the left (Vasavadi, Galolioand, Surwa). Thus, the river has a more extensive drainage system on right bank as compared to the left bank. The mean rainfall in basin is 625 mm. Temperature in the region during winter season varies from 4° to 15 °C. May is the hottest month in the region depicting maximum temperature variation from 40° to 45 °C (see Fig. 1).

3 Data Used

The study utilizes three different datasets, namely, station-based observed data, gridded data climate reanalysis data and satellite data. Table 1 provides the listing of the data collected for the analysis from different respective agencies.

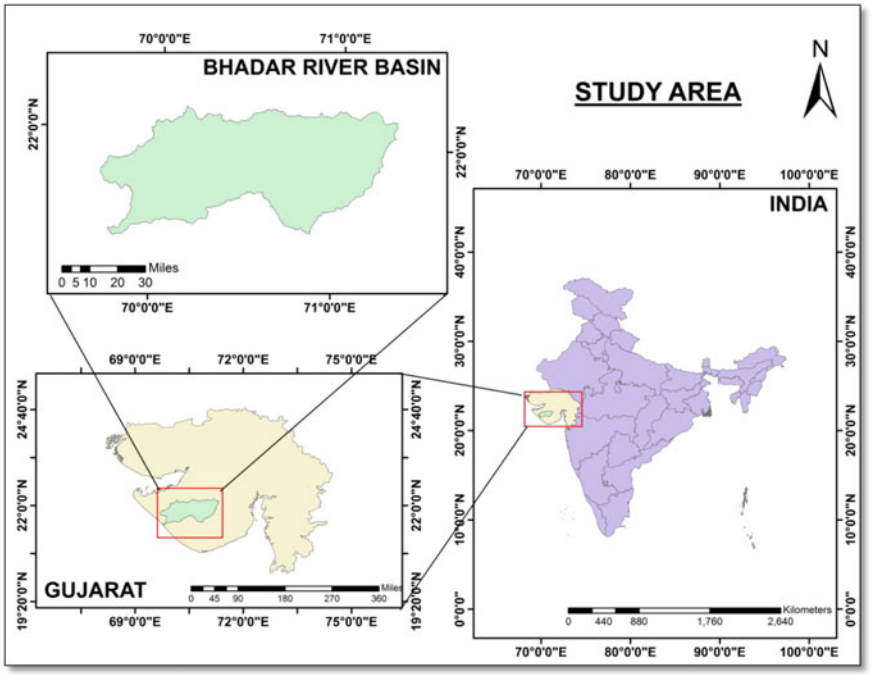

(a)

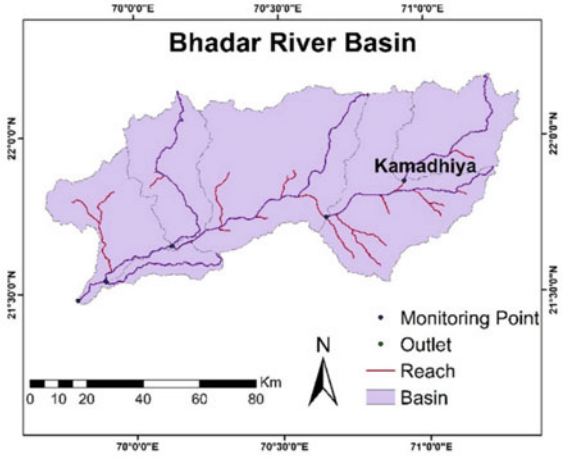

(b)

Fig. 1 **a** Location of Bhadar River Basin **b** Bhadar River Basin with Monitoring Station

Table 1 Data collection

Serial number	Data	Duration/ resolution	Source
1	Rain Gauge	1961–2020	State water data centre
2	River Gauge	1971–2020	State water data centre
3	Weather Station	2001–2020	State water data centre
4	Gridded Rainfall	1979–2021/ 0.25°X0.25°	IMD (https://imdpune.gov.in/)
5	SRTM-DEM	30 m	Earth explorer (https://earthexplorer.usgs.gov/)
6	Landuse/ landcover	2020/10 m	ESA sentinel-2 (Esri Inc.)
7	Soil Map	–	Food and agriculture organisation of united nations (https://www.fao.org/)

4 Methodology

The hydrological processes incorporated in the model are evapotranspiration (ET), infiltration, surface runoff, shallow and deep aquifer flows, percolation and channel routing [1]. As the study focused on climate change impacts on hydrology, the following equation is explained below. The following water balance equation is applied on SWAT model to represent basic hydrology of a watershed (see Fig. 2):

$$SW_t = SW_0 + \sum_{i=1}^{t} \left(R_{day} - Q_{\text{surf}} - E_a - W_{\text{seep}} - Q_{gw}\right)$$

where,

SW_t = Final soil water content (mm)

SW_0 = Initial soil water content (mm)

R_{day} = Amount of precipitation on day i (mm)

Q_{surf} = Amount of surface runoff on day i (mm)

E_{a} = Amount of evapotranspiration on day i (mm)

W_{seep} = Amount of percolation and bypass existing the soil profile bottom on day i (mm)

Q_{gw} = Amount of return flow on day i (mm).

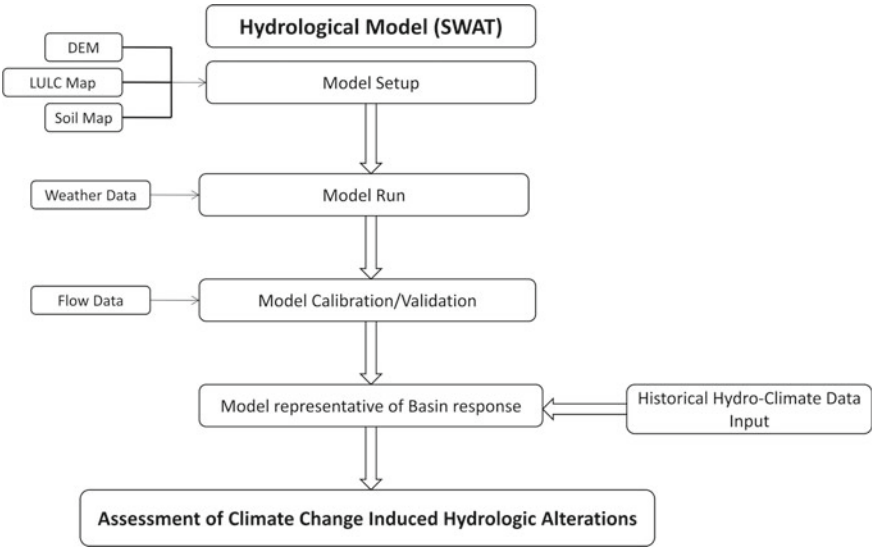

Fig. 2 Methodology flowchart

4.1 Model Evaluation Criteria

The model evaluation criteria signify how accurate a model performance is after run. It is measured relative to observed data. These are the statistical/mathematical coefficients to quantify the model performance. The most popularly used statistical validation indices, namely, Coefficient of Determination (R^2) and Nash–Sutcliffe Efficiency (NSE) are applied to determine how well hydrological model results fit with the observation. The range of coefficient of determination lies between 1 (perfect fit) and 1 (no fit at all).

$$R^2 = \left(\frac{\sum_{i=1}^{n} \left(Q_{\text{observed}} - Q_{\text{observed\_avg}}\right)\left(Q_{\text{simulated}} - Q_{\text{simulated\_avg}}\right)}{\left(\sum_{i=1}^{n} \left(Q_{\text{observed}} - Q_{\text{observed\_avg}}\right)^2 \sum_{i=1}^{n} \left(Q_{\text{simulated}} - Q_{\text{simulated\_avg}}\right)^2\right)^{0.5}} \right)^2 \tag{1}$$

where n is the number of events, $Q_{\text{simulated}}$ and Q_{observed} are simulated and observed runoff over the validation period.

NSE value ranges from 1 (best fit) to negative infinity. NSE is more stringent performance test than R^2 and is never greater than R^2. NSE observes how well the model simulated results matches with the observed data in relation to solely predicting the parameter of concern by using mean of the measured data over the evaluation time period. NSE of 0 indicates that predictive skill of model is the same as the time-series mean in terms of the sum of the squared error. Negative NSE indicates

that mean of observed data is better predictor than model simulated values, while NSE greater than 0 indicates that the model predicts measured data better than the observed mean values.

$$\mathrm{NSE} = 1 - \frac{\sum_{i=1}^{n}(Q\mathrm{measured}_i - Q\mathrm{simulated}_i)^2}{\sum_{i=1}^{n}(Q\mathrm{measured}_i - Q\mathrm{measured}_{\mathrm{avg}})^2}$$

where $Q\mathrm{measured}_i$ and $Q\mathrm{simulated}_i$ are the simulated and observed discharges at ith observation, respectively, and $Q\mathrm{measured}_{\mathrm{avg}}$ is the mean of observed data over the simulation period.

5 Results and Disscussion

For the Bhadar River, basin performance of the SWAT hydrologic model is evaluated using historical monthly streamflow data over the 20 year time period from 2001 to 2020 at the Kamadhiya River gauging station (latitude 21° 51′N, longitude 70° 55′E). The simulated and observed monthly streamflow for the calibration period at the Kamadhiya River gauging station is presented in Fig. 3. The simulation is firstly evaluated by visual examination of match between observed and predicted values. The hydrologic model results show good statistical correlation between model simulated and observed streamflow for calibration time period (2001–2014; 14 years) and also during the following validation period (2015–2020; 6 years). Average monthly flows were observed to be 10.61 m^3/s during the calibration period under the average monthly precipitation 56.47 mm. Performance measures indicate that the model is able to simulate river discharge with satisfactory level of match to the observed flow.

Figure 3 shows the observed versus simulated discharge graph at Kamadhiya gauging station during validation period. Table 2 shows the statistics summary of calibration and validation for the results using station as well as the gridded data.

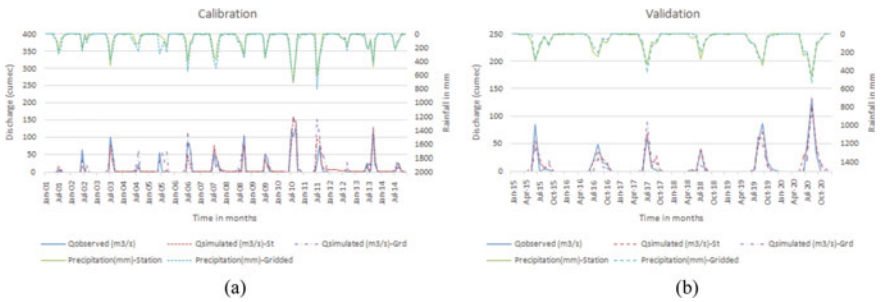

Fig. 3 Observed and SWAT Model simulated monthly total river discharge (bottom lines) along with precipitation observed with station data and gridded data (top lines) during calibration period (2001–2014) and validation period (2015–2020) for Bhadar River Basin

Table 2 Statistical indices of calibration and validation for Bhadar River Basin

Statistical Index	Station data	Gridded data
Calibration (2001–2014)		
R^2	0.76	0.75
NSE	0.74	0.59
Mean (Sim (Obs))	10.61(8.97)	13.49(8.97)
Validation (2015–2020)		
R^2	0.90	0.89
NSE	0.80	0.79
Mean (Sim (Obs))	10.13(9.51)	8.38(9.51)

The model performance is also assessed using statistical indices, NSE and R^2 in addition to graphical methods such as hydrograph. The mean flow values are calculated by comparing observed monthly flow to simulated monthly flow during the validation and calibration periods (see Fig. 4).

Overall, the performance of SWAT model is good in estimating streamflow as demonstrated by the value of coefficient of determination (R^2) 0.76 and Nash–Sutcliffe efficiency (NSE) 0.74. The model performance is evaluated over the 6 years validation period (2015–2020) following the calibration. The statistical indices for validation period are estimated as $R^2 = 0.90$, NSE = 0.89. These results show that the model performance is as good as for the calibration period. The model performance statistics for calibration and validation time period are presented in Table2. The results, therefore, confirm that calibration and validation are satisfactory and the model is successfully capturing the response of the watershed.

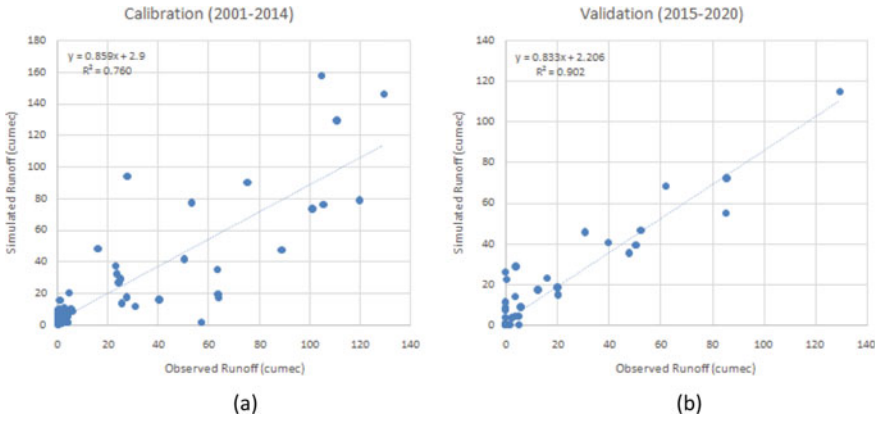

Fig. 4 Scatter plot of observed versus simulated runoff during calibration period (2001–2014) and validation period (2015–2020) for Bhadar River Basin

Table 3 Sensitive parameters of Bhadar River Basin

Serial number	Parameter	Min	Max	Best fitted value	Default value	New value
1	r__CN2.mgt	– 0.2	0.2	– 0.0676	87.06	81.174744
2	v__ALPHA_BF.gw	0	1	0.035	0.048	0.035
3	v__GW_DELAY.gw	30	450	407.579987	31	407.579987
4	v__GWQMN.gw	0	2	1.61	1	1.61
5	v__GW_REVAP.gw	0	0.2	0.1958	0.02	0.1958
6	v__ESCO.hru	0.8	1	0.8094	0.95	0.8094
7	v__CH_N2.rte	0	0.3	0.1107	0.014	0.1107
8	v__CH_K2.rte	0	500	11.125	0	11.125
9	v__ALPHA_BNK.rte	0	1	0.687	0	0.687
10	r__SOL_AWC(1).sol	– 0.2	0.4	0.1654	0.14	0.163156
11	r__SOL_K(1).sol	– 0.8	0.8	0.1424	3.16	3.609984
12	r__SOL_BD(1).sol	– 0.5	0.6	0.4031	1.5	2.10465
13	v__SFTMP.bsn	– 5	5	– 1.89	1	–1.89
14	v__SURLAG.bsn	0.05	24	21.437349	4	21.437349

Manual Calibration in SWAT:

Parameters indicating the diverse hydrological characteristics and conditions through the watershed are calibrated to physically plausible parameter values. The table of parameters is given below with fitted value and maximum and minimum range while simulation along with its default and new calibrated value. Best fit parameters are presented in Table 3. Figure 5 shows the estimation of different components of the hydrological cycle in the Bhadar River basin.

5.1 Climate Change Induced Hydrologic Alterations

The variation in river flow and other hydrologic parameters of the Bhadar River basin is shown in Fig. 6. It can be clearly observed that there is a larger fluctuation in the surface runoff as compared to the other water balance components. There is a jump in the surface runoff starting from the 2000 lasting till 2012. It is the same decade

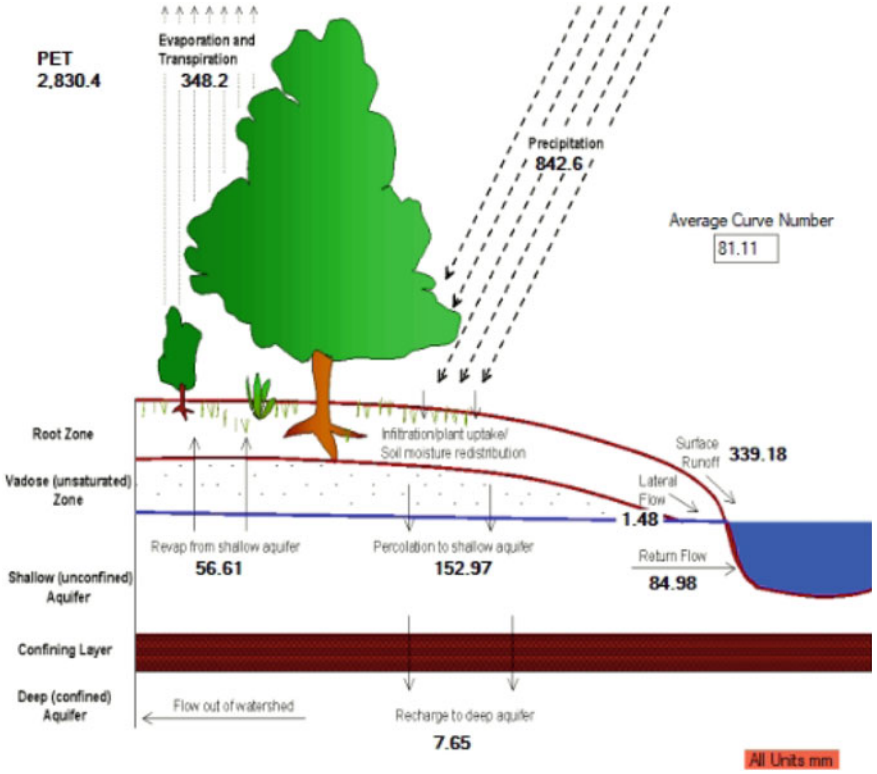

Fig. 5 Schematic diagram presenting different components of hydrologic response of Bhadar River Basin obtained by running SWAT model

for which rainfall changes its pattern. Also during this high period, two peaks were observed in the years 2005–06 and 2011–13. Percolation or groundwater recharge pattern is showing similar kind of variability as surface runoff but at a lower and smoother rate. Evaporation rate is observed less during rainfall deficient years but more or less it is uniform through the period. Also, at the end of simulation period, little rise in the rainfall-runoff pattern is observed, which may indicate starting of the rising limb.

The decade-wise variation in the hydrologic components of the Bhadar River basin is shown in Fig. 7. It can be observed that rainfall pattern has changed and also it has maximum impact on the runoff generation.

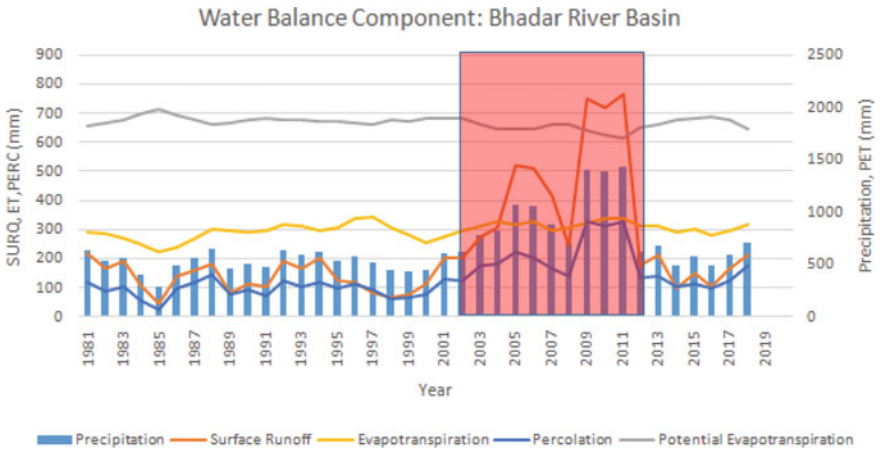

Fig. 6 Simulated water balance components namely potential evapotranspiration, percolation, evapotranspiration, surface runoff with observed rainfall (blue bars) for Bhadar River Basin, the red highlighted region shows time period of major changes in runoff condition

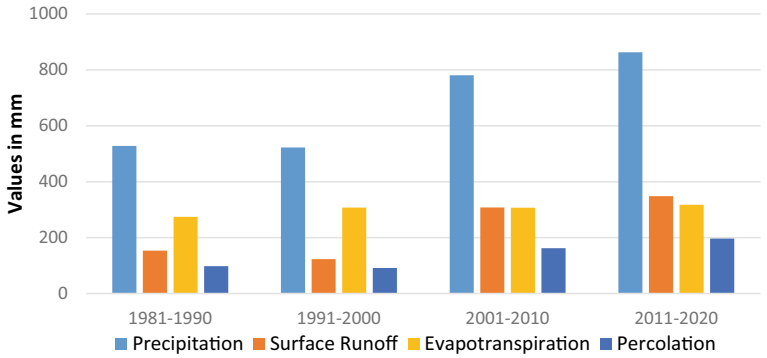

Fig. 7 Decadal average of simulated water balance components namely potential evapotranspiration, percolation, evapotranspiration, surface runoff with observed rainfall for Bhadar River Basin

As precipitation is the main driver of river flow, the variation in surface runoff, Evapotranspiration and percolation are plotted along with the change in annual precipitation. Decade wise percentage change in annual precipitation considering the reference decade as 1981–1990, for the three decades viz. 1991–2000, 2001–2010 and 2011–2020 is shown in Fig. 8. In the last three decades, precipitation has been increased by 63% and the result of SWAT model indicated that surface runoff increases by 126%.

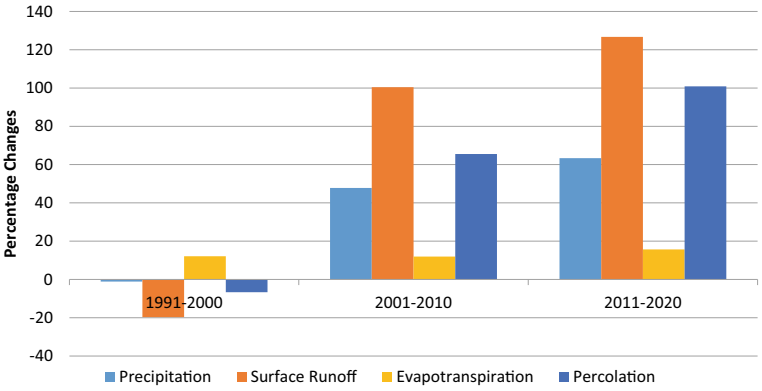

Fig. 8 Same as Fig. 7 but for percentage changes in water balance components

6 Conclusion

Assessing the impact of climate change on hydrologic alterations is crucial for depicting for the vulnerability of the water resources are of the great concern to the hydrologists, water manager and policy makers. The physically based semi-distributed SWAT model was capable of satisfactorily simulating the monthly flow of Bhadar River basin of Saurashtra Region.

The impact of climate change on hydrological variables in the Bhadar River basin has been studied using the Soil and Water Assessment Tool (SWAT). The model performance was tested for monthly flow at Kamadhiya gauging station under 14-year calibration (2001–2014) and 6-year validation period (2015–2020). The model results indicate satisfactory precision in fitting observed and simulated flow using various acceptable statistical indices. Result shows that SWAT model performs well with good R^2 (0.7583—calibration and 0.9021—validation) and NSE (0.9). The main objective of the present research is to study hydrological aspects such as runoff, evapotranspiration and percolation of the sub-basins. This research will contribute to the evaluation and planning water management policies and strategies under future climate conditions. This result may contribute to enhance the understanding of climate change and its induced hydrological alterations on water balance components in the region, which may finally facilitate the improvement of water management practices.

Acknowledgements Authors are thankful to State Water Data Centre, Gujarat for providing the required observational data to conduct the present study.

References

1. Arnold JG, Srinivasan R, Muttiah RS & Williams JR (1998) Large area hydrologic modeling and assessment part I: model development 1. JAWRA J Am Water Res Assoc 34(1):73–89
2. Carling PA, Leclair SF (2019) Alluvial stratification styles in a large, flash-flood influenced dryland river: the Luni River, Thar Desert, north-west India. Sedimentology 66(1):102–128
3. Frederick KD, Major DC (1997) Climate change and water resources. Clim Change 37(1):7–23
4. Gassman PW, Reyes MR, Green CH, Arnold JG (2007) The soil and water assessment tool: historical development, applications, and future research directions. Trans ASABE 50(4):1211–1250
5. Giupponi C, Gain AK (2017) Integrated water resources management (IWRM) for climate change adaptation. Reg Environ Change 17(7):1865–1867
6. Hendrickx JM, Walker GR (2017) Recharge from precipitation. In: Recharge of phreatic aquifers in (semi-) arid areas. Routledge, pp 19–111
7. Intergovernmental Panel on Climate Change (2018) Global warming of 1.5 °C: an IPCC special report on the impacts of global warming of 1.5 °C above pre-industrial levels and related global greenhouse gas emission pathways, in the context of strengthening the global response to the threat of climate change, sustainable development, and efforts to eradicate poverty. Intergovernmental Panel on Climate Change
8. Pallavi R, Rekha Rani K, Shashikanth K, Rajasekhar P & Shashtri H (2023) Intricate flood flow advancement modelling in the Krishna River Sub Basin, India. ISH J Hydraulic Eng 29(2):199–208
9. Loo YY, Billa L, Singh A (2015) Effect of climate change on seasonal monsoon in Asia and its impact on the variability of monsoon rainfall in Southeast Asia. Geosci Front 6(6):817–823
10. Oki T, Kanae S (2006) Global hydrological cycles and world water resources. Science 313(5790):1068–1072
11. Palmer MA, Reidy Liermann CA, Nilsson C, Flörke M, Alcamo J, Lake PS, Bond N (2008) Climate change and the world's river basins: anticipating management options. Front Ecol Environ 6(2):81–89
12. Schneider C, Laizé CLR, Acreman MC, Flörke M (2013) How will climate change modify river flow regimes in Europe? Hydrol Earth Syst Sci 17(1):325–339
13. Misra S, Sarkar S, Mitra P & Shastri HK (2022) Statistical downscaling of high resolution precipitation in India using convolutional long short term memory networks
14. Thomas J, Joseph S, Thrivikramji KP, Abe G, Kannan N (2012) Morphometrical analysis of two tropical mountain river basins of contrasting environmental settings, the southern Western Ghats, India. Environ Earth Sci 66:2353–2366
15. Wood EF, Roundy JK, Troy TJ, Van Beek LPH, Bierkens MF, Blyth E, Whitehead P et al (2011) Hyperresolution global land surface modeling: Meeting a grand challenge for monitoring Earth's terrestrial water. Water Resour Res 47(5)
16. Yang D, Yang Y, Xia J (2021) Hydrological cycle and water resources in a changing world: a review. Geogr Sustain 2(2):115–122

Mapping of Flood-Inundated Urban Regions Using Sentinel-1 SAR Imagery for the 2018 and 2019 Kerala Floods

K. S. S. Parthasarathy and Subrahmanya Kundapura

Abstract Floods are a common natural calamity causing an immense impact on the natural and human ecosystems around the world. A combination of unfavorable meteorological, hydrological, and physical conditions causes it. The study area is the Vembanad Lake System in Kerala, India comprising six watersheds: Periyar, Muvattupuzha, Meenachil, Manimala, Pamba, and Achenkovil that drains into the lake. The state faced severe flooding in 2018 and 2019 due to torrential rainfall. Thus, this study focuses on assessing flood inundation mapping utilizing Sentinel-1 SAR imagery in Google Earth Engine (GEE) for 2018 and 2019 since it simplifies and streamlines the complicated and time-consuming pre-processing of Sentinel-1 SAR images. These images are pre-processed, and the flooded areas are delineated. Change detection by image ratio method is utilized to identify the flood inundated and the most frequently flooded areas. The results show that 4% and 3.21% of the entire region were flooded in 2018 and 2019, respectively. In addition, 14.7 Km^2 of the urban area flooded in 2018, whereas 7.26 Km^2 of urban land flooded in the 2019 floods. Hence, these inundation maps can be utilized for risk assessment and primary preventive measures. It also serves as a tool to warn the residents in that region about the hazards and the possibility of inundations at the time of heavy downpours in the future.

Keywords Kerala floods · Remote sensing · SAR · Flood inundation mapping · Google earth engine

K. S. S. Parthasarathy (✉)
Department of Water Resources and Ocean Engineering, National Institute of Technology Karnataka, Surathkal, Mangaluru 575 025, India
e-mail: parthas1993@gmail.com

S. Kundapura
Faculty of Water Resources Engineering, Department of Water Resources and Ocean Engineering, National Institute of Technology Karnataka, Surathkal, Mangaluru 575 025, India
e-mail: subrahmanyakundapura@nitk.edu.in

S. Dutta and V. Chembolu (eds.), *Recent Development in River Corridor Management*, Lecture Notes in Civil Engineering 376, https://doi.org/10.1007/978-981-99-4423-1_20

1 Introduction

Floods are a typical catastrophic event that has a massive influence on natural and human habitats all over the world. A flood occurs when the river reaches an extremely high level, overflowing its banks and inundating the nearby neighborhoods [18]. Water is a valuable natural resource. However, flooding is a significant environmental problem that may cause socioeconomic losses and property damage [9]. Climatic changes have added to precipitation uncertainty in many regions of the world and occasional urban floods. Increased precipitation and related snowmelt and stream flows are projected to cause flooding, landslides, erosion, and damage to roads, embankments, and bridges due to climate change. These urban floods negatively impact the economy, livelihoods, and everyday activities [15]. Flood is a complex and site-dependent phenomenon that has piqued the attention of researchers in attempting to examine, analyze, and explain its causal aspects due primarily to significant damage to the environment inflicted by urban growth, downstream floodplain encroachment, habitat loss, and other reasons [6]. The increased urbanization of humanity causes the surface to be sealed, resulting in less seeping into the earth. In addition, building dykes results in the loss of natural reservoirs by cutting off the stream from the flood plain, stressing the ecology and perhaps causing a catastrophe and deterioration. Depletion of the environment's resources, such as the soil, water, and air, as well as the loss of ecosystems, habitats, and natural balance, are all instances of environmental degradation.

India is very vulnerable to floods, with more than 40 million hectares (mha) of the entire geographical area prone to flooding, which accounts for roughly 12.16% of the total area) [17]. The advancements in remote sensing and Geographic Information System (GIS) technology have made it possible to capture, monitor, and assess calamities. Because of remote sensing techniques, the availability of open-source data has become a valuable advantage throughout the catastrophe. In flood control, sensing images at optical and microwave wavelengths plays a significant role [7]. The constant monitoring facility sets the way for a warning system and plays a vital role in catastrophe preparedness efforts. The rapid development and accessibility of Synthetic Aperture Radar (SAR) data provide the potential for expanded study in various fields. Because the SAR can penetrate clouds, continual surveillance of flood occurrences is possible [16]. While flood mapping needs trained workers, conventional ground and aerial surveys are time-consuming. The ability to readily distinguish between land and water contrast is the main benefit of using SAR data [4]. Even though satellite remote sensing platforms record permanent surface water extent, microwave sensors using SAR imaging sensors can monitor floods in micro to moderate-size catchment regions in all weather conditions. Additionally, multidate images provide researchers with a significant resource for tracking changes or replicating the history of previous flash flood scenarios [17]. Hence, the present study evaluates the flood-inundated region during the 2018 and 2019 floods and estimation of flood-inundated areas from the prepared Land Use Land Cover (LULC) map.

2 Materials and Methods

2.1 Study Area

The study area comprises of Vembanad Lake system comprising of six watersheds, namely, Periyar, Muvattupuzha, Meenachil, Manimala, Pamba, and Achenkovil of latitude 9° 1′ 9″ N to 10° 20′ 22″ N and longitude of 76° 16′ 47″ E and 77° 24′ 43″ E comprising of area 12,183 Km^2 (Fig. 1). The Vembanad Lake encompasses an area of 1512 Km^2, making it India's second-largest wetland system. An area of 398.12 km^2 is located below the MSL, and a total of 763.23 km^2 is located below 1 m MSL. It is the longest lake in India and the largest lake in Kerala [14]. The study area's eastern and western sides are bounded by the Western Ghats and the Arabian Sea, respectively. The geology of the region comprises Charnockites, charnockite gneisses, and pyroxene-bearing granulites along the Western Ghats and the part of the study region [8]. The sedimentary formations of the Neogene and Quaternary periods are found in the western parts of the study area, along with the alluvial deposits in the coastal region. The region has a wet and maritime tropical climate comprising an average of 150 days a year. The state receives an average rainfall of 3000 mm/yr from the southwest and northeast monsoons, of which 65% accounts for the former [15]. The study area is frequently affected by the floods from the year 2018 followed by the years 2019, 2020, and 2021. Here, in this study, the extent of the 2018 and 2019 floods is considered.

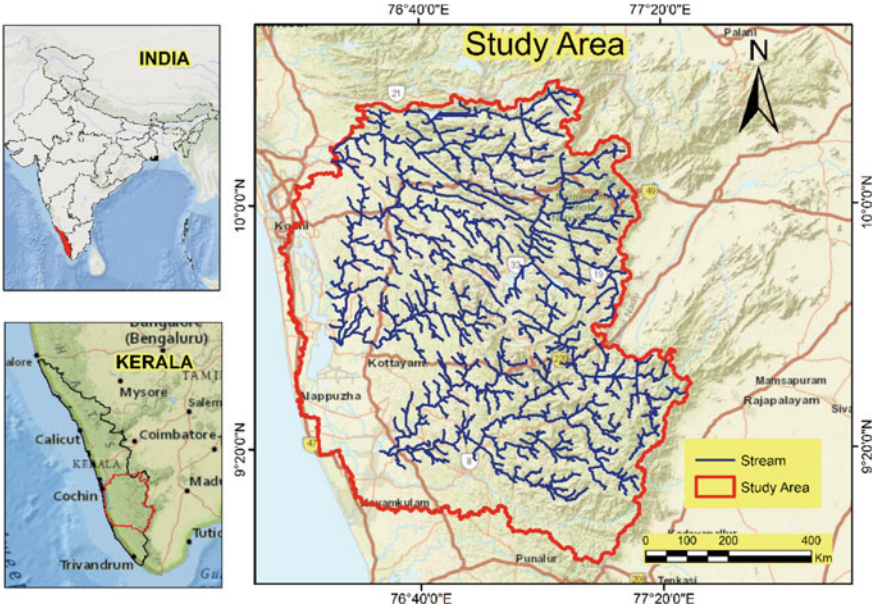

Fig. 1 Study area

2.2 2018 Kerala Floods

Kerala experienced substantial rainfall in August 2018, which was around 164% greater than the state's normal rainfall for that month. The intensity of the rain increased progressively beginning in June, contributing for a 15% increase above the normal rainfall of 749.6 mm. In July, rainfall totaled 857.4 mm, which was 18% more than the normal. In contrast, the first 20 days of August got 758.6 mm of rain instead of the typical 287.6 mm of rain, a 164% increase above the monthly average. All reservoirs were rapidly filling as the quantity of rainfall surpassed and continued throughout June. On the 8th and 9th of August 2018, Malappuram, Wayanad, Idukki, and Palakkad districts saw heavy rain, resulting in flooding in Wayanad and Idukki. Many reservoirs have attained their Full Reservoir Level (FRL) when water was discharged from catchments. Another strong rainstorm began on August 14th and lasted for a week till August 19th. While the state experienced 758.6 mm of rainfall in the first 20 days of August, 415 mm of rain occurred on 15–17 August 2018, causing catastrophic floods in 13 of Kerala's 14 districts. In addition to the heavy rain, the dams in FRL burst, causing major flooding across the area. According to the [3] study, dams in Kerala did neither increase nor decrease the quantity of flooding in the state. Because to above-average rainfall in the preceding months, the reservoirs were already at or near the FRL on August 14, 2018. Even if the reservoirs were less than the FRL, the scenario would remain the same since the rainfall was so severe for three days, and even four days in certain places.

Apart for Kasragode and Thiruvananthapuram, all regions of Kerala had abnormally significant precipitation. In which 50% of precipitation was measured in just 20 days, resulting in the severe flood. Even under little rain, the Kuttanad portion of Alappuzha district, which is below the MSL, is more susceptible to flooding. With the huge spell in July, the Kakki reservoir on the River Kakki was already full. The majority of Kuttanad was swamped by floodwater during the reservoir's discharge. If Kuttanad had not been inundated prior to the next spell, the reservoir's water level may have been reduced, saving the area from a catastrophic disaster. The heavy runoff from this reservoir water pooled in the Vembanad Lake, reducing its capacity. The decreased flow from the Thottappally barrage exacerbated floods in the Kuttanad area. This caused flooding in the low-lying areas of the Vembanad Lake, including the cities of Alappuzha, Kottayam, and Pathanamthitta.

2.3 2019 Kerala Floods

Three active spells—one in each of the months of July, August, and September—occurred in 2019 following their commencement, with the strongest spell taking place between the sixth and eleventh of August. After a somewhat drier than typical June and July, it is highly uncommon that the State got more than 150 mm of rain on 1 day, namely, on August 8, which resulted in floods in various sections of the state. The

daily rainfall deviation across Kerala is greater than 998% of normal as of August 8, 2019. While the 2018 floods saw scattered rainfall with less cumulative rainfall that fell fairly equally over a 24-h period, A few places in Kerala, most notably Kozhikode, Malappuram, and Idukki, have had rainfall surpassing 50 mm/2 h, according to 2 h of cumulative rainfall reported on August 8, 2019. The region affected by this occurrence was bigger than that commonly affected by cloudbursts or Mini Cloud Burst (MCB) events, which typically takes place in 50–100 square kilometers. A Mesoscale Cloudburst (MsCB) is defined as a geographically dispersed collection of pixels with high rainfall values. This Mesoscale convective storm delivered rainfall so strong that it earned the nickname "mini cloudburst" in contrast to the typical systems that develop near west coast of India. In Kerala's documented meteorological history during the monsoon season in August, this occurrence may be the first of its sort. After this MsCB occurrence, numerous areas of Malappuram and Kozhikode experienced flash floods [20].

2.4 Data Preparation

2.4.1 Processing of SAR Imagery

The flooded areas are delineated using multi-temporal Sentinel 1—Level 1—GRD (Ground Range Detected) digital data. Two polar-orbiting satellites operate C-band synthetic aperture radar imaging at 5.405 GHz as part of the Sentinel-1 program. The level-1 GRD product is a collection of SAR data detected, multi-looked, and projected to ground range using an Earth ellipsoid model. Due to the multi-look processing, the resultant output has nearly square spatial resolution and square pixel spacing, with decreased speckle. The pixel values represent the observed magnitude, but the phase information is lost. Sentinel-1 mission pioneer applications include maritime surveillance, land monitoring, and emergency management [5]. Google Earth Engine (GEE) is a cloud-based platform for effectively processing satellite data for research, education, and non-profit applications. It simplifies the specification of numerous modes of operation for combining input data and effectively producing composite, cloud-free, and multi-temporal datasets. To determine flood inundation extents. The Flood Mapping Algorithm (FMA) using GEE is utilized, which is widely used by various researchers to determine the flooded region [17, 19, 21]. It helps reduce time consumption and high processing load as the processing is all carried out in the GEE cloud infrastructure [14]. The image change detection method was used to identify flooded areas in multi-temporal SAR data. Change detection is often achieved by comparing before and after catastrophe reference data to flood images [7, 11].

Sentinel-1 images include erroneous noise (i.e., rigorous geometric, radiometric corrections, thermal, and speckle). All satellite data must be rigorously pre-processed before being used in any application. Pre-processing (Fig. 2) comprises (a) orbital file modification to eliminate orbital noise; and (b) thermal noise reduction is used to reduce noise from data collected by sensors on board the satellite during the

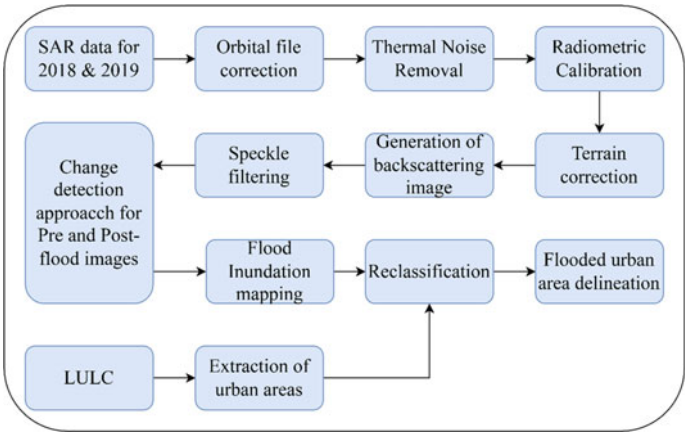

Fig. 2 The overall methodology of the study

data collection process. Thermal noise may affect the quality of the data in situations where the SAR system detects a low average signal response, such as ponds, stagnant water, streams, and so on; (c) in order to compare SAR images taken at various time periods, radiometric calibration, which calibrates RADAR reflectivity (DN) to backscattering coefficient (physical units), is employed; and (d) to address distortions including foreshortening, layover, and shadow effects in Sentinel-1 SLC (Single Look Complex) data, the data must be converted from slant range geometry to a map coordinate system which is known as Terrain correction. A speckle filter is used to smooth the images during the pre-processing of Sentinel-1 VV and VH SAR images. Change detection using image ratio analyzes the before and post-flooded images. As a consequence, an image containing flood and non-flood regions is produced. To distinguish the flooded and non-flooded regions, the image is subjected to a differential upper threshold.

2.4.2 Classification of LULC Map

Landsat 8 Top of Atmosphere (TOA) images from 2019 are utilized in the GEE environment for classification. In the images, the cloud cover is adjusted to less than 30%, and the Random Forest (RF) method is used to classify the LULC. The classification is achieved by using points and polygons to define the Area Of Interest (AOI) for the chosen image [1]. 15–35 pixels are chosen in each sample to provide a better AOI. The five primary categories are waterbody, built-up land, vegetation, barren land, and forest. For classification, each class was trained using 70–90 AOIs and validated with 65–80 AOIs. It also ensured that the data were dispersed and spectrally clean. Random stratified sampling is used to test accuracy, with the fewest possible observations selected randomly in each segment [14]. The built-up region is extracted from the LULC map and overlaid with the flooded region to extract the

flood-inundated urban region during the 2018 and 2019 floods. The methodology for the study is shown in Fig. 2.

3 Result and Discussion

The sentinel-1 SAR images of VV and VH polarization are acquired during the pre- and post-floods for 2018 and 2019. After pre-processing the images, a speckle filter of smoothing radius 50 is applied to smoothen the acquired images. The filtered image visualized differentiates the water and land before and after the flood occurrence in both 2018 (Figs. 3 and 4) and 2019 (Figs. 5 and 6).

A good polarization choice enhances the differentiation of flooded regions [10]. The results of our polarization configurations, as well as the contributions of Carreño Conde and De Mata Muñoz [2], Martinis and Rieke [12], Matgen et al. [13] in comparative studies of polarizations to monitor flood areas, reaffirm that the VH polarization is better suited for delimiting flooded areas. It produces very well and accurately defined surfaces, whereas VV polarization cannot. The roughness and complexity of the terrain significantly impact VV polarization. As a result, VH polarization is employed to identify the flooded zone further. The image ratio technique is carried out to delineate the flooded region from the non-flooded region.

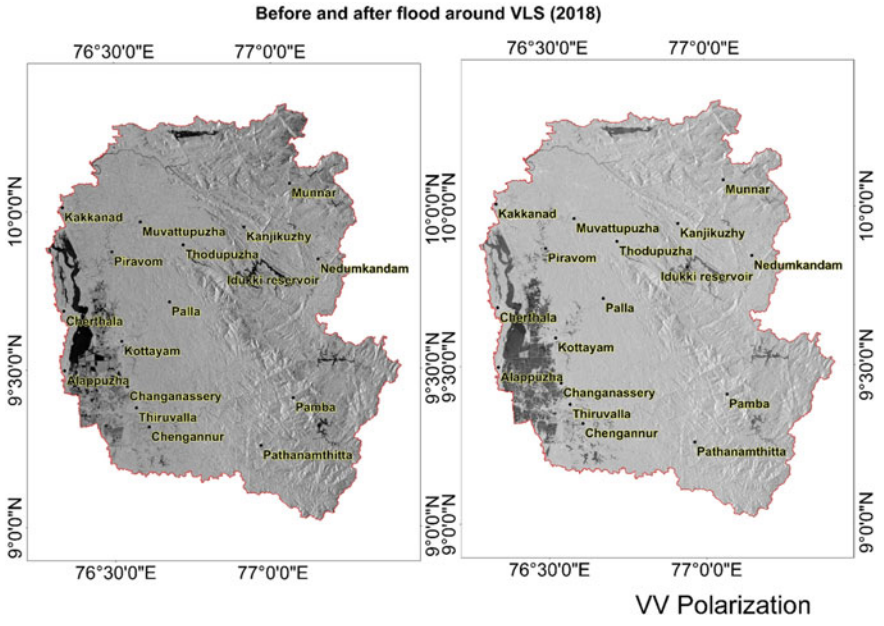

Fig. 3 VV polarization of before and after 2018 flood

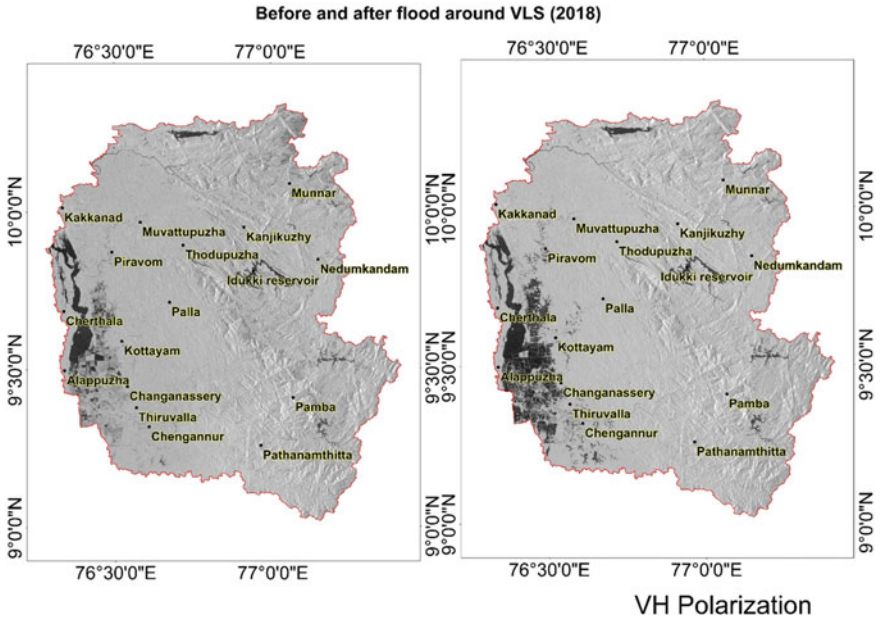

Fig. 4 VH polarization of before and after 2018 flood

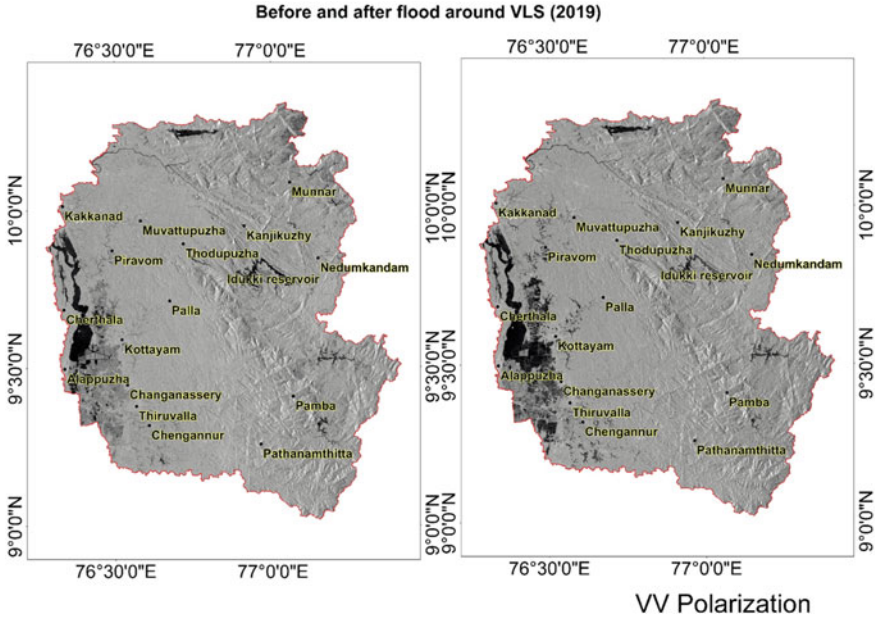

Fig. 5 VV polarization of before and after 2019 flood

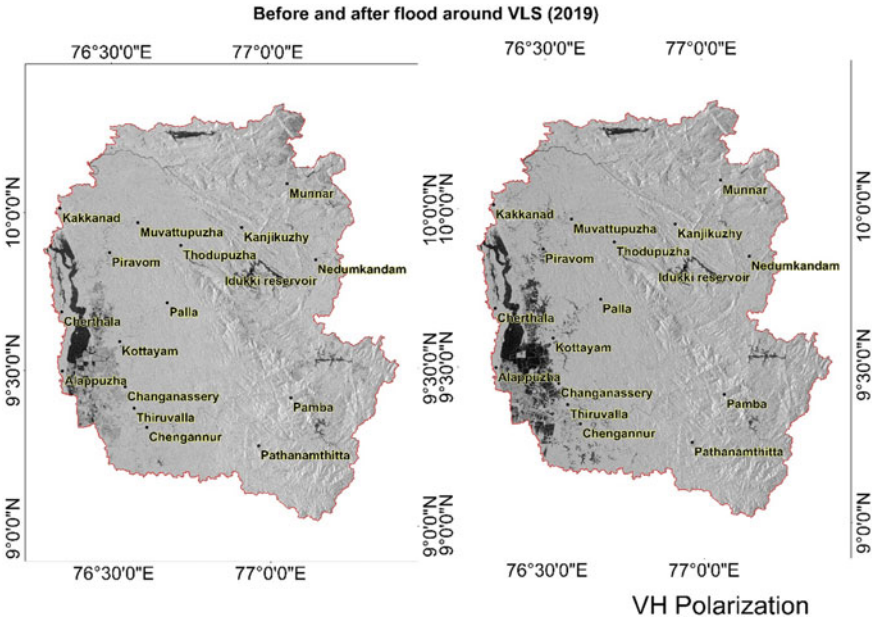

Fig. 6 VH polarization of before and after 2019 flood

In this process, a threshold of 1.20 is applied to delineate the flooded region properly. Figures 7 and 8 show the clear differentiation between the permanent water body from the flooded region.

Figure 7 shows the flood inundated region during the 2018 floods. The white patches show the flooded regions during the 2018 floods. It is found that the region surrounding the Vembanad Lake comprising mainly of Cherthala, Kottayam, Alappuzha, Changanassery, Thiruvalla, Piravom, and Chengannur are the severe flood-affected region in the study, which comprises 4% of the total study area. These are some of the important cities around the study and comprise a huge population. During the 2019 floods, the regions comprising Kottayam, Alappuzha, Changanassery, Thiruvalla, Piravom, and Chengannur are affected by the floods, comprising 3.21% of the study region. This shows the impact of the 2018 and 2019 floods around the important urban regions.

The LULC map (Fig. 9) is generated from the GEE using the RF algorithm and is extracted using Export.image.toDrive tool in GEE. The classified image has an accuracy and kappa coefficient of 91.19% and 88.16%, respectively. This demonstrates that the performance RF is better suited to multi-class issues and can manage minor classification variations [14].

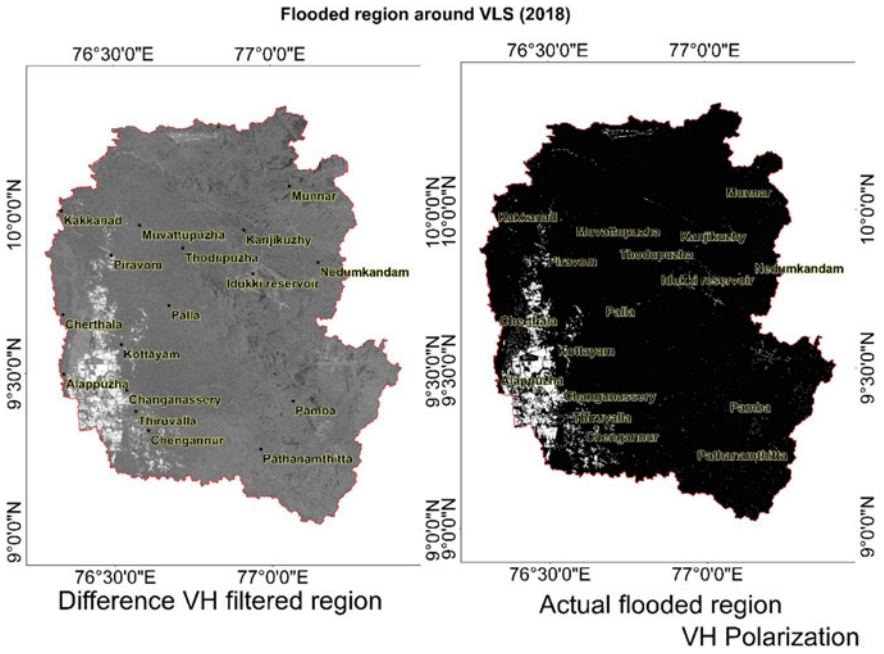

Fig. 7 Flooded region for 2018 flood

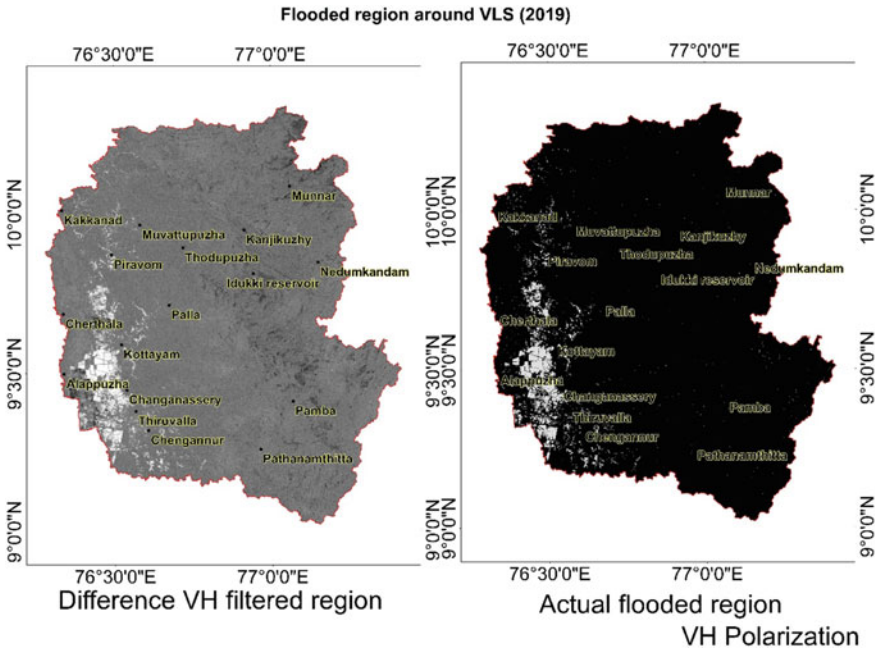

Fig. 8 Flooded region for 2019 flood

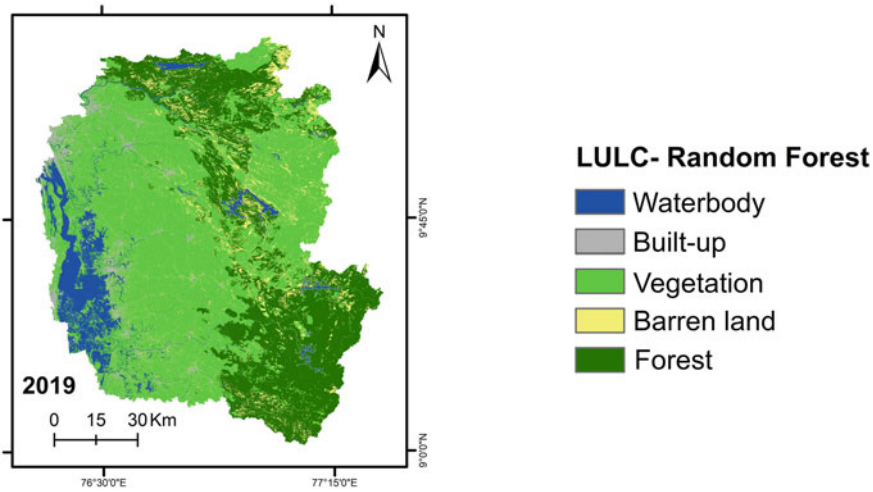

Fig. 9 LULC map for the year 2019

Thus, from the LULC map prepared, the built-up region is extracted and overlaid with the 2018 and 2019 flooded regions. Then the potentially flooded urban region is extracted by intersecting both the maps, and it found that an area of 14.7 Km^2 of the built-up land (Fig. 10) was inundated during the 2018 floods. This includes low-lying areas such as Changanassery, Alappuzha, Cherthala, and Thiruvalla. The 2019 floods affected an area of 7.26 Km^2 of built-up land (Fig. 9), comprising mainly the northern part of Kottayam, Cherthala, Alappuzha, and Chengannur. From the results, it is found that the regions such as Cherthala, Alappuzha, and Chengannur are the most frequently flood-affected regions, and serious mitigation measures have to be taken during the time of the flood.

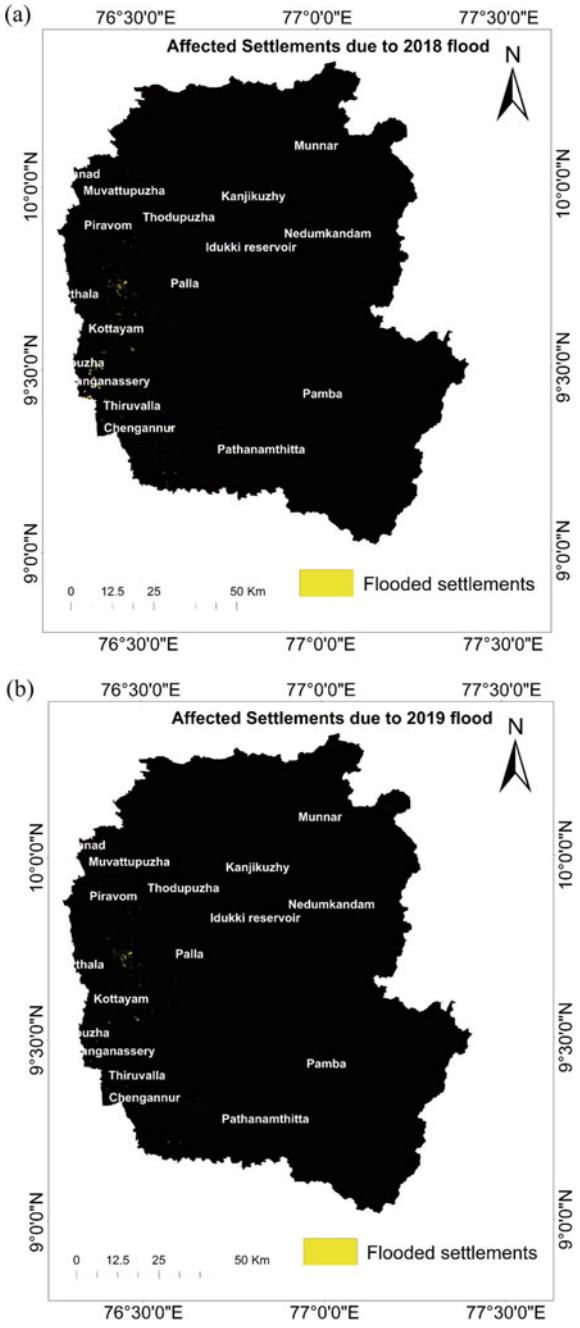

Fig. 10 Affected Settlements due to the 2018 (**a**) and 2019 (**b**) floods

4 Conclusion

From the results, it is observed that 4% and 3.21% area of the total region got flooded in 2018 and 2019, respectively. In addition, 14.7 Km^2 of the urban area flooded in 2018, whereas 7.26 Km^2 of urban land flooded in the 2019 floods. The primary ideas of mapping flood-inundated urban regions are risk assessment and primary preventive measures. It also serves as a tool to warn the residents of the region about the hazards and the possibility of inundations at the time of heavy downpours in the future. Land-use planners and government entities are obligated to inform local communities about the most recent flood susceptibility evaluations and the rules prohibiting new projects in areas with a high risk of flooding. It will also be a primary tool for the insurance companies to map the flood-affected built-up region, and this work can not only be restricted to the built-up region but can also be extended to map the flood-affected agricultural region.

References

1. Abijith D, Saravanan S (2021) Assessment of land use and land cover change detection and prediction using remote sensing and CA Markov in the northern coastal districts of Tamil Nadu, India. Environ Sci Pollut Res. https://doi.org/10.1007/s11356-021-15782-6
2. Carreño Conde F, De Mata Muñoz M (2019) Flood monitoring based on the study of sentinel-1 SAR images: the Ebro river case study. Water 11(12):2454. https://doi.org/10.3390/w11122454
3. CWC (2018) Kerala floods of August 2018 (August):46
4. Dewan AM, Kankam-Yeboah K, Nishigaki M (2006) Using synthetic aperture radar (SAR) data for mapping river water flooding in an urban landscape: a case study of greater Dhaka, Bangladesh. J Japan Soc Hydrol Water Resour 19(1):44–54. https://doi.org/10.3178/JJSHWR.19.44
5. ESA (2000) Sentinel: user-guides
6. Hong H, Panahi M, Shirzadi A, Ma T, Liu J, Zhu AX, Chen W, Kougias I, Kazakis N (2018) Flood susceptibility assessment in Hengfeng area coupling adaptive neuro-fuzzy inference system with genetic algorithm and differential evolution. Sci Total Environ 621:1124–1141. https://doi.org/10.1016/J.SCITOTENV.2017.10.114
7. Jacinth Jennifer J, Saravanan S, Abijith D (2020) Integration of SAR and multi-spectral imagery in flood inundation mapping–a case study on Kerala floods 2018. ISH J Hydraul Eng 28(1):480–490. https://doi.org/10.1080/09715010.2020.1791265
8. Jennifer JJ (2022) Feature elimination and comparison of machine learning algorithms in landslide susceptibility mapping. Environ Earth Sci 81(489). https://doi.org/10.1007/S12665-022-10620-5/FIGURES/15
9. Kalantari Z, Ferreira CSS, Koutsouris AJ, Ahmer AK, Cerdà A, Destouni G (2019) Assessing flood probability for transportation infrastructure based on catchment characteristics, sediment connectivity and remotely sensed soil moisture. Sci Total Environ 661:393–406. https://doi.org/10.1016/J.SCITOTENV.2019.01.009
10. Klemas V (2015) Remote sensing of floods and flood-prone areas: an overview. J Coast Res 314:1005–1013. https://doi.org/10.2112/JCOASTRES-D-14-00160.1
11. Manavalan R (2017) SAR image analysis techniques for flood area mapping-literature survey. Earth Sci Inform 10(1):1–14. https://doi.org/10.1007/S12145-016-0274-2/FIGURES/8

12. Martinis S, Rieke C (2015) Backscatter analysis using multi-temporal and multi-frequency SAR data in the context of flood mapping at River Saale, Germany. Remote Sens 7(6):7732–7752. https://doi.org/10.3390/rs70607732
13. Matgen P, Schumann G, Henry J-B, Hoffmann L, Pfister L (2007) Integration of SAR-derived river inundation areas, high-precision topographic data and a river flow model toward near real-time flood management. Int J Appl Earth Obs Geoinf 9(3):247–263. https://doi.org/10.1016/j.jag.2006.03.003
14. Parthasarathy KSS, Deka PC (2022) Spatio-temporal classification and prediction of land use and land cover change for the Vembanad Lake system, Kerala: a machine learning approach. Environ Sci Pollut Res 29(57):86220–86236. https://doi.org/10.1007/s11356-021-17257-0
15. Parthasarathy KSS, Deka PC, Saravanan S, Abijith D, Jacinth Jennifer J (2021) Assessing the impact of 2018 tropical rainfall and the consecutive flood-related damages for the state of Kerala, India. In: Disaster resilience and sustainability. Elsevier, pp 379–395
16. Rahman MR, Thakur PK (2018) Detecting, mapping and analysing of flood water propagation using synthetic aperture radar (SAR) satellite data and GIS: a case study from the Kendrapara District of Orissa State of India. Egypt J Remote Sens Sp Sci 21:S37–S41. https://doi.org/10.1016/j.ejrs.2017.10.002
17. Saravanan S, Abijith D (2022) Flood susceptibility mapping of Northeast coastal districts of Tamil Nadu India using multi-source geospatial data and machine learning techniques. Geocarto Int 1–30. https://doi.org/10.1080/10106049.2022.2096702
18. Subramanya K (2013) Engineering hydrology. Tata McGraw Hill Publishing Company Limited
19. Tiwari V, Kumar V, Matin MA, Thapa A, Ellenburg WL, Gupta N, Thapa S (2020) Flood inundation mapping-Kerala 2018; Harnessing the power of SAR, automatic threshold detection method and Google Earth Engine. PLoS One 15(8 August). https://doi.org/10.1371/journal.pone.0237324
20. Vijaykumar P, Abhilash S, Sreenath AV, Athira UN, Mohanakumar K, Mapes BE, Chakrapani B, Sahai AK, Niyas TN, Sreejith OP (2021) Kerala floods in consecutive years - Its association with mesoscale cloudburst and structural changes in monsoon clouds over the west coast of India. Weather Clim Extrem 33:100339. https://doi.org/10.1016/j.wace.2021.100339
21. Zhang M, Chen F, Liang D, Tian B, Yang A (2020) Use of sentinel-1 GRD SAR images to delineate flood extent in Pakistan. Sustainability 12(14):5784. https://doi.org/10.3390/SU12145784

Impact Assessment of Flood on Agricultural Land Using Cloud-Based Computing Platform in Kosi River Basin, North Bihar, India

Himanshu Kumar, Rohan Kumar, Sujay Dutta, and Magan Singh

Abstract Flooding is a major natural disaster in the Indian state of Bihar. The geographical setup of North Bihar increases the risk of floods and makes the region flood-prone. Recurring flood events in Bihar cause substantial loss of life and property every year. Rapid urbanization, deforestation, infrastructure development and erratic rainfall are the main causes of frequent floods in North Bihar. Public availability of geospatial datasets and free access to cloud-based geo-computing platform such as Google Earth Engine (GEE) are being commonly utilized for monitoring of flood events. The present work is aimed to examine the flood extent of the Kosi River Basin, Bihar and their impact on agricultural land using Sentinel-1 microwave and Sentinel-2A/B optical images. In this study, we found that a large portion of the Kosi River Basin was flooded during the monsoon season of 2020 and 2021. The inundation map has been prepared to visualize the extent of the flood, and it is expected that the results of the study can be used to inform decision-making by policymakers and other stakeholders to prioritize their efforts towards reducing the impact of floods and provide timely relief.

Keywords Agricultural land · Flood extent mapping · Google earth engine · Kosi river basin · Sentinel-1&2

H. Kumar (✉) · R. Kumar
Lovely Professional University, Phagwara 144001, India
e-mail: himanshukumar.gis@gmail.com

H. Kumar · M. Singh
ICAR-National Dairy Research Institute, Karnal 132001, India

S. Dutta
Space Application Centre, ISRO, Ahmedabad, Ambavadi 380015, India

S. Dutta and V. Chembolu (eds.), *Recent Development in River Corridor Management*,
Lecture Notes in Civil Engineering 376, https://doi.org/10.1007/978-981-99-4423-1_21

1 Introduction

Flood is a widespread, natural disaster that is a recurrent phenomenon due to the geographical and riverine structures of the Indian subcontinent. Unplanned urban development, changes in climate, land-use pattern, imbalanced rainfall are the major reasons for recurring floods in the Kosi River Basin in North Bihar, India. Thus affects the life, property of millions of people and adversely affects the local ecosystem. In Bihar, the main source of income is agriculture, which is severely destroyed by frequent floods every year and creates huge unemployment for the residents of the region.

Some past flood events in the Indo-Gangetic plain, such as the Kosi flood (2008) and the Bihar Ganga flood (2019), are examples of the increasing severity of hydrological disaster [3]. So, there is a need to develop the monitoring and early warning systems for vulnerable areas to reduce the adverse effects of floods. In this context, remote sensing satellites provide an efficient and cost-effective way to map and monitor flood events, especially in areas where ground surveys and aerial observations may be difficult or impossible to conduct. Satellites can capture images of flood-affected areas from space, providing a bird's eye view of the extent and severity of the flooding. These images are being used to extract flood maps and monitor the impact of flood on agricultural land [17, 10].

Nowadays, Synthetic Aperture Radar (SAR) datasets are being extensively utilized for flood hazard mapping due to their all-weather detecting capability. The Sentinel-1A (S-1A) and Sentinel-1B (S-1B) satellites were both launched by the European Space Agency (ESA) in during the years 2014–2016, respectively. It is providing high-resolution images of Earth's surface even in the absence of visible light, such as during cloudy weather or at night. This datasets are openly available to scientists and academics [19]. Its spatial resolution is 10 m and the revisit time is 5 days. Remotely sensed Earth observation datasets are gradually increasing for mapping of flood-prone areas [15].

Nowadays, various sources of remote sensing satellite datasets are freely accessible, such as https://earthexplorer.usgs.gov/, Bhuvan Portal, etc. However, satellite dataset processing is challenging due to the large resource requirements such as downloading storage and high configuration workstations.

Hence to overcome these problems, Google's GEE is an advanced cloud-computing platform for remote sensing dataset processing. The platform is also hosting up-to-date remote sensing (Landsat, Sentinel and MODIS archive) ready to use and its supporting datasets [10].

In the present study, Sentinel-2 MultiSpectral Instrument (MSI) data were used for agricultural land mapping, and Sentinel-1 SAR was used for flood occurrence and flood-affected agricultural land mapping. SAR remote sensing datasets have longer wavelengths, which can penetrate the cloud cover. Hence, it is a potential source for flood hazard mapping. This capability of SAR sensors to identify flood progression and flood affected agricultural land depends on various backscattering mechanisms such as biomass composition, soil condition, surface roughness of agricultural land

affected backscatter SAR signal [4]. For the identification of inundated pixels, several SAR-based flood identification techniques used scattering mechanism by applying backscatter thresholds to satellite imagery [5].

Nowadays, the change detection technique is a common approach for flood identification.

Likewise, various other methods and indices are available to extract waterbodies or flooded pixels such as normalized difference water index (NDWI) [13], modified normalized difference water index (MNDWI) [20], and recently developed, automated water extraction index (AWEI) by Feyisa et al. [6].

The NDWI is a widely used method for waterbody extraction. It is calculated as the difference between the near-infrared (NIR) and green bands, divided by their sum. This index is sensitive to water content, as water absorbs more NIR radiation and reflects more green radiation than other classes. Pixels with high NDWI values are classified as water.

Another widely used index for waterbody extraction is the MNDWI. The MNDWI is similar to the NDWI, but it uses shortwave infrared (SWIR) band instead of the NIR band. The SWIR band is more sensitive to water than the NIR band, especially in shallow water bodies. The MNDWI is calculated as the difference between the SWIR and green bands, divided by their sum.

Similarly, the AWEI is based on the NDWI and includes the blue band to improve the discrimination of water from other class. The AWEI is calculated as the sum of the green and blue bands, minus twice the NIR band, divided by the sum of the green and blue bands, plus twice the NIR band.

In the last decade, various research work has been conducted based on optical and SAR data to mitigate the impact of recurrent flood events in Bihar [12]. Presently, the flood extent of Kosi River Basin in North Bihar and their impact on agricultural land has been assessed using Sentinel-1 Microwave (SAR) and Sentinel-2A/B Optical (MSI) images in GEE platform during the monsoon season of 2020 and 2021.

2 Study Area

This study was conducted in Kosi River Basin of North Part of Bihar, India, which lies between latitude 26°41′3.206″ to 26°40′46.669″ and longitude 86°27′33″ to 87°39′13″ and covers about 10,934 km^2 (Fig. 1). The area is situated in the Indo-Gangetic plain, which is prone to floods due to its geographical location and topography. The state experiences floods due to heavy rainfall during the monsoon season. The average annual rainfall in Bihar is 1205 mm with an average of 52 rainy days. The summers are generally quite hot, with temperatures ranging from 35 °C to 40 °C, and the winters are fairly cool, with temperatures ranging from 10 °C to 20 °C. In recent years, Kosi belt has experienced devastating floods, which have caused significant damage to infrastructure, crops, and property, as well as loss of life. Floods have also led to the displacement of people, leading to economic and social problems. The government has undertaken several measures to mitigate the effects of floods in

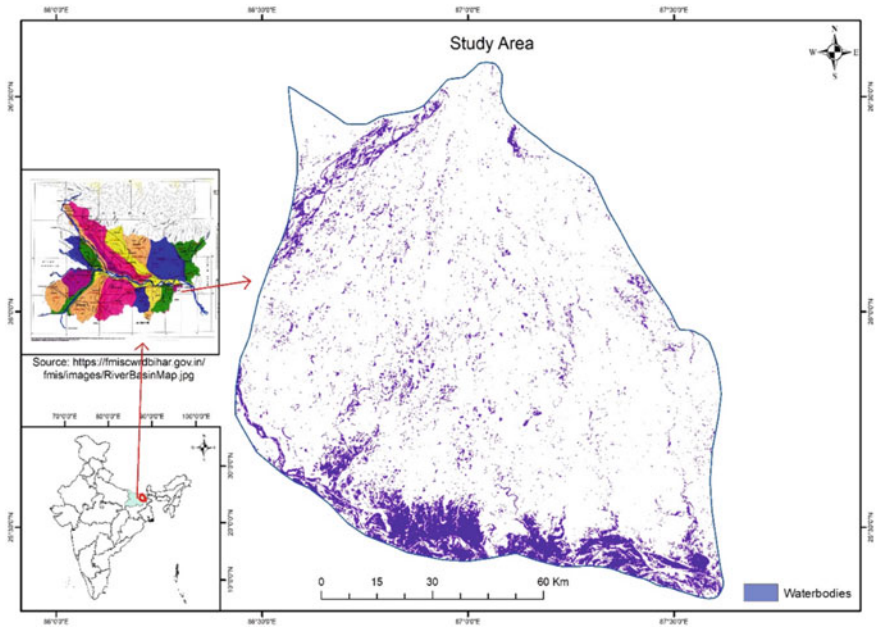

Fig. 1 Location map of Kosi River basin

the state. These measures include the construction of embankments and dams, the creation of flood shelters and the provision of relief and rehabilitation to affected people.

3 Data Used

In this study, Sentinel-1 and Sentinel-2 satellite imagery as well as SRTM (Shuttle Radar Topography Mission) datasets are commonly used in flood mapping (Table 1).

Table 1 Data utilized for present work

Data	Duration	Spatial resolution	Source	Use
Sentinel-1	June−October (2020 and 2021),	10 m	ESA	Flood extent map
Sentinel-2	March (2020 and 2021)	10 m	ESA	Land use mapping
SRTM	2000–2021	30 m	NGA and NASA	Terrain correction

4 Geo-Processing of Sentinel-1 Datasets

In the present work, publicly accessible Sentinel-1 data collected from ESA. VV + VH (vertical transmit, vertical receive (VV) and vertical transmit, horizontal receive (VH) polarization have been used in the present study due to conflict-free modes. These datasets are available on the GEE cloud platform with the SNAP (Sentinel Application Platform) software tool package. The SNAP is a software tool package developed by ESA for processing and analysing satellite data, including data from the Sentinel series of satellites. SNAP provides various tools for working with satellite data, including image processing, data visualization, and data analysis. Therefore, the GEE platform has been utilized for SAR data processing such as orbit, noise and radiometric correction.

SRTM (Shuttle Radar Topography Mission) dataset has been used for terrain corrections and converted backscatter intensity to decibels (dB) using the GEE platform. The SRTM dataset is a digital elevation model (DEM) of the Earth's surface created using radar dataset collected by "the Space Shuttle Endeavour during the Shuttle Radar Topography Mission in 2000". In GEE, the SRTM dataset is often used for terrain correction of satellite imagery. Terrain correction is the procedure of rectifying for variations in the Earth's topography to improve the accuracy of satellite imagery analysis. By using the SRTM dataset, GEE can correct distortions in the imagery caused by the Earth's topography, such as shadowing, foreshortening and layover [8]. We used all available Sentinel-1 datasets during June−October 2020 and June−October 2021 for flood hazard mapping.

5 Sentinel-2 MSI and Processing

Openly accessible high-resolution Sentinel-2 optical satellite imagery is capable to monitor the Earth's surface. This satellite has 10 m spatial resolution (band: 2, band: 3, band: 4 and band: 8). In recent years, several studies have utilized Sentinel-2 data for agriculture field mapping. Kobayashi et al. [14] used Sentinel-2 data to classify different crop types. Similarly, Karwariya et al. [21] used Sentinel-2 imagery for crop-type mapping.

Thus, Sentinel-2 datasets are utilized in the present study for agriculture field mapping. The least cloud-covered (<10%) imageries of March 2020 and March 2021 have been used with the help of available GEE Tools like "CLOUDY_PIXEL_PERCENTAGE". Moreover, the QA band of Sentinel-2A/B has been utilized to eliminate the cloud cover [10].

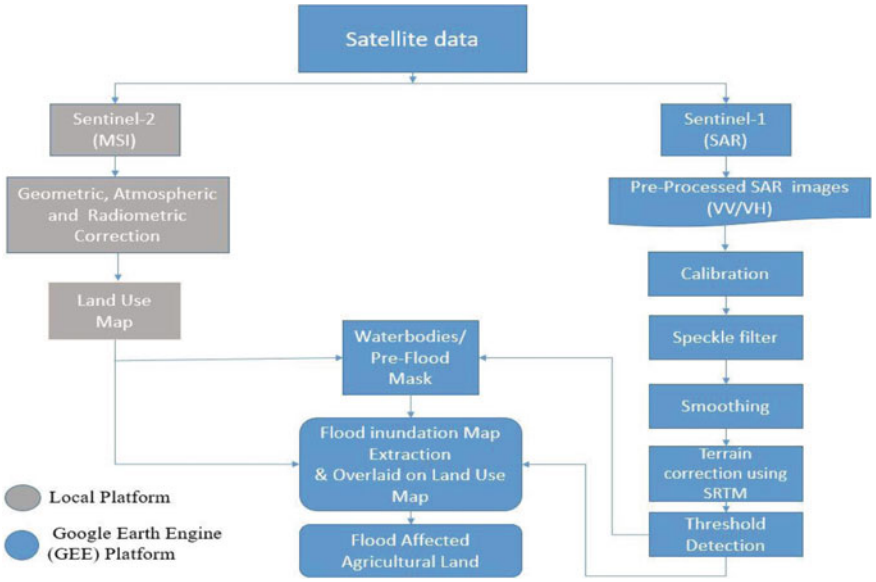

Fig. 2 Flowchart of the methodology

6 Methodology

In the present work, Sentinel-1A/B SAR data have been utilized for the identification of flood extent. The land use layer was generated by Sentinel-2 datasets to extract flood-affected cropland during flood events of 2020 and 2021. Threshold method was utilized for identification of inundated pixels. Because, an automated thresholding method distinguishes threshold values to differentiate water pixels from non-water pixels without requiring any training sample [11]. Then, the achieved inundation extent has been subtracted by the pre-flood layer of water bodies Fig. (2).

7 Google Earth Engine (GEE)

Microwave remote sensing dataset processing is a challenging task. But, GEE provides the best solution to process these datasets. It has capability to analyse a wide range of geospatial data using Google's infrastructure. In addition, it is also providing access to various satellite's data and other geospatial data that can be analysed and processed in real time using a variety of built-in algorithms and JavaScript codes. The entire process task is executed in GEE platform and JavaScript code is developed for flood extent and affected agricultural lands' demarcation (Fig. 3).

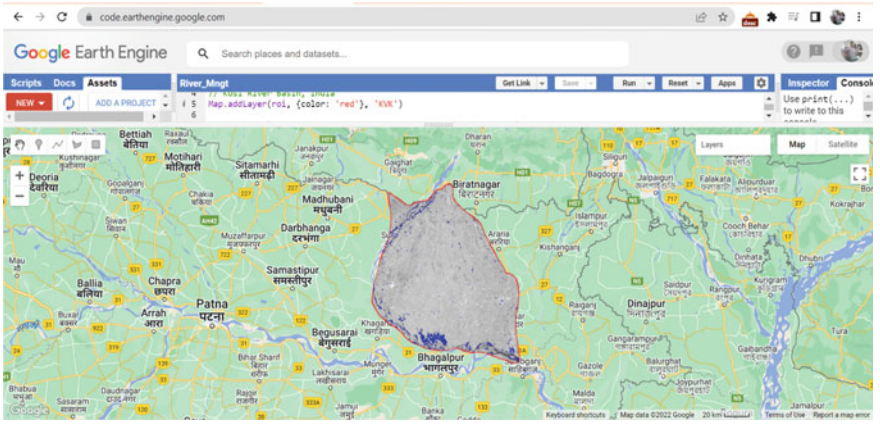

Fig. 3 GEE Platform's interface

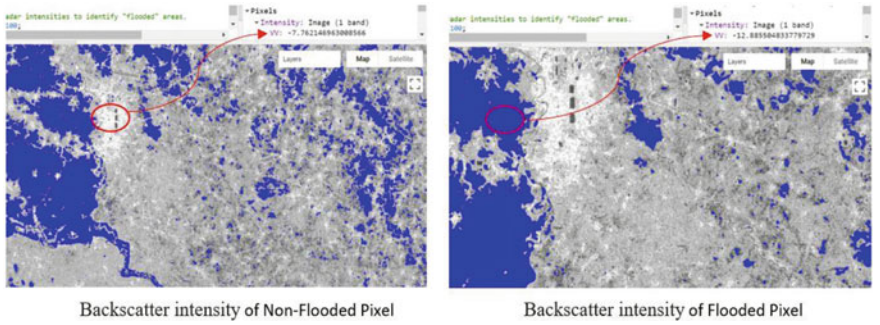

Fig. 4 Backscatter intensity map of flooded and Non-flooded pixels

8 Backscatter Intensity Pattern of Flooded and Non-Flooded Pixels

Backscatter Intensity gives an inference about the types of objects present on the earth surface. In SAR (Synthetic Aperture Radar) imaging, the backscatter intensity is the amount of radar energy that is reflected back to the radar antenna after it has been transmitted to the ground. This backscatter intensity depends on various factors, including the surface roughness, the moisture content and the structure of the target. The pixels with low grayscale intensity resemble water features while high-intensity pixels resemble man-made or 175 non-water features [7] (Fig. 4).

Table 2 Statistics of flood event

Land use type	Geographic area in hectare (km^2)	Total flood-affected area (km^2)		Affected area in %	
		2020	2021	2020	2021
Cropland	9449.73	871.37	1078.85	9.22	11.42
Built-up land	84.89	0.83	0.35	0.98	0.41
Shrubland	418.15	116.08	114.89	27.76	27.48
Fallow land	57.3	6.26	5.35	10.92	9.34
Water bodies	473.09	197.92	214.55	41.84	45.35
Plantations	37.07	0.17	0.46	0.46	1.24
Wetlands	414.02	49.51	94.19	11.96	22.75
Total	10,934.25	1242.14	1508.64	11.36	13.80

9 Results and Discussion

The study shows that large proportion of Kosi River Basin was affected due to severe floods, around 1242.14 km^2 in 2020 and 1508.64 km^2 in 2021. In 2020, 871.37 km^2 and, in 2021, 1078.85 km^2 of agricultural land were submerged due to floods.

The large population of Bihar is dependent on agriculture which is most affected by the floods every year. Detailed affected area and affected population are shown in detail in Table 2.

The analysis also indicates that around 116.08 km^2 of scrublands, 6.26 km^2 of fallow land 0.17 hectares of plantation area were inundated in 2020 and 114.89 km^2 of scrubland, 5.35 km^2 of fallow land, 0.46 km^2 of plantation were inundated in 2021.

10 Flood Progression Assessment

The study employed VV polarization to map flood, which is ranging from –8 dB to –12 dB (Fig. 5). High VV values were associated with non-water features, while waterbodies showed low backscatter response.

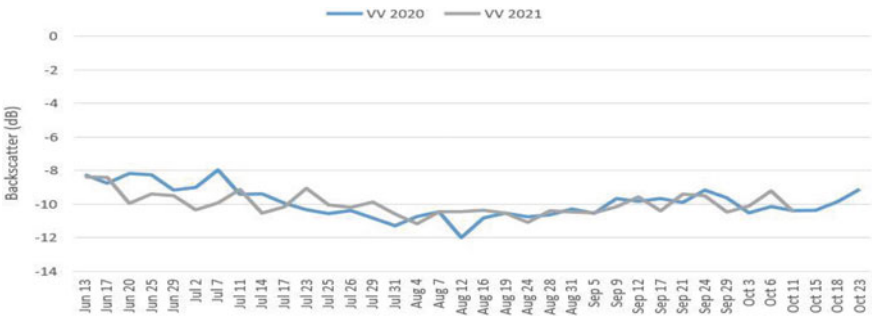

Fig. 5 Backscatter response of VV ranges of Sentinel-1 SAR datasets

11 Pre-Flood Land Use Map

Remote Sensing satellite data are most important for land use and change detection mapping. Sentinel-2 datasets were employed in the study to generate the land use layer using an RF model. Random Forest is a machine learning algorithm that can be used for classification tasks, including land use mapping. The algorithm works by building a decision tree based on a subset of the input data and then combining multiple decision trees to create an ensemble model. The RF algorithm can effectively classify the input data (Satellite imagery) into different land use categories, based on the spectral characteristics of the imagery. By using Sentinel-2A/B images and Random Forest algorithms on the GEE platform, land use maps were generated with high accuracy and efficiency (Fig. 6).

12 Flood Progression Map of 2020 and 2021

Sentinel-l SAR satellite data and a thresholding approach have been used to map the flood extent in Kosi River Basin, Bihar. Then, flood extent was overlaid on generated pre-flood land use map (Fig. 6) to get the affected class by floods 2020 and 2021.

Whereas, in the 2020 flood events, about 9.22% cropland, 1% built-up land, 27.76% scrubland, 10.92 fallow land, 0.46% plantation and 11.96% wetland were submerged in the study area (Fig. 7). In 2020, the floods submerged about 9.22% of cropland, 1% of built-up land, 27.76% of scrubland, 10.92% of fallow land, 0.46% of plantation and 11.96% of wetland in the study area. While, about 11.42% of cropland, 0.41% of built-up land, 27.48% of scrubland, 9.34 of fallow land, 1.24% of plantation and 22.75% of wetland were submerged in the 2021 flood events (Fig. 8).

The floods had a significant impact on croplands, which are areas used for agricultural purposes. This could lead to a decrease in food production and affect the

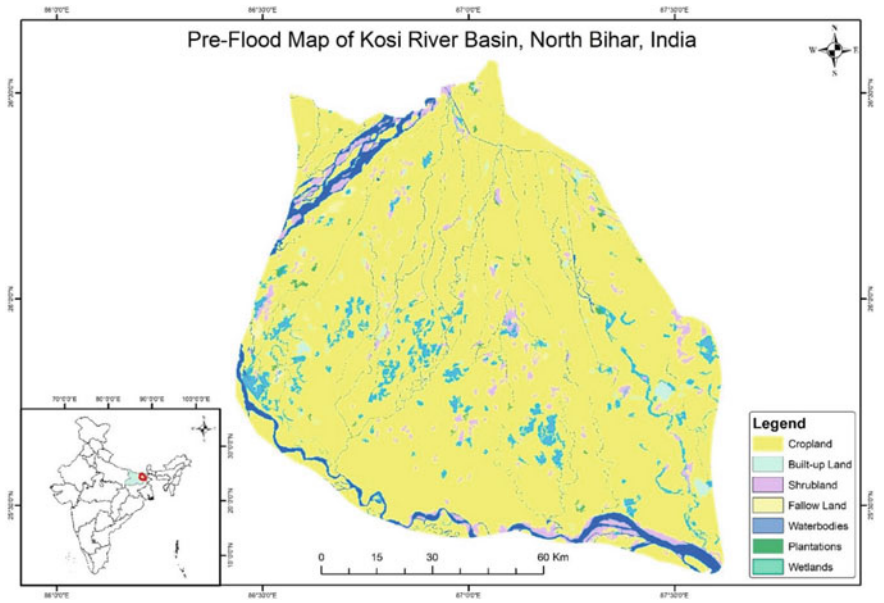

Fig. 6 Pre-flood map with different land classes

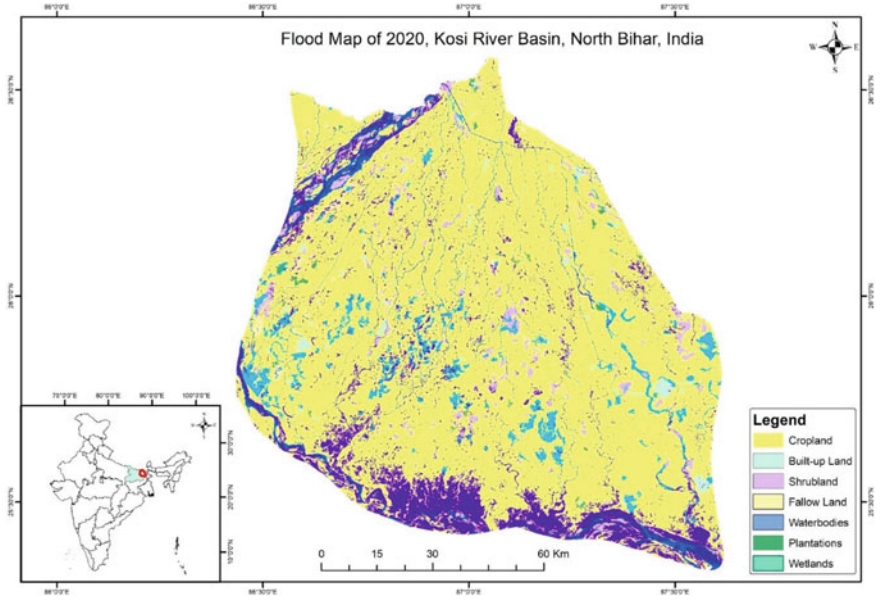

Fig. 7 Flood map of 2020

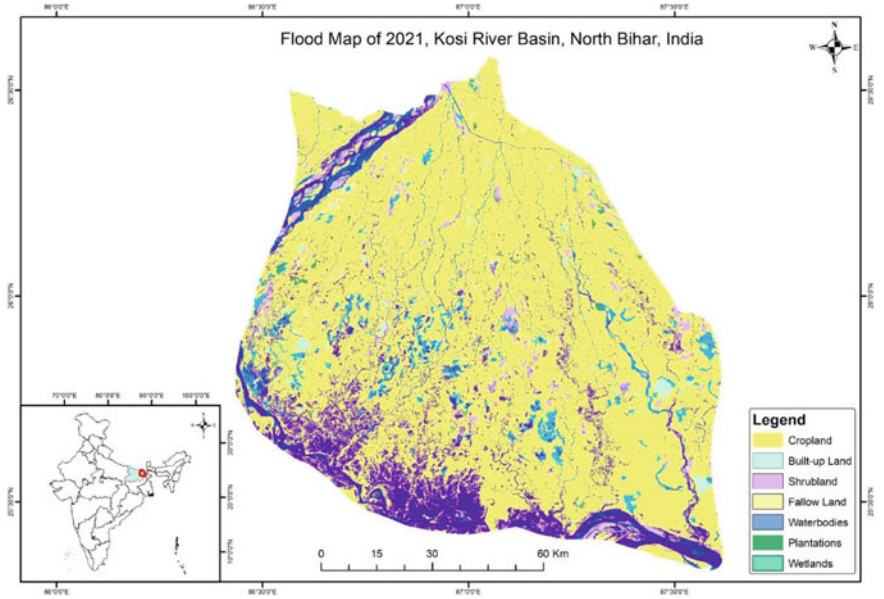

Fig. 8 Flood map of 2021

livelihoods of people who rely on agriculture for their income. The impact on built-up land, which includes residential and commercial areas, is relatively low but still significant as it could lead to damage to buildings and infrastructure.

Scrubland, which is vegetation that is not dense enough to be classified as forest, was the most affected land type in both 2020 and 2021 floods. The impact on fallow land, which is land that is left uncultivated for a period of time, was also significant. The floods could lead to erosion and soil degradation, making it difficult to use the land for agricultural purposes in the future.

Plantations, which are areas where trees are planted for commercial purposes, were also affected by the floods. The impact on wetlands, which are areas that are saturated with water, was significant in both years. Wetlands are essential ecosystems that provide a range of ecosystem services, including water purification and habitat for wildlife.

It is observed that the floods had a significant impact on various types of land in the study area during the flood events of 2020 and 2021, with the 2021 floods affecting a larger area of land than the 2020 floods. The impact on croplands, fallow land and wetlands is particularly concerning as it could affect food production, local ecosystem and biodiversity. They purify, restore and recharge groundwater, and maintain water quality, vegetation, flora and fauna. Further studies are needed to assess the long-term impact of the floods on the affected areas.

13 Conclusion

In this study, a JavaScript code is evolved for efficient processing of massive data which enables flood mapping through remotely sensed imageries. Here, we found that around ~11.36% (1242.14 km^2) area of study area is flooded in 2020. As of 2021 floods, about ~13.80% (1508.64 km^2) area of study area is also flooded in 2021. In the floods of 2021, about 2.44% more area of Kosi River Basin has been flooded as compared to the floods of 2020 in Bihar, India. The generated flood maps and flood-affected agricultural land can be utilized by policymakers, as major benefit of the study.

References

1. Adriaan, Jacobus, Prins, and, Adriaan, Van, Niekerk (2021) Crop type mapping using LiDAR, Sentinel-2 and aerial imagery with machine learning algorithms. Geo-Spat Inf Sci 24(2):215–227. https://doi.org/10.1080/10095020.2020.1782776
2. Bhuvan Portal. https://bhuvan.nrsc.gov.in/home/index.php
3. Bhatt CM, Gupta A, Roy A, Dalal P, Chauhan P (2021) Geospatial analysis of September, 2019 floods in the lower gangetic plains of Bihar using multi-temporal satellites and river gauge data. Geomat Nat Haz Risk 12(1):84–102. https://doi.org/10.1080/19475705.2020.1861113
4. Liu CA, Chen ZX, Yun SH, Chen JS, Hasi T, Pan HZ (2019) Research advances of SAR remote sensing for agriculture applications: A review. J Integr Agric 18(3): 506–525. https://doi.org/10.1016/S2095-3119(18)62016-7
5. Chini M, Hostache R, Giustarini L, Matgen P (2017) A hierarchical split-based approach for parametric thresholding of SAR images: Flood inundation as a test case. IEEE Trans Geosci Remote Sens 55(12):6975–6988. https://doi.org/10.1109/TGRS.2017.2737664
6. Feyisa GL, Meilby H, Fensholt R, Proud SR (2014) Automated water extraction index: A new technique for surface water mapping using Landsat imagery. Remote Sens Environ 140:23–35. https://doi.org/10.1016/j.rse.2013.08.029
7. Ghosh S, Kumar D, Kumari R (2022) Evaluating the impact of flood inundation with the cloud computing platform over vegetation cover of Ganga Basin during COVID-19. Spat Inf Res 30:291–308. https://doi.org/10.1007/s41324-022-00430-z
8. Gorelick N, Hancher M, Dixon M, Ilyushchenko S, Thau D, Moore R (2017) Google earth engine: Planetary-scale geospatial analysis for everyone. Remote Sens Environ 202:18–27. https://doi.org/10.1016/j.rse.2017.06.031
9. https://earthexplorer.usgs.gov/
10. Kumar H, Karwariya SK, Kumar R (2022) Google earth engine-based identification of flood extent and flood-affected paddy rice fields using sentinel-2 MSI and sentinel-1 SAR data in Bihar state, India. J Indian Soc Remote Sens 50:791–803. https://doi.org/10.1007/s12524-021-01487-3
11. Liang J, Liu D (2020) A local thresholding approach to flood water delineation using Sentinel-1 SAR imagery. ISPRS J Photogramm Remote Sens 159:53–62. https://doi.org/10.1016/J.ISPRSJPRS.2019.10.017
12. Martinis S, Twele A, Strobl C, Kersten J, Stein E (2013) A multi-scale flood monitoring system based on fully automatic MODIS and TerraSAR-X processing chains. Remote Sens 5(11):5598–5619. https://doi.org/10.3390/rs5115598
13. McFeeters SK (1996) The use of the Normalized Difference Water Index (NDWI) in the delineation of open water features. Int J Remote Sens 17(7):1425–1432. https://doi.org/10.1080/01431169608948714

14. Kobayashi N, Tani H, Wang X, Sonobe R (2020) Crop classification using spectral indices derived from Sentinel-2A imagery. J Inf Telecommun 4(1):67–90. https://doi.org/10.1080/24751839.2019.1694765
15. Schumann GJ, Brakenridge GR, Kettner AJ, Kashif R, Niebuhr E (2018) Assisting flood disaster response with earth observation data and products: A critical assessment. Remote Sens 10(8):1230. https://doi.org/10.3390/rs10081230
16. Sentinel Application Platform (SNAP). https://step.esa.int/main/toolboxes/snap/
17. Sinha R, Bapalu GV, Singh LK, Rath B (2008) Flood risk analysis in the Kosi river basin, north Bihar using multi-parametric approach of Analytical Hierarchy Process (AHP). J Indian Soc Remote Sens. 36:335–349. https://doi.org/10.1007/s12524-008-0034-y
18. Sinha R, Bapalu GV, Singh LK et al (2008) Flood risk analysis in the Kosi river basin, north Bihar using multi-parametric approach of Analytical Hierarchy Process (AHP). J Indian Soc Remote Sens 36:335–349. https://doi.org/10.1007/s12524-008-0034-y
19. Torres R, Snoeij P, Geudtner D, Bibby D, Davidson M, Attema E, Potin P, Traver IN (2012) GMES Sentinel-1 mission. Remote Sens Environ 120:9–24. https://doi.org/10.1016/j.rse.2011.05.028
20. Xu H (2006) Modification of normalized difference water index (NDWI) to enhance open water features in remotely sensed imagery. Int J Remote Sens 27(14):3025–3033. https://doi.org/10.1080/01431160600589179
21. Karwariya S, Dutta S, Singh M, Kumar H, Kumar S, Meena VK, Bhattacharya BK (2022) Estimating fodder crops area using multi-date high resolution satellite data- a case study in Madhya Pradesh, India. Range Manag Agrofor 43(1):19–24

Geospatial Technology for Upland Catchment Management

An Optimal Sampling Design to Capture the Watershed-Scale Soil Moisture Dynamic in a Tropical Agricultural Watershed of Eastern India

Gurjeet Singh and Rabindra Kumar Panda

Abstract Understanding the soil moisture dynamic at the watershed-scale is essential for hydrological applications (i.e., drought monitoring, flood forecasting, irrigation, etc.) and river basin management activities. Globally, in-situ measured accurate soil moisture data at the watershed-scale is quite scarce due to the high maintenance cost of large-density sensor networks and complex/challenging conditions for soil moisture field campaigns. Characterizing the soil moisture variability at the watershed-scale requires a robust in-situ monitoring strategy at the point-scale to balance representativeness and minimization of monitoring cost. Thus, this study determined an optimal sampling design to capture the spatiotemporal variability of soil moisture at the watershed-scale. The study was conducted for the typical eastern Indian conditions of extreme seasonal variability that lead from very wet (during monsoon) to dry (during hot summer). Soil moisture measurements were carried out at 83 locations in an agricultural watershed of 500 km^2 for 56 days across a year. A hand-held soil moisture probe (ThetaProbe) was used for the measurements from June 2016 to July 2017. Based on the analyzes of 41,832 measurements collected during field measurements, it was found that the maximum numbers of required locations necessary to estimate watershed-mean soil moisture within ±2% absolute error are 30. Moreover, the five most representative locations identified through time stability analysis were found to be sufficient for capturing the temporal pattern of watershed-mean soil moisture with a root-mean-square error of ±2.17%. The findings will be helpful in providing guidelines for optimizing short-term measurement and a robust sensor network to assess the watershed-scale soil moisture dynamics.

Keywords Soil moisture · Spatiotemporal variability · Tropical watershed · Time stability · Watershed-scale

G. Singh (✉)
Department of Civil and Environmental Engineering, Michigan State University, East Lansing, MI 48824, USA
e-mail: singhg23@msu.edu

R. K. Panda
Centre for Climate Smart Agriculture, Siksha 'O' Anusandhan University, 751030, Bhubaneswar, Odisha, India

S. Dutta and V. Chembolu (eds.), *Recent Development in River Corridor Management*, Lecture Notes in Civil Engineering 376, https://doi.org/10.1007/978-981-99-4423-1_22

1 Introduction

Surface soil moisture is a key dynamic hydrological state variable [28] that affects various hydrological process. Spatiotemporal variation of surface soil moisture significantly affects the watershed-scale soil moisture dynamics, which may result in variations of surface atmospheric feedback, runoff dynamics, groundwater recharge, and crop yield. Understanding surface soil moisture dynamics at a watershed-scale with reasonable temporal and spatial resolution is required for hydrological modeling [7, 19, 30], climate modeling and weather prediction [1, 12, 20] and agricultural modeling [2, 23, 31]. Thus, precise measurements of surface soil moisture at the watershed-scale are necessary to fulfill the requirements of various applications.

The spatiotemporal variation in geophysical characteristics such as rainfall, vegetation cover, soil properties, and topography over a watershed-scale makes soil moisture distribution highly nonlinear across time and space. Therefore, measuring soil moisture in a large watershed (>100 km^2) to represent the average soil moisture dynamic accurately is challenging. The conventional in-situ point scale measurement (i.e., gravimetric sampling) of soil moisture is precise. Still, gravimetric sampling is not practicable for watershed-scale soil moisture measurement, where many in-situ observations are needed at frequent intervals. The use of electronic sensors-based geophysical techniques with fixed-type automatic data-logging devices for continuous in-situ soil moisture measurement eliminates the need for time-intensive gravimetric sampling [6]. But, it is expensive to maintain a sufficiently large-density sensor network for watershed-scale soil moisture assessment. Soil moisture scaling theory and soil moisture spatiotemporal variability analysis reveals that a reliable estimate of large-scale soil moisture could be obtained using a few-point observation [3, 10, 13, 22]. Inline this context, past studies show the potential of soil moisture spatiotemporal variability analysis with a few statistical analyzes to determine the number of required samples (NRS) to estimate mean soil moisture of a large area [3–5, 14, 29]. In addition, a hypothesis on the temporal stability of soil moisture spatial pattern [27] provided an opportunity to minimize the NRS to capture the temporal pattern of the soil moisture over a large region [4, 5, 10 and 11].

Notably, these studies also suggested that areal mean soil moisture assessment using a few-point observation and scale of temporal stability must be established using dense soil moisture measurements over a large region. However, due to expenses and limited conditions experienced in soil moisture field campaigns, monitoring is complex, and soil moisture spatiotemporal variability analysis in an area greater than 100 km^2 [5] is poorly understood. Over the past, studies focused on measuring soil moisture and its variability analysis either favoring the large spatial scale [8, 14, 17, 18] or long time periods [4, 15, 16, 21], but very few consider both of them [5, 9]. Besides, tropical regions are rarely studied for soil moisture variability analysis, which may hold key differences from previous studies due to very high variability in soil moisture from very dry to very wet soil conditions.

In view of the facts mentioned above, the present study aimed to investigate the long-term soil moisture spatiotemporal variability over a large tropical agricultural

watershed (>100 km^2) for the optimal sampling design of soil moisture measurements. For this objective, frequent in-situ measurements at various point locations were carried out in an eastern Indian watershed of 500 km^2 to capture different soil wetness conditions for a year.

2 Study Area and Measurements

2.1 Study Area

An agricultural watershed, namely, Rana watershed of approximately 500 km^2, located in the middle region of the Mahanadi River basin of eastern India, is selected for this study (Fig. 1). The climate of the watershed is tropical, having marked seasonality in rainfall with the long dry season. The average annual rainfall of the study area is 1458 mm, mainly occurring (about 70%) in the southwest monsoon season of June to September [24]. Due to the tropical climate, the study area experiences very high temperatures during April and May. The mean annual temperature of this region is 27.4 °C with maximum and minimum temperatures of 42.2 °C and 11.3 °C. Due to the high climate variability, the study watershed experiences varying soil wetness conditions, i.e., very dry to very wet and back to very dry conditions. Paddy is a dominant crop in the study region and is usually cultivated during the southwest monsoon season. Elevation in the watershed ranges between 22 and 299 m (see Fig. for the topography view). Based on the soil textural analysis of various locations of the watershed it was found that soil texture class of the watershed varies considerably from sandy loam to clay, where a major portion of the watershed has sandy loam, followed by sandy clay loam and clay loam.

2.2 Soil Moisture Measurements

With the aim of achieving dense sampling at a large spatial scale for a long period, 83 locations (i.e., 79 agricultural fields and 4 grasslands) were selected within the watershed of 500 km^2 for measuring soil moisture (see Fig. 1). In addition to the vegetation, the criteria for choosing the sampling locations were geophysical characteristics that affect the spatiotemporal variation of the soil moisture, such as soil texture and elevation. The choice of sampling periods was based on the criterion of minimum interaction with human activities, such as tillage. Therefore, soil moisture measurements were initiated in June when the paddy crop was planted in most fields. Samplings were not carried out for a one-month duration (10 December 2016−10 January 2017) due to tillage activities after the paddy crop in a few areas of the watershed for the cultivation of pulse crops (i.e., moong). Overall, soil moisture measurements were conducted for nearly one year, from 20 June 2016 to 12 July

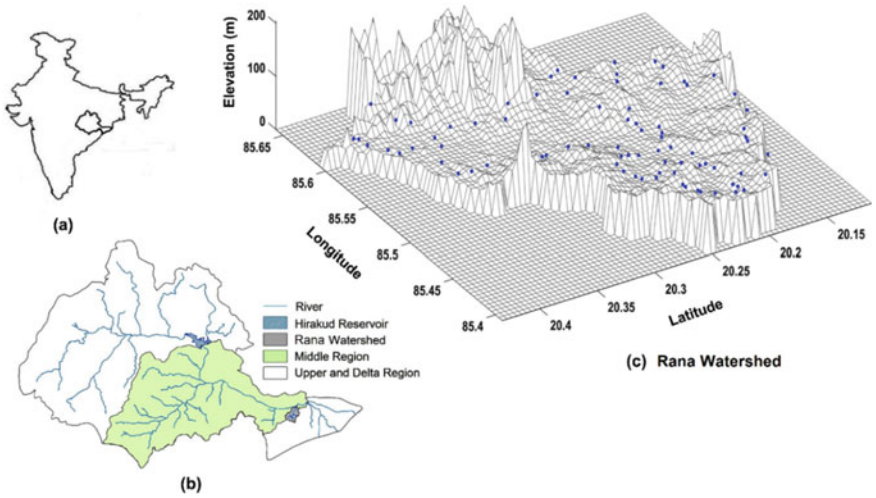

Fig. 1 **a** Location of Mahanadi river basin in India **b** Location of the study area, Rana watershed in Mahanadi River basin **c** Topographic overhead view of Rana watershed with sampling locations

2017, to capture the entire range of soil moisture variability from dry to wet and wet to dry conditions. Due to unfavorable conditions, sampling was not carried out frequently from August to October because of heavy rainfall and standing water in most paddy fields. Similarly, measurements were not taken frequently in April and May because of the soil's hardness (i.e., very dry condition). Overall, a total of 56 days of soil moisture sampling was carried out in one year. A view of soil moisture measurements during field campaigns is presented in Fig. 2a. The temporal pattern of the watershed-mean soil moisture based on soil moisture sampling at 83 sampling locations is also shown in Fig. 2b.

Soil moisture was sampled using an impedance probe (ThetaProbe, type ML3 and HH2 recording device, Delta-T Devices, Cambridge, England) which consists of four sharpened, 6 cm long stainless-steel rods. For each sampling location, three-point measurements of ThetaProbe were taken at 10–15 m separation distances, and each measurement consisted of three ThetaProbe samples. A total of nine ThetaProbe samples were taken from each sampling location to reduce the uncertainty in the estimates of mean soil moisture of a sampling location. Figure 3 shows a view of the sampling design and soil moisture measurements. During each sampling day, 747 soil moisture measurements were carried out, and a total of 41,832 samples were collected in 56 sampling days. In addition, on each sampling day, 10% of the total locations were also sampled with gravimetric sampling. Gravimetric samples were taken adjacent to one of the ThetaProbe samples with a soil core sampler having a fixed volume of 137 cm^3 with a 6 cm depth. The measured impedance from ThetaProbe was calibrated using gravimetric-based volumetric soil moisture content. A single generalized calibration of Thetaprobe was developed [25] for the watershed and used for precise soil moisture measurements at each sampling location.

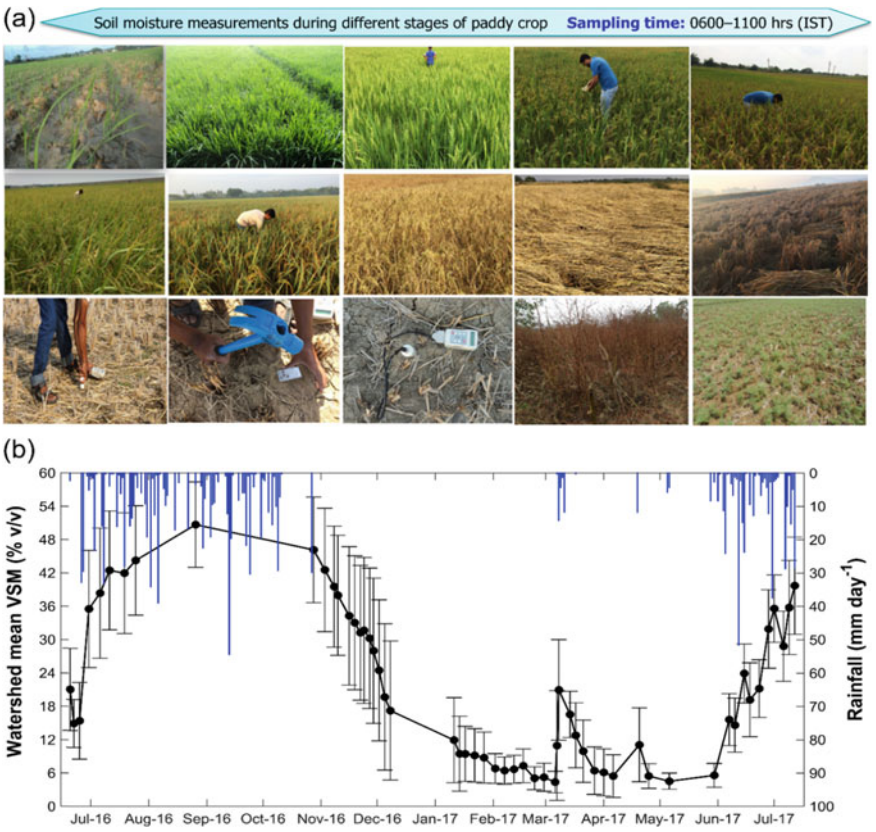

Fig. 2 **a** A view of soil moisture measurements during different stages of the paddy crop and field conditions throughout the year. **b** Temporal pattern of the watershed-mean volumetric soil moisture (VSM), along with error bars of ± 1 standard deviation in space. The blue bars represent a variation of daily rainfall measured by a weather station in the watershed

3 Methodology

The statistical properties of each sampling day and whole field campaign are analyzed in terms of their variability in space and time for the soil moisture spatiotemporal variability analysis as given below:

Let θ_{ijk} the soil moisture measured at point i, sampling location j and sampling day k, then the spatial mean of the sampling location and sampling day, $\overline{\theta_{jk}}$, is given by.

$$\overline{\theta_{jk}} = \frac{1}{N_p} \sum_{i=1}^{N_p} \theta_{ijk} \tag{1}$$

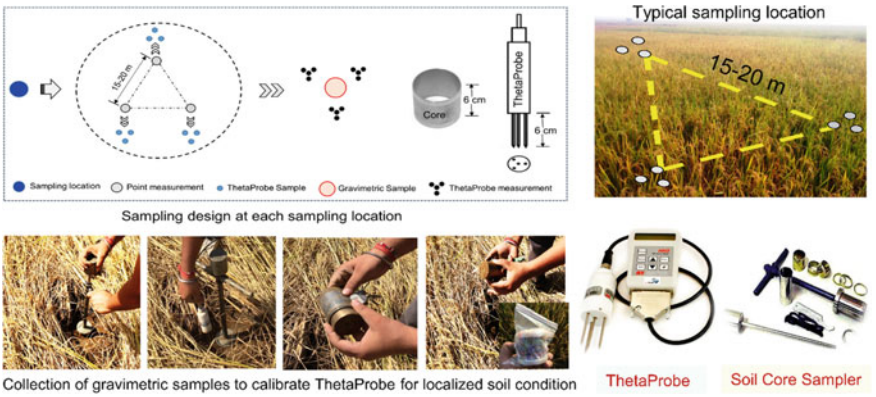

Fig. 3 Sampling design at each sampling location, where a large blue circle represents the sampling location and three-point measurements at the sampling location forming a triangle is shown with a gray circle. Small black circles show the shape of ThetaProbe measurement, and the red circle represents the position of the gravimetric sample. A view of the gravimetric sample collection in the rice field is presented through photographs

where N_p is the number of measurement points at the sapling location j. Similarly, the spatial mean of each sampling day, $\overline{\theta_k}$, can be defined as.

$$\overline{\theta_k} = \frac{1}{N}\sum_{j=1}^{N}\overline{\theta_{jk}} \tag{2}$$

where N is the number of sampling locations. Also, the temporal mean for each sampling location, $\overline{\theta_j}$, can be defined as:

$$\overline{\theta_j} = \frac{1}{M}\sum_{k=1}^{M}\overline{\theta_{jk}} \tag{3}$$

where M is the number of sampling days.

The coefficient of variation of each sampling day in space, CV_k, is calculated as follows:

$$CV_k = \frac{\sigma_k}{\overline{\theta_k}} = \frac{\sqrt{\frac{1}{N-1}\sum_{j=1}^{N}\left(\overline{\theta_{jk}} - \overline{\theta_k}\right)^2}}{\overline{\theta_k}} \tag{4}$$

where σ_k is the standard deviation in space for a sampling day.

Determination of standard deviation helps in the assessment of an optimal number of sampling locations (ONL) for estimating the mean soil moisture within a specified range of absolute error. The robust monitoring strategy has been optimized for

the watershed-mean soil moisture assessment through soil moisture spatiotemporal variability analysis using a statistical approach and time stability method.

3.1 ONL Analyzes Using a Statistical Approach

ONL, for watershed-mean soil moisture ($\overline{\theta_k}$) assessment within a specific value of absolute error, has been determined using Eq. 5 given by Gilbert (1987) and is expressed as:

$$ONL = \left(t_{1-\alpha/2, ONL-1} \frac{\sigma_E}{AE}\right)^2 \tag{5}$$

where σ_E is a standard error, $t_{1\text{-}\alpha/2,ONL\text{-}1}$ is the value of the student's t-distribution at a significance level α, and depending on the sample dimensions ONL; AE represents the absolute error (% v/v). If a reliable value of σ_E is not available, CV can be used to estimate ONL (Gilbert, 1987). For this, a functional relationship between the CV_k as well as σ_k and the $\overline{\theta_k}$ is investigated. An exponential function $CV_k = k_1 . e^{-k_2\overline{\theta_k}}$ was used to fit the CV_k -$\overline{\theta_k}$ relationship for characterizing the variations of soil moisture, as usually employed for soil moisture campaigns [3, 14], where k_1 and k_2 are the model fitting parameters. Based on the CV_k -$\overline{\theta_k}$ fitting, a relationship between σ_k and $\overline{\theta_k}$ can be derived as $\sigma_k = k_1 . \overline{\theta_k} . e^{-k_2\overline{\theta_k}}$. Further, the σ_k -$\overline{\theta_k}$ relationship is used to calculate the uncertainty in watershed-mean soil moisture assessment from a certain number of soil moisture samples, including its evolution with drying or wetting.

Moreover, the exponential law described by CV_k -$\overline{\theta_k}$, is employed to determine the ONL to achieve a specified uncertainty using σ_k -$\overline{\theta_k}$. Equation 6 is solved by an iterative procedure to estimate the ONL at a 5% significance level for different absolute errors (AE). The iterative process is repeated until $|ONL_l - ONL_{l-1}| \leq \varepsilon$, where ε is a control value, 0.5 in this study.

$$ONL_l = \left(t_{0.975, ONL_{(l-1)}-1} \frac{k_1 . \overline{\theta_k} . e^{-k_2\overline{\theta_k}}}{AE}\right)^2, \quad l = 1, 2, 3, \ldots \tag{6}$$

The statistical approach quantifies the ONL to determine the sampling size for capturing the spatial variability of soil moisture at the watershed-scale. But most hydrological applications require a temporal pattern of watershed-mean soil moisture. Besides, the exact position of the ONL in the study domain is essential to set up a soil moisture sensor network. Since the statistical approach fails to characterize the temporal pattern of the watershed-mean soil moisture, a time stability method is used to identify locations where the soil moisture can be considered "representative" of the entire area of study at the temporal scale.

3.2 ONL Analyzes Using Temporal Stability Analysis

The temporal stability analysis [27] identifies the sampling locations that maintain a consistent temporal relationship with the areal mean soil moisture with little variability. This study conducts temporal stability analysis based on the parametric test of the relative differences in soil moisture. For each sampling location j and total sampling days M, the mean relative difference of soil moisture, $\overline{\delta_j}$ (% v/v), and variance of the relative difference, $\sigma(\delta_j)^2$, is estimated as:

$$\overline{\delta_j} = \frac{1}{M} \sum_{k=1}^{M} \frac{\overline{\theta_{jk}} - \overline{\theta_k}}{\overline{\theta_k}} \tag{7.1}$$

$$\sigma(\delta_j)^2 = \frac{1}{M-1} \sum_{k=1}^{M} \left(\frac{\overline{\theta_{jk}} - \overline{\theta_k}}{\overline{\theta_k}} - \overline{\delta_j} \right)^2 \tag{7.2}$$

$\overline{\delta_j}$, at a sampling location computes the location's bias and helps to identify whether a particular location is wetter or drier than the areal mean. Generally, a "representative" location to capture the temporal pattern of the areal mean soil moisture can be identified by the low value of $\left|\overline{\delta_j}\right|$ and/or standard deviation of the relative difference, $\sigma(\delta_j)$. [17] considered combining $\overline{\delta_j}$ and $\sigma(\delta_j)$ statistical metrics relative difference and presented a comprehensive evaluation criterion (CEC) to include both the bias and accuracy to locate the best time-stable locations.

$$CEC_j = \sqrt{\left(\overline{\delta_j}\right)^2 + \sigma\left(\delta_j\right)^2} \tag{8}$$

Based on the rank-ordered CEC_j, the sampling location with the highest time stability is identified as the one with the lowest CEC_j value.

4 Results and Discussion

The temporal pattern of measured soil moisture was found to be highly linked to rainfall (see Fig. 2b). The measured soil moisture statistical analysis shows that the spatial CV_k ranges between 0.151 and 0.901. CV_k was found to be very high during dry periods, whereas low in wet periods and, on average equal to 0.404. On the other hand, the temporal CV_j was found to have an average of 0.723, considerably higher than CV_k, and ranges between 0.578 and 0.887. This confirms that soil moisture temporal variability is more significant than spatial variability and indicates that ONL to capture the temporal pattern of the watershed-mean soil moisture can be derived in this study region. The high CV_k value follows the findings reported in the past investigation on soil moisture variability in relation to the spatial variability of

soil moisture and the dimension of the investigated area [3–5, 14]. Specifically, the spatial CV_k increases with the increase in the area, where average CV_k ranges from 0.06 to 0.20 for the area of 1 m^2 and 250 km^2, respectively, at 0–15 cm depth in central Italy [5]. Comparing σ_k and CV_k values presented in [14], the values found for the eastern Indian watershed are very similar.

4.1 ONL to Capture Watershed-Mean Soil Moisture

Based on the in-situ measurements, an analytical relationship was fitted between $\overline{\theta_k}$ and the CV_k for the growing season, non-growing season, and the whole year, as presented in Table 1, and Fig. 4a. Further, the fitted parameters of CV_k verses $\overline{\theta_k}$ relationship were utilized to derive a relationship between σ_k verses $\overline{\theta_k}$ as shown in Fig. 4b to capture the spatial variability of soil moisture. The distribution of σ_k verses $\overline{\theta_k}$ shows that σ_k increases until $\overline{\theta_k}$ reaches around 30% and decreases beyond that, whereas CV_k shows a rapid decreasing pattern with increasing $\overline{\theta_k}$. It was also observed that CV_k has a very less scattered pattern as $\overline{\theta_k}$ decreases during the growing season but is found to be a widely scattered pattern during the non-growing season. Overall, a decreasing exponential pattern of $CV_k - \overline{\theta_k}$ and a convex upward trend in $\sigma_k - \overline{\theta_k}$ reported in this study is similar to those reported in previous studies across the world [3–5, 13, 14, 17] (Fig. 4).

Further, the fitted decreasing exponential pattern of CV_k, $\overline{\theta_k}$ was used to quantify the ONL as a function of the average wetness condition and in relation to a prefixed significance level and varying absolute errors. Figure 5a. demonstrates the ONL (using Eq. 6) to capture the watershed-mean soil moisture with a 5% significance level and within an absolute error of ±2%, during different seasons. The ONLs were found to be equal to 30 for the growing season and fewer for the non-growing season, equivalent to 20, whereas a maximum ONL of 25 is needed for the whole year to assess watershed-mean soil moisture. The maximum ONL found to be 30 that is during the growing season confirms the effectiveness of the sampling design adopted for this study, where 83 locations were monitored. Analysis of different absolute errors for ONL shows that fewer resources are needed on higher absolute error (> ±2%) for watershed-mean soil moisture estimation (Fig. 5b). The reported analysis reveals that ~10 to 15 sampling locations are sufficient to capture the spatial pattern of the watershed-mean having an area of 500 km^2 with a more relevant range of absolute

Table 1 The exponential fitting parameters of CV_k versus $\overline{\theta_k}$ relationship and the corresponding coefficient of determination (R^2)

Season	CV_k versus $\overline{\theta_k}$ relationship		
	k_1	k_2	R^2
Growing season	1.537	− 0.043	0.994
Non-growing season	0.592	− 0.028	0.543
Whole year	0.573	− 0.020	0.498

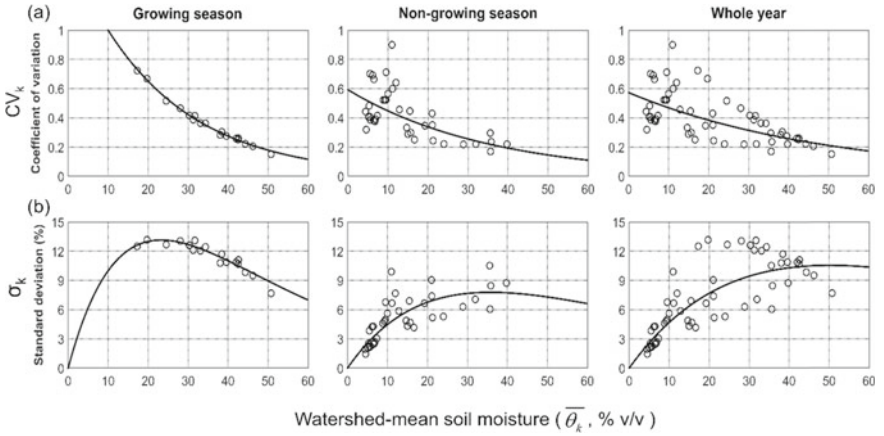

Fig. 4 Analytical relationship between watershed-mean soil moisture ($\overline{\theta_k}$) and statistical characteristics **a** coefficient of variation (CV_k), **b** standard deviation (σ_k) of soil moisture measurements at watershed-scale during each sampling day for the growing season, non-growing season, and the whole year

error between ±4% and ±6%. The ONL obtained in this study matches with the ONL found for different hydroclimatic regions and geomorphological conditions with varying spatial scales, ranging between 15 and 40 sampling locations [4, 5, 14]. Since the computation of the "average" error on the soil moisture temporal pattern is necessary [4]), a temporal pattern of spatial mean soil moisture is analyzed to assess ONL for a reliable estimate of watershed-mean soil moisture.

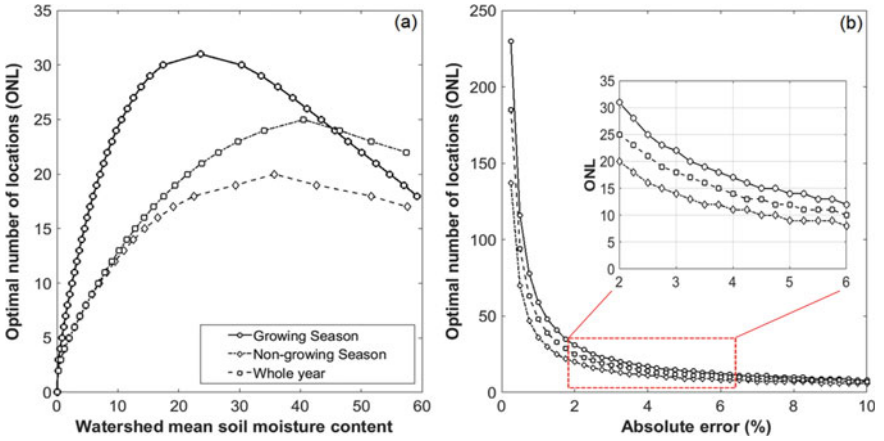

Fig. 5 The optimal number of locations to capture the watershed-mean soil moisture at a 5% significance level during different seasons **a** with ±2% absolute error and **b** at different absolute errors

4.2 *ONL to Capture the Temporal Pattern of Watershed-Mean Soil Moisture*

The most temporally stable locations that can serve as representative locations to capture the watershed-mean soil moisture were identified using time stability analysis based on the parametric test of relative differences (Eq. 7). Figure 6a shows the time stability characteristics, mean relative difference ($\overline{\delta_j}$), ranked from smallest to largest along with ± 1 standard deviation. The sampling locations representing positive $\overline{\delta_j}$ values constantly overestimate the watershed-mean soil moisture, whereas negative values of $\overline{\delta_j}$ represents underestimation of the watershed-mean soil moisture consistently. Generally, the range of variation in $\overline{\delta_j}$ increases with the investigated area size [5]. The *CEC* (Eq. 8) has the ability to effectively eliminate systematic bias as well as accurately capture the watershed-mean soil moisture at each sampling time. The selected most time-stable location based on the lowest CEC value was found to capture the watershed-mean soil moisture with a high correlation ($R^2 = 0.852$) but with a high Root-Mean-Square error (RMSE) of 5.573%. Though only one representative location has the capability to capture the temporal variation pattern of the watershed-mean soil moisture with high correlation, it fails to provide a reasonable accuracy (RMSE of $\pm 4\%$ or better). Notably, this contradicts the previous study's finding [5], where one representative site can capture the temporal pattern of areal mean soil moisture with reasonable accuracy at a regional scale of 200 km^2. In further analysis, it was found that the five most time-stable locations of the study watershed can capture watershed-mean soil moisture with an excellent correlation ($R^2 = 0.981$) and RMSE of $\pm$ 2.17%. The scatter plot in Fig. 6b shows ensemble soil moisture of the identified five best time-stable locations that can represent watershed-mean soil moisture with an error range of $\pm 4\%$. These analyzes imply that the five time-stable sampling locations could be utilized to capture the temporal pattern of watershed-mean soil moisture with reasonable accuracy and confirm the robust optimal sampling design for the watershed of 500 km^2. The spatial distribution of the five most time-stable locations in the watershed along with other sampling locations (Fig. 7), shows that identified sampling locations are well distributed across the watershed. Remarkably it was also found that the identified time-stable locations have different elevations and soil texture conditions.

5 Conclusion

On the analyzes of 41,832 in-situ soil moisture samples collected during one year at 83 sampling locations in a watershed of 500 km^2, it can be concluded that the dense in-situ measurements help to characterize the soil moisture spatiotemporal variability at the watershed-scale. The characterization of soil moisture spatiotemporal variability reveals that sampling at a few locations (~30 locations) is sufficient for capturing the spatial pattern of the soil moisture at a watershed of 500 km^2. In

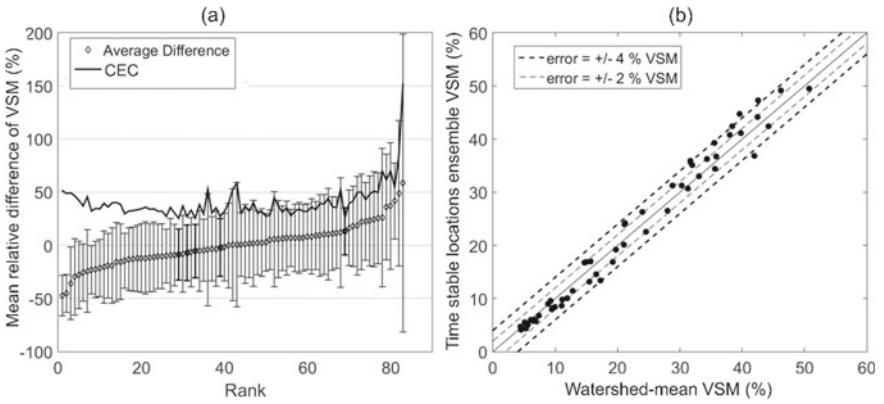

Fig. 6 **a** Rank ordered mean relative difference of soil moisture at each sampling location with ±1 standard deviation error bars. The solid line is a comprehensive evaluation criterion (CEC) to identify the best time-stable locations. The thick bars are the five best time-stable locations in the watershed based on the CEC. **b** Comparison of watershed-mean VSM with the ensemble VSM of the identified five best time-stable locations to achieve a reasonable accuracy (RMSE of ±4% or better)

comparison, very fewer resources, and nearly five representative or time-stable locations are required to capture the temporal variation pattern of the watershed-mean soil moisture within an RMSE of ~ ±2%. However, the optimal sampling design strategy must be transferred to ungauged regions to avoid the monitoring cost of dense measurements. The selection of representative locations a priori in ungauged areas to capture the temporal variation pattern of the areal mean soil moisture is possible with various geophysical characteristics information. A few past studies [17, 26], reveal that soil properties and topography are significant geophysical parameters that jointly control spatiotemporal persistence. However, more detailed investigations are needed towards transferring optimal sampling design strategy to the ungauged area by assessing the effects of heterogeneities of similar or different geophysical properties in other regions and for different space and time scales. In this study, a large soil moisture dataset at a watershed-scale has been generated through several intensive field campaigns for tropical regions where soil moisture information is sparse. The optimal sampling design based on long-term intensive sampling can be utilized as a guideline for designing a robust sensor-based network at the watershed-scale and could be helpful in planning sampling for satellite soil moisture product validation. The data used for optimal sampling design focuses only on one watershed in the tropical region of India. Therefore, further analysis is needed using in-situ soil moisture measurements of other watersheds in tropical climates and possibly other climate regions to assess the applicability of such an approach.

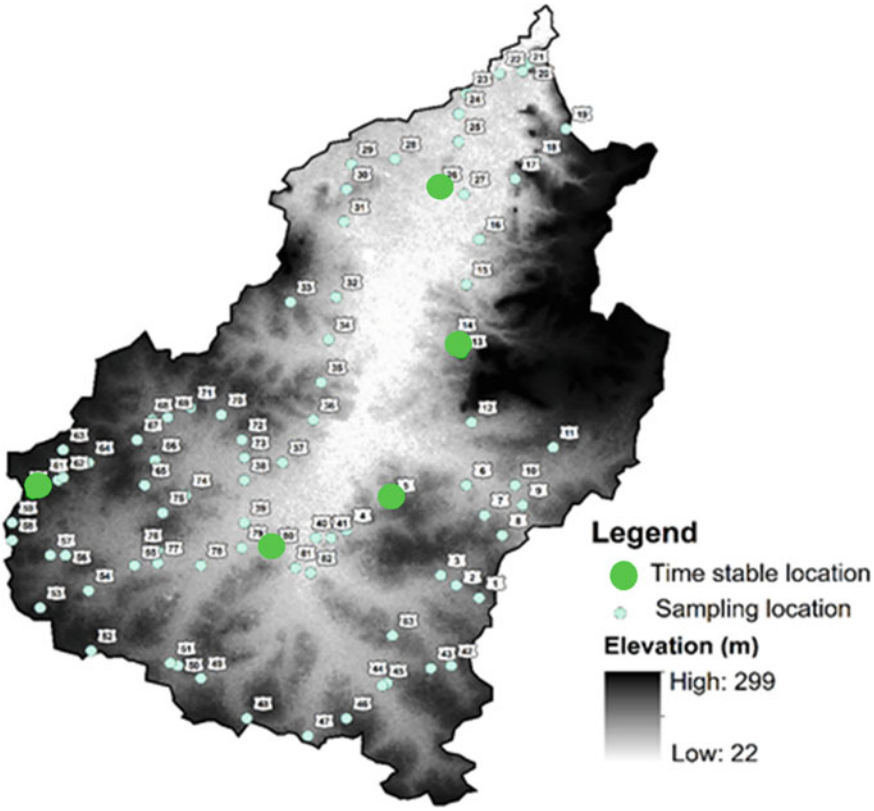

Fig. 7 The elevation map of the watershed shows 83 soil moisture sampling locations. Locations marked with a circle are the five most representative or time-stable locations of the watershed

References

1. Albergel C, Calvet JC, De Rosnay P, Balsamo G, Wagner W, Hasenauer S, Mahfouf JF (2010) Cross-evaluation of modelled and remotely sensed surface soil moisture with in situ data in Southwestern France. Hydrol Earth Syst Sci 14(11):2177–2191
2. Bolten JD, Crow WT, Jackson TJ, Zhan X, Reynolds CA (2010) Evaluating the utility of remotely sensed soil moisture retrievals for operational agricultural drought monitoring. IEEE J Sel Top Appl Earth Obs Remote Sens 3(1):57–66
3. Brocca L, Morbidelli R, Melone F, Moramarco T (2007) Soil moisture spatial variability in experimental areas of central Italy. J Hydrol 333(2–4):356–373
4. Brocca L, Melone F, Moramarco T, Morbidelli R (2010) Spatial-temporal variability of soil moisture and its estimation across scales. Water Resour Res 46(2):1–14
5. Brocca L, Tullo T, Melone F, Moramarco T, Morbidelli R (2012) Catchment scale soil moisture spatial-temporal variability. J Hydrol 422–423:63–75
6. Bogena HR, Herbst M, Huisman JA, Rosenbaum U, Weuthen A, Vereecken H (2010) Potential of wireless sensor networks for measuring soil water content variability. Vadose Zone J 9(4):1002–1013

7. Chen F, Crow WT, Starks PJ, Moriasi DN (2011) Improving hydrologic predictions of a catchment model via assimilation of surface soil moisture. Adv Water Resour 34(4):526–536
8. Choi M, Jacobs JM (2011) Spatial soil moisture scaling structure during soil moisture experiment 2005. Hydrol Process 25(6):926–932
9. Cosh MH, Jackson TJ, Moran S, Bindlish R (2008) Temporal persistence and stability of surface soil moisture in a semi-arid watershed. 112:304–313
10. Cosh MH, Stedinger JR, Brutsaert W (2004) Variability of surface soil moisture at the watershed scale. Water Resour Res 40(12):1–9
11. Cosh MH, Jackson TJ, Starks P, Heathman G (2006) Temporal stability of surface soil moisture in the Little Washita River watershed and its applications in satellite soil moisture product validation. 323:168–177
12. Entekhabi D (1995) Recent advances in land-atmosphere interaction research. Rev Geophys 33(S2):995–1003
13. Famiglietti J (1999) Ground-based investigation of soil moisture variability within remote sensing footprints during the Southern Great Plains 1997(SGP97) Hydrology Experiment. Water Resour Res 35(6):1839–1851
14. Famiglietti JS, Ryu D, Berg AA, Rodell M, Jackson TJ (2008) Field observations of soil moisture variability across scales. Water Resour Res 44(1):1–16
15. Hu W, Shao M, Han F, Reichardt K (2011) Spatio-temporal variability behaviour of land surface soil water content in shrub- and grassland. Geoderma 162(3–4):260–272
16. Hu W, Shao M, Han F, Reichardt K, Tan J (2010) Watershed scale temporal stability of soil water content. Geoderma 158(3–4):181–198
17. Jacobs JM, Mohanty BP, Hsu EC, Miller D (2004) SMEX02: Field scale variability, time stability and similarity of soil moisture. Remote Sens Environ 92(4):436–446
18. Joshi C, Mohanty BP, Jacobs JM, Ines AVM (2011) Spatiotemporal analyses of soil moisture from point to footprint scale in two different hydroclimatic regions. Water Resour Res 47 (1)
19. Koster RD, Mahanama SPP, Livneh B, Lettenmaier DP, Reichle RH (2010) Skill in streamflow forecasts derived from large-scale estimates of soil moisture and snow. Nat Geosci 3:613
20. Koster RD, Dirmeyer PA, Guo Z, Bonan G, Chan E, Cox P, Yamada T (2004) Regions of strong coupling between soil moisture and precipitation. Science 305(5687):1138–1140
21. De Lannoy GJM, Houser PR, Verhoest NEC, Pauwels VRN, Gish TJ (2007) Upscaling of point soil moisture measurements to field averages at the OPE3 test site. J Hydrol 343(1–2):1–11
22. Mohanty BP, Skaggs TH (2001) Spatio-temporal evolution and time-stable characteristics of soil moisture within remote sensing footprints with varying soil, slope, and vegetation. Adv Water Resour 24(9–10):1051–1067
23. Narasimhan B, Srinivasan R (2005) Development and evaluation of Soil Moisture Deficit Index (SMDI) and Evapotranspiration Deficit Index (ETDI) for agricultural drought monitoring. Agric For Meteorol 133(1):69–88
24. Singh G, Panda RK, Nair A (2020) Regional scale trend and variability of rainfall pattern over agro-climatic zones in the mid-Mahanadi River basin of eastern India. J. Hydro-environ. Res. 29:5–19
25. Singh G, Panda RK, Bisht DS (2021) Improved generalized calibration of an impedance probe for soil moisture measurement at regional scale using Bayesian neural network and soil physical properties. J Hydrol Eng 26(3):04020068
26. Singh G, Panda RK, Mohanty BP (2019) Spatiotemporal analysis of soil moisture and optimal sampling design for regional-scale soil moisture estimation in a tropical watershed of India. Water Resource Research. 55(3):2057–2078
27. Vachaud G, Passerat De Silans A, Balabanis P, Vauclin M (1985) Temporal stability of spatially measured soil water probability density function1. Soil Sci Soc Am J 49:822–828
28. Vinnikov KY, Robock A, Qiu S, Entin JK, Owe M, Choudhury BJ, Njoku EG (1999) Satellite remote sensing of soil moisture in Illinois, United States. J Geophys Res: Atmos 104(D4):4145–4168
29. Wang C, Zuo Q, Zhang R (2008) Estimating the necessary sampling size of surface soil moisture at different scales using a random combination method. J Hydrol 352(3–4):309–321

30. Western AW, Grayson RB, Blöschl G (2002) Scaling of soil moisture: A hydrologic perspective. Annu Rev Earth Planet Sci 30(1):149–180
31. de Wit AJW, van Diepen CA (2007) Crop model data assimilation with the Ensemble Kalman filter for improving regional crop yield forecasts. Agric For Meteorol 146(1–2):38–56

Modeling Snow and Glacier Melt Runoff in the Beas River Basin Using SRM Degree Day

Gopinadh Rongali, Ashok K. Keshari, Rakesh Khosa, and Ashvani K. Gosain

Abstract The runoff from snow and glacier melt is one of the most important sources of freshwater for the ever-present Himalayan Rivers. Satellite imagery and Geographic Information System (GIS) tools like Digital Elevation Model (DEM) and simulation models have been highly useful in figuring out and connecting between theoretical concepts and actual conditions in hilly and difficult-to-reach places. The present study uses a variety of geospatial tools, including Remote Sensing (RS), GIS, and the snowmelt runoff model (SRM), to estimate snow and glacier melt runoff in the Beas River basin of the Western Himalayas. This research used Landsat-8 snow cover data, Advanced Spaceborne Thermal Emission and Reflection Radiometer (ASTER) DEM, GIS, and ultimately the Windows Version of the Snowmelt Runoff Model (WinSRM) to estimate the snow and glacier melt runoff in the Beas River basin up to Pandoh Dam. The SRM has been done using hydro-meteorological data from the years 2013 to 2015. Remote sensing data was utilized to calculate the Beas River's temporal Snow Cover Area (SCA) from 2013 to 2015, and DEM was used to identify elevation zones and aspect maps. The findings showed that there is little difference between the calculated runoff (772.51 m^3/s) and the observed runoff (802.47 m^3/s). The data analysis shows that the SRM model is the most effective method for calculating runoff from snow and glacier melt in mountainous regions. For the period of April 2013 to October 2015, the overall coefficient of correlation (R^2) accuracy of SRM for a portion of the Beas River basin is 0.77. Snowmelt accounts for around 6.68% of the total stream flow at Pandoh Dam in the Beas River basin.

G. Rongali (✉) · A. K. Keshari · R. Khosa · A. K. Gosain
Department of Civil Engineering, Indian Institute of Technology Delhi, New Delhi, India
e-mail: gopinadh01@gmail.com

A. K. Keshari
e-mail: akeshari@civil.iitd.ac.in

R. Khosa
e-mail: rkhosa@civil.iitd.ac.in

A. K. Gosain
e-mail: gosain@civil.iitd.ac.in

S. Dutta and V. Chembolu (eds.), *Recent Development in River Corridor Management*,
Lecture Notes in Civil Engineering 376, https://doi.org/10.1007/978-981-99-4423-1_23

Keywords Remote sensing · Snow and glacier melt runoff · Snow cover area · Temperature index model · SRM · GIS

1 Introduction

The management of vast catchments' water resources depends on the understanding of water flow. Estimating and predicting the runoff from melting snow and glaciers and the resulting stream flow from different catchments is crucial for planning, managing projects in river valleys, and understanding various hydro-meteorological processes. Together with giving accurate predictions of runoff volumes, this is essential for predicting water supplies, issuing flood warnings, managing water resources, and navigating. In alpine basins with high snowmelt runoff, the daily streamflow is simulated and predicted using the Martinec model, commonly known as the Martinec-Rango model. SRM's runoff calculations seem to be quite simple to comprehend. Various academics have used the model to date on more than 100 basins located in 29 different countries [2]. SRM can evaluate and estimate snow melt runoff in mountain basins. Using a known or anticipated discharge value as the starting point, a model run may last an indefinite number of days. The SRM requires knowledge about the amount of snow cover (S), temperature (T), and precipitation (P) for different elevation zones. The collection of spatial and temporal information on expansive catchments requires the use of remote sensing.

For the three months of April, May, and June of 1969, Daoo and Shirvaikar [1]calculated the discharge from snowmelt in the Beas River watershed in the Himalayas using the energy balance approach. Then they contrasted their findings with the River's snowmelt discharge. According to Gupta et al. [4], melting snow may significantly alter how much water flows in a river. For predicting snowmelt runoff, this knowledge is crucial. Kumar et al. [6] performed snow cover mapping and snow melt runoff modeling using satellite data as input. Nagler and Rott [12] devised a method for snow mapping in mountain areas and glaciers based on C-band European Remote Sensing (ERS) Synthetic Aperture Radar (SAR) images from repeat orbits, and the SRM has been tested for two drainage basins in the Austrian Alps. For basins in the Austrian Zillertal Alps that are a component of a network of reservoirs for hydropower production, Nagler and Rott [13] conducted real-time projections of the snow melt flow up to six days in advance. Additionally, Nagler and Rott [14] developed maps of melting snow using an autonomous snow mapping system based on change detection and SAR data from the Alpine basin Tuxbach in the Eastern Alps. Prasad and Roy [16] found that anticipating snowmelt runoff is critical for hydropower generation and water management in India's Western Himalayan Rivers during non-monsoon season. Singh et al. [18] investigated the relating air temperature to the depletion of snow-covered area in a Himalayan basin. The average contribution of snow and glacier melt runoff to the annual flow of the Beas River at Pandoh Dam was calculated using the water balance approach by Kumar et al. [7]. Singh et al. [19] studied a comparative hydrological approach to control the transfer of

hydrologic characteristics from gauged to ungauged catchments. According to Yuan et al. [22], the precipitation in the mid-Tianshan mountains was related to the Pacific North American (PNA) pattern. Engelhardt et al. [3] assessed the mass balance and outflow over 60 years for the Chhota Shigri glacier. Bhattacharya et al. 2019 only examined a small number of precipitation datasets or failed to consider reanalysis products.

Snowmelt contributes more to streamflow as the basin's elevation rises while rain's contribution decreases. Snowmelt runoff dominates the runoff over 3000 m of elevation. It is always challenging to regularly map and monitor snow cover and glaciers in these steep locations due to the difficulty of access to and the scarcity of ground observation sites. As a result, this study has been made to simulate the snow and glacier melt runoff using the Snowmelt Runoff Model for Windows (WinSRM) with the aid of Landsat-8 satellite data, Remote Sensing (RS), and Geographic Information System (GIS).

2 The Study Area

The Beas River basin up to Pandoh Dam is the subject of current research (Fig. 1). One of the largest tributaries of the Indus River system, the Beas River basin is located between 31° and 32° N and 77° and 78° E. It starts in Rothang Pass, 3900 m above sea level, and travels through Larji before turning right and heading southwest till it reaches Pandoh dam. The catchment area's rocks have sharp slopes and are often deserted. Between Pandoh Dam and the Parbati sub-northeast watershed, the elevation ranges from 846 to 6500 m. A significant stretch of the river is covered in wintertime snow, which feeds the Beas River throughout the summer. Water is transferred from the Beas River to the Satluj River via Pandoh Dam so that Dehar Power Plant may generate electricity.

3 Methodology

The Beas River basin up to Pandoh Dam has been utilized to estimate snow and glacier melt flow using Landsat-8 snow cover data, ASTER DEM with RS and GIS, and WinSRM. Hydro-meteorological data from the years 2013 to 2015 was used to complete the SRM. To calculate the Beas River temporal SCA from 2013 to 2015, Landsat-8 data were used. Aspect maps and elevation zones were later created using the DEM. The temperature index-based snow and glacier melt runoff simulation model developed by SRM was used in this study to simulate runoff from snow and glacier melt. The daily hydro-meteorological data—rainfall and temperature—for three stations were acquired from the MOSDAC website (https://www.mosdac.gov.in/) and used to simulate snow and glacier melt runoff.

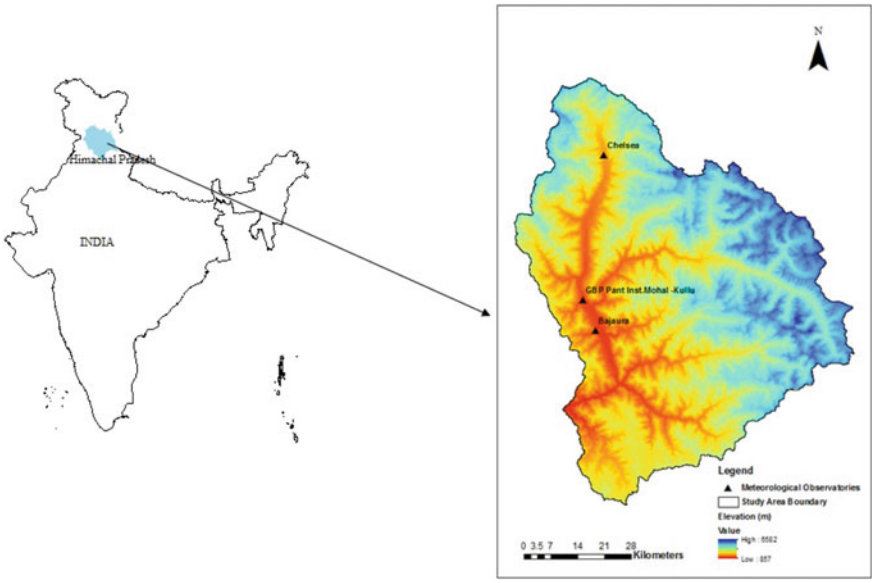

Fig. 1 Himachal Pradesh's beas river basin

SRM has been developed to simulate and forecast daily streamflow in mountain basins where snowmelt is a primary runoff factor. As satellite remote sensing of snow cover has improved, SRM is being deployed in even larger basins. Also, the World Meteorological Organization (WMO) evaluated SRM for runoff simulations and partly recreated circumstances of real-time runoff predictions with success ([20, 21]). Equation (1) explains how the projected recession flow is multiplied with the water produced by snowmelt and rainfall to produce the daily outflow from the basin:

$$Q_{n+1} = [C_{Sn} \cdot a_n(T_n + \Delta T_n)S_n + C_{Rn}P_n]\frac{A \cdot 10000}{86400}(1 - k_{n+1}) + Q_n k_{n+1} \quad (1)$$

where Q = Average daily discharge [m^3 s^{-1}], C = Runoff coefficient (runoff/precipitation) expresses losses, with c_S Snow melting and c_R to rain, a = Degree-day factor [cm^o $C^{-1}d^{-1}$] 1° day snowmelt depth, ΔT = Lapse rate adjustment while extrapolating station temperature to average basin or zone elevation [°C d], S = Snow coverage ratio, P = Runoff-causing precipitation [cm]. TCRIT assesses if this contribution is rain and immediate. TCRIT stores fresh snow over snow-free areas until melting occurs. A = Area of the basin or zone [km^2], k = Recession coefficient shows discharge drop without snowmelt or rain: $k = \frac{Q_{m+1}}{Q_m}$ (m, m + 1 are the sequence of days during a true recession flow period), n = Discharge period in days. Equation 1 assumes an 18-h lag between the daily temperature cycle and discharge cycle. The nth day's degree-days correlate to the (n + 1)th day's discharge. Various lag times

can be introduced by a subroutine, $\frac{10000}{86400}$ = Conversion factor from cm·km^2 d^{-1} to m^3 s^{-1}.

T, S, and P are daily variables; cR, cS, lapse rate to estimate T, TCRIT, k, and lag time are basin- or climate-specific. If the basin's elevation range exceeds 500 m, it should be separated into 500 m zones. The model equation for a 1500-m height range and three zones A, B, and C is:

$$Q_{n+1} = \left\{ \begin{array}{l} [c_{SAn} \cdot a_{An} (T_n + \Delta T_{An}) S_{An} + c_{RAn} P_{An}] \frac{A_A \cdot 10000}{86400} \\ +[c_{SBn} \cdot a_{Bn} (T_n + \Delta T_{Bn}) S_{Bn} + c_{RBn} P_{Bn}] \frac{B_B \cdot 10000}{86400} \\ +[c_{SCn} \cdot a_{Cn} (T_n + \Delta T_{Cn}) S_{Cn} + c_{RCn} P_{Cn}] \frac{C_C \cdot 10000}{86400} \end{array} \right\} (1 - k_{n+1}) + Q_n k_{n+1} \quad (2)$$

SRM may operate in simulation mode without updating. The accuracy of the simulation is only evaluated using the discharge data. In ungauged basins, the simulation is initiated using an estimated discharge derived from a neighbring gauged basin. The simulation in the Beas River basin was conducted using the program WinSRM version 1.12, which simulates snow and glacier melt runoff. This fundamental strategy has been used to estimate runoff from snow and glacier melt (Fig. 2). The temperature index of degree-day method is the name of the technique.

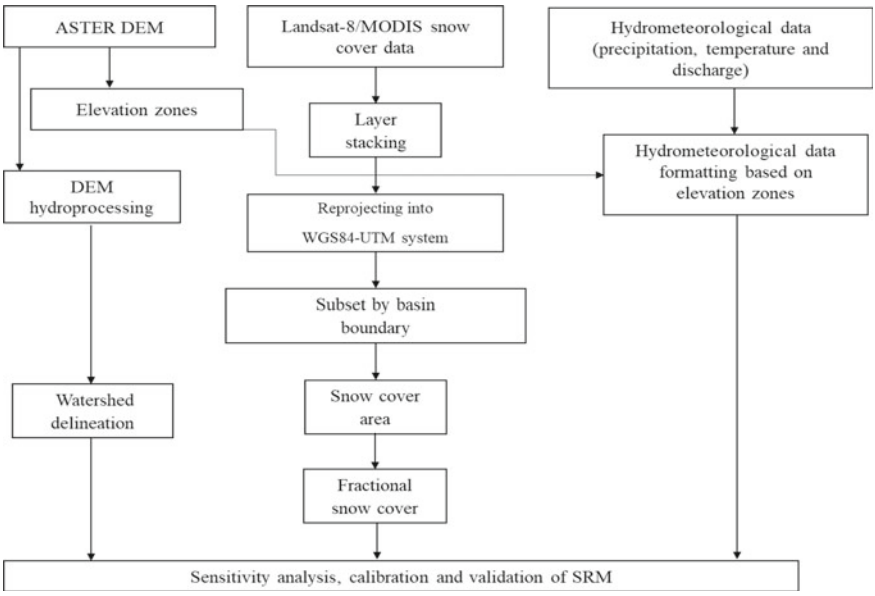

Fig. 2 Flowchart of the snow melt runoff model (SRM)

The meteorological network for data gathering in the Himalayan highlands is quite subpar maximum and minimum temperatures, humidity, and wind speed are readily available. Since temperature indices are regarded to be the most accurate technique to quantify the heat transfer processes that take place when snow melts, they are often used to determine how quickly snow melts. The complicated energy balance that results in snow melt has been determined by using the air temperature in degrees per day as an indication. A degree day is the amount of heat that lingers for 24 h when a temperature deviates 1 °C from the reference temperature. The most popular phrase connecting daily snow melt to temperature index is,

$$M = D_f(T_i - T_b) \tag{3}$$

M = Water melted in cm/sec, Df = Degree-day factor (cm ºC day^{-1}), Ti = Index air temperature (ºC), T_b = Base temperature (usually 0 ºC).

R^2 and D_v as defined below are two criteria which are calculated by the model automatically [11].

$$R^2 = 1 - \frac{\sum_{i=1}^{n} (Q_i - Q_j)^2}{\sum_{i=1}^{n} (Q_i - \bar{Q}_j)^2} \tag{4}$$

$$D_v = \frac{V_R - V_{R'}}{V_R} \text{X}100 \tag{5}$$

where R^2 is a measure of model efficiency [−], Q_i is measured daily discharge [m^3s^1], Q_j is simulated daily discharge [m^3s^1], $\overline{Q}$ is the average daily discharge for the simulation year or simulation season [m^3s^1], n is the number of daily discharge values [−], D_v is the percentage difference between the total measured and simulated runoff [%], V_R is measured runoff volume [m^3] and V'$_R$is simulated runoff R volume [m^3].

4 Results and Discussion

The ASTER GDEM has been used to create the 12 elevation bands or zones, each of which is 500 m wide (Fig. 3), for the study area selected river basin, with the exception of A and L. These elevation bands and zones have been used to calculate the mean elevation of each elevation zone. The catchment area distribution for different altitudinal zones is shown by the hypsometric curve in Fig. 4, and Table 1 provides the characteristics of each zone (Fig. 5).

The watershed has been categorized and separated into elevation zones using ArcGIS functions for snow and glacier melt runoff modeling using SRM. With the changing height and geographical breadth of the DEM of the catchment, 12 elevation

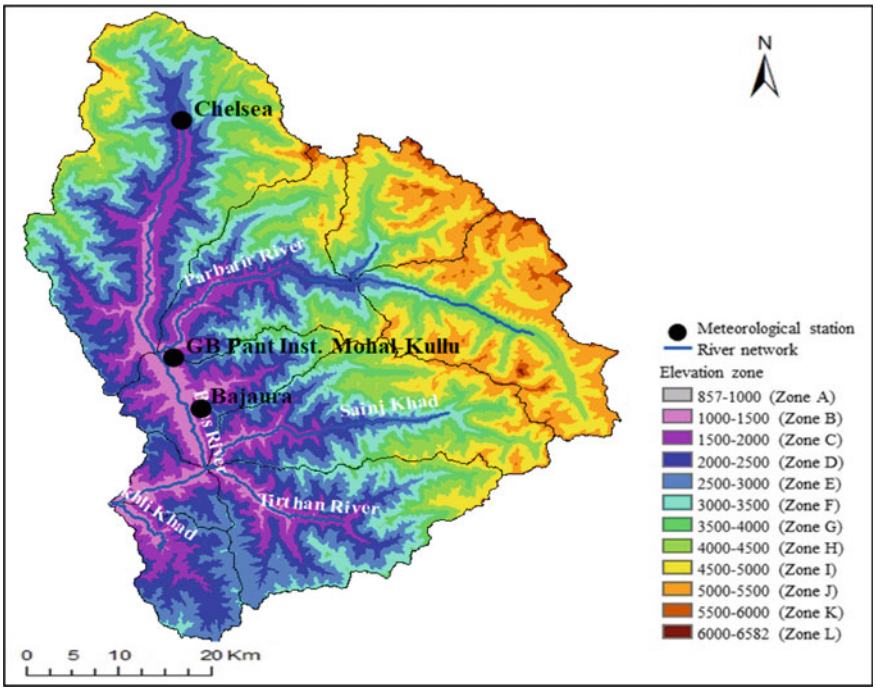

Fig. 3 GDEM of the Beas river basin showing the 12 altitudinal zones used in this investigation

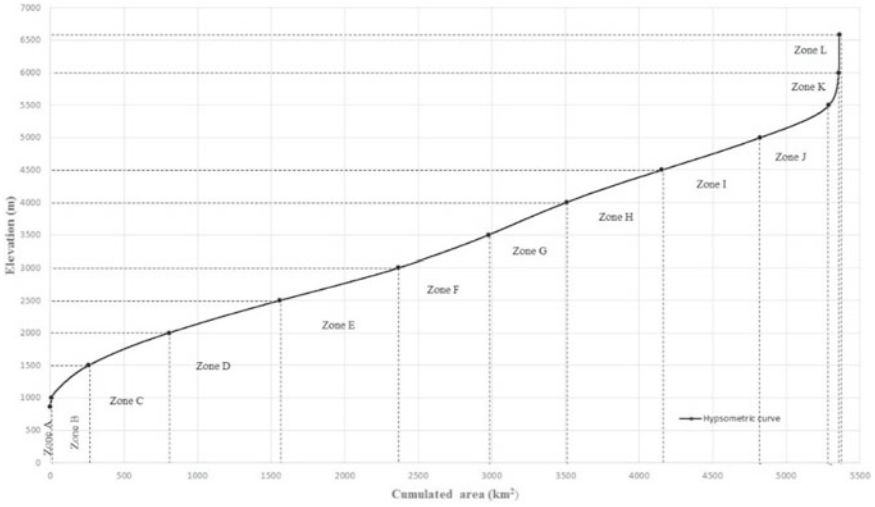

Fig. 4 Beas river basin hypsometric curve showing area in 12 elevation zones

Table 1 DEM of Beas river basin elevation zones

Zone	Elevation range (m)	Area (%)	Area (km^2)	Cumulative area (km^2)
A	857–1000	0.17	9.4	9.4
B	1000–1500	4.69	252.8	262.2
C	1500–2000	10.17	547.7	809.9
D	2000–2500	14.07	757.5	1567.4
E	2500–3000	15	808	2375.4
F	3000–3500	11.39	613.6	2989
G	3500–4000	9.88	532.2	3521.2
H	4000–4500	12.10	651.6	4172.8
I	4500–5000	12.46	671.2	4844
J	5000–5500	8.68	467.4	5311.4
K	5500–6000	1.23	66.5	5377.9
L	6000–6582	0.09	4.9	5382.8

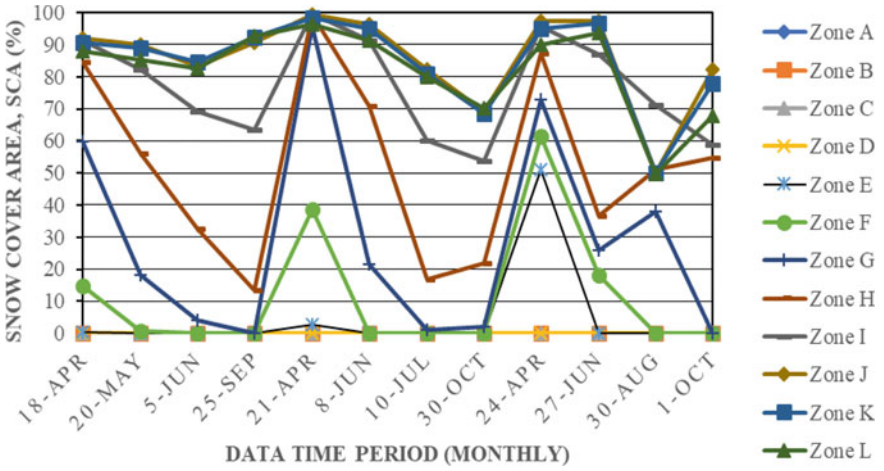

Fig. 5 Snow cover distribution in the Beas River watershed during 2013–2015

zones have been defined based on the elevation range between the lowest (857 m) and highest (6582 m) sites in the watershed. The computations in SRM are based on these zones. For the purpose of computing snowmelt runoff, many variables and parameters have been described and extrapolated to each elevation zone individually since all of these components change with the variation in elevation. The elevation zones, area, and elevation curve are used to determine the basin characteristics.

The Beas Basin is divided into 12 (500-m) elevation bands by the digital elevation model. It is possible to calculate each zone's mean elevation using height bands. To

calculate degree-day factors and extrapolate base station temperatures to various altitudes, this mean elevation is employed. The degree-day factor, temperature distribution within each elevation zone, and Thiessen polygon-based rainfall distribution are the meteorological factors that were deduced. Three hydro-meteorological stations are used to capture data on temperature and rainfall. Temperature and rainfall readings are point measurements; thus they are transformed using the Thiessen polygon technique to spatial data. Thiessen's polygon and elevation zones are used to calculate weighted rainfall for SRM.

For calibration and validation purposes in SRM, numerous parameters must be parameterized. Table 2 provides the parameters that were employed in the current study's simulation utilizing SRM. For calibration and SRM validation, the time frames April 2013–July 2014 and October 2014–October 2015, respectively, were employed. SRM automatically calculates and displays R^2 and Dv after each run as accuracy metrics. Table 3 shows the SRM snowmelt runoff calibration and validation results. According to the table, the value of R^2 fluctuates between 0.74 and 0.77 over the simulated period from April 2013–October 2015. The observed runoff ranges from 22,931.47 to 23,762.97 m^3 (10^6 m^3), with an average of 724.22 to 750.48 m^3/s. The calculated runoff ranges from 27,805.12 to 25,087.34 m^3 (10^6 m^3), with an average of 880.72−794.54 m^3/s. Between 2013–14 and 2014–15, the volume difference ranges from 3.61 to 9.76%. In comparison to the simulation years 2013–14 and 2014–15, the available rainfall data for this period could not adequately represent rainfall in the entire basin, which may be the primary cause of the volume difference for the periods 2013–14 and 2014–15. These data were only available from three rain gauge stations.

While the highest runoff is seen in August, mostly because of monsoonal rains, the SMR began rising in the spring–summer (April–May) season. This is primarily

Table 2 SRM calibration parameter range

Parameters	Range		Description
	Min	Max	
Temperature lapse rate (°C/100 m)	0.71	0.87	Constant for all the zones
Degree-day factor (cm $°C^{-1}d^{-1}$)	0.55	0.75	Varies month wise and zone wise
Critical temperature; TCRIT (°C)	0	2.0	0.0 for Zone-1 to 3, increasing from 0.75 to 2.0 from Zone-4 to 12
Time lag (hr)	6	18	6 h for Zone-1 to 3, 12 h for Zone-4 & 5, 15 h for Zone-6 & 7 and 18 h for Zone-8 to 12
Runoff coefficient for snow, CS	0.15	0.20	Varies month wise and zone wise
Runoff coefficient for rain, CR	0.10	0.15	Varies month wise and zone wise
Rainfall contributing area, RCA	0	1	Varies month wise and zone wise. (1 for lower zones in all months)
Xcoeff	0.80	1.06	Constant for all the zones
Ycoeff	0.02	0.02	Varies month wise

Table 3 Simulation results for Beas River basin up to Pandoh dam, 2013–2015

Period	Runoff volume (10^6 m^3)		Average Runoff (m^3/s)		Volume difference, D_v (%)	Coefficient of determination, R^2
	measured	computed	measured	computed		
2013–14	22,931.47	23,762.97	724.22	750.48	3.61	0.74
2014–15	25,087.34	27,805.12	880.72	794.54	9.76	0.77

because of a rise in air temperature. Between October and April, snowmelt is minimal. The simulation shows that SMR is the region's primary supply of freshwater throughout the year, with the exception of the monsoon. Rain on snow and regular rainfall-runoff contributions are substantially larger than the typical SMR because of the rise in temperature and precipitation during the monsoon. The basin SCA primarily melts in the summer, which has led to an increase in calculated and observed runoff in these months. Due to cold air temperatures and short days, snowmelt is minimal throughout the winter, particularly between December and February. During the monsoon season from mid-June to July, rainfall is considerable, which leads to high calculated and observed runoff values. Runoff is directly proportional to rainfall, with runoff coefficients determining the quantity of rainfall that is converted to runoff [10]. SRM relies on snow and rain runoff coefficients and the degree-day factor.

The biggest discrepancy is the time at which the observed and calculated discharge maxima occur. The recession coefficient, a crucial component of SRM since (1-k) represents the fraction of the daily melt water output that manifests as runoff right away, is utilized to correct and eliminate these mistakes [11]. The k value has been calculated by plotting the values of Qn and Qn + 1 against one another. The discharge data of Pandoh Dam have been collected from (https://cds.climate.copernicus.eu/) and utilized for the years 2013–2015 in order to estimate the k values for the study region. This dataset offers a gridded river discharge time record that has been simulated. It is a creation of the Global Flood Awareness System (GloFAS) that provides a consistent worldwide depiction of a significant hydrological variable. Two auxiliary files for interpretation are included with this dataset, one of which contains upstream area data and the other contains elevation data. Peak discharge values of the computed and measured runoff change directly with the runoff coefficient, and the location of flow peaks are primarily controlled by X and Y coefficients. During the monsoon season, when there is a lot of heavy rain, there are more peak flows, so the X and Y coefficients need to be adjusted more. The SRM's inability to accurately simulate peak discharge is also attributed to the dearth of adequate rainfall data for each elevation zone in the basin.

It has been assumed that the long-term average of the effective snowmelt input to the basin (after losses are taken into account) can be used to calculate the contribution of the snowmelt component to the total runoff at the outlet since SRM does not separate the snowmelt runoff component and the rain-induced runoff component from the total runoff.

5 Conclusions

Estimating snow and glacier melt runoff is important in India's Western Himalayan Rivers for hydropower generation and water management during the non-monsoon season. This research uses remotely sensed snow cover area data from the Landsat-8 as well as local daily temperature and precipitation data to model runoff in a mountainous basin with predominant snow cover.

WinSRM predicts snow and glacier melt runoff for the Beas River basin, which lacks data. SCA was developed from Landsat-8 images, ASTER GDEM, and hydro-meteorological data. The distribution of parameters according to elevation zone and, subsequently, the SMR output, is made possible by the elevation zone method, which raises the caliber of SRM simulations. Runoff coefficients, recession coefficients, and the degree-day factor are the SRM calibration parameters that are the most sensitive.

From April through June, as the air temperature progressively rises, the contribution from snowmelt predominates. The monsoon season has the highest discharge (combined snow and glacier melt, rainfall, and runoff) throughout the research period (July to September). Beginning in October, snowmelt reduces over the winter months. The average measured runoff volume is 24009.40 (10^6 m^3), the average measured runoff is 802.47 (m^3/s), the average computed runoff is 25784.04 (10^6 m^3), the average computed runoff is 772.51 (m^3/s), and the average volume difference is (+) 6.68% for the snowmelt season in the Beas River basin for the simulation period of April 2013–October 2015.

Acknowledgements We acknowledge MOSDAC for supplying the hydro-meteorological data for the research on their website (https://www.mosdac.gov.in/). Additionally, we appreciate the Landsat-8 and ASTER GDEM data provided by the USGS Earth Explorer website and the discharge data for Pandoh Dam provided by the CDS (https://cds.climate.copernicus.eu) website.

References

1. Daoo VJ, Shirvaikar VV (1978) Snow melt run off estimate from the Beas catchment in the Himalayas using energy balance techniques. ArchivfürMeteorologie, Geophys Und Bioklimatol, Ser B 26(2–3):183–192
2. DeWalle D, Rango A (2008) Snowmelt-Runoff Model (SRM). Principles of snow hydrology. Cambridge University Press, Cambridge, pp 306–364
3. Engelhardt M, Ramanathan AL, Eidhammer T, Kumar P, Landgren O, Mandal A, Rasmussen ROY (2017) Modelling 60 years of glacier mass balance and runoff for ChhotaShigri Glacier, Western Himalaya, Northern India. J Glaciol 63(240):618–628
4. Gupta RP, Duggal AJ, Rao SN, Sankar G, Singhal BBS (1982) Snow-cover area versus snowmelt runoff relation and its dependence on geomorphology—a study from the Beas catchment (Himalayas, India). J Hydrol 58(3–4):325–339
5. Kulkarni AV, Singh SK, Mathur P, Mishra VD (2006) Algorithm to monitor snow cover using AWiFS data of RESOURCESAT-1 for the Himalayan region. Int J Remote Sens 27(12):2449–2457

6. Kumar VS, Paul PR, Rao CLR, Haefner H (1993) Srtowmelt runoff forecasting studies in Himalayan Basins. In: Snow and Glacier Hydrology, Proceedings of the Kathmandu Symposium. IAHS Publication, Kathmandu, pp 85–94
7. Kumar V, Singh P, Singh V (2007) Snow and glacier melt contribution in the Beas River at Pandoh dam, Himachal Pradesh, India. Hydrol Sci J 52(2):376–388
8. Mandal A, Ramanathan A, Azam MF, Angchuk T, Soheb M, Kumar N, Singh VB (2020) Understanding the interrelationships among mass balance, meteorology, discharge and surface velocity on ChhotaShigri Glacier over 2002–2019 using in situ measurements. J Glaciol 66(259):727–741
9. Martinec J (1975) Snowmelt-runoff model for stream flow forecasts. Hydrol Res 6(3):145–154
10. Martinec J, Rango A (1986) Parameter values for snowmelt runoff modelling. J Hydrol 84(3–4):197–219
11. Martinec J, Rango A, Roberts RT (2008) Snowmelt Runoff Model (SRM) User's Manual New Mexico State University. Las Cruces, New Mexico, 175
12. Nagler T, Rott H (1997) The application of ERS-1 SAR for snowmelt runoff modelling. IAHS Publ-Ser Proc Rep-Intern Assoc Hydrol Sci 242:119–128
13. Nagler T, Rott H (1998) SAR tools for snowmelt modelling in the project HydAlp. In: IGARSS'98. Sensing and Managing the Environment. 1998 IEEE International Geoscience and Remote Sensing. Symposium Proceedings. (Cat. No. 98CH36174) (vol 3, pp 1521–1523). IEEE
14. Nagler T, Rott H (2000) Retrieval of wet snow by means of multitemporal SAR data. IEEE Trans Geosci Remote Sens 38(2):754–765
15. Northern Khorasan Water Regional Company (2013) Physiography. Meteorol Hydrol Stud Rep
16. Prasad VH, Roy PS (2005) Estimation of snowmelt runoff in Beas Basin, India. Geocarto Int 20(2):41–47
17. Rango A, Martinec J (1998) The snowmelt runoff model (SRM) user/s manual, version 4. fttp. *hydrolab. arsusda. gov/pub/srm/srm4. pdf*
18. Singh P, Bengtsson L, Berndtsson R (1995) Relating air temperature to the depletion of snow-covered area in a Himalayan basin. Nordic Hydrol 34:267–280
19. Singh R, Archfield SA, Wagener T (2014) Identifying dominant controls on hydrologic parameter transfer from gauged to ungauged catchments–A comparative hydrology approach. J Hydrol 517:985–996
20. World Meteorological Organization (1986) Intercomparison of models of snowmelt runoff. WMO Operational Hydrology Report no. 23, WMO Report no. 646. World Meteorological Organization, Geneva, Switzerland
21. World Meteorological Organization (1992) Simulated Real-Time intercomparison of hydrological models. Secretariat of the World meteorological organization.
22. Yuan F, Hao Z, Berndtsson R, Jiang P, Yasuda H (2016) The mass balance of glacier No. 1 at the headwaters of the Urumqi River in relation to northern hemisphere teleconnection patterns. Water 8(3):100

Development of a Fully Automated Atmospheric Correction Technique for Applications in Google Earth Engine

Riddick Kakati, S. K. Dwivedy, and Subashisa Dutta

Abstract For any satellite-based study, ground-based reflectance values are required. Nowadays, these ground-based reflectance products are provided by all the major space agencies, commonly designated as level 2 products. However, the availability of the level 2 products takes some time and once in a while, these products are not available. For the development of near real-time monitoring systems, this poses a major problem, and thus it becomes necessary to correct the raw satellite imagery by using atmospheric correction techniques. The Dark Object Subtraction technique (DOS) is one such commonly used technique used previously in many studies. However, it requires the manual selection of the darkest pixels in the imagery, thus making it unsuitable for automation-based systems. This study aims to automate the process of Dark Object Subtraction Sentinel 2A raw satellite imageries within the Google Earth Engine platform. Mean annual LULC maps generated using automated Dark Object Subtraction could replicate the level 2 product quite accurately. These classified imageries for July 2018−July 2019 produced overall classification accuracies of 74.13 and 67.24% using Random Forest Classifier and Support Vector Machines, respectively, compared to 68.96% obtained for both the classification algorithms using level 2 products. In the period July 2019−July 2020, it was obtained as 81.03 and 77.58%, respectively, compared to 79.31% for the same, and for July 2020- July 2021, it was 72.41 and 68.96% against 68.96 and 67.24%. The automated Dark Object Subtraction technique can thus be employed to develop near real-time automated satellite imagery-based systems within the Google Earth Engine platform.

Keywords Atmospheric correction · Dark object subtraction · Google earth engine · Sentinel 2A · LULC

R. Kakati (✉) · S. Dutta
Department of Civil Engineering, IIT Guwahati, Guwahati, India
e-mail: riddick.kakati@iitg.ac.in

S. K. Dwivedy
Department of Mechanical Engineering, IIT Guwahati, Guwahati, India

S. Dutta and V. Chembolu (eds.), *Recent Development in River Corridor Management*,
Lecture Notes in Civil Engineering 376, https://doi.org/10.1007/978-981-99-4423-1_24

1 Introduction

A variety of earth monitoring applications, including the assessment of the global energy balance and the detection of changes in land cover, have long advocated the use of satellite imagery. Problems arise due to the presence of the atmosphere because solar EMR reflected by the Earth and measured by the detectors in the satellite must travel through its way from the sun to the Earth and back. When EMR travels through the atmosphere, it comes into contact with molecules of the various gases and the particles that make up the atmosphere. Scattering and absorption are the two basic processes that are often used to characterize this interaction [10]. Electromagnetic radiation undergoes a transformation when it interacts with Earth's surface. During this process, path radiance refers to emitted radiation that does not interact with the earth before entering detectors. This path radiance is typically undesirable information since it tells nothing about the character of the land surface [1, 8]. Water and vegetation, which are not as reflective as other surfaces, have a greater effect on the atmosphere. This is a particularly serious issue for applications that rely on multispectral satellite data for monitoring, including those in agriculture and land use research. It affects the quantity of electromagnetic radiation perceived by the array of detectors in a satellite, which changes with wavelength [4, 5, 10, 13]. Thus, atmospheric correction is necessary, particularly for Rayleigh scattering generated by gases, water vapour and aerosols which affects the bands near the visible part of the electromagnetic spectrum [13]. The data from the sensor (called digital number, DN) needs to be free from atmospheric interferences, which can be achieved through the generation of surface reflectance, which normalises data from different time periods and sources. Radiative transfer codes (RTC) help in determining an accurate relationship between surface reflectance and radiance of the sensor by the use of atmospheric optical depth on the date of satellite pass [12]. An RTC with realistically simulated atmospheres may be used instead of actual weather data when actual data is unavailable. For a variety of simulated atmospheres, aerosol kinds, sun zenith angles, and ground altitudes, [15] proposed employing a library of atmospheric correction functions created using an RTC to predict surface reflectance. For situations when no atmospheric data is available, this library might allow for "rapid" analysis of satellite images. Using a NxN pixel window and suitable weighting factors for the difference in reflectance, the estimate was further enhanced by approximating a correction for the adjacency effect. But the high cost and prolonged implementation process associated with an RTC make it challenging for applications, which require rapid and frequent generation of processed data.

There have been a number of proposals for easier atmospheric correction techniques for images in the visible and near infrared spectra that are gathered by satellites [7, 9, 14, 17]. The amount and precision of atmospheric data needed to apply a simplified technique vary widely, and very few procedures may be used when no atmospheric data is available. To save the hassle of taking separate readings of the atmosphere and the site itself, it is also possible to extrapolate information about atmospheric conditions from the image itself. Surface reflectance factors are often

retrieved using scene-derived atmospheric information in conjunction with an RTC in image-based atmospheric correction methods. In order to estimate path radiance, [2] used a clear lake in the image, and then used a radiative transfer algorithm to deduce atmospheric transmittance and downwelling irradiance from this estimate. Recently, several investigations have relied on a simplified version of this technique known as the dark object subtraction approach [5, 6, 11, 13].

The Dark Object Subtraction (DOS) technique eliminates the requirement for radiative transfer coding by subtracting the path radiance from the scene's darkest object, which need not be a body of pure water. This is accomplished by disregarding the transmittance and downwelling radiance components [5]. Images where scattering is the primary cause of attenuation benefit from the dark object subtraction approach for correction [12]. It is based on the concept that some of the image's pixels should be black (zero reflectance), and these pixels are referred to as "dark objects". Examples of objects with DN values of zero or close to zero include dark areas cast by shadows and bodies of clear water. A first order atmospheric adjustment, such as the one achieved by the Simple Dark Object Subtraction approach [16], [19], is preferable to no correction at all. The approach involves selecting a constant haze value (DN) for each spectral band by attributing the influence of the atmosphere to the smallest DN value in the histogram of the whole scene. The improved Dark Object Subtraction [4] approach tends to rectify the Haze in terms of atmospheric scattering and path radiance by using the power law of the relative scattering effect of the atmosphere.

The COST Dark Object Subtraction (DOS) approach [5] was automated inside the Google Earth Engine platform in this study. Processing raw images with the automated DOS technique will allow the development of near real-time monitoring systems, which is especially important because the generation of level 2 surface reflectance products takes some time and also, often times, these tiles are not available. The results obtained were validated using commonly used supervised machine learning based classification algorithms viz., Random Forest Classifier and Support Vector Machines.

2 Methodology

2.1 DOS Model [5]

The following equation may be used as a generic representation of the DN values captured by imaging systems:

$$DN_i(X, Y) = G_i \times [L_\lambda(X, Y)] + O_i \tag{1}$$

where,

$DN_i(X, Y)$ = pixel (X, Y) output DN in the band i,

G_i = band i gain factor,

$L_\lambda(X, Y)$ = pixel (X, Y) radiance in the band i,

O_i = band i offset.

Rearranging Eq. (1), the following equation for radiance $[L_\lambda(X, Y)]$ is obtained.

$$L_\lambda(X, Y) = \frac{DN_i(X, Y) - O_i}{G_i} \tag{2}$$

To convert these radiances to surface reflectance, the general model as per Moran, 1992 is given as.

$$\rho_i(X, Y) = \frac{\pi \times (L_\lambda(X, Y) - H_i)}{\tau_{vi} \times \left[E_o \times Cos(\theta_z) \times \tau_{zi} + E_{down}\right]} \tag{3}$$

where,

$\rho_i(X, Y)$ = Surface reflectance

H_i = The path radiance

τ_{vi} = Atmospheric transmittance from the ground surface to satellite

E_o = Solar spectral irradiance of the sun on a perpendicular surface outside the atmosphere ($Wm^{-2}sr^{-1}\mu m^{-1}$)

θ_z = Sun zenith angle

τ_{zi} = Atmospheric transmittance from sun to the ground surface

E_{down} = Surface downwelling spectral irradiance due to scattered solar flux in the atmosphere ($Wm^{-2}\mu m^{-1}$)

In this model, the improved DOS technique [5] suggested the following values:

$\tau_{zi} = (\theta_z)$; $\tau_{vi} = 1(fornadirview)$; $E_{down} = 0$ and H_i = Dark object (Value of darkest pixel in image).

The reader may refer to the article by [5] for more details on the model.

2.2 *Random Forest Classifier [3]*

The random forest classifier uses a collection of tree classifiers from a supplied input vector. Each of the tree classifiers is produced from a random vector sampled separately from the input vector and which then searches, on a unit scale, for the most popular class. In this study, a random forest classifier was used, which builds a tree using a random feature or feature combination at each node. Bagging was used for each feature/feature combination, which is a technique for generating a training dataset by randomly drawing with replacement N samples, where N is the size of

the original training set. Attribute selection in random forest is done using the Gini Index, which measures the relevance of an attribute with the class. The Gini index is defined as follows for a given training set T, where we randomly choose one instance (pixel) and assign it to a class C_i.

$$\sum\sum_{j\neq i}(f(C_i,T)/|T|)\left(f\left(C_j,T\right)/|T|\right)$$

where the probability that the example belongs to class C_i is denoted by $f(C_i,T)/|T|$.

When a tree is expanded to its maximum depth on fresh training data, a new set of features is learned. Parameters that must be set by the user while creating a random forest classifier are the number of trees to be produced and the number of characteristics to be utilized at each node. Selective feature searching is performed at each node to find the optimal branching. Thus, N trees make up the random forest classifier, with N being the user-defined maximum number of trees to be produced. Each instance from the datasets is then sent down to each of the N trees to be classified. In such situation, the forest will choose the category that received the most votes (out of a possible N).

2.3 Support Vector Machines [18]

Support Vector Machines (SVM) is based on statistical learning theory, whose goal is to locate the thresholds that will result in the most effective class separation. In a two class problem where the classes can be separated using linear features, SVMs choose a hyperplane that creates the most separation between them. The gap between the two classes is measured by adding together their respective nearest spots' distances to the hyperplane. Standard Quadratic Programming (QP) optimization methods may be used to the issue of maximising the margin. The margin is calculated based on the vectors or points that are closest to the hyperplane, which are referred to as "support vectors". If the two classes cannot be separated linearly, SVMs will look for the hyperplane that minimizes a quantity proportional to the amount of misclassification mistakes while maximizing the margin. SVMs can also be modified to work with nonlinear decision spaces. To lessen the computational burden of working with high-dimensional feature spaces, kernel functions are used.

2.4 Model Setup

2.4.1 Dark Object Subtraction

This study uses Google Earth Engine, which is a cloud- server based computational platform for planetary-scale geospatial analysis. The GUI consists of a code editor, a console and a file explorer. The Sentinel 2A Level 1 C dataset used for the analysis was downloaded from the data catalogue within the interface. Then this dataset was processed through the code editor using Eq. (3) to obtain the surface reflectance values. To obtain the darkest pixel value, each raster was converted to a dictionary datatype, which consists of key-value pairs. This was done using the built in function "*ee.Dictionary*". In this study, the key corresponded to the pixel value and the value corresponded to the count of that pixel value. Then, a histogram was generated for the dictionary variable using the built in function "*ee.Reducer.histogram*". Now, this histogram will automatically generate a key having 0 value and its number of occurences. To remove such values, the built in signum function was first used to identify the 0 values, and then the mask built in function was used to remove those values. The first value in the dictionary variable remaining after removing the 0 value corresponds to the darkest pixels in the imagery.

2.4.2 Classifiers

Both the Random Forest and SVM classifiers were trained to identify six classes viz., agriculture, barren land, forest, river, urban and wetland. Training and testing data were selected using Google Earth Pro, where the true colour satellite imageries were used for generating the ground truth. The details of the number of elements within each class used for ground truths are listed in Fig. 1.

2.5 Calibration and Validation

The automated Dark Object Subtraction technique was calibrated using Eq. (3). For validation, Sentinel 2 Level 1C satellite tiles in the period of July 2018−July 2019, July 2019−July 2020 and July 2020−July 2021 were selected for a region (Fig. 2) that spanned roughly 100 kms upstream and downstream of Guwahati, India. Then, a Land Use Land Cover (LULC) classification was carried out using Random Forest classifier and Support Vector Machines to evaluate the classification accuracy obtained by the automated Dark Object Subtraction corrected imagery and the Sentinel Level 2 surface reflectance product.

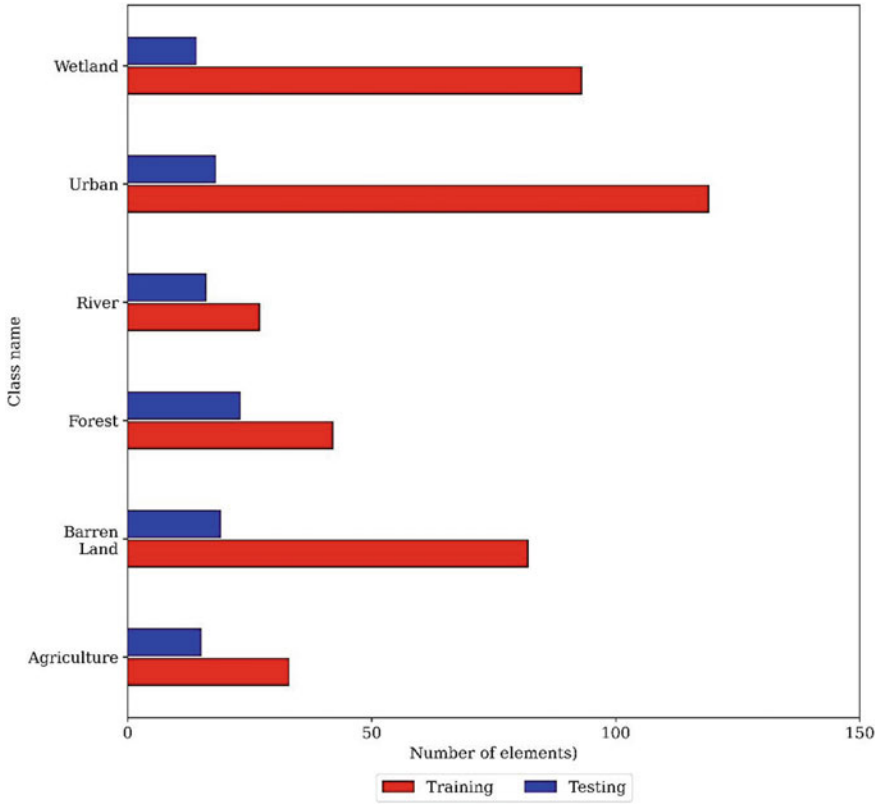

Fig. 1 Ground truth details

3 Results and Discussion

To obtain surface reflectance images from the Sentinel 2A raw level 1C images, the automated DOS algorithm was executed within Google Earth Engine code editor. The resulting images were extracted and classified using both random forest classifier and support vector machine algorithms. On the other hand, Sentinel 2A level 2 surface reflectance images were also extracted and classified using the same classifiers. The performance of the automated DOS algorithm was evaluated through classification accuracy using the confusion matrix method. Figure 5 shows the overall classification accuracies and the Cohen Kappa scores obtained after the classification.

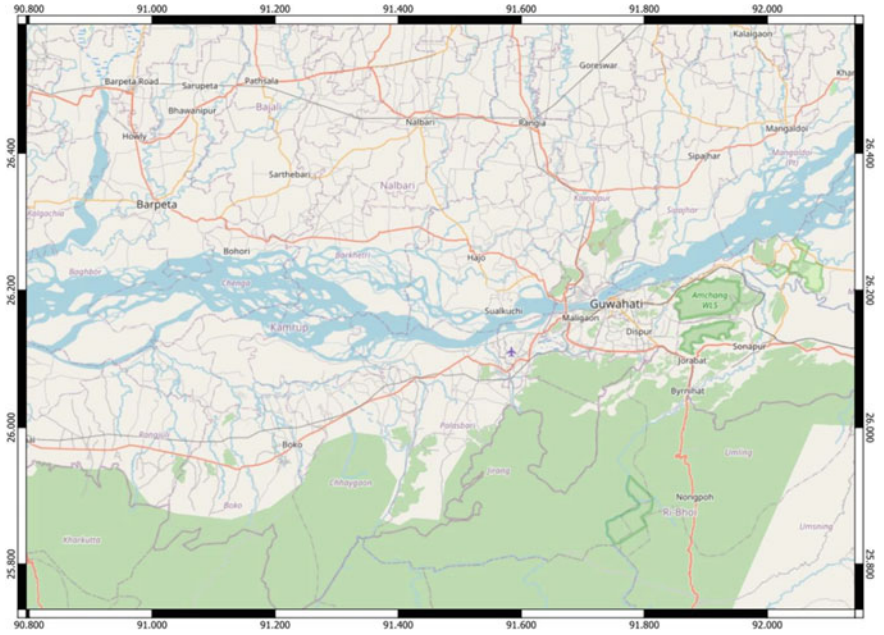

Fig. 2 Study area

3.1 Random Forest Classifier

The random forest classifier was implemented through a script within the code editor in Google Earth Engine to identify six classes, based on the training data provided for each class. Analyses was carried out for the period of July 2018−July 2019, July 2019−July 2020 and July 2020−July 2021. For this case, overall classification accuracies of 74.13, 81.03 and 72.41% were obtained for the periods July 2018−July 2019, July 2019−July 2020 and July 2020−July 2021 respectively for the automated DOS algorithm. Similarly, 68.96, 79.31 and 68.96% were obtained respectively for the Sentinel level 2 product. In this case, it can be observed that the automated DOS based image had a better classification accuracy than the Sentinel Level 2 image. On plotting the change in area obtained for both automated DOS and Sentinel 2A level 2 image (Fig. 3), it can be observed that for the classes barren land, urban, river and agriculture, the trends are similar. The difference in trend for the forest and wetland classes may be attributed to their mixed spectral response, due to which there were some classification errors in these two classes, as reflected in the overall classification accuracies.

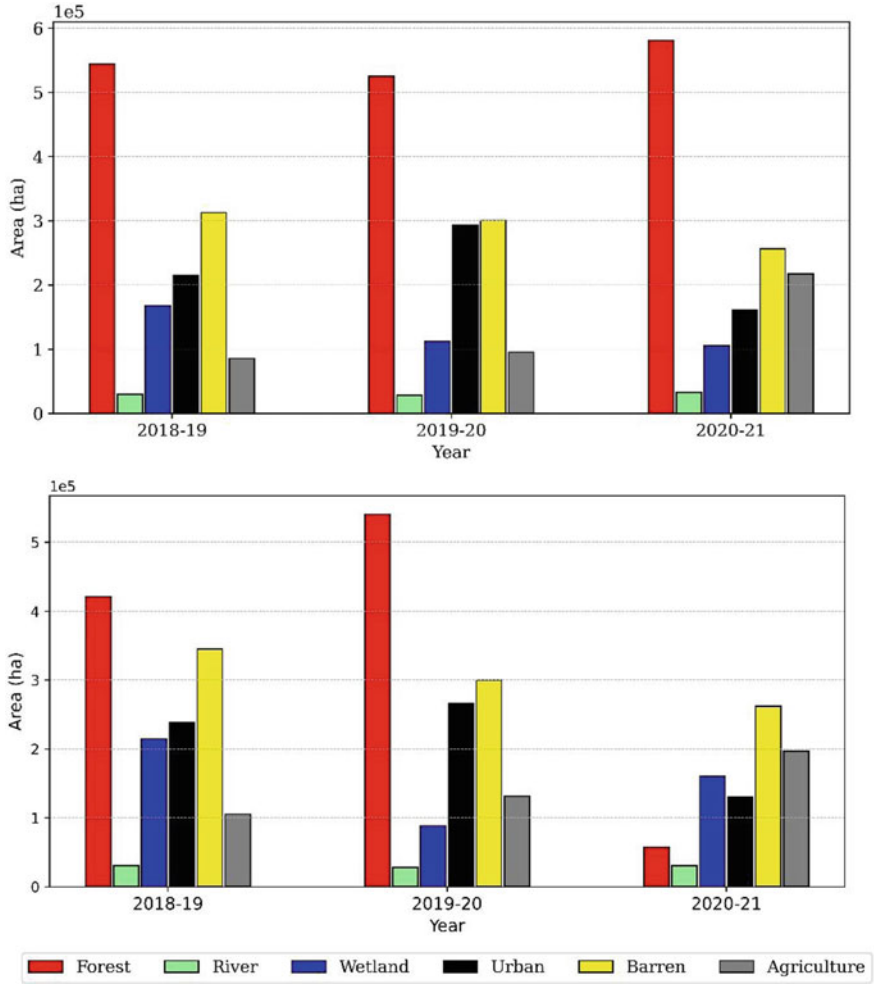

Fig. 3 Plots showing change in area for each class for automated DOS (top) and Sentinel 2A level 2 image (bottom) using random forest classifier

3.2 Support Vector Machines

The Support Vector Machines algorithm was also implemented through Google Earth Engine to identify six classes, similar to the Random Forest Classifier. For this case, overall classification accuracies of 67.24, 77.58 and 68.96% were obtained for the periods July 2018−July 2019, July 2019−July 2020 and July 2020−July 2021 respectively for the automated DOS algorithm. Similarly, 68.96, 79.31 and 67.24% were obtained respectively for the Sentinel level 2 product. In this case, it can be observed that the automated DOS based image had a slightly lower classification

accuracy than the Sentinel Level 2 image for the first two periods, but was slightly higher for the last period. On plotting the change in area obtained for both automated DOS and Sentinel 2A level 2 image (Fig. 4), it can be observed that other than river class, all the other classes are showing similar trends. The difference in trend for the river class may be attributed to their mixed spectral response with wetland, due to which there were some classification errors in these two classes, as reflected in the confusion matrices as well as in the classification accuracy.

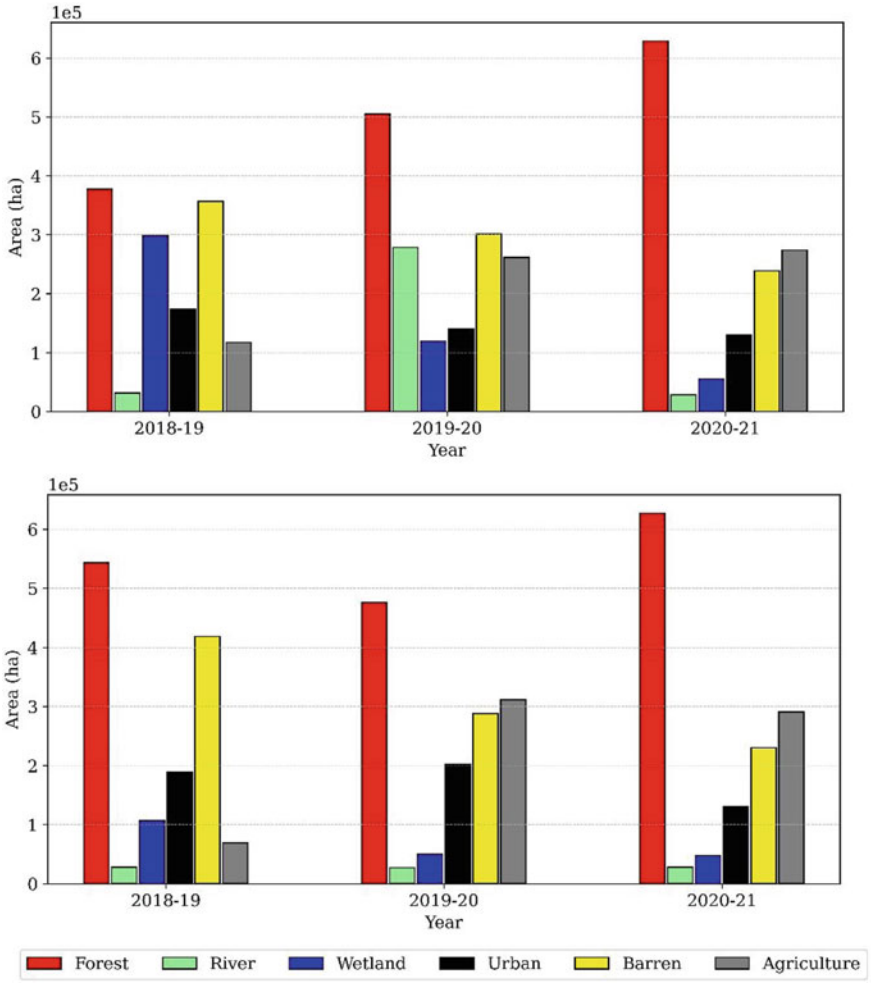

Fig. 4 Plots showing change in area for each class for automated DOS (top) and Sentinel 2A level 2 image (bottom) using support vector machines

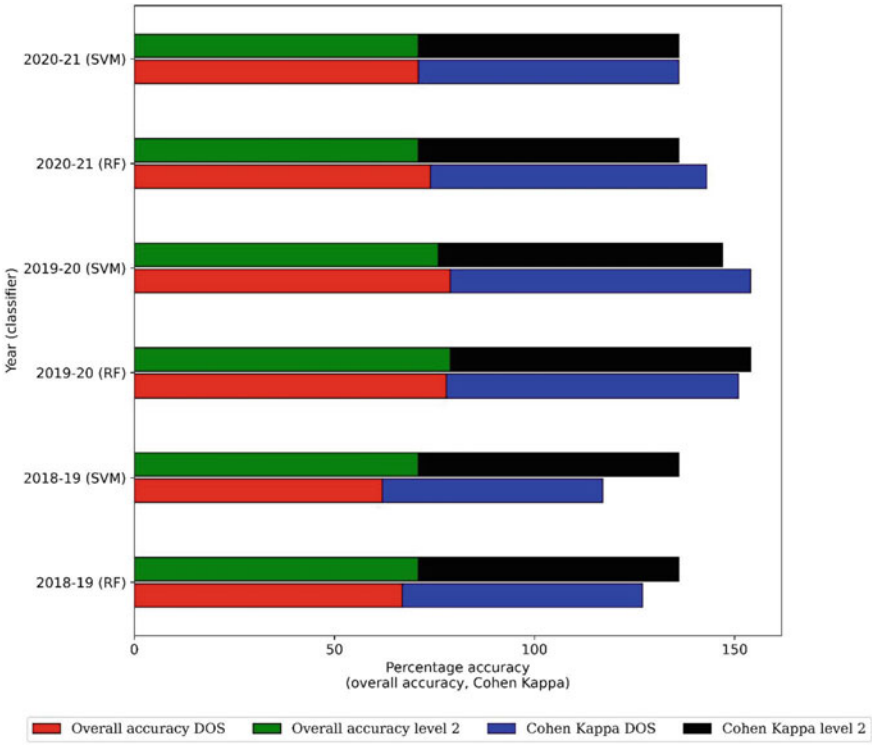

Fig. 5 Overall results obtained after image classification

4 Conclusion

Dark object subtraction is a widely used image-based atmospheric correction technique. In this study, it has been automated for use in the development of near real-time monitoring applications. It has been observed that the performance of automated DOS technique was nearly the same as that of the Sentinel 2 level 2 surface reflectance product, in terms of classification accuracies using the Random Forest and Support Vector Machines classification algorithms. For July 2018−July 2019, overall classification accuracies of 74.13 and 67.24% using Random Forest Classifier and Support Vector Machines, respectively were obtained, compared to 68.96% for both the classification algorithms using level 2 products. In the period July 2019−July 2020, it was obtained as 81.03 and 77.58%, respectively, compared to 79.31% for the same, and for July 2020−July 2021, it was 72.41 and 68.96% against 68.96 and 67.24%. It was also observed that in terms of the confusion matrices and the change in area of land use classes, the automated DOS produced quite similar behaviour as compared to the Sentinel 2A level 2 product. The main objective of this study was just to compare the performance of the automation product with the processed surface reflectance product, hence the classification results obtained have not been analysed further.

References

1. Adams JB, Gillespie AR (2006) Remote sensing of landscapes with spectral images: A physical modeling approach. Cambridge University Press
2. Ahern FJ, Goodenough DG, Jain SC, Rao VR, Rochon G (1977) Use of clear lake as standard reflectors for atmospheric measurement. In: ERIM Proc. of the 11th Intern Symp on Remote Sensing of Environment, vol 1
3. Breiman L (2001) Random forests. Mach Learn 45(1):5-32
4. Chavez PS Jr (1988) An improved dark-object subtraction technique for atmospheric scattering correction of multispectral data. Remote Sens Environ 24(3):459–479
5. Chavez PS (1996) Image-based atmospheric corrections-revisited and improved. Photogramm Eng Remote Sens 62(9):1025–1035
6. Ding H, Shi J, Wang Y, Wei L (2015) An improved dark-object subtraction technique for atmospheric correction of Landsat 8. In: MIPPR 2015: Remote sensing image processing, geographic information systems, and other applications, vol 9815. SPIE, pp 128–135
7. Dozier J, Frew J (1981) Atmospheric corrections to satellite radiometric data over rugged terrain. Remote Sens Environ 11:191–205
8. Gao J (2009) Digital analysis of remotely sensed imagery. McGraw-Hill Education
9. Kneizys FX (1988) Users guide to LOWTRAN 7 (No. 1010). Air Force Geophysics Laboratory, United States Air Force
10. Lillesand T, Kiefer RW, Chipman J (2015) Remote sensing and image interpretation. John Wiley & Sons
11. Li Z, Duan P, Hu S, Li M, Kang X (2022) Fast hyperspectral image dehazing with dark-object subtraction model. IEEE Geosci Remote Sens Letters
12. Moran MS, Jackson RD, Slater PN, Teillet PM (1992) Evaluation of simplified procedures for retrieval of land surface reflectance factors from satellite sensor output. Remote Sens Environ 41(2–3):169–184
13. Mustak S (2013) Correction of atmospheric haze in Resourcesat-1 Liss-4 Mx Data for urban analysis: an improved dark object subtraction approach. Int Arch Photogramm, Remote Sens Spat Inf Sci 1:W3
14. Otterman J, Fraser RS (1976) Earth-atmosphere system and surface reflectivities in arid regions from Landsat MSS data. Remote Sens Environ 5:247–266
15. Richter R (1990) A fast atmospheric correction algorithm applied to Landsat TM images. Title Remote Sens 11(1):159–166
16. Rowan LC, Wetlaufer PH, Stewart JH (1976) Discrimination of rock types and detection of hydrothermally altered areas in south-central Nevada by the use of computer-enhanced ERTS images
17. Singh SM (1988) Estimation of multiple reflection and lowest order adjacency effects on remotely-sensed data. Int J Remote Sens 9(9):1433–1450
18. Vapnik V (1999) The nature of statistical learning theory. Springer science & business media
19. Vincent R (1973) An ERTS multispectral scanner experiment for mapping iron compounds
20. Wicaksono P, Hafizt M (2018) Dark target effectiveness for dark-object subtraction atmospheric correction method on mangrove above-ground carbon stock mapping. IET Image Proc 12(4):582–587

Prioritizing Areas Prone to Critical Soil Erosion by Using Multiple Criteria Decision Analysis and GIS Techniques

Thallam Prashanth, Sayantan Ganguly, and Manoj Gummadi

Abstract In India, due to uneven rainfall distribution and land use changes, soil erosion patterns vary spatially and temporally significantly. Soil erosion refers to the detachment of soil particles on the land surface due to natural geological processes and transport by means of natural geological agents like water, wind, etc. It may accelerate due to poor land management and anthropogenic activities. The eroded soil particles cause sedimentation in reservoirs and reduce the carrying capacity of waterbodies, leading to changes in water quality and alteration of the cross-section of rivers. This study integrates Analytical Hierarchical Process (AHP) and Fuzzy Analytical Hierarchical Process (FAHP) to identify the areas prone to critical soil erosion. The areas prone to soil erosion are identified by integrating drainage density, elevation, ground slope, land use land cover (LULC), rainfall, and soil map. Soil erosion-prone areas obtained using AHP and FAHP are cross-verified by performing river bank shifting analysis using multi-temporal global surface waterbodies data on Google Earth Engine (GEE). River bank shifting analysis calculates the amount of the area (in hectares) prone to soil erosion and deposition at a frequency of every 5 years from 2000–2020, using a Geographic Information System (GIS). This study is aimed to reduce the investments, is weather independent, and prioritizes areas prone to soil erosion temporally and spatially.

Keywords Soil erosion · Analytical hierarchical process · Fuzzy analytical hierarchical process · Geographic information system · Remote sensing

T. Prashanth (✉)
Research Scholar, Department of Civil Engineering, Indian Institute of Technology Ropar, Nangal Road, Rupnagar, Punjab 140001, India
e-mail: thallam.21cez0007@iitrpr.ac.in

S. Ganguly
Assistant Professor, Department of Civil Engineering, Indian Institute of Technology Ropar, Nangal Road, Rupnagar, Punjab 140001, India
e-mail: sayantan.ganguly@iitrpr.ac.in

M. Gummadi
GIS Analyst, Geo Climate Risk Solutions Pvt Ltd, Vishakhapatnam 530048, India
e-mail: manugummadi@gmail.com

S. Dutta and V. Chembolu (eds.), *Recent Development in River Corridor Management*, Lecture Notes in Civil Engineering 376, https://doi.org/10.1007/978-981-99-4423-1_25

1 Introduction

Soil erosion is one of the significant soil threats in India, due to uneven distribution and intensification of rainfall [10]. Soil erosion is the process of exfoliation of the top layer of soil on the earth's surface governed by natural agents like water, wind, etc., or anthropogenic forces affecting the riverine ecosystem and increasing the hazards. Soil erosion reduces the storage capacity and decreases the water quality by increasing suspended solids in the surface waterbodies [4]. It also leads to changes in the cross-section of the surface waterbodies, river bank shifting, stream piracy, changes in the flow direction, meandering, formation of oxbow lakes, morphological parameters (areal, linear, relief parameters), and stream bifurcation. For instance, [11] studied soil erosion of the Indravati catchment using the Universal Soil Loss Equation (USLE) model. The authors predicted the sediment yield using empirical equations and validated the results with observed data. [3] identified environmentally stressed areas to conserve soil by determining the weightage for various factors responsible for soil erosion using Analytical Hierarchical Process (AHP). Cartwright et al. [2] mapped the areas of higher erosion potential using AHP, Weighted Linear Combination (WLC), ensemble model (average of WLC and AHP method), Revised Universal Soil Loss Equation (RUSLE) and Soil Water Assessment Tool (SWAT). They concluded that all methods provided more accurate results but AHP and ensemble model both consumed less time. [7] analyzed the river bank erosion, deposition, and bar dynamics using multi-temporal Landsat satellite images from 1973 to 2015 and concluded that both banks have experienced dynamic forms of aggradations and degradation processes resulting in channel shifting. The National Institute of Hydrology, Roorkee, published a report in 2013 on "Morphological Study on Sutlej River" to identify the river course of the Sutlej River by using LISS-II and LISS-III satellite imagery and also studied river bank shifting analysis using Survey of India (SOI) toposheets. The survey concluded that erosion and deposition rates of soil sediments were increasing with time [5]. Saadon et al. [8] developed an empirical model to estimate river bank erosion rates by using different types of independent parameters like hydraulic characteristics (near bank velocity, boundary shear stress, shear velocity, etc.), bank and soil properties (height, angle of the bank, etc.), bank resistance and sediment supply (concentration of the suspended sediment).

Due to variations in rainfall and temperature patterns, it is essential to study riverbank soil erosion with respect to space and time. In this study, remote sensing technique is used in monitoring the riverbank shift along the channel length in every 5 years. This type of study is weather independent and reduces investments. The analysis can be done for a more extensive stretch in a shorter period and with less manpower.

The main objectives of the present study are.

(a) To map the areas prone to higher soil erosion using Analytical Hierarchy Process (AHP) and Fuzzy Analytical Hierarchy Process (F-AHP).
(b) To determine the erosion and deposition rates with respect to time with the frequency of every 5 years using multi-temporal global surface water datasets.
(c) Validation of the higher soil erosion zones obtained from AHP and F-AHP with multi-temporal global surface water datasets.

2 Study Area

Figure 1 This study is carried out for a segment of the Sutlej basin in Himachal Pradesh. The Sutlej basin originates near the Manasarovar Lake in China and extends towards Shipkila District in Himachal Pradesh and finally spreads through Punjab, India. The study area extends from 31° north to 33° north latitude and 76° east to 79° east longitude. The ground elevation of the study area is obtained from the Advanced Spaceborne Thermal Emission and Reflection Radiometer Digital Elevation Model (ASTER-DEM) ranging from 486 to 6665 m while the slope ranges from 0 to 80%. As per the soil data provided by the Food and Agricultural Organization (FAO), the study area is comprised of four different types of soils: clay, sandy loam, loamy sand, and loam. As per the data obtained from Climate Research Unit (CRU), the rainfall varies from 252 to 951 mm.

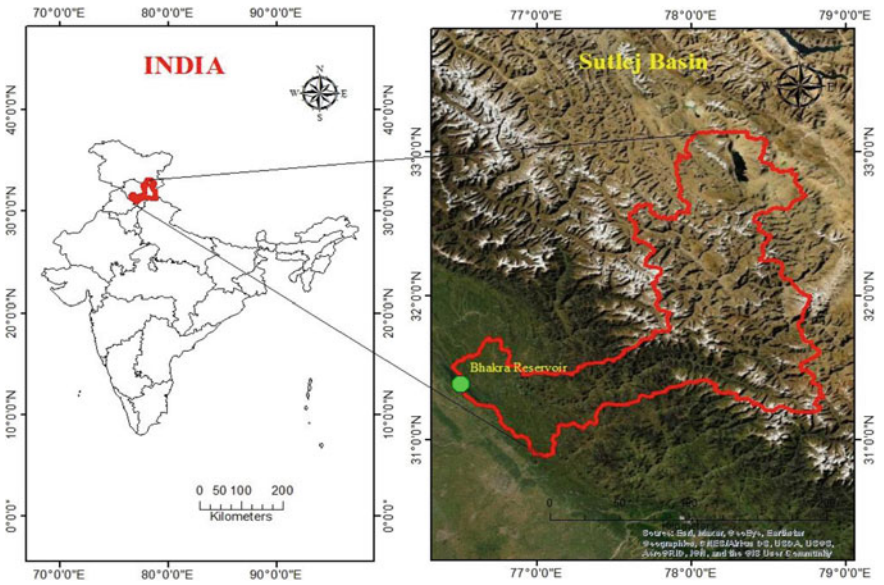

Fig. 1 Sutlej Basin in Himachal Pradesh

3 Methodology

3.1 Data Collections

The ASTER DEM (Fig. 2) is obtained from the USGS Earth Explorer website. By using Arc-GIS and DEM, ground slope (Fig. 3) and drainage density (Fig. 4) are determined. The supervised classification was performed on the Sentinel-2 satellite image in August 2020 using Google Earth Engine (GEE) for the study area. Figure 6 explains the basic classification of Land Use Land Cover (LULC); some classes are identified, like waterbodies, agriculture, forest, built-up, etc. As per the soil data (Fig. 5) provided by Food and Agricultural Organization (FAO) at a 1:5,000,000 scale, the study area comprises of four different types of soils clay, sandy loam, loamy sand, and loam. The rainfall data (Fig. 7) is obtained from the CRU website and are converted from raster to points for performing spatial interpolation by using Inverse Distance Weighing (IDW) method.

The parameters selected in this study to prioritize the areas susceptible to soil erosion are Elevation, ground slope, drainage density, soil, rainfall and land use land cover. The soil particles in the streambed in contact with the flow, tend to move due to the hydraulic drag action of water. Velocity of the flow, on the other hand, increases due to an increase in the slope. Thus the soil tends to erode, getstransported towards the medium slopes and finally settles at the low slope regions (deltaic regions). The soil type is a major factor affecting erosion because it is responsible for the formation of the stream. For instance, as clay is less permeable, when rainfall occurs, it absorbs a small amount of the water and the larger amount generates surface runoff. Sand is more permeable than clay due to larger interconnectivity of the pores. During rainfall the sand absorbs water and therefore the formation of the stream quality decreases due to the presence of coarse-grained soil. The drainage density derived from the DEM data is essential because soil erosion increases due to water accumulation from different streams. As the flow accumulation increases, the drainage density also increases due to the presence of an abundant higher-order stream in an area. LULC is used because the runoff depends on the type of land use. Runoff is more in waterbodies due to the accumulation of water from different directions and therefore it is a more critical factor in categorizing zones of soil erosion. Soil erosion is also large in agriculture but it is also significantly less compared to erosion near river banks. In built-up areas, runoff is more, and soil erosion is less.

3.2 Estimation of Soil Erosion Susceptibility Using AHP and F-AHP

Analytical Hierarchy Process (AHP) is the best method for decision-making and resolving conflicts when several alternatives and criteria. AHP is a process of developing a hierarchical framework keeping its goal or objective at the primary level,

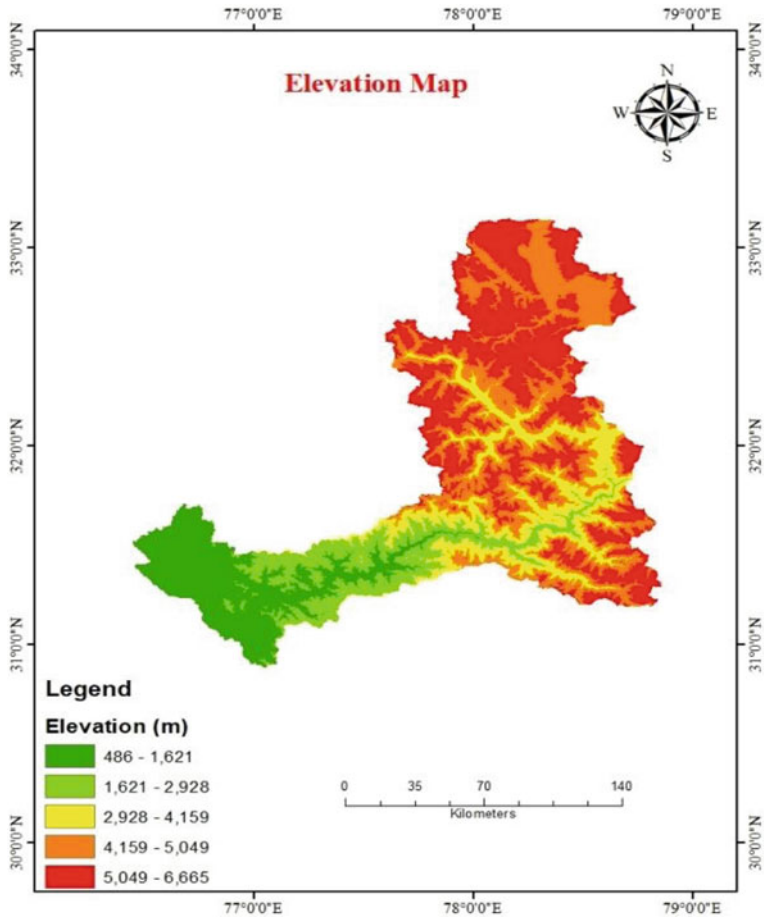

Fig. 2 Elevation map

criteria at the secondary level and possible alternatives at the tertiary level [9]. AHP relies on expert judgment and their assumptions.

Fuzzy is said to be non-clear. One should apply certain logic to make it clearly known as Fuzzy Logic. Fuzzy mathematics and Analytical Hierarchical process are integrated to evaluate the uncertainty and imprecision problems carried out in AHP. In some cases, we cannot rely on expert judgments; F-AHP plays a crucial role in solving uncertainty.

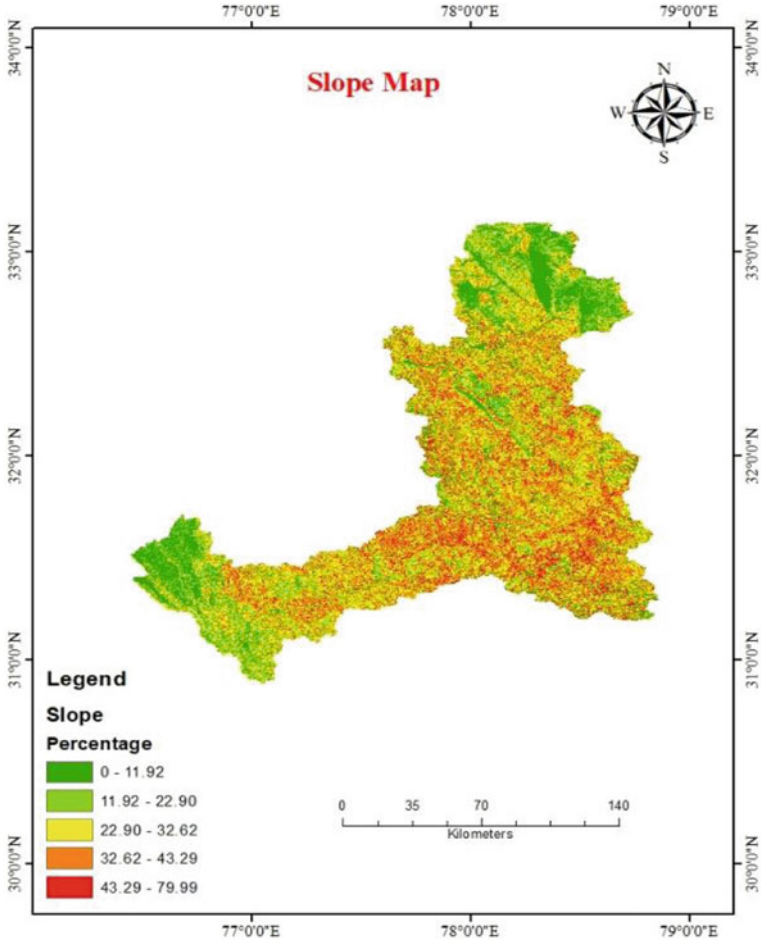

Fig. 3 Slope map

3.2.1 Estimation of Weightage of Parameters Involved in Mapping Soil-Erosion Sustainability Using AHP

Based on the assumptions and suggestions with respect to a goal provided in the literature, the first step is to construct a pair-wise comparison matrix in AHP. The pair-wise comparison (Table 2) matrix provides the relative importance (Table 1) of one attribute with respect to other attributes to achieve a goal/objective.

A normalized pair-wise comparison matrix (Table 3) is constructed by calculating the ratio between the scale and the sum of their scales, as shown in Table 1. All the values within the matrix lie between 0 & 1 by performing normalization. Criteria weightage is calculated by the average of each row for corresponding criteria. Finally, the criteria weightage is converted to a percentage.

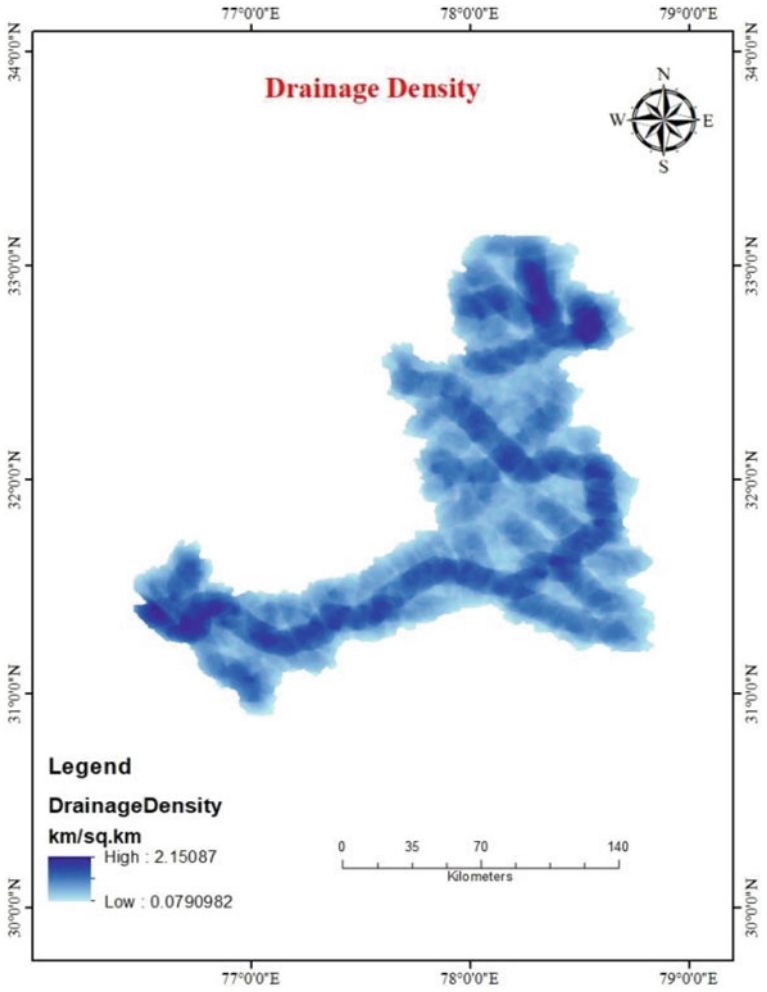

Fig. 4 Drainage density

The consistency matrix is constructed by the product of scale in a pair-wise comparison matrix (Table 1) and criteria weightage. Based on the literature, the pair-wise comparison matrix is considered consistent when the consistency ratio < 0.1. The weighted sum in Table 4 is calculated by the sum of elements in the corresponding criteria. The ratio in Table 4 is calculated between the weighted sum and criteria weightage. The formulas required for the calculations are listed below:

$$\lambda_{max} = \frac{sum\ of\ ratios}{number\ of\ criterias} = 6.51$$

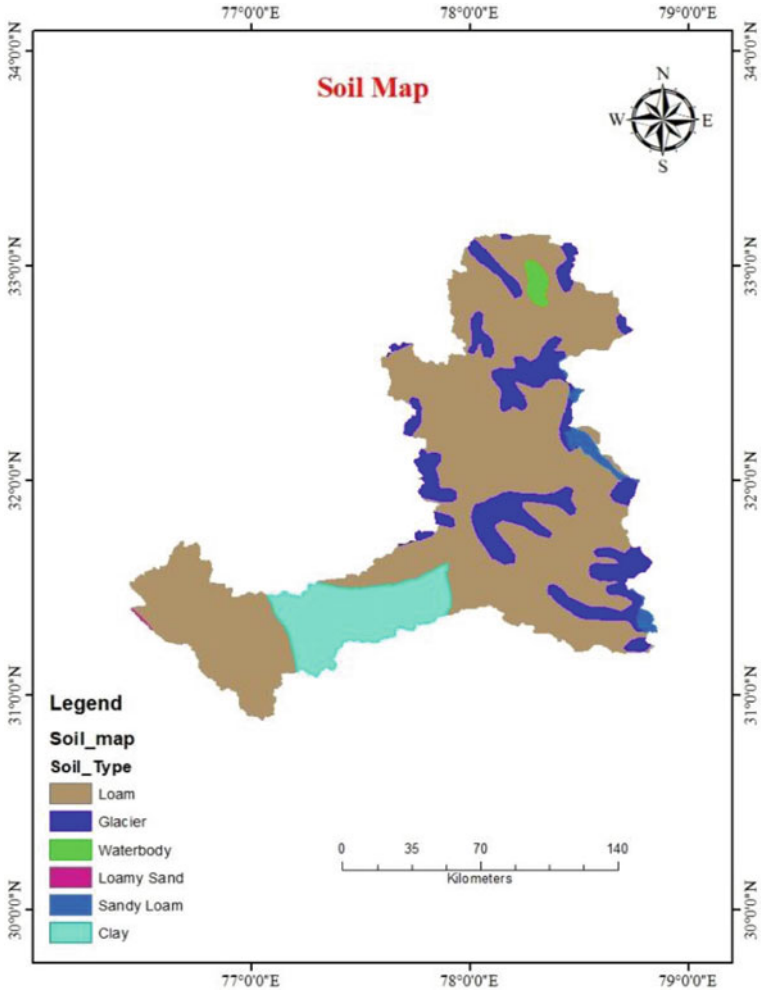

Fig. 5 Soil map

$$Consistency\ Index = CI = \frac{\lambda_{max} - n}{n - 1} = 0.1$$

$$Random\ Consistency\ Index\ for n = 6\ given\ in\ saaty\ table = 1.24$$

$$Consistency\ Ratio = \frac{Consistency\ Index}{Random\ Consistency\ Index} = 0.085 < 0.1(check)$$

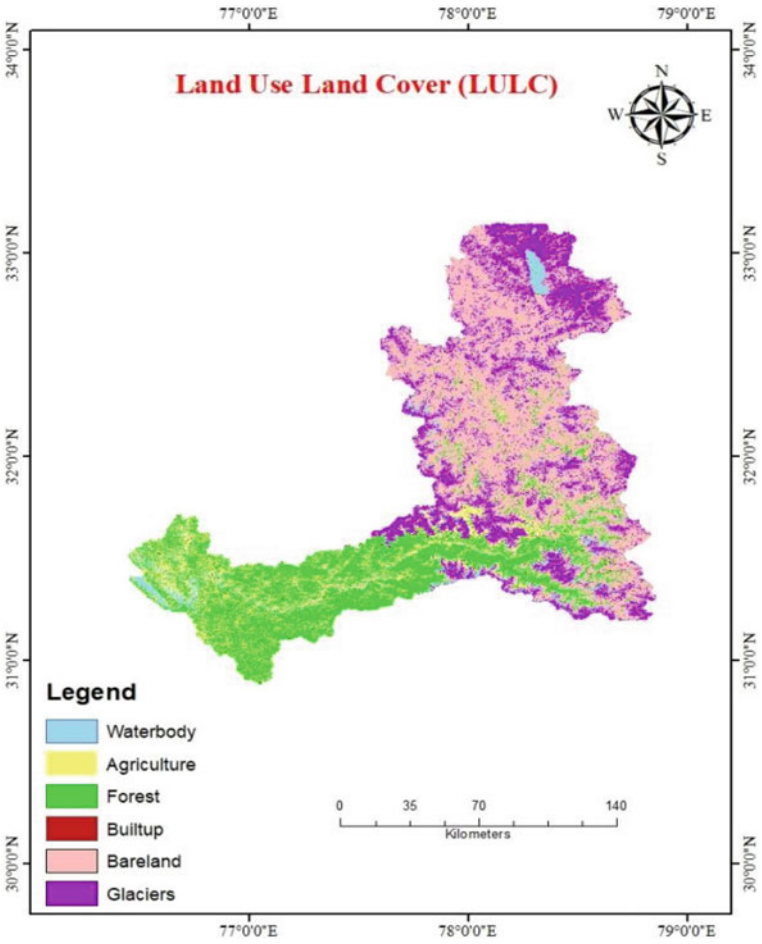

Fig. 6 Land use land cover map

3.2.2 Estimation of Weightage of Parameters Involved in Mapping Soil-Erosion Sustainability Using F-AHP

The pair-wise comparison matrix developed in AHP is converted into a Fuzzy triangular scale to solve uncertainty in the model by using scales mentioned in Table 1 and the weights are calculated. Fuzzy-AHP was proposed by [1] in which geometric mean is used to calculate weights.

After converting the pair-wise comparison matrix to the Fuzzified pair-wise comparison matrix (Table 5), the fuzzy geometric mean in Table 6 is calculated by multiplying all lower limit elements and power rise to 1/number of elements. The same method is applied to calculate the geometric mean for the middle and upper limits respectively. The fuzzy weights in Table 6 are determined by multiplying fuzzy

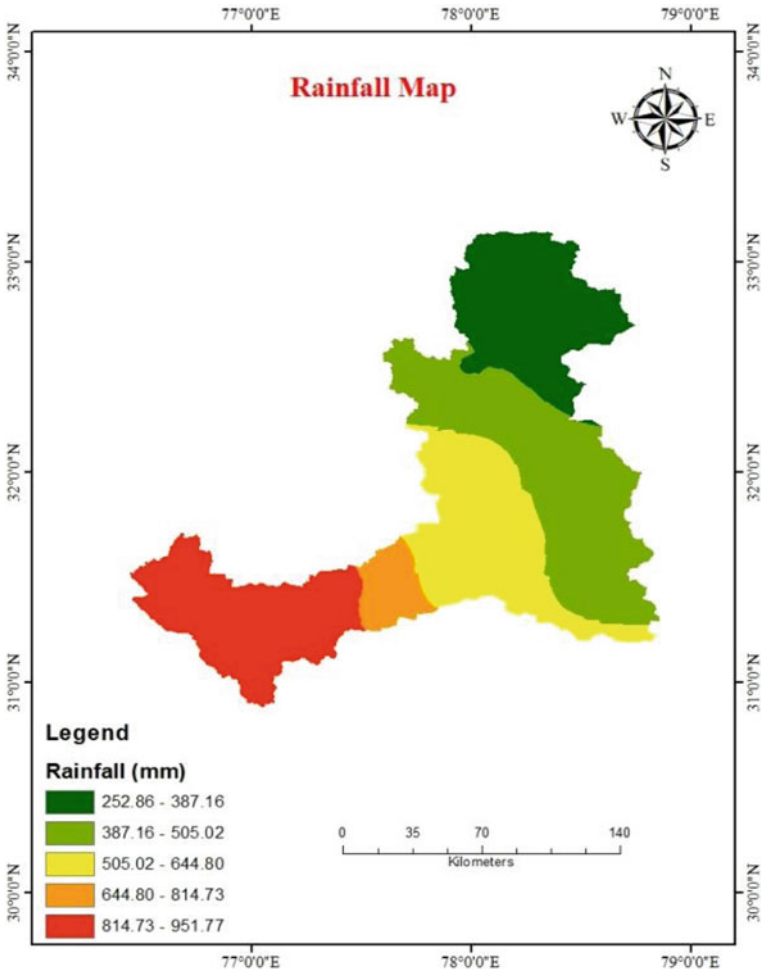

Fig. 7 Rainfall map

geometric means with the inverse of their sum. The criteria weights are determined by the average of the lower, middle, and upper limits. Normalized weights in Table 6 are obtained by calculating the ratio between the weightage criteria and their sum.

After determining Weightages using AHP and F-AHP methods, all the raster layers are re-sampled using the re-sampling tool in Arc-GIS. After re-sampling, the weightage overlay analysis is performed for the calculated weights using AHP and F-AHP. The respective rankings are provided in Table 7. The rankings in Table 7 range from 1 to 5. 1 denoting the area or alternative prone to less soil erosion while 5 represents the area prone to higher soil erosion. After performing weightage overlay analysis, the results are compared with multi-temporal satellite images.

Table 1 Scale of relative importance to achieve our goal/Objective

AHP Scale	Fuzzy scale	Importance
1	(1, 1, 1)	Equal
2	(1, 2, 3)	Intermediate
3	(2, 3, 4)	Moderate
4	(3, 4, 5)	Intermediate
5	(4, 5, 6)	Strong
6	(5, 6, 7)	Intermediate
7	(6, 7, 8)	Very strong
8	(7, 8, 9)	Intermediate
9	(9, 9, 9)	Extreme
1/3,1/5,1/7,1/9		Values of the inverse comparison

Table 2 Pair-wise comparison matrix

Goal/Objective	Drainage density	Rainfall	Elevation	Slope	Soil	LULC
Drainage density	1.00	5.00	5.00	6.00	5.00	5.00
Rainfall	0.20	1.00	3.00	2.00	3.00	3.00
Elevation	0.20	0.33	1.00	4.00	2.00	2.00
Slope	0.17	0.50	0.25	1.00	2.00	1.00
Soil	0.20	0.33	0.50	0.50	1.00	2.00
LULC	0.20	0.33	0.50	1.00	0.50	1.00
SUM	1.97	7.50	10.25	14.50	13.50	14.00

Table 3 Normalized Pair-wise comparison matrix

Goal/ Objective	Drainage density	Rainfall	Elevation	Slope	Soil	LULC	Weighted sum	Criteria weightage
Drainage density	0.51	0.67	0.49	0.41	0.37	0.36	0.47	46.74
Rainfall	0.10	0.13	0.29	0.14	0.22	0.21	0.18	18.37
Elevation	0.10	0.04	0.10	0.28	0.15	0.14	0.14	13.51
Slope	0.08	0.07	0.02	0.07	0.15	0.07	0.08	7.74
Soil	0.10	0.04	0.05	0.03	0.07	0.14	0.07	7.44
LULC	0.10	0.04	0.05	0.07	0.04	0.07	0.06	6.21

Table 4 Calculating consistency

Goal/ Objective	Drainage density	Rainfall	Elevation	Slope	Soil	LULC	Weighted sum	Criteria weightage	Ratio
Drainage density	0.47	0.92	0.68	0.46	0.37	0.31	3.21	0.47	6.86
Rainfall	0.09	0.18	0.41	0.15	0.22	0.19	1.25	0.18	6.79
Elevation	0.09	0.06	0.14	0.31	0.15	0.12	0.87	0.14	6.46
Slope	0.08	0.09	0.03	0.08	0.15	0.06	0.49	0.08	6.35
Soil	0.09	0.06	0.07	0.04	0.07	0.12	0.46	0.07	6.18
LULC	0.09	0.06	0.07	0.08	0.04	0.06	0.40	0.06	6.43
								Sum	39.06

Table 5 Fuzzified Pair-wise comparison matrix

Goal/ Objective	Drainage density	Rainfall	Elevation	Slope	Soil	LULC
Drainage density	(1,1,1)	(4,5,6)	(4,5,6)	(5,6,7)	(4,5,6)	(4,5,6)
Rainfall	(1/6,1/5,1/4)	(1,1,1)	(2,3,4)	(1,2,3)	(2,3,4)	(2,3,4)
Elevation	(1/6,1/5,1/4)	(1/4,1/3,1/2)	(1,1,1)	(3,4,5)	(1,2,3)	(1,2,3)
Slope	(1/7,1/6,1/5)	(1/3,1/2,1/1)	(1/5,1/4,1/3)	(1,1,1)	(1,2,3)	(1,1,1)
Soil	(1/6,1/5,1/4)	(1/4,1/3,1/2)	(1/3,1/2,1/1)	(1/3,1/2,1/1)	(1,1,1)	(1,2,3)
LULC	(1/6,1/5,1/4)	(1/4,1/3,1/2)	(1/3,1/2,1/1)	(1/1,1/1,1/1)	(1/3,1/2,1/1)	(1,1,1)

4 Results and Discussion

The areas prone to critical soil erosion are mapped using AHP and F-AHP methods. These results are compared with multi-temporal Landsat satellite images. Figures 8 and 9 show the areas prone to critical soil erosion using AHP and F-AHP. Areas prone to critical soil erosion are classified as very low, low, moderate, high and very high.

In this study, remote sensing plays a vital role in data acquisition and GIS helps to analyze data. The surface waterbodies datasets from 2000–2020 at a frequency of every 5 years are extracted from global surface waterbodies datasets which are available in the Google earth engine platform [6].

Figure 10 shows the surface waterbodies in the Sutlej basin at a frequency of every 5 years from 2000–2020. The unchanged area in every two years is determined by using the intersection tool in Arc-GIS. The amount of the area eroded is quantified by

Table 6 Calculation of weightage for each criteria

Goal/ Objective	Fuzzy geometric mean	Fuzzy weights	Criteria weights	Normalized weights	Normalized weights (%)
Drainage density	(3.29, 3.94, 4.56)	(0.325, 0.486, 0.722)	0.511	0.48	47.56
Rainfall	(1.049, 1.486, 1.906)	(0.103, 0.183, 0.301)	0.195	0.18	18.15
Elevation	(0.707 ,1.01, 1.333)	(0.0698, 0.124, 0.211)	0.134	0.12	12.47
Slope	(0.452, 0.588, 0.764)	(0.0446,0.072, 0.121)	0.0792	0.07	7.37
Soil	(0.408, 0.567, 0.849)	(0.0403, 0.07, 0.134)	0.0814	0.08	7.58
LULC	(0.408, 0.505, 0.707)	(0.0403, 0.0623, 0.119)	0.0738	0.07	6.87
Sum	(6.314, 8.1, 10.119)	Sum	1.0744		

identifying the difference between the area of the previous year and the unchanged area. The area where sediment gets deposited is determined by calculating the difference between the area of the following year and the unchanged area. Figure 11 shows the variation in erosion and deposition rates every 5 years. Here in this study, for every 5 years, the deposited area is observed to be greater than the eroded area. It is because the eroded area quantified is the erosion only due to runoff. The deposited area is due to area eroded by rainfall, runoff, wind, lack of agricultural practices, etc.

5 Conclusions

The Integrated GIS-AHP tool determines the spatial variation of soil erosion hazard effectively. The results obtained from AHP and Fuzzy AHP are verified with multi-temporal global surface water datasets (30 m resolution). The Fuzzy AHP provided more accurate results as compared to multi-temporal global surface water datasets. This research signifies and proves to be a crucial tool in speculating the soil erosion hazards assessment with the integration of AHP and GIS techniques. The approach used in determining soil erosion hazard qualitatively and quantitatively over a comparatively large area concluded in a smaller time frame. Soil erosion in the basin is found to be increasing with time. As the erosion increases with time, it can decrease the water storage capacity in reservoirs and cause inconvenience for

Table 7 Rankings for each alternative present in each criterion

Criteria	Range	Resample	Rank
Drainage density	0.079–0.597	1	2
	0.597–1.114	2	3
	1.114–1.632	3	4
	1.632–2.15	4	5
Elevation	486–1621	1	1
	1621–2928	2	2
	2928–4159	3	3
	4159–5049	4	4
	5049–6665	5	5
Slope	0–11.92	1	1
	11.92–22.9	2	2
	22.9–32.62	3	3
	32.62–43.29	4	4
	43.29–79.99	5	5
Soil	Loam	1	5
	Glacier	2	1
	Waterbody	3	2
	Loamy sand	4	4
	Sandy loam	5	4
	Clay	6	3
Rainfall	252.86–387.16	1	1
	387.16–505.02	2	2
	505.02–644.8	3	3
	644.8–814.73	4	4
	814.73–951.77	5	5
LULC	Waterbody	1	5
	Agriculture	2	4
	Forest	3	2
	Builtup	4	1
	Bareland	5	3
	Glacier/snow	6	1

the safe operation of turbines. Thus, it is necessary to provide river bank management, protection, agricultural practices and continuous monitoring to prevent soil erosion in erosion-prone zones. These results are also helpful for the soil and water conservation departments.

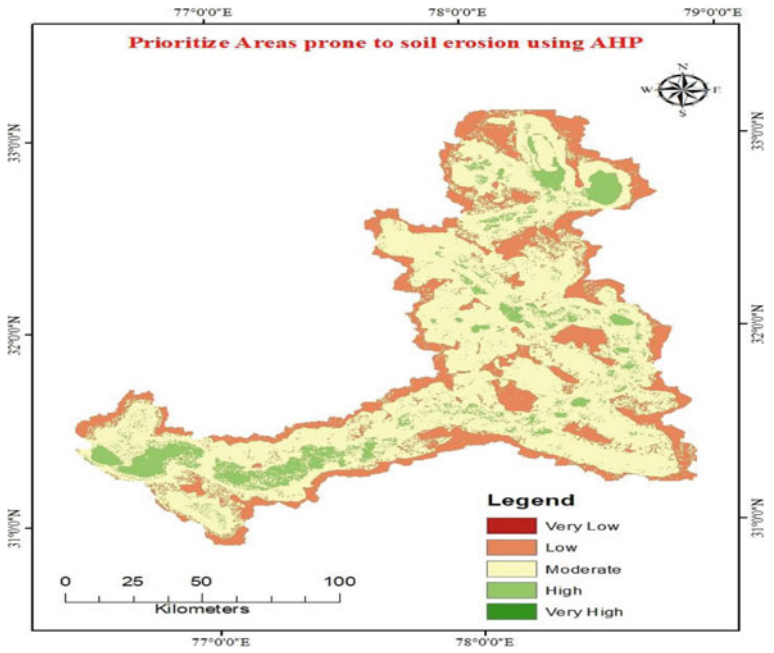

Fig. 8 Areas prone to critical soil erosion using AHP

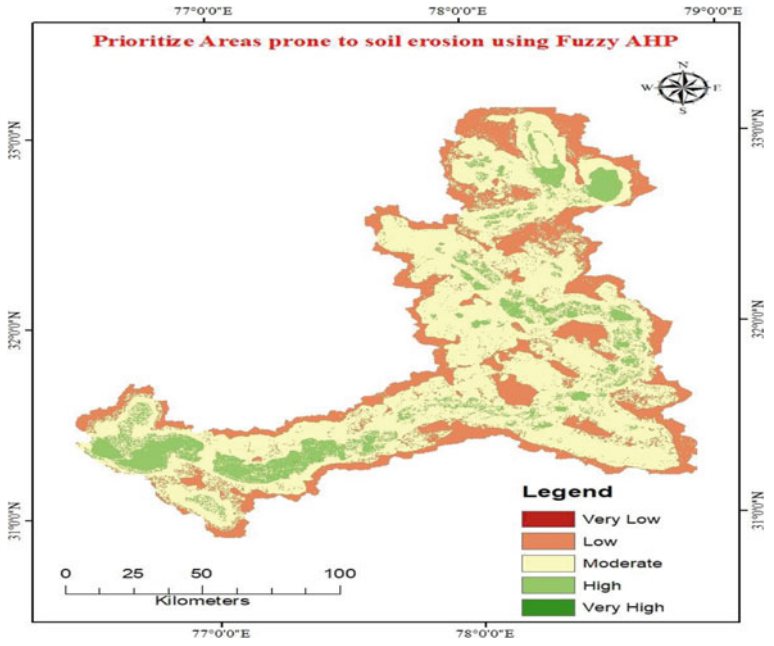

Fig. 9 Areas prone to critical soil erosion using F-AHP

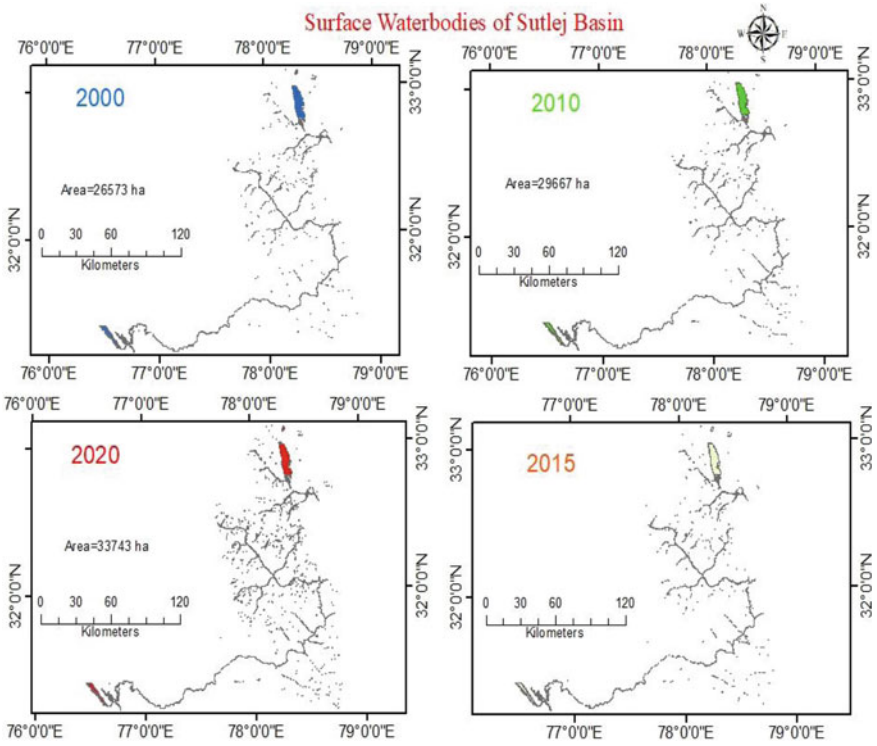

Fig. 10 Surface waterbodies of Sutlej basin

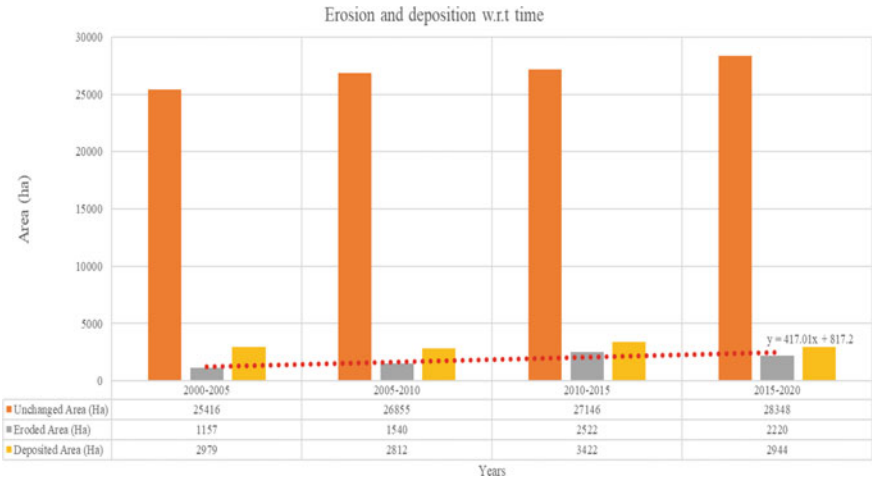

Fig. 11 Erosion and deposition rates with respect to time

References

1. Buckley JJ (1985) Fuzzy hierarchical analysis*. In: Fuzzy Sets and Systems (Vol. 17).
2. Cartwright JH, Shammi SA, Rodgers III JC (2022) Use of multi-criteria decision analysis (mcda) for mapping erosion potential in gulf of Mexico Watersheds. Water 14(12):1923
3. Jaiswal R, Thomas T, Galkate R, Ghosh N, Singh S (2013) Watershed prioritization using saaty's AHP based decision support for soil conservation measures. Water Resour Manag 27. https://doi.org/10.1007/s11269-013-0494-x
4. Mishra CD et al (2019) Priority assessment of sub-watershed based on optimum number of parameters using fuzzy-AHP decision support system in the environment of RS and GIS. J Indian Soc Remote Sens 47(4):603–617
5. NIH Roorkee (2013) A report on morphological study of the Sutlej river
6. Pekel J-F et al. (2016) High-resolution mapping of global surface water and its long-term changes. Nature 540.7633: 418–422
7. Rahman A, Yunus A, Pal P (2017) Analysis on river bank erosion-accretion and bar dynamics using multi-temporal satellite images. Am J Water Resour 5:132–141. https://doi.org/10.12691/ajwr-5-4-6
8. Saadon A, Abdullah J, Muhammad N, Ariffin J, Julien P (2020) Predictive models for the estimation of riverbank erosion rates. CATENA 196:1–12. https://doi.org/10.1016/j.catena.2020.104917
9. Saaty TL, Vargas LG (2012) Models, Methods, Concepts & Applications of the Analytic Hierarchy Process, vol 175. Springer US. https://doi.org/10.1007/978-1-4614-3597-6
10. Shukla S, Jain SK, Kansal ML, Chandniha SK (2017) Assessment of sedimentation in Pong and Bhakra reservoirs in Himachal Pradesh, India, using geospatial technique. Remote Sens Appl: Soc Environ 8:148–156. https://doi.org/10.1016/j.rsase.2017.08.008
11. Vemu S, Pinnamaneni UB (2011) Estimation of spatial patterns of soil erosion using remote sensing and GIS: a case study of Indravati catchment. Nat Hazards 59(3):1299–1315. https://doi.org/10.1007/s11069-011-9832-6

Irrigation Water Requirement and Irrigation Schedule of Sugarcane in Kurnool District, Andhra Pradesh

Souvick Kumar Shaw, Anurag Sharma, and Kishanjit Kumar Khatua

Abstract The present chapter includes irrigation water requirement and irrigation schedule of sugarcane estimated by CROPWAT 8.0 under the existing soil and climatic condition of Kurnool District, Andhra Pradesh. Along with that, some important conservative and non-conservative crop characteristics of sugarcane are determined by AQUACROP 6.1 under standard conditions. The reference crop evapotranspiration was calculated by Penman–Monteith method based on FAO and effective rainfall was determined by fixed percentage method available in CROPWAT 8.0 for the year 2005. 78% of total water consumption is needed through irrigation for sugarcane to meet its crop evapotranspiration under standard condition. Dry yield was obtained as 7563 kg/ha. Higher water demand was seen during winter and summer seasons for sugarcane. The results of this research may be beneficial for proper assessment of water demand of crops and evaluation of crop phenology to ensure effective utilization of available water resources for Irrigation Authority of Kurnool District to cultivate sugarcane.

Keywords Crop water requirement · Irrigation schedule · Conservative and non-conservative crop characteristics · Standard conditions · AQUACROP 6.1

1 Introduction

India has only 2.4% of land surface and 4% of fresh water surface in the world. As significant surface water scarcity is increasing day by day, so, increasing water demand for irrigation becomes national importance for any country for utilizing water

S. K. Shaw · A. Sharma (✉) · K. K. Khatua
Department of Civil Engineering, National Institute of Technology, Rourkela, India
e-mail: sharmaan@nitrkl.ac.in

S. K. Shaw
e-mail: 521ce1009@nitrkl.ac.in

K. K. Khatua
e-mail: kkkhatua@nitrkl.ac.in

S. Dutta and V. Chembolu (eds.), *Recent Development in River Corridor Management*,
Lecture Notes in Civil Engineering 376, https://doi.org/10.1007/978-981-99-4423-1_26

resources, conservation of water for modern irrigation approaches and management policy and practice [1]. India is constantly facing drought situation and is in urgent need of water to enhance the irrigation operation for different crops. The rainfall distribution was insufficient and irregular for the year 2005 of Kurnool District. A very less amount of rainfall was occurring during post-monsoon season (i.e. December–February) and most of the rabi crops and perennial crops had faced a significant water stress at the root zone during this year affecting the productivity. Crop water requirement of various crops and climatic water balance was evaluated in different Agro-Ecological Unit's (AEU's) by using evapotranspiration as well as effective rainfall data in Palakkad District, Kerala [2]. Water requirement of crop and irrigation scheduling was studied for some major crops in Dhi-Qar province, Southern Iraq by using CROPWAT 8.0 [3]. Guidelines for the evaluation of reference crop evapotranspiration (ETo), crop evapotranspiration under standard and non-standard conditions, irrigation water balance and yield reduction under some adverse field conditions, are illustrated in 'FAO - Irrigation and drainage Paper 56' [4]. To enhance the estimation of needed yield under significant water scarcity scenario, 'AQUACROP' model is used widely. Canopy growth profile, canopy senescence and stomatal closure, and harvestable index are some of the essential crop characteristics [5]. An empirical model has been established to build a relationship between crop production and evapotranspiration in AQUACROP by using the linear dependency of biomass with transpiration within a range of water deficit [6]. Crop yield prediction models have a significant contribution in estimating food demand with existing population under available climatic and environmental conditions [7]. AQUACROP software demands a limited set of input variables which makes this software both simple and effective as compared to models [8].

The objectives of this present study are lying (i) to estimate the reference crop evapotranspiration and effective rainfall by CROPWAT 8.0; (ii) to show the contribution of effective rainfall in CWR and to develop irrigation scheduling of sugarcane; (iii) to study the crop characteristics for sugarcane under limited set conditions by AQUACROP 6.1 model.

2 Materials and Methodology

2.1 Study Area

Monthly climatic and meteorological data for 2005 were taken at Kurnool district, Andhra Pradesh. This district is located between 14°54′ N to 16°18′N latitude and 76°58′E to 79°34′E longitude and altitude of 94.5 m from m.s.l. The mean monthly temperature is lying between 21.5 °C and 36 °C during winter and summer seasons respectively. Some major crops are cultivated here i.e. cotton, sunflower, groundnut, rice, onion, sorghum etc. under tropical climate. Net irrigated area of Kurnool district is 1757 km^2, gross irrigated area is 2126 km^2 and rainfed area is 6858 km^2. Major

sources of irrigation water are canals, tanks, tube wells etc. Besides that, groundwater can be used for agricultural purposes.

2.2 Data Collection

2.2.1 Climatic and Meteorological Data

The climatic and meteorological data consists of monthly mean maximum and minimum temperature, sunshine hours, radiation, wind speed and relative humidity. These data are taken from CLIMWAT 2.0 for 2005 and are taken as input parameters to determine ETo by Penman–Monteith method according to FAO guidelines.

2.2.2 Crop Data

The value of crop coefficient (Kc) was taken from FAO -Irrigation and Drainage paper 56 [4]. Planting and harvesting date for sugarcane is 15/09/2005 and 14/09/2006 respectively and the type of soil was medium (loam) soil.

2.3 Theory and Methods

The reference crop evapotranspiration is evaluated as in Eq. (1) (Reddy 2020).

$$\mathrm{ETo} = [0.408\,\Delta\,(\mathrm{Rn} - \mathrm{G}) + \gamma\,(900/\mathrm{T} + 273)\,(\mathrm{e_s} - \mathrm{e_a})\,\mathrm{u_2}]/[\Delta + \gamma\,(1 + 0.34\mathrm{u_2})] \quad (1)$$

where, Δ = slope of the curve between saturation vapor pressure and temperature in [KPa/°C]; Rn = net heat radiation in [MJ/m^2/day]; G = soil heat flux in [MJ/m^2/day]; γ = psychometric constant in [KPa/°C]; ($\mathrm{e_s} - \mathrm{e_a}$) = saturation vapor pressure deficit in [KPa]; T = mean air temperature in [°C], $\mathrm{u_2}$ = wind speed at a height of 2 m from the ground surface in [m/s].

The crop evapotranspiration (ETc) is estimated by multiplying Kc with reference crop evapotranspiration (ETo) given by Eq. (2) [4].

$$\mathrm{ETc} = \mathrm{Kc} \times \mathrm{ETo} \quad (2)$$

where, ETc is crop evapotranspiration under standard condition obtained from single crop coefficient approach in [mm]; Kc is crop coefficient.

Effective rainfall is the amount of water, which is directly consumed by any plant and it is calculated after accounting for all the losses i.e. initial abstraction, infiltration loss, percolation loss, evaporation loss etc. [9]. In this present study, effective rainfall

was determined based on the fixed percentage method available in CROPWAT 8.0 as in Eq. (3).

$$ER = a \cdot P_{total} \tag{3}$$

where, ER is effective rainfall in [mm]; a is fraction of total rainfall getting converted into ER (user defined parameter); P_{total} is total amount of rainfall in [mm].

3 Results and Discussions

3.1 Reference Crop Evapotranspiration and Effective Rainfall

Reference crop evapotranspiration had been evaluated based on the available climatic parameters for the year 2005 for Kurnool district. The monthly climatic and meteorological data, daily ETo is represented in Table 1 [3].

From Table 1, it is clear that reference crop evapotranspiration was increasing during January to June and decreasing during July to December. The highest ETo was observed in May i.e. 7.94 mm/day whereas it achieved its minimum value in

Table 1 Kurnool district: weather station data and reference crop evapotranspiration in 2005

Month	Min Temp	Max Temp	Relative humidity	Wind speed	Sunshine hours	Radiation	ETo
	[°C]	[°C]	[%]	[km/day]	[hours]	[MJ/m^2/day]	[mm/day]
January	17.0	31.3	47	104	8.8	18.8	3.99
February	19.3	34.3	37	112	9.3	21.1	4.90
March	22.5	37.5	30	121	9.7	23.5	5.94
April	26.0	39.3	34	138	9.2	23.6	6.66
May	27.2	40.0	37	225	8.3	22.3	7.94
June	25.0	35.6	54	354	5.8	18.3	7.19
July	23.8	32.5	64	363	4.4	16.2	5.75
August	23.5	32.1	63	302	4.9	16.9	5.48
September	23.3	31.9	65	207	5.5	17.3	4.83
October	22.4	32.4	61	95	8.7	20.7	4.58
November	19.2	31.0	56	78	7.7	17.6	3.73
December	16.6	30.3	51	69	8.4	17.7	3.40
Average	22.1	34.0	50	181	7.6	19.5	5.37

December i.e. 3.4 mm/day. The differences in ETo values show the variation in the climatic parameters of this study area.

Low relative humidity, high monthly mean temperature, and high wind speed reflect increasing trend of evapotranspiration mainly in summer season [10].

The monthly effective rainfall was determined by the fixed percentage method as described in Eq. (3) by considering the value of 'a' as 0.8 and the results are shown in Fig. 1. In most of the cases, the effective rainfall is considered to be 80% of total rainfall for a rainfall value of less than 100 mm in a month [11]. In this present study, monthly rainfall value was below 100 mm except for the month of July, August and September in 2005 (Fig. 2) for Kurnool district. So, the value of the fraction (a) was taken as 0.8 as insufficient information is available from local conditions for this study area.

From Fig. 2, it can be observed that the distribution of effective rainfall shows almost uniform variation from January to March and then increasing from April to September and finally decreasing from September to December. Also, the rainfall distribution pattern for 2005 was irregular. Maximum effective rainfall depth was 102.4 mm in the month of September and there was negligible quantity of rainfall in the month of January, March and December. Almost 68.5% of effective rainfall was occurring in the monsoon season and around 20.6% was occurring during post-monsoon season.

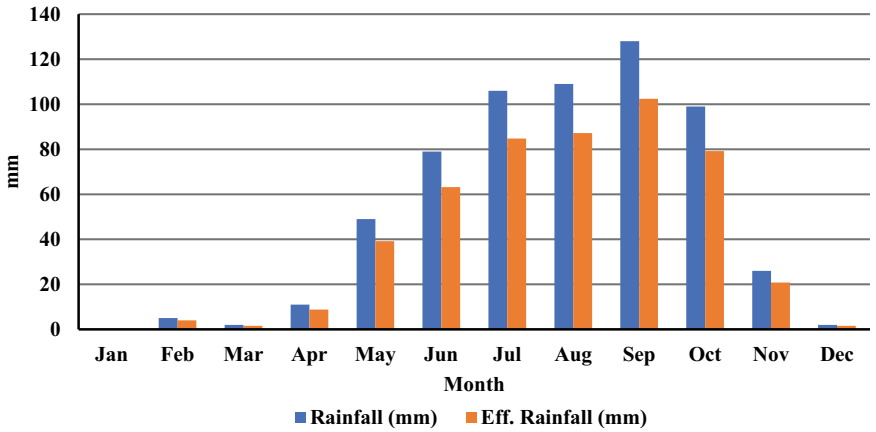

Fig. 1 Variation of monthly rainfall and effective rainfall of Kurnool district in 2005

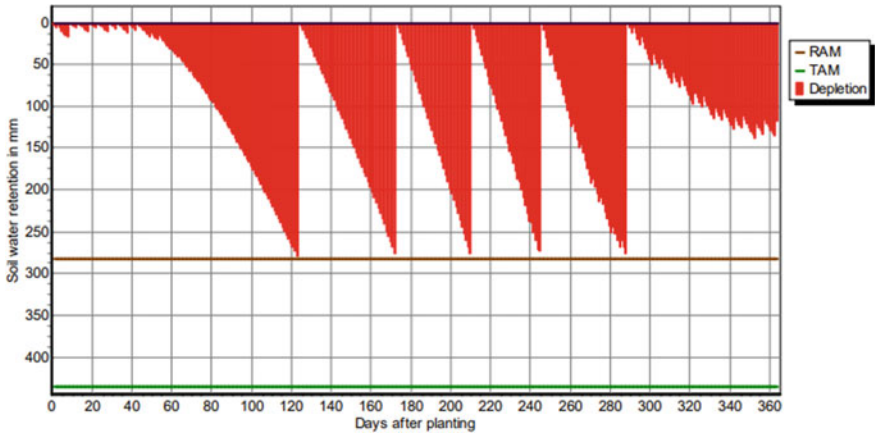

Fig. 2 Soil water retention—growing length curve for sugarcane

3.2 Crop Water Requirement (CWR) and Irrigation Scheduling

Irrigation water for sugarcane was determined by considering available climatic, soil and crop parameters. Crops have different water needs based on the site for agriculture, soil texture, method of agriculture, climatic condition of that place, and effective rainfall and it is not uniformly distributed throughout the entire growing cycle of crops [12]. Irrigation schedule provides important information about the timing of irrigation, controlling the application and discharge of water in an effective and systematic way and also it improves the well-developed irrigation management in the field [3].

Tables 2 and 3 show the crop water requirement and irrigation schedule for sugarcane respectively.

For sugarcane, effective rainfall only satisfied 23.6% of its crop water demand. So, a significant water requirement would be satisfied by irrigation. Being a perennial crop, it needs water throughout its entire growing period for its growth. Around 20.6 and 10.8% of effective rainfall satisfied the crop water demand for sugarcane during post-monsoon season of 2005 and pre-monsoon season of 2006 respectively. So, sugarcane can utilize a significant amount of water during monsoon period of 2006. A significant amount of water from irrigation was needed from January to June i.e. almost 1243.7 mm which constitutes 60% of crop water requirement. Kc value is more at the time of transplantation and it was significantly falling from its initial stage to crop development stage up to 2nd week of October. After that it would increase almost linearly up to the end of its mid-season stage and then was falling down from the end of mid-season to the end of late season stage of crop development at a lower slope. Initially, the crop requires less amount of water with a large irrigation interval as it is few centimeters high. So, a very small canopy covers the ground and

Table 2 CWR for sugarcane

Month	Decade	Stage	Kc	ETc	ETc	Eff rain	Irr. Req
[–]	[–]	[–]	[coeff]	[mm/day]	[mm/dec]	[mm/dec]	[mm/dec]
Sep	2	Init	0.77	3.7	22.2	21.6	0.0
Sep	3	Init	0.40	1.9	19.0	32.8	0.0
Oct	1	Init	0.40	1.9	18.7	30.1	0.0
Oct	2	Deve	0.43	2.0	19.7	28.1	0.0
Oct	3	Deve	0.57	2.4	26.8	21.0	5.8
Nov	1	Deve	0.71	2.9	28.7	12.2	16.5
Nov	2	Deve	0.85	3.2	31.9	5.1	26.8
Nov	3	Deve	0.99	3.6	36.0	3.6	32.4
Dec	1	Deve	1.13	3.9	39.0	1.7	37.3
Dec	2	Mid	1.23	4.1	40.7	0.0	40.7
Dec	3	Mid	1.24	4.4	48.1	0.0	48.0
Jan	1	Mid	1.24	4.7	47.0	0.0	46.9
Jan	2	Mid	1.24	4.9	49.4	0.0	49.4
Jan	3	Mid	1.24	5.3	58.5	0.1	58.4
Feb	1	Mid	1.24	5.7	56.9	1.1	55.9
Feb	2	Mid	1.24	6.1	60.7	1.6	59.1
Feb	3	Mid	1.24	6.5	51.9	1.2	50.7
Mar	1	Mid	1.24	6.9	69.2	0.5	68.7
Mar	2	Mid	1.24	7.4	73.5	0.1	73.4
Mar	3	Mid	1.24	7.7	84.1	1.1	83.1
Apr	1	Mid	1.24	8.0	79.5	1.4	78.0
Apr	2	Mid	1.24	8.3	82.5	1.9	80.6
Apr	3	Mid	1.24	8.8	87.8	5.6	82.1
May	1	Mid	1.24	9.5	94.7	9.9	84.8
May	2	Mid	1.24	10.1	100.8	13.3	87.5
May	3	Mid	1.24	9.7	106.6	15.9	90.7
Jun	1	Mid	1.24	9.2	92.1	18.5	73.6
Jun	2	Late	1.22	8.7	87.4	21.2	66.2
Jun	3	Late	1.16	7.8	78.2	23.5	54.6
Jul	1	Late	1.11	6.9	68.7	26.4	42.2
Jul	2	Late	1.06	6.0	60.1	29.1	31.0
Jul	3	Late	1.01	5.7	62.2	29.1	33.1
Aug	1	Late	0.96	5.3	53.4	28.4	24.9
Aug	2	Late	0.91	5.0	49.8	28.5	21.2
Aug	3	Late	0.86	4.5	49.5	30.4	19.1

(continued)

Table 2 (continued)

Month	Decade	Stage	Kc	ETc	ETc	Eff rain	Irr. Req
Sep	1	Late	0.80	4.1	40.5	33.6	6.9
Sep	2	Late	0.77	3.7	14.8	14.4	0.0
Total					2090.2	492.9	1629.7

Table 3 Irrigation schedule for sugarcane

Date	Day	Stage	Rain	Ks	Eta	Depl	Net Irr	Deficit	Loss	Gr. Irr	Flow
[–]	[–]	[–]	[mm]	[fract.]	[%]	[%]	[mm]	[mm]	[mm]	[mm]	[l/s/ha]
16 Jan	124	Mid	0.0	1.00	100	65	284.8	0.0	0.0	406.9	0.38
6 Mar	173	Mid	0.0	1.00	100	65	284.0	0.0	0.0	405.7	0.96
13 Apr	211	Mid	1.2	1.00	100	66	285.2	0.0	0.0	407.4	1.24
18 May	246	Mid	0.0	1.00	100	65	283.7	0.0	0.0	405.2	1.34
30 Jun	289	End	0.0	1.00	100	66	285.5	0.0	0.0	407.9	1.10
14 Sep	End	End	0.0	1.00	0	27					

Kc is low. Whereas, a considerable evaporation can take place from soil resulting high value of soil evaporation coefficient (Ke) at this phase [13]. But during the crop development and mid-season stage, almost maximum canopy (70–80%) covers the ground resulting in high leaf area index [4] and flowering stage starts at this phase. So, productivity will be high and significant transpiration takes place from the plant stomata [4].

Table 3 shows the irrigation schedule for sugarcane for the condition refill soil at field capacity and irrigation at critical depletion, available in CROPWAT 8.0. The first watering was done 124 days after its transplantation. The irrigation interval was fixed at 49 days, 38 days, 35 days and 43 days from the consecutive watering. Sugarcane has faced no significant moisture deficit at the root zone as Ks was unity. So, adjusted evapotranspiration almost meets crop evapotranspiration. Initially, the flow rate was low and it was significantly increased by 152.6% during its mid-season stage. Higher flow rate through irrigation can be observed during its mid-season stage (April–May) as effective rainfall was low to meet the water needs. NIR was obtained as 1423.2 mm and GIR was 2033.1 mm. In this present study, GIR is obtained by considering an application efficiency of 70%.

Net irrigation requirement (NIR) is the amount of water that can be needed for a plant to attain the water content of existing soil up to field capacity to enhance the growth of plant [3]. It can be calculated by considering an extra amount of water required for leaching with crop evapotranspiration (ETc). Gross irrigation requirement (GIR) is determined from NIR by adopting suitable irrigation efficiency based on the type of irrigation. Some portion of water is used by evaporation, surface runoff, interception loss as well as percolation loss. So, moisture deficit can be seen at the root zone resulting in depletion of total available water. Different irrigation

water requirement is given in Eqs. (4), (5) and (6)

$$\text{ETc} = \text{Cu} - \text{Eff.rain} \tag{4}$$

$$\text{NIR} = \text{ETc} + \text{leaching requirement} \tag{5}$$

$$\text{GIR} = \text{NIR}/\eta\text{a} \tag{6}$$

where, ETc is daily crop evapotranspiration [mm/day]; Cu is daily consumptive use of water [mm/day]; ηa is the application efficiency.

Figure 2 shows the soil water retention—growing length curve for sugarcane. In the figure, TAM is the total available moisture [mm]; RAW is the readily available moisture [mm]. RAW is a fraction of TAW which a plant takes from the soil moisture zone without any occurrence of water stress. TAM and RAM were uniform throughout the entire growing cycle of sugarcane resulting in the constant crop height and RAW was almost 64% of TAW. Initially, the moisture depletion was observed after 65 days from its transplantation. Therefore, it did not affect the crop growth, but at the time of harvesting it was low and the variation of moisture depletion showed a marginal difference throughout the initial to mid-season stage.

3.3 Crop Characteristics

Some major conservative and non-conservative crop characteristics were studied under limited set conditions in AQUACROP 6.1 model for sugarcane. Crop parameters are used to evaluate rooting depth, growth of canopy, biomass and crop yield [14]. Conservative crop parameters include base temperature, canopy development with crop period, biomass and yield. Whereas, non-conservative crop parameters may consist of management dependent parameters, crop phenology and soil characteristics [5]. AQUACROP model shows variation of canopy growth profile with transpiration rate by considering canopy development, leaf area expansion, senescence and harvest index [5]. In AQUACROP, yield is obtained by multiplying the harvest index with the biomass and biomass can be determined from Eq. (7).

$$\text{B} = \text{WP*} \times \sum \frac{\text{Tr}}{\text{ETo}} \tag{7}$$

where, B is the daily biomass [ton/ha]; WP* is normalized water productivity at an atmospheric CO_2 concentration of 369.41 ppm [g/m^2]; Tr is the daily crop transpiration [mm] [5].

Table 4 shows the crop characteristics for sugarcane. Initially, due to high initial canopy cover, LAI was high resulting in more transplantation from the plant stomata. Maximum canopy cover was achieved at the crop development stage and the crop

senescence occurred at 266 days after the formation of maximum canopy cover. The rate of root zone development was faster for sugarcane. Hence, maximum crop height could be achieved within the minimum possible time after transplantation. Being a C4 type crop, the tangent of the line between biomass and $\sum \frac{Tr}{ETo}$ is high as compared to C3 type of crop due to a less efficient carbon assimilation process resulting in high WP* [6]. No water stress was seen during canopy expansion, stomatal closure, and early senescence resulting in high production of crops, thus, actual biomass production tends to be the same as the potential biomass. The growth of canopy cover shows a non-linear relationship with the growing period for sugarcane as given by Eq. (8)

$$GCC = -0.0034B^2 + 1.4412B - 18.672 \tag{8}$$

where, GCC is the growth of canopy cover [%] and B is the crop growing period [days].

Growth of canopy cover (GCC) basically shows the canopy development at different stages of crop growth starting from emergence to its full maturity. Prior to harvesting, canopy senescence occurs and maximum canopy cover can be attained during flowering stage.

The root zone development for sugarcane shows a linear relationship with the growing period according to Eq. (9) (Fig. 3)

$$Zr = 0.0453 \cdot B + 0.2798 \tag{9}$$

where, Zr is the root zone depth [m].

4 Conclusion

The evaluation of crop water requirement, irrigation schedule and crop characteristics were studied in this present study for sugarcane. All the simulations were performed in CROPWAT 8.0 and AQUACROP 6.1 model. The major outcomes of this research are being discussed below:

(1) Average daily reference crop evapotranspiration (ETo) was 5.37 mm/day and it shows an increasing trend during dry season and vice-versa.
(2) A significant amount of crop water demand was satisfied by irrigation for sugarcane being a perennial crop.
(3) CWR for sugarcane was estimated as 2090 mm. It will require more amount of water for its maturity and consequently, it will have more ETc.
(4) Root zone development shows a linear variation with the growing period for sugarcane whereas variation of GCC was non-linear with crop growing period.

Table 4 Crop characteristics for sugarcane

Crop characteristics	Parameter	Unit	Observation/ Value/Remark
Canopy cover	Growth of initial canopy	[–]	Very high canopy cover
	Initial Canopy Cover (CC_o)	[–]	0.74
Type of planting method: transplantation	Canopy size	[cm^2/ plant]	20
	Plant density	[Plants/ ha]	37,037
Canopy development	Canopy expansion	[–]	Fast expansion
	Maximum Canopy Cover (CCx)	[%]	90
	Canopy decline	[–]	Very slow decline
Time to reach at different growth stages from sowing	Recovered	[days]	7
	Maximum canopy	[days]	64
	Senescence	[days]	330
	Maturity	[days]	365
Flowering and yield formation	Length building up HI	[days]	NA
	Duration of flowering	[days]	NA
Time to reach at flowering, maturity and potential vegetative growth from sowing	Flowering	[days]	65
	Maturity	[days]	102
	Potential vegetative growth	[days]	75
Root deepening: very deep-rooted crop	Maximum effective rooting depth	[m]	3.00
	Average root zone expansion	[cm/day]	4.9
	From day 1 after sowing to maximum depth	[days]	61
Crop production (No Water, Fertility or Salinity Stress)	Type of Crop	[–]	C4
	WP*	[g/m^2]	30.0
	Reference Harvest Index (HI)	[%]	35
	Biomass	[Ton/ha]	21.608
	Dry yield	[Ton/ha]	7.563
	ET water productivity	[Kg/m^3]	2.29
	HI adjusted	[%]	NA

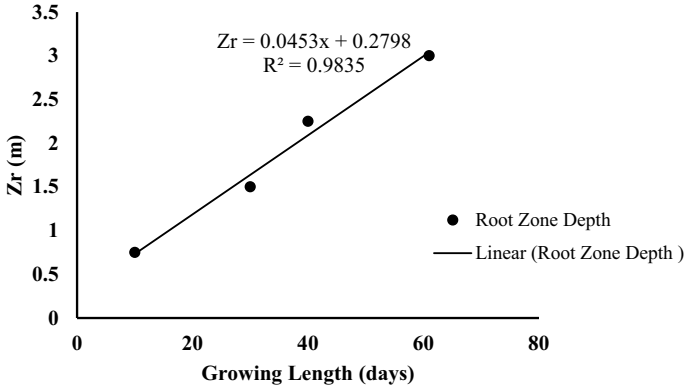

Fig. 3 Variation of Root zone development with growing length for sugarcane

Acknowledgements This present research has not been completed without the expertise, immense hard work, continuous motivation and innovative ideas of Prof. K.K Khatua and Prof. A. Sharma. We are specially very grateful to Irrigation Authority of Kurnool District for providing a lot of information for this research. Last but not the least, we are thankful to each and every faculty of Civil Department, NIT Rourkela for their continuous support and encouragement towards this work.

References

1. Babu RG, Babu GR, Kumar HH (2015) Estimation of crop water requirement, effective rainfall and irrigation water requirement for vegetable crops using CROPWAT. Int J Agric Eng 8(1):15–20
2. Surendran U, Sushanth CM, Mammen G, Joseph EJ (2015) Modelling the crop water requirement using FAO-CROPWAT and assessment of water resources for sustainable water resource management: a case study in Palakkad district of humid tropical Kerala, India. Aquat Procedia 4:1211–1219
3. Ewaid SH, Abed SA, Al-Ansari N (2019) Crop water requirements and irrigation schedules for some major crops in Southern Iraq. Water 11(4), article number 756
4. Allen RG, Pereira LS, Raes D, Smith M (1998) Crop evapotranspiration—Guidelines for computing crop water requirements—FAO Irrigation and drainage paper 56. FAO—Food and Agriculture Organization of the United Nations, Rome, ISBN 92-5-104219-5
5. Steduto P, Raes D, Hsiao TC, Fereres E, Heng L, Izzi G, Hoogeveen J (2009) AquaCrop: a new model for crop prediction under water deficit conditions. FAO, Rome 33(80):285–292
6. Salman M, García Vila M, Fereres Castiel E, Raes D, Steduto P (2021) The AquaCrop model–Enhancing crop water productivity
7. Abrha B, Delbecque N, Raes D, Tsegay A, Todorovic M, Heng LEE, Vanutrecht E, Geerts S, Garcia-Vila M, Deckers S (2012) Sowing strategies for barley (Hordeum vulgare L.) based on modelled yield response to water with AquaCrop. Exp Agric 48(2):252–271
8. Raes D, Steduto P, Hsiao TC, Fereres E (2009) AquaCrop—the FAO crop model to simulate yield response to water: II. Main algorithms and software description. Agron J 101(3):438–447
9. Sulaiman SO, Kamel AH, Sayl KN, Alfadhel MY (2019) Water resources management and sustainability over the Western desert of Iraq. Environ Earth Sci 78(16):1–15

10. Alemayehu YA, Steyn JM, Annandale JG (2009) FAO-type crop factor determination for irrigation scheduling of hot pepper (Capsicum annuum L.) cultivars. S Afr J Plant Soil 26(3):186–194
11. Clarke D, Smith M, El-Askari K (2001) CropWat for Windows: user guide. IHE, Oak Brook, IL, USA
12. de Azevedo PV, de Souza CB, da Silva BB, da Silva VP (2007) Water requirements of pineapple crop grown in a tropical environment, Brazil. Agric Water Manag 88(1–3):201–208
13. Najm ABA, Abdulhameed IM, Sulaiman SO (2020) Water requirements of crops under various Kc coefficient approaches by using water evaluation and planning (WEAP). Int J Des Nat Ecodyn 15(5):739–748
14. DeTar WR (2008) Yield and growth characteristics for cotton under various irrigation regimes on sandy soil. Agric Water Manag 95(1):69–76

Correction to: Influence of Lateral Connectivity on Channel Characteristics in (Post)Glacial Landscapes

Marwan A. Hassan, Mike Turley, David A. Reid, Stephen Bird, and Porter Abbey

Correction to:
Chapter "Influence of Lateral Connectivity on Channel Characteristics in (Post)Glacial Landscapes" in: S. Dutta and V. Chembolu (eds.), *Recent Development in River Corridor Management*, Lecture Notes in Civil Engineering 376, https://doi.org/10.1007/978-981-99-4423-1_1

In the original version of the chapter, the following correction has been incorporated: In the chapter "Influence of Lateral Connectivity on Channel Characteristics in (Post)Glacial Landscapes" the author's last name was misspelled as last name of Porter Abbey was unfortunately published with an error (Porter Abby). The correction chapter and the book have been updated with the changes.

The updated version of this chapter can be found at
https://doi.org/10.1007/978-981-99-4423-1_1

S. Dutta and V. Chembolu (eds.), *Recent Development in River Corridor Management*,
Lecture Notes in Civil Engineering 376, https://doi.org/10.1007/978-981-99-4423-1_27